PROGRESS IN THEORETICAL CHEMISTRY AND PHYSICS

Recent Advances in the Theory of Chemical and Physical Systems

Jean-Pierre Julien,
Jean Maruani, Didier Mayou,
Stephen Wilson and
Gerardo Delgado-Barrio (Eds.)

Springer

RECENT ADVANCES IN THE THEORY OF CHEMICAL AND PHYSICAL SYSTEMS

Progress in Theoretical Chemistry and Physics

VOLUME 15

The titles published in this series are listed at the end of this volume.

Recent Advances in the Theory of Chemical and Physical Systems

Proceedings of the 9th European Workshop on Quantum Systems in Chemistry and Physics (QSCP-IX) held at Les Houches, France, in September 2004

Edited by

JEAN-PIERRE JULIEN
Laboratoire d'Etudes des Propriétés Electroniques des Solides, CNRS and UJF, Grenoble, France

JEAN MARUANI
Laboratoire de Chimie Physique, CNRS and UPMC, Paris, France

DIDIER MAYOU
Laboratoire d'Etudes des Propriétés Electroniques des solides, CNRS and UJF, Grenoble, France

STEPHEN WILSON
Rutherford Appleton Laboratory, Oxfordshire, U.K.

and

GERARDO DELGADO-BARRIO
Instituto de Matemáticas y Física Fundamental, CSIC, Madrid, Spain

Springer

A C.I.P. Catalogue record for this book is available from the Library of Congress.

ISBN-10 1-4020-4527-1 (HB)
ISBN-13 978-1-4020-4527-1 (HB)
ISBN-10 1-4020-4528-X (e-book)
ISBN-13 978-1-4020-4528-8 (e-book)

Published by Springer,
P.O. Box 17, 3300 AA Dordrecht, The Netherlands.

www.springer.com

Printed on acid-free paper

Printed in the Netherlands.

Progress in Theoretical Chemistry and Physics

A series reporting advances in theoretical molecular and material sciences, including theoretical, mathematical and computational chemistry, physical chemistry and chemical physics

Aim and Scope

Science progresses by a symbiotic interaction between theory and experiment: theory is used to interpret experimental results and may suggest new experiments; experiment helps to test theoretical predictions and may lead to improved theories. Theoretical Chemistry (including Physical Chemistry and Chemical Physics) provides the conceptual and technical background and apparatus for the rationalisation of phenomena in the chemical sciences. It is, therefore, a wide ranging subject, reflecting the diversity of molecular and related species and processes arising in chemical systems. The book series *Progress in Theoretical Chemistry and Physics* aims to report advances in methods and applications in this extended domain. It will comprise monographs as well as collections of papers on particular themes, which may arise from proceedings of symposia or invited papers on specific topics as well as initiatives from authors or translations.

The basic theories of physics – classical mechanics and electromagnetism, relativity theory, quantum mechanics, statistical mechanics, quantum electrodynamics – support the theoretical apparatus which is used in molecular sciences. Quantum mechanics plays a particular role in theoretical chemistry, providing the basis for the valence theories which allow to interpret the structure of molecules and for the spectroscopic models employed in the determination of structural information from spectral patterns. Indeed, Quantum Chemistry often appears synonymous with Theoretical Chemistry: it will, therefore, constitute a major part of this book series. However, the scope of the series will also include other areas of theoretical chemistry, such as mathematical chemistry (which involves the use of algebra and topology in the analysis of molecular structures and reactions); molecular mechanics, molecular dynamics and chemical thermodynamics, which play an important role in rationalizing the geometric and electronic structures of molecular assemblies and polymers, clusters and crystals; surface, interface, solvent and solid-state effects; excited-state dynamics, reactive collisions, and chemical reactions.

Recent decades have seen the emergence of a novel approach to scientific research, based on the exploitation of fast electronic digital computers. Computation provides a method of investigation which transcends the traditional division between theory and experiment. Computer-assisted simulation and design may afford a solution to complex problems which would otherwise be intractable to theoretical analysis, and may also

provide a viable alternative to difficult or costly laboratory experiments. Though stemming from Theoretical Chemistry, Computational Chemistry is a field of research in its own right, which can help to test theoretical predictions and may also suggest improved theories.

The field of theoretical molecular sciences ranges from fundamental physical questions relevant to the molecular concept, through the statics and dynamics of isolated molecules, aggregates and materials, molecular properties and interactions, and the role of molecules in the biological sciences. Therefore, it involves the physical basis for geometric and electronic structure, states of aggregation, physical and chemical transformations, thermodynamic and kinetic properties, as well as unusual properties such as extreme flexibility or strong relativistic or quantum-field effects, extreme conditions such as intense radiation fields or interaction with the continuum, and the specificity of biochemical reactions.

Theoretical chemistry has an applied branch – a part of molecular engineering, which involves the investigation of structure–property relationships aiming at the design, synthesis and application of molecules and materials endowed with specific functions, now in demand in such areas as molecular electronics, drug design or genetic engineering. Relevant properties include conductivity (normal, semi- and supra-), magnetism (ferro- or ferri-), optoelectronic effects (involving nonlinear response), photochromism and photoreactivity, radiation and thermal resistance, molecular recognition and information processing, and biological and pharmaceutical activities, as well as properties favouring self-assembling mechanisms and combination properties needed in multifunctional systems.

Progress in Theoretical Chemistry and Physics is made at different rates in these various research fields. The aim of this book series is to provide timely and in-depth coverage of selected topics and broad-ranging yet detailed analysis of contemporary theories and their applications. The series will be of primary interest to those whose research is directly concerned with the development and application of theoretical approaches in the chemical sciences. It will provide up-to-date reports on theoretical methods for the chemist, thermodynamician or spectroscopist, the atomic, molecular or cluster physicist, and the biochemist or molecular biologist who wish to employ techniques developed in theoretical, mathematical or computational chemistry in their research programmes. It is also intended to provide the graduate student with a readily accessible documentation on various branches of theoretical chemistry, physical chemistry and chemical physics.

CONTENTS

PREFACE

This volume contains twenty-six papers selected from the scientific contributions to the *Ninth European Workshop on Quantum Systems in Chemistry and Physics (QSCP-IX)*, which was held at *Les Houches*, France, in September 2004. About sixty scientists from twenty countries attended the meeting, which addressed the state of the art; they identified new trends and considered future evolution of both methods and applications in the field.

The *QSCP-IX* workshop took place at the world-renowned conference centre of *Les Houches*, which is owned and operated by the *Université Joseph-Fourier Ecole de Physique*. The *Les Houches* facility is situated in the French Alps, overlooking the famous winter resort of *Chamonix*, with stunning views of Europe's tallest mountain, *Mont-Blanc*: http://lepes.grenoble.cnrs.fr/QSCP9/.

The *QSCP-Les Houches* workshop was divided into five morning and four afternoon plenary sessions, during which a total of 46 lectures, each of 30 min, were delivered by leading experts. There were also two evening sessions where 32 posters were presented, each being first described in a 3-min oral presentation. We are very grateful to both oral speakers and poster presenters, for their energy and enthusiasm made the workshop the stimulating experience that it was.

The *QSCP-IX* workshop followed a format that has evolved over the eight previous *QSCP* meetings, beginning with that organised by Pr Roy McWeeny at *San Miniato*, near Pisa, in 1996. At the *QSCP-Les Houches* workshop there were sessions on:

"Density matrices and density functionals",
"Electron correlation treatments: CI and MB methods",
"Relativistic formulations and effects",
"Valence theory; chemical bonding and bond breaking",
"Nuclear motion; vibronic effects, flexible molecules",
"Response theory; properties and spectra",
"Atoms and molecules in strong electric and magnetic fields",
"Condensed matter; clusters and crystals, surfaces and interfaces",
"Molecular electronics; molecular materials",
"Reactive collisions and chemical reactions",
"Computational chemistry, biochemistry and chemical physics".

The *QSCP* workshops have created a unique forum in Europe for open discussion and exchange of ideas. They facilitate cooperation on the development of advanced methods for the description of quantum systems and their applications in chemistry, physics, and the molecular sciences. Workshops since 2000 have been organized by Professor Aristides Mavridis (Athens) on the *Island of Spetses*, Greece, in September 2003; Professor Ivan Hubač (Bratislava) at *Casta Papiernicka*, Slovakia, in September 2002; and Doctors Yavor Delchev and Alia Tadjer (Sofia) in the *Boyana Presidential Residence*, Bulgaria, in April 2001.

The twenty-six papers collected in this volume have been divided into four sections, each addressing different aspects of the study of quantum systems in chemistry and physics. These are:

Part I: Quantum Chemical Methods
Part II: Relativistic and Heavy-Element Systems
Part III: Complexes and Clusters
Part IV: Complex Systems.

We are pleased to acknowledge the support given to the *QSCP-Les Houches* workshop by the *Centre National de la Recherche Scientifique* (*CNRS), Départements Chimie et SPM*, the *Région Rhône-Alpes*, the *Conseil Général de Haute-Savoie* and the *City of Grenoble*.

The efforts of all members of the Local Organizing Committee were very much appreciated, especially the invaluable work of Mrs Karen Guibreteau, Conference Secretary. The supportive help of the team of *Les Houches* centre, particularly Brigitte Rousset and Isabelle Lelièvre, is also gratefully acknowledged. Special thanks are due to Martial Ducloy, Director of the *Les Houches* facility, for offering us the opportunity to hold *QSCP-IX* in this prestigious location.

Professor Daudel acted as Honorary President of the *Centre de Mécanique Ondulatoire Appliquée* (*CMOA)* for the award of the *Promising Scientist Prize*, which was won by Professor Piotr Piecuch (Michigan State University, USA). An impressive ceremony took place at the meeting banquet, held in the restaurant *La Calèche* at *Chamonix-Mont Blanc*. The Prize was awarded at the headquarters of *UNESCO* in Paris: http://www.ccr.jussieu.fr/lcpmr/prize.html.

We hope that, in this volume, we have captured some of the stimulating developments described during the *QSCP-IX* workshop, and that the readers will be fired with as much enthusiasm in consulting these proceedings as were the workshop participants during their time at *Les Houches*.

Jean-Pierre Julien
Jean Maruani
Didier Mayou
Stephen Wilson
Gerardo Delgado-Barrio

PART I

QUANTUM CHEMICAL METHODS

THEORY AND COMPUTATION IN THE STUDY OF MOLECULAR STRUCTURE

H. M. QUINEY
School of Physics,
The University of Melbourne,
Victoria 3010, Australia

AND

S. WILSON
Rutherford Appleton Laboratory,
Oxfordshire OX11 0QX, England

Abstract. In this paper, we advocate the use of literate programming techniques in molecular physics and quantum chemistry. With a suitable choice of publication medium, literate programming allows both a theory and corresponding computer code to be placed in the public domain and subject to the usual "open criticism and constructive use" which form an essential ingredient of the scientific method.

The use of literate programming methods leads naturally to structure and standardization in computer code. In turn, this structure leads to subroutine libraries and we describe the specification of a *basic tensor algebra subroutine library*, which we have recently developed, and which we expect to prove useful in a range of applications.

We briefly consider the use of literate programming techniques in enhancing *collaborative virtual environments*, which facilitate developed cooperation between geographically distributed sites.

1. Introduction

Ziman has noted that the fact that a piece of scientific research is published often transcends in importance the details of its contents or the medium of communication. In his book *"Real Science: What it is, and what it means"*, he emphasizes that an important characteristic of a published piece of work is that it is [1]

J.-P. Julien et al. (eds.),
Recent Advances in the Theory of Chemical and Physical Systems, 3–12.

> "fully and freely available for open criticism and constructive use"

It is our submission that failure to publish computer code, together with its documentation, and the resulting lack of "open criticism and constructive use" has hampered the development of computational molecular physics and quantum chemistry. It is high probable that similar statements could be made about many other areas of computational science and engineering.

In this paper, we advocate the use of literate programming methods, first introduced by Knuth [2], but now little used [3], as a means of placing computer code in the public domain along side the associate theoretical apparatus. Such publication not only places the work in the body of scientific knowledge but also serves to establish authorship.

This paper is arranged as follows: In section 2, we give a brief overview of the philosophy of literate programming. In section 3, we emphasize the benefits of documenting code and consider the consequences of failing to do so. As we have explained above, publication is seen as fundamental to progress in science, in general, and so, in section 4, we consider publication in the context of literate programming. The practicalities of literate programming are considered in section 5. The use of literate programming in developing libraries is considered in section 6 whilst in section 7 devolved collaboration using literate programming methods is briefly discussed. Section 8 contains some final comments.

2. Literate programming

D.E. Knuth introduced the concept of literate programming in 1984. He

> "believe[d] that the time [was] ripe for significantly better documentation of programs, and that we [could] best achieve this by considering programs to be works of literate."

This requires a radical shift of emphasis in the writing of computer programs. Knuth suggests that

> "instead of imagining that our main task is to instruct a computer what to do"

we should

> "concentrate rather on explaining to human beings what we want a computer to do"

The task facing a literate programmer extends beyond that of a computer programmer. The literate programmer must strive not only to create correct and efficient code, but also a description of the theoretical concepts that lie behind the code.

Literate programming is a system of programming for the generation of structured and documented programs. As Knuth puts it,

> "The practitioner of literate programming can be regarded as an essayist, whose main concern is with exposition and excellence of style.

> Such an author, with thesaurus in hand, chooses the names of variables carefully and explains what each variable means. He or she strives for a program that is comprehensive because its concepts have been introduced in an order that is best for human understanding, using a mixture of formal and informal methods that reinforce each other."

Thus literate programming appears ideally suited to the task of publication in computational molecular physics and quantum chemistry, and indeed, in other computational sciences and in engineering. This task must entail placing both the theoretical model and the associated computer code in the public domain, where they can be subjected to the "open criticism and constructive use" which forms an integral part of the scientific method.

Traditionally, computer programs for molecular physics and quantum chemistry have consisted of FORTRAN code annotated by comments describing the function of variables, of various pieces of code and subroutines. Literate programming changes the emphasis. Instead of the code containing the relevant documentation, literate programs consists of documentation containing the code. The literate program is a document intended to be read by humans with code contained between "code delimiters" from which it can be extracted and processed by literate programming tools prior to execution on a computer.

3. Documentation

The importance of program documentation is widely recognized. In 1991, Cordes and Brown [4] put is as follows:-

> "The ability to comprehend a program written by other individuals is becoming increasingly important in software development. Given that the general cost of program maintenance may reach 60 per cent of the total software costs associated with a certain product, a real demand exists for systems that can present the program text in a readable, understandable format."

Literate programming afford such a system.

The failure to document a particular piece of code has several negative consequences, but before considering these let us consider the reasons why authors fail to document. We have identified a number of motives for this failing:-

1. 'Lack of resources' is the most often given reason for not documenting a code. Slater [5] writes

   > "Both management pressure and programmer's instincts lead documentation to be left late and under-resourced."

   He continues

   > "This is bad strategy in the longer term."

because an undocumented or poorly documented code is more difficult and therefore more costly both to maintain and develop.

2. Some code authors take the attitude that

   "if it was hard to write it should be hard to use"

   and either do not document or poorly document their code.
3. Often secrecy is a motive for failing to document code. This may be to prevent collaboration or to restrict collaboration.
4. Secrecy is often required to maintain commercial confidentiality and this may be another reason given for failure to document. However, commercial code must be maintained and developed and this can only be done efficiently and cost-effectively if the code is documented.
5. A lack of documentation may conceal plagiarism. Code may have been "acquired" either illegally or improperly and this is concealed by omitting documentation.
6. Ignorance may also be a reason for not documenting a piece of code, which has been acquired properly or legally, but is not understood. The code may performs a particular task, given what seems to be plausible input, but its operation may not be understood.

Of course, none of these reasons stand up to scrutiny.

Failure to document makes code more costly to maintain and develop, but it has a more serious consequence: even if it is made freely available, the code is not placed in the public domain in a form in which it can readily be comprehended by others. It is not subject, therefore, to the normal scientific processes of "open criticism and constructive use".

4. Publication

In an article published in 2003 in the journal *Software - Practice and Experience*, Thimbleby [3] makes the observation that, in the computer science literature, it is

> "routine to describe programming ideas without publishing, let alone depositing, the relevant code, programs or underlying algorithms for community access."

He continues

> "... after almost 20 years the use of literate programming for publishing code in the mainstream literature is now negligible. In whatever ways people may be using literate programming internally in software development projects ..., it is evidently not addressing the needs of the broader research community."

He offers reasons for this lack of use:

> "Probably the main reason for literate programming failing to survive in the literature is that it imposes its own styles and conventions ...,

which adds significantly to the 'noise' of a paper and makes it harder to conform to journal styles."

Thimbleby also recognized that

"... it has become inappropriate for commercial reasons to publish code."

The computer science community have produced a significant literature on methods for implementing literate programming, including CWEB, FWEB, and *elucidative programming*. The computational science community, including computational molecular physics and quantum chemistry, have not explored the application of these methods.

5. The practicalities of literate programming

In the original implementation described by Knuth, literate programs combine text and code in a single file called a WEB file. The literate programming approach does not restrict the language employed to generate the text, although TEXor LATEXare most commonly used. Here we shall use LATEX. The code may be written in FORTRAN, C or even, as in Knuth's original work, PASCAL Here we shall use C.

The WEB file is not employed directly. It is first processed by one of two commands:- `weave` and `tangle`. The `weave` command generates a LATEX file which can be processed further to produce a formatted document in the usual manner. So the file `example.web` would be processed as follows:-

```
weave example.web > example.tex
latex example.tex > example.dvi
dvips example.dvi > example.ps
```

The command `tangle` generates a C file from the WEB file which can then be processed to produce an executable program. The same WEB file, `example.web`, would be processed as follows:-

```
tangle example.web > example.c
gcc example.c > example
example < example.in > example.out
```

A number of schemes for formatting the WEB file can be envisaged. We are not advocating any particular scheme here. Knuth suggested using the character "@" to delimit different fragments of the WEB file. In his original scheme, the WEB file has the following structure:-

@
LATEX code describing the C code which follows
@
C code corresponding to the LATEX above.
@
LATEX code describing the C code which follows
@
C code corresponding to the LATEX above.

@
LaTeX code describing the C code which follows
@
C code corresponding to the LaTeX above.
... ...

but a number of other possible implementation have been proposed.

We have recently given examples of the application of literate programming methods in quantum chemistry. In a paper entitled *"Literate programming in quantum chemistry: A simple example"* [6], we describe an application to the calculation of an approximation to the ground state energy of the helium atom. The paper, we submit, demonstrates the pedagogical advantages of literate programming. In a second paper, entitled *"Literate programming in quantum chemistry: A collaborative approach to code development for molecular electronic structure theory"* [7], we describe the use of literate programming method in collaborative code development. We are also preparing a volume with the title *"Literate programming in quantum chemistry: An introduction"* [8].

6. Literate programming and libraries

The adoption of literate programming methods should lead naturally to structure in a computer program. If we are to consider "programs to be works of literature" then, just as a book is divided into parts and chapters, and the chapters are further divided into sections and subsections, perhaps supplemented by appendices, the "literate" approach to programming leads to a modularity of the code. This modularity leads in turn to the concept of a library, a set of fundamental building blocks from which large codes can be synthesized.

A well known example of a library of fundamental routines upon which large codes are based is the Basic Linear Algebra Subroutines or BLAS. In 1973, Hanson, Krogh and Lawson [9] identified the advantages of adopting a set of basic linear algebra subroutines for vector-vector operations in linear algebra. Following the development of vector processing and parallel processing with hierarchical memories, extensions of the BLAS were proposed, first to handle matrix-vector operations [10] [11], - the Level 2 BLAS or BLAS2, and then matrix-matrix operations [12] [13] [14] - the Level 3 BLAS or BLAS3. The BLAS has found application in numerical libraries such as the NAG library and in a wide range of application software. Carefully tailored implementations of the BLAS, often provided by hardware vendors, have often provided near optimal performance on a wide range of machines by effectively exploiting their vector and/or parallel processing capabilities. The "Level 3 *BLAS*" have proved to be particularly useful in obtaining close to peak performance on many modern computer architectures because they

amortize the cost of obtaining data from main memory by reusing data in the cache or high level memory.

We propose [15] a set of basis tensor algebra subroutines or BTAS. Tensors and tensor operators arise in many fields in the computational sciences, including computational quantum chemistry. The nomenclature BTAS(m, n), with $m \geq n$, where m and n are the respective ranks of the tensors, is proposed to establish a high level classification of tensor operations. The BTAS can be classified as follows:-

BTAS$(1,0)$ BTAS$(1,1)$

BTAS$(2,0)$ BTAS$(2,1)$ BTAS$(2,2)$

BTAS$(3,0)$ BTAS$(3,1)$ BTAS$(3,2)$ BTAS$(3,3)$

BTAS$(4,0)$ BTAS$(4,1)$ BTAS$(4,2)$ BTAS$(4,3)$ BTAS$(4,4)$ ...

BTAS$(m,0)$ collects simple operations on tensors of rank m, *e.g.* copying. BTAS$(1,1)$ is equivalent to BLAS1, BTAS$(2,1)$ is equivalent to BLAS2, and BTAS$(2,2)$ to BLAS3.

Let us briefly recall a few of the basics of the algebra of tensors. An nth rank tensor in m-dimensional space is an object with n indices and m^n components. For a general tensor a distinction is made between contravariant (upper) indices and covariant (lower) indices. A tensor of rank $m_1 + m_2$ may have m_1 contravariant indices and m_2 covariant indices. The order of the indices is significant. Tensors can be classified according to whether they are

(i) symmetric with respect to the permutation of a pair of indices, *i.e.*

$$A_{i\ldots j\ldots k\ldots l} = A_{i\ldots k\ldots j\ldots l} \tag{1}$$

(ii) antisymmetric with respect to the permutation of a pair of indices, *i.e.*

$$A_{i\ldots j\ldots k\ldots l} = -A_{i\ldots k\ldots j\ldots l} \tag{2}$$

A general tensor can be written as a sum of a symmetric and an antisymmetric component.

The use of literate programming techniques means that we can clearly indicate contravariant and covariant indices in the LaTeX fragment describing code for BTAS.

7. Literate programming and devolved collaboration

It has been noted that the literate programming paradigm is well suited to collaborative projects [16]. The phenomenal growth in the power of computing machines in the second half of the twentieth century was accompanied during its last two decades by an equally spectacular growth in the network connecting these machines. This has created the new opportunities for collaborative research across geographically distributed sites, often in

different time zones. (The present work, for instance, was undertaken on distant continents.)

A collaborative virtual environment [17] is one that actively supports human-human communication in addition to human-machine communication and which uses a Virtual Environment as the user interface. One of the present authors (SW) was involved in the establishment of a *"European Metalaboratory for ab initio multireference quantum chemical methods"*[1], which, in addition to developing new quantum chemical methodology, planned the development of a pilot suite of capabilities for remote scientific collaboration between geographically distributed sites by creating a prototypical environment tailored to the needs of the quantum chemistry community. Such an environment might provide a cross-platform suite of audio, video, screen sharing, white board, and other tools for discussions, seminars, exchange of draft manuscripts, LaTeXdocuments, preprints and reprints, data preparation and analysis, program execution, training, *etc.* We submit that, in the development of new methodology and associated computer code, literate programming techniques, in that they actively support communication between humans in addition to human-machine communication, provides a promising mechanism for the exchange of information within a collaborative virtual environment for quantum chemistry especially when the collaborators are geographically distributed.

8. Final remarks

The historical record of computational molecular physics and quantum chemistry, with its huge legacy of largely undocumented code written largely in every dialect of FORTRAN, strongly indicates that the adoption of the literate programming paradigm would yield widespread benefits. The evidence suggests that many of these codes will, if they are properly maintained, outlive their designers, to be harnessed in unforeseen applications. A code that is is well-documented is more likely to be used widely, and to be revised regularly as newer, more efficient algorithms are developed. While our own interests are in the development of public domain and open source software, the model seems also to offer advantages to commercial developers who may very well wish to employ highly skilled programmers

[1] An EU COST project under action D23 'Metachem: Metalaboratories for Complex Computational Applications in Chemistry'. Project number: D23/0001/01: 'European Metalaboratory for multireference quantum chemical methods' (01/02/200118/07/2005). Participants: P. Čársky, J. Pittner (J. Heyrovsky Institute, Prague, Czech Republic), I. Hubač (Comenius University, Slovakia), S. Wilson (Rutherford Appleton Laboratory, UK), W. Wenzel (Universität Dortmund Germany), L. Meissner (Nicholas Copernicus University Poland), V. Staemmler (Ruhr Universität Bochum Germany), C. Tsipis (Aristotle University of Thessaloniki, Greece), A. Mavridis (National and Kapodistrian University of Athens, Greece).

who may be otherwise unfamiliar with the highly specialized algorithms of molecular physics and quantum chemistry.

This change in style requires, perhaps, a commensurate change of perception that reflects more accurately the technological developments and economic imperatives that shape modern research. The very considerable investments that have been made in the development of code should be accorded the same respect and recognition that has been traditionally associated with scholarly works in books and journals. Given the central role that computer programs now play in molecular physics and quantum chemistry and the complexity, subtlety, and beauty of the scientific ideas that they embody, the construction of these codes should, as Knuth contends, rightly be a regarded as an essential act of communication, rather than just a base commodity, or a necessary evil.

In this paper, we have discussed the application of literate programming methods in computational molecular physics and quantum chemistry. The widespread adoption of these methods could significantly enhance the development of both theory and computer code. Similar benefits could be forthcoming in other areas of computational science and engineering. Literate programs should be considered "to be works of literature" [2] and will therefore naturally lead to a highly structured and modular programming style. The widespread adoption of such as style could significantly enhance the development of both theory and computer code in many areas of computational science and engineering.

References

1. J. Ziman, *Real Science. What it is, and what it means*, Cambridge University Press (2000).
2. D.E. Knuth, *Literate Programming*, The Computer Journal **27:2**, 97 (1984).
3. H. Thimbleby, Software - Practice and Experience **33**, 975 (2003).
4. D. Cordes and M. Brown, Computer **24**, 52 (1991).
5. J. Slater, in *Supercomputational Science*, ed: R.G. Evans and S. Wilson, Plenum Press, New York (1991).
6. H.M. Quiney and S. Wilson, *Literate programming in quantum chemistry: A simple example*, Intern. J. Quantum Chem. Vol. 104, p. 430 (2005).
7. H.M. Quiney and S. Wilson, *Literate programming in quantum chemistry: A collaborative approach to code development for molecular electronic structure theory*, Molec. Phys. **103**, 389 (2005).
8. H.M. Quiney and S. Wilson, *Literate programming in quantum chemistry: An introduction, (in preparation).*
9. R. Hanson, F. Krogh and C. Lawson, SIGNUM Newl. **8**, 16 (1973).
10. J.J. Dongarra, J.J. Du Croz, S.J. Hammarling and R.J. Hanson, ACM Trans. Math. Softw. **14**, 1 (1988).
11. J.J. Dongarra, J.J. Du Croz, S.J. Hammarling and R.J. Hanson, ACM Trans. Math. Softw. **14**, 18 (1988).
12. J.J. Dongarra, J.J. Du Croz, I.S. Duff and S.J. Hammarling, ACM Trans. Math. Softw. **16**, 1 (1990).

13. S.P. Datardina, J.J. Du Croz, S.J. Hammarling and M.W. Pont, J. C Lang. Transl. **3**, 295 (1992).
14. J.J. Du Croz, P.J.D. Mayes, J. Wasniewski and S. Wilson, Parallel Computing **8**, 345 (1988).
15. H.M. Quiney and S. Wilson, *(work in progress)*.
16. N. Ramsey and C. Marceau (1991) Software - Practice and Experience **21**, 677.
17. E.F. Churchill, D.N. Snowdon and A.J. Munro (Eds.), *Collaborative Virtual Environments*, Springer, Berlin (2001).

COUPLED-CLUSTER AND CONFIGURATION-INTERACTION APPROACHES TO QUASIDEGENERACY

JOSEF PALDUS
Department of Applied Mathematics,
University of Waterloo,
Ontario, Canada N2L 3G1
and
Department of Chemistry and
Guelph-Waterloo Center for Graduate Work in Chemistry,
Waterloo Campus, University of Waterloo,
Ontario, Canada N2L 3G1

AND

XIANGZHU LI
Department of Applied Mathematics,
University of Waterloo,
Ontario, Canada N2L 3G1

Abstract. The capability of the variational and perturbative-type approaches to the many-electron correlation problem – as represented by the configuration interaction (CI) and coupled cluster (CC) theories – to describe, respectively, the nondynamic and dynamic correlation effects, is emphasized, and its exploitation in the design of the so-called externally corrected CC methods, as well as in the formulation of Davidson-type corrections that are based on the CC theory, at both single reference and multireference levels, is reviewed. The performance of various methods of this type is illustrated on the DZP H4 model that consists of two interacting and slightly stretched hydrogen molecules in a trapezoidal geometry. This often studied model enables a continuous transition from the degenerate to the nondegenerate regime by varying the degree of quasidegeneracy via a single geometric parameter. In this way the role of higher-than-pair clusters, particularly in the presence of intruder states, can be explored and the performance of various approaches that exploit the complementarity of the CI and CC approaches can be evaluated.

J.-P. Julien et al. (eds.),
Recent Advances in the Theory of Chemical and Physical Systems, 13–43.

1. Introduction

The computation of *ab initio* potential energy curves (PECs) or surfaces (PESs) for a multitude of energetically low-lying states, within a wide range of molecular geometries that involve various dissociation channels – particularly when a sufficiently high accuracy is required, as when computing the ro-vibrational levels and the corresponding spectra or in reaction dynamics calculations – represents a very challenging problem. There are essentially two types of approaches that can be employed for this purpose, namely those of a variational or perturbative variety. These may be either of a single reference (SR) or of a multireference (MR) type. Clearly, when dealing with several states that belong to the same symmetry species, the latter MR versions are called for.

The typical variational approaches are represented by the configuration interaction (CI) method, usually restricted to single (S) and double (D) excitations for reasons of feasibility, i.e., by the SR-CISD or MR-CISD methods (see, e.g., Refs. [1, 2]). Presently, large-scale versions of these methods represent the most useful tool for the above mentioned purposes of PESs generation, in spite of their size-inextensive character that is routinely, though only partially, overcome via various semiempirical, Davidson-type corrections [3–10]. In spite of the arbitrariness of these *ex post* corrections that account for the missing dynamic correlation, the great advantage of the CI approaches is their ability to handle the static and nondynamic correlation effects in a very efficient and automatic manner, not to mention their universality and the existence of generally very efficient and well-converging algorithms.

The perturbative-type approaches are then typified by the coupled-cluster (CC) methods [11–14], whose superiority over the finite-order many-body perturbation theory (MBPT) is well documented (for and overview, see, e.g., Refs. [15–25] and references therein). Although all approaches that are based on the Rayleigh-Schrödinger perturbation theory are *size-extensive*, the great advantage of the CC methods is their efficient handling of dynamical correlations. The standard SR CCSD method – eventually supplemented by a perturbative correction for the triples (T) in its widely used CCSD(T) version [26,27] – is the method of choice when high accuracy and reliability are called for [28]. Unfortunately, in view of the perturbative nature of the triples correction, the standard CCSD(T) method breaks down in the presence of quasidegeneracy. This breakdown can be to a large extent averted by an appropriate renormalization of the triples correction via the completely renormalized (CR) or renormalized (R) CCSD(T) methods, as recently introduced by Kowalski and Piecuch [29–31].

The only, yet essential, limitation that is imposed on the SR version of the CC theory is the nondegeneracy of the reference configuration $|\Phi\rangle$

employed. Nonetheless, even in many highly quasidegenerate situations, the standard CCSD method performs surprisingly well and is invariably superior to the finite-order MBPT, which also requires a considerable computational effort when going beyond the second order. For closed-shells, one usually employs the restricted Hartree-Fock (RHF) wave function as a reference, and in high-spin open-shell cases, either the restricted open-shell (ROHF), or even the unrestricted (UHF), HF wave functions are used for this purpose. Clearly, in the latter case, the spin-symmetry is broken, which may result in various shortcomings (see, e.g., Ref. [21]). For this reason, both fully [32, 33] and approximately [34–40] spin adapted versions of the SR CCSD method have been developed. The fully spin-adapted version relies on the unitary group approach (UGA) to the many-electron correlation problem (see, e.g., Refs. [41–43] and references therein) and can properly handle the static correlation in low-lying singlet excited states, as well as the high-spin doublet and triplet states [32].

Needless to say, the quasidegeneracy is invariably encountered when breaking genuine chemical bonds, as well as in most open-shell situations that are encountered when handling, for example, low-spin excited states or various radicaloid species. A deteriorating performance of the standard SR CCSD method in such situations can be at least partially offset by an explicit consideration of higher-than-pair clusters, namely of quadruples (Q) and/or triples (T), via the full CCSDT [44–46], CCSDTQ [47,48], or higher order [49] methods. Unfortunately, this results in a drastic increase in computational cost, so that these approaches are restricted to small systems and moderate basis sets. Moreover, in many instances (see, e.g., Ref. [50] and below), even these high-order CC approaches become inadequate. Thus, while all SR CC approaches are inherently size-extensive, they lack the ability to account for nondynamic correlations. Indeed, in addition to the size-extensive property (as guaranteed by the absence of unlinked contributions to the energy), one has to take care of the so-called *size-consistency* by choosing a flexible enough reference configuration, or a set of such configurations, that is capable to correctly describe the dissociation channels of interest, particularly those involving open-shell species. For this reason, a considerable attention was given to the MR CC approaches.

Unfortunately, in contrast to the CI method, an extension of the SR CC theory to the MR case is far from being straightforward, since there is no unique way in which to generalize the SR exponential Ansatz for the exact N-electron wave function $|\Psi\rangle$, i.e.,

$$|\Psi\rangle = \exp(T)|\Phi\rangle\,, \qquad T = \sum_{k=1}^{N} T_k\,, \qquad T_k = \sum_j (t_k)_j G_j^{(k)}\,, \tag{1}$$

when more than one reference configuration is required. Here, as in the following text, $G_j^{(k)}$ designates a k-fold excitation operator relative to the reference (here $|\Phi\rangle$), leading to the k-fold excited configuration state $|\Xi_j^{(k)}\rangle = G_j^{(k)}|\Phi\rangle\,, \langle\Phi|\Xi_j^{(k)}\rangle = 0$. Thus, when we wish to employ a model space $\mathcal{M}_0$ that is spanned by M suitable configurations $|\Phi_i\rangle$, $i = 1, 2, \cdots, M$ (represented by either the Slater determinants or spin-adapted configurations), so that $\dim\mathcal{M}_0 = M$, we have essentially two options how to proceed (for an overview, see, e.g., Refs. [16, 18, 21, 24]).

On the one hand, we can strive for *a single* cluster operator T, defining the valence universal wave operator U, $U = \exp(T)$, which will transform all the model space states $|\Phi_i\rangle$ into some linear combinations of the exact states $|\widetilde{\Psi}_i\rangle$, $i = 1, 2, \cdots, M$, which in turn span the target space $\mathcal{M}$, i.e.,

$$|\widetilde{\Psi}_i\rangle = U|\Phi_i\rangle, \qquad U = \exp(T), \tag{2}$$

The desired exact states $|\Psi_i\rangle$, given as linear combinations of $|\widetilde{\Psi}_i\rangle$ (see Sec. 2), are then obtained by diagonalizing the effective Hamiltonian $H^{\text{eff}} = PHUP$, defined on $\mathcal{M}_0$, as guaranteed by the projector P onto $\mathcal{M}_0$, i.e.,

$$P = \sum_{i=1}^{M} P_i, \qquad P_i = |\Phi_i\rangle\langle\Phi_i|\,. \tag{3}$$

Alternatively, we can define *different* cluster operators $T(i)$, one for each reference $|\Phi_i\rangle$, so that

$$U = \sum_{i=1}^{M} \exp[T(i)]P_i, \tag{4}$$

and

$$|\widetilde{\Psi}_i\rangle = \exp[T(i)]\,|\Phi_i\rangle\,. \tag{5}$$

The former approach is referred to as the *valence universal* (VU) or *Fock space* MR CC method [51–54] and the latter one as the *state universal* (SU) or *Hilbert space* method [55]. In spite of a great number of papers devoted to both the VU and SU approaches, very few actual applications have been carried out since their inception more than two decades ago. Certainly, no general-purpose codes have been developed. This is not so much due to the increased complexity of the MR formalism relative to the SR one, as it is due to a number of genuine obstacles that have yet to be overcome.

While each approach has its own peculiarities, one common obstacle arises due to the so-called *intruder states*. These are the states from the orthogonal complement ${\mathcal{M}_0}^{\perp}$ of $\mathcal{M}_0$, whose energy falls within the interval of energies characterizing the reference configurations spanning $\mathcal{M}_0$ or lies

close to this interval. Thus, similarly as in the SR formalism, in which case we require the reference configuration $|\Phi\rangle$ not to be quasidegenerate, it is essential in the MR version of the CC theory that the energies of reference configurations are well separated from those spanning ${\mathcal{M}_0}^{\perp}$.

The above requirement is further complicated by the fact that in order to achieve the exact size-extensivity of the theory, one should employ the so-called *complete model space* (CMS), which is spanned by configurations corresponding to all possible occupations of valence orbitals. Such CMS, however, will often involve high-energy configurations, thus enhancing the probability for the occurrence of intruders. For this reason, much work has been devoted to the design of MR CC formalisms that are based on *incomplete model spaces* (IMSs). Unfortunately, even with IMSs the problem of intruders often persists, since it is difficult to define an intruder-free model space in the entire range of geometries of interest.

In the VU case, we encounter additional complications: In order to unambiguously define the VU cluster operator one has to consider not only the system of interest, but also an entire sequence of daughter systems that arise by a sequential ionization of valence electrons, until the closed-shell state involving only the core electrons is reached (for a precise formulation of the valence universality, see Refs. [18,56]). This, in turn, may lead to genealogy problems, since one often encounters multiple solutions at various stages of ionization [57] (note that the target space $\mathcal{M}$ is far from being unambiguous). For these and other reasons, we focus in the following on the SU-type formalism.

In order to gain a better insight into the structure of the SU CC formalism, we have carried out the cluster analysis of the exact full CI (FCI) wave functions, using the SU CC Ansatz [58], for an extensively studied $(H_2)_2$ model system [59,60]. This enabled us to explore the importance of various components of the SU CC equations, as well as to assess the role of higher-than-pair clusters (see also Ref. [61] for the analysis of VU and SU cluster relations). Based on this experience, we have formulated the SU CCSD formalism that employs a *general model space* (GMS), which is spanned by an arbitrarily selected set of configurations, regardless the splitting of orbitals into the core, valence (or active), and excited (or virtual) subsets [62]. Here we relied on the so-called *intermediate normalization*,

$$\langle \Phi_i | \widetilde{\Psi}_j \rangle = \delta_{ij} \,, \tag{6}$$

which is essential if we wish to carry out the above mentioned cluster analysis that is based on the SU Ansatz and which greatly simplifies the effective Hamiltonian formalism on which all MR CC formalisms are based. This in turn requires the imposition of the so-called *C-conditions* on the internal cluster amplitudes, as will be explained below.

We have carried out several applications showing the promise of this procedure [63,64], as well as addressed the question of the size-consistency and size-extensivity [65–67], to which we wish to turn our attention again in this paper. Finally, we have also extended the idea of *externally corrected* (ec) SR CCSD methods [68–70] (see also Refs. [21, 24]) to the MR case, introducing the (N, M)-CCSD method [71], which exploits an N-reference (NR) CISD wave functions as a source of higher-than-pair clusters in an M-reference SU CCSD method. Both the GMS and (N, M)-CCSD allow us to avoid the undesirable intruder states, while providing very encouraging results.

Let us recall, finally, that ec CCSD approaches exploit the complementarity of the CI and CC methods in their handling of the dynamic and nondynamic correlations. While we use the CI as an external source of higher than pair clusters, Meissner *et al.* [10,72–74] exploit the CC method to correct the CI results (thus designing the CC-based Davidson-type corrections). This aspect will also be addressed below.

Thus, following a brief exposition of the necessary formalism, introducing the required terminology and notation, we shall discuss the questions of size-consistency and size-extensivity in the MR context. We shall further illustrate these aspects using both the existing and new data.

2. Theory

2.1. EFFECTIVE HAMILTONIAN FORMALISM

We recall that the *effective Hamiltonian formalism* considers a model space $\mathcal{M}_0$ together with a target space $\mathcal{M}$,

$$\mathcal{M}_0 = \mathrm{Span}\{|\Phi_i\rangle\} = \mathrm{Span}\{|\widetilde{\Phi}_i\rangle\}\,, \qquad \langle\Phi_i|\Phi_j\rangle = \delta_{ij}\,, \tag{7}$$

$$\mathcal{M} = \mathrm{Span}\{|\Psi_i\rangle\} = \mathrm{Span}\{|\widetilde{\Psi}_i\rangle\}\,, \qquad \langle\Psi_i|\Psi_j\rangle = \delta_{ij}\,, \tag{8}$$

where

$$\dim \mathcal{M}_0 = \dim \mathcal{M} = M\,, \qquad i, j = 1, 2, \cdots, M, \tag{9}$$

with the relevant states interrelated via the projection operator P, Eq. (3), and its "inverse", the wave operator U, as follows (for an overview, see, e.g., Refs. [16, 18, 21, 24])

$$P|\Psi_i\rangle = |\widetilde{\Phi}_i\rangle\,, \qquad P|\widetilde{\Psi}_i\rangle = |\Phi_i\rangle\,, \tag{10}$$

$$U|\widetilde{\Phi}_i\rangle = |\Psi_i\rangle\,, \qquad U|\Phi_i\rangle = |\widetilde{\Psi}_i\rangle\,. \tag{11}$$

Clearly, while the configurations $|\Phi_i\rangle$ are mutually orthonormal, and similarly for $|\Psi_i\rangle$, their tilded counterparts are not, and none of the target states $|\Psi_i\rangle$ is orthogonal to $\mathcal{M}_0$. Thus, relating the two basis sets of $\mathcal{M}_0$ as follows

$$|\widetilde{\Phi}_i\rangle = \sum_j c_{ij}|\Phi_j\rangle\,, \qquad \mathbf{C} = \| \; c_{ij} \; \|\,, \qquad \det \mathbf{C} \neq 0\,, \tag{12}$$

we see that the target states are related by the corresponding inverse transformation, namely

$$|\Psi_i\rangle = U|\widetilde{\Phi}_i\rangle = \sum_j c_{ij}|\widetilde{\Psi}_j\rangle\,. \tag{13}$$

Assuming, now, the intermediate normalization, Eq. (6), we find that

$$\langle\Phi_j|\widetilde{\Phi}_i\rangle = c_{ij} = \langle\Phi_j|\Psi_i\rangle\,, \tag{14}$$

and writing the target state exact wave functions $\{|\Psi_i\rangle\}$ (or, in fact, any MR CI wave functions) in the form

$$|\Psi_i\rangle = \sum_{|\Phi_j\rangle\in\mathcal{M}_0} c_{ij}|\Phi_j\rangle + \sum_{|\Xi_j\rangle\in{\mathcal{M}_0}^{\perp}} d_{ij}|\Xi_j\rangle\,, \qquad \mathbf{D} = \| \; d_{ij} \; \|\,, \tag{15}$$

with $\{|\Xi_j\rangle\}$, $\langle\Xi_i|\Xi_j\rangle = \delta_{ij}$, spanning ${\mathcal{M}_0}^{\perp}$, while for $|\widetilde{\Psi}_i\rangle$ we get

$$|\widetilde{\Psi}_i\rangle = |\Phi_i\rangle + \sum_{|\Xi_j\rangle\in{\mathcal{M}_0}^{\perp}} b_{ij}|\Xi_j\rangle\,, \tag{16}$$

where the coefficient matrix $\mathbf{B}$ is given by

$$\mathbf{B} = \| \; b_{ij} \; \| = \mathbf{C}^{-1}\mathbf{D}\,. \tag{17}$$

Note that all the above expressions characterize the effective Hamiltonian formalism *per se*, and are independent of a particular form of the wave operator U. Indeed, this formalism can be exploited directly, without any cluster Ansatz for the wave operator U (see Ref. [75]). We also see that by relying on the intermediate normalization, we can easily carry out the SU-Ansatz-based cluster analysis: We only have to transform the relevant set of states into the form given by Eq. (16) and employ the SU CC Ansatz,

$$|\widetilde{\Psi}_i\rangle = U|\Phi_i\rangle = \exp[T(i)]|\Phi_i\rangle\,. \tag{18}$$

Then we can employ the same procedure (in fact the same codes) as in the SR case by considering the model space configuration $|\Phi_i\rangle$ as a new reference (or Fermi vacuum) for each $|\widetilde{\Psi}_i\rangle$.

2.2. GMS SU CCSD FORMALISM

We shall now employ the SU Ansatz for the wave operator U, Eq. (4), with the cluster operator $T(i)$ having the same general form as in the SR case, namely

$$T(i) = \sum_{k=1}^{N} T_k(i)\,, \qquad T_k(i) = \sum_j t_j^{(k)}(i) G_j^{(k)}(i)\,. \tag{19}$$

Here $G_j^{(k)}(i)$ designates the k-th rank excitation operator relative to $|\Phi_i\rangle$ and $t_j^{(k)}(i)$ is the corresponding cluster amplitude. In the standard SU CC approach that employs a CMS, only excitations out of $\mathcal{M}_0$ are allowed. When we employ a GMS, we have to take a special care of the excitations that interconnect reference configurations within $\mathcal{M}_0$ (cf. also Refs. [76,77]), which we shall refer to as the *internal* excitations. This can be done in a way that preserves the intermediate normalization, Eq. (6), if we employ the C-conditions mentioned earlier (cf. also Ref. [55]). For this purpose, we thus distinguish the *internal* and the *external* excitation operators $G_j^{(k)}(i)$ – and similarly for the corresponding cluster amplitudes $t_j^{(k)}(i)$ – according to whether the resulting configuration belongs to $\mathcal{M}_0$ or not, i.e., whether

$$G_j^{(k)}(i)|\Phi_i\rangle \in \mathcal{M}_0 \qquad \text{or} \qquad G_j^{(k)}(i)|\Phi_i\rangle \in \mathcal{M}_0{}^{\perp}\,, \tag{20}$$

respectively.

Now, the external cluster amplitudes are again given by the usual MR SU CCSD equations [55], namely

$$\langle G_l^{(k)}(i)\Phi_i|\overline{H}|\Phi_i\rangle = \sum_{j(\neq i)} \Gamma^{ij}(l) H_{ji}^{(\mathrm{eff})}\,, \qquad \overline{H} = \exp[-T(i)] H \exp[T(i)]\,, \tag{21}$$

where $H_{ji}^{(\mathrm{eff})}$ designates the matrix element of the effective Hamiltonian,

$$H_{ji}^{(\mathrm{eff})} = \langle \Phi_j | H \exp[T(i)] | \Phi_i \rangle\,, \tag{22}$$

and $\Gamma^{ij}(l)$ is the coupling coefficient

$$\Gamma^{ij}(l) = \langle G_l^{(k)}(i)\Phi_i| \exp[-T(i)] \exp[T(j)] |\Phi_j\rangle\,, \tag{23}$$

while the internal cluster amplitudes are determined via the C-conditions [62].

The C-conditions ascertain the validity of the intermediate normalization, Eq. (6), by requiring that the off-diagonal transformed coefficients $\widetilde{c}_{ij}$ that are associated with the reference configurations $|\Phi_j\rangle$, $(j \neq i)$ in the target wave function $|\widetilde{\Psi}_i\rangle$ must vanish, since

$$\widetilde{\mathbf{C}} = \| \widetilde{c}_{ij} \| = \mathbf{C}^{-1}\mathbf{C} = \mathbf{I}\,, \tag{24}$$

I being the identity matrix. Introducing an explicit notation for the excitation operators, which specifies the hole and particle (spin) orbitals as, respectively, the subscripts and superscripts,

$$G_l^{(k)}(i) \equiv G_{P_1P_2\cdots P_k}^{Q_1Q_2\cdots Q_k}(i)\,, \qquad G_l^{(k)}(i)|\Phi_i\rangle \in \mathcal{M}_0\,, \tag{25}$$

(and similarly for the cluster amplitudes $t_l^{(k)}(i)$ and coefficients $\widetilde{c}_{ij}$), the C-conditions simply require that

$$\widetilde{c}_{P_1P_2\cdots P_k}^{Q_1Q_2\cdots Q_k}(i) = 0\,. \tag{26}$$

Thus, with the exception of one-body clusters ($k = 1$), the internal cluster amplitudes do not simply vanish, but are given by the cluster amplitudes of lower rank.

When $k = 1$, the C-conditions, Eq. (26), imply that the internal one-body cluster amplitudes vanish,

$$t_P^Q(i) = 0\,, \qquad G_P^Q(i)|\Phi_i\rangle \in \mathcal{M}_0\,, \tag{27}$$

while for the two-body internal amplitudes we find the relationships

$$t_{P_1P_2}^{Q_1Q_2}(1) = t_{P_1}^{Q_2}(1)\,t_{P_2}^{Q_1}(1) - t_{P_1}^{Q_1}(1)\,t_{P_2}^{Q_2}(1) \tag{28}$$

and

$$t_{Q_1Q_2}^{P_1P_2}(2) = t_{Q_1}^{P_2}(2)\,t_{Q_2}^{P_1}(2) - t_{Q_1}^{P_1}(2)\,t_{Q_2}^{P_2}(2)\,, \tag{29}$$

assuming that

$$|\Phi_2\rangle = G_{P_1P_2}^{Q_1Q_2}|\Phi_1\rangle\,. \tag{30}$$

Similar relationships easily follow for higher-order amplitudes [62].

Once all the relevant cluster amplitudes have been determined by solving the SU CCSD equations, Eq. (21), while taking into account the C-conditions, we obtain the desired energies and eigenstates by diagonalizing the effective Hamiltonian. For details, we refer the reader to [62].

2.3. SIZE-CONSISTENCY AND SIZE-EXTENSIVITY

There has been much confusion and misunderstanding concerning these concepts. In the context of SR theories, the size-consistency usually implies the ability of the reference to properly describe the dissociation process at hand. With the exception of closed-shell systems dissociating into the closed-shell fragments (as, for example, in the case of van der Waals complexes involving closed shell species), the standard RHF reference is not size-consistent whenever we break genuine chemical bonds, while the UHF (with all its shortcomings) will usually fit the bill. The size-extensivity, on the other hand, implies the absence of unlinked contributions to the energy,

so that for noninteracting subsystems A and B of the parent species AB, the energy will be additive, i.e., when

$$\mathrm{AB} \longrightarrow \mathrm{A} + \mathrm{B}\,, \tag{31}$$

we have that in the separated limit

$$E(\mathrm{A} + \mathrm{B}) = E(\mathrm{A}) + E(\mathrm{B})\,. \tag{32}$$

In other words, we get the same result by considering (A+B) as a supersystem as when handling A and B subsystems separately. This is especially important for extended systems, involving n subsystems, in which case the limiting process $n \to \infty$ will only make sense if the energy is strictly linear in n in the noninteracting limit.

It is well known that the CC and MBPT energies are size-extensive, while this is not the case for truncated CI methods. Indeed, it is not difficult to verify (see, e.g., Ref. [8]) that for a system consisting of n subsystem [e.g., $(\mathrm{He})_n$], the CISD energy is proportional to $\sqrt{n}$ rather than to n. This is easy to comprehend when we realize that by restricting the excitations to, say, doubles, we ignore simultaneous double excitations on the subsystems A and B when considering the supersystem (A+B), which now represent quadruples, while such excitations are taken into account when handling the systems A and B individually.

In the context of the MR-type methods, the concept of size-extensivity takes on a much broader meaning. Until recently [65], this fact has not been explicitly pointed out as fas as we know, since most discussions focused solely on the lowest state or, at most, on one state at a time. Thus, when we consider the dissociation process (31), assuming that the subsystems A and B involve M_A and M_B states, respectively, with energies $E_i(\mathrm{X})$, $i = 1, \cdots, M_\mathrm{X}$, X = A, B, we must generally require that the additivity rule

$$E_{ij}(\mathrm{A} + \mathrm{B}) = E_i(\mathrm{A}) + E_j(\mathrm{B}), \quad i = 1, \cdots, M_\mathrm{A},\, j = 1, \cdots, M_\mathrm{B} \tag{33}$$

holds for all $M_\mathrm{A} \times M_\mathrm{B}$ states of the (A+B) supersystem. For this to be the case, the model space for the supersystem must be given by a tensor product of subsystem model spaces [65], i.e.,

$$\mathcal{M}_0(A + B) = \mathcal{M}_0(A) \otimes \mathcal{M}_0(B)\,. \tag{34}$$

Moreover, it can be shown [62,65–67] that the C-conditions not only warrant the validity of the intermediate normalization, but also imply an extensive cancellation of unlinked terms both in the effective Hamiltonian $H^{(\mathrm{eff})}$ and in the coupling coefficients $\Gamma^{ij}(l)$.

In any case, we believe that for the purposes of PESs generation, the size-consistency, as characterized by Eq. (33), is much more essential than an eventual small deviation from the size-extensivity. This is not only cor-

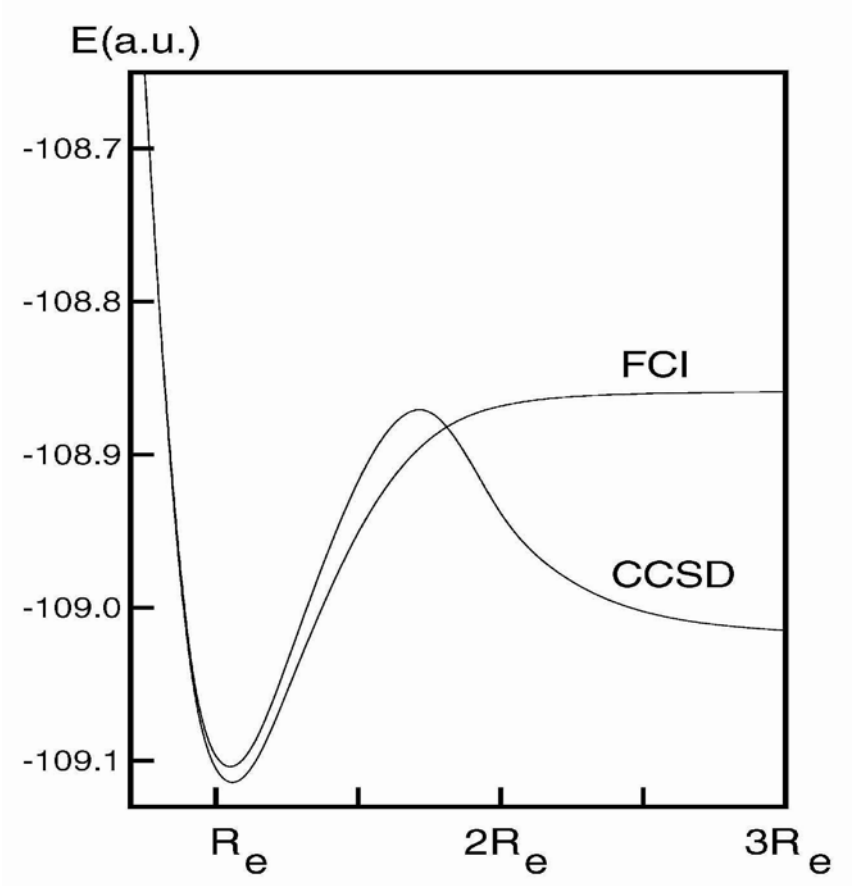

Figure 1. The PECs for the DZ model of N_2 as obtained with the FCI and CCSD methods.

roborated by the MR CI results, but also by a relative success of Brillouin-Wigner-type MR CC approaches [78–81] that are "manifestly" size-inextensive. In each case, an *a posteriori* account of size-extensivity, which is in general only approximate, yields useful results. Further, the validity of Eq. (33) for any pair of noninteracting subsystems, will also warrant the correct dependence on the subsystem number in the separated limit.

The essential role of the size-consistency in molecular applications is strikingly conspicuous already in the SR case. Indeed, the SR CCSD method is "manifestly" size-extensive, yet it fails when breaking genuine chemical bonds, as the well-known examples illustrate [82, 83]. This breakdown is of course most prominent when multiple bonds are involved, as the example of the CCSD PEC for N_2, shown in Fig. 1, clearly illustrates [83]. Note that even when we employ the UHF reference, we will not generate a smooth PEC in view of the presence of the triplet instability (see, e.g., [84, 85] and references therein), whose onset occurs at an intermediately stretched geometry [86].

2.4. EXTERNALLY-CORRECTED AND STATE-SPECIFIC METHODS

As already alluded to above, there exists a definite complementarity between the variational CI approaches and the perturbative CC methods [70]. The former ones, as represented by the limited CISD or MR CISD methods, are size-inextensive, but efficiently account for static and nondynamic correlations, while the CC and MBPT approaches are size-extensive at any level of truncation, but fail in the case of degeneracy or even strong quasidegeneracy. Thus, the CI approaches can simultaneously handle a multitude of states of an arbitrary spin multiplicity, regardless of the presence of quasidegeneracy or even degeneracy, while lacking in the description of dynamic correlation due to a multitude of highly excited states, unless excessively large dimensions can be afforded. On the other hand, the CC approaches are size-extensive at any level of truncation and account very efficiently for dynamic correlation, thanks to the exponential Ansatz for the wave operator, yet encounter serious difficulties in the presence of significant quasidegeneracy. In view of this complementarity and the fact that both CI and CC approaches are equivalent in their FCI and FCC limit, a conjoint treatment, if at all feasible, seems to be very desirable. This is precisely the idea behind the ec CC methods [68–70].

2.4.1. *Single-reference methods*

In the SR case, where the energy is completely determined by the one- and two-body cluster amplitudes T_1 and T_2, the availability of the exact three- and four-body cluster amplitudes T_3 and T_4 enables us to recover the exact FCI or FCC energy by solving the SR CCSD equations, in which we have accounted for the terms involving higher-than-pair clusters (i.e., for T_3 and T_4). Thus, even when we employ approximate three- or four-body amplitudes, or in fact even a small subset of the most important ones, we can significantly improve the CCSD result, particularly in the presence of quasidegeneracy, when higher-than-pair clusters become prominent.

After exploring various possibilities for an affordable and efficient external source of higher-than-pair clusters [68–70], a modest MR CISD wave functions turned out to represent an optimal choice. These can be easily transformed into the intermediately normalized SR CI form, with any configuration chosen as a reference and, subsequently, cluster analyzed to yield a set of the most important three- and four-body cluster amplitudes. This is precisely the essence of the RMR CCSD method [87–90], which proved to be capable to satisfactorily describe the stretching even of a triple bond. For example, using only eight-reference (8R) RMR CCSD, we were able to generate a PEC for N_2 yielding highly accurate ro-vibrational levels [91]: The fundamental Raman band frequencies were computed with an error of less than 1 cm^{-1} and for the vibrationally excited bands the spectra were faithfully reproduced up to a constant shift of about 7 cm^{-1}.

Although the RMR CCSD method (and similarly other ec CCSD methods) is essentially a corrected SR CCSD method, it must be classified as a *state selective* or a *state specific* (SS) MR CC approach, since it exploits the information originating from the MR CI wave function. It may also be characterized as an *amplitude correcting* ec CCSD or SS MR CC method in contrast to the *energy correcting* procedures [82, 83, 92]: In the former case the external source is employed in the computation of cluster amplitudes and the energy is obtained via the standard CCSD expression. In contrast, the energy correcting methods use standard CCSD amplitudes and employ the external information when evaluating the energy, just as the standard (i.e., not ec) "internally" energy correcting procedures, such as CCSD(T). In fact, we can use an MR CISD wave function for the direct energy correction, if in the standard CCSD energy expression we replace the reference configuration $|\Phi\rangle$ by the MR CISD wave function, say $|\chi\rangle$.

Generally, in the ec energy correcting approaches one employs the so-called *asymmetric energy formula* [82]

$$\mathcal{E} \equiv \mathcal{E}(\chi, \Psi) = D^{-1} \langle \chi | H | \Psi \rangle \,, \qquad D = \langle \chi | \Psi \rangle \,, \tag{35}$$

with the only requirement that $|\chi\rangle$ is not orthogonal to $|\Psi\rangle$, so that the denominator D does not vanish. Now, if $|\Psi\rangle$ is the exact wave function (e.g., FCI or FCC), we recover the exact energy using any $|\chi\rangle$. Likewise, when $|\Psi\rangle$ is an approximate wave function, but $|\chi\rangle$ is exact, we again recover the exact energy. Of course, in practice, neither $|\Psi\rangle$ nor $|\chi\rangle$ will be exact. For example, in the standard CCSD approach, we have $|\Psi\rangle = \exp(T_1 + T_2)\,|\Phi\rangle$ and $|\chi\rangle = |\Phi\rangle$. Note that nothing will change if $|\chi\rangle$ also involves singly and doubly excited configurations that are accounted for in the CCSD procedure. In fact, we can write [82]

$$\begin{aligned} \mathcal{E}(\chi, \Psi) &= E_{\rm CCSD} + D^{-1} \sum_{k>(2)} \langle \chi | \exp(T) | \Phi_k \rangle \langle \Phi_k | \overline{H} | \Phi \rangle \,, \\ D &= \langle \chi | \exp(T) | \Phi \rangle \,, \end{aligned} \tag{36}$$

where $k > (2)$ implies that the summation extends over higher than doubly excited configurations $|\Phi_k\rangle$, since otherwise $\mathcal{E} = E_{\rm CCSD}$ (see Ref. [82] for details). Here we must emphasize the close relationship of the ec energy corrected approaches with the *method of moments CC theory* and the related renormalized CCSD(T) and similar methods as pursued by Piecuch and Kowalski [29–31].

We distinguish the above mentioned procedures by the following acronyms: Let $\mathcal{N}$ stands either for an N reference model space (NR) or for (N, n_a), which designates a complete active space (CAS) with N electrons and n_a active orbitals. Then $\mathcal{N}$-RMR CCSD designates an amplitude corrected ec CCSD using $\mathcal{N}$-CISD as the external source, while CCSD-[$\mathcal{N}$] labels the corresponding energy corrected CCSD. Combining both corrections we have $\mathcal{N}_1$-RMR CCSD-[$\mathcal{N}_2$].

The idea of the ec methodology originated in our studies of semi-empirical cyclic polyene models C_NH_N with a nondegenerate ground state ($N = 4\nu + 2$, $\nu = 1, 2, \cdots$), representing a very demanding electron correlation problem. Indeed, for large N and/or coupling constant (i.e., small resonance integral β), the CCSD method [93] (or even higher order CCSDT or CCSDTQ methods [50]) completely breaks down due to the presence of severe quasidegeneracy (and, thus, an increasing prominence of higher-order clusters, in particular of T_4 [94]). On the other hand, the UHF wave function (of the different-orbitals for different spin or DODS type) supplies the exact solution in the fully correlated limit ($\beta = 0$), and can thus serve as an external source of T_4 clusters (in a singlet projected form no odd-numer-of-times excited clusters appear due to spin restrictions).

It can be shown [95] that in such a case the T_4 contribution cancels the exclusion principle violating (EPV) quadratic terms [59]. This realization led us to the formulation of the so-called ACPQ method (CCSD with an approximate account for quadruples) [95], as well as to CCDQ′ and CCSDQ′ [86], the latter also accounting for singles. Up to a numerical factor of 9 for one term involving triplet-coupled *pp-hh* t_2 amplitudes [95], this approach is identical with an earlier introduced CCSD-D(4,5) approach [59] and an independently developed ACCD method of Dykstra *et al.* [96, 97]. This method arises from CCSD by simply discarding the computationally most demanding (i.e., nonfactorizable) terms (see Refs. [59, 95–97] for details).

Another way to exploit the complementarity of CI and CC approaches was explored earlier by Meissner *et al.* [10]. Instead of using CI as a source of higher-than-pair clusters and correcting CCSD, it exploits the CC theory to correct the MR CISD results. In the spirit of an earlier work on Davidson-type corrections for SR CISD [10], Meissner *et al.* formulated a CCSD-based corrections for both SR [72] and MR [74] CISD. The latter was later extended to higher lying excited states [73].

We must, finally, mention the SS approaches that employ a genuine MR SU CC formalism, yet focus on one state at a time by neglecting the coupling with other states. Such an approach was pursued earlier by Kucharski and Bartlett [98] and, most recently by Mukherjee and collaborators [99, 100], who distinguish the *relaxed* and *nonrelaxed* versions of their formalism.

2.4.2. *Multireference methods*

The three- and four-body clusters play an even more important role in MR CC theories. In contrast to the SR formalism, where the energy is fully determined by one- and two-body clusters, the higher-than-pair clusters enter already the effective Hamiltonian. Consequently, even with the exact one- and two-body amplitudes, we can no longer recover the exact energies [71]. Here we must also keep in mind that the excitation order of various configurations from $\mathcal{M}_0^{\perp}$ is not uniquely defined, since a given configuration

can arise via excitations from different references. Nonetheless, when we employ the exact higher-order cluster amplitudes to correct the SU CCSD equations (including the effective Hamiltonian), we again recover the exact result, as in the SR formalism. However, in contrast to the SR case, we may now require even higher-than-four-body clusters for this purpose.

It turns out that MR CISD represents again the most suitable source of the required higher-order clusters. Carefully chosen small reference space MR CISD involves a very small, yet representative, subset of such cluster amplitudes. Moreover, in this way we can also overcome the eventual intruder state problems by including such states in MR CISD, while excluding them from GMS SU CCSD. In other words, while we may have to exclude some references from $\mathcal{M}_0$ in order to avoid intruders, we can safely include them in the MR CISD model space $\mathcal{M}_1$. In fact, we can even choose the CMS for $\mathcal{M}_1$. Thus, designating the dimensions of $\mathcal{M}_0$ and $\mathcal{M}_1$ spaces by M and N, respectively, we refer to the ec SU CCSD method employing an NR-CISD as the external source by the acronym (N, M)-CCSD. Thus, with this notation, we have that $(N, 1)$-CCSD $\equiv$ NR-RMR CCSD and $(0, M)$-CCSD $\equiv$ MR SU CCSD. Also, $(0, 1)$-CCSD $\equiv$ SR CCSD. For details of this procedure and its applications we refer the reader to Refs. [63, 64, 71].

Let us, finally, reiterate that, similarly as the MR CISD method can serve as an external source for correcting CCSD approaches, we can conversely use CCSD to formulate Davidson-type corrections for MR CISD, both for the lowest-lying [72, 74] and the higher-lying states [73].

In the following section, it will be our objective to compare the performance of these various approaches, using the same model system.

3. An Illustrative Example

In order to demonstrate and elucidate the above outlined assertions, we shall employ a well-studied model system consisting of four hydrogen atoms, namely the so-called H4 model [59]. In contrast to the original minimum basis set (MBS) H4 model [59], we shall rely on its double-zeta plus polarization (DZP) version [60], which emphasizes the dynamic correlation component (note that the MBS H4 model involves only one quadruply-excited state). Nonetheless, just as the MBS model, the DZP H4 model enables us to explore the capability of a studied method to handle the nondynamic correlation, whose importance varies as we proceed from a completely degenerate to a nondegenerate limit by varying a single geometric parameter.

The H4 model has been widely used in the past, particularly in its original MBS version, to evaluate the efficiency of various approaches to the many-electron correlation problem. It consists of four hydrogen atoms that are arranged in a trapezoidal configuration with equal and fixed internuclear H–H separations of 2 Å. Its geometry is thus fully determined by a single parameter α determining the $\measuredangle(H_1H_2H_3)$ and $\measuredangle(H_2H_3H_4)$ angles as follows

$$\measuredangle(H_1H_2H_3) = \measuredangle(H_2H_3H_4) = (\alpha + \tfrac{1}{2})\pi\,. \tag{37}$$

In the $\alpha = 0$ limit, we thus deal with the fully degenerate square configuration, while the $\alpha = 0.5$ limit characterizes a nondegenerate linear arrangement. The internuclear separation of 2 Å between the nearest neighboring atoms corresponds to that of a slightly stretched H_2 molecule and is used to emphasize the quasidegeneracy and intruder state effects. The latter is particularly apparent when we employ the linear version of the SU CCSD formalism (L-CCSD), as shown in detail earlier for various MBS H_4 models [101]. The H4 model may also be conceived to represent two slightly-stretched, interacting H_2 molecules in a trapezoidal arrangement and the transition from the degenerate square configuration to the nondegenerate linear one as a model of a single-bond breaking. In our examples, we use both the existing and new data ias obtained with various CI and CC methods.

The exact FCI, as well as the RHF and UHF energies, and the corresponding correlation energies of our DZP H4 model are listed in Table I.

Table I. The RHF, UHF, and FCI ground state energies (in a.u.) and the corresponding correlation energies $\Delta E_{\rm corr} = E(\mathrm{RHF}) - E(\mathrm{FCI})$ and $\Delta E^{\rm UHF}_{\rm corr} = E(\mathrm{UHF}) - E(\mathrm{FCI})$ (in mH) for the DZP H4 model with $0 \le \alpha \le 0.5$.

α	E(RHF)	E(UHF)	E(FCI)	$\Delta E_{\rm corr}$	$\Delta E^{\rm UHF}_{\rm corr}$
0	−1.931750	−2.023191	−2.063112	131.362	39.921
0.01	−1.951444	−2.027357	−2.069401	117.957	42.044
0.02	−1.969599	−2.032340	−2.079470	109.871	47.130
0.05	−2.015652	−2.050315	−2.114299	97.647	63.984
0.1	−2.069109	−2.081256	−2.160115	91.006	78.859
0.15	−2.101808	−2.105761	−2.188929	87.121	83.168
0.2	−2.121595	−2.122762	−2.206548	84.953	83.786
0.3	−2.141080	−2.141131	−2.224122	83.042	82.991
0.4	−2.148427	−2.148427	−2.230887	82.460	82.460
0.5	−2.150367	−2.150367	−2.232700	82.333	82.333

We see that the largest correlation effects are associated with the degenerate $\alpha = 0$ geometry and that these effects steadily decrease as we approach the nondegenerate linear geometry at $\alpha = 0.5$. We also see that the UHF method can account for a substantial part (i.e., for about 70 %) of the correlation energy in the degenerate limit. Consequently, in the UHF case, the correlation effects initially increase with the increasing value of α, reaching a shallow maximum in the interval $0.15 \leq \alpha \leq 0.2$ and then marginally decrease to the RHF values, becoming identical with the standard RHF related value for $\alpha \geq 0.3$, since for these geometries the UHF becomes identical with RHF, which is no longer triplet (or nonsinglet) unstable [86] (cf. Refs. [84, 85]).

Even though a significant portion of the correlation energy is accounted for at the UHF level in the degenerate and quasidegenerate regions, where the RHF solution is triplet unstable, the UHF solution never yields the exact FCI energy, as in the case of cyclic polyenes (cf., e.g., Ref. [93]). Consequently, the UHF-based methods, such as the ACPQ, ACCSD, CCSDQ′, etc., can only be partially successful, not to mention their lack of triples contribution. Nonetheless, these methods always represent an improvement over the standard CCSD, while requiring less computational effort.

3.1. CI-TYPE APPROACHES

Let us first consider CI results that are summarized in Table II. Note that here, as well as in the subsequent tables, we list the differences from the exact FCI energies in millihartrees (mH). The relative percentage errors are not given and may be easily evaluated by relying on the data given in Table I. We also point out that, generally, an important feature of the computed potentials for the subsequent generation of the ro-vibrational levels and the corresponding spectra, obtained by solving the Schrödinger equation for the nuclear motion, is the overall shape of the PECs or PESs, rather than the absolute energy values, which involve anyway an arbitrary energy shift. Thus, in addition to the energy differences from the exact FCI values we also indicate at the bottom of each subsequent table the so-called *nonparallelism error* (NPE), which is defined as the difference between the maximal and minimal deviations from the FCI potential within a given range of geometries. Note, however, that unless the energy deviations from the FCI potential are strictly monotonic within the considered interval, the given NPE values only represent a lower bound to the actual NPE. Nevertheless, these NPEs represent a useful overall characteristic of the quality of the generated PECs or PESs.

Comparing the SR, two-reference (2R), four-reference (4R), and (2/2)R energy differences in Table II, we immediately notice a great improvement

Table II. The SR, 2R, 4R and (2/2)R CISD ground state energies together with various Davidson-type corrections relative to the FCI energy (in mH) for the DZP H4 model with $0 \leq \alpha \leq 0.5$. The nonparallelism errors (NPE) are givenin the last two rows. See the text for details.

	CISD				Davidson-type corrections [c]					
					SR [d]		MR			
α	SR	2R	4R[a]	(2/2)R [a,b]	DC	RDC	SQDC [e]	SGDC [f]	$\Delta_{\mathrm{MRCI}}^{(2R)}$ [g]	$\Delta_{\mathrm{MRCI}}^{(2/2)\mathrm{R}}$ [a,b]
0	14.424	1.802	1.590	1.488	−30.599	−58.785	−2.849	0.983	–	–
0.01	10.148	1.772	1.557	1.461	−17.409	−26.873	−2.889	0.951	0.700	0.378
0.02	7.598	1.707	1.494	1.402	−11.177	−15.398	−2.918	0.892	–	–
0.05	4.740	1.507	1.311	1.230	−5.298	−6.499	−2.817	0.746	0.643	0.363
0.1	3.485	1.277	1.107	1.037	−3.358	−3.939	−2.396	0.634	0.529	0.290
0.15	2.995	1.133	0.976	0.911	−2.819	−3.251	−2.034	0.581	0.476	0.257
0.2	2.744	1.039	0.886	0.827	−2.599	−2.970	−1.791	0.547	0.451	0.243
0.3	2.532	0.939	0.788	0.733	−2.445	−2.773	−1.541	0.510	0.431	0.232
0.4	2.467	0.903	0.748	0.696	−2.408	−2.725	−1.448	0.497	0.428	0.230
0.5	2.453	0.894	0.738	0.686	−2.402	−2.716	−1.425	0.494	0.427	0.229
NPE	11.971	0.909	0.852	0.802	28.197	56.069	1.493	0.489	–	–
rNPE[h]	7.695	0.878	0.819	0.775	15.007	24.157	1.493	0.457	0.273	0.149

[a] (2/2)R designates a 6-dimensional two-electron/two-orbital spin- and spatial-symmetry nonadapted model space, while 4R is a 4-dimensional model space spanned by the four $M_S = 0$ determinants.
[b] Ref. [72]
[c] Refs. [3–7, 9, 10, 60, 72, 73]
[d] Standard Davidson correction (DC) and renormalized DC (RDC) for SR CISD [3–6]
[e] Scalar quasidgenerate DC (SQDC) for MR CISD [7, 60]
[f] Scalar generalized DC (SGDC) for MR CISD [10, 60]
[g] Ref. [73]
[h] Nonparallelism error for a restricted interval $0.01 \leq \alpha \leq 0.5$.

of the MR CISD results over the SR CISD ones. While there is only a small difference between the 2R- and 4R- or (2/2)R-CISD energies (3rd and 4th or 5th columns of Table II, respectively), there is a dramatic improvement over the SR CISD, particularly in the degenerate and highly-quasidegenerate regions, the corresponding NPEs being reduced by an order of magnitude.

Considering, next, various Davidson-type corrections (DCs), we see that the standard DC, and especially the renormalized DC (RDC), grossly overcorrect the SR CISD results, particularly in the quasidegenerate region of geometries. The so-called scalar quasidegenerate DC (SQDC) [7,60] and the scalar generalized DC (SGDC) [10, 60], applied to the 2R-CISD energies, perform much better, particularly the latter one, whose NPE amounts to only about half a millihartree. By far superior are, however, the corrections that are based on the CCSD theory [72–74]. Although the authors of these corrections do not provide the results for the fully degenerate case ($\alpha = 0$), both results for the restricted region $0.01 \leq \alpha \leq 0.5$ (rNPE) are excellent, reducing the SGDC rNPE by the factor of two or more. This improvement is most significant in the highly quasidegenerate region of geometries, as expected.

3.2. CC-TYPE APPROACHES

Turning, next, our attention to the CC methods, we first consider the SR approaches. These results are summarized in Table III. We first note a much better performance of SR CCSD over the SR CISD (2nd column in Tables III and II, respectively): The CCSD deviations from FCI are much smaller than the CISD ones, as are the corresponding NPEs. This seems to be a general feature of the SR CCSD method, which often performs amazingly well even in severely quasidegenerate situations.

Considering the ec CCSD SR approaches, we notice an excellent performance of both the 2R- and 4R- or (2/2)R-RMR CCSD methods, yielding better results than the corresponding MR-CISD (cf. Table II) that is employed as the external source. Particularly in the latter case, the NPE is only about half a millihartree. Similarly well-behaved is the energy correcting CCSD-[2R] method, yielding qualitatively identical results as does the 2R-RMR CCSD method. In fact, the 2R-RMR CCSD-[2R] approach (8th column in Table III), combining both the amplitude and energy corrections, also yields very similar results. Clearly, a simultaneous application of both types of corrections, employing the same external source, does not bring any additional improvement, at least in this case: The corresponding NPE is almost the same as that of CCSD-[2R] and only marginally better than the 2R-RMR CCSD one. This is not surprising, since both 2R-RMR CCSD and CCSD-[2R] already provide very good results for our H4 model.

Table III. The SR CCSD[a], 2R-, 4R- and (2/2)R-RMR CCSD[a,b], CCSD-[2R][c], CCSD-[(4/4)][c], and 2R-RMR CCSD-[2R][c], as well as ACCSD′ [d], ACCSD′[T][d], CCSD[T][d], CCSDQ′ [d], and CCSDQ′[T][d] ground state energies relative to the FCI energy (in mH) for the DZP H4 model with $0 \leq \alpha \leq 0.5$. The nonparallelism errors (NPE) are given in the last two rows. See the text for details.

	SR	*N*R-RMR CCSD			CCSD-	CCSD-	2R-RMR	ACCSD′	ACCSD′	CCSD	CCSDQ′	CCSDQ′
α	CCSD	2R	4R	(2/2)R	[2R]	[(4/4)] [e]	CCSD-[2R]		-[T]	-[T]		-[T]
0	5.508	1.098	0.877	0.762	1.048	6.769	1.065	4.802	−5.732	−3.968	6.334	−3.070
0.01	3.602	0.992	0.768	0.656	0.974	4.247	0.986	1.747	−3.737	−1.013	4.363	−0.192
0.02	2.431	0.890	0.671	0.563	0.891	2.765	0.887	0.718	−2.481	−0.276	3.073	0.405
0.05	1.262	0.700	0.500	0.406	0.714	1.315	0.713	0.436	−0.878	0.040	1.595	0.384
0.1	0.911	0.558	0.387	0.306	0.575	0.885	0.570	0.507	−0.346	0.076	1.012	0.180
0.15	0.811	0.497	0.341	0.267	0.512	0.782	0.509	0.494	−0.255	0.073	0.841	0.103
0.2	0.770	0.468	0.318	0.250	0.481	0.750	0.479	0.470	−0.243	0.067	0.778	0.075
0.3	0.748	0.446	0.297	0.234	0.457	0.741	0.454	0.437	−0.264	0.058	0.748	0.058
0.4	0.750	0.442	0.291	0.230	0.453	0.748	0.453	0.420	−0.286	0.056	0.750	0.056
0.5	0.752	0.441	0.290	0.229	0.454	0.751	0.453	0.415	−0.294	0.055	0.752	0.055
NPE	4.760	0.657	0.587	0.533	0.595	6.028	0.612	4.387	5.489	4.044	5.586	3.475
rNPE[f]	2.854	0.551	0.478	0.427	0.521	3.506	0.533	1.332	3.494	1.089	3.615	0.597

[a] Ref. [87]
[b] Refs. [71, 82]
[c] Ref. [82]
[d] Ref. [86]
[e] (4/4) designates the 4-electron/4-orbital CAS CI.
[f] Nonparallelism error for a restricted interval $0.01 \leq \alpha \leq 0.5$.

Interestingly enough, when we use the (4/4) complete active space (CAS) CI, involving four electrons distributed over four (lowest-lying) orbitals, as the external source for the energy correction, we obtain a slightly inferior results (7th column of Table II) even to the uncorrected SR CCSD. The reason for this lies in the fact that the (4/4) CAS CI involves only one quadruply excited configuration. Even though the latter is the most important quadruple, it is not able to correct the large discrepancy between the CCSD and FCI energies in the degenerate region at and around $\alpha = 0$. Indeed, at $\alpha = 0$, both the ground state reference $|\Phi_0\rangle$, and its HOMO-LUMO doubly excited $|\Phi_1\rangle$ configuration ($|\Phi_0\rangle$ and $|\Phi_1\rangle$ spanning the 2R model space), have the same weight, so that almost all double excitations from $|\Phi_1\rangle$ represent quadruples relative to $|\Phi_0\rangle$. Clearly, all these quadruples must be accounted for in order to correct for the quasidegeneracy. As pointed out in [82], this result also indicates that the CAS-SCF-type wave functions are unlikely to be very effective in the energy-correcting CCSD approaches.

Let us, finally, consider some of the UHF-based approaches (see Refs. [86, 93, 95] for details). The ACCSD′ results yield improved energies relative to the standard SR CCSD, even though the NPEs for the whole region are almost the same, and only the ACCSD′ rNPE is significantly better than the SR CCSD one. Adding the perturbative correction for triples overcorrects the ACCSD′ energies. This is not surprising, since the perturbative triple corrections generally break down in highly quasidegenerate situations, as witnessed by numerous results for various diatomics (see, e.g., Refs. [21, 24, 88]). When these corrections are applied to the SR CCSD energies, they perform well in the nondegenerate region of geometries, as expected, but again overcorrect in the degenerate and quasidegenerate situations. Nonetheless, the NPE of ∼1 mH represents a great improvement over the SR CCSD result. Similar statements apply to CCSDQ′, which may be regarded as the UHF-amplitude-corrected CCSD, and to its triple-corrected version CCSDQ′[T] [86, 95]. Obviously, the correction for triples, which cannot be accounted for by using the singlet-projected UHF wave function, plays here an important role, as also observed in Ref. [102]. Of course, the perturbative account of triples is useful only in the nondegenerate region.

Next, we consider the MR CC results that are summarized in Tables IV and V for the ground and the excited state of the same symmetry species (namely $^1A_1$), respectively. For the ground state, the standard 2R-SU CCSD ≡ (0,2)-CCSD provides a great improvement over the SR CCSD in the degenerate and quasidegenerate regions of geometries, as it should. Unfortunately, due to the presence of intruder states, the MR description deteriorates as we approach the nondegenerate regime (see Ref. [101] for

Table IV. Various SU, SS and BW MR-CCSD ground state energies relative to the FCI energy (in mH) for the DZP H4 model with $0 \leq \alpha \leq 0.5$. The nonparallelism errors (NPE) are given in the last two rows. See the text and Table II for details.

	(N,M)-CCSD [a]				$H^{(\mathrm{eff})}$ [d]		SS-MRCC [g]		BW
α	(0,2) [b]	(2,2) [c]	(4,2) [c]	(2/2,2) [c]	A [e]	B [f]	un-relaxed	relaxed	MR-CCSD [h]
0	−0.686	0.836	0.623	0.511	1.528	−0.128	−0.196	−0.279	–
0.01	−0.594	0.814	0.600	0.491	1.499	−0.125	−0.103	−0.187	−0.012
0.02	−0.409	0.773	0.560	0.456	1.433	−0.112	0.053	−0.020	–
0.05	−0.084	0.649	0.449	0.358	1.258	−0.085	–	–	0.454
0.1	−0.173	0.517	0.335	0.261	1.077	−0.083	0.501	0.443	0.582
0.15	−0.622	0.440	0.261	0.199	0.942	−0.107	–	–	0.590
0.2	−1.187	0.395	0.211	0.157	0.848	−0.136	–	–	0.579
0.3	−1.998	0.367	0.166	0.121	0.784	−0.171	–	–	0.559
0.4	−2.308	0.368	0.155	0.113	0.797	−0.186	0.554	0.383	0.551
0.5	−2.379	0.370	0.153	0.112	0.808	−0.190	1.130	0.221	0.548
NPE	−2.295	0.469	0.470	0.399	0.744	0.107	1.326	0.722	–
rNPE [i]	−2.295	0.447	0.447	0.379	0.715	0.107	1.233	0.630	0.602

[a] Ref. [71]
[b] Refs. [87,103,104]
[c] Refs. [71,82]
[d] Refs. [58,71]
[e] T_1 and T_2 from SU CCSD and T_3 and T_4 from 2R-CISD.
[f] T_1 and T_2 from FCI and T_3 and T_4 from 2R-CISD.
[g] Ref. [100]
[h] Ref. [79] These results do not involve any size-extensivity corrections.
[i] Nonparallelism error for a restricted interval $0.01 \leq \alpha \leq 0.5$.

a detailed study of intruders in the case of the MBS H4 model), yielding inferior results to the SR CCSD.

The detrimental effect of the intruders can be efficiently alleviated by employing the ec version employing the 2R- and 4R-CISD higher-than-pair cluster amplitudes, as witnessed by the (2,2)-, (4,2)-, and (2/2,2)-CCSD results (columns 3–5 of Table IV and columns 6–8 of Table V). These results provide a particularly significant improvement over the standard 2R-SU CCSD in the nondegenerate regime. We also note that while for the ground state the (2,2)- and (4,2)- or (2/2,2)-CCSD results are very similar, the latter approximation gives a much improved result for the excited state, yielding roughly the same NPE for both states.

In this regard, it is interesting to compare these ec results with those of Meissner *et al.* [72–74], which use the CC-based corrections for MR CISD. Although the absolute energy deviations are very similar for both (2,2)-CCSD (3rd column of Table IV) and $\Delta_{\mathrm{MRCI}}^{(2\mathrm{R})}$ (10th column of Table II), the latter gives a better rNPE (unfortunately, the $\alpha = 0$ result is not available for the $\Delta_{\mathrm{MRCI}}^{(2\mathrm{R})}$ correction). This fact can most likely be ascribed to the fact that the MR CI method is ideal for a simultaneous handling of a number of low-lying states. Yet, for the excited state, while the $\Delta_{\mathrm{MRCI}}^{(2\mathrm{R})}$ NPE is again significantly better than the (2,2)-CCSD one (11th and 6th columns of Table V, respectively), the (2/2,2)-CCSD NPE is better by about a factor of two than the $\Delta_{\mathrm{MRCI}}^{(2\mathrm{R})}$ NPE. Note also that for the excited state, the SR CISD gives about the same NPE as for the ground state, while 2R-CISD deteriorates in the nondegenerate region, so that the corresponding NPE is almost three-times as large as for the ground state.

A very instructive result is also obtained by evaluating the ec $H^{(\mathrm{eff})}$, using in each case the three- and four-body amplitudes provided by the 2R-CISD, while employing the exact FCI one- and two-body amplitudes (approximation B given in the 7th and 10th columns in Tables IV and V, respectively) on the one hand, and the 2R-SU CCSD amplitudes (approximation A given in the 6th and 9th columns in Tables IV and V, respectively) on the other hand [58,71]. We emphasize that in contrast to the (2,2)-CCSD approach, the three- and four-body amplitudes are only used in the evaluation of $H^{(\mathrm{eff})}$ and not in the computation of the one- and two-body amplitudes as in the (2,2)-CCSD method. Consequently, for the ground state, the A approximation yields inferior results to the (2,2)-CCSD ones, the energy deviations being about twice as large as in the proper ec SU CCSD and,

Table V. The FCI (in a.u.) and various CISD, SU CCSD, and BW CCSD excited state energies relative to the FCI energy (in mH) for the DZP H4 model with $0 \leq \alpha \leq 0.5$. The nonparallelism errors (NPE) are given in the last two rows. See the text for details.

		CISD		(N,M)-CCSD [a]				$H^{(\mathrm{eff})}$ [b]			BW MR-
α	FCI	SR	2R	(0,2)	(2,2)	(4,2)	(2/2,2)	A [c]	B [d]	$\Delta_{\mathrm{MRCI}}^{(\mathrm{2R})}$ [e]	CCSD [f]
0	−1.981434	16.842	1.645	3.373	0.916	0.537	0.305	1.158	0.128	–	–
0.01	−1.980637	20.120	1.701	3.299	0.934	0.545	0.307	1.206	0.125	0.718	3.078
0.05	−1.944499	22.593	2.165	3.060	1.161	0.671	0.381	1.717	0.085	1.015	3.085
0.1	−1.900893	21.122	3.016	3.490	1.546	0.844	0.472	2.240	0.083	1.234	3.744
0.15	−1.877185	19.352	3.918	3.462	1.970	1.032	0.581	1.898	0.107	1.143	3.903
0.2	−1.866764	18.045	4.414	2.767	2.275	1.149	0.640	0.733	0.136	0.808	3.329
0.3	−1.861977	16.774	4.521	1.724	2.559	1,192	0.613	−1.057	0.171	0.457	2.329
0.4	−1.863818	16.392	4.413	1.654	2.686	1.186	0.566	−1.451	0.186	0.590	2.207
0.5	−1.865105	16.317	4.374	1.726	2.729	1.184	0.551	−1.460	0.190	0.669	2.250
NPE	–	6.276	2.876	1.836	1.813	0.655	0.335	3.700	0.107	–	–
rNPE[g]	–	6.276	2.820	1.836	1.795	0.647	0.333	3.700	0.107	0.777	1.696

[a] Ref. [71]
[b] Refs. [58, 71]
[c] T_1 and T_2 from SU CCSD and T_3 and T_4 from 2R-CISD.
[d] T_1 and T_2 from FCI and T_3 and T_4 from 2R-CISD.
[e] Ref. [73]
[f] Ref. [79] These results do not involve any size-extensivity corrections.
[g] Nonparallelism error for a restricted interval $0.01 \leq \alpha \leq 0.5$.

similarly, for the corresponding NPEs. On the other hand, using the exact one- and two-body amplitudes obtained by the cluster analysis of the FCI wave functions, we recover almost exact energies for both states, resulting in a very small NPE ($\sim$ 0.1 mH), regardless whether the degenerate limit is included or not. In fact, for reasons explained in detail in Ref. [58], the absolute values of the energy deviations from FCI in the B approximation are identical for both states and only differ in sign.

Considering, next, the SS results obtained by Mukherjee's group [100] (cf. 8th and 9th columns in Table IV), we see that the unrelaxed version deteriorates in the nondegenerate limit, while the relaxed version performs rather well when the absolute values of deviations are considered, slightly overestimating the FCI energies in the degenerate limit and underestimating them in the mid-region of geometries (reaching a maximum at $\alpha \approx 0.1$). Consequently, the unrelaxed NPEs exceed 1 mH level, while the relaxed ones are similar to the A approximation of $H^{(\mathrm{eff})}$ (column 6 of Table IV), but inferior to both (2,2)- and (2/2,2)-CCSD NPEs. Unfortunately, Mukherjee *et al.* [100] focused their work on the lowest state only and do not provide any results for the excited state.

Finally, in the last column of Tables IV and V, we have also included the results obtained with the single-root Brillouin-Wigner (BW) version of the MR SU CCSD method [78–81]. Note that these results were not "a posteriori" corrected for the size-extensivity. Similarly as in the standard SU CCSD method, BW MR CCSD works best in the degenerate limit and deteriorates in both the intermediate and nondegenerate regions. The corresponding rNPE for the ground state is about the same as for the relaxed SS-MRCC and somewhat inferior to the ec SU CCSD ones. For the excited state, the deviations from FCI are about the same as for the standard SU CCSD, as is the corresponding rNPE, but significantly inferior to (2/2,2)-CCSD.

4. Conclusions

The above presented data clearly demonstrate the usefulness of the ec CC approaches at both the SR and MR levels. While in the SR case the energy is fully determined by the one- and two-body clusters, and the truncation of the CC chain of equations at the CCSD level can be made exact by accounting for the three- and four-body clusters, the MR case is much more demanding, since the higher-than-pair clusters appear already in the effective Hamiltonian. An introduction of the "external corrections" is thus

even more important, and thus useful, in the MR case, particularly in the presence of the intruder state(s), which can be often accommodated in this manner. Relying on the GMS-version of the SU MRCC theory at the CCSD level [62] we can thus avoid the intruder state problems by a suitable choice of a GMS, as well as via the external corrections based on the MR CISD wave functions. The GMS SU CCSD test calculations for a number of model systems, for which the exact FCI results are available and in which the intruder state problems are present, yielded most satisfactory results [64].

Numerous earlier studies of the ec CC methods clearly indicate that the modest size MR CISD wave functions represent the most suitable and easily available source of higher-than-pair clusters for this purpose (see Ref. [21] for an overview). Indeed, these wave functions can be easily transformed to a SR form, whose cluster analysis is straightforward. Moreover, the resulting three- and four-body amplitudes represent only a very small subset of all such amplitudes, namely those which are most important, and which at the same time implicitly account for all higher-order cluster components that are present in the MR CISD wave functions.

The results that examine the role of various cluster components in the effective Hamiltonian clearly indicate a relative insensitivity of the resulting energies to the choice of the three- and four-body clusters on the one hand and, on the other hand, the crucial role played by the one- and two-body clusters, as one would expect. The latter clusters may thus be conveniently accounted for by relying on the ec GMS SU CCSD method, namely via (M, N)-CCSD.

We have also seen that the said complementarity of the CC and CI approaches can be exploited in a "reversed" order, namely that we can rely on the MR CISD results and adjust them for their lack of dynamical correlation via the Davidson-like corrections that are based on the CC theory, as proposed by Meissner *et al.* [10, 72–74]. We have seen that, at least for the studied DZP H4 model, either variant leads to excellent results.

The SS approaches, proposed by Mukherjee's group [99, 100], in either relaxed or nonrelaxed version, also lead to much improved potentials, at least for the lowest energy level. Unfortunately, we are not aware of any information concerning their performance for the excited states of the same symmetry species as the lowest level state, either for the H4 model or other species that the authors considered.

The BW SU CCSD methods [78–81] also provide a viable alternative and their recently introduced GMS version [105] should further enhance their capabilities.

We can thus conclude that the complementarity of the CI and CC approaches in their ability to account, respectively, for the nondynamic and dynamic correlation effects, is worthy of a further pursuit in view of their relative affordability and due to the fact that both types of wave functions are simply related via the exponential Ansatz and yield the same exact result in their respective FCI and FCC limit.

Acknowledgements

Continued support by NSERC (J.P.) is gratefully acknowledged. The senior author also wishes to express his appreciation and gratitude to the organizers of the QSCP-IX meeting for the most interesting program and a very congenial and stimulating atmosphere.

References

1. I. Shavitt, *The Method of Configuration Interaction.* In: H. F. Schaefer III (Ed.) *Methods of Electronic Structure Theory; Modern Theoretical Chemistry*, Vol. 3. (Plenum, New York, 1977), pp. 189–275; *The Treatment of Electron Correlation: Where Do We Go from Here?* In: C. E. Dykstra (Ed.) *Advanced Theories and Computational Approaches to the Electronic Structure of Molecules* (Reidel, Dordrecht, 1984), pp. 185–196.
2. R. McWeeny, *Methods of Molecular Quantum Mechanics*, 2nd edn. (Academic, London, 1989).
3. R. Langhoff and E. R. Davidson, Int. J. Quantum Chem. **8**, 61 (1974).
4. E. R. Davidson and D. W. Silver, Chem. Phys. Lett. **52**, 403 (1977).
5. R. J. Bartlett and I. Shavitt, Int. J. Quantum Chem., Symp. **11**, 165 (1977); **12**, 543 (1978) (E).
6. P. E. M. Siegbahn, Chem. Phys. Lett. **55**, 386 (1978).
7. P. J. Bruna, S. D. Peyerimhoff, P. J. Buenker, Chem. Phys. Lett. **72**, 278 (1980).
8. J. Paldus, P. E. S. Wormer, F. Visser, and A. van der Avoird, J. Chem. Phys. **76**, 2458 (1982).
9. K. Jankowski, L. Meissner, and J. Wasilewski, Int. J. Quantum Chem. **28**, 931 (1985).
10. L. Meissner, Chem. Phys. Lett. **146**, 204 (1988); **263**, 351 (1996) and references therein.
11. J. Čížek, J. Chem. Phys. **45**, 4256 (1966).
12. J. Čížek, Adv. Chem. Phys. **14**, 35 (1969).
13. J. Čížek and J. Paldus, Int. J. Quantum Chem. **5**, 359 (1971).
14. J. Paldus, J. Čížek, and I. Shavitt, Phys. Rev. A **5**, 50 (1972).
15. R. J. Bartlett, J. Phys. Chem. **93**, 1693 (1989).
16. J. Paldus, *Coupled Cluster Theory.* In: S. Wilson and G. H. F. Diercksen (Eds.) *Methods in Computational Molecular Physics*, NATO ASI series, Series B: Physics, Vol. 293. (Plenum, New York, 1992), pp. 99–194.
17. R. J. Bartlett and J. F. Stanton, (1994) *Applications of Post-Hartree-Fock Methods: A Tutorial.* In: K. B. Lipkowitz and D. B. Boyd (Eds.) *Reviews in Computational Chemistry*, Vol. 5. (VCH Publishers, New York, 1994), pp. 65–169.
18. J. Paldus, *Algebraic Approach to Coupled Cluster Theory.* In: G. L. Malli (Ed.) *Relativistic and Correlation Effects in Mmolecules and Solids*, NATO ASI series, Series B: Physics, Vol. 318. (Plenum, New York, 1994), pp. 207–282.

19. R. J. Bartlett, *Coupled Cluster Theory: An Overview of Recent Developments.* In: D. R. Yarkony (Ed.) *Modern Electronic Structure Theory*, Vol. 2. (World Scientific, Singapore, 1995), pp. 1047–1131.
20. J. Gauss, *Coupled Cluster Theory.* In: P. von R. Schleyer (Ed.) *Encyclopedia of Computational Chemistry*, Vol. 1. (Wiley, New York, 1998), pp. 615–636.
21. J. Paldus and X. Li, Adv. Chem. Phys. **110**, 1 (1999).
22. T. D. Crawford and H. F. Schaefer III, *An Introduction to Coupled Cluster Theory for Computational Chemists.* In: K. B. Lipkowitz and D. B. Boyd (Eds.) *Reviews in Computational Chemistry*, Vol. 14, Chap. 2. (Wiley, New York, 2000), pp. 33–136.
23. J. F. Stanton and J. Gauss, Int. Rev. Phys. Chem. **19**, 61 (2000).
24. J. Paldus, *Coupled Cluster Methods.* In: S. Wilson (Ed.) *Handbook of Molecular Physics and Quantum Chemistry*, Vol. 2, Part 3, Chap. 19. (Wiley, Chichester, 2003), pp. 272–313.
25. I. Shavitt and R. J. Bartlett, *Many-Body Methods in Quantum Chemistry* (Cambridge University Press, Cambridge, 2005), in press.
26. K. Raghavachari, J. Chem. Phys. **82**, 4607 (1985).
27. M. Urban, J. Noga, S. J. Cole, and R. J. Bartlett, J. Chem. Phys. **83**, 4041 (1985).
28. T. J. Lee, G. E. Scuseria, *Achieving Chemical Accuracy with Coupled-Cluster Theory.* In: S. R. Langhoff (Ed.) *Quantum Mechanical Electronic Structure Calculations with Chemical Accuracy* (Kluwer, Dordrecht, 1995), pp. 47–108.
29. P. Piecuch and K. Kowalski, *In Search of the Relationship between Multiple Solutions Characterizing Coupled-Cluster Theories.* In: J. Leszczynski (Ed.) *Computational Chemistry: Review of Current Trends*, Vol. 5. (World Scientific, Singapore, 2000), pp. 1–104; P. Piecuch, K. Kowalski, I. S. O. Pimienta, and M. J. McGuire, Int. Rev. Phys. Chem. **21**, 527 (2002); P. Piecuch, K. Kowalski, I. S. O. Pimienta, P.-D. Fan, M. Lodriguito, M. J. McGuire, S. A. Kucharski, T. Kuś, and M. Musiał, Theor. Chem. Acc. **112**, 349 (2004).
30. K. Kowalski and P. Piecuch, J. Chem. Phys. **113**, 18, 5644, 8490 (2000); **115**, 643, 2966 (2001); **116**, 7411 (2002); Chem. Phys. Lett. **334**, 89 (2001); **347**, 237 (2001).
31. K. Kowalski and P. Piecuch, J. Mol. Struct. (Theochem) **547**, 191 (2001); J. Chem. Phys. **120**, 1715 (2004) and references therein.
32. X. Li and J. Paldus, J. Chem. Phys. **101**, 8812 (1994).
33. B. Jeziorski, J. Paldus, and P. Jankowski, Int. J. Quantum Chem. **56**, 129 (1995).
34. C. L. Janssen and H. F. Schaefer III, Theor. Chim. Acta **79**, 1 (1991).
35. M. Urban, P. Neogrády, and I. Hubač, *Spin Adaptation in the Open-Shell Coupled-Cluster Theory with a Single Determinant Restricted Hartree-Fock Reference.* In: R. J. Bartlett (Ed.) *Recent Advances in Coupled-Cluster Methods. Recent Advances in Computational Chemistry*, Vol. 3. (World Scientific, Singapore, 1997), pp. 275–306.
36. P. J. Knowles, C. Hampel, and H.-J. Werner, J. Chem. Phys. **99**, 5219 (1993).
37. D. Jayatilaka and G. S. Chandler, Mol. Phys. **92**, 471 (1997) and references therein.
38. T. D. Crawford, T. J. Lee, N. C. Handy, and H. F. Schaefer III, J. Chem. Phys. **107**, 9980 (1997).
39. P. G. Szalay and J. Gauss, J. Chem. Phys. **112**, 4027 (2000) and references therein.
40. I. Berente, P. G. Szalay, and J. Gauss, J. Chem. Phys. **117**, 7872 (2002).
41. J. Paldus, (1994) *Many-Electron Correlation Problem and Lie Algebras.* In: *Contemporary Mathematics*, Vol. 160. (American Mathematical Society, Providence, RI, 1994), pp. 209–236 and references therein.
42. J. Paldus, *Dynamical groups.* In: G. W. F.Drake (Ed.) *Atomic, Molecular and Optical Physics Handbook*, Sec. 2, *Mathematical Methods*, Chap. 4. (American Institute of Physics, New York, 1996), pp. 65–75 and references therein.
43. F. A. Matsen and R. Pauncz, *The Unitary Group in Quantum Chemistry* (Elsevier, Amsterdam, 1986).
44. J. Noga and R. J. Bartlett, J. Chem. Phys. **86**, 7041 (1987); **89**, 3401 (1988) (E).
45. G. E. Scuseria and H. F. Schaefer III, Chem. Phys. Lett. **152**, 382 (1988).
46. J. D. Watts and R. J. Bartlett, J. Chem. Phys. **93**, 6104 (1990).

47. S. A. Kucharski and R. J. Bartlett, Theor. Chim. Acta **80**, 387 (1991); J. Chem. Phys. **97**, 4282 (1992).
48. N. Oliphant and L. Adamaowicz, J. Chem. Phys. **95**, 6645 (1991); P. Piecuch and L. Adamaowicz, J. Chem. Phys. **100**, 5792 (1994).
49. M. Musiał, S. A. Kucharski and R. J. Bartlett, J. Chem. Phys. **116**, 4382 (2002).
50. R. Podeszwa, S. A. Kucharski, and Z. Stolarczyk, J. Chem. Phys. **116**, 480 (2002).
51. I. Lindgren, Int. J. Quantum Chem., Symp. **12**, 33 (1978).
52. I. Lindgren and D. Mukherjee, Phys. Rep. **151**, 93 (1987).
53. A. Landau, E. Eliav, and U. Kaldor, *Intermediate Hamiltonian Fock-Space Coupled-Cluster Method and Applications.* In: R. F. Bishop, T. Brandes, K. A. Gernoth, N. R. Walet, and Y. Xian (Eds.) *Recent Progress in Many-Body Theories, Advances in Quantum Many-Body Theories*, Vol. 6. (World Scientific, Singapore, 2002), pp. 355–364 and references therein.
54. D. Mukherjee and S. Pal, Adv. Quantum Chem. **20**, 292 (1981) and references therein.
55. B. Jeziorski and H. J. Monkhorst, Phys. Rev. A **24**, 1668 (1981).
56. B. Jeziorski and J. Paldus, J. Chem. Phys. **90**, 2714 (1989).
57. K. Jankowski, J. Paldus, I. Grabowski, and K. Kowalski, J. Chem. Phys. **97**, 7600 (1992); **101**, 1759 (1994) (E); **101**, 3085 (1994).
58. J. Paldus and X. Li, J. Chem. Phys. **118**, 6769 (2003).
59. K. Jankowski and J. Paldus, Int. J. Quantum Chem. **18**, 1243 (1980).
60. J. Paldus, P. E. S. Wormer, and M. Benard, Coll. Czech. Chem. Commun. **53**, 1919 (1988).
61. K. Jankowski, J. Paldus, and J. Wasilewski, J. Chem. Phys. **95**, 3549 (1991).
62. X. Li and J. Paldus, J. Chem. Phys. **119**, 5320 (2003).
63. X. Li and J. Paldus, J. Chem. Phys. **119**, 5346 (2003).
64. X. Li and J. Paldus, J. Chem. Phys. **120** 5890 (2004).
65. X. Li and J. Paldus, Int. J. Quantum Chem. **99**, 914 (2004).
66. J. Paldus, X. Li, Coll. Czech. Chem. Commun. **69**, 90 (2004).
67. J. Paldus, X. Li, and N. D. K. Petraco, J. Math. Chem. **35**, 213 (2004).
68. J. Paldus and J. Planelles, Theor. Chim. Acta **89**, 13 (1994); J. Planelles, J. Paldus, and X. Li, *ibid.* **89**, 33, 59 (1994); G. Peris, J. Planelles, and J. Paldus, Int. J. Quantum Chem. **62**, 137 (1997); X. Li, G. Peris, J. Planelles, F. Rajadell, and J. Paldus, J. Chem. Phys. **107**, 90 (1997); G. Peris, F. Rajadell, X. Li, J. Planelles, and J. Paldus, Mol. Phys. **94**, 235 (1998); G. Peris, J. Planelles, J.-P. Malrieu, and J. Paldus, J. Chem. Phys. **110**, 11 708 (1999).
69. L. Stolarczyk, Chem. Phys. Lett. **217**, 1 (1994).
70. J. Paldus and X. Li, *Electron Correlation in Small Molecules: Grafting CI onto CC.* In: P. Surján (Ed.) *Correlation and Localization*, Series in: *Topics in Current Chemistry*, Vol. 203. (Springer, Berlin, 1999), pp. 1–20; X. Li and J. Paldus, *Simultaneous Account of Dynamic and Nondynamic Correlations Based on Complementarity of CI and CC Approaches.* In: M. R. Hoffmann and K. G. Dyall (Eds.) *Low-Lying Potential Energy Surfaces*, ACS Symposium Series No. 828 (ACS Books, Washington, 2002), pp. 10–30.
71. X. Li and J. Paldus, J. Chem. Phys. **119**, 5334 (2003).
72. L. Meissner and I. Grabowski, Chem. Phys. Lett. **300**, 53 (1999).
73. L. Meissner and M. Nooijen, Chem. Phys. Lett. **316**, 501 (2000).
74. L. Meissner, J. Gryniaków, and I. Hubač, Chem. Phys. Lett. **397**, 34 (2004).
75. H. Meißner and E. O. Steinborn, Int. J. Quantum Chem. **63**, 257 (1997); H. Meißner and J. Paldus, J. Chem. Phys. **113**, 2594, 2612, 2622 (2000); H. Meißner and J. Paldus, Coll. Czech. Chem. Commun. **66**, 1164 (2001) and references therein.
76. L. Meissner, S. A. Kucharski, and R. J. Bartlett, J. Chem. Phys. **91**, 6187 (1989).
77. L. Meissner and R. J. Bartlett, J. Chem. Phys. **92**, 561 (1990).
78. I. Hubač, *Size Extensive Brillouin-Wigner Coupled-Cluster Theory.* In: A. Tsipis, V. S. Popov, D. R. Herschbach, and J. S. Avery (Eds.) *New Methods in Quantum*

Theory, NATO ASI Series, Series 3: High Technology, Vol. 8. (Kluwer, Dordrecht, 1996), pp. 183-202.
79. J. Mášik and I. Hubač, Adv. Quantum Chem. **31**, 75 (1999) and references therein.
80. J. Pittner, P. Nachtigall, P. Čársky, J. Mášik, and I. Hubač, J. Chem. Phys. **110**, 10 275 (1999); I. Hubač and S. Wilson, J. Phys. B **33**, 365 (2000); I. Hubač, J. Pittner, and P. Čársky, J. Chem. Phys. **112**, 8779 (2000).
81. J. Pittner, O. Demel, P. Čársky, and I. Hubač, Int. J. Mol. Sci. **2**, 281 (2002); J. Pittner, P. Čársky, and I. Hubač, Int. J. Quantum Chem. **90**, 1031 (2002); J. Pittner, J. Šmydke, P. Čársky, and I. Hubač, J. Mol. Struct. (Theochem) **547**, 239 (2001); J. C. Sancho-García, J. Pittner, P. Čársky, and I. Hubač, J. Chem. Phys. **112**, 8785 (2000); J. Pittner, P. Nachtigall, P. Čársky, and I. Hubač, J. Phys. Chem. A **105**, 1354 (2001); I. S. K. Kerkines, J. Pittner, P. Čársky, A. Mavridis, and I. Hubač, J. Chem. Phys. **117**, 9733 (2002); J. Pittner, J. Chem. Phys. **118**, 10 876 (2003).
82. X. Li and J. Paldus, J. Chem. Phys. **115**, 5759 (2001).
83. X. Li and J. Paldus, J. Chem. Phys. **115**, 5774 (2001).
84. J. Paldus, *Hartree-Fock Stability and Symmetry Breaking.* In: R. Carbó and M. Klobukowski (Eds.) *Self-Consistent Field: Theory and Applications* (Elsevier, Amsterdam, 1990), pp. 1–45.
85. J. L. Stuber and J. Paldus, *Symmetry Breaking in the Independent Particle Model.* In: E. J. Brändas and E. S. Kryachko (Eds.) *Fundamental World of Quantum Chemistry, A Tribute Volume to the Memory of Per-Olov Löwdin*, Vol. 1. (Kluwer, Dordrecht, 2003), pp. 67–139.
86. P. Piecuch, R. Toboła, and J. Paldus, Phys. Rev. A **54**, 1210 (1996).
87. X. Li and J. Paldus, J. Chem. Phys. **107**, 6257 (1997).
88. X. Li and J. Paldus, J. Chem. Phys. **108**, 637 (1998).
89. Chem. Phys. Lett. **286**, 145 (1998); Coll. Czech. Chem. Commun. **63**, 1381 (1998); J. Chem. Phys. **110**, 2844 (1999).
90. X. Li and J. Paldus, Mol. Phys. **98**, 1185 (2000); Int. J. Quantum Chem. **80**, 743 (2000); X. Li, J. Mol. Struct. (Theochem) **547**, 69 (2001).
91. X. Li and J. Paldus, J. Chem. Phys. **113**, 9966 (2000).
92. X. Li and J. Paldus, J. Chem. Phys. **117**, 1941 (2002); **118**, 2470 (2003); J. Paldus and X. Li, Coll. Czech. Chem. Commun. **68**, 554 (2003).
93. J. Paldus, M. Takahashi, and R. W. H. Cho, Phys. Rev. B **30**, 4267 (1984).
94. J. Paldus and M. J. Boyle, Int. J. Quantum Chem. **22**, 1281 (1982).
95. J. Paldus, J. Čížek, and M. Takahashi, Phys. Rev. A **30**, 2193 (1984).
96. R. A. Chiles and C. E. Dykstra, Chem. Phys. Lett. **80**, 69 (1981); S. M. Bachrach, R. A. Chiles, and C. E. Dykstra, J. Chem. Phys. **75**, 2270 (1981); C. E. Dykstra, S.-Y. Liu, M. F. Daskalakis, J. P. Lucia, and M. Takahashi, Chem. Phys. Lett. **137**, 266 (1987); C. E. Dykstra and E. R. Davidson, Int. J. Quantum Chem. **78**, 226 (2000).
97. C. E. Dykstra, *Ab Initio Calculation of the Structure and Properties of Molecules* (Elsevier, Amsterdam, 1988).
98. S. A. Kucharski and R. J. Bartlett, J. Chem. Phys. **95**, 8227 (1991); A. Balková, S. A. Kucharski and R. J. Bartlett, Chem. Phys. Lett. **182**, 511 (1991); P. G. Szalay and R. J. Bartlett, J. Chem. Phys. **101**, 4936 (1994).
99. U. S. Mahapatra, B. Datta, and D. Mukherjee, Mol. Phys. **94**, 157 (1998); Chem. Phys. Lett. **299**, 42 (1999); U. S. Mahapatra, B. Datta, B. Bandyopadhyay, and D. Mukherjee, Adv. Quantum Chem. **30**, 163 (1998).
100. U. S. Mahapatra, B. Datta, and D. Mukherjee, J. Chem. Phys. **110**, 6171 (1999).
101. J. Paldus, P. Piecuch, L. Pylypow, and B. Jeziorski, Phys. Rev. A **47**, 2738 (1993); P. Piecuch and J. Paldus, Phys. Rev. A **49**, 3479 (1994).

102. S. A. Kucharski, A. Balková, and R. J. Bartlett, Theor. Chim. Acta **80**, 321 (1991).
103. P. Piecuch and J. Paldus, J. Chem. Phys. **101**, 5875 (1994).
104. A. Balková, S. A. Kucharski, L. Meissner, and R. J. Bartlett, Theor. Chim. Acta **80**, 335 (1991).
105. J. Pittner, X. Li, and J. Paldus, Mol. Phys. Vol. 103, 2239 (2005).

NONITERATIVE COUPLED-CLUSTER METHODS FOR EXCITED ELECTRONIC STATES

PIOTR PIECUCH[1,2], MARTA WŁOCH, MARICRIS LODRIGUITO AND JEFFREY R. GOUR
Department of Chemistry, Michigan State University, East Lansing, MI 48824, USA

Abstract. New classes of noniterative coupled-cluster (CC) methods, which improve the results of the standard equation-of-motion (EOM) and response CC calculations for excited states dominated by two-electron transitions and excited-state potential energy surfaces along bond breaking coordinates, are reviewed. All of the methods discussed in this article are derived from the method of moments of CC equations (MMCC) and all of them are characterized by the relatively low computer costs which are similar to those characterizing the popular ground-state CCSD(T) theory. Three types of approaches are discussed: (i) the externally corrected MMCC approaches employing the configuration interaction and multi-reference perturbation theory wave functions, (ii) the completely renormalized EOMCC methods, including their most recent extension to excited states of radicals and other open-shell systems, and (iii) the new classes of MMCC and completely renormalized EOMCC theories employing the left eigenstates of the similarity-transformed Hamiltonian used in CC/EOMCC theory.

1. Introduction

The single-reference coupled cluster (CC) theory [1–5] has become a standard computational tool for studying ground-state molecular properties [6–10]. The basic approximations, such as CCSD (coupled cluster singles and doubles approach) [11–15], and the noniterative CCSD[T] [16, 17] and CCSD(T) [18] methods, in which the cleverly designed corrections due to

[1]Corresponding author. E-mail address: piecuch@cem.msu.edu.
[2]Also at: Department of Physics and Astronomy, Michigan State University, East Lansing, MI 48824, USA.

J.-P. Julien et al. (eds.),
Recent Advances in the Theory of Chemical and Physical Systems, 45–106.

triple excitations are added to the CCSD energy, can be routinely applied to molecules containing dozens of light atoms, several transition metal atoms, hundreds of electrons, and hundreds or even thousands of basis functions (see, e.g., Refs. [19, 20]). The CCSD(T) method is currently available in the majority of popular quantum chemistry software packages, enabling highly accurate *ab initio* calculations of useful molecular properties by experts as well as non-experts.

One of the biggest challenges in CC theory is the development of highly accurate and affordable methods for excited electronic states that would match the ease of applicability characterizing the ground-state CCSD and CCSD(T) approaches. The most promising candidates in this area are the linear-response CC theory [21–25] and the closely related equation-of-motion CC (EOMCC) [26–29] and symmetry-adapted cluster configuration interaction (SAC-CI) [30–34] methods. For example, the linear response CCSD [24, 25] and EOMCCSD [26–28] approximations, which are characterized by the manageable computational steps that scale as $\mathcal{N}^6$ with the system size, provide reliable information about excited states dominated by one-electron transitions. The problem is that the linear response CCSD and EOMCCSD methods cannot describe excited states having significant double excitation components and excited-state potential energy surfaces along bond beaking coordinates [35–54]. High-level EOMCC methods including higher–than–double excitations, such as the recently implemented full EOMCCSDT (EOMCC singles, doubles, and triples) [43, 44, 55, 56] and EOMCCSDTQ (EOMCC singles, doubles, triples, and quadruples) [46, 57] approaches, provide an excellent description of excited states dominated by doubles [43, 44, 46, 49] and excited-state potential energy surfaces [44], but large costs of the EOMCCSDT and EOMCCSDTQ calculations, which are defined by the iterative steps that scale as $\mathcal{N}^8$ and $\mathcal{N}^{10}$ with the system size, respectively, limit their applicability to small molecules with 2–3 light atoms and relatively small basis sets (the EOMCC schemes with up to pentuple and even hextuple excitations have been implemented too [57], but the $\mathcal{N}^{12}$ and $\mathcal{N}^{14}$ scalings of the resulting EOMCCSDTQP and EOMCCSDTQPH methods with the system size make these approaches completely impractical, since problems that one can tackle with such approaches are of the type of problems that can be handled by the full configuration interaction theory; moreover, the role of higher–than–quadruple excitations in the EOMCC calculations of interest in chemistry is virtually none [57]). Other, less expensive, ways of incorporating triple or triple and quadruple excitations in the EOMCC or linear response CC formalisms must be developed in order to make these methods applicable to a wide range of molecular problems and excited states dominated by either one- or two-electron transitions.

In order to improve the accuracy of EOMCCSD or linear response CCSD calculations in applications involving states having significant doubly excited contributions, while keeping the computer costs at the reasonably low level, a few iterative and noniterative EOMCC and linear response CC approximations including triple excitations have been proposed. The examples are the iterative EOMCCSDT-n approaches and their noniterative EOMCCSD(T), EOMCCSD($\tilde{\text{T}}$), and EOMCCSD(T$'$) counterparts [35, 36] or the linear-response CC methods such as CC3 [38–41] and CCSDR(3) [40, 41], which use elements of many-body perturbation theory (MBPT) to estimate triples effects. All of these methods are characterized by the relatively inexpensive $\mathcal{N}^7$ steps and all of them improve the EOMCCSD/linear response CCSD results for excited states dominated by two-electron transitions, but there are many cases where the results of EOMCCSDT-n, EOMCCSD(T), CC3, and similar calculations are far from satisfactory. This can be illustrated by the large 0.4–0.5 and 0.9 eV errors in the description of the lowest $^1\Pi_g$ and $^1\Delta_g$ states of the C_2 molecule, respectively, by the EOMCCSDT-1 and CC3 approaches [41] or the failure of the CC3 and CCSDR(3) methods to provide accurate information about excited-state potential energy surfaces along bond breaking coordinates [58] (cf., also, Ref. 51 for an additional analysis). Problems encountered in the EOMCCSDT-n, EOMCCSD(T), CC3, and similar calculations, when excited states dominated by doubles and excited-state potential energy surfaces are examined, should not come as a surprise. Similar failures are observed in the ground-state CCSD(T) calculations. The CCSD(T) method works well for closed-shell molecules near the equilibrium geometries, but it completely fails when chemical bonds are stretched or broken (see, e.g., Refs. 8, 49, 50, 52, and references therein). As is the case with the ground-state CCSD(T) approach, the EOMCC/response CC methods of the EOMCCSDT-n, EOMCCSD(T), or CC3 type are based on the conventional arguments originating from MBPT and these arguments do not apply to quasi-degenerate situations, such as bond breaking or excited states dominated by two-electron transitions. We can improve the results for excited states dominated by doubles and excited-state potential energy surfaces by switching to the recently developed active-space variant of the full EOMCCSDT approach, in which the leading triples contributions of the EOMCCSDT method are selected with the help of active orbitals, reducing the computer costs of full EOMCCSDT calculations quite substantially if the number of active orbitals is small [42–44], but it is desirable to explore alternative approaches, which would combine the ease-of-use of the noniterative single-reference CC/EOMCC approximations, such as CCSD(T) or EOMCCSD(T), with the effectiveness with which the expensive full EOMCCSDT or EOMCCSDTQ approaches handle excited states dominated by doubles and excited-state potential energy surfaces.

In the last three years, we have demonstrated that an excellent description of excited states dominated by double excitations and, to a large extent, excited-state potential energy surfaces along bond breaking coordinates can be obtained by using the completely renormalized (CR) EOMCCSD(T) approaches [49, 51–53, 59, 60] or one of the externally corrected variants of the excited-state generalization of the method of moments of CC equations (MMCC) [47–50, 52] (see Refs. [61–63] for the original papers on MMCC theory for ground electronic states). The CR-EOMCCSD(T) and other MMCC methods are based on a simple idea of improving the EOMCCSD or other EOMCC energies through the use of the suitably designed noniterative corrections due to triples or triples and quadruples that utilize the concept of the generalized moments of CC/EOMCC equations rather than the usual MBPT arguments exploited in the standard CCSD(T)/EOMCCSD(T), EOMCCSDT-n, CC3, and similar approaches. The CR-EOMCCSD(T) and other excited-state MMCC methods preserve the relatively low, $\mathcal{N}^6 - \mathcal{N}^7$-like, costs of the noniterative methods of the CCSD(T)/EOMCCSD(T) type, while providing considerable improvements in the EOMCCSD results and in the results of the EOMCCSDT-n, EOMCCSD(T), CC3, and similar calculations [47–53, 59, 60, 64].

As in the case of the ground-state MMCC and CR-CC methods [49, 50, 52, 61–63, 65–77], the key to a successful description of excited states by the CR-EOMCCSD(T) and other MMCC methods is the very good control of accuracy that all of these methods offer by directly addressing the quantity of interest, which is the difference between the exact, full CI, and EOMCC (e.g., EOMCCSD) energies. The MMCC formalism provides us with precise information about the many-body structure of these differences, suggesting several useful types of noniterative corrections to EOMCCSD or other EOMCC energies.

The purpose of the present paper is to review the most essential elements of the excited-state MMCC theory and various approximate methods that result from it, including the aforementioned CR-EOMCCSD(T) [49, 51, 52, 59] and externally corrected MMCC [47–50, 52] approaches. In the discussion of approximate methods, we focus on the MMCC corrections to EOMCCSD energies due to triple excitations, since these corrections lead to the most practical computational schemes. Although some of the excited-state MMCC methods have already been described in our earlier reviews [49, 50, 52], it is important that we update our earlier work by the highly promising new developments that have not been mentioned before. For example, since the last review [52], we have successfully extended the CR-EOMCCSD(T) methods to excited states of radicals and other open-shell systems [59]. We have also developed a new type of the externally cor-

rected excited-state MMCC methods employing inexpensive multi-reference MBPT (MRMBPT) wave functions in the design of noniterative corrections to EOMCCSD energies [78]. Finally, we have started exploring an entirely new idea of utilizing the left eigenstates of the CC/EOMCC similarity-transformed Hamiltonian (the CC/EOMCC "bra" wave functions) in the process of designing the noniterative MMCC corrections [79] and obtained the first evidence how accurate the CR-EOMCCSD(T) methods are in calculations of properties other than energy [59]. All of these new developments are discussed in the present review, along with the systematic description of other, more established, excited-state MMCC methods described in the earlier work.

2. Generalization of the method of moments of coupled-cluster equations to excited electronic states: Exact formalism

The key idea of the single-reference MMCC formalism [47–50, 52, 61–63] (cf. Refs. [80–82] for a multi-reference extension) is that of the state-selective, noniterative energy corrections

$$\delta_\mu^{(A)} \equiv E_\mu - E_\mu^{(A)}, \tag{1}$$

which, when added to the energies of ground ($\mu = 0$) and excited ($\mu > 0$) states, $E_\mu^{(A)}$, obtained in the standard CC/EOMCC calculations, such as CCSD/EOMCCSD, CCSDT/EOMCCSDT, etc. (designated here as method A), recover the corresponding exact, i.e. full CI, energies E_μ. The main goal of all approximate MMCC calculations, including the CR-EOMCCSD(T) [49, 51, 52, 59] approaches, the MMCC and CR-EOMCCSD(T) methods employing the left eigenstates of the similarity-transformed Hamiltonian [79], and the CI-corrected [47–50, 52] and MRMBPT-corrected [78] MMCC methods for excited electronic states discussed in this work, is to approximate corrections $\delta_\mu^{(A)}$, such that the resulting MMCC energies, defined as

$$E_\mu^{(\mathrm{MMCC})} = E_\mu^{(A)} + \delta_\mu^{(A)}, \tag{2}$$

are close to the corresponding full CI energies E_μ.

All ground- and excited-state MMCC approximations are obtained from the rigorous formulas for the exact corrections $\delta_\mu^{(A)}$ in terms of the generalized moments of CC/EOMCC equations, derived by Kowalski and Piecuch in Refs. [47, 61, 62] (cf., also, Refs. 49, 79). Since the proper introduction of these formulas requires an understanding of the underlying CC/EOMCC theory, we begin the discussion of the excited-state MMCC formalism with the key ingredients of the single-reference CC/EOMCC theory.

2.1. BASIC ELEMENTS OF COUPLED-CLUSTER AND EQUATION-OF-MOTION COUPLED-CLUSTER METHODS

The single-reference CC theory is based on the exponential ansatz for the ground-state wave function,

$$| \Psi_0\rangle = | \Psi_0^{(\mathrm{CC})}\rangle \equiv e^T | \Phi\rangle, \tag{3}$$

where T is the cluster operator (a particle-hole excitation operator) and $| \Phi\rangle$ is the reference determinant (often, the Hartree-Fock determinant). In all standard CC approximations, we truncate the many-body expansion for the cluster operator T at a given excitation level $m_A < N$, where N is the number of correlated electrons in a system. An example of the standard CC approximation is the CCSD method. In this case, $m_A = 2$ and the cluster operator T is approximated by

$$T^{(\mathrm{CCSD})} = T_1 + T_2, \tag{4}$$

where

$$T_1 = t_a^i a^a a_i \tag{5}$$

and

$$T_2 = \tfrac{1}{4}\, t_{ab}^{ij} a^a a^b a_j a_i \tag{6}$$

are the singly and doubly excited cluster components, t_a^i and t_{ab}^{ij} are the corresponding singly and doubly excited cluster amplitudes, $i, j, \ldots$ $(a, b, \ldots)$ are the single-particle states (spin-orbitals) occupied (unoccupied) in the reference determinant $|\Phi\rangle$, and a^p (a_p) are the usual creation (annihilation) operators associated with the orthonormal spin-orbitals $|p\rangle$. Here and elsewhere in the present paper, we use the Einstein summation convention over repeated upper and lower indices, so that the summation symbols corresponding to unrestricted summations over occupied and/or unoccupied spin-orbitals are omitted. The general form of the truncated cluster operator defining a standard CC approximation A, characterized by the excitation level m_A, is

$$T^{(A)} = \sum_{n=1}^{m_A} T_n, \tag{7}$$

where

$$T_n = \left(\frac{1}{n!}\right)^2 t_{a_1 \ldots a_n}^{i_1 \ldots i_n}\, a^{a_1} \cdots a^{a_n} a_{i_n} \cdots a_{i_1} \tag{8}$$

$(n = 1, \ldots, m_A)$ are the many-body components of $T^{(A)}$ and $t_{a_1 \ldots a_n}^{i_1 \ldots i_n}$ are the corresponding cluster amplitudes. The cluster amplitudes $t_{a_1 \ldots a_n}^{i_1 \ldots i_n}$ are determined by solving a coupled system of nonlinear and energy-independent

algebraic equations of the form:

$$\langle \Phi^{a_1\ldots a_n}_{i_1\ldots i_n}|\bar{H}^{(A)}|\Phi\rangle = 0, \;\; i_1 < \cdots < i_n, \;\; a_1 < \cdots < a_n, \tag{9}$$

where $n = 1, \ldots, m_A$,

$$\bar{H}^{(A)} = e^{-T^{(A)}} H e^{T^{(A)}} = (H e^{T^{(A)}})_C \tag{10}$$

is the similarity-transformed Hamiltonian of the CC/EOMCC theory, subscript C designates the connected part of the corresponding operator expression, and $|\Phi^{a_1\ldots a_n}_{i_1\ldots i_n}\rangle \equiv a^{a_1}\cdots a^{a_n} a_{i_n}\cdots a_{i_1}|\Phi\rangle$ are the n-tuply excited determinants relative to $|\Phi\rangle$. In particular, the standard CCSD equations for the singly and doubly excited cluster amplitudes t^i_a and t^{ij}_{ab}, defining T_1 and T_2, respectively, can be written as

$$\langle \Phi^a_i|\bar{H}^{(\mathrm{CCSD})}|\Phi\rangle = 0, \tag{11}$$

$$\langle \Phi^{ab}_{ij}|\bar{H}^{(\mathrm{CCSD})}|\Phi\rangle = 0, \quad i < j, \; a < b, \tag{12}$$

where

$$\bar{H}^{(\mathrm{CCSD})} = e^{-T^{(\mathrm{CCSD})}} H e^{T^{(\mathrm{CCSD})}} = (H e^{T^{(\mathrm{CCSD})}})_C \tag{13}$$

is the similarity-transformed Hamiltonian of the CCSD/EOMCCSD approach. The explicit and computationally efficient form of these and other equations used in CC calculations, in terms of one- and two-body matrix elements of the Hamiltonian in the normal-ordered form, $f^q_p \equiv \langle p|f|q\rangle$ and $v^{rs}_{pq} \equiv \langle pq|v|rs\rangle - \langle pq|v|sr\rangle$, respectively, where f is the Fock operator and v is the electron-electron repulsion term, and cluster amplitudes $t^{i_1\cdots i_n}_{a_1\ldots a_n}$ or, in the CCSD ($m_A = 2$) case, t^i_a and t^{ij}_{ab}, can be derived by applying diagrammatic techniques of many-body theory combined with diagram factorization methods which yield highly vectorized computer codes [59, 70, 83]. Once the system of equations, Eq. (9), is solved for $T^{(A)}$ or $t^{i_1\cdots i_n}_{a_1\ldots a_n}$ (or Eqs. (11) and (12) are solved for T_1 and T_2 or t^i_a and t^{ij}_{ab}), the CC energy corresponding to the standard method A is calculated using the equation

$$E^{(A)}_0 = \langle \Phi|\bar{H}^{(A)}|\Phi\rangle \equiv \langle \Phi|\bar{H}^{(A)}_{\mathrm{closed}}|\Phi\rangle, \tag{14}$$

where $\bar{H}^{(A)}_{\mathrm{closed}}$ is a "closed" part of $\bar{H}^{(A)}$ which is represented by those diagrams contributing to $\bar{H}^{(A)}$ that have no external (uncontracted) Fermion lines (as opposed to the "open" part of $\bar{H}^{(A)}$ which is represented by the diagrams having external or uncontracted Fermion lines).

The ground-state CC theory has a natural extension to excited electronic states $|\Psi_\mu\rangle$ via the EOMCC or linear response CC method, in which we write

$$|\Psi_\mu\rangle = |\Psi^{(\mathrm{CC})}_\mu\rangle \equiv R_\mu e^T|\Phi\rangle, \tag{15}$$

where T is obtained in the ground-state CC calculations and R_μ is a linear particle-hole excitation operator similar to T obtained by diagonalizing the similarity-transformed Hamiltonian $\bar{H} = e^{-T} H e^{T}$. As in the ground-state case, the standard EOMCC approximations are obtained by truncating the many-body expansion for the excitation operator R_μ at a given excitation level $m_A < N$, which is the same as the excitation level used to define the truncated form of T. Thus, in the EOMCCSD theory, which is a basic EOMCC approximation where m_A is set at 2, we write

$$R_\mu^{(\mathrm{CCSD})} = R_{\mu,0} + R_{\mu,1} + R_{\mu,2}, \tag{16}$$

where

$$R_{0,\mu} = r_0(\mu)\,\mathbf{1}, \tag{17}$$

$$R_{\mu,1} = r_a^i(\mu)\,a^a a_i, \tag{18}$$

and

$$R_{\mu,2} = \tfrac{1}{4}\,r_{ab}^{ij}(\mu)\,a^a a^b a_j a_i \tag{19}$$

are the reference, one-body, and two-body components of $R_\mu^{(\mathrm{CCSD})}$, and $r_0(\mu)$, $r_a^i(\mu)$, and $r_{ab}^{ij}(\mu)$ are the corresponding excitation amplitudes ($\mathbf{1}$ in Eq. (17) is a unit operator). In general, when T is approximated by $T^{(A)}$, Eq. (7), the corresponding excitation operator R_μ defining the EOMCC method A is approximated by

$$R_\mu^{(A)} = R_{\mu,0}^{(A)} + R_{\mu,\mathrm{open}}^{(A)}, \tag{20}$$

where the "open" part of $R_\mu^{(A)}$ is defined as

$$R_{\mu,\mathrm{open}}^{(A)} = \sum_{n=1}^{m_A} R_{\mu,n}, \tag{21}$$

with

$$R_{\mu,n} = \left(\frac{1}{n!}\right)^2 r_{a_1\ldots a_n}^{i_1\ldots i_n}(\mu)\,a^{a_1}\cdots a^{a_n} a_{i_n}\cdots a_{i_1} \tag{22}$$

representing the n-body components of $R_\mu^{(A)}$. The excitation amplitudes $r_{a_1\ldots a_n}^{i_1\ldots i_n}(\mu)$ defining $R_{\mu,\mathrm{open}}^{(A)}$ are obtained by solving the eigenvalue problem involving the similarity-transformed Hamiltonian $\bar{H}^{(A)}$ in the space spanned by the excited determinants $|\Phi_{i_1\ldots i_n}^{a_1\ldots a_n}\rangle$ with $n = 1, \ldots, m_A$, i.e.

$$\begin{aligned} \langle \Phi_{i_1\ldots i_n}^{a_1\ldots a_n} | (\bar{H}_{\mathrm{open}}^{(A)}\, R_{\mu,\mathrm{open}}^{(A)})_C | \Phi \rangle \;&=\; \omega_\mu^{(A)}\, r_{a_1\ldots a_n}^{i_1\ldots i_n}(\mu), \\ &\quad i_1 < \cdots < i_n,\;\; a_1 < \cdots < a_n, \end{aligned} \tag{23}$$

where

$$\bar{H}^{(A)}_{\rm open} = \bar{H}^{(A)} - \bar{H}^{(A)}_{\rm closed} = \bar{H}^{(A)} - E^{(A)}_0\,\mathbf{1} \tag{24}$$

is the "open" part of $\bar{H}^{(A)}$, represented by the diagrams of $\bar{H}^{(A)}$ that have external Fermion lines, and

$$\omega^{(A)}_\mu = E^{(A)}_\mu - E^{(A)}_0 \tag{25}$$

is the vertical excitation energy obtained with the EOMCC method A. In particular, the $r^i_a(\mu)$, and $r^{ij}_{ab}(\mu)$ amplitudes of the EOMCCSD theory and the corresponding excitation energies $\omega^{(\rm CCSD)}_\mu$ are obtained by diagonalizing the similarity-transformed Hamiltonian $\bar{H}^{(\rm CCSD)}$, Eq. (13), in the relatively small space of singly and doubly excited determinants $|\Phi^a_i\rangle$ and $|\Phi^{ab}_{ij}\rangle$. Equation (23) alone does not provide information about the coefficient $r_0(\mu)$ at the reference determinant $|\Phi\rangle$ in the corresponding EOMCC wave function $R^{(A)}_\mu e^{T^{(A)}}|\Phi\rangle$. This coefficient can be determined *a posteriori* using the equation

$$r_0(\mu) = \langle\Phi|(\bar{H}^{(A)}_{\rm open}\,R^{(A)}_{\mu,{\rm open}})_C|\Phi\rangle/\omega^{(A)}_\mu, \tag{26}$$

once the excitation amplitudes $r^{i_1\ldots i_n}_{a_1\ldots a_n}(\mu)$ defining $R^{(A)}_{\mu,{\rm open}}$ are known. For consistency of our presentation, we use the notation in which $\mu > 0$ means that we are dealing with excited states, whereas $\mu = 0$ corresponds to the ground-state problem. In particular, the excitation operator $R^{(A)}_\mu$ is formally defined as a unit operator when $\mu = 0$, i.e. $r_0(\mu = 0) = 1$ and $r^{i_1\ldots i_n}_{a_1\ldots a_n}(\mu = 0) = 0$ for $n \geq 1$, so that the EOMCC ansatz, Eq. (15), reduces to the ground-state CC ansatz, Eq. (3), in the ground-state, $\mu = 0$, case. With this definition of $R^{(A)}_{\mu=0}$, the EOMCC system of equations, Eq. (23), formally reduces to the standard system of the ground-state CC equations, Eq. (9), although we must, of course, remember that in the EOMCC calculations of excited states employing Eq. (23) we only solve for the excitation operator $R^{(A)}_\mu$ (or, for the corresponding excitation amplitudes $r^{i_1\ldots i_n}_{a_1\ldots a_n}(\mu)$) using the given values of cluster amplitudes $t^{i_1\ldots i_n}_{a_1\ldots a_n}$ defining the cluster operator $T^{(A)}$, obtained in the corresponding ground-state CC calculations that precede the excited-state EOMCC calculations.

The similarity-transformed Hamiltonians $\bar{H}^{(A)}$ or $\bar{H}^{(\rm CCSD)}$ are not hermitian, so that in addition to the right eigenstates $R^{(A)}_\mu|\Phi\rangle$ or $R^{(\rm CCSD)}_\mu|\Phi\rangle$, which define the "ket" CC/EOMCC or CCSD/EOMCCSD wave functions, we can also determine the left eigenstates of $\bar{H}^{(A)}$ or $\bar{H}^{(\rm CCSD)}$, $\langle\Phi|L^{(A)}_\mu$ or $\langle\Phi|L^{(\rm CCSD)}_\mu$, respectively, which define the corresponding "bra" CC/EOMCC or CCSD/EOMCCSD wave functions

$$\langle\tilde{\Psi}^{(\rm CC)}_\mu| = \langle\Phi|L_\mu e^{-T} \tag{27}$$

that match the "ket" states given by Eq. (15). Here, L_μ (in approximate methods, $L_\mu^{(A)}$ or $L_\mu^{(\mathrm{CCSD})}$) is a hole-particle deexcitation operator, so that, for example,

$$L_\mu^{(\mathrm{CCSD})} = L_{\mu,0} + L_{\mu,1} + L_{\mu,2}, \tag{28}$$

where

$$L_{0,\mu} = l_0(\mu)\,\mathbf{1}, \tag{29}$$

$$L_{\mu,1} = l_i^a(\mu)\,a^i a_a, \tag{30}$$

and

$$L_{\mu,2} = \tfrac{1}{4}\,l_{ij}^{ab}(\mu)\,a^i a^j a_b a_a \tag{31}$$

are the reference, one-body, and two-body components of $L_\mu^{(\mathrm{CCSD})}$, and $l_0(\mu)$, $l_i^a(\mu)$, and $l_{ij}^{ab}(\mu)$ are the corresponding deexcitation amplitudes. The right and left eigenstates of $\bar{H}^{(\mathrm{CCSD})}$ form a biorthonormal set,

$$\langle\Phi|L_\mu^{(\mathrm{CCSD})}\,R_\nu^{(\mathrm{CCSD})}|\Phi\rangle = \delta_{\mu,\nu}, \tag{32}$$

where $\delta_{\mu,\nu}$ is the usual Kronecker delta, so that the coefficient $l_0(\mu)$ at $\langle\Phi|$ in the left CCSD/EOMCCSD eigenstate $\langle\Phi|L_\mu^{(\mathrm{CCSD})}$ satisfies

$$l_0(\mu) = \delta_{\mu,0}, \tag{33}$$

meaning that $l_0(\mu) = 0$ in the excited-state ($\mu > 0$) case. In general, the deexcitation operators $L_\mu^{(A)}$ generating the left eigenstates of the similarity-transformed Hamiltonian $\bar{H}^{(A)}$, $\langle\Phi|L_\mu^{(A)}$, can be written as

$$L_\mu^{(A)} = L_{\mu,0}^{(A)} + L_{\mu,\mathrm{open}}^{(A)}, \tag{34}$$

where the "open" part of $L_\mu^{(A)}$ is defined as

$$L_{\mu,\mathrm{open}}^{(A)} = \sum_{n=1}^{m_A} L_{\mu,n}, \tag{35}$$

with

$$L_{\mu,n} = \left(\frac{1}{n!}\right)^2 l_{i_1\ldots i_n}^{a_1\ldots a_n}(\mu)\,a^{i_1}\cdots a^{i_n}a_{a_n}\cdots a_{a_1} \tag{36}$$

representing the n-body components of $L_\mu^{(A)}$. As in the CCSD case, the left and right eigenstates of $\bar{H}^{(A)}$, $\langle\Phi|L_\mu^{(A)}$ and $R_\mu^{(A)}|\Phi\rangle$, respectively, form a biorthonormal set,

$$\langle\Phi|L_\mu^{(A)}\,R_\nu^{(A)}|\Phi\rangle = \delta_{\mu,\nu}, \tag{37}$$

and the zero-body part of $L_\mu^{(A)}$ satisfies

$$L_{\mu,0}^{(A)} = \delta_{\mu,0}\,\mathbf{1}, \tag{38}$$

i.e. $L_{\mu,0}^{(A)}$ vanishes for excited states ($\mu > 0$), while being equal to the unit operator in the ground-state ($\mu = 0$) case. The deexcitation amplitudes $l_{i_1\ldots i_n}^{a_1\ldots a_n}(\mu)$ defining $L_{\mu,\mathrm{open}}^{(A)}$ are obtained by solving the left eigenvalue problem involving the similarity-transformed Hamiltonian $\bar{H}^{(A)}$ in the space spanned by the excited determinants $|\Phi_{i_1\ldots i_n}^{a_1\ldots a_n}\rangle$ with $n = 1, \ldots, m_A$,

$$\begin{aligned}\delta_{\mu,0}\,\langle\Phi|\bar{H}_{\mathrm{open}}^{(A)}|\Phi_{i_1\ldots i_n}^{a_1\ldots a_n}\rangle + \langle\Phi|L_{\mu,\mathrm{open}}^{(A)}\bar{H}_{\mathrm{open}}^{(A)}|\Phi_{i_1\ldots i_n}^{a_1\ldots a_n}\rangle &= \omega_\mu^{(A)}\, l_{i_1\ldots i_n}^{a_1\ldots a_n}(\mu),\\ i_1 < \cdots < i_n,\;\; a_1 < \cdots < a_n,&\end{aligned} \tag{39}$$

where $\omega_\mu^{(A)}$ is the vertical excitation energy, Eq. (25), and where we already used Eq. (38). In particular,

$$\begin{aligned}\langle\Phi|L_{\mu,\mathrm{open}}^{(A)}\bar{H}_{\mathrm{open}}^{(A)}|\Phi_{i_1\ldots i_n}^{a_1\ldots a_n}\rangle &= \omega_\mu^{(A)}\, l_{i_1\ldots i_n}^{a_1\ldots a_n}(\mu),\\ i_1 < \cdots < i_n,\;\; a_1 < \cdots < a_n,&\end{aligned} \tag{40}$$

in the excited-state ($\mu > 0$) case. When the ground-state ($\mu = 0$) case is considered, we usually write

$$L_0^{(A)} = \mathbf{1} + \Lambda^{(A)}, \tag{41}$$

where

$$\Lambda^{(A)} = \sum_{n=1}^{m_A} \Lambda_n \equiv L_{0,\mathrm{open}}^{(A)}, \tag{42}$$

with

$$\Lambda_n = \left(\frac{1}{n!}\right)^2 \lambda_{i_1\ldots i_n}^{a_1\ldots a_n}\, a^{i_1}\cdots a^{i_n} a_{a_n}\cdots a_{a_1}, \tag{43}$$

represents the well-known "lambda" operator of the analytic gradient CC theory [84]. The ground-state deexcitation amplitudes $\lambda_{i_1\ldots i_n}^{a_1\ldots a_n} \equiv l_{i_1\ldots i_n}^{a_1\ldots a_n}(0)$ that define the $\Lambda^{(A)}$ operator are obtained by solving the following system of linear equations (cf. Eq. (39)):

$$\begin{aligned}\langle\Phi|\bar{H}_{\mathrm{open}}^{(A)}|\Phi_{i_1\ldots i_n}^{a_1\ldots a_n}\rangle + \langle\Phi|\Lambda^{(A)}\,\bar{H}_{\mathrm{open}}^{(A)}|\Phi_{i_1\ldots i_n}^{a_1\ldots a_n}\rangle &= 0,\\ i_1 < \cdots < i_n,\;\; a_1 < \cdots < a_n.&\end{aligned} \tag{44}$$

The CCSD/EOMCCSD equations for the deexcitation amplitudes $l_i^a(\mu)$, $l_{ij}^{ab}(\mu)$, $\lambda_i^a \equiv l_i^a(0)$, and $\lambda_{ij}^{ab} \equiv l_{ij}^{ab}(0)$ are obtained by setting $m_A = 2$ in Eqs. (40) and (44).

If the only purpose of the calculation is to obtain energies $E_\mu^{(A)}$ or vertical excitation energies $\omega_\mu^{(A)}$ (in the $m_A = 2$ case, the EOMCCSD energies $E_\mu^{(\mathrm{CCSD})}$ and vertical excitation energies $\omega_\mu^{(\mathrm{CCSD})}$), the left eigenstates of $\bar{H}^{(A)}$ or $\bar{H}^{(\mathrm{CCSD})}$, $\langle\Phi|L_\mu^{(A)}$ or $\langle\Phi|L_\mu^{(\mathrm{CCSD})}$, respectively, are not needed and it is sufficient to solve the right eigenvalue problem involving $\bar{H}^{(A)}$ or $\bar{H}^{(\mathrm{CCSD})}$, Eq. (23). However, if one has to calculate properties other than energy, such as the expectation values and transition matrix elements involving the CC/EOMCC states $\langle\tilde{\Psi}_\mu|$ and $|\Psi_\nu\rangle$, both right and left eigenstates of $\bar{H}^{(A)}$ (or $\bar{H}^{(\mathrm{CCSD})}$) are important. Indeed, if θ is a property operator, we obtain

$$\langle\tilde{\Psi}_\mu^{(\mathrm{CC})}|\theta|\Psi_\nu^{(\mathrm{CC})}\rangle = \langle\Phi|L_\mu\,\overline{\theta}\,R_\nu|\Phi\rangle, \tag{45}$$

where $\overline{\theta} = e^{-T}\theta\,e^T = (\theta\,e^T)_C$. In particular, when $\theta = a^p a_q$ in Eq. (45), we can determine the CCSD or EOMCCSD one-body reduced density matrices in the CC/EOMCC electronic states $|\Psi_\mu\rangle$, designated by $\gamma_q^p(\mu) \equiv \gamma_q^p(\mu,\mu)$, or the corresponding transition one-body reduced density matrices $\gamma_q^p(\mu,\nu)$, $\mu \neq \nu$. We obtain,

$$\gamma_q^p(\mu,\nu) = \langle\Phi|L_\mu\,\overline{a^p a_q}\,R_\nu|\Phi\rangle. \tag{46}$$

We can use the above expressions to calculate electron densities and various (transition) one-body properties, including, for example, dipole and transition dipole moments,

$$\langle\tilde{\Psi}_\mu^{(\mathrm{CC})}|\theta|\Psi_\nu^{(\mathrm{CC})}\rangle = \theta_p^q\,\gamma_q^p(\mu,\nu), \tag{47}$$

where $\theta_p^q \equiv \langle p|\theta|q\rangle$ are matrix elements of the one-electron property operator θ and $\gamma_q^p(\mu,\nu)$ is defined by Eq. (46). In approximate CC/EOMCC calculations, the cluster operator T and the excitation and deexcitation operators R_μ and L_μ are, of course, replaced by their truncated forms ($T^{(A)}$, $R_\mu^{(A)}$, and $L_\mu^{(A)}$, respectively).

Although the main use of the left eigenstates of $\bar{H}^{(A)}$ or $\bar{H}^{(\mathrm{CCSD})}$ is the calculation of properties other than energy and analytic energy gradients (cf., e.g., Refs. [6, 7, 28, 29, 84–90]), other uses of $L_\mu^{(A)}$ are possible. In particular, as mentioned in the Introduction, the left eigenstates of $\bar{H}^{(A)}$ or $\bar{H}^{(\mathrm{CCSD})}$ (or the corresponding "bra" CC/EOMCC wave functions $\langle\tilde{\Psi}_\mu|$) can be used to design new types of noniterative MMCC corrections to standard CC/EOMCC energies. These new types of MMCC corrections exploiting the left eigenstates of the CC/EOMCC similarity-transformed Hamiltonians as well as other types of MMCC approaches to excited electronic states and their performance in benchmark calculations are reviewed in Section 3. The basic ideas behind the underlying MMCC theory are discussed in the next subsection.

2.2. NONITERATIVE CORRECTIONS TO COUPLED-CLUSTER AND EQUATION-OF-MOTION COUPLED-CLUSTER ENERGIES DEFINING THE EXACT METHOD OF MOMENTS OF COUPLED-CLUSTER EQUATIONS

We are now equipped with all of the basic concepts of the CC/EOMCC theory which are necessary to explain the noniterative MMCC approaches to ground and excited electronic states. In this section, we focus on the exact MMCC theory. The approximate MMCC schemes for excited electronic states, including the externally corrected MMCC approaches and the CR-EOMCCSD(T) theory, and their most recent analog based on the left eigenstates of the similarity-transformed Hamiltonian, are discussed in Section 3.

As described in Section 2.1, the standard CC and EOMCC equations are obtained by projecting $\bar{H}^{(A)}|\Phi\rangle$ and $\bar{H}^{(A)}R_\mu^{(A)}|\Phi\rangle$ on the excited determinants $|\Phi_{i_1\ldots i_n}^{a_1\ldots a_n}\rangle$ with $n = 1,\ldots,m_A$ that correspond to the particle-hole excitations included in the cluster operator $T^{(A)}$ and linear excitation operator $R_\mu^{(A)}$. The corresponding ground-state CC energy is obtained by projecting $\bar{H}^{(A)}|\Phi\rangle$ on the reference determinant $|\Phi\rangle$. It is, therefore, quite natural to expect that in order to correct the results of the standard CC/EOMCC calculations employing the cluster and excitation operators truncated at m_A-body terms, we have to consider the projections of $\bar{H}^{(A)}|\Phi\rangle$ and $\bar{H}^{(A)}R_\mu^{(A)}|\Phi\rangle$ on the excited determinants $|\Phi_{i_1\ldots i_k}^{a_1\ldots a_k}\rangle$ with $k > m_A$, which span the orthogonal complement of the subspace spanned by the reference determinant $|\Phi\rangle$ and the excited determinants $|\Phi_{i_1\ldots i_k}^{a_1\ldots a_k}\rangle$ with $k = 1,\ldots,m_A$. These projections, designated by $\mathfrak{M}_{\mu,a_1\ldots a_k}^{i_1\ldots i_k}(m_A)$, define the generalized moments of the CC/EOMCC equations corresponding to method A. We obtain [47–52, 61–63, 72, 74],

$$\mathfrak{M}_{\mu,a_1\ldots a_k}^{i_1\ldots i_k}(m_A) = \langle\Phi_{i_1\ldots i_k}^{a_1\ldots a_k}|(\bar{H}^{(A)}R_\mu^{(A)})|\Phi\rangle, \tag{48}$$

where $k > m_A$. Because of our convention in which $R_{\mu=0}^{(A)} = \mathbf{1}$, Eq. (48) includes the ground-state, $\mu = 0$, case. Indeed, when $\mu = 0$, moments $\mathfrak{M}_{\mu,a_1\ldots a_k}^{i_1\ldots i_k}(m_A)$, Eq. (48), reduce to the generalized moments of CC equations $\mathfrak{M}_{a_1\ldots a_k}^{i_1\ldots i_k}(m_A)$ defining approximation A [49, 50, 52, 61–63, 72, 74],

$$\mathfrak{M}_{0,a_1\ldots a_k}^{i_1\ldots i_k}(m_A) \equiv \mathfrak{M}_{a_1\ldots a_k}^{i_1\ldots i_k}(m_A) = \langle\Phi_{i_1\ldots i_k}^{a_1\ldots a_k}|\bar{H}^{(A)}|\Phi\rangle. \tag{49}$$

It can be demonstrated that once the cluster and excitation operators, $T^{(A)}$ and $R_\mu^{(A)}$, respectively, and the ground- and excited-state energies $E_\mu^{(A)}$ are determined by solving the relevant CC/EOMCC equations, Eqs. (9), (23), and (26), we can obtain the exact, full CI, energies E_μ by adding the

following state-selective corrections $\delta_\mu^{(A)}$ to energies $E_\mu^{(A)}$ [47–52, 61–63, 72]:

$$\begin{aligned}\delta_\mu^{(A)} &\equiv E_\mu - E_\mu^{(A)} \\ &= \sum_{n=m_A+1}^{N} \sum_{k=m_A+1}^{n} \langle \Psi_\mu | C_{n-k}(m_A)\, M_{\mu,k}(m_A) | \Phi \rangle / \\ &\quad \langle \Psi_\mu | R_\mu^{(A)} e^{T^{(A)}} | \Phi \rangle. \end{aligned} \tag{50}$$

Here,

$$C_{n-k}(m_A) = (e^{T^{(A)}})_{n-k} \tag{51}$$

is the $(n-k)$-body component of the exponential wave operator $e^{T^{(A)}}$, defining the CC method A, $|\Psi_\mu\rangle$ is the full CI wave function of the μ-th electronic state, and

$$M_{\mu,k}(m_A) = \left(\frac{1}{k!}\right)^2 \mathfrak{M}_{\mu,a_1\ldots a_k}^{i_1\ldots i_k}(m_A)\, a^{a_1}\cdots a^{a_k} a_{i_k}\cdots a_{i_1}, \tag{52}$$

where $\mathfrak{M}_{\mu,a_1\ldots a_k}^{i_1\ldots i_k}(m_A)$, $k > m_A$, represent the generalized moments of the CC/EOMCC equations corresponding to the approximate method A, as defined by Eq. (48). In particular, if we want to recover the full CI energies E_μ from the CCSD/EOMCCSD energies $E_\mu^{(\mathrm{CCSD})}$ (the $m_A = 2$ case), we have to add the following corrections $\delta_\mu^{(\mathrm{CCSD})}$ to energies $E_\mu^{(\mathrm{CCSD})}$:

$$\delta_\mu^{(\mathrm{CCSD})} = \sum_{n=3}^{N} \sum_{k=3}^{n} \langle \Psi_\mu | C_{n-k}(2)\, M_{\mu,k}(2) | \Phi \rangle / \langle \Psi_\mu | R_\mu^{(\mathrm{CCSD})} e^{T^{(\mathrm{CCSD})}} | \Phi \rangle. \tag{53}$$

Here, $T^{(\mathrm{CCSD})}$ and $R_\mu^{(\mathrm{CCSD})}$ are the cluster and excitation operators obtained in the CCSD and EOMCCSD calculations, Eqs. (4) and (16), respectively, $C_{n-k}(2)$ is the $(n-k)$-body component of $e^{T^{(\mathrm{CCSD})}}$, and

$$M_{\mu,k}(2) = \left(\frac{1}{k!}\right)^2 \mathfrak{M}_{\mu,a_1\ldots a_k}^{i_1\ldots i_k}(2)\, a^{a_1}\cdots a^{a_k} a_{i_k}\cdots a_{i_1}, \tag{54}$$

where

$$\mathfrak{M}_{\mu,a_1\ldots a_k}^{i_1\ldots i_k}(2) = \langle \Phi_{i_1\ldots i_k}^{a_1\ldots a_k} | (\bar{H}^{(\mathrm{CCSD})} R_\mu^{(\mathrm{CCSD})}) | \Phi \rangle, \tag{55}$$

with $k \geq 3$, are the generalized moments of the CCSD ($\mu = 0$) or EOMCCSD ($\mu > 0$) equations. The above equations for $\delta_\mu^{(A)}$ and $\delta_\mu^{(\mathrm{CCSD})}$, in terms of the generalized moments $\mathfrak{M}_{\mu,a_1\ldots a_k}^{i_1\ldots i_k}(m_A)$ and $\mathfrak{M}_{\mu,a_1\ldots a_k}^{i_1\ldots i_k}(2)$, respectively, can be obtained by considering the asymmetric energy expression,

$$\Lambda[\Psi] = \langle \Psi | (H - E_\mu^{(A)}) R_\mu^{(A)} e^{T^{(A)}} | \Phi \rangle / \langle \Psi | R_\mu^{(A)} e^{T^{(A)}} | \Phi \rangle, \tag{56}$$

referred to as the MMCC functional [47, 49, 50, 62, 72]. This expression satisfies the important property

$$\Lambda[\Psi_\mu] = E_\mu - E_\mu^{(A)}, \tag{57}$$

where E_μ is the exact, full CI, energy, if $|\Psi_\mu\rangle$ is a full CI state. We refer the reader to the original work by Kowalski and Piecuch [47, 62] and Appendices in Ref. [49] for the details of the derivation of Eq. (50) using functional $\Lambda[\Psi]$, Eq. (56). It is worth mentioning here that the applicability of the MMCC functional, Eq. (56), introduced by Kowalski and Piecuch for the ground-state problem in 2000 [62] and extended to excited states in 2001 [47], in direct calculations of the noniterative correction $\delta_0^{(\mathrm{CCSD})}$ to standard CCSD energy has been examined by Li and Paldus [91, 92]. These authors showed that the asymmetric energy expression represented by Eq. (56) is capable of improving the results of standard CC calculations at larger internuclear separations. The only problem with applying Eq. (56) "as is" is the fact that direct calculations of corrections $\delta_\mu^{(A)}$ using the MMCC functional are prohibitively expensive. After rewriting the MMCC functional, Eq. (56), in terms of the generalized moments of CC/EOMCC equations, as is done in Eqs. (50) and (53), one can propose a variety of relatively inexpensive CC/EOMCC approximations that the direct application of Eq. (56) cannot lead to. Li and Paldus have realized this and in subsequent papers (see, e.g., Ref. 93, 94) they used the expressions for the ground-state correction $\delta_0^{(\mathrm{CCSD})}$ which are identical to our Eq. (53). They have not studied the excited-state corrections $\delta_\mu^{(A)}$ though.

Equation (50) (or its CCSD/EOMCCSD-based analog, Eq. (53)) defines the exact MMCC formalism for ground and excited states. This equation allows us to improve the CC/EOMCC (e.g. CCSD/EOMCCSD) results, in a state-selective manner, by adding the noniterative corrections $\delta_\mu^{(A)}$ (in practice, one of the approximate forms of $\delta_\mu^{(A)}$ or $\delta_\mu^{(\mathrm{CCSD})}$), obtained using the information that can be directly extracted from the standard CC/EOMCC calculations, such as operators $T^{(A)}$ and $R_\mu^{(A)}$, matrix elements of $\bar{H}^{(A)}$, and generalized moments of the CC/EOMCC equations $\mathfrak{M}^{i_1\ldots i_k}_{\mu,a_1\ldots a_k}(m_A)$, to the CC/EOMCC energies $E_\mu^{(A)}$. The key quantities in Eq. (50) that require more attention and that are essential for designing the approximate forms of the MMCC corrections $\delta_\mu^{(A)}$ are the generalized moments $\mathfrak{M}^{i_1\ldots i_k}_{\mu,a_1\ldots a_k}(m_A)$, Eq. (48), and the many-body components of $e^{T^{(A)}}$ defining the $C_{n-k}(m_A)$ operators, Eq. (51). The $C_{n-k}(m_A)$ terms are very easy to calculate. The zero-body term, $C_0(m_A)$, equals 1; the one-body term, $C_1(m_A)$, equals T_1; the two-body term, $C_2(m_A)$, equals $T_2 + \frac{1}{2}T_1^2$ if $m_A \geq 2$; the three-body term $C_3(m_A)$ equals $T_1T_2 + \frac{1}{6}T_1^3$ if $m_A = 2$ and $T_3 + T_1T_2 + \frac{1}{6}T_1^3$ if $m_A \geq 3$,

etc. The determination of the generalized moments $\mathfrak{M}^{i_1\ldots i_k}_{\mu,a_1\ldots a_k}(m_A)$ is relatively straightforward too, particularly for the lower-order CC/EOMCC methods, such as CCSD and EOMCCSD (the $m_A = 2$ case). Indeed, the formula for the leading moment $\mathfrak{M}^{ijk}_{\mu,abc}(2)$, entering the basic MMCC(2,3) approximation discussed in Section 3 and corresponding to the projection of the CCSD/EOMCCSD equations on triply excited determinants $|\Phi^{abc}_{ijk}\rangle$, in terms of the many-body components of the CCSD/EOMCCSD similarity-transformed Hamiltonian $\bar{H}^{(\mathrm{CCSD})}$, Eq. (13), and the EOMCCSD excitation operator $R^{(\mathrm{CCSD})}_{\mu}$, Eq. (16), which enables us to correct the CCSD and EOMCCSD energies by considering the leading term in correction $\delta^{(\mathrm{CCSD})}_{\mu}$, Eq. (53), is [47–49, 51, 52, 59]

$$\begin{aligned}\mathfrak{M}^{ijk}_{\mu,abc}(2) &= \langle\Phi^{abc}_{ijk}|(\bar{H}^{(\mathrm{CCSD})}_2 R_{\mu,2})_C|\Phi\rangle \\ &\quad +\langle\Phi^{abc}_{ijk}|[\bar{H}^{(\mathrm{CCSD})}_3 (R_{\mu,1}+R_{\mu,2})]_C|\Phi\rangle \\ &\quad +\langle\Phi^{abc}_{ijk}|(\bar{H}^{(\mathrm{CCSD})}_4 R_{\mu,1})_C|\Phi\rangle + r_0(\mu)\,\mathfrak{M}^{ijk}_{abc}(2), \qquad (58)\end{aligned}$$

where the ground-state moment $\mathfrak{M}^{ijk}_{abc}(2)$, obtained by projecting the CCSD equations on triply excited determinants, is given by [51, 52]

$$\begin{aligned}\mathfrak{M}^{ijk}_{abc}(2) &= \langle\Phi^{abc}_{ijk}|[H_N(T_2 + T_1T_2 + \tfrac{1}{2}T_2^2 + \tfrac{1}{2}T_1^2T_2 \\ &\quad +\tfrac{1}{2}T_1T_2^2 + \tfrac{1}{6}T_1^3T_2)]_C|\Phi\rangle. \qquad (59)\end{aligned}$$

In the above equations, the operators $\bar{H}^{(\mathrm{CCSD})}_p$ represent the p-body components of $\bar{H}^{(\mathrm{CCSD})}$ and $H_N = H - \langle\Phi|H|\Phi\rangle$ is the Hamiltonian in the normal-ordered form. The fully factorized expression for the triply excited moments of the CCSD/EOMCCSD equations $\mathfrak{M}^{ijk}_{\mu,abc}(2)$, in terms of the amplitudes defining the CCSD/EOMCCSD cluster and excitation operators, T_1, T_2, $R_{\mu,0}$, $R_{\mu,1}$, and $R_{\mu,2}$, and molecular integrals f^q_p and v^{rs}_{pq}, which can be used in the efficient computer implementations of all MMCC(2,3) approximations, including the externally corrected MMCC(2,3) and CR-EOMCCSD(T) schemes, has the following form [59]:

$$\begin{aligned}\mathfrak{M}^{ijk}_{\mu,abc}(2) &= \mathscr{A}_{abc}\,\mathfrak{T}^{ijk}_{\mu,abc}(2) \\ &= \mathscr{A}_{abc}\{\,\mathscr{A}^{i/jk}[\,(\tfrac{1}{2}\bar{h}^{ie}_{ab}r^{jk}_{ec} - \tfrac{1}{2}\bar{h}^{jk}_{mc}r^{im}_{ab} - \tfrac{1}{2}I^{jk}_{mc}t^{im}_{ab} + I^{ie}_{ab}t^{jk}_{ec}) \\ &\quad +\tfrac{1}{2}r_0\,(\bar{h}^{ie}_{ab}t^{jk}_{ec} - I'^{jk}_{mc}t^{im}_{ab})\,]\,\}\,, \qquad (60)\end{aligned}$$

where, for simplicity, we dropped the symbol μ in the amplitudes $r^{jk}_{ec}(\mu)$, $r^{im}_{ab}(\mu)$, and $r_0(\mu)$. The antisymmetrizers $\mathscr{A}_{pqr}$, $\mathscr{A}_{p/qr}$, and $\mathscr{A}_{pq}$, which enter Eq. (60) directly or through the matrix elements of $\bar{H}^{\mathrm{CCSD}}$, and other

intermediates that are needed to construct Eq. (60) and that are listed in Table 1, are defined in a usual way,

$$\mathscr{A}_{pqr} \equiv \mathscr{A}^{pqr} = 1 - (pq) - (pr) - (qr) + (pqr) + (prq), \tag{61}$$

$$\mathscr{A}_{p/qr} \equiv \mathscr{A}^{p/qr} = 1 - (pq) - (pr), \tag{62}$$

and

$$\mathscr{A}_{pq} \equiv \mathscr{A}^{pq} = 1 - (pq), \tag{63}$$

with (pq) and (pqr) representing the cyclic permutations of two and three indices, respectively. The explicit spin-orbital expressions for one- and two-body matrix elements of $\bar{H}^{\rm CCSD}$, $\bar{h}^q_p$ and $\bar{h}^{rs}_{pq}$, respectively, and other recursively generated intermediates entering Eq. (60), in terms of cluster amplitudes t^i_a and t^{ij}_{ab}, excitation amplitudes $r^i_a \equiv r^i_a(\mu)$ and $r^{ij}_{ab} \equiv r^{ij}_{ab}(\mu)$, and molecular integrals f^q_p and v^{rs}_{pq}, are given in Table 1. Similar expressions can be given for the EOMCCSD moments $\mathfrak{M}^{i_1\ldots i_k}_{\mu,a_1\ldots a_k}(2)$ with $k \geq 4$ that enter the MMCC(2,4) and other higher-order MMCC schemes. In general, the generalized moments $\mathfrak{M}^{i_1\ldots i_k}_{\mu,a_1\ldots a_k}(m_A)$ corresponding to the CC/EOMCC approximation A can be calculated using the formula [47–52]:

$$\begin{aligned}\mathfrak{M}^{i_1\ldots i_k}_{\mu,a_1\ldots a_k}(m_A) &= \langle \Phi^{a_1\ldots a_k}_{i_1\ldots i_k} | (\bar{H}^{(A)}_{\rm open} R^{(A)}_{\mu,{\rm open}})_C | \Phi\rangle \\ &\quad + \sum_{p=m_A+1}^{k-1} \langle \Phi^{a_1\ldots a_k}_{i_1\ldots i_k} | (\bar{H}^{(A)}_p R^{(A)}_{\mu,k-p})_{DC} | \Phi\rangle \\ &\quad + r_0(\mu)\, \mathfrak{M}^{i_1\ldots i_k}_{a_1\ldots a_k}(m_A),\end{aligned} \tag{64}$$

where $r_0(\mu)$ is the coefficient at the reference determinant $|\Phi\rangle$ in the many-body expansion of $R^{(A)}_\mu|\Phi\rangle$, Eq. (20) (cf. Eq. (26) for the formula for $r_0(\mu)$), subscripts "open," C, and DC refer to open (i.e. having external lines), connected, and disconnected parts of a given operator expression, O_j represents the j-body component of operator O, and $\mathfrak{M}^{i_1\ldots i_k}_{a_1\ldots a_k}(m_A)$ are the generalized moments of the single-reference CC equations defined by Eq. (49).

In order to use Eqs. (50) and (53) in practical calculations, the following two issues must be addressed. First, the exact MMCC corrections $\delta^{(A)}_\mu$, Eq. (50), or $\delta^{({\rm CCSD})}_\mu$, Eq. (53), are represented by complete many-body expansions including the N-body contributions, where N is the number of electrons in a system, corresponding to all many-body components of the wave functions $|\Psi_\mu\rangle$ that enter Eqs. (50) and (53) (cf. the summations over n in Eqs. (50) and (53)). In order to develop practical MMCC methods, we must truncate the many-body expansions for $\delta^{(A)}_\mu$ or $\delta^{({\rm CCSD})}_\mu$, given by Eqs. (50) or (53), at some, preferably low, excitation level $m_B > m_A$. This leads to the MMCC(m_A, m_B) schemes [47–52, 61–63, 72]. Examples of these schemes are

TABLE 1. Explicit algebraic expressions for the matrix elements elements of $\bar{H}^{\rm CCSD}$ (designated by $\bar{h}$) and other intermediates (designated by I or ϑ) used to construct the triply excited moments of the CCSD/EOMCCSD equations, $\mathfrak{M}^{ijk}_{\mu,abc}(2)$, Eq. (60).

Intermediate	*Expression*[a]
$\bar{h}^a_i$	$f^a_i + t^m_e v^{ae}_{im}$
I^a_i	$-r^m_e v^{ae}_{mi}$
$\bar{h}^{bc}_{ai}$	$v^{bc}_{ai} - t^m_a v^{bc}_{mi}$
$\bar{h}^{ka}_{ij}$	$v^{ka}_{ij} + t^k_e v^{ea}_{ij}$
$\bar{h}^{cd}_{ab}$	$v^{cd}_{ab} + \frac{1}{2} t^{mn}_{ab} v^{cd}_{mn} - t^m_b \bar{h}^{cd}_{am} + t^m_a v^{cd}_{bm}$
$\bar{h}^{kl}_{ij}$	$v^{kl}_{ij} + \frac{1}{2} t^{kl}_{ef} v^{ef}_{ij} - t^k_e \bar{h}^{le}_{ij} + t^l_e v^{ke}_{ij}$
$\bar{h}^{jb}_{ia}$	$\vartheta^{jb}_{ia} - t^{jm}_{ea} v^{eb}_{im} - t^m_a \bar{h}^{jb}_{im}$
$\bar{h}^{ic}_{ab}$	$v^{ic}_{ab} + t^i_e v^{ec}_{ab} - t^m_a \bar{h}^{ic}_{mb} + t^m_b \vartheta^{ic}_{ma} - t^{im}_{ab} \bar{h}^c_m + t^{im}_{ae} \bar{h}^{ce}_{bm} - t^{im}_{be} v^{ce}_{am} + \frac{1}{2} t^{nm}_{ab} \bar{h}^{ic}_{nm}$
$\bar{h}^{jk}_{ia}$	$v^{jk}_{ia} + t^m_a \bar{h}^{jk}_{mi} - t^j_e v^{ke}_{ia} + \mathscr{A}^{jk} t^{km}_{ae} \bar{h}^{je}_{im} + t^{jk}_{ea} \bar{h}^e_i + t^k_e \vartheta^{je}_{ia} - \frac{1}{2} t^{jk}_{ef} v^{ef}_{ai}$
I^{ic}_{ab}	$\frac{1}{2} \bar{h}^{ec}_{ab} r^i_e - \bar{h}^{ec}_{bm} r^{im}_{ae} + \frac{1}{4} \bar{h}^{ic}_{mn} r^{mn}_{ab} - \bar{h}^{ic}_{mb} r^m_a$
I^{jk}_{ia}	$I^e_i t^{kj}_{ae} + \frac{1}{2} \bar{h}^{ef}_{ai} r^{kj}_{ef} - \bar{h}^{jk}_{im} r^m_a + \mathscr{A}^{jk} (\bar{h}^{je}_{im} r^{km}_{ae} + \bar{h}^{je}_{ia} r^k_e)$
I'^{jk}_{ia}	$\bar{h}^{jk}_{ia} - t^{jk}_{ea} \bar{h}^e_i$
ϑ^{jb}_{ia}	$v^{jb}_{ia} + t^j_e v^{eb}_{ia}$

[a] Summation over repeated upper and lower indices is assumed; $f^q_p = \langle p|f|q\rangle$ and $v^{rs}_{pq} = \langle pq|v|rs\rangle - \langle pq|v|sr\rangle$ are the one- and two-electron integrals in a molecular spin-orbital basis $\{p\}$ corresponding to the Fock operator (f) and the two-body part of the Hamiltonian (v).

the CI- and MRMBPT-corrected MMCC(2,3) methods [47, 49, 50, 52, 78] and the CR-EOMCCSD(T) approach [49, 51, 52, 59] discussed in Section 3, in which the suitably designed corrections $\delta^{(\rm CCSD)}_\mu$, based on the exact Eq. (53), are added to the CCSD/EOMCCSD energies. Alternatives to the MMCC(m_A, m_B) schemes are the approximate MMCC methods employing the left eigenstates of the similarity-transformed Hamiltonian $\bar{H}^{(A)}$ or $\bar{H}^{(\rm CCSD)}$ [79], in which the MMCC corrections $\delta^{(A)}_\mu$ or $\delta^{(\rm CCSD)}_\mu$ are first rewritten in a computationally convenient form that does not use the overlap denominators $\langle\Psi_\mu|R^{(A)}_\mu e^{T^{(A)}}|\Phi\rangle$ or $\langle\Psi_\mu|R^{(\rm CCSD)}_\mu e^{T^{(\rm CCSD)}}|\Phi\rangle$ entering Eqs. (50) and (53) (also discussed in Section 3). The second issue that needs to be addressed is the fact that the wave functions $|\Psi_\mu\rangle$ that enter the exact

Eqs. (50) and (53) are the full CI states. Thus, we must approximate wave functions $|\Psi_\mu\rangle$ in some way. A few different methods of approximating $|\Psi_\mu\rangle$ in Eq. (53), leading to the aforementioned externally corrected MMCC(2,3) approaches and CR-EOMCCSD(T) schemes, and their analogs exploiting the left eigenstates of $\bar{H}^{(\mathrm{CCSD})}$, and the performance of all of these methods in actual calculations of excited electronic states are discussed in the next section.

3. Approximate MMCC methods for excited states and their performance

There are two, essentially different, ways of approximating the MMCC corrections $\delta_\mu^{(A)}$, Eq. (50), that lead to relatively inexpensive, and therefore practical, computational schemes. In the first method, we assume that the CI expansions of the ground- and excited-state wave functions $|\Psi_\mu\rangle$ entering Eq. (50) are relatively short and do not contain higher–than–m_B-tuply excited components relative to the reference determinant $|\Phi\rangle$, where the excitation level m_B is not much higher than the excitation level m_A defining the CC/EOMCC approximation we are trying to improve. This leads to the externally (CI or MRMBPT) corrected MMCC(m_A, m_B) schemes [47–50, 52, 78] and the CR-EOMCCSD(T) method [49, 51, 52, 59]. We discuss these approaches first, focusing on the MMCC(m_A, m_B) methods with $m_A = 2$ and $m_B = 3$, which enable us to improve the results of the CCSD/EOMCCSD calculations by terms that represent the leading triples effects (see Section 3.1). In the second approach, discussed in Section 3.2, which leads to the MMCC(m_A, m_B)$_{\mathscr{L}}$ schemes, including the recently formulated [79] and promising CR-EOMCCSD(T)$_{\mathscr{L}}$ approximation, we rewrite the "bra" wave functions $\langle\Psi_\mu|$ in Eq. (50) in terms of the left eigenstates of $\bar{H}^{(A)}$. The main difference between the regular MMCC(m_A, m_B) approaches and the MMCC(m_A, m_B)$_{\mathscr{L}}$ methods is the absence of the overlap denominator $\langle\Psi_\mu|R_\mu^{(A)}e^{T^{(A)}}|\Phi\rangle$ in the MMCC(m_A, m_B)$_{\mathscr{L}}$ energy corrections. The information about this denominator, which enters the regular MMCC energy formula, Eq. (50), and which helps to improve the results for doubly excited states and excited-state potential energy surfaces along bond breaking coordinates, is incorporated in the MMCC(m_A, m_B)$_{\mathscr{L}}$ methods through the use of the left eigenstates of $\bar{H}^{(A)}$ ($\bar{H}^{(\mathrm{CCSD})}$ in the CR-EOMCCSD(T)$_{\mathscr{L}}$ case).

3.1. EXTERNALLY CORRECTED MMCC(2,3) SCHEMES AND THE CR-EOMCCSD(T) APPROACH

The MMCC(2,3), CR-EOMCCSD(T), and other MMCC(m_A,m_B) methods are obtained by assuming that the CI expansions of the ground- and excited-state wave functions $|\Psi_\mu\rangle$ entering Eq. (50) do not contain higher–than–m_B-tuply excited components relative to the reference $|\Phi\rangle$, where $m_A < m_B < N$. In all MMCC(m_A,m_B) approximations, we calculate the ground- and excited-state energies as follows [47–52, 61–63, 72]:

$$E_\mu^{(\mathrm{MMCC})}(m_A,m_B) = E_\mu^{(A)} + \delta_\mu(m_A,m_B), \tag{65}$$

where $E_\mu^{(A)}$ is the energy of the μ-th electronic state, obtained with some standard EOMCC method A, and

$$\begin{aligned}\delta_\mu(m_A,m_B) \;=\; & \sum_{n=m_A+1}^{m_B} \sum_{k=m_A+1}^{n} \langle\Psi_\mu|C_{n-k}(m_A) \\ & \times M_{\mu,k}(m_A)|\Phi\rangle / \langle\Psi_\mu|R_\mu^{(A)} e^{T^{(A)}}|\Phi\rangle\end{aligned} \tag{66}$$

is the relevant MMCC correction to $E_\mu^{(A)}$. As in the exact theory defined by Eq. (50), the generalized moments of the CC/EOMCC equations, $\mathfrak{M}^{i_1\ldots i_k}_{\mu,a_1\ldots a_k}(m_A)$, Eqs. (48) and (64), enter Eqs. (65) and (66) through quantities $M_{\mu,k}(m_A)|\Phi\rangle$, Eq. (52), and $C_{n-k}(m_A)$ are the many-body components of $e^{T^{(A)}}$, defined by Eq. (51), where $T^{(A)}$ is the cluster operator defining (along with the excitation operator $R_\mu^{(A)}$) the CC/EOMCC calculations A, whose results we are trying to correct.

We limit our discussion to the low-order MMCC(m_A,m_B) schemes with $m_A = 2$ and $m_B = 3$, which can be used to correct the results of the CCSD/EOMCCSD calculations for the effects of triple excitations (for the description of the MMCC(2,4) and other higher-order MMCC(m_A,m_B) methods, see Refs. [48–50, 52, 61–63, 72]). The MMCC(2,3) energy expression is as follows [47–52, 61–63, 72]:

$$E_\mu^{(\mathrm{MMCC})}(2,3) = E_\mu^{(\mathrm{CCSD})} + \langle\Psi_\mu|M_{\mu,3}(2)|\Phi\rangle / \langle\Psi_\mu|R_\mu^{(\mathrm{CCSD})} e^{T^{(\mathrm{CCSD})}}|\Phi\rangle, \tag{67}$$

where $E_\mu^{(\mathrm{CCSD})}$ is the CCSD ($\mu = 0$) or EOMCCSD ($\mu > 0$) energy, $T^{(\mathrm{CCSD})}$ is the cluster operator obtained in the CCSD calculations (cf. Eq. (4)), $R_\mu^{(\mathrm{CCSD})}$ is the corresponding excitation operator (cf. Eq. (16); when $\mu = 0$, $R_\mu^{(\mathrm{CCSD})} = \mathbf{1}$), and

$$M_{\mu,3}(2) = \tfrac{1}{36}\, \mathfrak{M}^{ijk}_{\mu,abc}(2)\, a^a a^b a^c a_k a_j a_i, \tag{68}$$

with $\mathfrak{M}^{ijk}_{\mu,abc}(2)$ representing the triply excited moments of the CCSD/EOMCCSD equations defined by Eqs. (58) and (59). These moments are easy to calculate. As implied by Eqs. (58) and (59), their determination requires the explicit consideration of the triples-reference, triples-singles, and triples-doubles blocks of the matrix representing the CCSD/EOMCCSD similarity-transformed Hamiltonian $\bar{H}^{\rm CCSD}$, Eq. (13). In consequence, the most expensive steps of the ground- and excited-state calculations using methods based on the MMCC(2,3) approximation are essentially identical to the $n_o^3 n_u^4$ noniterative steps of the ground-state CCSD(T) calculations (n_o and n_u are the numbers of occupied and unoccupied correlated orbitals, respectively). Similar remarks apply to the memory and disk-space requirements. Clearly, these are great simplifications in the computer effort, compared to the higher-level EOMCC approaches, such as EOMCCSDT [43, 44, 55, 56], particularly if we realize that we only have to use the T_1 and T_2 clusters, obtained in the CCSD calculations, to construct matrix elements of $\bar{H}^{(\rm CCSD)}$ that enter $\mathfrak{M}^{ijk}_{\mu,abc}(2)$, Eqs. (58) and (59). In practical implementations of all MMCC(2,3) methods, the simplifications are even greater, since, as shown by Eq. (60) and Table 1, we can calculate moments $\mathfrak{M}^{ijk}_{\mu,abc}(2)$ in a highly efficient manner, which leads to noniterative $n_o^3 n_u^4$ procedures, by using recursively generated intermediates and one- and two-body matrix elements of $\bar{H}^{(\rm CCSD)}$, $\bar{h}^q_p$ and $\bar{h}^{rs}_{pq}$, respectively, expressed in terms of the CCSD cluster amplitudes t^i_a and t^{ij}_{ab}, EOMCCSD excitation amplitudes $r^i_a(\mu)$ and $r^{ij}_{ab}(\mu)$, and molecular integrals f^q_p and v^{rs}_{pq}.

Depending on the form of the wave function $|\Psi_\mu\rangle$ in Eq. (67), we can distinguish between the externally corrected MMCC(2,3) approaches for excited states, which employ the inexpensive CI or MRMBPT (in general, non-CC) wave functions to approximate $|\Psi_\mu\rangle$ [47–50, 52, 61, 68, 78], and CR-EOMCCSD(T) methods, which are based on the perturbative analysis of the full EOMCCSDT problem to provide the approximate form of $|\Psi_\mu\rangle$ for MMCC(2,3) calculations [49, 51, 52, 59]. The CR-EOMCCSD(T) approaches can be viewed as the excited-state extensions of the ground-state CR-CCSD(T) method introduced in Refs. [61, 62] (see, also, Refs. [49, 50, 52, 63, 65, 67, 69, 70, 72, 73, 75, 76]). Externally corrected MMCC methods are very similar, in the overall idea, to the large class of the externally corrected CC methods pioneered by Paldus and collaborators, in which CC and non-CC concepts are combined together to improve CC results in the presence of quasi-degeneracies [8, 17, 95–102]. In particular, the CI-corrected MMCC methods discussed in this work, which were originally introduced in the context of the ground-state calculations by Piecuch and Kowalski in Ref. 61, are very similar to the so-called energy-corrected CC approaches of Li and Paldus [91–94]. We begin the discussion of MMCC(2,3) methods with the externally corrected approaches.

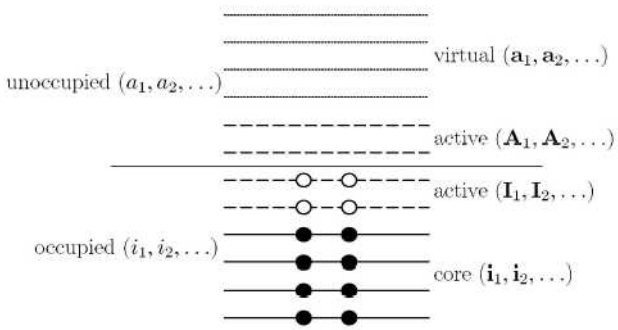

Figure 1. The orbital classification used in the active-space CI, MRMBPT, and the CI- and MRMBPT-corrected MMCC methods, such as MMCC(2,3)/CI and MMCC(2,3)/PT. Core, active, and virtual orbitals are represented by solid, dashed, and dotted lines, respectively. Full and open circles represent core and active electrons of the reference determinant $|\Phi\rangle$ (the closed-shell reference $|\Phi\rangle$ is assumed).

3.1.1. *The CI- and MRMBPT-corrected MMCC(2,3) methods*

In the CI-corrected MMCC(2,3) approach and other CI-corrected MMCC(m_A, m_B) methods for excited states, originally introduced in Refs. [47, 48], we replace the wave functions $|\Psi_\mu\rangle$ in Eqs. (66) and (67) by the wave functions obtained in inexpensive CI calculations that provide a qualitatively correct description of the ground and excited states of interest. One of the best choices of the CI wave functions $|\Psi_\mu\rangle$ for such calculations is provided by the multi-reference-like, active-space CI approaches, such as CISDt. In this case, following the philosophy of multi-reference calculations, we divide the available spin-orbitals into four groups (see Figure 1) of core spin-orbitals ($\mathbf{i}_1$, $\mathbf{i}_2$, ... or $\mathbf{i}$, $\mathbf{j}$, ...), active spin-orbitals occupied in reference $|\Phi\rangle$ ($\mathbf{I}_1$, $\mathbf{I}_2$, ... or $\mathbf{I}$, $\mathbf{J}$, ...), active spin-orbitals unoccupied in reference $|\Phi\rangle$ ($\mathbf{A}_1$, $\mathbf{A}_2$, ... or $\mathbf{A}$, $\mathbf{B}$, ...), and virtual spin-orbitals ($\mathbf{a}_1$, $\mathbf{a}_2$, ... or $\mathbf{a}$, $\mathbf{b}$, ...). The choice of active spin-orbitals (typically, a few highest-energy occupied spin-orbitals and a few lowest-energy unoccupied spin-orbitals) is dictated by the dominant orbital excitations in the ground and excited states that we would like to calculate. An example of the good choice of active orbitals for the calculations of the valence excited states of CH^+ can be found in Table 2.

In the specific case of the CI-corrected MMCC(2,3) approach, very good results are obtained when the wave function $|\Psi_\mu\rangle$ in Eq. (67) is replaced by the wave function obtained in the active-space CISDt calculations, which

is defined as follows:

$$|\Psi_\mu^{(\mathrm{CISDt})}\rangle = (C_{\mu,0} + C_{\mu,1} + C_{\mu,2} + c_{\mu,3})|\Phi\rangle, \tag{69}$$

where

$$C_{\mu,0} = c_0(\mu)\,\mathbf{1}, \tag{70}$$

$$C_{\mu,1}|\Phi\rangle = c_a^i(\mu)\,a^a a_i = \sum_{i,a} c_a^i(\mu)\,a^a a_i, \tag{71}$$

and

$$C_{\mu,2} = \tfrac{1}{4}\,c_{ab}^{ij}(\mu)\,a^a a^b a_j a_i = \sum_{i<j,a<b} c_{ab}^{ij}(\mu)\,a^a a^b a_j a_i \tag{72}$$

are the excitation operators defining the reference, singly excited, and doubly excited contributions to $|\Psi_\mu^{\mathrm{CISDt}}\rangle$, and

$$c_{\mu,3} = \sum_{i<j<\mathbf{K},\mathbf{A}<b<c} c_{\mathbf{A}bc}^{ij\mathbf{K}}(\mu)\,a^{\mathbf{A}} a^b a^c a_{\mathbf{K}} a_j a_i \tag{73}$$

are the internal and semi-internal triples containing at least one active occupied and one active unoccupied spin-orbital indices, designated by **K** and **A**, respectively. The CISDt method can be viewed as an inexpensive variant of the CI singles, doubles, and triples (CISDT) approximation, in which the complete set of triple excitations is replaced by a relatively small set of triples defined by Eq. (73). The final energy expression defining the CISDt-corrected MMCC(2,3) method, referred to as the MMCC(2,3)/CI approximation, is:

$$E_\mu^{(\mathrm{MMCC/CI})}(2,3) = E_\mu^{(\mathrm{EOMCCSD})} + \sum_{i<j<\mathbf{K},\mathbf{A}<b<c} [c_{\mathbf{A}bc}^{ij\mathbf{K}}(\mu)]^*\,\mathfrak{M}_{\mu,\mathbf{A}bc}^{ij\mathbf{K}}(2)/D_\mu^{\mathrm{CISDt}}, \tag{74}$$

where $\mathfrak{M}_{\mu,\mathbf{A}bc}^{ij\mathbf{K}}(2)$ represent the subset of all triply excited moments of the CCSD/EOMCCSD equations defined by Eqs. (58) and (59) and

$$D_\mu^{\mathrm{CISDt}} \equiv \langle\Psi_\mu^{\mathrm{CISDt}}|R_\mu^{(\mathrm{CCSD})}e^{T^{(\mathrm{CCSD})}}|\Phi\rangle = \Delta_{\mu,0}^{\mathrm{CISDt}} + \Delta_{\mu,1}^{\mathrm{CISDt}} + \Delta_{\mu,2}^{\mathrm{CISDt}} + \Delta_{\mu,3}^{\mathrm{CISDt}} \tag{75}$$

is the overlap denominator $\langle\Psi_\mu|R_\mu^{(\mathrm{CCSD})}e^{T^{(\mathrm{CCSD})}}|\Phi\rangle$ appearing in the general Eq. (67), written for the wave function $|\Psi_\mu\rangle = |\Psi_\mu^{(\mathrm{CISDt})}\rangle$, Eq. (69). The $\Delta_{\mu,0}^{\mathrm{CISDt}}$, $\Delta_{\mu,1}^{\mathrm{CISDt}}$, $\Delta_{\mu,2}^{\mathrm{CISDt}}$, and $\Delta_{\mu,3}^{\mathrm{CISDt}}$ terms that contribute to the denominator D_μ^{CISDt}, Eq. (75), are defined as

$$\Delta_{\mu,0}^{\mathrm{CISDt}} = [c_0(\mu)]^*\,r_0(\mu), \tag{76}$$

$$\Delta_{\mu,1}^{\rm CISDt} = \sum_{i,a} [c_a^i(\mu)]^* \, \beta_a^i(\mu), \tag{77}$$

$$\Delta_{\mu,2}^{\rm CISDt} = \sum_{i<j,a<b} [c_{ab}^{ij}(\mu)]^* \, \beta_{ab}^{ij}(\mu), \tag{78}$$

and

$$\Delta_{\mu,3}^{\rm CISDt} = \sum_{i<j<\mathbf{K},\mathbf{A}<b<c} [c_{\mathbf{A}bc}^{ij\mathbf{K}}(\mu)]^* \, \beta_{\mathbf{A}bc}^{ij\mathbf{K}}(\mu), \tag{79}$$

where $c_0(\mu)$, $c_a^i(\mu)$, $c_{ab}^{ij}(\mu)$, and $c_{\mathbf{A}bc}^{ij\mathbf{K}}(\mu)$ are the CI coefficients obtained in the variational CISDt calculations for the μ-th electronic state and $r_0(\mu)$,

$$\beta_a^i(\mu) = \langle \Phi_i^a | (R_{\mu,1} + R_{\mu,0} T_1) | \Phi \rangle, \tag{80}$$

$$\beta_{ab}^{ij}(\mu) = \langle \Phi_{ij}^{ab} | [R_{\mu,2} + R_{\mu,1} T_1 + R_{\mu,0} (T_2 + \tfrac{1}{2} T_1^2)] | \Phi \rangle, \tag{81}$$

and

$$\beta_{abc}^{ijk}(\mu) = \langle \Phi_{ijk}^{abc} | [R_{\mu,2} T_1 + R_{\mu,1} (T_2 + \tfrac{1}{2} T_1^2) + R_{\mu,0} (T_1 T_2 + \tfrac{1}{6} T_1^3)] | \Phi \rangle \tag{82}$$

are the coefficients at the reference determinant $|\Phi\rangle$ and singly, doubly, and triply excited determinants, $|\Phi_i^a\rangle$, $|\Phi_{ij}^{ab}\rangle$, and $|\Phi_{ijk}^{abc}\rangle$ respectively, in the CI expansion of the CCSD/EOMCCSD wave function $R_\mu^{\rm (CCSD)} e^{T^{\rm (CCSD)}} |\Phi\rangle$, which can be easily determined using the CCSD/EOMCCSD cluster and excitation amplitudes t_a^i, t_{ab}^{ij}, $r_0(\mu)$, $r_a^i(\mu)$, and $r_{ab}^{ij}(\mu)$. As in the case of moments $\mathfrak{M}_{\mu,\mathbf{A}bc}^{ij\mathbf{K}}(2)$, we only need a subset of all triexcited coefficients $\beta_{abc}^{ijk}(\mu)$, Eq. (82), defined through active spin-orbital indices as $\beta_{\mathbf{A}bc}^{ij\mathbf{K}}(\mu)$, to calculate the triply excited contribution $\Delta_{\mu,3}^{\rm CISDt}$, Eq. (79), to the denominator $D_\mu^{\rm CISDt}$. One can easily extend the above MMCC(2,3)/CI approximation to higher-order CI-corrected MMCC(m_A, m_B) schemes, such as MMCC(2,4)/CI, which describes the combined effect of triple and quadruple excitations that are defined through active orbitals in a similar way as the triple excitations of the CISDt wave functions (see, e.g., Refs. [48, 49, 52]).

One of the main advantages of the CI-corrected MMCC schemes, including MMCC(2,3)/CI, is a very good control of the quality of wave functions $|\Psi_\mu\rangle$ used to construct the noniterative corrections $\delta_\mu(m_A, m_B)$, which is accomplished through the judicious choice of active orbitals that can always be adjusted to excited states of a given type or, when the potential energy surfaces are examined, to a given type of bond breaking. Another advantage of the CI-corrected MMCC methods is their relatively low computer cost, which is a consequence of the fact that it is usually sufficient to use very small active orbital spaces to obtain good results (cf., e.g., Table 2 and Figure 2). The relatively low cost of the CI-corrected MMCC

calculations can be explained by using the CISDt-corrected MMCC(2,3) approach, defined by Eq. (74), as an example. As one can see, we do not have to determine the entire set of the triexcited moments $\mathfrak{M}^{ijk}_{\mu,abc}(2)$ in the MMCC(2,3)/CI calculations. This alone leads to considerable savings in the computer effort, since we only have to construct $\sim N_o N_u n_o^2 n_u^2$ moments $\mathfrak{M}^{ij\mathbf{K}}_{\mu,\mathbf{A}bc}(2)$, where N_o (N_u) is the number of active orbitals occupied (unoccupied) in $|\Phi\rangle$, which is a small fraction of all $\sim n_o^3 n_u^3$ moments $\mathfrak{M}^{ijk}_{\mu,abc}(2)$ when $N_o \ll n_o$ and $N_u \ll n_u$. Moreover, the $\sim n_o^3 n_u^4$ steps related to the construction of moments $\mathfrak{M}^{ijk}_{\mu,abc}(2)$reduce to the $\mathcal{N}^5$-like $N_o N_u n_o^2 n_u^3$ steps in the MMCC(2,3)/CI calculations. There is an additional cost related to the CISDt calculations, needed to generate the $|\Psi_\mu^{\mathrm{CISDt}}\rangle$ wave functions, but again the usual $n_o^3 n_u^5$ steps of the parent CISDT calculations reduce to the considerably less expensive $N_o N_u n_o^2 n_u^4$ steps in the CISDt case. All these factors contribute to the relatively low cost of the MMCC(2,3)/CI calculations. The number of triples used in the CISDt-corrected MMCC(2,3) calculations is usually very small (no more than $\sim$ 30 % of all triples; sometimes even less than that [47–49, 52, 68]). The CPU times required to construct the relevant corrections $\delta_\mu(2,3)$ to CCSD/EOMCCSD energies are often on the order of the CPU time of a single CCSD/EOMCCSD iteration [47–49, 52, 68].

We illustrate the performance of the CISDt-corrected MMCC(2,3) approach using excited states of the CH^+ ion as an example (see Table 2 and Figure 2). We are comparing the MMCC(2,3)/CI results for a few low-lying excited states of CH^+ of the $^1\Sigma^+$, $^1\Pi$, and $^1\Delta$ symmetries, obtained with the [5*s*3*p*1*d*/3*s*1*p*] basis set described in Ref. [103] and the ground-state restricted Hartree-Fock (RHF) orbitals, with the results of the corresponding full CI calculations reported in Refs. [45, 103]. Along with the MMCC(2,3)/CI and full CI data, we show the EOMCCSD and full EOMCCSDT results (the latter ones obtained in Ref. [44]) and the results obtained with the perturbative triples CC3 model [39] (see Table 2). In addition, in Figure 2, we compare the potential energy curves for excited states of CH^+, obtained with the MMCC(2,3)/CI approach, with the corresponding EOMCCSD and full CI curves on the one hand and the potential energy curves resulting from the CISDt calculations, which are used to generate wave functions $|\Psi_\mu\rangle$ for the MMCC(2,3)/CI method, on the other hand. In calculating the CISDt wave functions $|\Psi_\mu^{(\mathrm{CISDt})}\rangle$ and in calculating the final MMCC(2,3)/CI energies, we used a small active space consisting of the highest-energy occupied orbital, 3σ, and three lowest-energy unoccupied orbitals, $1\pi_x \equiv 1\pi$, $1\pi_y \equiv 2\pi$, and 4σ. This choice of active space reflects the nature of orbital excitations defining the valence excited states of CH^+ shown in Table 2 and Figure 2 (see Refs. [42, 43, 47] for details).

TABLE 2. A comparison of the MMCC(2,3)/CI, MMCC(2,3)/PT, CR-EOMCCSD(T), and CR-EOMCCSD(T)$_{\mathscr{L}}$ vertical excitation energies of the CH^+ ion, as described by the [5s3p1d/3s1p] basis set of Olsen *et al.* [103], at the equilibrium geometry, with the exact, full CI, data and other CC results.[a]

State	*Full CI*[b]	*EOMCCSD*[c]	*CC3*[d]	*EOMCCSDT*[c]	*MMCC(2,3)/CI*[e,f]	*MMCC(2,3)/PT*[f,g]	*CR-EOMCCSD(T)*[h]	*CR-EOMCCSD(T)*$_{\mathscr{L}}$[i]
$2\ ^1\Sigma^+$	8.549	0.560	0.230	0.074	0.084	0.102	0.117	0.106
$3\ ^1\Sigma^+$	13.525	0.055	0.016	0.001	0.000	0.052	0.011	0.020
$4\ ^1\Sigma^+$	17.217	0.099	0.026	-0.002	0.015		0.025	0.022
$1\ ^1\Pi$	3.230	0.031	0.012	-0.003	0.007	0.015	0.007	0.017
$2\ ^1\Pi$	14.127	0.327	0.219	0.060	0.105	-0.176	0.113	0.135
$1\ ^1\Delta$	6.964	0.924	0.318	0.040	0.051	0.090	0.027	0.032
$2\ ^1\Delta$	16.833	0.856	0.261	-0.038	0.006		-0.002	-0.030

[a] The full CI values are the excitation energies. All other values are the deviations from the full CI results. The $n\ ^1Y$ energy is the vertical excitation energy from the ground state ($X\ ^1\Sigma^+ \equiv 1\ ^1\Sigma^+$) to the n-th singlet state of symmetry Y. All energies are in eV. The equilibrium bond length in CH^+ is 2.13713 bohr.
[b] From Ref. [103].
[c] From Ref. [44].
[d] From Ref. [39].
[e] From Refs. [47, 48].
[f] The active space consisted of the 3σ, $1\pi_x \equiv 1\pi$, $1\pi_y \equiv 2\pi$, and 4σ orbitals.
[g] From Ref. [78].
[h] The CR-EOMCCSD(T),ID result taken from Ref. [51].
[i] From Ref. [79].

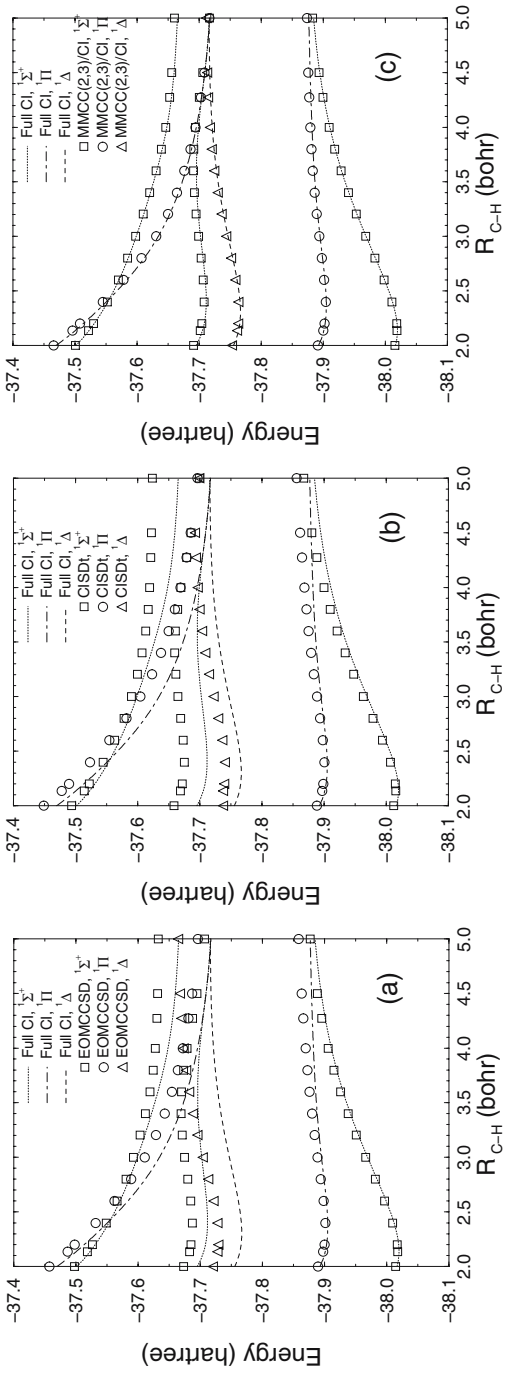

Figure 2. Potential energy curves for the CH^+ ion (energies in hartree and the C–H distance in bohr; see Refs. [44, 47] for the EOMCCSD and MMCC(2,3)/CI data; see Refs. [45, 103] for the full CI data). The results include the ground state and the two lowest excited states of the $^1\Sigma^+$ symmetry (the full CI curves are indicated by the dotted lines and other results are represented by □), the lowest two $^1\Pi$ states (the full CI curves are indicated by the dashed-dotted lines and other results are represented by ○), and the lowest $^1\Delta$ state (the full CI curve is indicated by the dashed line and other results are indicated by △). (a) A comparison of the EOMCCSD and full CI results. (b) A comparison of the CISDt and full CI results. (c) A comparison of the MMCC(2,3)/CI and full CI results.

We begin our discussion with the vertical excitation energies at the equilibrium geometry, $R_{\mathrm{C-H}} = R_e = 2.13713$ bohr, shown in Table 2. In this case, the doubly excited nature of the first-excited $^1\Sigma^+$ ($2\ ^1\Sigma^+$) state and of the lowest two $^1\Delta$ states $1\ ^1\Delta$ and $2\ ^1\Delta$, and the partially biexcited character of the second $^1\Pi$ state $2\ ^1\Pi$ (cf. Refs. [42, 43, 47, 103]) cause significant problems for the EOMCCSD approach. The errors in the EOMCCSD excitation energies for these four states, relative to the corresponding full CI values, are 0.560, 0.924, 0.856, and 0.327 eV, respectively. The CC3 method reduces these large errors to 0.219–0.318 eV, but if we want to obtain errors which are less than 0.1 eV with the standard EOMCC methodology, we must use the full EOMCCSDT approach (or its active-space EOMCCSDt variant [43, 44]). The full EOMCCSDT approach reduces the relatively large unsigned errors in the EOMCCSD results for the $2\ ^1\Sigma^+$, $1\ ^1\Delta$, $2\ ^1\Delta$, and $2\ ^1\Pi$ states to 0.074, 0.040, 0.038, and 0.060 eV, respectively.

As shown in Table 2, the inexpensive MMCC(2,3)/CI approach is capable of providing the results of full EOMCCSDT quality. Indeed, the errors in the vertical excitation energies for the $2\ ^1\Sigma^+$, $1\ ^1\Delta$, $2\ ^1\Delta$, and $2\ ^1\Pi$ states of CH^+ that have large double excitation components, obtained with the noniterative MMCC(2,3)/CI approximation, are 0.006–0.105 eV. This should be compared to the 0.327–0.924 eV errors in the EOMCCSD results, the 0.219–0.318 eV errors obtained with the CC3 method, and the 0.504–0.882 eV errors obtained with the CISDt approach used to construct wave functions $|\Psi_\mu\rangle$ for the MMCC(2,3)/CI calculations [47, 48]. For the remaining states shown in Table 2 (the third and fourth $^1\Sigma^+$ states and the lowest-energy $^1\Pi$ state), the errors in the CISDt-corrected MMCC(2,3) results, relative to full CI, are 0.000–0.015 eV. Again, the only standard EOMCC method that can compete with the MMCC(2,3)/CI approach is the expensive full EOMCCSDT approximation.

The excellent performance of the CISDt-corrected MMCC(2,3) approximation is not limited to vertical excitation energies at the equilibrium geometry. As shown in Figure 2 (c), the MMCC(2,3)/CI method is capable of providing a highly accurate description of entire excited-state potentials of CH^+. The very large (often > 1 eV) errors in the EOMCCSD and CISDt results for the excited-state potential energy curves, relative to the corresponding full CI curves (cf. Figures 2 (a) and (b)) are reduced in the MMCC(2,3)/CI calculations to 0.00–0.10 eV. For example, the errors in the EOMCCSD excitation energies, relative to full CI, for the three lowest excited states of the $^1\Sigma^+$ symmetry, the two lowest $^1\Pi$ states, and the two lowest $^1\Delta$ states are 0.668, 0.124, 0.256, 0.109, 0.564, 1.114, and 2.095 eV, respectively, at $R_{\mathrm{C-H}} = 1.5R_e$, and 0.299, 0.532, 0.771, 0.234, 0.467, 1.178, and 3.950 eV, respectively, at $R_{\mathrm{C-H}} = 2R_e$ [44]. Our

MMCC(2,3)/CI method reduces these large unsigned errors to 0.072, 0.005, 0.025, 0.024, 0.059, 0.065, and 0.086 eV, respectively, at $R_{\mathrm{C-H}} = 1.5R_e$, and 0.074, 0.048, 0.046, 0.045, 0.007, 0.079, and 0.029 eV, respectively, at $R_{\mathrm{C-H}} = 2R_e$ [47, 48]. As in the $R_{\mathrm{C-H}} = R_e$ case, the only standard EOMCC approach that can provide the results of this high quality is the expensive full EOMCCSDT method [44]. Interestingly enough, the MMCC(2,3)/CI approximation is capable of providing the reasonably correct description of the asymptotic region of the potential energy curves of CH^+, restoring almost perfectly, for example, the degeneracy of the $2\ ^1\Sigma^+$, $2\ ^1\Pi$, and $1\ ^1\Delta$ states in the $R_{\mathrm{C-H}} = \infty$ limit, which is severely broken by all EOMCC/response CC doubles models, including the standard EOMCCSD approach (cf. Figures 2 (a) and (c); see, also, Refs. [45, 47]). There is no need to reoptimize orbitals to obtain an accurate description of excited states of CH^+ in the MMCC(2,3)/CI calculations (the ordinary RHF orbitals are sufficient) and the required computer effort is small. For example, the fraction of all triples used in the MMCC(2,3)/CISDt calculations discussed here was, depending of state's symmetry, 26–29 % [47, 48].

The CI-corrected MMCC methods provide us with an excellent description of excited states dominated by double excitations and excited-state potentials along bond breaking coordinates, but one may think of reducing the costs of the CISDt-corrected MMCC(2,3) and similar calculations even further by replacing the CI wave functions $|\Psi_\mu\rangle$ in the MMCC(m_A, m_B) energy expressions, Eqs. (65) and (66), by the wave functions obtained with low-order MRMBPT approaches. We have recently implemented the pilot version of one of the possible MRMBPT-corrected MMCC(2,3) approaches, referred here and elsewhere in this article to as the MMCC(2,3)/PT method [78], in which we proceed as follows: First, as in all multi-reference calculations, and in analogy to the CISDt calculations discussed above, we divide the available spin-orbitals into core, active, and virtual categories, as shown in Figure 1. By distributing active electrons among active spin-orbitals in all possible ways, we produce a certain number (designated here by M) of reference determinants $|\Phi_p\rangle$, which span the complete model space or P-space $\mathscr{M}_0$. With the judicious choice of active spin-orbitals, we can assume that the linear combinations of reference determinants $|\Phi_p\rangle$, $p = 1, \ldots, M$,

$$|\bar{\Psi}_\mu^{(P)}\rangle = \sum_{p=1}^{M} \bar{c}_{p\mu} |\Phi_p\rangle, \tag{83}$$

where the coefficients $\bar{c}_{p\mu}$ and the corresponding eigenvalues $\bar{E}_\mu$ are obtained by diagonalizing the Hamiltonian in the model space $\mathscr{M}_0$, represent reasonable zero-order approximations to the ground- and excited states

$|\Psi_\mu\rangle$ and energies E_μ of interest. Once the model space $\mathscr{M}_0$ is defined, we consider all singly and doubly excited determinants with respect to each reference $|\Phi_p\rangle$, $p = 1, \ldots, M$, which span the Q-space (a subspace of the orthogonal complement $\mathscr{M}_0^\perp$), as is often done in multi-reference CISD calculations, and define the wave functions $|\Psi_\mu\rangle$, which will eventually be used to design the MMCC/PT (e.g. MMCC(2,3)/PT) energy corrections, as

$$|\Psi_\mu\rangle = \sum_{p=1}^{M} c_{p\mu}|\Phi_p\rangle + \sum_{q=M+1}^{R} c_{q\mu}|\Phi_q\rangle, \tag{84}$$

where $|\Phi_p\rangle$, $p = 1, \ldots, M$, are the reference determinants and $|\Phi_q\rangle$, $q = M+1, \ldots, R$, are the Q-space determinants, as defined above. We estimate the values of the coefficients $c_{p\mu}$, $p = 1, \ldots, M$, and $c_{q\mu}$, $q = M+1, \ldots, R$, in Eq. (84) by applying the partitioning technique to the Hamiltonian matrix in the space spanned by the P-space and Q-space determinants $|\Phi_p\rangle$ and $|\Phi_q\rangle$, respectively. Thus, if $\mathbf{C}_{P\mu}$ and $\mathbf{C}_{Q\mu}$ are the column vectors of coefficients $c_{p\mu}$ with $p = 1, \ldots, M$ and $c_{q\mu}$ with $q = M+1, \ldots, R$, respectively, and if $\mathbf{H}_{PP}$, $\mathbf{H}_{PQ}$, $\mathbf{H}_{QP}$, and $\mathbf{H}_{QQ}$ are the corresponding PP, PQ, QP, and QQ blocks of the Hamiltonian, we can write the Hamiltonian eigenvalue problem for the wave functions $|\Psi_\mu\rangle$, Eq. (84), as follows:

$$\begin{pmatrix} \mathbf{H}_{PP} & \mathbf{H}_{PQ} \\ \mathbf{H}_{QP} & \mathbf{H}_{QQ} \end{pmatrix} \begin{pmatrix} \mathbf{C}_{P\mu} \\ \mathbf{C}_{Q\mu} \end{pmatrix} = E_\mu \begin{pmatrix} \mathbf{C}_{P\mu} \\ \mathbf{C}_{Q\mu} \end{pmatrix}. \tag{85}$$

If we approximate the QQ block of the Hamiltonian, $\mathbf{H}_{QQ}$, by the diagonal matrix elements $\langle\Phi_q|H|\Phi_q\rangle$, we can immediately write

$$\mathbf{C}_{Q\mu} \approx (E_\mu \mathbf{1} - \mathbf{D}_Q)^{-1} \mathbf{H}_{QP} \mathbf{C}_{P\mu}, \tag{86}$$

or, more explicitly,

$$c_{q\mu} \approx \sum_{p=1}^{M} (E_\mu - \langle\Phi_q|H|\Phi_q\rangle)^{-1} \langle\Phi_q|H|\Phi_p\rangle\, c_{p\mu}, \quad (q = M+1, \ldots, R), \tag{87}$$

where $\mathbf{D}_Q$ in Eq. (86) is the diagonal part of $\mathbf{H}_{QQ}$. In the MRMBPT scheme used in our pilot implementation of the MMCC(2,3)/PT method [78], we obtain the approximate values of the coefficients $c_{q\mu}$, $q = M+1, \ldots, R$, by replacing the energies E_μ and coefficients $c_{p\mu}$, $p = 1, \ldots, M$, in Eq. (87) by the zero-order energies $\bar{E}_\mu$ and coefficients $\bar{c}_{p\mu}$, respectively, resulting from the diagonalization of the Hamiltonian in the model space $\mathscr{M}_0$ (diagonalization of $\mathbf{H}_{PP}$). We use the resulting approximate values of the coefficients $c_{q\mu}$,

$$\bar{c}_{q\mu} = \sum_{p=1}^{M} (\bar{E}_\mu - \langle\Phi_q|H|\Phi_q\rangle)^{-1} \langle\Phi_q|H|\Phi_p\rangle\, \bar{c}_{p\mu}, \quad (q = M+1, \ldots, R), \tag{88}$$

along with the coefficients $\bar{c}_{p\mu}$ obtained by diagonalizing $\mathbf{H}_{PP}$, to define the wave functions

$$|\bar{\Psi}_\mu\rangle = \sum_{p=1}^{M} \bar{c}_{p\mu}|\Phi_p\rangle + \sum_{q=M+1}^{R} \bar{c}_{q\mu}|\Phi_q\rangle, \tag{89}$$

which can be used instead of the wave functions $|\Psi_\mu\rangle$ in the MMCC(m_A, m_B) energy expressions, Eqs. (65) and (66), to define the MMCC(m_A, m_B)/PT approximations.

In the specific case of the MMCC(2,3)/PT approximation, we go one step further and, after rewriting each $|\bar{\Psi}_\mu\rangle$, Eq. (89), in the form of the CI expansion relative to the reference determinant $|\Phi\rangle$ used in the CCSD and EOMCCSD calculations whose results we want to improve,

$$|\bar{\Psi}_\mu\rangle = (\bar{C}_{\mu,0} + \bar{C}_{\mu,1} + \bar{C}_{\mu,2} + \bar{C}_{\mu,3} + \cdots)|\Phi\rangle, \tag{90}$$

where

$$\bar{C}_{\mu,0} = \bar{c}_0(\mu)\,\mathbf{1}, \tag{91}$$

$$\bar{C}_{\mu,1}|\Phi\rangle = \bar{c}_a^i(\mu)\,a^a a_i = \sum_{i,a} \bar{c}_a^i(\mu)\,a^a a_i, \tag{92}$$

$$\bar{C}_{\mu,2} = \tfrac{1}{4}\,\bar{c}_{ab}^{ij}(\mu)\,a^a a^b a_j a_i = \sum_{i<j,a<b} \bar{c}_{ab}^{ij}(\mu)\,a^a a^b a_j a_i, \tag{93}$$

and

$$\bar{C}_{\mu,3} = \tfrac{1}{36}\,\bar{c}_{abc}^{ijk}(\mu)\,a^a a^b a^c a_k a_j a_i = \sum_{i<j<k,a<b<c} \bar{c}_{abc}^{ijk}(\mu)\,a^a a^b a^c a_k a_j a_i \tag{94}$$

are the corresponding particle-hole excitation operators relative to $|\Phi\rangle$ defining the reference, singly excited, doubly excited, and triply excited contributions to $|\bar{\Psi}_\mu\rangle$, we truncate the CI expansion for the MRMBPT wave function $|\bar{\Psi}_\mu\rangle$, Eq. (90), at triply excited determinants (the $\bar{C}_{\mu,3}|\Phi\rangle$ term). As a result, the final energy formula for the MMCC(2,3)/PT energy, obtained by replacing $|\Psi_\mu\rangle$ in Eq. (67) by $|\bar{\Psi}_\mu\rangle$, Eq. (90), truncated at triply excited determinants relative to $|\Phi\rangle$, is

$$E_\mu^{(\mathrm{MMCC/PT})}(2,3) = E_\mu^{(\mathrm{EOMCCSD})} + \sum_{i<j<k,a<b<c} [\bar{c}_{abc}^{ijk}(\mu)]^*\,\mathfrak{M}_{\mu,abc}^{ijk}(2)/\bar{D}_\mu, \tag{95}$$

where the triply excited moments $\mathfrak{M}_{\mu,abc}^{ijk}(2)$ are defined by Eqs. (58) and (59) (and calculated using Eq. (60)), and

$$\bar{D}_\mu \equiv \langle\bar{\Psi}_\mu|R_\mu^{(\mathrm{CCSD})}e^{T^{(\mathrm{CCSD})}}|\Phi\rangle = \bar{\Delta}_{\mu,0} + \bar{\Delta}_{\mu,1} + \bar{\Delta}_{\mu,2} + \bar{\Delta}_{\mu,3} \tag{96}$$

is the overlap denominator $\langle\Psi_\mu|R_\mu^{(\mathrm{CCSD})}e^{T^{(\mathrm{CCSD})}}|\Phi\rangle$ entering Eq. (67), written for the wave function $|\Psi_\mu\rangle = |\bar{\Psi}_\mu\rangle$, Eq. (90), truncated at triples. The $\bar{\Delta}_{\mu,0}$, $\bar{\Delta}_{\mu,1}$, $\bar{\Delta}_{\mu,2}$, and $\bar{\Delta}_{\mu,3}$ contributions to the denominator $\bar{D}_\mu$, Eq. (96), are calculated as

$$\bar{\Delta}_{\mu,0} = [\bar{c}_0(\mu)]^* \, r_0(\mu), \tag{97}$$

$$\bar{\Delta}_{\mu,1} = \sum_{i,a} [\bar{c}_a^i(\mu)]^* \, \beta_a^i(\mu), \tag{98}$$

$$\bar{\Delta}_{\mu,2} = \sum_{i<j,a<b} [\bar{c}_{ab}^{ij}(\mu)]^* \, \beta_{ab}^{ij}(\mu), \tag{99}$$

and

$$\bar{\Delta}_{\mu,3} = \sum_{i<j<k,a<b<c} [\bar{c}_{abc}^{ijk}(\mu)]^* \, \beta_{abc}^{ijk}(\mu), \tag{100}$$

where $\bar{c}_0(\mu)$, $\bar{c}_a^i(\mu)$, $\bar{c}_{ab}^{ij}(\mu)$, and $\bar{c}_{abc}^{ijk}(\mu)$ are the CI coefficients obtained by rewriting the MRMBPT wave function, $|\bar{\Psi}_\mu\rangle$, Eq. (89), in the single-reference CI form of Eq. (90), and $r_0(\mu)$, $\beta_a^i(\mu)$, $\beta_{ab}^{ij}(\mu)$, and $\beta_{abc}^{ijk}(\mu)$ are the coefficients at the reference determinant $|\Phi\rangle$ and singly, doubly, and triply excited determinants, $|\Phi_i^a\rangle$, $|\Phi_{ij}^{ab}\rangle$, and $|\Phi_{ijk}^{abc}\rangle$ respectively, in the CI expansion of the CCSD/EOMCCSD wave function $R_\mu^{(\mathrm{CCSD})}e^{T^{(\mathrm{CCSD})}}|\Phi\rangle$ (for the formulas for the coefficients $\beta_a^i(\mu)$, $\beta_{ab}^{ij}(\mu)$, and $\beta_{abc}^{ijk}(\mu)$, see Eqs. (80)–(82), respectively). Although the summations over i, j, k, a, b, c in Eqs. (95) and (100) have the form of the complete summations over triples, in reality the wave functions $|\bar{\Psi}_\mu\rangle$, Eq. (89), contain only a small subset of all triples, once we rewrite each $|\bar{\Psi}_\mu\rangle$ in the form of the single-reference CI expansion, Eq. (90). This is a consequence of using active orbitals in designing the model space $\mathscr{M}_0$, which limit triple excitations relative to the reference $|\Phi\rangle$ to a small class of triple excitations that carry a certain number of active spin-orbital indices. Although the actual number of triples in $|\bar{\Psi}_\mu\rangle$ depends on the dimension of the active space used in the MRMBPT calculations, in analogy to the MMCC(2,3)/CI calculations, we only need a subset of all triexcited coefficients $\beta_{abc}^{ijk}(\mu)$, Eq. (82), and a subset of triply excited moments $\mathfrak{M}_{\mu,abc}^{ijk}(2)$, Eqs. (58)–(60), which match the nonzero coefficients $\bar{c}_{abc}^{ijk}(\mu)$, to calculate the MMCC(2,3)/PT energy, Eq. (95). Again, as in the MMCC(2,3)/CI case, one can easily extend the above MMCC(2,3)/PT approximation to higher-order MRMBPT-corrected MMCC(m_A, m_B) schemes, such as the MMCC(2,4)/PT approach which describes the combined effect of selected triple and quadruple excitations introduced by the MRMBPT wave functions [78].

One of the main advantages of the MRMBPT-corrected MMCC schemes, such as MMCC(2,3)/PT, is their low cost, compared to the already rather

inexpensive CI-corrected MMCC methods. As in the case of the CI-corrected MMCC approaches, such as MMCC(2,3)/CI, in the MMCC(2,3)/PT method and other MRMBPT-corrected MMCC approximations we have a very good control of accuracy through active orbitals defining model space $\mathscr{M}_0$, which can always be adjusted to the excited states or the bond breaking problem of interest, but unlike in the MMCC/CI schemes, we do not have to solve the iterative CISDt or other CI-like equations to generate the wave functions $|\Psi_\mu\rangle$ that enter the corrections $\delta_\mu(m_A, m_B)$ of the MRMBPT-corrected MMCC theories. We calculate the relevant CI-like coefficients, such as $\bar{c}_0(\mu)$, $\bar{c}_a^i(\mu)$, $\bar{c}_{ab}^{ij}(\mu)$, and $\bar{c}_{abc}^{ijk}(\mu)$, by converting the relatively simple expressions that define the MRMBPT wave functions $|\bar{\Psi}_\mu\rangle$, Eq. (89), into the single-reference CI form defined by Eq. (90). Thus, the main computer effort goes into the calculations of a small subset of triexcited moments $\mathfrak{M}_{\mu,abc}^{ijk}(2)$, leading to the significant reduction of the $n_o^3 n_u^4$ steps that are normally needed to calculate all moments $\mathfrak{M}_{\mu,abc}^{ijk}(2)$.

We illustrate the performance of the MMCC(2,3)/PT approach using selected excited states of the CH^+ ion, as described by the $[5s3p1d/3s1p]$ basis set of Ref. [103] (see Table 2). As in the case of the MMCC(2,3)/CI approach, we compare the MMCC(2,3)/PT results with the full CI vertical excitation energies at the equilibrium geometry $R_{C-H} = R_e = 2.13713$ bohr, reported in Ref. [103], and the corresponding EOMCCSD, EOMCCSDT, and CC3 results reported in Refs. [39, 44]. In calculating the MRMBPT wave functions $|\bar{\Psi}_\mu\rangle$, Eqs. (89) and (90), we used the same small set of active orbitals consisting of the 3σ, $1\pi_x \equiv 1\pi$, $1\pi_y \equiv 2\pi$, and 4σ orbitals as employed in the MMCC(2,3)/CI calculations.

As shown in Table 2, the inexpensive MMCC(2,3)/PT approach is capable of providing the results which are practically as good as the excellent MMCC(2,3)/CI results. In the case of the $2\ ^1\Sigma^+$ and $1\ ^1\Delta$ states, which have a strong double excitation character, causing the EOMCCSD approach to fail, the MMCC(2,3)/PT corrections to CCSD/EOMCCSD energies produce the results of the EOMCCSDT quality, reducing the 0.560 and 0.924 eV errors in the EOMCCSD results to 0.102 and 0.090 eV, respectively. For these two states, the errors relative to full CI obtained with the noniterative MMCC(2,3)/PT approach are 2–3 times smaller than the errors obtained with the much more expensive and iterative CC3 method. For states such as $2\ ^1\Pi$, which have a partially biexcited character, and for states dominated by single excitations ($3\ ^1\Sigma^+$, $1\ ^1\Pi$), the MMCC(2,3)/PT results are as good as the CC3 results. Although in this pilot study, we could not find the MRMBPT wave functions that would have a significant overlap with the EOMCCSD wave functions for the higher-energy $4\ ^1\Sigma^+$ and $2\ ^1\Delta$ states,

so that we could not obtain the complete set of MMCC(2,3)/PT energies, we can conclude that the MMCC(2,3)/PT method is as accurate as the MMCC(2,3)/CI approximation. This is good news, since MMCC(2,3)/PT calculations are less expensive than MMCC(2,3)/CI calculations, as explained above. We have, in fact, the preliminary results for the excitation energies corresponding to stretched geometries of the CH^+ ion [78]. For example, the MMCC(2,3)/PT approach reduces the large, 0.299, 0.532, 0.234, 0.467, and 1.178 eV errors in the EOMCCSD results for the $2\ ^1\Sigma^+$, $3\ ^1\Sigma^+$, $1\ ^1\Pi$, $2\ ^1\Pi$, and $1\ ^1\Delta$ states at $R_{C-H} = 2R_e$ to -0.079, -0.021, 0.133, -0.123, and 0.005 eV, respectively. The MMCC(2,3)/CI approach offers a very similar error reduction, but we need to solve the iterative CISDt equations to obtain the wave functions $|\Psi_\mu^{(\mathrm{CISDt})}\rangle$, Eq. (69), to calculate the MMCC(2,3)/CI corrections. This is not needed in the MMCC(2,3)/PT calculations, which rely on the less expensive MRMBPT-like wave functions $|\bar{\Psi}_\mu\rangle$, Eq. (89), in the process of constructing the $\delta_\mu(2,3)$ corrections to the CCSD/EOMCCSD energies.

The CI- and MRMBPT-corrected MMCC approximations lead to significant improvements of the EOMCC excitation energies by constructing corrections $\delta_\mu(m_A, m_B)$ with the help of the wave functions $|\Psi_\mu\rangle$ obtained in the non-CC calculations that provide a reasonable, qualitatively correct description of the ground and excited states of interest. The question arises if we can achieve the same goal and similar accuracies by designing the MMCC corrections $\delta_\mu(m_A, m_B)$ using nothing else than the cluster and excitation operators obtained in the CC/EOMCC calculations. This question is addressed in the next subsection.

3.1.2. *The CR-EOMCCSD(T) approach: The "black-box" MMCC method for molecular excited states*

An interesting alternative to the externally corrected MMCC methods, discussed in Section 3.1.1, is offered by the CR-EOMCCSD(T) approach [49, 51, 52, 59]. The CR-EOMCCSD(T) method can be viewed as an extension of the ground-state CR-CCSD(T) approach of Refs. [61, 62], which overcomes the failures of the standard CCSD(T) approximations when diradicals [76, 104, 105] and potential energy surfaces involving single bond breaking and single bond insertion [49, 50, 52, 60–62, 65, 67, 69, 70, 72, 73] are examined, to excited states.

The CR-EOMCCSD(T) approach is a purely single-reference, "black-box" method based on the MMCC(2,3) approximation, in which the wave function $|\Psi_\mu\rangle$ entering Eq. (67) is designed by using the singly and doubly excited cluster amplitudes t_a^i and t_{ab}^{ij}, defining T_1 and T_2, respectively, obtained in the CCSD calculations, and the zero-, one- and two-body amplitudes $r_0(\mu)$, $r_a^i(\mu)$ and $r_{ab}^{ij}(\mu)$, defining $R_{\mu,0}$, $R_{\mu,1}$, and $R_{\mu,2}$, respectively,

obtained in the EOMCCSD calculations. As with all MMCC(2,3) methods, the CR-EOMCCSD(T) approach enables us to correct the results of the CCSD/EOMCCSD calculations through noniterative energy corrections due to triples.

The wave functions $|\Psi_\mu\rangle$ that are used to design triples corrections of the CR-EOMCCSD(T) theory are obtained by analyzing the EOMCCSDT eigenvalue problem, in which the most expensive triples-triples block of the CCSDT/EOMCCSDT similarity-transformed Hamiltonian matrix is approximated by its diagonal and in which the T_3 cluster contributions to matrix elements of the CCSDT/EOMCCSDT similarity-transformed Hamiltonian are neglected. Depending on additional approximations in the resulting wave functions $|\Psi_\mu\rangle$, we can propose several variants of the CR-EOMCCSD(T) theory [51, 52]. In the following, we focus on variant ID (the CR-EOMCCSD(T),ID method), which represents one of the most complete versions of the CR-EOMCCSD(T) approach and which often provides the most accurate description of excited states when compared to the remaining CR-EOMCCSD(T) approximations [51–53]. Since we discuss here only one variant of the CR-EOMCCSD(T) theory, namely, the CR-EOMCCSD(T),ID method, we drop ",ID" from the acronym CR-EOMCCSD(T),ID, remembering that from now on CR-EOMCCSD(T) will stand in this paper for the CR-EOMCCSD(T),ID approach. In the CR-EOMCCSD(T) $\equiv$ CR-EOMCCSD(T), ID method, the wave function $|\Psi_\mu\rangle$ that enters Eq. (67), designated as $|\Psi_\mu^{(\text{CR-EOMCCSD(T)})}\rangle$, is defined as follows [51, 52, 59]:

$$\begin{aligned}
|\Psi_\mu^{(\text{CR-EOMCCSD(T)})}\rangle &= \bar{P}(R_{\mu,0}+R_{\mu,1}+R_{\mu,2}+\tilde{R}_{\mu,3})e^{T_1+T_2}|\Phi\rangle \\
&= \{R_{\mu,0}+(R_{\mu,1}+R_{\mu,0}T_1) \\
&\quad +[R_{\mu,2}+R_{\mu,1}T_1+R_{\mu,0}(T_2+\tfrac{1}{2}T_1^2)] \\
&\quad +[\tilde{R}_{\mu,3}+R_{\mu,2}T_1+R_{\mu,1}(T_2+\tfrac{1}{2}T_1^2) \\
&\quad +R_{\mu,0}(T_1T_2+\tfrac{1}{6}T_1^3)]\}|\Phi\rangle, \qquad (101)
\end{aligned}$$

where $\bar{P}$ is a projection operator on the subspace spanned by the reference $|\Phi\rangle$ and all singly, doubly, and triply excited determinants. The triple excitation operator $\tilde{R}_{\mu,3}$, entering Eq. (101), is calculated as

$$\tilde{R}_{\mu,3} = \tfrac{1}{36}\,\tilde{r}^{ijk}_{abc}(\mu)\; a^a a^b a^c a_k a_j a_i, \qquad (102)$$

where

$$\tilde{r}^{ijk}_{abc}(\mu) = \mathfrak{M}^{ijk}_{\mu,abc}(2)/D^{ijk}_{\mu,abc} \qquad (103)$$

are the approximate values of the triple excitation amplitudes $r^{ijk}_{abc}(\mu)$ resulting from the analysis of the full EOMCCSDT eigenvalue problem [51]. As

one can see, we calculate the approximate amplitudes $\tilde{r}^{ijk}_{abc}(\mu)$ using exactly the same set of triply excited moments $\mathfrak{M}^{ijk}_{\mu,abc}(2)$ of the CCSD/EOMCCSD equations that enters the MMCC(2,3) energy expression, Eq. (67). The $D^{ijk}_{\mu,abc}$ quantities that enter Eq. (103) represent the perturbative denominators for triple excitations, which are defined as follows [51, 52, 59]:

$$\begin{aligned} D^{ijk}_{\mu,abc} &= E^{(\mathrm{CCSD})}_{\mu} - \langle \Phi^{abc}_{ijk}|\bar{H}^{(\mathrm{CCSD})}|\Phi^{abc}_{ijk}\rangle \\ &= \omega^{(\mathrm{CCSD})}_{\mu} - \langle \Phi^{abc}_{ijk}|\bar{H}^{(\mathrm{CCSD})}_{1}|\Phi^{abc}_{ijk}\rangle \\ &\quad -\langle \Phi^{abc}_{ijk}|\bar{H}^{(\mathrm{CCSD})}_{2}|\Phi^{abc}_{ijk}\rangle \\ &\quad -\langle \Phi^{abc}_{ijk}|\bar{H}^{(\mathrm{CCSD})}_{3}|\Phi^{abc}_{ijk}\rangle, \end{aligned} \tag{104}$$

where $\bar{H}^{(\mathrm{CCSD})}_{p}$, $p = 1 - 3$, are the one-, two-, and three-body components of the CCSD/EOMCCSD similarity-transformed Hamiltonian $\bar{H}^{(\mathrm{CCSD})}$, respectively, and $\omega^{(\mathrm{CCSD})}_{\mu}$ is the EOMCCSD vertical excitation energy.

The use of the diagonal elements of the triples-triples block of the $\bar{H}^{(\mathrm{CCSD})}$ matrix rather than the more usual MBPT-like differences of bare spin-orbital energies $(\epsilon_a + \epsilon_b + \epsilon_c - \epsilon_i - \epsilon_j - \epsilon_k)$ in the definition of the denominators $D^{ijk}_{\mu,abc}$, which are needed to define the approximate triexcited amplitudes $\tilde{r}^{ijk}_{abc}(\mu)$, has a positive effect on the overall accuracies of the CR-EOMCCSD(T) calculations, while facilitating the open-shell implementation of the CR-EOMCCSD(T) method employing the restricted open-shell Hartree-Fock (ROHF) orbitals [59]. Indeed, the use of spin-orbital energy differences $(\epsilon_a + \epsilon_b + \epsilon_c - \epsilon_i - \epsilon_j - \epsilon_k)$ instead of the complete form of the diagonal matrix elements of $\bar{H}^{(\mathrm{CCSD})}$ involving triply excited determinants to define the denominator $D^{ijk}_{\mu,abc}$, Eq. (104), would lead to formal and practical difficulties related to the choice of the unperturbed Hamiltonian to define orbital energies because of the presence of the off-diagonal matrix elements in the spin-orbital form of the Fock matrix written for the ROHF orbitals (see Refs. [54, 85, 86, 106] for a discussion of serious problems that appear in the ROHF-based implementations of the CCSD(T) and CC3 methods). The use of the complete form of triexcited moments $\mathfrak{M}^{ijk}_{\mu,abc}(2)$, as defined by Eqs. (58)–(60), and the use of the complete form of the denominator $D^{ijk}_{\mu,abc}$, Eq. (104), in which all terms resulting from $\langle \Phi^{abc}_{ijk}|\bar{H}^{(\mathrm{CCSD})}|\Phi^{abc}_{ijk}\rangle$ are retained, as is done in the CR-EOMCCSD(T) approach discussed here, enables us to avoid these problems, which complicate the ROHF-based implementations of the CCSD(T) [85, 86, 106] and CC3 [54] methods, since we never have to worry about what terms in the Hamiltonian should be regarded as the zero-order terms to calculate the approximate triple excitation operator $\tilde{R}_{\mu,3}$, Eq. (102). This is one of the many advantages of the

MMCC-based CR-EOMCCSD(T) theory over the conventional treatment of triple excitations, such as CCSD(T) and CC3.

The above equations enable us to calculate the CR-EOMCCSD(T) energies by replacing $|\Psi_\mu\rangle$ in Eq. (67) by $|\Psi_\mu^{(\text{CR-EOMCCSD(T)})}\rangle$, Eq. (101). The resulting energy formula,

$$E_\mu^{(\text{CR-EOMCCSD(T)})} = E_\mu^{(\text{CCSD})} + \langle\Psi_\mu^{(\text{CR-EOMCCSD(T)})}|M_{\mu,3}(2)|\Phi\rangle / \langle\Psi_\mu^{(\text{CR-EOMCCSD(T)})}|R_\mu^{(\text{CCSD})}e^{T^{(\text{CCSD})}}|\Phi\rangle, \quad (105)$$

applies to ground and excited states (ground states when $\mu = 0$ and excited states when $\mu > 0$). In particular, we obtain the ground-state CR-EOMCCSD(T) energies by replacing $R_{\mu,0}$, $R_{\mu,1}$, and $R_{\mu,2}$ in Eq. (101) by $\mathbf{1}$, 0, and 0, respectively, and $\tilde{R}_{\mu,3}$, Eq. (102), by $\tilde{R}_{0,3} = \frac{1}{36}\,\tilde{r}_{abc}^{ijk}(0)\; a^a a^b a^c a_k a_j a_i$, where $\tilde{r}_{abc}^{ijk}(0) = \mathfrak{M}_{abc}^{ijk}(2)/D_{0,abc}^{ijk}$, with $\mathfrak{M}_{abc}^{ijk}(2)$ representing the triply excited moments of the CCSD equations, Eq. (59), and $D_{0,abc}^{ijk}$ given by Eq. (104) in which $\mu = 0$ and $\omega_0^{(\text{CCSD})} = 0$. The state-selective nature of the CR-EOMCCSD(T) method, in which the ground- and excited-state energies are obtained in separate, yet related, calculations using Eq. (105) and wave functions $|\Psi_\mu^{(\text{CR-EOMCCSD(T)})}\rangle$ that result from the analysis of the EOMCCSDT equations including the ground-state problem, leads to a much better balance between the energies of ground and excited states compared to the standard EOMCCSD(T), EOMCCSD($\tilde{\text{T}}$), EOMCCSD(T$'$) [35, 36], and CCSDR(3) [40, 41] calculations [51, 52]. In the standard approaches of the EOMCCSD(T) type, one focuses on directly improving the EOMCCSD vertical excitation energies and this leads to large discrepancies between the accuracies of the excited-state energies obtained from the EOMCCSD(T), EOMCCSD($\tilde{\text{T}}$), EOMCCSD(T$'$), and CCSDR(3) calculations and the ground-state energies calculated with the CCSD or CCSD(T) approaches (see Ref. [51] for a detailed discussion). Moreover, as shown, for example, in Refs. [51, 58], the standard noniterative methods of the EOMCCSD(T) type and their iterative analogs of the EOMCCSDT-n or CC3 type cannot be used to study excited-state potentials along bond breaking coordinates. As shown below, the CR-EOMCCSD(T) method is more robust in this regard, allowing one to explore large fragments of excited-state potential energy surfaces, even when the ground state is characterized by a large degree of nondynamic correlation.

The above Eq. (105) is a general expression. Let us briefly discuss the more explicit formulas for the CR-EOMCCSD(T) energies $E_\mu^{(\text{CR-EOMCCSD(T)})}$. In the most efficient implementations of the CR-EOMCCSD(T) approach reported in Refs. [51, 59], we rewrite Eq. (105)

as follows [59]:

$$E_\mu^{(\text{CR-EOMCCSD(T)})} = E_\mu^{(\text{CCSD})} + N_\mu^{\text{CR(T)}}/D_\mu^{\text{CR(T)}}, \tag{106}$$

where

$$N_\mu^{\text{CR(T)}} = \sum_{i<j<k,a<b<c} [\gamma_{abc}^{ijk}(\mu)]^* \, \mathfrak{M}_{\mu,abc}^{ijk}(2) \tag{107}$$

and

$$D_\mu^{\text{CR(T)}} = \Delta_{\mu,0}^{\text{CR(T)}} + \Delta_{\mu,1}^{\text{CR(T)}} + \Delta_{\mu,2}^{\text{CR(T)}} + \Delta_{\mu,3}^{\text{CR(T)}} \tag{108}$$

are the numerator ($\langle \Psi_\mu^{(\text{CR-EOMCCSD(T)})} | M_{\mu,3}(2) | \Phi \rangle$) and denominator ($\langle \Psi_\mu^{(\text{CR-EOMCCSD(T)})} | R_\mu^{(\text{CCSD})} e^{T^{(\text{CCSD})}} | \Phi \rangle$) terms appearing in Eq. (105). As already explained, the triply excited moments of the CCSD/EOMCCSD equations, $\mathfrak{M}_{\mu,abc}^{ijk}(2)$, are most efficiently calculated with the help of Eq. (60). The $\gamma_{abc}^{ijk}(\mu)$ amplitudes that enter the numerator term $N_\mu^{\text{CR(T)}}$, Eq. (107), represent the coefficients at the triply excited determinants $|\Phi_{ijk}^{abc}\rangle$ in the CI expansion of $|\Psi_\mu^{(\text{CR-EOMCCSD(T)})}\rangle$,

$$\gamma_{abc}^{ijk}(\mu) = \langle \Phi_{ijk}^{abc} | \Psi_\mu^{(\text{CR-EOMCCSD(T)})} \rangle = \tilde{r}_{abc}^{ijk}(\mu) + \beta_{abc}^{ijk}(\mu), \tag{109}$$

where $\tilde{r}_{abc}^{ijk}(\mu)$ and $\beta_{abc}^{ijk}(\mu)$ are given by Eqs. (103) and (82), respectively. The $\Delta_{\mu,0}^{\text{CR(T)}}$, $\Delta_{\mu,1}^{\text{CR(T)}}$, $\Delta_{\mu,2}^{\text{CR(T)}}$, and $\Delta_{\mu,3}^{\text{CR(T)}}$ terms that contribute to the denominator $D_\mu^{\text{CR(T)}}$, Eq. (108), are defined as

$$\Delta_{\mu,0}^{\text{CR(T)}} = |r_0(\mu)|^2, \tag{110}$$

$$\Delta_{\mu,1}^{\text{CR(T)}} = \sum_{i,a} |\beta_a^i(\mu)|^2, \tag{111}$$

$$\Delta_{\mu,2}^{\text{CR(T)}} = \sum_{i<j,a<b} |\beta_{ab}^{ij}(\mu)|^2, \tag{112}$$

and

$$\Delta_{\mu,3}^{\text{CR(T)}} = \sum_{i<j<k,a<b<c} [\gamma_{abc}^{ijk}(\mu)]^* \, \beta_{abc}^{ijk}(\mu), \tag{113}$$

where $r_0(\mu)$, $\beta_a^i(\mu)$, and $\beta_{ab}^{ij}(\mu)$ are the coefficients at the reference determinant $|\Phi\rangle$ and singly and doubly excited determinants, $|\Phi_i^a\rangle$ and $|\Phi_{ij}^{ab}\rangle$, respectively, in the CI expansion of the CCSD or EOMCCSD wave functions $R_\mu^{(\text{CCSD})} e^{T^{(\text{CCSD})}} |\Phi\rangle$ (for the formulas for $\beta_a^i(\mu)$ and $\beta_{ab}^{ij}(\mu)$, see Eqs. (80) and (81), respectively). The key elements of the algorithm that leads

to the highly efficient general-purpose computer implementation of the CR-EOMCCSD(T) approach, based on Eq. (106), are shown in Figure 3. As one can read from Figure 3, we calculate moments $\mathfrak{M}^{ijk}_{\mu,abc}(2)$ "on the fly" in the explicit loop over $i<j<k$ and there is no explicit loop over $a<b<c$. Instead, we calculate the entire set of moments $\mathfrak{M}^{ijk}_{\mu,abc}(2)$ corresponding to all values of a,b,c and fixed values of indices i,j,k from the $i<j<k$ loop, which are stored in a relatively small array of dimension n_u^3. This is done to achieve a high efficiency of the resulting CR-EOMCCSD(T) code. Indeed, we could choose an alternative coding strategy and calculate moments $\mathfrak{M}^{ijk}_{\mu,abc}(2)$ for $i<j<k$ and $a<b<c$ only, but this would have to be done at the expense of the high degree of vectorization characterizing Eq. (60) and the algorithm shown in Figure 3, which significantly benefits from the use of fast matrix multiplication routines from the `BLAS` library in determining $\mathfrak{M}^{ijk}_{\mu,abc}(2)$. For example, if we used the explicit $i<j<k$ and $a<b<c$ loops, the calculation of the $\frac{1}{2}\bar{h}^{ie}_{ab}r^{jk}_{ec}$ term in Eq. (60), which is one of the terms that defines the $n_o^3n_u^4$ scaling of the CR-EOMCCSD(T) theory, would split into a very large number of $\sim\frac{1}{36}\,n_o^3n_u^3$ very short matrix multiplications, each involving the summation over a single index e only. Each of these matrix multiplications is fast, but we would have to repeat them as many times as the number of elements in the $i<j<k$ and $a<b<c$ loops and this would result in a much slower code. By having the explicit loop over $i<j<k$ only, the summation over e for the entire set of all a,b,c values entering the $\bar{h}^{ie}_{ab}r^{jk}_{ec}$ term is performed with a single call to the `BLAS` matrix multiplication routine, which is a much more efficient use of fast matrix multipliers. At the same time, by calculating moments $\mathfrak{M}^{ijk}_{K,abc}(2)$ in the explicit loop over $i<j<k$, we keep the memory requirements at the relatively low level that does not exceed n_u^3 words when we execute Eq. (60). As a result, the memory requirements of the CR-EOMCCSD(T) calculations are defined by the $t^{im}_{ae}\bar{h}^{ec}_{mb}$, $-t^{im}_{be}v^{ec}_{ma}$, and $-\bar{h}^{ec}_{bm}r^{im}_{ae}$ terms that enter the definitions of $\bar{h}^{ic}_{ab}$ and I^{ic}_{ab} in Table 1. These memory requirements are $2n_on_u^3$ words. The calculation of moments $\mathfrak{M}^{ijk}_{\mu,abc}(2)$ in the explicit loop over $i<j<k$ and for all values of a,b,c to achieve a high degree of vectorization creates an impression that the operation count in our algorithm is artificially increased by a factor of 6, compared to the use of the explicit $i<j<k$ and $a<b<c$ loops, but this is a false impression. To avoid overcomputing, which the calculation involving all a,b,c values seems to imply, while enhancing, at the same time, the performance through a highly efficient use of the `BLAS` matrix multiplication routines, instead of enforcing the correct symmetry of $\mathfrak{M}^{ijk}_{\mu,abc}(2)$ with respect to permutations of indices a,b,c during the determination of $\mathfrak{M}^{ijk}_{\mu,abc}(2)$, we first calculate the nonsym-

metric quantity $\mathfrak{T}^{ijk}_{\mu,abc}(2)$ for the given i,j,k values from the $i<j<k$ loop and for all a,b,c values (see Eq. (60)). Once this is done, we have at our disposal all of the relevant $\mathfrak{T}^{ijk}_{\mu,abc}(2)$ values that are needed to construct the final $\mathfrak{M}^{ijk}_{\mu,abc}(2)$ moment, which is obtained by simply adding the six values of $\mathfrak{T}^{ijk}_{\mu,abc}(2)$ that correspond to six permutations of indices a,b,c, with the appropriate permutation signs, as in the definition of the antisymmetrizer $\mathscr{A}_{abc}$, Eq. (61). In other words, the antisymmetrization over a,b,c is done at the very end, once all six numerical values of $\mathfrak{T}^{ijk}_{\mu,abc}(2)$ that correspond to six permutations of indices a,b,c are determined.

By following the algorithm described in Figure 3 and by using the idea of recursively generated intermediates in the calculation of the triply excited moments $\mathfrak{M}^{ijk}_{\mu,abc}(2)$ (cf. Eq. (60) and Table 1) and the CR-EOMCCSD(T) corrections $\delta^{\rm CR(T)}_\mu = N^{\rm CR(T)}_\mu/D^{\rm CR(T)}_\mu$ to CCSD/EOMCCSD energies, we achieve a very high degree of efficiency of the CR-EOMCCSD(T) computer codes. In particular, the most expensive steps of the CR-EOMCCSD(T) codes based on the algorithm described in Figure 3 scale as $n_o^2n_u^4$ in the iterative CCSD and EOMCCSD parts and $n_o^3n_u^4$ in the noniterative part associated with the determination of the CR-EOMCCSD(T) corrections $\delta^{\rm CR(T)}_\mu$. Specifically, the CPU time required to calculate the triples correction $\delta^{\rm CR(T)}_\mu$ for a given excited state is twice or three times the CPU time required to calculate the standard (T) correction of the ground-state CCSD(T) method (for the ground state, the timings of CR-EOMCCSD(T) and CCSD(T) calculations are essentially the same). For comparison, the full EOMCCSDT approach involves a lot more expensive and iterative $n_o^3n_u^5$ steps. The CC3 method, with its iterative $n_o^3n_u^4$ steps, is less time-consuming compared to EOMCCSDT, but the need to perform iterative $\mathscr{N}^7$-like calculations makes the CC3 approach considerably more expensive than the CR-EOMCCSD(T) method. At the same time, as shown in Table 2, the CR-EOMCCSD(T) results are more accurate than the corresponding CC3 results. In fact, they are almost as good as the results of full EOMCCSDT calculations (see Tables 2 and 3; see Refs. [49, 51, 52] for other examples).

Let us, therefore, illustrate the performance of the CR-EOMCCSD(T) approach by a few examples of benchmark calculations (for the realistic applications of the CR-EOMCCSD(T) approach, see, for example, Refs. [51, 52, 64]). As in the case of the MMCC(2,3)/CI and MMCC(2,3)/PT methods, we begin our discussion with the electronic excitations in the CH^+ ion, as described by the $[5s3p1d/3s1p]$ basis set of Ref. [103] (see Table 2). A comparison of the vertical excitation energies, corresponding to the three lowest-energy excited states of the $^1\Sigma^+$ symmetry and two lowest-energy states of the $^1\Pi$ and $^1\Delta$ symmetries, obtained at the equilibrium geometry

Solve the CCSD/EOMCCSD equations

LOOP OVER μ

Compute the CCSD/EOMCCSD total energy $E_\mu^{(\mathrm{CCSD})}$

Compute $\Delta_{\mu,0}^{\mathrm{CR(T)}}$, $\Delta_{\mu,1}^{\mathrm{CR(T)}}$, and $\Delta_{\mu,2}^{\mathrm{CR(T)}}$, Eqs. (110)–(112), respectively

DENOM = $\Delta_{\mu,0}^{\mathrm{CR(T)}}$ + $\Delta_{\mu,1}^{\mathrm{CR(T)}}$ + $\Delta_{\mu,2}^{\mathrm{CR(T)}}$

SUM = 0.0

LOOP OVER i<j<k

Calculate $\mathfrak{T}_{\mu,abc}^{ijk}(2)$ for all values of a, b, c using Eq. (60)

Calculate $\mathfrak{M}_{\mu,abc}^{ijk}(2)$ by antisymmetrizing $\mathfrak{T}_{\mu,abc}^{ijk}(2)$, as in Eq. (60)

LOOP OVER a<b<c

Calculate $D_{\mu,abc}^{ijk}$, Eq. (104)

Calculate $\tilde{r}_{abc}^{ijk}(\mu)$, Eq. (103)

Calculate $\beta_{abc}^{ijk}(\mu)$, Eq. (82)

Calculate $\gamma_{abc}^{ijk}(\mu)$, Eq. (109)

SUM = SUM + $\gamma_{abc}^{ijk}(\mu)$ * $\mathfrak{M}_{\mu,abc}^{ijk}(2)$

DENOM = DENOM + $\gamma_{abc}^{ijk}(\mu)$ * $\beta_{abc}^{ijk}(\mu)$

END OF LOOP OVER a<b<c

END OF LOOP OVER i<j<k

CORR = SUM/DENOM

$E_\mu^{(\text{CR-EOMCCSD(T)})} = E_\mu^{(\mathrm{CCSD})}$ + CORR

END OF LOOP OVER μ

Figure 3. The key elements of the algorithm used to calculate the CR-EOMCCSD(T) energy, Eq. (106).

$R_{\mathrm{C-H}} = R_e = 2.13713$ bohr with the CR-EOMCCSD(T) approach, with the analogous results obtained in the EOMCCSD, CC3, EOMCCSDT, and full CI calculations reported in Refs. [39, 44, 103] is given in Table 2. As one can see, the relatively inexpensive CR-EOMCCSD(T) method, which has the ease-of-use of the standard ground-state CCSD(T) approach, pro-

vides the results of the EOMCCSDT quality, particularly for the $2\ ^1\Sigma^+$, $1\ ^1\Delta$, and $2\ ^1\Delta$ states that are dominated by double excitations, for which the standard EOMCCSD approach fails. Indeed, the CR-EOMCCSD(T) approach reduces the 0.560, 0.924, and 0.856 eV errors obtained with the EOMCCSD method for the $2\ ^1\Sigma^+$, $1\ ^1\Delta$, and $2\ ^1\Delta$ states of CH^+ to 0.117, 0.027, and -0.002 eV, respectively. In fact, the CR-EOMCCSD(T) results for the $2\ ^1\Sigma^+$, $1\ ^1\Delta$, and $2\ ^1\Delta$ states are considerably better than the results of the iterative triples CC3 calculations, which give 0.230–0.318 eV errors in this case. Similar remarks apply to the $2\ ^1\Pi$ state, which has a partially biexcited character (see Table 2). For the remaining three states that are dominated by singles (the $3\ ^1\Sigma^+$, $4\ ^1\Sigma^+$, and $1\ ^1\Pi$ states), the CR-EOMCCSD(T) method improves the relatively good EOMCCSD results, reducing the 0.031–0.099 eV errors obtained with the EOMCCSD approach to 0.007–0.025 eV, which is more or less the same level of accuracy as observed in the CC3 calculations. The overall accuracy of the CR-EOMCCSD(T) approach, which is a relatively inexpensive "black-box" method, is as good as the accuracy of the MMCC(2,3)/CI approximation, which requires choosing active orbitals and performing additional CISDt calculations.

As shown in Refs. [51, 52], the excellent performance of the CR-EOMCCSD(T) approach is not limited to the equilibrium geometry. For example, the CR-EOMCCSD(T) method is capable of reducing the large unsigned errors of 0.299, 0.532, 0.234, 0.467, and 1.178 eV, obtained in the EOMCCSD calculations for CH^+ at $R_{\text{C-H}} = 2R_e$ for the $2\ ^1\Sigma^+$, $3\ ^1\Sigma^+$, $1\ ^1\Pi$, $2\ ^1\Pi$, and $1\ ^1\Delta$ states, to 0.093, 0.084, 0.061, 0.018, and 0.009 eV, respectively [51, 52]. At the significantly stretched nuclear geometries of CH^+, such as $R_{\text{C-H}} = 2R_e$, the CR-EOMCCSD(T) approach has some problems with the higher-energy $4\ ^1\Sigma^+$ and $2\ ^1\Delta$ states, but even in this case we observe considerable improvements in the poor EOMCCSD results when the CR-EOMCCSD(T) method is employed (see Refs. [51, 52] for further details). Similar remarks apply to excited-state potential energy surfaces along bond breaking coordinates of other molecules, including strongly multi-reference systems, such as ozone [107] and C_2 [53]. For example, in a recent study [53], we have examined the performance of the CR-EOMCCSD(T) method employing RHF orbitals in the calculations of ground- and excited-state potential energy curves of C_2, as described by the 6-31G* basis set [108]. In addition to the ground-state ($X\ ^1\Sigma_g^+$) curve, we have examined two lowest-energy excited states of the $^1\Delta_g$ and $^1\Sigma_g^+$ symmetries, designated as the $B\ ^1\Delta_g$ and $B'\ ^1\Sigma_g^+$ states, respectively. The CR-EOMCCSD(T) results have been compared with the full CI curves for the $X\ ^1\Sigma_g^+$, $B\ ^1\Delta_g$, and $B'\ ^1\Sigma_g^+$ states of the C_2/6-31G* molecule reported by Abrams and Sherrill [109]. Our findings are summarized in Figure 4. As

one can see, the $X\ ^1\Sigma_g^+$, $B\ ^1\Delta_g$, and $B'\ ^1\Sigma_g^+$ potential curves of C_2 create a significant challenge for the standard CCSD and EOMCCSD approaches. If we focus on the C–C distances ranging between 1.1 and 1.8 Å, the errors in the CCSD and EOMCCSD results for the $X\ ^1\Sigma_g^+$, $B\ ^1\Delta_g$, and $B'\ ^1\Sigma_g^+$ states are 0.76–1.52 eV, 2.77–3.48 eV, and 2.43–3.18 eV, respectively. In particular, the error in the EOMCCSD vertical excitation energy corresponding to the $X\ ^1\Sigma_g^+ \to B\ ^1\Delta_g$ transition at the approximate equilibrium geometry $R_{C-C} = 1.25$ Å, relative to the full CI value of 2.43 eV, is 1.98 eV. A similarly large error in the EOMCCSD result for the $X\ ^1\Sigma_g^+ \to B\ ^1\Delta_g$ vertical transition in C_2 was observed earlier by Christiansen *et al.* [41]. These authors used a modified version of the aug-cc-pVDZ basis set [110, 111] and noted that even the iterative CC3 and EOMCCSDT-1 methods, which account for the triples effects, produce large errors on the order of 0.9 eV, when the $B\ ^1\Delta_g$ state is examined. In fact, in a more recent study [49], Piecuch *et al.* showed that the lowest $^1\Delta_g$ state of C_2 cannot be accurately described by the full EOMCCSDT approach, which gives an error on the order of 0.4 eV, when the modified variant of the aug-cc-pVDZ basis set used by Christiansen *et al.* is employed. The only standard EOMCC method, which is capable of providing an accurate description of the $B\ ^1\Delta_g$ state of C_2, is the prohibitively expensive full EOMCCSDTQ approach [46].

As shown in Figure 4, the CCSD and EOMCCSD potentials are not only characterized by huge errors, as described above; they are also qualitatively incorrect. For example, the $B\ ^1\Delta_g$ potential curve is shifted to higher energies so much that it crosses the $B'\ ^1\Sigma_g^+$ curve; this is completely wrong since the full CI calculations show that the $B\ ^1\Delta_g$ curve should cross the $X\ ^1\Sigma_g^+$ potential, not the $B'\ ^1\Sigma_g^+$ curve. In addition, the small, ~ 0.4 eV energy gap corresponding to an avoided crossing of the $X\ ^1\Sigma_g^+$ and $B'\ ^1\Sigma_g^+$ full CI states at $R \approx 1.7$ Å is absent in the CCSD/EOMCCSD calculations. The extremely poor performance of the standard EOMCCSD approach for the $B\ ^1\Delta_g$ and $B'\ ^1\Sigma_g^+$ states of C_2 confirms the well-known fact that the EOMCCSD method cannot describe excited-state potential energy surfaces along bond-breaking coordinates and excited states dominated by two-electron transitions (in this case, the $1\pi_u^2 \to 3\sigma_g^2$ double excitations relative to the RHF reference determinant).

The CR-EOMCCSD(T) approach dramatically improves the poor CCSD/EOMCCSD results. This can be seen by comparing the CCSD/EOMCCSD and full CI potential energy curves with the CR-EOMCCSD(T) potential curves shown in Figure 4. Although the CR-EOMCCSD(T) method cannot accurately describe the $B\ ^1\Delta_g$ and $B'\ ^1\Sigma_g^+$ excited states in the asymptotic region [53] (not shown in Figure 4), the CR-EOMCCSD(T) results for the $X\ ^1\Sigma_g^+$, $B\ ^1\Delta_g$ and $B'\ ^1\Sigma_g^+$ states in the

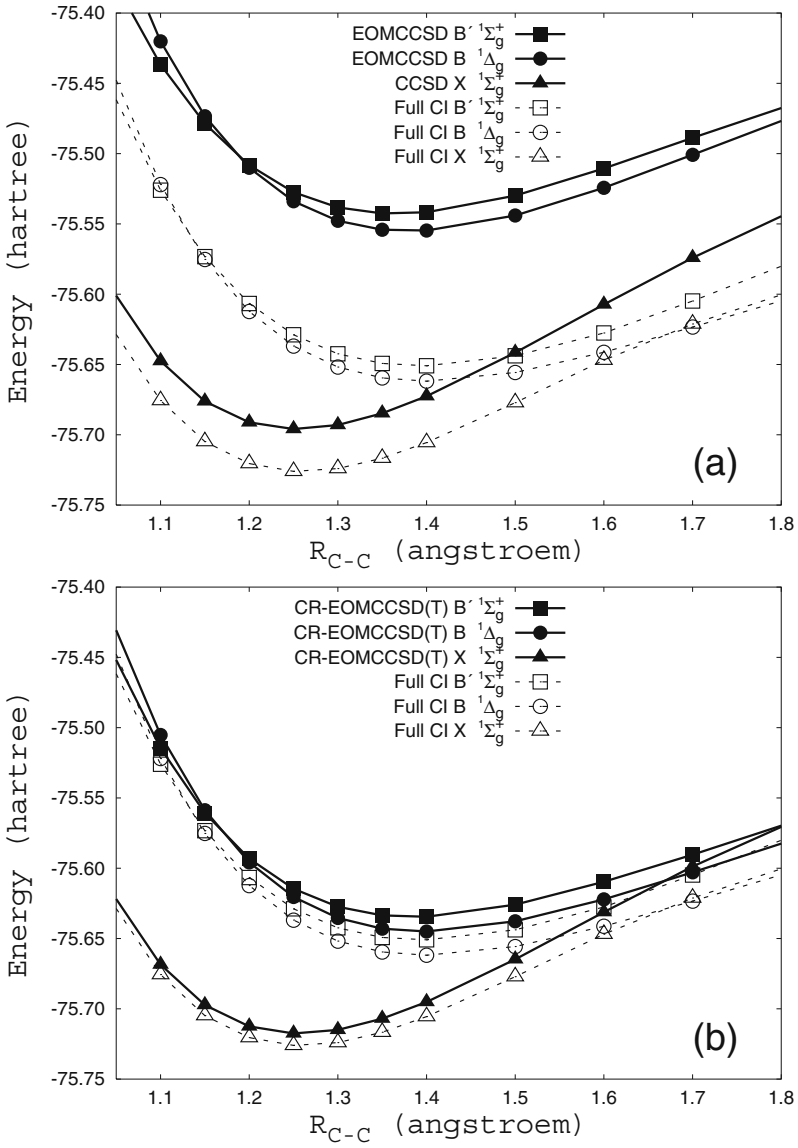

Figure 4. Potential energy curves for the C_2 molecule (energies in hartree and the C–C distance in Å; the CCSD/EOMCCSD and full CI data taken from Refs. [53, 109]; the CR-EOMCCSD(T)≡CR-EOMCCSD(T),ID data has not been published before). The results include the ground state, $X\ ^1\Sigma_g^+$, and the lowest excited states of the $^1\Delta_g$ and $^1\Sigma_g^+$ symmetries, $B\ ^1\Delta_g$ and $B'\ ^1\Sigma_g^+$. The full CI curves are indicated by the dashed lines and open symbols and the CC/EOMCC curves are indicated by the solid lines and filled symbols. (a) A comparison of the CCSD/EOMCCSD and full CI results. (b) A comparison of the CR-EOMCCSD(T) and full CI results.

spectroscopic 1.1 Å$\leq R_{C-C} \leq$ 1.8 Å region are quite good, particularly if we take into consideration the single-reference character and the relatively low cost of the CR-EOMCCSD(T) calculations and the challenge that the low-lying electronic states of C_2 create for single-reference methods [53, 109]. The CR-EOMCCSD(T) approach reduces the 0.76–1.52 eV, 2.77–3.48 eV, and 2.43–3.18 eV errors obtained in the CCSD/EOMCCSD calculations for the $X\ ^1\Sigma_g^+$, $B\ ^1\Delta_g$ and $B'\ ^1\Sigma_g^+$ states of C_2 in the 1.1 Å$\leq R_{C-C} \leq$ 1.8 Å region to 0.19–0.81 eV, 0.45–0.61 eV, and 0.28–0.49 eV, respectively. In particular, the large, 1.98 eV, error in the EOMCCSD vertical excitation energy corresponding to the $X\ ^1\Sigma_g^+ \rightarrow B\ ^1\Delta_g$ transition at the approximate equilibrium geometry $R_{C-C} = 1.25$ Å reduces to 0.22 eV, when the CR-EOMCCSD(T) method is employed. A similarly impressive error reduction in the EOMCCSD results for the $X\ ^1\Sigma_g^+ \rightarrow B\ ^1\Delta_g$ vertical transition in C_2 was observed in our recent CR-EOMCCSD(T), MMCC(2,3)/CI, and MMCC(2,4)/CI calculations employing the modified aug-cc-pVDZ basis set of Christiansen *et al.* [48, 49, 51, 52].

The CR-EOMCCSD(T) curves for the $X\ ^1\Sigma_g^+$, $B\ ^1\Delta_g$ and $B'\ ^1\Sigma_g^+$ states of C_2 are almost parallel to the corresponding full CI curves. Indeed, the nonparallelity errors (NPE's; NPE is defined as the difference between the maximum and minimum errors along a potential energy curve) obtained with the CR-EOMCCSD(T) approach in the 1.1 Å$\leq R_{C-C} \leq$ 1.8 Å region are 0.62, 0.16, and 0.21 eV for the $X\ ^1\Sigma_g^+$, $B\ ^1\Delta_g$ and $B'\ ^1\Sigma_g^+$ states, respectively. This should be compared to the NPE values of 0.76, 0.71, and 0.75 eV, respectively, obtained in the EOMCCSD calculations. We can reduce the NPE values obtained with the CR-EOMCCSD(T),ID method discussed here even further if we employ variant III of the CR-EOMCCSD(T) approach [51, 52]. As shown in Ref. [53], the NPE values obtained with variant III of the CR-EOMCCSD(T) method for the $X\ ^1\Sigma_g^+$, $B\ ^1\Delta_g$ and $B'\ ^1\Sigma_g^+$ states in the 1.1 Å$\leq R_{C-C} \leq$ 1.8 Å region are 0.36, 0.06, and 0.16 eV, respectively.

As shown in Figure 4, the CR-EOMCCSD(T) approach restores the crossing of the $X\ ^1\Sigma_g^+$ and $B\ ^1\Delta_g$ states in the $R \approx 1.7$ Å region. It also brings the $X\ ^1\Sigma_g^+$ and $B'\ ^1\Sigma_g^+$ states much closer to each other in the $R = 1.6 - 1.8$ Å region, trying to mimic the existence of an avoided crossing between these two states that the standard CCSD/EOMCCSD methods fail to describe. The only problem is that variant ID of the CR-EOMCCSD(T) theory brings the nearly degenerate $X\ ^1\Sigma_g^+$ and $B'\ ^1\Sigma_g^+$ states too close to each other, so that they become virtually degenerate. As shown in Ref. [53], this problem can be eliminated by replacing the denominators $D^{ijk}_{\mu,abc}$, Eq. (104), that are used to define the approximate triexcited amplitudes $\tilde{r}^{ijk}_{abc}(\mu)$ by the MBPT-like energy differences $[\omega_\mu^{(CCSD)} - (\epsilon_a + \epsilon_b + \epsilon_c - \epsilon_i - \epsilon_j - \epsilon_k)]$,

but then one looses some of the high accuracy of the CR-EOMCCSD(T),ID and CR-EOMCCSD(T),III results. This problem will have to be addressed in the future.

Finally, before discussing our recent attempt to formulate the MMCC methods employing left eigenstates of the CC/EOMCC similarity-transformed Hamiltonian [79], let us mention that the very good performance of the CR-EOMCCSD(T) approach is not limited to singlet electronic states or closed-shell molecules. We have recently developed the highly efficient computer codes for the CR-EOMCCSD(T) calculations for non-singlet electronic states of radical and other open-shell systems, as described by the ROHF orbitals [59]. We have tested these codes on excited states of several open shell systems, including the CH radical, which poses a serious challenge to standard EOMCC and response CC methods, such as EOMCCSD and CC3 [54], since some of the low-lying states of CH have a large double excitation character which requires a highly accurate determination of the triples effects (T_3 and $R_{\mu,3}$) in CC/EOMCC calculations. This can be seen in Table 3, where we characterize the low-lying excited states of CH by the reduced excitation level (REL) defined as [59]

$$\text{REL} \;=\; \sum_{n=0}^{2} n\,\langle\Phi|(R_{\mu,n})^{\dagger}R_{\mu,n}|\Phi\rangle \,/\, \sum_{n=0}^{2}\langle\Phi|(R_{\mu,n})^{\dagger}R_{\mu,n}|\Phi\rangle, \quad (114)$$

where $R_{\mu,n}$, $n = 0-2$, are the zero-, one-, and two-body components of the excitation operator $R_{\mu}^{(\text{CCSD})}$ obtained in the EOMCCSD calculations. The REL ≈ 1.0 value implies that a given excited state is dominated by singles and REL ≈ 2.0 for excited states dominated by doubles. As shown in Table 3, the $a\ ^4\Sigma^-$ and $A\ ^2\Delta$ states of CH are dominated by single excitations, whereas the $B\ ^2\Sigma^-$ and $C\ ^2\Sigma^+$ states have a considerable multi-reference character [112] and significant contributions from double excitations.

Shown in Table 3 are the total and adiabatic excitation energies T_e, obtained with the aug-cc-pVTZ basis set [110, 111], and the dipole moments μ, obtained with the aug-cc-pVDZ basis set [110, 111], in various electronic states of CH. We compare the CR-EOMCCSD(T) results for the total and adiabatic excitation energies and dipole moments with the corresponding results of the CCSD/EOMCCSD calculations and the recently reported [46] results of the full CCSDT/EOMCCSDT calculations employing the unrestricted Hartree-Fock (UHF) reference. The relevant experimental data, including the T_e and μ values and the equilibrium bond lengths used in the CC/EOMCC calculations, were taken from Refs. [113–119]. The CCSD/EOMCCSD and CCSDT/EOMCCSDT values of the dipole moments were obtained analytically, using the right and left eigenstates of the relevant similarity-transformed Hamiltonians, as described in Section

2.1 (see Eqs. (45)–(47)). The CR-EOMCCSD(T) values of μ were obtained numerically using the finite-field method.

As shown in Table 3, the CR-EOMCCSD(T) approach provides a uniformly accurate description of the excited states of CH, independent of their (singly or doubly excited, doublet or quartet) character. The CR-EOMCCSD(T) adiabatic excitation energies T_e obtained with the aug-cc-pVTZ basis set are within 0.07–0.33 eV from experiment. This includes the $B\ ^2\Sigma^-$ and $C\ ^2\Sigma^+$ states dominated by two-electron transitions, for which the EOMCCSD approach fails, producing the 1.19 and 1.42 eV errors, respectively, when the aug-cc-pVTZ basis set is employed. The CR-EOMCCSD(T) approach reduces these large errors to 0.07 and 0.15 eV, respectively, which is a considerable improvement. The overall description of the excited states of CH listed in Table 3 by the CR-EOMCCSD(T) approach is almost as good as that obtained with the full CCSDT/EOMCCSDT method, particularly for the most challenging $B\ ^2\Sigma^-$ and $C\ ^2\Sigma^+$ states dominated by doubles. In general, the differences between the CR-EOMCCSD(T) and CCSDT/EOMCCSDT values of T_e obtained here with the aug-cc-pVTZ basis set range between 0.06 eV for the $C\ ^2\Sigma^+$ state and 0.26 eV for the $A\ ^2\Delta$ state, which is a very good agreement, particularly if we realize that the CR-EOMCCSD(T) method employs the iterative $n_o^2n_u^4$ and noniterative $n_o^3n_u^4$ steps, which are much less expensive than the iterative $n_o^3n_u^5$ steps of the full CCSDT/EOMCCSDT approach.

The above similarities between the results of the CR-EOMCCSD(T) and CCSDT/EOMCCSDT calculations can also be observed when we examine the total energies of various excited states of CH listed in Table 3. The differences between the CR-EOMCCSD(T) and the corresponding EOMCCSDT total energies of the excited states of CH given in Table 3 range between 2.7 and 9.8 millihartree (the difference between the CCSDT and CR-EOMCCSD(T) ground-state energies is only 0.5 millihartree). This is very encouraging, particularly when we realize that a few millihartree differences between the CR-EOMCCSD(T) and EOMCCSDT energies are very small when compared to the magnitude of triples effects in the excited-state calculations. These effects, as measured by the differences between the EOMCCSDT and EOMCCSD energies, can be on the order of 50 millihartree (cf., e.g., the 46.6 and 53.3 millihartree differences between the EOMCCSDT and EOMCCSD energies for the $B\ ^2\Sigma^-$ and $C\ ^2\Sigma^+$ states, respectively, in Table 3). Finally, it is quite encouraging to observe that the CR-EOMCCSD(T) method is capable of substantially improving the CCSD/EOMCCSD results for the dipole moments in ground and excited states. For the $X\ ^2\Pi$, $a\ ^4\Sigma^-$, and $A\ ^2\Delta$ states, the agreement between the EOMCCSDT and CR-EOMCCSD(T) values of μ shown in Table 3 is virtually perfect. For the most challenging $B\ ^2\Sigma^-$, and $C\ ^2\Sigma^+$ states dominated

TABLE 3. Total energies (E), adiabatic excitation energies (T_e), reduced excitations level (REL) values, and dipole moments (μ) of the ground and low-lying excited states of the CH radical, as obtained with the aug-cc-pVTZ (E, T_e, and REL) and aug-cc-pVDZ (μ) basis sets [110, 111]. Experimental data and nuclear geometries used in the CC/EOMCC calculations[a] are taken from Refs. [113–119].

State	*Method*	*E/hartree*	T_e/eV	*REL*	$\mu/debye$
$X\ ^2\Pi$	CCSD	-38.409232			1.39
	CCSDT[b]	-38.413493			1.37
	CR-EOMCCSD(T)	-38.412954			1.37
	Experiment				1.46 ± 0.06[c]
$a\ ^4\Sigma^-$	EOMCCSD	-38.372480	1.00	1.15	0.66
	EOMCCSDT[b]	-38.386466	0.74		0.65
	CR-EOMCCSD(T)	-38.379436	0.91		0.64
	Experiment		0.74[d]		
$A\ ^2\Delta$	EOMCCSD	-38.289817	3.25	1.12	0.82
	EOMCCSDT[b]	-38.305291	2.94		0.81
	CR-EOMCCSD(T)	-38.295500	3.20		0.81
	Experiment		2.87[e]		0.77 ± 0.07[f]
$B\ ^2\Sigma^-$	EOMCCSD	-38.246634	4.42	1.81	0.97
	EOMCCSDT[b]	-38.293254	3.27		1.27
	CR-EOMCCSD(T)	-38.296665	3.16		1.14
	Experiment		3.23[g]		
$C\ ^2\Sigma^+$	EOMCCSD	-38.212223	5.36	1.89	0.76
	EOMCCSDT[b]	-38.265474	4.03		0.87
	CR-EOMCCSD(T)	-38.262752	4.09		0.85
	Experiment		3.94[h]		

[a] The equilibrium geometries used in the CC/EOMCC calculations were taken from experiment. They are: $r_e = 1.1197868$ Å for the $X\ ^2\Pi$ state [113], $r_0 = 1.0977$ Å for the $a\ ^4\Sigma^-$ state [114], $r_e = 1.1031$ Å for the $A\ ^2\Delta$ state [113], $r_e = 1.1640$ Å for the $B\ ^2\Sigma^-$ state [115], and $r_e = 1.1143$ Å for the $C\ ^2\Sigma^+$ state [116].
[b] The UHF-based CCSDT/EOMCCSDT results reported in Ref. [46].
[c] From Ref. [117].
[d] From Ref. [118].
[e] From Ref. [113].
[f] From Ref. [119].
[g] From Ref. [115].
[h] From Ref. [116].

by double excitations, the CR-EOMCCSD(T) approach provides substantial improvements in the EOMCCSD dipole moment values, reducing the

0.30 and 0.11 debye errors relative to the corresponding full EOMCCSDT results to 0.13 and 0.02 debye, respectively.

All of the above examples show that the externally corrected MMCC(2,3) approaches and the more "black-box" CR-EOMCCSD(T) method offer considerable improvements in the EOMCCSD results, particularly when the excited states of interest are dominated by two-electron transitions or when the excited-state potential energy surfaces along bond breaking coordinates are examined. The CR-EOMCCSD(T) approach and other MMCC(2,3) schemes are capable of improving the results of CC3 and other standard EOMCC/response CC calculations that incorporate triples effects in an approximate way, bringing the excitation energies closer to the corresponding full EOMCCSDT and full CI values. Other examples of the successful applications of the excited-state MMCC(2,3) and CR-EOMCCSD(T) methods can be found elsewhere [48, 49, 51, 52, 60, 64, 107]. In the next section, we focus on one of the most recent advances in the excited-state MMCC theory, which is the development of MMCC and CR-EOMCC approximations that use the left eigenstates of the CC/EOMCC similarity-transformed Hamiltonian.

3.2. THE MMCC SCHEMES EXPLOITING THE LEFT EIGENSTATES OF THE SIMILARITY-TRANSFORMED HAMILTONIAN: THE CR-EOMCCSD(T)$_{\mathscr{L}}$ APPROACH

All MMCC methods discussed in the previous section are obtained by extracting the leading terms from the exact MMCC expressions for the noniterative corrections $\delta_\mu^{(A)}$, Eq. (50), or $\delta_\mu^{(\mathrm{CCSD})}$, Eq. (53), which, when added to the energies obtained in the standard CC/EOMCC calculations, $E_\mu^{(A)}$ or $E_\mu^{(\mathrm{CCSD})}$, respectively, recover the exact (i.e. full CI) energies E_μ of the electronic states of interest. The resulting MMCC(m_A, m_B) methods are characterized by the presence of the denominator terms $\langle\Psi_\mu|R_\mu^{(A)}e^{T^{(A)}}|\Phi\rangle$ or $\langle\Psi_\mu|R_\mu^{(\mathrm{CCSD})}e^{T^{(\mathrm{CCSD})}}|\Phi\rangle$ that renormalize the resulting corrections $\delta_\mu(m_A, m_B)$ to provide the desired improvements in the CC/EOMCC results for the excited states dominated by double excitations and for the molecular potential energy surfaces along bond breaking coordinates (see, e.g., Refs. [61–63, 66, 76] for a detailed discussion of the role of the $\langle\Psi_0|e^{T^{(A)}}|\Phi\rangle$ and $\langle\Psi_0|e^{T^{(\mathrm{CCSD})}}|\Phi\rangle$ denominator terms in improving the ground-state CC results). The calculation of these overlap denominator terms for the wave functions $|\Psi_\mu\rangle$ defining the externally corrected MMCC(m_A, m_B) methods and the CR-EOMCCSD(T) approach constitutes a very small fraction of the total computer effort related to the determination of the $\delta_\mu(m_A, m_B)$ corrections, but usually these denominators introduce small size extensivity errors, estimated at ~ 0.5 % of the total

correlation energy in the ground-state calculations [49, 77] (size extensivity is defined here as the absence of disconnected diagrams in the MBPT expansion of the electronic energy; this is not necessarily the same as the ability of a given method to describe bond breaking or separation of a given system into noninteracting fragments; for example, size inextensive methods, such as MRCI, can describe all kinds of system fragmentations, while some size extensive approaches, such as CCSD(T), fail to describe bond breaking). The size extensivity errors in the externally corrected MMCC(m_A, m_B) and CR-EOMCCSD(T) calculations are much smaller than the errors obtained with the standard CCSD, CCSD(T), EOMCCSD, and similar methods when potential energy surfaces along bond breaking coordinates and reaction pathways are examined [49, 105], but it is always interesting to look for new alternatives that might eliminate the size extensivity problem from approximate MMCC calculations. Kowalski and Piecuch have recently developed the rigorously size extensive extension of the ground-state CR-CC methods, such as CR-CCSD(T), by introducing a new concept of the numerator-denominator connected MMCC expansions and the idea of local renormalization [77], but it is quite difficult to extend these considerations to excited states at this time. Moreover, the problem of size extensivity of the EOMCC results for excited states is much more complicated than the extensivity of the ground-state CC calculations, since approximate EOMCC methods, such as EOMCCSD, whose results we are trying to improve here, are not size extensive [25, 59, 120–122]. The EOMCCSD method is only size intensive, meaning that it can provide the correct description of an idealized separation of a given many-electron system into two noninteracting fragments, in which only one of the two separated fragments is singly excited [25] (as shown later by Meissner [122], the EOMCCSD approach can also describe one-electron charge-transfer excitations between separated fragments). Unfortunately, this property of EOMCCSD does not eliminate the size extensivity error from the EOMCCSD and other truncated EOMCC calculations. Although we cannot address all of these issues here, it may be worth contemplating new classes of MMCC methods that might potentially reduce the extensivity errors through the elimination of the overlap denominators $\langle \Psi_\mu | R_\mu^{(A)} e^{T^{(A)}} | \Phi \rangle$ or $\langle \Psi_\mu | R_\mu^{(\mathrm{CCSD})} e^{T^{(\mathrm{CCSD})}} | \Phi \rangle$ from the noniterative corrections $\delta_\mu^{(A)}$ or $\delta_\mu^{(\mathrm{CCSD})}$.

We have recently started exploring MMCC methods which are based on the new forms of the expressions for the corrections $\delta_\mu^{(A)}$ or $\delta_\mu^{(\mathrm{CCSD})}$ that do not use the overlap denominator terms $\langle \Psi_\mu | R_\mu^{(A)} e^{T^{(A)}} | \Phi \rangle$ and $\langle \Psi_\mu | R_\mu^{(\mathrm{CCSD})} e^{T^{(\mathrm{CCSD})}} | \Phi \rangle$ [79]. The key to such methods is the use of the left eigenstates of the similarity-transformed Hamiltonians $\bar{H}^{(A)}$ or $\bar{H}^{(\mathrm{CCSD})}$. This is based on an observation that the CC/EOMCC "bra" state $\langle \tilde{\Psi}_\mu^{(\mathrm{CC})} |$,

Eq. (27), and the "ket" CC/EOMCC state $|\Psi_\mu^{(\mathrm{CC})}\rangle$, Eq. (15), satisfy (cf. Eq. (37))

$$\langle\tilde{\Psi}_\mu^{(\mathrm{CC})}|\Psi_\mu^{(\mathrm{CC})}\rangle = 1, \tag{115}$$

so that in the exact, full CI, limit the $\langle\tilde{\Psi}_\mu^{(\mathrm{CC})}|$ "bra" state represents the renormalized form of the "ket" state $|\Psi_\mu^{(\mathrm{CC})}\rangle$ (this should be contrasted with the fact that, in general, $\langle\Psi_\mu^{(\mathrm{CC})}|\Psi_\mu^{(\mathrm{CC})}\rangle \neq 1$).

The main idea of the MMCC methods exploiting the left eigenstates of $\bar{H}^{(A)}$ is the following representation of the exact, full CI "bra" state $\langle\Psi_\mu|$ entering Eqs. (50) and (53) [79]:

$$\langle\Psi_\mu| = \langle\Phi|\mathscr{L}_\mu\, e^{-T^{(A)}}. \tag{116}$$

Here, $T^{(A)}$ is the cluster operator for the CC method A, whose results we would like to improve (cf. Eq. (7)), and

$$\mathscr{L}_\mu = \sum_{n=0}^{N} \mathscr{L}_{\mu,n}, \tag{117}$$

where

$$\mathscr{L}_{\mu,n} = \left(\frac{1}{n!}\right)^2 \ell_{i_1\ldots i_n}^{a_1\ldots a_n}(\mu)\, a^{i_1}\cdots a^{i_n} a_{a_n}\cdots a_{a_1} \tag{118}$$

is the n-body component of $\mathscr{L}_\mu$, is the suitably chosen deexcitation operator such that $\langle\Phi|\mathscr{L}_\mu = \langle\Psi_\mu|e^{T^{(A)}}$ (obviously, such operator always exists). We can further decompose the operator $\mathscr{L}_\mu$ into $\mathscr{L}_\mu^{(A)}$ and $\delta\mathscr{L}_\mu^{(A)}$,

$$\mathscr{L}_\mu = \mathscr{L}_\mu^{(A)} + \delta\mathscr{L}_\mu^{(A)}, \tag{119}$$

where

$$\mathscr{L}_\mu^{(A)} = \sum_{n=0}^{m_A} \mathscr{L}_{\mu,n} \tag{120}$$

and

$$\delta\mathscr{L}_\mu^{(A)} = \sum_{n=m_A+1}^{N} \mathscr{L}_{\mu,n}, \tag{121}$$

with m_A representing the excitation level defining the CC/EOMCC method A. Since we can always normalize the full CI "bra" state $\langle\Psi_\mu|$, which enters Eqs. (50) and (53), in an arbitrary manner without changing the values of corrections $\delta_\mu^{(A)}$ and $\delta_\mu^{(\mathrm{CCSD})}$, we choose the normalization of $\langle\Psi_\mu|$, Eq. (116), such that

$$\langle\Phi|\mathscr{L}_\mu^{(A)} R_\mu^{(A)}|\Phi\rangle = 1. \tag{122}$$

Equation (122) looks like Eq. (37), but this is where the similarities between $\langle\Phi|\mathscr{L}_\mu^{(A)}$ and the left eigenstate $\langle\Phi|L_\mu^{(A)}$, corresponding to the right eigenstate $R_\mu^{(A)}|\Phi\rangle$ of $\bar{H}^{(A)}$, end. The $\langle\Phi|\mathscr{L}_\mu^{(A)}$ state is only one of the two contributions to $\langle\Phi|\mathscr{L}_\mu = \langle\Psi_\mu|e^{T^{(A)}}$, as defined by Eq. (119), whereas $\langle\Phi|L_\mu^{(A)}$ is the true left eigenstate of $\bar{H}^{(A)}$ corresponding to $R_\mu^{(A)}|\Phi\rangle$. The $\langle\Phi|\mathscr{L}_\mu^{(A)}$ and $\langle\Phi|L_\mu^{(A)}$ states can be numerically similar, but they are formally not identical unless $m_A = N$ and $\delta\mathscr{L}_\mu^{(A)} = 0$.

With the above representation of the full CI "bra" state $\langle\Psi_\mu|$, Eq. (116), and with the normalization of $\langle\Psi_\mu|$ defined by Eq. (122), we can rewrite Eq. (50) for the exact value of the correction $\delta_\mu^{(A)}$ in the following way [79]:

$$\delta_\mu^{(A)} \equiv E_\mu - E_\mu^{(A)} = \sum_{n=m_A+1}^{N} \langle\Phi|\mathscr{L}_{\mu,n}\, M_{\mu,n}(m_A)|\Phi\rangle, \tag{123}$$

where the operators $M_{\mu,n}(m_A)$ are defined in terms of the generalized moments of CC/EOMCC equations of method A, $\mathfrak{M}^{i_1\ldots i_n}_{\mu,a_1\ldots a_n}(m_A)$, via Eq. (52). By using Eqs. (52) and (118), we can immediately write

$$\delta_\mu^{(A)} = \sum_{n=m_A+1}^{N} \sum_{i_1<\cdots<i_n,a_1<\cdots<a_n} \ell^{a_1\ldots a_n}_{i_1\ldots i_n}(\mu)\, \mathfrak{M}^{i_1\ldots i_n}_{\mu,a_1\ldots a_n}(m_A), \tag{124}$$

where the generalized moments of CC/EOMCC equations are defined by Eqs. (48) and (49) and $\ell^{a_1\ldots a_n}_{i_1\ldots i_n}(\mu)$ are the deexcitation amplitudes defining the n-body components of $\mathscr{L}_\mu$. We only need the amplitudes $\ell^{a_1\ldots a_n}_{i_1\ldots i_n}(\mu)$ and moments $\mathfrak{M}^{i_1\ldots i_n}_{\mu,a_1\ldots a_n}(m_A)$ with $n > m_A$ to construct Eq. (124).

As one can see, the main difference between the new MMCC expression for the exact correction $\delta_\mu^{(A)}$, given by Eqs. (123) and (124), and the original MMCC formula, Eq. (50), is the absence of the overlap denominator term $\langle\Psi_\mu|R_\mu^{(A)}e^{T^{(A)}}|\Phi\rangle$ in Eqs. (123) and (124). This may be a useful feature in calculating the approximate values of corrections $\delta_\mu^{(A)}$, particularly when the lack of rigorous size extensivity of the MMCC(m_A,m_B) methods discussed in the previous section becomes an issue. Another difference is the absence of the $C_{n-k}(m_A)$ terms representing the $(n-k)$-body components of $e^{T^{(A)}}$ in Eqs. (123) and (124). One can rather easily show [79] that these terms can be summed over to $e^{T^{(A)}}$, which cancels out the $e^{-T^{(A)}}$ operator entering the formula for $\langle\Psi_\mu|$, Eq. (116).

The details of the derivation of Eqs. (123) and (124) will be described elsewhere [79]. Let us only mention that one can derive Eqs. (123) and (124) by using the original MMCC formula for the correction $\delta_\mu^{(A)}$, Eq. (50), in

which the exact "bra" state $\langle\Psi_\mu|$ is replaced by Eq. (116), or by replacing the wave function $\langle\Psi|$ in the MMCC functional, Eq. (56), by $\langle\Psi_\mu|$, Eq. (116), and by exploiting the resolution of identity in the N-electron Hilbert space in a manner which is analogous to the original derivation of the MMCC energy expressions [47, 62] (see, also, Ref. [49]). The overlap denominator term $\langle\Psi_\mu|R_\mu^{(A)}e^{T^{(A)}}|\Phi\rangle$ entering Eqs. (50) and (56) disappears from the resulting expressions for $\delta_\mu^{(A)}$, since

$$\langle\Phi|\mathscr{L}_\mu\, R_\mu^{(A)}|\Phi\rangle = \langle\Phi|\mathscr{L}_\mu^{(A)}\, R_\mu^{(A)}|\Phi\rangle + \langle\Phi|(\delta\mathscr{L}_\mu^{(A)})\, R_\mu^{(A)}|\Phi\rangle = 1. \tag{125}$$

In arriving at Eq. (125), we used Eqs. (119) and (122), and the obvious fact that $\langle\Phi|(\delta\mathscr{L}_\mu^{(A)})\, R_\mu^{(A)}|\Phi\rangle = 0$ (cf. the definition of $\delta\mathscr{L}_\mu^{(A)}$, Eq. (121); $\delta\mathscr{L}_\mu^{(A)}$ contains n-body components with $n > m_A$, whereas the n-body components of $R_\mu^{(A)}$ have $n \le m_A$).

The question arises how to use Eqs. (123) and (124) in practice. In analogy to the MMCC(m_A, m_B) schemes defined by Eqs. (65) and (66), we can introduce the MMCC(m_A, m_B)$_\mathscr{L}$ methods in which we calculate the energy as follows [79]:

$$E_\mu^{(\mathrm{MMCC})}(m_A, m_B)_\mathscr{L} = E_\mu^{(A)} + \delta_\mu(m_A, m_B)_\mathscr{L}, \tag{126}$$

where $m_B > m_A$ and and where

$$\begin{aligned}\delta_\mu(m_A, m_B)_\mathscr{L} &= \sum_{n=m_A+1}^{m_B} \langle\Phi|\mathscr{L}_{\mu,n}\, M_{\mu,n}(m_A)|\Phi\rangle \\ &= \sum_{n=m_A+1}^{m_B} \sum_{i_1<\cdots<i_n, a_1<\cdots<a_n} \ell_{i_1\ldots i_n}^{a_1\ldots a_n}(\mu)\, \mathfrak{M}_{\mu,a_1\ldots a_n}^{i_1\ldots i_n}(m_A)\end{aligned} \tag{127}$$

is the relevant correction to the CC/EOMCC energy $E_\mu^{(A)}$. An example of the MMCC(m_A, m_B)$_\mathscr{L}$ method might be the MMCC(2,3)$_\mathscr{L}$ approximation, in which, in analogy to the MMCC(2,3) methods discussed in the previous section, we correct the results of the CCSD/EOMCCSD calculations by adding the corrections

$$\delta_\mu(2,3)_\mathscr{L} = \langle\Phi|\mathscr{L}_{\mu,3}\, M_{\mu,3}(m_A)|\Phi\rangle = \sum_{i<j<k, a<b<c} \ell_{ijk}^{abc}(\mu)\, \mathfrak{M}_{\mu,abc}^{ijk}(2) \tag{128}$$

to the CCSD/EOMCCSD energies $E_\mu^{(\mathrm{CCSD})}$.

As in the case of the MMCC(2,3) schemes, discussed in Section 2, we can use Eq. (128) to design the analog of the CR-EOMCCSD(T) method employing the left eigenstates of $\bar{H}^{(\mathrm{CCSD})}$. In order to accomplish this and formulate the resulting CR-EOMCCSD(T)$_\mathscr{L}$ approximation, we have to come

up with the approximate form of the three-body operator $\mathscr{L}_{\mu,3}$, which uses the standard elements of the CCSD/EOMCCSD theory, such the CCSD cluster operators T_1 and T_2 and the zero-, one- and two-body components of the left eigenstate $\langle\Phi|L_\mu^{(\mathrm{CCSD})}$ of the CCSD/EOMCCSD similarity-transformed Hamiltonian $\bar{H}^{(\mathrm{CCSD})}$. The desired approximate form of $\mathscr{L}_{\mu,3}$ that can be used to formulate the CR-EOMCCSD(T)$_{\mathscr{L}}$ approximation can be obtained by analyzing the equation

$$\langle\Phi|\mathscr{L}_\mu\,\bar{H}^{(\mathrm{CCSD})} = E_\mu\,\langle\Phi|\mathscr{L}_\mu, \tag{129}$$

which is equivalent to the Schrödinger equation $H|\Psi_\mu\rangle = E_\mu|\Psi_\mu\rangle$ or, more precisely, to its adjoint form $\langle\Psi_\mu|H = E_\mu\,\langle\Psi_\mu|$ if $\langle\Phi|\mathscr{L}_\mu\,e^{-T^{(\mathrm{CCSD})}}$ is the exact, full CI "bra" state $\langle\Psi_\mu|$. By right-projecting Eq. (129) on the triply excited determinants $|\Phi_{ijk}^{abc}\rangle$, while approximating the operator $\mathscr{L}_\mu$ by $L_\mu^{(\mathrm{CCSD})} + \tilde{\mathscr{L}}_{\mu,3}$, where $\langle\Phi|L_\mu^{(\mathrm{CCSD})}$ is the left eigenstate of the $\bar{H}^{(\mathrm{CCSD})}$ obtained in the CCSD/EOMCCSD calculations and $\tilde{\mathscr{L}}_{\mu,3}$ is an approximate form of the three-body component $\mathscr{L}_{\mu,3}$, and by replacing the exact energy E_μ in the resulting equation by the CCSD/EOMCCSD energy $E_\mu^{(\mathrm{CCSD})}$, while approximating the triples-triples block of the matrix representing $\bar{H}^{(\mathrm{CCSD})}$ by its diagonal, we obtain

$$\mathscr{L}_{\mu,3} \approx \tilde{\mathscr{L}}_{\mu,3} = \tfrac{1}{36}\,\tilde{\ell}_{ijk}^{abc}(\mu)\,a^i a^j a^k a_c a_b a_a, \tag{130}$$

where

$$\tilde{\ell}_{ijk}^{abc}(\mu) = \langle\Phi|L_\mu^{(\mathrm{CCSD})}\bar{H}^{(\mathrm{CCSD})}|\Phi_{ijk}^{abc}\rangle / D_{\mu,abc}^{ijk}, \tag{131}$$

with $D_{\mu,abc}^{ijk}$ defined by Eq. (104). An elementary diagrammatic analysis of Eq. (131) shows that

$$\begin{aligned}\tilde{\ell}_{ijk}^{abc}(\mu) \;=\; & \langle\Phi|[L_{\mu,1}\bar{H}_2^{(\mathrm{CCSD})} + L_{\mu,2}\bar{H}_1^{(\mathrm{CCSD})} \\ & +(L_{\mu,2}\bar{H}_2^{(\mathrm{CCSD})})_C]|\Phi_{ijk}^{abc}\rangle / D_{\mu,abc}^{ijk},\end{aligned} \tag{132}$$

where $L_{\mu,1}$ and $L_{\mu,2}$ are the one- and two-body components of $L_\mu^{(\mathrm{CCSD})}$ obtained by solving the left CCSD ($\mu = 0$) and EOMCCSD ($\mu > 0$) equations (Eqs. (44) and (40), respectively, where $m_A = 2$) and $\bar{H}_1^{(\mathrm{CCSD})}$ and $\bar{H}_2^{(\mathrm{CCSD})}$ are the one and two-body components of $\bar{H}^{(\mathrm{CCSD})}$. The final CR-EOMCCSD(T)$_{\mathscr{L}}$ energy is calculated as [79]

$$E_\mu^{(\text{CR-EOMCCSD(T)}_{\mathscr{L}})} = E_\mu^{(\mathrm{CCSD})} + \sum_{i<j<k,a<b<c} \tilde{\ell}_{ijk}^{abc}(\mu)\,\mathfrak{M}_{\mu,abc}^{ijk}(2), \tag{133}$$

where $\mathfrak{M}^{ijk}_{\mu,abc}(2)$ are the triply excited moments of the CCSD ($\mu = 0$) or EOMCCSD ($\mu > 0$) equations that one can calculate using Eq. (60) and $\tilde{\ell}^{abc}_{ijk}(\mu)$ is defined by Eq. (132). The above expression applies to ground ($\mu = 0$) and excited ($\mu > 0$) states. In the former case, we simply replace the one- and two-body components of $L^{(\mathrm{CCSD})}_{\mu}$ in Eq. (132) by the one- and two-body operators Λ_1 and Λ_2 obtained by solving the linear system of the CCSD "lambda" equations, Eq. (44), where $A = \mathrm{CCSD}$ and $m_A = 2$. One can easily verify that the ground-state CR-EOMCCSD(T)$_{\mathscr{L}}$ energy reduces to the energy expression defining the CCSD(2)$_T$ approach of Refs. [75, 123] if the denominator $D^{ijk}_{0,abc}$ in Eq. (132) written for the $\mu = 0$ case is replaced by the usual MBPT-like difference of bare spin-orbital energies for triples, $(\epsilon_i + \epsilon_j + \epsilon_k - \epsilon_a - \epsilon_b - \epsilon_c)$ (see Refs. [124–131] for the related approaches).

The CR-EOMCCSD(T)$_{\mathscr{L}}$ method is essentially as inexpensive as the CR-EOMCCSD(T) approach of Refs. [49, 51, 52, 59], discussed in Section 3.1.2. Thus, the most expensive steps of the CR-EOMCCSD(T)$_{\mathscr{L}}$ approach scale as $n_o^2 n_u^4$ in the iterative CCSD and EOMCCSD parts and $n_o^3 n_u^4$ in the noniterative part associated with the determination of the triples correction $\sum_{i<j<k,a<b<c} \tilde{\ell}^{abc}_{ijk}(\mu)\, \mathfrak{M}^{ijk}_{\mu,abc}(2)$. The only essential difference between the CR-EOMCCSD(T) and CR-EOMCCSD(T)$_{\mathscr{L}}$ methods is the need to solve the CCSD "lambda" equations and the left EOMCCSD equations, in addition to solving the usual CCSD equations and right EOMCCSD equations, in the CR-EOMCCSD(T)$_{\mathscr{L}}$ calculations. The CCSD "lambda" equations and the left EOMCCSD equations are characterized by the $n_o^2 n_u^4$ steps which are similar to the usual $n_o^2 n_u^4$ steps of CCSD/EOMCCSD. Thus, the costs of the CR-EOMCCSD(T)$_{\mathscr{L}}$ and CR-EOMCCSD(T) calculations are not much different.

The CR-EOMCCSD(T)$_{\mathscr{L}}$ method is currently under development, so that we cannot show too many examples of the actual applications yet. However, we have already tested the CR-EOMCCSD(T)$_{\mathscr{L}}$ approach using the electronic excitations in the CH^+ ion as an example. The CR-EOMCCSD(T)$_{\mathscr{L}}$ results for the three lowest-energy excited states of the $^1\Sigma^+$ symmetry and two lowest-energy states of the $^1\Pi$ and $^1\Delta$ symmetries, obtained at the equilibrium geometry $R_{\mathrm{C-H}} = R_e = 2.13713$ bohr and the same [5s3p1d/3s1p] basis set of Ref. [103] as used in the MMCC(2,3)/CI, MMCC(2,3)/PT, and CR-EOMCCSD(T) calculations discussed in Section 3.1, are shown in Table 2. As one can see, the CR-EOMCCSD(T)$_{\mathscr{L}}$ approach is as effective in improving the EOMCCSD results as the CR-EOMCCSD(T) method analyzed in Section 3.1.2. This is particularly true for the 2 $^1\Sigma^+$, 1 $^1\Delta$, and 2 $^1\Delta$ states that are dominated by double excitations, for which the CR-EOMCCSD(T)$_{\mathscr{L}}$ approach provides the results of the full EOMCCSDT quality, reducing the large 0.560, 0.924, and 0.856

eV errors in the EOMCCSD calculations for the 2 $^1\Sigma^+$, 1 $^1\Delta$, and 2 $^1\Delta$ states to 0.106, 0.032, and -0.030 eV, respectively. As in the case of the externally corrected MMCC(2,3) methods and CR-EOMCCSD(T) approach, the CR-EOMCCSD(T)$_{\mathscr{L}}$ results for the 2 $^1\Sigma^+$, 1 $^1\Delta$, and 2 $^1\Delta$ states are considerably better than the results of the iterative CC3 calculations. A similar superiority of the CR-EOMCCSD(T)$_{\mathscr{L}}$ approach over the CC3 method is observed for the partially biexcited 2 $^1\Pi$ state, for which the 0.327 and 0.219 eV errors obtained with the EOMCCSD and CC3 approaches, respectively, reduce to 0.135 eV, when the CR-EOMCCSD(T)$_{\mathscr{L}}$ method is employed. For the remaining excited states listed in Table 2 that are dominated by one-electron transitions (the 3 $^1\Sigma^+$, 4 $^1\Sigma^+$, and 1 $^1\Pi$ states), the CR-EOMCCSD(T)$_{\mathscr{L}}$ approach is as accurate as the CC3 method, i.e. only slightly less accurate than the full EOMCCSDT approach. The overall accuracy of the CR-EOMCCSD(T)$_{\mathscr{L}}$ approach, which represents a new type of "black-box" MMCC approximation, is very similar to the accuracy of the externally corrected MMCC(2,3) methods and CR-EOMCCSD(T) approach.

The performance of the CR-EOMCCSD(T)$_{\mathscr{L}}$ method, which is based on the modified form of the MMCC formalism that no longer needs the overlap denominators of the $\langle\Psi_\mu|R_\mu^{(\mathrm{CCSD})}e^{T^{(\mathrm{CCSD})}}|\Phi\rangle$ type to improve the EOMCCSD energies, is very encouraging. However, we have to perform a larger number of calculations to see if CR-EOMCCSD(T)$_{\mathscr{L}}$ offers the same level of consistency in applications involving singly and doubly excited states as other MMCC approximations. The results of our findings will be reported elsewhere [79].

4. Summary and concluding remarks

We have provided a comprehensive discussion of new classes of noniterative CC/EOMCC methods, developed by our group, that can provide an accurate description of excited electronic states, particularly the most challenging excited states dominated by two-electron transitions and excited-state potential energy surfaces along bond breaking coordinates which require a well-balanced description of dynamic and nondynamic correlation effects. All of the methods discussed in this article are derived from the more general MMCC formalism, which is based on the idea of correcting standard CC/EOMCC results, originating, for example, from CCSD and EOMCCSD calculations, through the *a posteriori* noniterative energy corrections that in the exact limit of the MMCC theory recover the exact, full CI energies of the electronic states of interest. The key elements in designing the MMCC corrections to CC/EOMCC energies are the generalized moments of the CC/EOMCC equations, which can be rather easily extracted from

the approximate CC/EOMCC calculations whose results we would like to improve, particularly when one is interested in correcting the results of basic CCSD/EOMCCSD calculations.

We have discussed three classes of excited-state MMCC methods: (i) the externally corrected MMCC approaches employing the configuration interaction and multi-reference perturbation theory wave functions, (ii) the CR-EOMCC methods, such as CR-EOMCCSD(T), and (iii) the new classes of MMCC and CR-EOMCC theories employing the left eigenstates of the similarity-transformed Hamiltonian used in the CC/EOMCC theory. The first class of externally corrected MMCC theories is based on the idea of combining the information that originates from the CC/EOMCC calculations (the cluster and excitation amplitudes that define a given CC/EOMCC approximation and the corresponding generalized moments) with the approximate wave functions obtained in some low-order non-CC calculations that can provide a qualitatively correct description of the bond breaking process or excited states of interest. In our discussion of the externally corrected MMCC methods, we have focused on the MMCC(2,3)/CI and MMCC(2,3)/PT methods that can be used to correct the results of the CCSD/EOMCCSD calculations for the effects of triple excitations, as described by combining the triply excited moments of the CCSD/EOMCCSD equations with the wave functions originating from the low-order CISDt and MRMBPT calculations.

The idea of CR-EOMCC methods, such as CR-EOMCCSD(T), is entirely different. In this case, we design the MMCC corrections to the CC/EOMCC energies due to higher-order excitations without resorting to any non-CC calculations. For example, in the CR-EOMCCSD(T) approach discussed in this article, we design the corrections to the CCSD/EOMCCSD energies due to triples using the singly and doubly excited clusters obtained in the CCSD calculations, the zero-, one-, and two-body components of the linear excitation operator defining the EOMCCSD approach, and the triply excited moments of the CCSD/EOMCCSD equations. Thus, the CR-EOMCCSD(T) approach and other CR-EOMCC approximations are similar in spirit to the popular computational "black-box" methods, such as CCSD(T). In particular, the computer costs of the CR-EOMCCSD(T) method per single electronic state are more or less the same as the costs of the CCSD(T) calculations: both are the relatively inexpensive iterative $\mathscr{N}^6$ and noniterative $\mathscr{N}^7$ procedures. The same remark applies to the externally corrected MMCC(2,3)/CI and MMCC(2,3)/PT methods, although one has to perform the additional CISDt and low-order MRMBPT calculations, in addition to the CCSD and EOMCCSD calculations, to obtain the MMCC(2,3)/CI and MMCC(2,3)/PT triples corrections. Moreover, one has to select active orbitals to carry out the MMCC(2,3)/CI

and MMCC(2,3)/PT calculations, so that the externally corrected MMCC methods are not as easy to use as the purely single-reference CR-EOMCCSD(T) approach. On the other hand, the choice of active orbital space for the MMCC(2,3)/CI and MMCC(2,3)/PT calculations is often obvious if we have some *a priori* knowledge of the orbital excitations that dominate the electronic excitations of interest.

The third and the most recent group of the MMCC and CR-EOMCC methods is based on the idea of renormalizing the triples and other higher-order corrections to CCSD/EOMCCSD or other CC/EOMCC energies in situations involving two-electron excitations and excited-state potential energy surfaces along bond breaking coordinates through the left eigenstates of the similarity-transformed Hamiltonian used in the CC/EOMCC calculations. The left eigenstates of the similarity-transformed Hamiltonian used in the CC/EOMCC theory enable us to eliminate the overlap denominators that are present in other methods based on the original MMCC theory. This may have some advantages in situations where the presence of disconnected diagrams in the CR-EOMCCSD(T) triples corrections resulting from the use of the overlap denominators creates a potential problem. One of the approximations in this category, which we discussed in greater detail, is the CR-EOMCCSD(T)$_{\mathscr{L}}$ approach, which is a promising candidate for the "black-box" method for the calculations of excited states dominated by single or double excitations that has computer costs similar to those of CCSD(T) or CR-EOMCCSD(T).

In a few numerical examples, we have demonstrated that all of the above MMCC and CR-EOMCC methods provide considerable improvements in the EOMCCSD results, particularly when the excited states of interest gain a significant double excitation or multi-reference character. The MMCC(2,3)/CI, MMCC(2,3)/PT, CR-EOMCCSD(T), and CR-EOMCCSD(T)$_{\mathscr{L}}$ methods can often compete with the much more expensive EOMCCSDT approach. In fact, there are cases, such as the lowest-energy $^1\Delta_g$ state of the C_2 molecule, where the MMCC(2,3)/CI and CR-EOMCCSD(T) methods balance the ground and excited state correlation effects better than full EOMCCSDT. Even if this particular case is a result of the fortuitous cancellation of errors, it is very encouraging to see that the low-cost and easy-to-use MMCC(2,3)/CI, MMCC(2,3)/PT, CR-EOMCCSD(T), and CR-EOMCCSD(T)$_{\mathscr{L}}$ methods can be as accurate as the high-level and very expensive EOMCC methods, such as EOMCCSDT.

Acknowledgements

One of us (P.P.) would like to thank Professors Jean-Pierre Julien and Jean Maruani for inviting him to give a talk at the Ninth European Workshop

on Quantum Systems in Chemistry and Physics (QSCP-IX), where some of the results discussed in this contribution were presented. P.P. would like to thank Dr. Stephen Wilson and Professor Jean Maruani for encouraging him to write this review article. This work has been supported by the Chemical Sciences, Geosciences and Biosciences Division, Office of Basic Energy Sciences, Office of Science, U.S. Department of Energy (Grant No. DE-FG02-01ER15228) and the National Science Foundation (Grant No. CHE-0309517; both awards provided to P.P.). Additional support has been provided by the National Science Foundation REU Program in the Department of Chemistry at Michigan State University (J.R.G.).

References

1. F. Coester, *Nucl. Phys.* **7**, 421 (1958).
2. F. Coester and H. Kümmel, *Nucl. Phys.* **17**, 477 (1960).
3. J. Čížek, *J. Chem. Phys.* **45**, 4256 (1966).
4. J. Čížek, *Adv. Chem. Phys.* **14**, 35 (1969).
5. J. Čížek and J. Paldus, *Int. J. Quantum Chem.* **5**, 359 (1971).
6. R.J. Bartlett, in: *Modern Electronic Structure Theory*, Part I, edited by D.R. Yarkony (World Scientific, Singapore, 1995), pp. 1047-1131.
7. J. Gauss, in: *Encyclopedia of Computational Chemistry*, edited by P.v.R. Schleyer, N.L. Allinger, T. Clark, J. Gasteiger, P.A. Kollman, H.F. Schaefer III, and P.R. Schreiner (Wiley, Chichester, U.K., 1998), Vol. 1, pp. 615-636.
8. J. Paldus and X. Li, *Adv. Chem. Phys.* **110**, 1 (1999).
9. T.D. Crawford and H.F. Schaefer III, *Rev. Comp. Chem.* **14**, 33 (2000).
10. J. Paldus, in: *Handbook of Molecular Physics and Quantum Chemistry*, edited by S. Wilson (Wiley, Chichester, 2003), Vol. 2, pp. 272-313.
11. G.D. Purvis III and R.J. Bartlett, *J. Chem. Phys.* **76**, 1910 (1982).
12. G.E. Scuseria, A.C. Scheiner, T.J. Lee, J.E. Rice, and H.F. Schaefer III, *J. Chem. Phys.* **86**, 2881 (1987).
13. G.E. Scuseria, C.L. Janssen, and H.F. Schaefer III, *J. Chem. Phys.* **89**, 7382 (1988).
14. T.J. Lee and J.E. Rice, *Chem. Phys. Lett.* **150**, 406 (1988).
15. P. Piecuch and J. Paldus, *Int. J. Quantum Chem.* **36**, 429 (1989).
16. M. Urban, J. Noga, S.J. Cole, and R.J. Bartlett, *J. Chem. Phys.* **83**, 4041 (1985).
17. P. Piecuch and J. Paldus, *Theor. Chim. Acta* **78**, 65 (1990).
18. K. Raghavachari, G.W. Trucks, J.A. Pople and M. Head-Gordon, *Chem. Phys. Lett.* **157**, 479 (1989).
19. M. Schütz, *J. Chem. Phys.* **116**, 8772 (2002).
20. R.M. Olson, S. Varganov, M.S. Gordon, S. Chretien, H. Metiu, P. Piecuch, K. Kowalski, S.A. Kucharski, and M. Musiał, *J. Am. Chem. Soc.* **127**, 1049 (2005).
21. H. Monkhorst, *Int. J. Quantum Chem. Symp.* **11**, 421 (1977).
22. E. Dalgaard and H. Monkhorst, *Phys. Rev. A* **28**, 1217 (1983).
23. M. Takahashi and J. Paldus, *J. Chem. Phys.* **85**, 1486 (1986).
24. H. Koch and P. Jørgensen, *J. Chem. Phys.* **93**, 3333 (1990).
25. H. Koch, H.J.Aa. Jensen, P. Jørgensen, and T. Helgaker, *J. Chem. Phys.* **93**, 3345 (1990).
26. J. Geertsen, M. Rittby, and R.J. Bartlett, *Chem. Phys. Lett.* **164**, 57 (1989).
27. D.C. Comeau and R.J. Bartlett, *Chem. Phys. Lett.* **207**, 414 (1993).
28. J.F. Stanton and R.J. Bartlett, *J. Chem. Phys.* **98**, 7029 (1993).
29. P. Piecuch and R.J. Bartlett, *Adv. Quantum Chem.* **34**, 295 (1999).
30. H. Nakatsuji and K. Hirao, *Chem. Phys. Lett.* **47**, 569 (1977).

31. H. Nakatsuji and K. Hirao, *J. Chem. Phys.* **68**, 2053, 4279 (1978).
32. H. Nakatsuji, *Chem. Phys. Lett.* **59**, 362 (1978).
33. H. Nakatsuji, *Chem. Phys. Lett.* **67**, 329, 334 (1979).
34. H. Nakatsuji, in: *Computational Chemistry: Reviews of Current Trends*, edited by J. Leszczyński (World Scientific, Singapore, 1997), Vol. 2, pp. 62-124.
35. J.D. Watts and R.J. Bartlett, *Chem. Phys. Lett.* **233**, 81 (1995).
36. J.D. Watts and R.J. Bartlett, *Chem. Phys. Lett.* **258**, 581 (1996).
37. J.D. Watts and R.J. Bartlett, *J. Chem. Phys.* **101**, 3073 (1994).
38. H. Koch, O. Christiansen, P. Jørgensen, and J. Olsen, *Chem. Phys. Lett.* **244**, 75 (1995).
39. O. Christiansen, H. Koch, and P. Jørgensen, *J. Chem. Phys.* **103**, 7429 (1995).
40. O. Christiansen, H. Koch, and P. Jørgensen, *J. Chem. Phys.* **105**, 1451 (1996).
41. O. Christiansen, H. Koch, P. Jørgensen, and J. Olsen, *Chem. Phys. Lett.* **256**, 185 (1996).
42. K. Kowalski and P. Piecuch, *J. Chem. Phys.* **113**, 8490 (2000).
43. K. Kowalski and P. Piecuch, *J. Chem. Phys.* **115**, 643 (2001).
44. K. Kowalski and P. Piecuch, *Chem. Phys. Lett.* **347**, 237 (2001).
45. A.I. Krylov, C.D. Sherrill, and M. Head-Gordon, *J. Chem. Phys.* **113**, 6509 (2000).
46. S. Hirata, *J. Chem. Phys.* **121**, 51 (2004).
47. K. Kowalski and P. Piecuch, *J. Chem. Phys.* **115**, 2966 (2001).
48. K. Kowalski and P. Piecuch, *J. Chem. Phys.* **116**, 7411 (2002).
49. P. Piecuch, K. Kowalski, I.S.O. Pimienta and M.J. McGuire, *Int. Rev. Phys. Chem.* **21**, 527 (2002).
50. P. Piecuch, K. Kowalski, I.S.O. Pimienta, and S.A. Kucharski, in: *Low-Lying Potential Energy Surfaces*, ACS Symposium Series, Vol. 828, edited by M.R. Hoffmann and K.G. Dyall (American Chemican Society: Washington, D.C., 2002), pp. 31-64.
51. K. Kowalski and P. Piecuch, *J. Chem. Phys.* **120**, 1715 (2004).
52. P. Piecuch, K. Kowalski, I.S.O. Pimienta, P.-D. Fan, M. Lodriguito, M.J. McGuire, S.A. Kucharski, T. Kuś, and M. Musiał, *Theor. Chem. Acc.* **112**, 349 (2004).
53. C.D. Sherrill and P. Piecuch, *J. Chem. Phys.* **122**, XXX (2005), in press [to appear in April 1, 2005 issue].
54. C.E. Smith, R.A. King, and T.D. Crawford, *J. Chem. Phys.* **122**, 054110 (2005).
55. M. Włoch, M. Musiał, and S.A. Kucharski, *Ann. Pol. Chem.* Soc. **1**, 255 (2001).
56. S.A. Kucharski, M. Włoch, M. Musiał, and R.J. Bartlett, *J. Chem. Phys.* **115**, 8263 (2001).
57. M. Kállay and J. Gauss, *J. Chem. Phys.* **121**, 9257 (2004).
58. H. Larsen, J. Olsen, P. Jørgensen, and O. Christiansen, *J. Chem. Phys.* **113**, 6677 (2000); **114**, 10985 (2001) [Erratum].
59. M. Włoch, J.R. Gour, K. Kowalski, and P. Piecuch, *J. Chem. Phys.*, in press.
60. R.K. Chaudhuri, K.F. Freed, G. Hose, P. Piecuch, K. Kowalski, M. Włoch, S. Chattopadhyay, D. Mukherjee, Z. Rolik, Á. Szabados, G. Tóth, and P.R. Surján, *J. Chem. Phys.* **122**, XXX (2005), in press [to appear in April 1, 2005 issue].
61. P. Piecuch and K. Kowalski, in: *Computational Chemistry: Reviews of Current Trends*, edited by J. Leszczyński (World Scientific, Singapore, 2000), Vol. 5, pp. 1-104.
62. K. Kowalski and P. Piecuch, *J. Chem. Phys.* **113**, 18 (2000).
63. K. Kowalski and P. Piecuch, *J. Chem. Phys.* **113**, 5644 (2000).
64. S. Coussan, Y. Ferro, M. Rajzmann, A. Trivella, P. Roubin, R. Wieczorek, P. Piecuch, K. Kowalski, M. Włoch, S.A. Kucharski, and M. Musiał, in preparation for *J. Phys. Chem. A*.
65. K. Kowalski and P. Piecuch, *Chem. Phys. Lett.* **344**, 165 (2001).
66. P. Piecuch, S.A. Kucharski, and K. Kowalski, *Chem. Phys. Lett.* **344**, 176 (2001).
67. P. Piecuch, S.A. Kucharski, V. Špirko, and K. Kowalski, *J. Chem. Phys.* **115**, 5796 (2001).

68. P. Piecuch, K. Kowalski, and I.S.O. Pimienta, *Int. J. Mol. Sci.* **3**, 475 (2002).
69. M.J. McGuire, K. Kowalski, and P. Piecuch, *J. Chem. Phys.* **117**, 3617 (2002).
70. P. Piecuch, S.A. Kucharski, K. Kowalski, and M. Musiał, *Comp. Phys. Commun.* **149**, 71 (2002).
71. I.S.O. Pimienta, K. Kowalski, and P. Piecuch, *J. Chem. Phys.* **119**, 2951 (2003).
72. P. Piecuch, K. Kowalski, P.-D. Fan, and I.S.O. Pimienta, in: *Advanced Topics in Theoretical Chemical Physics*, Vol. 12 of *Progress in Theoretical Chemistry and Physics*, edited by J. Maruani, R. Lefebvre, and E. Brändas (Kluwer, Dordrecht, 2003), pp. 119-206.
73. M.J. McGuire, K. Kowalski, P. Piecuch, S.A. Kucharski, and M. Musiał, *J. Phys. Chem. A* **108**, 8878 (2004).
74. P.-D. Fan, K. Kowalski, and P. Piecuch, *Mol. Phys.*, in press.
75. S. Hirata, P.-D. Fan, A.A. Auer, M. Nooijen, and P. Piecuch, *J. Chem. Phys.* **121**, 12197 (2004).
76. M.J. McGuire and P. Piecuch, *J. Am. Chem. Soc.* **127**, 2608 (2005).
77. K. Kowalski and P. Piecuch, *J. Chem. Phys.* **122**, 074107 (2005).
78. M. Lodriguito, K. Kowalski, M. Włoch, and P. Piecuch, in preparation for *J. Chem. Phys.*
79. P. Piecuch, M. Włoch, and J.R. Gour, in preparation for *J. Chem. Phys.*
80. K. Kowalski and P. Piecuch, *J. Mol. Struct.: THEOCHEM* **547**, 191 (2001).
81. P. Piecuch and K. Kowalski, *Int. J. Mol. Sci.* **3**, 676 (2002).
82. K. Kowalski and P. Piecuch, *Mol. Phys.* **102**, 2425 (2004).
83. S.A. Kucharski and R.J. Bartlett, *Theor. Chim. Acta* **80**, 387 (1991).
84. E.A. Salter, G.W. Trucks, and R.J. Bartlett, *J. Chem. Phys.* **90**, 1752 (1989).
85. J.D. Watts, J. Gauss, and R.J. Bartlett, *J. Chem. Phys.* **98**, 8718 (1993).
86. J. Gauss, W.J. Lauderdale, J.F. Stanton, J.D. Watts, and R.J. Bartlett, *Chem. Phys. Lett.* **182**, 207 (1991).
87. J. Gauss, J.F. Stanton, and R.J. Bartlett, *J. Chem. Phys.* **95**, 2623 (1991).
88. J. Gauss, J.F. Stanton, and R.J. Bartlett, *J. Chem. Phys.* **95**, 2639 (1991).
89. J. Gauss and J.F. Stanton, *Phys. Chem. Chem. Phys.* **2**, 2047 (2000).
90. J. Gauss and J.F. Stanton, *J. Chem. Phys.* **116**, 1773 (2002).
91. X. Li and J. Paldus, *J. Chem. Phys.* **115**, 5759 (2001).
92. X. Li and J. Paldus, *J. Chem. Phys.* **115**, 5774 (2001).
93. X. Li and J. Paldus, *J. Chem. Phys.* **117**, 1941 (2002).
94. X. Li and J. Paldus, *J. Chem. Phys.* **118**, 2470 (2003).
95. J. Paldus, J. Čížek, and M. Takahashi, *Phys. Rev. A* **30**, 2193 (1984).
96. P. Piecuch, R. Toboła, and J. Paldus, *Phys. Rev. A* **54**, 1210 (1996).
97. J. Paldus and J. Planelles, *Theor. Chim. Acta* **89**, 13 (1994).
98. G. Peris, J. Planelles, and J. Paldus, *Int. J. Quantum Chem.* **62**, 137 (1997).
99. L. Stolarczyk, *Chem. Phys. Lett.* **217**, 1 (1994).
100. X. Li and J. Paldus, *J. Chem. Phys.* **107**, 6257 (1997).
101. X. Li and J. Paldus, *J. Chem. Phys.* **108**, 637 (1998).
102. X. Li and J. Paldus, *Chem. Phys. Lett.* **286**, 145 (1998).
103. J. Olsen, A.M. Sánchez de Merás, H.J.Aa. Jensen, and P. Jørgensen, *Chem. Phys. Lett.* **154**, 380 (1989).
104. I. Özkan, A. Kinal, and M. Balci, *J. Phys. Chem. A* **108**, 507 (2004).
105. A. Kinal and P. Piecuch, *J. Am. Chem. Soc.*, submitted.
106. T.D. Crawford and H.F. Schaefer III, *J. Chem. Phys.* **104**, 6259 (1996).
107. K. Kowalski and P. Piecuch, unpublished.
108. W.J. Hehre, R. Ditchfield, and J.A. Pople, *J. Chem. Phys.* **56**, 2257 (1972).
109. M. L. Abrams and C. D. Sherrill, *J. Chem. Phys.* **121**, 9211 (2004).
110. T.H. Dunning, Jr., *J. Chem. Phys.* **90**, 1007 (1989).
111. R.A. Kendall, T.H. Dunning Jr., and R.J. Harrison, *J. Chem. Phys.* **96**, 6769 (1992).

112. A. Kalemos, A. Mavridis, and A. Metropoulos, *J. Chem. Phys.* **111**, 9536 (1999).
113. M. Zachwieja, *J. Mol. Spectrosc.* **170**, 285 (1995).
114. T. Nelis, J.M. Brown, and K.M. Evenson, *J. Chem. Phys.* **92**, 4067 (1990).
115. R. Kepa, A. Para, M. Rytel, and M. Zachwieja, *J. Mol. Spectrosc.* **178**, 189 (1996).
116. K.P. Huber and G. Herzberg, *Molecular Spectra and Molecular Structure: Constants of Diatomic Molecules* (Van Nostrand Reinhold, New York, 1979).
117. D.H. Phelps and F.W. Dalby, *Phys. Rev. Lett.* **16**, 3 (1966).
118. A. Kasdan, E. Herbst, and W.C. Lineberger, *Chem. Phys. Lett.* **31**, 78 (1975).
119. T.C. Steimle, D.F. Nachman, D.A. Fletcher, and J.M. Brown, *J. Mol. Spectrosc.* **138**, 222 (1989).
120. D. Mukhopadhyay, S. Mukhopadhyay, R. Chaudhuri, and D. Mukherjee, *Theor. Chim. Acta* **80**, 441 (1991).
121. L. Meissner and R.J. Bartlett, *J. Chem. Phys.* **94**, 6670 (1991).
122. L. Meissner and R.J. Bartlett, *J. Chem. Phys.* **102**, 7490 (1995).
123. S. Hirata, M. Nooijen, I. Grabowski and R.J. Bartlett, *J. Chem. Phys.* **114**, 3919 (2001); **115**, 3967 (2001) [Erratum].
124. S.R. Gwaltney and M. Head-Gordon, *Chem. Phys. Lett.* **323**, 21 (2000).
125. S.R. Gwaltney, C.D. Sherrill, M. Head-Gordon, and A.I. Krylov, *J. Chem. Phys.* **113**, 3548 (2000).
126. S.R. Gwaltney and M. Head-Gordon, *J. Chem. Phys.* **115**, 2014 (2001).
127. S.R. Gwaltney, E.F.C. Byrd, T. Van Voorhis, and M. Head-Gordon, *Chem. Phys. Lett.* **353**, 359 (2002).
128. M. Head-Gordon, T. Van Voorhis, S.R. Gwaltney, and E.F.C. Byrd, in: *Low-Lying Potential Energy Surfaces*, ACS Symposium Series, Vol. 828, edited by M.R. Hoffmann and K.G. Dyall (American Chemican Society, Washington, D.C., 2002), pp. 93-108.
129. J.F. Stanton, *Chem. Phys. Lett.* **281**, 130 (1997).
130. D.T. Crawford and J.F. Stanton, *Int. J. Quantum Chem.* **70**, 601 (1998).
131. S.A. Kucharski and R.J. Bartlett, *J. Chem. Phys.* **108**, 5243 (1998).

EXCITED STATE SELF-CONSISTENT FIELD THEORY USING EVEN-TEMPERED PRIMITIVE GAUSSIAN BASIS SETS

V. N. GLUSHKOV

Department of Physics,
National University of Dnepropetrovsk,
49050 per. Nauchny 13,
Dnepropetrovsk,
Ukraine

AND

S. WILSON

Rutherford Appleton Laboratory,
Chilton, Oxfordshire OX11 0QX,
England †

Abstract. A practical Hartree-Fock theory of atomic and molecular electronic structure is developed for individual electronically excited states that does not involve off-diagonal Lagrange multipliers. An easily implemented method for taking the orthogonality constraints into account, which has been proposed earlier by one of us, is used to impose the orthogonality of the Hartree-Fock excited state wave function of interest to states of lower energy. The applicability of systematic sequence of even-tempered basis sets with the orbital exponents, ζ_p, defined by the geometric series $\zeta_p = \alpha\beta^p$ is examined in Hartree-Fock energy calculations for excited states which have the same spatial and spin symmetry as the ground state. It is shown that a simple reoptimization of the α and β parameters leads to a sequence of even-tempered basis sets capable of supporting high accuracy for excited state energies of some simple atoms.

† email:quantumsystems@gmail.com

J.-P. Julien et al. (eds.),
Recent Advances in the Theory of Chemical and Physical Systems, 107–126.

1. Introduction

Modern many-body methods have become sufficiently refined that the major source of error in most *ab initio* calculations of molecular properties is today associated with truncation of one-particle basis sets (*e.g.* [1]- [4]); that is, with the accuracy with which the algebraic approximation is implemented. The importance of generating systematic sequences of basis sets capable of controlling basis set truncation error has been emphasized repeatedly in the literature (see [4] and references therein). The study of the convergence of atomic and molecular structure calculations with respect to basis set extension is highly desirable. It allows examination of the convergence of calculations with respect to basis set size and the estimation of the results that would be obtained from complete basis set calculations.

Most contemporary schemes for designing atomic and molecular Gaussian basis sets (*e.g.* [4]- [7]) exploit, in one form or another, the idea of even-tempered basis sets [8], [9] (see also [4]), which have exponents, ζ_p, defined by the geometric series:

$$\zeta_p = \alpha\beta^p,\ p = 1, 2, ..., M \tag{1}$$

The parameters α and β must be taken to be functions of M, the number of basis functions, *i.e.* $\alpha = \alpha(M)$ and $\beta = \beta(M)$, if the Gaussian sets defined by (1) are to become complete in the appropriate subspace as $M \to \infty$. In particular, Schmidt and Ruedenberg shown that the following conditions

$$\begin{aligned} \lim_{M\to\infty} \alpha(M) &= 0 \\ \lim_{M\to\infty} \beta(M) &= 0 \\ \lim_{M\to\infty} [\beta(M)]^M &= \infty \end{aligned} \tag{2}$$

must be satisfied if an even-tempered basis set is to approach completeness as $M \to \infty$. Recently, Kryachko and Wilson [10] have generalized the empirical prescription (1) proposing a more flexible choice of the parameters α and β.

Applications based on the even-tempered prescription (1) have shown that it can lead to atomic and diatomic Hartree-Fock ground state energies of an accuracy approaching that achieved in numerical Hartree-Fock calculations [4][1]. It is conjectured that a comparable accuracy can be achieved for small polyatomic molecules [12], [13] by constructing basis sets according to the prescription established for diatomic molecules. Similar procedures can

[1]See [11] for a recent review of applications of even-tempered basis set to the calculation of accurate molecular polarizabilities and hyperpolarizabilities within the matrix Hartree-Fock approximation. In [11] the results finite basis set Hartree-Fock calculations are compared with finite difference Hartree-Fock calculations.

be used in calculations which go beyond the Hartree-Fock approximation and take account of electron correlation effects [12], [14] and in calculations which adopt a relativistic formalism and use the Dirac-Hartree-Fock approximation [15], [16].

There is far less reported experience for *ab initio* studies of electronically excited states than for ground states. Matrix Hartree-Fock calculations for excited states cannot be considered routine. Often the same basis set is used for both the ground and excited state even though as long ago as 1958 Shull and Löwdin [17] demonstrated

"the desirability of using different basis sets for different states."

This approach can provide a more compact representation of the accurate excited state wave functions than the use of a common basis set for ground and excited state. Most commonly used approaches for excited states in use today are based on multireference techniques. Such techniques include configuration interaction, the multiconfigurational self-consistent field method and its "complete active space" variant designated CASSCF, multireference perturbation theory and multireference coupled cluster expansions. Whilst these methods are indispensable in studies of systems where single-configuration methods cannot be applied; for example, when the weight of the Hartree-Fock configuration in the wave function of the full configuration interaction expansion is less than ~ 0.9 [18]; it is clear that orbitals of a single-configuration together with a basis set that has been specifically optimized for a given excited state will probably prove more appropriate for the development of *many-body* correlation methods.

Existing open-shell self-consistent field methods for ground states cannot be applied directly to excited states of the same symmetry as a lower state without 'variational collapse'; that is, the approximation to the excited state wave function is contaminated by components of a lower state. Several useful methods have been proposed to overcome the 'variational collapse' problem and a number of different schemes have been proposed for obtaining Hartree-Fock wave functions for excited states [19]- [24]. Some of these approaches [19]- [21], [24]explicitly introduce orthogonality constraints to lower states. Other methods [22], [23] introduce this restriction implicitly. In both types of scheme, the excited state self-consistent field wave function of interest is orthogonal to the wave function for a lower state or states of the same symmetry, but this lower state or states are not necessarily the best self-consistent field functions for these states [24]. An interesting ensemble Hartree-Fock approach [25], based on the extended Raleigh-Ritz variational principle [26] have been also proposed. This is a good compromise in applications to the excited state problem within the framework of density functional theory and has found application in wave function based formulation as well [27]. However, in density functional theory calculations

for excited states reported so far this scheme does not provide an accuracy comparable with that achieved for ground state calculations.

It is worth noting that the methods mentioned give rise to Hartree-Fock equations based on different Fock operators for the various orbitals of the same spin. This implies that off-diagonal Lagrange multipliers appear which cannot be eliminated by a suitable unitary transformation. Moreover, the complications arise when excited states above the first one are considered (see, *e.g.* [25] for further details).

This paper is arranged as follows:- in Section 2, we develop an alternative Hartree-Fock method for excited states that does not involve off-diagonal Lagrange multipliers and avoids complications when applied to excited states lying above the first excited state. A simple and easily implemented technique for taking orthogonality constraints into account, which has been proposed earlier by one of us [28]- [30], was used to enforce the orthogonality of an excited state wave function of interest to lower functions of the same symmetry. In Section 3, we investigate the use of a systematic sequence of even-tempered basis sets for *matrix* Hartree-Fock calculations of excited state energies. We examine the convergence of the excited state energy expectation values with respect to basis set size and the accuracy supported by different sequences. One has been shown that a simple reoptimization of the α and β parameters in (1) leads to a sequence of even-tempered basis sets capable of supporting high accuracy for excited state energies of simple atoms. Concluding remarks are given in Section 4.

2. Hartree-Fock equations for excited states

2.1. ORTHOGONALITY CONSTRAINTS FOR SINGLE DETERMINANTAL WAVE FUNCTIONS

Before deriving the Hartree-Fock equations for the excited state orbitals, we consider the orthogonality constraints imposed on these orbitals.

The *exact* many-electron wave function for an excited state, Ψ_i, $i \neq 0$, satisfies orthogonality conditions with respect to other many-electron state including the ground state, Ψ_0. For example, for the first excited state with many-electron wave function Ψ_1 we have

$$\langle \Psi_0 | \Psi_1 \rangle = 0 \tag{3}$$

The exact ground state wave function, Ψ_0, can be written

$$\Psi_0 = \Phi_0 + \chi_0 \tag{4}$$

where Φ_0 is the many-electron ground state Hartree-Fock wave function and χ_0 is the correlation correction. Without loss of generality, we can require that the Hartree-Fock ground state wave function and its correlation correction be orthogonal

$$\langle \Phi_0 | \chi_0 \rangle = 0 \tag{5}$$

Similarly, the exact excited state wave function, Ψ_1, can be written

$$\Psi_1 = \Phi_1 + \chi_1 \tag{6}$$

where Φ_1 is the many-electron excited state Hartree-Fock wave function and χ_1 is the corresponding correlation correction. Again, without loss of generality, we can require that Φ_1 and χ_1 be orthogonal

$$\langle \Phi_1 | \chi_1 \rangle = 0 \tag{7}$$

Substituting (6) into (3) we get

$$\begin{aligned} \langle \Psi_0 | \Psi_1 \rangle &= \langle \Psi_0 | \Phi_1 \rangle + \langle \Psi_0 | \chi_1 \rangle \\ &= 0 \end{aligned} \tag{8}$$

If we require that the Hartree-Fock wave function for the excited state be orthogonal to the exact ground state wave function then we have

$$\langle \Psi_0 | \Phi_1 \rangle = 0 \tag{9}$$

which implies, from (8), that

$$\langle \Psi_0 | \chi_1 \rangle = 0 \tag{10}$$

It is then easily shown that

$$\frac{\langle \Phi_1 | \, H \, | \Phi_1 \rangle}{\langle \Phi_1 | \Phi_1 \rangle} \geqslant \mathcal{E}_1 \tag{11}$$

where $\mathcal{E}_1$ is the exact energy of the excited state and H is the total electronic hamiltonian operator. However, equations (9) and (11) cannot be used directly because the exact wave function for the ground state, Ψ_0, is, of course, unknown.

Substituting (4) and (6) into (3) we have

$$\begin{aligned} \langle \Psi_0 | \Psi_1 \rangle &= \langle \Phi_0 | \Phi_1 \rangle + \langle \Phi_0 | \chi_1 \rangle + \langle \chi_0 | \Phi_1 \rangle + \langle \chi_0 | \chi_1 \rangle \\ &= 0 \end{aligned} \tag{12}$$

or

$$\langle \Phi_0 | \Phi_1 \rangle = - \left[\langle \Phi_0 | \chi_1 \rangle + \langle \chi_0 | \Phi_1 \rangle + \langle \chi_0 | \chi_1 \rangle \right] \tag{13}$$

We see the the Hartree-Fock wave functions, Φ_0 and Φ_1, do not, in general, satisfy orthogonality constraints analogous to those obeyed by the exact wave functions. However, we may impose constraints upon the Hartree-Fock function without loss of generality so that, for example,

$$\langle \Phi_0 | \Phi_1 \rangle = 0. \tag{14}$$

From (13) we see that this constraint requires that

$$\langle\Phi_0|\chi_1\rangle + \langle\chi_0|\Phi_1\rangle = -\langle\chi_0|\chi_1\rangle \tag{15}$$

The imposition of the orthogonality constraint (14) to an approximate lower state wave function, such as the Hartree-Fock function, does not, in general yield an excited state energy which is an upper bound to the exact excited state energy. An upper bound to the excited state energy is obtained if we impose the additional constraint

$$\langle\Phi_0|\, H\, |\Phi_1\rangle = 0 \tag{16}$$

In practice, if the lower state energy and the corresponding wave function are known accurately then the coupling matrix element $\langle\Phi_0|\, H\, |\Phi_1\rangle$ is small. Experience shows that, because the finite basis set approximation is more restrictive for Φ_1 than it is for Φ_0, the calculated excited state energy lies above the corresponding exact value.

The imposition of the constraint (14) is important since *(i)* any lack of orthogonality of the Hartree-Fock wave functions may lead to excited state energies lying below the corresponding exact energies (For example, Cohen and Kelly [32] found for the He atom the first singlet excited state energy $E_1 = -2.16984$ Hartree, whereas the observed energy $E_{1,exact} = -2.14598$ Hartree (see also [33]).); *(ii)* it facilitates the development of a simple perturbation theory expansion for correlation effects in excited states [31]; *(iii)* it allows the study of properties which depend on the wave functions of different states, *e.g.* in the evaluation of transition properties (see also [24]).

We shall be concerned with ground and excited electronic states which can be adequately described by a single determinantal wave function, *i.e.* doublet states, triplet states, *etc.* with spin $S \neq 0$). Let Φ_0 be the Slater determinant constructed from a set of spin-orbitals consisting of spatial part $|\varphi_{0i^\alpha}\rangle$, $(i^\alpha = 1, 2, ..., n^\alpha)$ associated with α spin functions and orbitals $|\varphi_{0i^\beta}\rangle$, $(i^\beta = 1, 2, ..., n^\beta)$ associated with β spin functions, *i.e.*

$$\Phi_0 = (N!)^{-\frac{1}{2}} \det|\varphi_{01^\alpha}\alpha, ..., \varphi_{0n^\alpha}\alpha; \varphi_{01^\beta}\beta, ..., \varphi_{0n^\beta}\beta| \tag{17}$$

Without loss of generality, we define $n^\alpha > n^\beta, n^\alpha + n^\beta = N$, where N is a number of electrons and $S = S_z = (n^\alpha - n^\beta)/2$ is the total spin. Similarly, Φ_1 is a single determinant wave function for the first excited state:

$$\Phi_1 = (N!)^{-\frac{1}{2}} \det|\varphi_{11^\alpha}\alpha, ..., \varphi_{1n^\alpha}\alpha; \varphi_{11^\beta}\beta, ..., \varphi_{1n^\beta}\beta| \tag{18}$$

It is well known that the orthogonality constraint for functions (17) and (18)

$$\langle\Phi_0|\Phi_1\rangle = 0 \tag{19}$$

can be written in terms of the spatial orbitals in the form

$$\begin{aligned}\langle\Phi_0|\Phi_1\rangle &= \det|\langle\varphi_{01}{}^{\alpha}|\varphi_{11}{}^{\alpha}\rangle ... \langle\varphi_{0n}{}^{\alpha}|\varphi_{1n}{}^{\alpha}\rangle| \times \\ &\quad \det|\langle\varphi_{01}{}^{\beta}|\varphi_{1n}{}^{\alpha}\rangle ... \langle\varphi_{0n}{}^{\beta}|\varphi_{1n}{}^{\beta}\rangle| \\ &= 0 \end{aligned} \tag{20}$$

The annihilation of either one of the two determinants in (20) leads to fulfillment of the orthogonality condition (19). From energy considerations and previous computational experience, we impose the orthogonality restrictions only via the first determinant which is associated with the α set and involves the occupied orbital highest in energy.

As is well known, the condition

$$\det|\langle\varphi_{01^{\alpha}}|\varphi_{11^{\alpha}}\rangle ... \langle\varphi_{0n^{\alpha}}|\varphi_{1n^{\alpha}}\rangle| = 0$$

is fulfilled if either the rows or columns in the first overlap determinant are linearly dependent. Therefore, two *physically* different schemes are possible to satisfy (20):
either

$$\sum_{j}^{n^{\alpha}} b_j^1 \langle\varphi_{0i^{\alpha}}|\varphi_{1j^{\alpha}}\rangle = 0, \quad i = 1, 2, ..., n^{\alpha} \tag{21}$$

or

$$\sum_{i}^{n^{\alpha}} b_i^0 \langle\varphi_{0i^{\alpha}}|\varphi_{1j^{\alpha}}\rangle = 0, \quad j = 1, 2, ..., n^{\alpha} \tag{22}$$

Eq.(21) requires that all occupied ground state orbitals be orthogonal to a linear combination of the excited state orbitals $\sum_j^{n^{\alpha}} b_j^1 |\varphi_{1j^{\alpha}}\rangle$, which describes an excited electronic state. Eq.(22) requires the orthogonality of all occupied excited state orbital associated with α spin functions to the arbitrary vector $\sum_i^{n^{\alpha}} b_i^0 |\varphi_{0i^{\alpha}}\rangle$ from the subspace of the occupied ground state orbitals associated with α spin functions. In general, the coefficients b_i^0 can be determined by minimizing the excited state Hartree-Fock energy. However, calculations show that the choice

$$\sum_{i}^{n^{\alpha}} b_i^0 |\varphi_{0i^{\alpha}}\rangle = |\varphi_{0n^{\alpha}}\rangle , \tag{23}$$

where $\varphi_{0n^{\alpha}}$ is the orbital from the ground state Slater's determinant with the highest energy, leads to a minimum energy for the excited state. In the limit of a complete basis set the schemes defined by (21) and (22), certainly, yield the same energy values.

In this work, we use the second scheme, *i.e.* that defined by equation (22), which upon using (23) becomes

$$\langle\varphi_{0n^{\alpha}}|\varphi_{1j^{\alpha}}\rangle = 0, \quad j = 1, 2, ..., n^{\alpha} \tag{24}$$

to impose the orthogonality constraint (19). Equation (24) can be rewritten in symmetrical form, which is useful when deriving the Hartree-Fock equations, as follows:

$$\langle\varphi_{1j^\alpha}|\varphi_{0n^\alpha}\rangle\,\langle\varphi_{0n^\alpha}|\varphi_{1j^\alpha}\rangle = 0,\;\; j = 1, 2, ..., n^\alpha \tag{25}$$

or, since the left-hand side of (25) is not negative

$$\sum_{j}^{n^\alpha} \langle\varphi_{1j^\alpha}|P_n^\alpha|\varphi_{1j^\alpha}\rangle = 0 \tag{26}$$

where P_n^α is the projection operator

$$P_n^\alpha = |\varphi_{0n^\alpha}\rangle\,\langle\varphi_{0n^\alpha}| \tag{27}$$

We shall now follow the unrestricted Hartree-Fock (UHF) formalism to obtain a restricted high-spin open-shell functions as proposed in [34], [35]. In order to eliminate spin contamination in the UHF function Φ_1, the following 'spin purity' constraint is imposed on the spatial orbitals:

$$\langle\Phi_1|\left[\mathbf{S^2} - \mathbf{S(S+1)}\right]|\Phi_1\rangle = 0 \tag{28}$$

This restriction can be also written in terms of orthogonality constraints [35]:

$$\sum_{i}^{n^\beta} \langle\varphi_{1i^\beta}|Q^\alpha|\varphi_{1i^\beta}\rangle = 0 \tag{29}$$

with

$$Q^\alpha = I - P^\alpha \tag{30}$$

Here I is identity operator and P^α is the orthoprojector on the subspace of occupied α-orbitals, *i.e.*

$$P^\alpha = \sum_{i}^{n^\alpha} |\varphi_{1i^\alpha}\rangle\,\langle\varphi_{1i^\alpha}| \tag{31}$$

Eq.(29) means that the set of orbitals associated with the β spin functions lies completely within the space defined by the set associated with the α spin functions.

The Hartree-Fock equations for excited states can now be obtained by constructing a functional consisting of the UHF energy expression together with terms imposing the orthogonality constraints (26) and (29) by the method of Lagrange undetermined multipliers. In particular, the constraints (26) and (29) multiplied by Lagrange multipliers λ_1 and λ_2, respectively, are

added to the UHF energy $E_1^{UHF} = \langle\Phi_1|\, H\,|\Phi_1\rangle$, so as to give the following functional

$$\mathcal{E}_{UHF} = E_1^{UHF} + \lambda_1 \sum_i^{n^\beta} \langle\varphi_{1i^\beta}|Q^\alpha|\varphi_{1i^\beta}\rangle + \lambda_2 \sum_i^{n^\alpha} \langle\varphi_{1j^\alpha}|P_n^\alpha|\varphi_{1j^\alpha}\rangle \tag{32}$$

2.2. VARIATIONAL DERIVATION OF HARTREE-FOCK EQUATIONS FOR EXCITED STATES

The Hartree-Fock like equations for the excited orbitals can be derived by varying the functional (32). The stationary condition has the form

$$\begin{aligned} \delta\mathcal{E}_{UHF} &= \delta\left[E_1^{UHF} + \lambda_1 \sum_i^{n^\beta} \langle\varphi_{1i^\beta}|Q^\alpha|\varphi_{1i^\beta}\rangle + \lambda_2 \sum_i^{n^\alpha} \langle\varphi_{1j^\alpha}|P_n^\alpha|\varphi_{1j^\alpha}\rangle\right] \\ &= 0 \end{aligned} \tag{33}$$

In practical applications, we invariably invoke the algebraic approximation by parametrizing the orbitals in a finite basis set. This approximation may be written

$$|\varphi_1\rangle = P\,|\varphi_1\rangle \tag{34}$$

where P is an orthoprojector defined by a chosen basis set with dimension M_1, *i.e.*

$$P = \sum_{p,q}^{M_1} |\chi_p^1\rangle \left(\mathbf{S^{-1}}\right)_{pq} \langle\chi_q^1| \tag{35}$$

where $\mathbf{S}$ is the overlap matrix with elements $\langle\chi_p|\chi_q\rangle$ and $\mathbf{S^{-1}}$ is its inverse so that

$$|\varphi_1\rangle = \sum_{p,q}^{M_1} |\chi_p^1\rangle \left(\mathbf{S^{-1}}\right)_{pq} \langle\chi_q^1|\varphi_1\rangle \tag{36}$$

is the approximation of the orbital $|\varphi_1\rangle$ in the given basis set. It should be stressed that, in general, the basis set for the excited state,

$$\left\{\chi_p^1; p = 1, 2, ..., M_1\right\}, \tag{37}$$

is distinct from that for the ground state,

$$\left\{\chi_p^0; p = 1, 2, ..., M_0\right\}. \tag{38}$$

The stationary condition (33) leads, after some manipulation, to the following equations

$$\begin{aligned} &P(\mathbf{F}^\alpha - \lambda_\mathbf{1}\mathbf{P}^\beta + \lambda_\mathbf{2}\mathbf{P}_\mathbf{n}^\alpha - \varepsilon_\mathbf{i}^\mathbf{a})\mathbf{P}\,|\varphi_{\mathbf{1i}^\alpha}\rangle = \mathbf{0}, && i^\alpha = 1, 2, ..., n^\alpha, ..., M_1 \\ &&& \lambda_1, \lambda_2 \to \infty \\ &P(\mathbf{F}^\beta + \lambda_\mathbf{1}\mathbf{Q}^\alpha - \varepsilon_\mathbf{i}^\beta)\mathbf{P}\,|\varphi_{\mathbf{1i}^\beta}\rangle = \mathbf{0}, && i^\beta = 1, 2, ..., n^\beta, ..., M_1 \end{aligned}$$

Here $\mathbf{F}^{\alpha}$ and $\mathbf{F}^{\beta}$ are the standard UHF Fock operators constructed from the excited state orbitals φ_{1i} .

Unlike the traditional approaches to this constrained variational problem (*e.g.* [36]), we shall apply a method for determining the Lagrangian multipliers λ_1, λ_2 which has been designated *tocia* for "*t*aking the *o*rthogonality *c*onstraints *i*nto *a*ccount". This method was proved to be a useful tool for solving tasks which can be formulated in terms of eigenvalue problems with orthogonalities constraints [30], [31], [34], [35], [37], [27]. According to the *tocia* method, the terms $\lambda_1 P^{\beta}$ and $\lambda_1 Q^{\alpha}$, $\lambda_1 \to \infty$, ensure spin purity (see [34], [35] for more details) whereas the term $\lambda_2 P_n^{\alpha}$, $\lambda_2 \to \infty$, provides for the orthogonality of states. This result can be easily extended to the higher energy levels. For example, in the case of the second excited state the operator P_n^{α} should be substituted by the orthoprojector

$$P_n^{\alpha} = |\varphi_{0n^{\alpha}}\rangle \langle \varphi_{0n^{\alpha}}| + |\varphi_{1n^{\alpha}}\rangle \langle \varphi_{1n^{\alpha}}| \, , etc., \tag{39}$$

i.e. the problem of how to choose a determinantal wave function for the higher excitations does not appear. In the *tocia* method, the only addition computation required, beyond that arising in the standard UHF scheme, is the evaluation of the overlap matrix element $\langle \varphi_{0n^{\alpha}} | \varphi_{1j^{\alpha}} \rangle$. In practical calculations, the value λ_1 is taken to be $\sim 100 - 500$ a.u. so as toensure spin purity [35], whereas taking $\lambda_2 > 1000$ a.u. ensures that $\langle \Phi_0 | \Phi_1 \rangle < 10^{-6} - 10^{-6}$ [27].

3. Implementation of the algebraic approximation for excited states

In this section, we turn to the approximation of the excited state in a finite basis set. In particular, we describe three different schemes for developing systematic sequences of even-tempered basis sets for excited states which will approach the exact solution in the limit $M_1 \to \infty$. We define each scheme, which we label (a), (b) and (c) in turn.

In each scheme, we generate a sequence of even-tempered basis sets, with exponents given by (1), in which the parameters vary as a function of M, the basis set size, in such a way that the conditions (2) are satisfied and the basis set becomes formally complete in the limit $M \to \infty$.

In the scheme which we label (a), the same basis set is employed for both the ground and excited state. Therefore, the same integrals over basis functions are used for both states. The values of the even-tempered parameters α and β for $M = 6$ are those which were optimized for the ground state of the atom as reported by Schmidt and Ruedenberg [9]. These values are given in Table 1 of reference [9]. Larger basis sets were generated by means of the recursion formulae [10]:

$$\alpha\,[M] = \left[\frac{\beta\,[M]-1}{\beta\,[M-1]-1}\right]^{a} \alpha\,[M-1] \tag{40}$$

and

$$\ln(\beta\,[M]) = \left[\frac{M}{M-1}\right]^{b} \ln\beta\,[M-1] \tag{41}$$

with the values of a and b taken from the work of Schmidt and Ruedenberg [9]. These values are given in Table 3 of reference [9].

In scheme (b) the basis set is optimized by invoking the variation principle for each state considered. For the ground state the optimized values of the even-tempered parameters α_0 and β_0 given by Schmidt and Ruedenberg [9] are used. We add the subscript "0" to distinguish ground state values. For the excited state optimal α_1 and β_1 values for a sequence of M_1 values are determined.

In our third scheme, which we label (c), we optimized the parameter α and β the smallest basis set considered, *i.e.* $M = 6$ and then determine values of these parameters for the basis sets of larger size by using the recursions (40) and (41) with the values of a and b taken from the work of Schmidt and Ruedenberg [9].

Each of these schemes lead to sequences of basis sets which satisfy the limits (2) and therefore lead to complete basis sets in the limit $M_1 \to \infty$. We performed prototype calculations on some simple atoms in order to study the rate of convergence of the excited state energies and the accuracy which could be supported before problems associated with the precision of our calculations arising from computational linear dependence became significant. In particular, we studied the ^3S states of the He atom corresponding to the configurations $1s2s$, $1s3s$ and $1s4s$, the ^3S states of the Li atom corresponding to the configurations $1s^2 3s$ and $1s^2 4s$, and the ^3S states of the Be atom corresponding to the configurations (He) $2s3s$ and (He) $2s4s$.

4. Results and discussions

4.1. MATRIX HARTREE-FOCK ENERGIES FOR EXCITED STATES

The ground and excited state matrix Hartree-Fock energies for the He, Li and Be atoms are presented in Tables 1, 2 and 3, respectively. All energies are given in atomic units, (Hartree). In each of these tables, we label the columns according to the three schemes, *(a)*, *(b)* and *(c)*, described above for generating sequences of even-tempered basis sets. We consider each system in turn.

For the excited states of the He atom considered in Table 1 the numerical Hartree-Fock energies are known from reference [38] to be - $E(1s2s) = -2.174\ 26$ Hartree, $E(1s3s) = -2.068\ 49$ Hartree, $E(1s4s) = -2.036\ 44$ Hartree. For none of the three states considered does the sequence of basis sets constructed according to scheme (a) achieve satisfactory accuracy. For the $1s2s$ state, the energy supported by the largest basis set, *i.e.* $M = 72$, is in error by ~ 0.8 mHartree For the $1s3s$ state this error is ~ 0.056 Hartree,

TABLE 1. Self-Consistent Field energies (in hartree) of the He atom for some ^{3}S excited states as a function of the size, M, of the even-tempered basis set used to parametrize the orbitals. In the column headed *(a)*: the same even-tempered basis set optimized for the ground state, is used for all states; *(b)*: the even-tempered basis set is optimized for each state; *(c)*: the even-tempered parameters α and β are optimized for each basis set for the smallest basis set ($M = 6$) and larger basis sets are generated using the recursions.

^{3}S $1s2s$

M	*(a)*	*(b)*	*(c)*
6	-1.834 615 14	-2.169 691 48	-2.169 691 48
12	-2.095 895 65	-2.174 206 91	-2.174 162 33
18	-2.141 254 61	-2.174 249 90	-2.174 247 58
24	-2.157 041 32	-2.174 250 75	-2.174 250 59
30	-2.164 213 86	-2.174 250 77	-2.174 250 76
42	-2.170 129 77	-2.174 250 78	-2.174 250 78
54	-2.172 286 98	-	-
60	-2.172 843 71	-	-
72	-2.173 481 74	-	-

^{3}S $1s3s$

M	*(a)*	*(b)*	*(c)*
6	1.737 069 70	-2.059 022 84	-2.059 022 85
12	-1.109 789 95	-2.068 339 06	-2.067 689 10
18	-1.584 292 85	-2.068 479 75	-2.068 450 41
24	-1.760 644 49	-2.068 484 72	-2.068 473 85
30	-1.849 814 46	-2.068 484 93	-2.068 483 86
42	-1.937 546 88	-2.068 484 96	-2.068 484 88
54	-1.979 772 36	-	-
60	-1.993 383 33	-	-
72	-2.012 555 80	-	-

^{3}S $1s4s$

M	*(a)*	*(b)*	*(c)*
6	17.382 628 04	-2.001 929 36	-2.001 929 36
12	2.016 029 12	-2.036 247 88	-2.035 012 30
18	-0.098 971 53	-2.036 416 13	-2.036 012 02
24	-0.816 612 58	-2.036 434 95	-2.036 412 98
30	-1.160 495 08	-2.036 435 84	-2.036 418 53
42	-1.486 125 49	-2.036 436 41	-2.036 436 07
54	-1.640 053 15	-	-
60	-1.689 869 35	-	-
72	-	-	-

whilst for the $1s4s$ state the calculation with the largest basis set failed to converge and for the next largest set the error is ~ 0.348 Hartree. Not surprisingly, a basis set designed for the ground state supports an increasingly poor description of excited states as the level of excitation increases. Equally, it is not surprising that if the sequence of even-tempered basis sets for each excited state is optimized independently then the matrix Hartree-Fock energies converge to values in good agreement with the corresponding numerical Hartree-Fock energies. Whatismore this level of agreement is achieve for basis sets only 42 functions in the case of the He states considered here. Scheme (c) leads to sequences of energies which begin, of course, with values equal to those for scheme (b) when $M = 6$ and converge almost as rapidly towards the numerical Hartree-Fock values. For the $1s2s$ state schemes (b) and (c) lead to energies which agree to all figures quoted, *i.e.* 0.01 μHartree when $M = 42$. For the $1s3s$ state there is a difference of ~ 0.08 μHartree between the energies supported by the two schemes when $M = 42$. The corresponding energy difference for the $1s4s$ state is ~ 0.34 μHartree.

For the excited states of the Li atom considered in Table 2 the numerical Hartree-Fock energies are known [38] to be as follows: $E(1s^2 3s) = -7.310\ 22$ Hartree, $E(1s^2 4s) = -7.274\ 88$ Hartree. For neither of the two states considered does the sequence of basis sets constructed according to scheme (a) achieve satisfactory accuracy. Furthermore, convergence of the self-consistent field procedure was not achieved for basis sets larger than $M = 54$. For the $1s^2 3s$ state, the largest basis set gave an energy which differs from the numerical Hartree-Fock value by ~ 0.3 mHartree. The corresponding difference for the $1s^2 4s$ state is significantly larger at ~ 15.3 mHartree. For scheme (b) a basis set of 42 functions supports an energy which differs from the numerical hartree-Fock value by just ~ 0.01 mHartree for the $1s^2 3s$ state and by less than 0.01 mHartree for the $1s^2 4s$ state. Scheme (c) results in a comparable level of accuracy to that achieved with scheme (b) for both of the states considered.

For the two excited states of the Be atom considered in Table 3 the numerical Hartree-Fock energies are known [38] to be as follows: E([He]2s3s) $= -14.377\ 54$ Hartree, E([He]2s4s) $= -14.324\ 66$ Hartree. For scheme (a) the iterative process failed to converge for basis sets containing more than 72 functions. For the [He]2s3s state, the largest basis set supports an energy expectation value which is within ~ 0.2 mHartree of the numerical Hartree-Fock value, whilst for the [He]2s4s state, the corresponding difference is ~ 16.7 mHartree. Again, a basis set designed for the ground state supports an increasingly poor description of excited states as the level of excitation increases. When the sequence of even-tempered basis sets are individually optimized for a particular state (scheme (b)) an accuracy of ~ 0.04 mHartree is supported for the [He]2s3s state and ~ 0.05 mHartree for the [He]2s4s state. A comparable accuracy is observed for the excited

TABLE 2. Self-Consistent Field energies (in hartree) of ^{2}S excited states of the Li atom as a function of the size, M, of the even-tempered basis set used to parametrize the orbitals. In the column headed *(a)*: the same even-tempered basis set optimized for the ground state, is used for all states; *(b)*: the even-tempered basis set is optimized for each state; *(c)*: the even-tempered parameters α and β are optimized for each basis set for the smallest basis set ($M = 6$) and larger basis sets are generated using the recursions.

$1s^2 3s$			
M	*(a)*	*(b)*	*(c)*
6	-6.841 521 95	-7.268 417 74	-7.268 417 74
12	-7.261 404 14	-7.309 776 81	-7.309 197 38
18	-7.295 552 02	-7.310 193 98	-7.310 186 74
24	-7.304 099 99	-7.310 207 15	-7.310 205 26
30	-7.307 239 87	-7.310 207 73	-7.310 207 50
42	-7.309 318 77	-7.310 207 76	-7.310 207 76
54	-7.309 888 96	-	-

$1s^2 4s$			
M	*(a)*	*(b)*	*(c)*
6	-1.780 422 08	-7.154 657 33	-7.154 657 33
12	-6.740 485 93	-7.273 656 76	-7.271 672 62
18	-7.085 615 24	-7.274 850 25	-7.274 830 78
24	-7.176 272 56	-7.274 878 70	-7.274 861 99
30	-7.213 866 71	-7.274 883 70	-7.274 880 24
42	-7.244 980 78	-7.274 883 90	-7.274 883 86
54	-7.257 576 14	-	-

state energies of the Be atom corresponding to scheme (c) in which only the basis set for $M = 6$ is optimized.

4.2. SEQUENCIES OF EVEN-TEMPERED BASIS SETS FOR EXCITED STATES

It is of interest to examine the parameters α and β defining the even-tempered basis sets used in calculating the energies reported in Table 1, 2 and 3. Let us note that α has dimensions bohr^{-2} whereas β is a dimensionless quantity.

The optimized α and β parameters for the ground states of He, Li and Be are given in Table 1 of the work of Schmidt and Ruedenberg [9] for the smaller basis sets considered in this work. The ground state parameters for larger basis sets were obtained by using the recursions (40) and (41) to

TABLE 3. Self-Consistent Field energies (in hartree) of the Be atom for some ^{3}S excited states as a function of the size, M, of the even-tempered basis set used to parametrize the orbitals. In the column headed *(a)*: the same even-tempered basis set optimized for the ground state, is used for all states; *(b)*: the even-tempered basis set is optimized for each state; *(c)*: the even-tempered parameters α and β are optimized for each basis set for the smallest basis set ($M = 6$) and larger basis sets are generated using the recursions.

$(He)2s3s$

M	*(a)*	*(b)*	*(c)*
6	-13.685 973 24	-14.287 433 98	-14.287 433 98
12	-14.308 751 64	-14.376 551 31	-14.376 157 39
18	-14.355 839 67	-14.377 477 84	-14.377 452 53
24	-14.368 148 73	-14.377 497 90	-14.377 496 50
30	-14.372 823 26	-14.377 498 69	-14.377 498 56
42	-14.376 028 85	-14.377 498 74	-14.377 498 74
54	-14.376 949 34	-	-
60	-14.377 148 28	-	-
72	-14.377 351 93	-	-

$(He)2s4s$

M	*(a)*	*(b)*	*(c)*
6	-5.206 147 93	-14.103 283 99	-14.103 283 99
12	-13.459 627 62	-14.322 849 81	-14.320 183 66
18	-14.013 438 62	-14.324 551 09	-14.324 462 05
24	-14.159 808 90	-14.324 607 13	-14.324 583 56
30	-14.221 078 84	-14.324 610 93	-14.324 607 87
42	-14.272 399 38	-14.324 611 21	-14.324 611 13
54	-14.293 550 25	-	-
60	-14.299 788 29	-	-
72	-14.307 983 38	-	-

extend the Schmidt-Ruedenberg sets. These are the parameters determined by Schmidt and Ruedenberg for the corresponding ground states which were used in the present study to obtain the excited state energies in the columns headed *(a)* in Tables 1, 2 and 3.

In Tables 4 and 5, the even-tempered basis set α and β parameters corresponding to the columns headed *(b)* and *(c)* in Table 1 for the helium atom are given, respectively. The parameters obtained by optimization of α and β with respect to the energy for each size of a basis set, that is scheme *(b)* are given in Table 4. They should be compared with the parameters obtained from the recursion formulae (40) and (41) according to scheme *(c)* in which the parameters α and β were only optimized for the smallest

TABLE 4. Optimized even-tempered parameters α and β for ^{3}S excited states of He as a function of size of basis set.

	$1s2s$		$1s3s$		$1s4s$	
M	α	β	α	β	α	β
6	0.009 397	4.210 973	0.001 684	4.979 103	0.000 376	5.420 623
12	0.009 088	2.641 628	0.002 742	2.758 438	0.000 924	3.033 467
18	0.008 243	2.211 957	0.002 785	2.202 424	0.001 226	2.212 713
24	0.007 443	1.999 366	0.001 967	1.999 755	0.001 232	1.932 314
30	0.006 989	1.897 299	0.002 043	1.845 165	0.001 176	1.794 637
42	0.005 045	1.702 089	0.002 176	1.661 148	0.001 068	1.666 500

TABLE 5. Even-tempered α and β parameters for ^{3}S states of He from the recursion formulae.

	$1s2s$		$1s3s$		$1s4s$	
M	α	β	α	β	α	β
6	0.009 397	4.210 973	0.001 684	4.979 103	0.000 376	5.420 623
12	0.007 565	2.858 623	0.001 339	3.230 871	0.000 297	3.437 767
18	0.006 755	2.396 799	0.001 189	2.653 847	0.000 263	2.794 540
24	0.006 262	2.154 050	0.001 099	2.355 565	0.000 243	2.464 841
30	0.005 918	2.000 886	0.001 036	2.169 343	0.000 229	2.260 108
42	0.005 453	1.814 036	0.000 952	1.944 419	0.000 210	2.014 071

basis set, *i.e.* $M = 6$.

Tables 6 and 7 display the corresponding values of α and β for the lithium atom; Table 6 giving the optimized values (scheme *(b)*) and Table 7 giving the values obtained by using the recursions (40) and (41) after optimizing the values for the smallest basis set (scheme *(c)*).

In Tables 8 and 9, the even-tempered parameters for the two excited states of the beryllium atom considered in this work are presented, with Table 8 giving the parameters obtained according to scheme *(b)* in which the parameters were fully optimized and Table 9 giving the parameters obtained by means of scheme *(c)* in which the parameters α and β were only optimized for the smallest basis set, *i.e.* $M = 6$.

Comparing the parameters given in Tables 4-9, it can be seen that the fully optimized values of β (scheme *(b)*) display a similar behavior to the values obtained from recursion formulae (40) and (41) after optimizing the value for the smallest basis set. In contrast, for the α parameters resulting from schemes *(b)* and *(c)* some differences can be observed.

The energy expectation values resulting from schemes *(b)* and *(c)* are

TABLE 6. Optimized even-tempered α and β parameters for ^{2}S states of Li as a function of size of basis set

	$1s^2 3s$		$1s^2 4s$	
M	α	β	α	β
6	0.002 164	5.321 302	0.000 473	6.009 700
12	0.002 993	2.961 293	0.000 276	3.364 387
18	0.003 087	2.323 756	0.000 565	2.497 936
24	0.002 937	2.046 230	0.000 659	2.067 042
30	0.002 715	1.894 460	0.000 509	1.928 593
42	0.002 446	1.707 018	0.000 493	1.699 996

TABLE 7. Even-tempered α and β parameters for ^{2}S states of Li from the recursion formulae.

	$1s^2 3s$		$1s^2 4s$	
M	α	β	α	β
6	0.002 164	5.321 302	0.000 473	6.009 700
12	0.001 811	3.172 344	0.000 393	3.450 384
18	0.001 654	2.533 693	0.000 358	2.711 044
24	0.001 559	2.219 463	0.000 337	2.352 045
30	0.001 491	2.029 298	0.000 322	2.136 548
42	0.001 399	1.806 306	0.000 302	1.885 728

seen to be very close together. This observation can be explained by noting that the energy surface in the space of the parameters α and β has a smooth structure. However, it should also be noted that the energy expectation value is more sensitive to variation of the parameter β than to that of α.

It has been demonstrated that for the excited states of the atoms He, Li and Be considered in the present work, a simple optimization of the α and β parameters for each size of basis set leads to a sequence of even-tempered basis sets capable of supporting high accuracy in Hartree-Fock calculations for excited state energies of atoms. Furthermore, optimization of the α and β parameters for the smallest basis set in a sequence, $M = 6$ in the present study, followed by application of the recursion formulae (40) and (41) represents a good compromise which undoubtedly proved useful in case where full optimization of these parameters for each size of basis set is computationally demanding.

TABLE 8. Optimized even-tempered α and β parameters for ^{3}S states of Be as a function of size of basis set.

	[He] $2s3s$		[He] $2s4s$	
M	α	β	α	β
6	0.004 884	5.142 401	0.001 057	5.809 367
12	0.004 799	2.947 601	0.001 459	3.191 957
18	0.004 552	2.370 166	0.001 709	2.424 045
24	0.004 237	2.083 730	0.001 736	2.080 558
30	0.003 912	1.921 824	0.001 663	1.899 549
42	0.003 667	1.745 016	0.001 537	1.719 092

TABLE 9. Even-tempered α and β parameters for ^{3}S states of Be from recursion formulae.

	[He] $2s3s$		[He] $2s4s$	
M	α	β	α	β
6	0.004 884	5.142 401	0.001 057	5.809 367
12	0.003 925	3.125 481	0.000 842	3.402 319
18	0.003 513	2.513 894	0.000 751	2.692 540
24	0.003 264	2.210 162	0.000 696	2.344 631
30	0.003 092	2.025 281	0.000 659	2.134 569
42	0.002 859	1.807 301	0.000 608	1.888 741

5. Concluding remarks

We have presented a practical Hartree-Fock theory of atomic and molecular electronic structure for individual electronically excited states that does not involve the use of off-diagonal Lagrange multipliers. An easily implemented method for taking the orthogonality constraints into account (*tocia*) has been used to impose the orthogonality of the Hartree-Fock excited state wave function of interest to states of lower energy.

The applicability of systematic sequence of even-tempered basis sets with the exponents, ζ_p, defined by the geometric series $\zeta_p = \alpha\beta^p$, has been examined in Hartree-Fock energy calculations for excited states which have the same spatial and spin symmetry as the ground state. It is shown that a simple reoptimization of the α and β parameters leads to a sequence of even-tempered basis sets capable of supporting high accuracy for excited state energies of some simple atoms, He, Li and Be. In contrast, simply using even-tempered basis sets designed for the corresponding ground states leads to significant loss of accuracy.

It has been demonstrated that a sequence of basis sets generated with schemes designated *(b)* and *(c)* are capable of supporting high accuracy for excited state energies of the atoms. Optimization of the α and β parameters only for the smallest basis set (scheme *(c)*) lead to energies which are in a good agreement with those obtained in a case where these parameters were optimized for each size of basis set (scheme *(b)*). It must be concluded that schemes *(b)* and *(c)*support comparable accuracies in the energies of all states.

Finally, we remark that, although the in the present study attention has been focussed on the excited states of some simple atomic systems, the method described here can be applied to molecular systems where they can be expected to support high accuracy as well as providing a suitable reference with respect to which well-founded many-body expansions for correlation effects can be developed.

References

1. E.R. Davidson and D.F. Feller, Chem. Rev. **86**, 681 (1986)
2. S. Wilson, Adv. Chem. Phys. **67**, 439 (1987)
3. S. Wilson, in: *New Methods in Quantum Theory*, Ed. C.A. Tsipis, V.S. Popov, D.R. Herschbach and J.S. Avery, NATO ASI Series 3, V.8, p. 437-461, Kluwer Academic Publishers, Dordrecht, 1996
4. S. Wilson, in *Handbook of Molecular Physics and Quantum Chemistry*, **2**, *Molecular Electronic Structure*, ed. S. Wilson, P.F. Bernath and R. McWeeny, Wiley, Chichester (2003)
5. T.H. Dunning, Jr., J. Chem .Phys. **90**, 1007 (1989)
6. J. Almlof and P.R. Taylor, J.Chem.Phys. **86**, 4070 (1987)
7. T. Helgaker and P.R. Taylor, in: *Modern Electronic Structure Theory*, Part 11, Ed. D. Yarkony, pp. 727-856, World Scientific (1995)
8. R.S. Raffenetti and K. Rudenberg, J. Chem. Phys. **59**, 5978 (1973).
9. M.W. Schmidt and K. Rudenberg, J. Chem. Phys. **71**, 3951 (1979)
10. E.S. Kryachko and S. Wilson, Int.J.Quant.Chem. **93**, 112 (2003)
11. J. Kobus, D. Moncrieff and S. Wilson, J. Comp. Meth. Sci. & Eng. **4**, 611 (2004)
12. D. Moncrieff and S. Wilson, J. Phys. B: At. Mol. Opt. Phys. **29**, 6009 (1996)
13. D. Moncrieff and S. Wilson, J. Phys. B: At. Mol. Opt. Phys. **28**, 4007 (1995)
14. D. Moncrieff and S. Wilson, J. Phys. B: At. Mol. Opt. Phys. **29**, 2425 (1996)
15. H.M. Quiney, I.P. Grant and S. Wilson, J. Phys. B: At. Mol. Opt. Phys. **23**, L271 (1990)
16. H.M. Quiney, V.N. Glushkov and S. Wilson, Int. J. Quantum Chem. **89**, 227 (2002)
17. H. Shull and P.-O. Löwdin, Phys.Rev. **110**, 1466 (1958)
18. K. Anderssom and B.O. Roos, in: *Modern Electronic Structure Theory*, Part 11, Ed. D. Yarkony, pp. 55-109, World Scientific (1995)
19. K. Morokuma and S. Iwata, Chem. Phys. Lett. **16**, 195 (1972)
20. R. McWeeny, Molec. Phys. **28**, 1273 (1974)
21. J. Mrozek and A. Golebiewski, Int. J. Quant. Chem. **12**, 207 (1977)
22. E.R.Davidson, L.Z. Stenkamp CF Int.J.Quant.Chem. (Symp). 10, 21.(1976)
23. E.R. Davidson and E.L. McMurchie, in: *Excited States* **5**, 1 (1985)
24. R. Colle, A. Fortunelli and O. Salwetti, Theor. Chim. Acta. **71**, 467 (1987)
25. N. Gidopoulos and A. Theophilou, Phil. Mag. **69**, 1067 (1994)
26. A. Theophilou, J. Phys. C, **12**, 5419 (1979)
27. N. Gidopoulos, V.N. Glushkov and S. Wilson, Proc.R. Soc. Lond. A., **457**, 1657 (2002)

28. V.N. Glushkov, A.Ya. Tsaune and Z. Vychisl, Matem. & Mat. Phys. **25**, 298 (1985)
29. V.N. Glushkov, Opt. Spectrosc. **93**, 15 (2002)
30. V.N. Glushkov, J. Math. Chem. **31**, 91 (2002)
31. V.N. Glushkov and A.Ya. Tsaune, Opt. Spectrosc. **87**, 267 (1999)
32. M. Cohen and P.S. Kelly, Can. J. Phys. **43**, 1867 (1965)
33. H. Tatewaki, T. Koga, Y. Sakai and A.J. Thakkar, J. Chem. Phys. **101**, 4945 (1994)
34. V.N. Glushkov, Chem. Phys. Lett. **273**, 122 (1997)
35. V.N. Glushkov, Int. J. Quant. Chem. **99**, 236 (2004)
36. P.E. Gill and M. Murray, *Numerical methods for constrained optimization*, London. Academic Press (1978)
37. V.N. Glushkov, Chem. Phys. Lett. **287**, 189 (1998)
38. C. Froese, J. Chem. Phys. **47**, 4010 (1967)

PRACTICABLE FACTORIZED TDLDA FOR ARBITRARY DENSITY- AND CURRENT-DEPENDENT FUNCTIONALS

V. O. NESTERENKO
Bogoliubov Laboratory of Theoretical Physics, Joint Institute for Nuclear Research, Dubna, Moscow region, 141980, Russia

J. KVASIL
Department of Nuclear Physics, Charles University, CS-18000 Prague 8, Czech Republic

AND

P.-G. REINHARD
Institut für Theoretische Physik, Universität Erlangen, D-91058, Erlangen, Germany

Abstract. We propose a practicable method for describing linear dynamics of different finite Fermi systems. The method is based on a general self-consistent procedure for factorization of the two-body residual interaction. It is relevant for diverse density- and current-dependent functionals and, in fact, represents the self-consistent separable random-phase approximation (RPA), hence the name SRPA. SRPA allows to avoid diagonalization of high-rank RPA matrices and thus dwarfs the calculation expense. Besides, SRPA expressions have a transparent analytical form and so the method is very convenient for the analysis and treatment of the obtained results. SRPA demonstrates high numerical accuracy. It is very general and can be applied to diverse systems. Two very different cases, the Kohn-Sham functional for atomic clusters and Skyrme functional for atomic nuclei, are considered in detail as particular examples. SRPA treats both time-even and time-odd dynamical variables and, in this connection, we discuss the origin and properties of time-odd currents and densities in initial functionals. Finally, SRPA is compared with other self-consistent approaches for the excited states, including the coupled-cluster method.

J.-P. Julien et al. (eds.),
Recent Advances in the Theory of Chemical and Physical Systems, 127–150.

1. Introduction

The time-dependent local-density-approximation theory (TDLDA) is widely used for description of dynamics of diverse quantum systems such as atomic nuclei, atoms and molecules, atomic clusters, etc. (see for more details [1–5]). However, even in the linear regime, this theory is plagued by dealing with high-rank matrices which make the computational effort too expensive. This is especially the case for non-spherical systems with their demanding configuration space. For example, in the Random Phase Approximation (RPA), a typical TDLDA theory for linear dynamics, the rank of the matrices is determined by the size of the particle-hole 1ph space which becomes really huge for deformed and heavy spherical systems. The simplest RPA versions, like the sum rule approach and local RPA (see hierarchy of RPA methods in [6]) deal with a few collective variables instead of a full 1ph space and thus avoid the problem of high-rank matrices. But these versions cannot properly describe gross-structure of collective modes and the related property of the Landau damping (dissipation of the collective motion over nearby 1ph excitations).

In this connection, we propose a method [7–10] which combines accuracy and power of involved RPA versions with simplicity and physical transparency of the simplest ones and thus is a good compromise between these two extremes. The method is based on the self-consistent *separable* approximation for the *two-body* residual interaction which is factorized into a sum of weighted products of *one-body* operators. Hence the method is called as separable RPA (SRPA). It should be emphasized that the factorization is self-consistent and thus does not result in any additional parameters. Expressions for the one-body operators and their weights are inambiguously derived from the initial functional. The factorization has the advantage to shrink dramatically the rank of RPA matrix (usually from $r = 10^3 - 10^6$ to $r = 2 - 14$) and thus to minimize the calculation expense. Rank of SRPA matrix is determined by the number of the separable terms in the expansion for the two-body interaction. Due to effective self-consistent procedure, usually a few separable terms (or even one term) are enough for a good accuracy. Ability of SRPA to minimize the computational effort becomes really decisive in the case of non-spherical systems with its huge 1ph configuration space. SRPA formalism is quite simple and physically transparent, which makes the method very convenient for the analysis and treatment of the numerical results. Being self-consistent, SRPA allows to extract spurious admixtures connected with violation of the translational or rotational invariance. As is shown below, SRPA exhibits accuracy of most involved RPA versions but for the much less expense. Since SRPA exploits the full 1ph space, it equally well treats collective and non-collective states and, what is very important, fully describes the Landau damping, one of the most important properties of collective motion. SRPA is quite general and can be

applied to diverse finite Fermi systems (and thus to different functionals), including those tackling both time-even densities and time-odd currents. The latter is important not only for nuclear Skyrme functionals [11, 12] which exploits a variety of time-even and time-odd variables but also for electronic functionals whose generalized versions deal with basic current densities (see e.g. [13]).

SRPA has been already applied for atomic nuclei and clusters, both spherical and deformed. To study dynamics of valence electrons in atomic clusters, the Konh-Sham functional [14,15]was exploited [7,8,16,17], in some cases together with pseudopotential and pseudo-Hamiltonian schemes [16]. Excellent agreement with the experimental data [18] for the dipole plasmon was obtained. Quite recently SRPA was used to demonstrate a non-trivial interplay between Landau fragmentation, deformation splitting and shape isomers in forming a profile of the dipole plasmon in deformed clusters [17].

In atomic nuclei, SRPA was derived [9,10,19] for the demanding Skyrme functional involving a variety of densities and currents (see [20] for the recent review on Skyrme forces). SRPA calculations for isoscalar and isovector giant resonances (nuclear counterparts of electronic plasmons) in doubly magic nuclei demonstrated high accuracy of the method [10].

In the present paper, we give a detail, maybe even tutorial, description of SRPA, consider and discuss its most important particular cases and compare it with alternative approaches, including the equation-of-motion method in the coupled-cluster theory. We thus pursue the aim to advocate SRPA for researchers from other areas, e.g. from the quantum chemistry.

The paper is organized as follows. In Section 2, derivation of the the SRPA formalism is done. Relations of SRPA with other alternative approaches are commented. In Sec. 3, the method to calculate SRPA strength function (counterpart of the linear response theory) is outlined. In Section 4, the particular SRPA versions for the electronic Kohn-Sham and nuclear Skyrme functionals are specified and the origin and role of time-odd currents in functionals are scrutinized. In Sec. 5, the practical SRPA realization is discussed. Some examples demonstrating accuracy of the method in atomic clusters and nuclei are presented. The summary is done in Sec. 6. In Appendix A, densities and currents for Skyrme functional are listed. In Appendix B, the optimal ways to calculate SRPA basic values are discussed.

2. Basic SRPA equations

RPA problem becomes much simpler if the residual two-body interaction is factorized (reduced to a separable form)

$$\sum_{h_1,h_2,p_1,p_2} < h_2p_2|\hat{V}_{res}|p_1h_1 > a^+_{p_1}a^+_{p_2}a_{h_2}a_{h_1} \to \sum_{k,k'=1}^{K} [\kappa_{kk'}\hat{X}_k\hat{X}_{k'} + \eta_{kk'}\hat{Y}_k\hat{Y}_{k'}] \tag{1}$$

where

$$\hat{X}_k = \sum_{ph} < p|\hat{X}_k|h > a_p^+ a_h, \quad \hat{Y}_k = \sum_{ph} < p|\hat{Y}_k|h > a_p^+ a_h$$

are time-even and time-odd one-body operators, respectively. Further, a_p^+ (a_h) is the creation (annihilation) operator of the particle state p (hole state h); K is the number of the separable terms.

Conceptually, the self-consistent procedure outlined below was first proposed in [21].

2.1. TIME-DEPENDENT HAMILTONIAN

The system is assumed to undergo small-amplitude harmonic vibrations around HF ground state. The starting point is a general time-dependent energy functional

$$E(J_\alpha(\vec{r},t)) = \int \mathcal{H}(J_\alpha(\vec{r},t))d\vec{r} \tag{2}$$

depending on an arbitrary set of densities and currents defined through the corresponding operators as

$$J_\alpha(\vec{r},t) =< \Psi(t)|\hat{J}_\alpha(\vec{r})|\Psi(t) >= \sum_h^{occ} \varphi_h^*(\vec{r},t)\hat{J}_\alpha(\vec{r})\varphi_h(\vec{r},t) \tag{3}$$

where $\Psi(t)$ is the many-body function of the system as a Slater determinant, and φ_h^* is the wave function of the hole (occupied) single-particle state. In general, the set (3) includes both time-even and time-odd densities and currents, see examples in the Appendix A.

Time-dependent mean-field Hamiltonian directly follows from (2)-(3):

$$\hat{h}(\vec{r},t)\varphi_h = \frac{\delta\mathcal{H}}{\delta\varphi_h^*} = \sum_\alpha \frac{\delta\mathcal{H}}{\delta J_\alpha}\frac{\delta J_\alpha}{\delta\varphi_h^*} = \sum_\alpha \frac{\delta\mathcal{H}}{\delta J_\alpha}\hat{J}_\alpha\varphi_h. \tag{4}$$

In the small-amplitude regime, the densities are decomposed into static part and small time-dependent variation

$$J_\alpha(\vec{r},t) = \bar{J}_\alpha(\vec{r}) + \delta J_\alpha(\vec{r},t). \tag{5}$$

Then, to the linear order for $\delta J_\alpha(\vec{r},t)$, the mean-field Hamiltonian (4) can be decomposed into static and time-dependent response parts

$$\begin{aligned} \hat{h}(\vec{r},t) &= \hat{h}_0(\vec{r}) + \hat{h}_{res}(\vec{r},t), \\ &= \sum_\alpha [\frac{\delta\mathcal{H}}{\delta J_\alpha}]_{J=\bar{J}}\hat{J}_\alpha(\vec{r}) + \sum_{\alpha,\alpha'} [\frac{\delta^2\mathcal{H}}{\delta J_\alpha \delta J_{\alpha'}}]_{J=\bar{J}}\delta J_{\alpha'}(\vec{r},t)\hat{J}_\alpha(\vec{r}) \end{aligned} \tag{6}$$

and thus we get the time-dependent Hamiltonian $\hat{h}_{res}(\vec{r},t)$ responsible for the collective motion.

2.2. SCALING PERTURBATION

Now we should specify the response Hamiltonian $\hat{h}_{res}(\vec{r},t)$. For this aim, we use the scaling transformation and define the perturbed many-body wave function of the system as

$$|\Psi(t)>=\prod_{k=1}^{K} exp[-iq_k(t)\hat{P}_k]exp[-ip_k(t)\hat{Q}_k]|0> . \tag{7}$$

Here both the perturbed wave function $|\Psi(t)>$ and static ground state wave function $|0>$ are Slater determinants; $\hat{Q}_k(\vec{r})$ and $\hat{P}_k(\vec{r})$ are generalized coordinate (time-even) and momentum (time-odd) hermitian operators with the propoerties.

$$\begin{aligned} \hat{Q}_k = \hat{Q}_k^+, \quad \hat{T}\hat{Q}_k\hat{T}^{-1} &= \hat{Q}_k, \\ \hat{P}_k = i[\hat{H},\hat{Q}_k]_{ph} = \hat{P}_k^+, \quad \hat{T}\hat{P}_k\hat{T}^{-1} &= -\hat{P}_k, \end{aligned} \tag{8}$$

They generate T-even and T-odd harmonic deformations $q_k(t)$ and $p_k(t)$; $\hat{T}$ is the time inversion operator.

Using Eqs. (3) and (7), the transition densities read

$$\begin{aligned} \delta J_\alpha(\vec{r},t) \quad &=< \Psi(t)|\hat{J}_\alpha|\Psi(t)> - <0|\hat{J}_\alpha|0>= \\ &= i\sum_k \{q_k(t) <0|[\hat{P}_k,\hat{J}_\alpha(\vec{r})]|0> + p_k(t) <0|[\hat{Q}_k,\hat{J}_\alpha(\vec{r})]|0>\} \end{aligned} \tag{9}$$

and the response Hamiltonian (6) is

$$\hat{h}(\vec{r},t) = \sum_{sk}\{q_k(t)\hat{X}_k(\vec{r}) + p_k(t)\hat{Y}_k(\vec{r})\} \tag{10}$$

where all the $\vec{r}$-dependent terms are collected into the hermitian one-body operators

$$\hat{X}_k(\vec{r}) = i\sum_{\alpha\alpha'}[\frac{\delta^2\mathcal{H}}{\delta J_\alpha \delta J_{\alpha'}}]_{J=\bar{J}} <0|[\hat{P}_k,\hat{J}_{\alpha'}]|0> \hat{J}_\alpha(\vec{r}), \tag{11}$$

$$\hat{Y}_k(\vec{r}) = i\sum_{\alpha\alpha'}[\frac{\delta^2\mathcal{H}}{\delta J_\alpha \delta J_{\alpha'}}]_{J=\bar{J}} <0|[\hat{Q}_k,\hat{J}_{\alpha'}]|0> \hat{J}_\alpha(\vec{r}) \tag{12}$$

with the properties

$$\hat{X}_k = \hat{X}_k^+, \quad T\hat{X}_kT^{-1} = \hat{X}_k, \quad \hat{X}_k^* = \hat{X}_k, \tag{13}$$

$$\hat{Y}_k = \hat{Y}_k^+, \quad T\hat{Y}_kT^{-1} = -\hat{Y}_k, \quad \hat{Y}_k^* = -\hat{Y}_k. \tag{14}$$

As is shown below, $\hat{X}_k$ and $\hat{Y}_k$ are just the T-even and T-odd operators to be exploited in the separable expansion (1).

In the derivation above, we used the property of hermitian operators with a definite T-parity

$$< 0|[\hat{A}, \hat{B}]|0 >= 0, \quad \text{if} \quad T\hat{A}T^{-1} = T\hat{B}T^{-1} \tag{15}$$

which states that the average of the commutator vanishes if the operators $\hat{A}$ and $\hat{B}$ are of the same T-parity. This property allows to classify operators with a definite T-parity in the SRPA formalism and thus to make the formalism simple and transparent. For example, in Eqs. (11)-(12), T-even and T-odd densities $\hat{J}_\alpha(\vec{r})$ contribute separately to $\hat{X}_k$ and $\hat{Y}_k$.

To complete the construction of the separable expansion (1), we should yet determine the strength matrices $\kappa_{kk'}$ and $\eta_{kk'}$. This can be done through variations of the basic operators

$$\begin{aligned} \delta\hat{X}_k(t) \quad &\equiv < \Psi(t)|\hat{X}_k|\Psi(t) > - < 0|\hat{X}_k|0 >= \\ &= i\sum_{k'} q_{k'}(t) < 0|[\hat{P}_{k'}, \hat{X}_k]|0 >= -\sum_{k'} q_{k'}(t)\kappa^{-1}_{k'k} \, , \end{aligned} \tag{16}$$

$$\begin{aligned} \delta\hat{Y}_k(t) \quad &\equiv < \Psi(t)|\hat{Y}_k|\Psi(t) > - < 0|\hat{Y}_k|0 >= \\ &= i\sum_{k'} p_{k'}(t) < 0|[\hat{Q}_{k'}, \hat{Y}_k]|0 >= -\sum_{k'} p_{k'}(t)\eta^{-1}_{k'k} \end{aligned} \tag{17}$$

where we introduce symmetric inverse strength matrices

$$\begin{aligned} \kappa^{-1}_{k'k} \quad &= \kappa^{-1}_{kk'} = -i < 0|[\hat{P}_{k'}, \hat{X}_k]|0 >= \\ &= \int d\vec{r} \sum_{\alpha\alpha'} [\frac{\delta^2\mathcal{H}}{\delta J_{\alpha'}\delta J_\alpha}] < 0|[\hat{P}_k, \hat{J}_\alpha]|0 >< 0|[\hat{P}_{k'}, \hat{J}_{\alpha'}]|0 >, \end{aligned} \tag{18}$$

$$\begin{aligned} \eta^{-1}_{k'k} \quad &= \eta^{-1}_{kk'} = -i < 0|[\hat{Q}_{k'}, \hat{Y}_k]|0 > \\ &= \int d\vec{r} \sum_{\alpha\alpha'} [\frac{\delta^2\mathcal{H}}{\delta J_{\alpha'}\delta J_\alpha}] < 0|[\hat{Q}_k, \hat{J}_\alpha]|0 >< 0|[\hat{Q}_{k'}, \hat{J}_{\alpha'}]|0 > . \end{aligned} \tag{19}$$

Then one gets

$$-\sum_k \kappa_{k'k}\delta\hat{X}_k(t) \quad = \quad q_{k'}(t), \tag{20}$$

$$-\sum_{sk} \eta_{k'k}\delta\hat{Y}_k(t) \quad = \quad p_{k'}(t) \tag{21}$$

and the response Hamiltonian (10) acquires the form

$$\hat{h}(\vec{r}, t) = -\sum_{kk'} \{\kappa_{kk'}\delta\hat{X}_k(t)\hat{X}_{k'}(\vec{r}) + \eta_{kk'}\delta\hat{Y}_k(t)\hat{Y}_{k'}(\vec{r})\}. \tag{22}$$

Following [1], the response Hamiltonian (22) leads to the same eigenvalue problem as the separable Hamiltonian

$$\hat{H}_{RPA} = \hat{h}_0 + \hat{V}_{res}, \tag{23}$$

with

$$\hat{V}_{res} = -\frac{1}{2}\sum_{kk'}[\kappa_{kk'}\hat{X}_k\hat{X}_{k'} + \eta_{kk'}\hat{Y}_k\hat{Y}_{k'}] \tag{24}$$

(see also discussion in the next subsections).

In principle, we already have in our disposal the SRPA formalism for description of the collective motion in space of collective variables. Indeed, Eqs. (11), (12), (18), and (19) deliver one-body operators and strength matrices we need for the separable expansion of the two-body interaction. The number K of the collective variables $q_k(t)$ and $p_k(t)$ and separable terms depends on how precisely we want to describe the collecive motion (see discussion in Section 4). For $K = 1$, SRPA converges to the sum rule approach with a one collective mode [6]. For $K > 1$, we have a system of K coupled oscillators and SRPA is reduced to the local RPA [6, 24] suitable for a rough description of several modes and or main gross-structure efects. However, SRPA is still not ready to describe the Landau fragmentation. For this aim, we should consider the detailed 1ph space. This will be done in the next subsection.

2.3. INTRODUCTION OF 1PH SPACE

Collective modes can be viewed as superpositions of 1ph configurations. It is convenient to define this relation by using the Thouless theorem which establishes the connection between two arbitrary Slater determinants [25]. Then, the perturbed many-body wave function reads

$$|\Psi(t)>=(1+\sum_{ph} c_{ph}(t)\hat{A}^{+}_{ph})|\Psi_0> \tag{25}$$

where

$$\hat{A}^{+}_{ph} = a^{\dagger}_{p}a_h \tag{26}$$

is the creation operator of 1ph pair and

$$c_{ph}(t) = c^{+}_{ph}e^{i\omega t} + c^{-}_{ph}e^{-i\omega t} \tag{27}$$

is the harmonic time-dependent particle-hole amplitude. T-even $q_k(t)$ and T-odd $p_k(t)$ collective variables can be also specified as harmonic oscillations

$$\begin{aligned} q_k(t) &= \bar{q}_k cos(\omega t) = \frac{1}{2}\bar{q}_k(e^{i\omega t} + e^{-i\omega t}), \\ p_k(t) &= \bar{p}_k sin(\omega t) = \frac{1}{2i}\bar{p}_k(e^{i\omega t} - e^{-i\omega t}). \end{aligned} \tag{28}$$

Substituting (10) and (25) into the time-dependent HF equation

$$i\frac{d}{dt}|\Psi(t)>=(\hat{h}_0+\hat{h}_{res}(t))|\Psi(t)>, \tag{29}$$

one gets, in the linear approximation, the relation between $c^{\pm}_{ph}$ and collective deformations $\bar{q}_k$ and $\bar{p}_k$

$$c^{\pm}_{ph}=-\frac{1}{2}\frac{\sum_{k'}[\bar{q}_{k'}<ph|\hat{X}_{k'}|0>\mp i\bar{p}_{k'}<ph|\hat{Y}_{k'}|0>]}{\varepsilon_{ph}\pm\omega}, \tag{30}$$

where ε_{ph} is the energy of 1ph pair.

In addition to Eqs. (17)-(18), the variations $\delta\hat{X}_k(t)$ and $\delta\hat{Y}_k(t)$ can be now obtained with the alternative perturbed wave function (25):

$$\delta\hat{X}_{k'}(t) = \sum_{ph}(c_{ph}(t)^*<ph|\hat{X}_{k'}|0>+c_{ph}(t)<0|\hat{X}_{k'}|ph>), \tag{31}$$

$$\delta\hat{Y}_{k'}(t) = \sum_{ph}(c_{ph}(t)^*<ph|\hat{Y}_{k'}|0>+c^s_{ph}(t)<0|\hat{Y}_{k'}|ph>). \tag{32}$$

It is natural to equate the dynamical variations of the basic operators $\delta\hat{X}_k$ and $\delta\hat{Y}_k$, obtained with the scaling (7) and Thouless (25) perturbed wave functions. This provides the additional relation between the amplitudes $c^{\pm}_{ph}$ and deformations $\bar{q}_k$ and $\bar{p}_k$ and finally result in the system of equations for the unknowns $\bar{q}_k$ and $\bar{p}_k$.

By equating (17)-(18) and (31)-(32) we get

$$-\sum_k q_k(t)\kappa^{-1}_{kk'} = \sum_{ph}(c_{ph}(t)^*<ph|\hat{X}_{k'}|0>+c_{ph}(t)<0|\hat{X}_{k'}|ph>), \tag{33}$$

$$-\sum_k q_k(t)\eta^{-1}_{kk'} = \sum_{ph}(c_{ph}(t)^*<ph|\hat{Y}_{k'}|0>+c_{ph}(t)<0|\hat{Y}_{k'}|ph>). \tag{34}$$

Substituting (27)-(30) into these expressions and collecting, for example, the terms at $e^{i\omega t}$, one finally gets

$$\begin{aligned}\sum_k \{\bar{q}_k[F^{(XX)}_{k'k}-\kappa^{-1}_{kk'}]+\bar{p}_kF^{(XY)}_{k'k}\}=0,\\ \sum_k \{\bar{q}_kF^{(YX)}_{k'k}+\bar{p}_k[F^{(YY)}_{k'k}-\eta^{-1}_{kk'}]\}=0\end{aligned} \tag{35}$$

with

$$F^{(XX)}_{k'k} = \sum_{ph}\frac{1}{\varepsilon^2_{ph}-\omega^2}\{<ph|\hat{X}_k|0>^*<ph|\hat{X}_{k'}|0>(\varepsilon_{ph}+\omega) + <ph|\hat{X}_k|0><0|\hat{X}_{k'}|ph>(\varepsilon_{ph}-\omega)\}, \tag{36}$$

$$F^{(YX)}_{k'k} = -i\sum_{ph}\frac{1}{\varepsilon^2_{ph}-\omega^2}\{<ph|\hat{Y}_k|0>^*<ph|\hat{X}_{k'}|0>(\varepsilon_{ph}+\omega) + <ph|\hat{Y}_k|0><0|\hat{X}_{k'}|ph>(\varepsilon_{ph}-\omega)\}, \quad (37)$$

$$F^{(XY)}_{k'k} = i\sum_{ph}\frac{1}{\varepsilon^2_{ph}-\omega^2}\{<ph|\hat{X}_k|0>^*<ph|\hat{Y}_{k'}|0>(\varepsilon_{ph}+\omega) + <ph|\hat{X}_k|h><0|\hat{Y}_{k'}|ph>(\varepsilon_{ph}-\omega)\}, \quad (38)$$

$$F^{(YY)}_{k'k} = \sum_{ph}\frac{1}{\varepsilon^2_{ph}-\omega^2}\{<ph|\hat{Y}_k|0>^*<ph|\hat{Y}_{k'}|0>(\varepsilon_{ph}+\omega) + <ph|\hat{Y}_k|0><0|\hat{Y}_{k'}|ph>(\varepsilon_{ph}-\omega)\}. \quad (39)$$

Equating determinant of the system (35) to zero, we get the dispersion equation for RPA eigenvalues ω_ν.

2.4. NORMALIZATION CONDITION

By definition, RPA operators of excited one-phonon states read

$$\hat{Q}^+_\nu = \frac{1}{2}\sum_{ph}\{c^{\nu-}_{ph}\hat{A}^+_{ph} - c^{\nu+}_{ph}\hat{A}_{ph}\} \quad (40)$$

and fulfill

$$[\hat{Q}_\nu, \hat{Q}^+_{\nu'}] = \delta_{\nu,\nu'}, \quad [\hat{Q}^+_\nu, \hat{Q}^+_{\nu'}] = [\hat{Q}_\nu, \hat{Q}_{\nu'}] = 0, \quad (41)$$

where $\hat{A}^+_{ph}$ and $c^{\nu\pm}_{ph}$ are given by (26) and (30), respectively. In the quasiboson approximation for $\hat{A}^+_{ph}$, the normalization condition $[\hat{Q}_\nu, \hat{Q}^+_\nu] = 1$ results in the relation

$$\sum_{ph}\{(c^{\nu-}_{ph})^2 - (c^{\nu+}_{ph})^2\} = 2. \quad (42)$$

Using (30), it can be reformulated in terms of the RPA matrix coefficients (36)-(39):

$$\sum_{ph}\{(c^{\nu-}_{ph})^2 - (c^{\nu+}_{ph})^2\} \quad (43)$$

$$= \sum_{kk'}\frac{1}{4}\{\bar{q}^\nu_{k'}\bar{q}^\nu_k\frac{\partial F^{(XX)}_{k'k}(\omega_\nu)}{\partial\omega_\nu} + 2\bar{q}^\nu_{k'}\bar{p}^\nu_k\frac{\partial F^{(YX)}_{k'k}(\omega_\nu)}{\partial\omega_\nu} + \bar{p}^\nu_{k'}\bar{p}^\nu_k\frac{\partial F^{(YY)}_{k'k}(\omega_\nu)}{\partial\omega_\nu}\} = 2N_\nu.$$

The variables $\bar{q}^\nu_k$ and $\bar{p}^\nu_k$ should be finally normalized by the factor $1/\sqrt{N_\nu}$.

2.5. GENERAL DISCUSSION

Eqs. (11), (12), (18), (19), (30), (35)-(39), and (40)-(43) constitute the basic SRPA formalism. It is worth now to comment some essential points:

• One may show (e.g. by using a standard derivation of the matrix RPA) that the separable Hamiltonian (23)-(24) with (40) results in the SRPA equations (35)-(39) if to express unknowns $c_{ph}^{\nu\pm}$ through $\bar{q}_{\bar{k}}$ and $\bar{p}_{\bar{k}}$. Generally, RPA equations for unknowns $c_{ph}^{\nu\pm}$ require the RPA matrix of the high rank equal to size of the $1ph$ basis. The separable approximation allows to reformulate the RPA problem in terms of much more compact unknows $\bar{q}_{\bar{k}}$ and $\bar{p}_{\bar{k}}$ (see relation (30) and thus to minimize the computational effort. As is seen from (35), the rank of the SRPA matrix is equal to a double number K of the separable operators and hence is low.
• The number of RPA eigen-states ν is equal to the number of the relevant $1ph$ configurations used in the calculations. In heavy nuclei and atomic clusters, this number ranges the interval 10^3-10^6. For every RPA state ν, Eq. (35) delivers a particular set of the amplitudes $\bar{q}_{sk}^{\nu}$ and $\bar{p}_{sk}^{\nu}$ which, following Eq. (30), self-consistently regulate relative contrubutions of different T-even and T-odd oscillating densities to the ν-state.
• Eqs. (11), (12), (18), (19) relate the basic SRPA values with the starting functional and input operators $\hat{Q}_k$ and $\hat{P}_k$ by a simple and physically transparent way. This makes SRPA very convenient for the analysis and treatment of the obtained results.
• It is instructive to express the basic SRPA operators via the separable residual interaction (24):

$$\hat{X}_k = [\hat{V}_{res}, \hat{P}_k]_{ph}, \qquad \hat{Y}_k = [\hat{V}_{res}, \hat{Q}_k]_{ph} \tag{44}$$

where the index ph means the $1ph$ part of the operator. It is seen that the T-odd operator $\hat{P}_k$ retains the T-even part of V_{res} to build $\hat{X}_k$. Vice versa, the commutator with the T-even operator $\hat{Q}_k$ keeps the T-odd part of V_{res} to build $\hat{Y}_k$.
• Some of the SRPA values read as averaged commutators between T-odd and T-even operators. This allows to establish useful relations with other models. For example, (18), (19) and (44) give

$$\kappa_{k'k}^{-1} = -i < 0|[\hat{P}_{k'}, \hat{X}_k]|0 > = -i < 0|[\hat{P}_{k'}, [\hat{V}_{res}, \hat{P}_k]]|0 >, \tag{45}$$

$$\eta_{k'k}^{-1} = -i < 0|[\hat{Q}_{k'}, \hat{Y}_k]|0 > = -i < 0|[\hat{Q}_{k'}, [\hat{V}_{res}, \hat{Q}_k]]|0 > . \tag{46}$$

The similar double commutators but with the full Hamiltonian (instead of the residual interaction) correspond to m_3 and m_1 sum rules, respectively, and so represent the spring and inertia parameters [24] in the basis of collective generators $\hat{Q}_k$ and $\hat{P}_k$. This allows to establish the connection of the SRPA with the sum rule approach [22, 23] and local RPA [24].

Besides, the commutator form of SRPA values can considerably simplify their calculation (see discussion in the Appendix B).
• SRPA restores the conservation laws (e.g. translational invariance) violated by the static mean field. Indeed, let's assume a symmetry mode with

the generator $\hat{P}_{\rm sym}$. Then, to keep the conservation law $[\hat{H}, \hat{P}_{\rm sym}] = 0$, we simply have to include $\hat{P}_{\rm sym}$ into the set of the input generators $\hat{P}_k$ together with its complement $\hat{Q}_{\rm sym} = i[\hat{H}, \hat{P}_{\rm sym}]$.

• SRPA equations are very general and can be applied to diverse systems (atomic nuclei, atomic clusters, etc.) described by density and current-dependent functionals. Even Bose systems can be covered if to redefine the many-body wave function (25) exhibiting the perturbation through the elementary excitations. In this case, the Slater deterninant for 1ph excitations should be replaced by a perturbed many-body function in terms of elementary bosonic excitations.

• In fact, SRPA is the first TDLDA iteration with the initial wave function (7). A single iteration is generally not enough to get the complete convergence of TDLDA results. However, SRPA calculations demonstrate that high accuracy can be achieved even in this case if to ensure the optimal choice of the input operators $\hat{Q}_k$ and $\hat{P}_k$ and keep sufficient amount of the separable terms (see discussion in Sec. 5). In this case, the first iteration already gives quite accurate results.

• There are some alternative RPA schemes also delivering self-consistent factorization of the two-body residual interaction, see e.g. [21, 27–29] for atomic nuclei and [30, 31] for atomic clusters. However, these schemes are usually not sufficiently general. Some of them are limited to analytic or simple numerical estimates [21, 27, 30], next ones start from phenomenological single-particle potentials and thus are not fully self-consistent [28], the others need a large number of the separable terms to get an appropriate numerical accuracy [29,31]. SRPA has evident advantages as compared with these schemes.

• After solution of the SRPA problem, the Hamiltonian (23)-(24) is reduced to a composition of one-phonon RPA excitations

$$\hat{H} = \sum_{\nu} \omega_\nu \hat{Q}^+_\nu \hat{Q}_\nu \tag{47}$$

where one-phonon operators are given by (40) – (41). Then, it is easy to get expressions of the equation-of-motion (EOM) method:

$$[\hat{H}, \hat{Q}^+_\nu] = \omega_\nu \hat{Q}^+_\nu, \quad [\hat{H}, \hat{Q}_\nu] = -\omega_\nu \hat{Q}_\nu. \tag{48}$$

So, SRPA and EOM with the Hamiltonian (23)-(24) are equivalent. This allows to to establish the connection between the SRPA and couled-cluster EOM method with the single reference (see for reviews [32–35]). SRPA uses the excitation operators involving only singles (1ph) and so generally carries less correlations than EOM-CC. At the same time, SRPA delivers very elegant and physically transparent calculations scheme and, as is shown in our calculations, the correlations included to the SRPA are often quite

enough to describe linear dynamics. It would be interesting to construct the approach combining advantages of SRPA and EOM-CC.

3. Strength function

In study of response of a system to external fields, we are usually interested in the average strength function instead of the responses of particular RPA states. For example, giant resonances in heavy nuclei are formed by thousands of RPA states whose contributions in any case cannot be distinguished experimentally. In this case, it is reasonable to consider the averaged response described by the strength function. Besides, the calculation of the strength function is usually much easier.

For electric external fields of multipolarity $E\lambda\mu$, the strength function can be defined as

$$S_L(E\lambda\mu;\omega) = \sum_\nu \omega_\nu^L M^2_{\lambda\mu\nu} \zeta(\omega-\omega_\nu) \tag{49}$$

where

$$\zeta(\omega-\omega_j) = \frac{1}{2\pi}\frac{\Delta}{(\omega-\omega_\nu)^2+(\Delta/2)^2} \tag{50}$$

is Lorentz weight with an averaging parameter Δ and

$$M_{\lambda\mu\nu} = \frac{1}{2}\sum_{ph} < ph|\hat{f}_{\lambda\mu}|0 > (c^{\nu-}_{ph} + c^{\nu+}_{ph}) \tag{51}$$

is the transition matrix element for the external field

$$\hat{f}_{\lambda\mu} = \frac{1}{1+\delta_{\mu,0}} r^\lambda (Y_{\lambda\mu} + Y^\dagger_{\lambda\mu}). \tag{52}$$

It is worth noting that, unlike the standard definition of the strength function with using $\delta(\omega-\omega_\nu)$, we exploit here the Lorentz weight. It is very convenient to simulate various smoothing effects.

The explicite expression for (49) can be obtained by using the Cauchy residue theorem. For this aim, the strength function is recasted as a sum of ν residues for the poles $z=\pm\omega_\nu$. Since the sum of all the residues (covering all the poles) is zero, the residues with $z=\pm\omega_\nu$ (whose calculation is time consuming) can be replaced by the sum of residies with $z=\omega\pm i(\Delta/2)$ and $z=\pm\varepsilon_{ph}$ whose calculation is much less expensive (see details of the derivation in [8]).

Finally, the strength function for L=0 and 1 reads as

$$\begin{aligned} S_L(E\lambda\mu,\omega) &= \frac{1}{\pi}\Im\left[\frac{z^L \det|B(z)|}{\det|F(z)|}\right]_{z=\omega+i(\Delta/2)} \\ &+ 2\sqrt{2}\sum_{ph}^{K_p,K_h>0} \varepsilon^L_{ph} < ph|\hat{f}_{\lambda\mu}|0 >^2 \zeta(\omega-\varepsilon_{ph}). \end{aligned} \tag{53}$$

The first term in (53) is contribution of the residual two-body interaction while the second term is the unperturbed (purely $1ph$) strength function. Further, $F(z)$ is determinant of the RPA symmetric matrix (35) of the rank $2K$, where K is the number of the initial operators $\hat{Q}_k$. The symmetric matrix B of the rank $(2K+1)$ is defined as

$$\begin{aligned} B_{nn'}(z) &= F_{nn'}(z), \\ B_{2K+1,2K+1}(z) &= 0, \quad B_{2K+1,n}(z) = B_{n,2K+1}(z) = A_n(z) \end{aligned} \tag{54}$$

where $n, n' = 1, ..., 2K$ and left (right) indexes define lines (columns).

The values $A_n(z)$ read

$$\begin{aligned} A^{(X)}_{n=2k-1}(E\lambda\mu, z) &= 4 \sum_{ph}^{K_p,K_h>0} \frac{\varepsilon_{ph} < ph|\hat{X}_k|0 >< ph|\hat{f}_{\lambda\mu}|0 >}{\varepsilon^2_{ph} - z^2} \\ A^{(Y)}_{n=2k}(E\lambda\mu, z) &= 4 \sum_{ph}^{K_p,K_h>0} \frac{z< ph|\hat{Y}_k|0 >< ph|\hat{f}_{\lambda\mu}|0 >}{\varepsilon^2_{ph} - z^2}. \end{aligned} \tag{55}$$

They form the right and low borders of the determinant B thus fringering the RPA determinant F. The values $-A_n(z)$ in the most right column have the same indices as the corresponding strings of the RPA determinant. The values $A_n(z)$ in the lowest line have the same indices as the corresponding columns of the RPA determinant.

Derivation of the strentth function, given above, deviates from the standard one in the lineary response theory. Besides, the SRPA deals with the Lorentz weight instead of $\delta(\omega - \omega_\nu)$ used in the linear response theory. At the same time, SRPA strength function and lineary response theory are conceptually the same approaches. Since the linear response theory is widely used in the coupled-cluster (CC) method, it would be interesting to consider the implementation of SRPA stength function method to CC. The linear response theory is widely used in the coupled-cluster (CC) method. In this connection, it would be interesting to enlarge the SRPA stength function method to CC.

4. Particular cases for clusters and nuclei

4.1. KOHN-SHAM FUNCTIONAL FOR ATOMIC CLUSTERS

Kohn-Sham functional for atomic clusters reads

$$E_{\rm tot}(t) = E_{\rm kin}(t) + E_{xc}(t) + E_C(t) = \int d\vec{r}\mathcal{H}(\rho(\vec{r}, t)) \tag{56}$$

where

$$E_{\rm kin}(t) = \frac{\hbar^2}{2m_e} \int d\vec{r}\, \tau(\vec{r}, t)\ , \tag{57}$$

$$E_{xc}(t) = \int d\vec{r}\,\rho(\vec{r},t)\,\epsilon_{xc}(\rho\,(\vec{r},t))\ , \tag{58}$$

$$E_C(t) = \frac{e^2}{2}\int\int d\vec{r}d\vec{r}_1\frac{(\rho(\vec{r},t)-\rho_i(\vec{r}))(\rho(\vec{r}_1,t)-\rho_i(\vec{r}_1))}{|\vec{r}-\vec{r}_1|} \tag{59}$$

are kinetic, exchange-correlation (in the local density approximation), and Coulomb terms, respectively. Further, $\rho_i(\vec{r})$ is the ionic density and $\rho(\vec{r},t)$ and $\tau(\vec{r},t)$ are density and kinetic energy density of valence electrons.

In atomic clusters, oscillations of valence electrons are generated by time-dependent variations of the electronic T-even density $\rho(\vec{r},t)$ only. So, one may neglect in the SRPA formalism all T-odd densities and their variations $p_k(t)$. This makes SRPA equations especially simple. In particular, the density variation (9) is reduced to

$$\begin{aligned}\delta\rho(\vec{r},t) &= i\sum_k q_k(t) < 0|[\hat{P}_k,\hat{\rho}(\vec{r})]|0 > \\ &= -4i\sum_k q_k(t)\sum_{ph}^{K_p,K_h>0} < ph|\hat{P}_k|0 > \Re< ph|\hat{\rho}|0 > \\ &= i\sum_k q_k(t)\delta\rho(\vec{r})\end{aligned} \tag{60}$$

where

$$< ph|\hat{P}_k|0 >= 2i\varepsilon_{ph} < ph|\hat{Q}_k| >, \tag{61}$$

$$\delta\rho(\vec{r}) = -\frac{\hbar^2}{2m_e}(\vec{\bigtriangledown}\bar{\rho}(\vec{r})\cdot\vec{\bigtriangledown}Q_k(\vec{r}) + 2\bar{\rho}(\vec{r})\bigtriangleup Q_k(\vec{r})). \tag{62}$$

Here, $\Re< ph|\hat{\rho}|0 >$ is the transition density and $\bar{\rho}(\vec{r})$ is the static ground state density of valence electrons.

It is seen from (60)-(61) that there are two alternative ways to calculate the density variation: i) through the transition density and matrix elements of $\hat{Q}_k$-operator and ii) through the ground state density. The second way is the most simple. It becomes possible because, in atomic clusters, V_{res} has no T-odd $\hat{Y}_k$-operators and thus the commutator of $\hat{Q}_k$ with the full Hamiltonian is reduced to the commutator with the kinetic energy term only:

$$\hat{P}_k = i[\hat{H},\hat{Q}_k]_{ph} = i[\hat{h}_0,\hat{Q}_k]_{ph} = -i\frac{\hbar^2}{2m_e}[\vec{\bigtriangledown}^2,\hat{Q}_k]_{ph}. \tag{63}$$

This drastically simplifies SRPA expressions and allows to present them in terms of the static ground state density. The scaling tranformation (7) loses exponents with $p_k(t)$ and reads

$$|\Psi(t)>=\prod_{k=1}^{K} exp\{-iq_k(t)\hat{P}_k\}|0>\ . \tag{64}$$

Other SRPA equations are reduced to

$$\begin{aligned}\hat{X}_k(\vec{r}) &= i[\frac{\delta^2\mathcal{H}}{\delta\rho\delta\rho}]_{\rho=\bar{\rho}} < 0|[\hat{P}_k,\hat{\rho}]|0 > \hat{\rho}(\vec{r}) \\ &= (\frac{\partial^2\mathcal{H}_{xc}}{\partial\rho\partial\rho})_{\rho=\bar{\rho}}\delta\rho(\vec{r}) + e^2\int d\vec{r}_1\frac{\delta\rho(\vec{r}_1)}{|\vec{r}-\vec{r}_1|}, \end{aligned} \tag{65}$$

$$\begin{aligned}\kappa^{-1}_{k'k} &= \kappa^{-1}_{kk'} = -i < 0|[\hat{P}_{k'},\hat{X}_k]|0 > \\ &= \int d\vec{r}\{\frac{\delta^2\mathcal{H}}{\delta\rho\delta\rho}\}_{\rho=\bar{\rho}} < 0|[\hat{P}_k,\hat{\rho}]|0 >< 0|[\hat{P}_{k'},\hat{\rho}]|0 > \\ &= -\int d\vec{r}X_k(\vec{r})\delta\rho(\vec{r}), \end{aligned} \tag{66}$$

$$\sum_k \bar{q}^\nu_k\{F^{(XX)}_{k'k} - \kappa^{-1}_{kk'}]\} = 0, \tag{67}$$

$$c^{\nu\pm}_{ph} = -\frac{1}{2}\frac{\sum_k \bar{q}^\nu_k < ph|\hat{X}_k|0 >}{\varepsilon_{ph} \pm \omega_\nu}, \tag{68}$$

$$\sum_{ph}\{(c^{\nu-}_{ph})^2 - (c^{\nu+}_{ph})^2\} = \sum_{kk'}\frac{1}{4}\bar{q}^\nu_k\bar{q}^\nu_{k'}\frac{\partial F^{(XX)}_{kk'}(\omega_\nu)}{\partial\omega_\nu} = 2N_\nu. \tag{69}$$

It is seen that the basic operator (65) and strength matrix (66) have now simple expressions via $\delta\rho(\vec{r})$ from (62). The operator (65) has exchange-correlation and Coulomb terms. For electric multipole oscillations (dipole plasmon, ...), the Coulomb term dominates.

In recent years, there appear some new functionals where the current of electrons instead of their density is used as a basic variable [13]. SRPA equations for this case can be straightforwardly obtained from the general formalism given in Sec. 2.

4.2. SKYRME FUNCTIONAL FOR ATOMIC NUCLEI

Nuclear interaction is very complicated and its explicit form is still unknown. So, in practice different approximations to nuclear interaction are used. Skyrme forces [11,12] represent one of the most successful approximations where the interaction is maximally simplified and, at the same time, allows to get accurate and universal description of both ground state properties and dynamics of atomic nuclei (see [20] a for recent review). Skyrme forces are contact, i.e. $\sim \delta(\vec{r}_1 - \vec{r}_2)$, which minimizes the computational effort. In spite of this dramatic simplification, Skyrme forcese well reproduce properties of most spherical and deformed nuclei as well as characteristics of nuclear matter and neutron stars. Additional advantage of the Skyrme interaction is that its parameters are directly related to the basic nuclear

properties: incompressibility, nuclear radii, masses and binding energies, etc. SRPA for Skyrme forces was derived in [9, 10, 19, 26].

Although Skyrme forces are relatively simple, they are still much more demanding than the Coulomb interaction. In particular, they deal with a variety of diverse densities and currents. The Skyrme functional reads [12, 36, 37]

$$E = \int d\vec{r} \left(\mathcal{H}_{\rm kin} + \mathcal{H}_{\rm Sk}(\rho_s, \tau_s, \vec{\sigma}_s, \vec{j}_s, \vec{J}_s) + \mathcal{H}_{\rm C}(\rho_p) \right), \tag{70}$$

where

$$\mathcal{H}_{\rm kin} = \frac{\hbar^2}{2m}\tau, \tag{71}$$

$$\mathcal{H}_{\rm C} = \frac{e^2}{2}\int d\vec{r}' \rho_p(\vec{r}) \frac{1}{|\vec{r}-\vec{r}'|}\rho_p(\vec{r}') - \frac{3}{4}e^2(\frac{3}{\pi})^{\frac{1}{3}}[\rho_p(\vec{r})]^{\frac{4}{3}}, \tag{72}$$

$$\begin{aligned}\mathcal{H}_{\rm Sk} = {} & \frac{b_0}{2}\rho^2 - \frac{b_0'}{2}\sum_s \rho_s^2 - \frac{b_2}{2}\rho\Delta\rho + \frac{b_2'}{2}\sum_s \rho_s\Delta\rho_s \\ & + \frac{b_3}{3}\rho^{\alpha+2} - \frac{b_3'}{3}\rho^\alpha \sum_s \rho_s^2 \\ & + b_1(\rho\tau - \vec{j}^2) - b_1'\sum_s(\rho_s\tau_s - \vec{j}_s^2) \\ & - b_4\left(\rho\vec{\nabla}\vec{\Im} + \vec{\sigma}\cdot(\vec{\nabla}\times\vec{j})\right) - b_4'\sum_s\left(\rho_s(\vec{\nabla}\vec{\Im}_s) + \vec{\sigma}_s\cdot(\vec{\nabla}\times\vec{j}_s)\right) \\ & + \tilde{b}_4\left(\vec{\sigma}\vec{T} - \vec{\Im}^2\right) + \tilde{b}_4'\sum_s\left(\vec{\sigma}_s\vec{T}_s - \vec{\Im}_s^2\right)\end{aligned} \tag{73}$$

are kinetic, Coulomb and Skyrme terms respectively. The isospin index $s = n, p$ covers neutrons (n) and protons (p). Densities without this index involve both neutrons and protons, e.g. $\rho = \rho_p + \rho_n$. Parameters b and α are fitted to describe ground state properties of atomic nuclei.

The functional includes diverse densities and currents, both neutrons and protons. They are naturally separated into two groups: 1) T-even density $\rho_s(\vec{r})$, kinetic energy density $\tau_s(\vec{r})$ and spin orbital density $\vec{\Im}_s(\vec{r})$ and 2) T-odd spin density $\sigma_s(\vec{r})$, current $\vec{j}_s(\vec{r})$ and vector kinetic energy density $\vec{T}_s(\vec{r})$. Explicit expressions for these densities and currents, as well as for their operators, are given in the appendix A. Only T-even densities contribute to the ground state properties of nuclei with even numbers of protons and neutrons (and thus with T-even wave function of the ground state). Instead, both T-even and T-odd densities participate in generation of nuclear oscillations. Sec. 2 delivers the SRPA formalism for this general case.

4.3. T-ODD DENSITIES AND CURRENTS

Comparison of the Kohn-Sham and Skyrme functionals leads to a natural question why these two functionals exploit, for the time-dependent problem, so different sets of basic densities and currents? If the Kohn-Sham functional is content with one density, the Skyrme forces operate with a diverse set of densities and currents, both T-even and T-odd. Then, should we consider T-odd densities as genuine for the description of dynamics of finite many-body systems or they are a pequliarity of nuclear forces? This question is very nontrivial and still poorly studied. We present below some comments which, at least partly, clarify this point.

Actual nuclear forces are of a finite range. These are, for example, Gogny forces [40] representing more realistic approximation of actual nuclear forces than Skyrme approximation. Gogny interaction has no any velocity dependence and fulfills the Galilean invariance. Instead, two-body Skyrme interaction depends on relative velocities $\vec{k} = 1/2i \cdot (\vec{\nabla}_1 - \vec{\nabla}_2)$, which just simulates the finite range effects [20].

The static Hartree-Fock problem assumes T-reversal invariance and T-even single-particle density matrix. In this case, Skyrme forces can be limited by only T-even densities: $\rho_s(\vec{r})$, $\tau_s(\vec{r})$ and $\vec{\Im}_s(\vec{r})$. In the case of dynamics, the density matrix is not already T-even and aquires T-odd components [12]. This fact, together with velocity dependence of the Skyrme interaction, results in appearance in the Skyrme functional of T-odd densities and currents: $\vec{s}_s(\vec{r})$, $\vec{j}_s(\vec{r})$ and $\vec{T}_s(\vec{r})$ [12,36]. Hence the origin of T-odd densities in the Skyrme functional. However, this is not the general case for nuclear forces.

As compared with the Kohn-Sham functional for electronic systems, the nuclear Skyrme functional is less genuine. The main (Coulomb) interaction in the Kohn-Sham problem is well known and only exchange and corellations should be modeled. Instead, in the nuclear case, even the basic interaction is unknown and should be approximated, e.g. by the simple contact interaction in Skyrme forces.

The crudeness of Skyrme forces has certain consequences. For example, the Skyrme functional has no any exchange-correlation term since the relevant effects are supposed to be already included into numerous Skyrme fitting parameters. Besides, the Skyrme functional may accept a diverse set of T-even and T-dd densities and currents. One may say that T-odd densities appear in the Skyrme functional partly because of its specific construction. Indeed, other effective nuclear forces (Gogny [40] , Landau-Migdal [41]) do not exploit T-odd densities and currents for description of nuclear dynamics.

Implementation of a variety of densities and currents in the Skyrme fuctional has, however, some advantages. It is known that different projectiles and external fields used to generate collective modes in nuclear reactions

are often selective to particular densities and currents. For example, some elastic magnetic collective modes (scissors, twist) are associated with variations in the momentum space while keeping the common density $\rho_s(\vec{r})$ about constant. T-odd densities and currents can play here a significant role while Skyrme forces obtain the advantage to describe the collective motion by a natural and physically transparent way.

Relative contributions of T-odd densities to a given mode should obviously depend on the character of this mode. Electric multipole excitations (plasmons in atomic clusters, $E\lambda$ giant resonances in atomic nuclei) are mainly provided by T-even densities (see e.g. [19]). Instead, T-odd densities and currents might be important for magnetic modes and maybe some exotic (toroidal, ...) electric modes.

It worth noting that T-odd denstities appear in the Skyrme functional in the specific combinations $\rho_s\tau_s - \vec{j}_s^2$, $\rho_s(\vec{\nabla}\vec{\Im}_s) + \vec{\sigma}_s \cdot (\vec{\nabla} \times \vec{j}_s)$, and $\vec{\sigma}_s\vec{T}_s - \vec{\Im}_s^2$. Following [37], this ensures Skyrme forces to fulfill the local gauge invariance (and Galilean invariance as the particular case). The velocity-independent finite-range Gogny forces also keep this invariance. Being combined into specific combinations, T-odd densities do not require any new Skyrme parameters [37]. So, the parameters fitted to the static nuclear properties with T-even densities only, are enough for description of the dynamics as well.

The time-dependent density functional theory [38] for electronic systems is usually implemented at adiabatic local density approximation (ALDA) when density and single-particle potential are supposed to vary slowly both in time and space. Last years, the current-dependent Kohn-Sham functionals with a current density as a basic variable were introduced to treat the collective motion beyond ALDA (see e.g. [13]). These functionals are robust for a time-dependent linear response problem where the ordinary density functionals become strongly nonlocal. The theory is reformulated in terms of a vector potential for exchange and correlations, depending on the induced *current* density. So, T-odd variables appear in electronic functionals as well.

In general, the role of T-odd variables in dynamics of finite many-body systems is still rather vague. This fundamental problem devotes deep and comprehensive study.

5. Choice of initial operators

It is easy to see that, after choosing the initial operators $\hat{Q}_k(\vec{r})$, all other SRPA values can be straightforwardly determined following the steps

$$\hat{Q}_k \;\Rightarrow < |[\hat{Q}_k, \hat{J}_\alpha]| > \Rightarrow\; \hat{Y}_k,\; \eta^{-1}_{kk'} \;\Rightarrow\; \hat{P}_k \;\Rightarrow < |[\hat{P}_k, \hat{J}_\alpha]| > \Rightarrow\; \hat{X}_k,\; \kappa^{-1}_{kk'}.$$

As was mentioned above, the proper choice of initial operators $\hat{Q}_k(\vec{r})$ is crucial to achieve good convergence of the separable expansion (1) with a minimal number of separable operators.

SRPA itself does not give a recipe to determine $\hat{Q}_k(\vec{r})$. But choice of these operators can be inspired by physical and computational arguments. The operators should be simple and universal in the sense that they can be applied equally well to all modes and excitation channels. The main idea is that the initial operators should result in exploration of different spatial regions of the system, the surface and interior. This suggests that the leading scaling operator should have the form of the applied external field in the long-wave approximation, for example,

$$\hat{Q}^{\lambda\mu}_{k=1}(\vec{r}) = r^{\lambda}(Y_{\lambda\mu}(\Omega) + \text{h.c.}). \tag{74}$$

Such a choice results in the separable operators (11), (12) and (65) most sensitive to the surface of the system. This is evident in (65) where $\delta\rho(\vec{r}) \propto \vec{\bigtriangledown}\bar{\rho}(\vec{r})$ is peaked at the surface. Many collective oscillations manifest themselves as predominantly surface modes. As a result, already one separable term generating by (74) usually delivers a quite good description of collective excitations like plasmons in atomic clusters and giant resonances in atomic nuclei. The detailed distributions depends on a subtle interplay of surface and volume vibrations. This can be resolved by taking into account the nuclear interior. For this aim, the radial parts with larger powers $r^{\lambda+n_k}Y_{\lambda\mu}$ and spherical Bessel functions can be used, much similar as in the local RPA [24]. This results in the shift of the maxima of the operators (11), (12) and (65) to the interior. Exploring different conceivable combinations, one may found a most efficient set of the initial operators.

For description of the dipole plasmon in atomic clusters, the set of hermitian operators

$$Q^{\lambda_k\mu}_{k}(\vec{r}) = r^{\lambda_k+n_k}(Y_{\lambda_k\mu}(\Omega) + Y^{\dagger}_{\lambda_k\mu}(\Omega)) \tag{75}$$

with $\lambda_k n_k = 10, 12, 14$ and $\mu = 0, 1$ is usually enough [8,17]. As is seen from Fig. 1, we successfully reproduce gross structure of the dipole plasmon in light axially-deformed sodium clusters (some discrepancies for the lightest cluster Na^{+}_{11} arise because of the roughness of the ionic jellium approximation for smallest samples). Already one initial operator is usually enough to reproduce the energy of the dipole plasmon and its branches but in this case the plasmon acquires some artificial strength in its right flank and thus the overestimated width [7]. This problem can be solved by adding two more initial operators. The calculations for a variety of spherical alkali metal clusters [16] as well as for deformed clusters of a medium size [17] show that SRPA correcly describes not only gross structure of the dipole plasmon but also its Landau damping and width.

For the description of giant resonances in atomic nuclei, we used the set of initial operators [10]

$$\hat{Q}_k(\vec{r}) = R_k(r)(Y_{\lambda\mu}(\Omega) + \text{h.c.}) \tag{76}$$

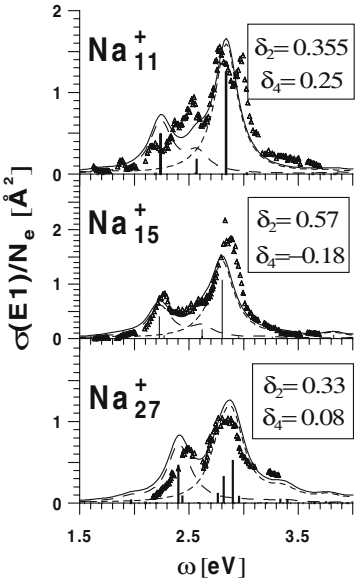

Figure 1. Photoabsorption cross section for the dipole plasmon in axially deformed sodium clusters, normalized to the number of valence electrons N_e. The parameters of quadrupole and hexadecapole deformations are given in boxes. The experimental data [39] (triangles) are compared with SRPA results given as bars for RPA states and as the strength function (49) smoothed by the Lorentz weight with $\Delta = 0.25$ eV. Contributions to the strength function from μ =0 and 1 dipole modes (the latter has twice larger strength) are exhibited by dashed curves. The bars are given in $eV\AA^2$.

with

$$R_k(r) = \begin{cases} r^\lambda, & k=1 \\ j_\lambda(q_\lambda^k r), & k=2,3,4 \end{cases} \tag{77}$$

$$q_\lambda^k = a_k \frac{z_\lambda}{R_{\rm diff}}, \quad a_2=0.6\ , a_3=0.9\ , a_4=1.2$$

where $R_{\rm diff}$ is the diffraction radius of the actual nucleus and z_λ is the first root in of the spherical Bessel function $j_\lambda(z_\lambda) = 0$. The separable term with $k = 1$ is mainly localized at the nuclear surface while the next terms are localized more and more in the interior. This simple set seems to be a best compromise for the description of nuclear giant resonances in light and heavy nuclei. Fig. 2 demonstrates that already one separable term (k=1) can be enough to get a reasonable agreement with the exact results. For k=1, the calculations are especially simple and results are easily analyzed.

The sets (75)-(77) are optimal for description of electric collective modes ($E\lambda$ plasmons in clusters and giant resonances in nuclei). For description of magnetic modes, the initial operator should resemble the T-odd magnetic external field. So, in this case we should start from the initial operators

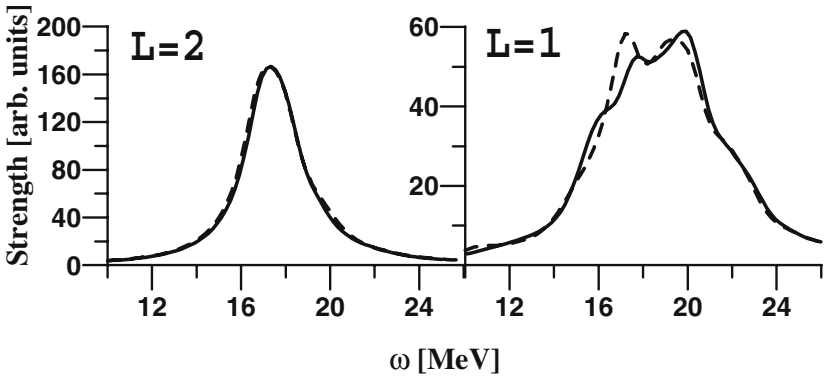

Figure 2. Isoscalar E2 and isovector E1 giant resonances in ^{40}Ca calculated with SkM* forces. The results are exhibited for full (exact) RPA (solid curve) and SRPA with $k = 1$ (dotted curve).

$\hat{P}_k$ in the form of the magnetic multipole transition operator in the long-wave approximation. The T-even operators $\hat{Q}_k$ are then obtained from the connection $\hat{Q}_k = i[\hat{H}, \hat{P}_k]$.

6. Summary

We presented fully self-consistent separable random-phase-approximation (SRPA) method for description of linear dynamics of different finite Fermi-systems. The method is very general, physically transparent, convenient for the analysis and treatment of the results. SRPA drastically simplifies the calculations. It allows to get a high numerical accuracy with a minimal computational effort. The method is especially effective for systems with a number of particles $10 - 10^3$, where quantum-shell effects in the spectra and responses are significant. In such systems, the familiar macroscopic methods are too rough while the full-scale microscopic methods are too expensive. SRPA seems to be here the best compromise between quality of the results and the computational effort. As the most involved methods, SRPA describes the Landau damping, one of the most important characteristics of the collective motion. SRPA results can be obtained in terms of both separate RPA states and the strength function (linear response to external fields).

The particular SRPA versions for electronic Kohn-Sham and nuclear Skyrme functional were considered and examples of the calculations for the dipole plasmon in atomic clusters and giant resonances in atomic nuclei were presented. SRPA was compared with alternative methods, in particular with EOM-CC. It would be interesting to combine advantages of SRPA and couled-cluster approach in one powerful method.

Appendix A: Densities and currents for Skyrme functional

In Skyrme forces, the complete set of the densities involves the ordinary density, kinetic-energy density, spin-orbital density, current density, spin density and vector kinetic-energy density:

$$
\begin{aligned}
\rho_s(\vec{r},t) &= \sum_{h\epsilon s}^{occ} \varphi_h^*(\vec{r},t)\varphi_h(\vec{r},t), & \hat{T}\rho\hat{T}^{-1} &= \rho \\
\tau_s(\vec{r},t) &= \sum_{h\epsilon s}^{occ} \vec{\nabla}\varphi_h^*(\vec{r},t)\cdot\vec{\nabla}\varphi_h(\vec{r},t), & \hat{T}\tau\hat{T}^{-1} &= \tau \\
\vec{\Im}_s(\vec{r},t) &= -i\sum_{h\epsilon s}^{occ} \varphi_h^*(\vec{r},t)(\vec{\nabla}\times\hat{\vec{\sigma}})\varphi_h(\vec{r},t), & \hat{T}\vec{\Im}\hat{T}^{-1} &= \vec{\Im} \\
\vec{j}_s(\vec{r},t) &= -\frac{i}{2}\sum_{h\epsilon s}^{occ}\left[\varphi_h^*(\vec{r},t)\vec{\nabla}\varphi_h(\vec{r},t) - \vec{\nabla}\varphi_h^*(\vec{r},t)\varphi_h(\vec{r},t)\right], & \hat{T}\vec{j}\hat{T}^{-1} &= -\vec{j} \\
\vec{\sigma}_s(\vec{r}) &= \sum_{h\epsilon s}^{occ} \varphi_h^*(\vec{r},t)\hat{\vec{\sigma}}\varphi_h(\vec{r},t), & \hat{T}\vec{\sigma}\hat{T}^{-1} &= -\vec{\sigma} \\
\vec{T}_s(\vec{r}) &= \sum_{h\epsilon s}^{occ} \vec{\nabla}\varphi_h^*(\vec{r},t)\hat{\vec{\sigma}}\cdot\vec{\nabla}\varphi_h(\vec{r},t), & \hat{T}\vec{\sigma}\hat{T}^{-1} &= -\vec{\sigma}
\end{aligned}
$$

where the sum runs over the occupied (hole) single-particle states h. The associated operators are

$$
\begin{aligned}
\hat{\rho}_s(\vec{r}) &= \sum_{i=1}^{N_s}\delta(\vec{r}_i-\vec{r}), \\
\hat{\tau}_s(\vec{r}) &= \sum_{i=1}^{N_s}\overleftarrow{\nabla}\delta(\vec{r}_i-\vec{r})\vec{\nabla}, \\
\hat{\vec{\Im}}_s(\vec{r}) &= \sum_{i=1}^{N_s}\delta(\vec{r}_i-\vec{r})\vec{\nabla}\times\hat{\vec{\sigma}}, \\
\hat{\vec{j}}_s(\vec{r}) &= \frac{1}{2}\sum_{i=1}^{N_s}\left\{\vec{\nabla},\delta(\vec{r}_i-\vec{r})\right\}, \\
\hat{\vec{\sigma}}_s(\vec{r}) &= \sum_{i=1}^{N_s}\delta(\vec{r}_i-\vec{r})\hat{\vec{\sigma}}, \\
\hat{\vec{T}}_s(\vec{r}) &= \sum_{i=1}^{N_s}\overleftarrow{\nabla}\delta(\vec{r}_i-\vec{r})\vec{\nabla}\hat{\vec{\sigma}},
\end{aligned}
$$

where $\hat{\vec{\sigma}}$ is the Pauli matrix, N_s is number of protons or neutrons in the nucleus.

Appendix B: Presentation of responses and strength matrices through the matrix elements

Responses $< 0|[\hat{P}_k, \hat{J}_{\alpha'}]|0 >$ and $< 0|[\hat{Q}_k, \hat{J}_{\alpha'}]|0 >$ in (11)-(12) and inverse strength matrices in (18)-(19) read as the averaged commutators

$$< 0|[\hat{A}, \hat{B}]|0 > \quad \text{with} \quad T\hat{A}T^{-1} = -T\hat{B}T^{-1}. \tag{78}$$

Calculation of these values can be greatly simplified if to express them through the $1ph$ matrix elements of the operators $\hat{A}$ and $\hat{B}$.

In the case of the strength matrices, the matrix elements are real for T-even operators and image for T-odd operators and thus we easily get

$$\kappa^{-1}_{k'k} = -i < 0|[\hat{P}_{k'}, \hat{X}_k]|0 >= 4i \sum_{ph}^{K_p,K_h>0} < ph|\hat{P}_{k'}|0 >< ph|\hat{X}_k]|0 >, \tag{79}$$

$$\eta^{-1}_{k'k} = -i < 0|[\hat{Q}_{k'}, \hat{Y}_k]|0 >= -4i \sum_{ph}^{K_p,K_h>0} < ph|\hat{Q}_{k'}|0 >< ph|\hat{Y}_k]|0 > \tag{80}$$

where K_p and K_h are projections of the momentum of particle and hole states onto quantization axis of the system.

The case of responses is more involved in the sense that matrix elements of the second operator in the commutator are transition densities which are generally complex. However, the first operator in the commutator still has real (for T-even $\hat{A}$) or image (for T-odd $\hat{A}$) matrix elements and so the averages can be finally reduced to

$$< 0|[\hat{Q}_k, \hat{J}_\alpha]|0 > \;=\; 4i \sum_{ph}^{K_p,K_h>0} < ph|\hat{Q}_k|0 > \Im < ph|\hat{J}_\alpha|0 >, \tag{81}$$

$$< 0|[\hat{P}_k, \hat{J}_\alpha]|0 > \;=\; -4 \sum_{ph}^{K_p,K_h>0} < ph|\hat{P}_k|0 > \Re < ph|\hat{J}_\alpha|0 >, \tag{82}$$

where $\Im$ and $\Re$ result in image and real parts of the transition densities.

The matrix elements for operator $\hat{P}_k$ read

$$< ph|\hat{P}_k|0 >= i2\varepsilon_{ph} < ph|\hat{Q}_k|0 > - < ph|\hat{Y}_k|0 > . \tag{83}$$

References

1. D.J. Row, *Nuclear Collective Motion* (Methuen, London, 1970).
2. P. Ring and Schuck, *The Nuclear Many-Body Problems*, (Springer-Verlag, Berlin, 1980).
3. R.M. Dreizler and E.K.U. Gross, *Density Functional Theory: An approach to the Quantum Many-Body Problem* (Springer-Verlag, Berlin, 1990).

4. G.F. Bertsch and R. Broglia, *Oscillations in Finite Quantum Systems* (Cambridge University Press, Cambridge, 1994).
5. P.-G. Reinhard and E. Suraud, *Introduction to Cluster Dynamics* (Willey-VCH, Berlin, 2003).
6. P.-G. Reinhard and Y.K. Gambhir, Ann. Physik, **1** 598 (1992).
7. V.O. Nesterenko, W. Kleinig, V.V. Gudkov, and N. Lo Iudice, Phys. Rev. A **56**, 607 (1998);
8. W. Kleinig, V.O. Nesterenko, and P.-G. Reinhard, Ann. Phys. (NY) **297**, 1 (2002).
9. J. Kvasil, V.O. Nesterenko, and P.-G. Reinhard, in Proceed. of 7th Inter. Spring Seminar on Nuclear Physics, Miori, Italy, 2001, edited by A.Covello, World Scient. Publ., p.437 (2002); arXiv nucl-th/00109048.
10. V.O. Nesterenko J. Kvasil, and P.-G. Reinhard, Phys. Rev. C **66**, 044307 (2002).
11. T.H.R. Skyrme, Phil. Mag. **1**, 1043 (1956); D. Vauterin, D.M. Brink, Phys. Rev. C**5**, 626 (1972).
12. Y.M. Engel, D.M. Brink, K. Goeke, S.J. Krieger, and D. Vauterin, Nucl. Phys. A**249**, 215 (1975).
13. G. Vignale and W. Kohn, Phys. Rev. Lett. **77** 2037 (1996); G. Vignale, C.A. Ullrich and S. Conti, Phys. Rev. Lett. **79** 4878 (1997).
14. W. Kohn and L. Sham, Phys. Rev. **140** A1133 (1965).
15. O. Gunnarson and B.I. Lundqvist, Phys. Rev. B**13**, 4274 (1976).
16. W. Kleinig, V.O. Nesterenko, P.-G. Reinhard, and Ll. Serra, Eur. Phys. J. D**4**, 343 (1998).
17. V.O. Nesterenko, W. Kleinig, and P.-G. Reinhard, Eur. Phys. J. D**19**, 57 (2002).
18. H. Haberland and M. Schmidt, Eur. Phys. J. D**6**, 109 (1999).
19. V.O. Nesterenko, J. Kvasil, P.-G. Reinhard, W. Kleinig, and P. Fleischer, Proc. of the 11-th International Symposium on Capture-Gamma-Ray Spectroscopy and Related Topics, ed. by J.Kvasil, P.Cejnar, M.Krticka, Prague, 2002, Word Scientific Singapore, p. 143 (2003).
20. M. Bender, P.-H. Heenen, and P.-G. Reinhard, Rev. Mod. Phys. **75**, 121 (2003).
21. E. Lipparini and S. Stringari, Nucl. Phys. A**371**, 430 (1981).
22. O. Bohigas, A.M. Lane, J. Martorell, Phys. Rep. **51**, 267 (1979).
23. E. Lipparini ans S. Stringari, Phys. Rep. **175**, 104 (1989).
24. P.-G. Reinhard, N. Brack, O. Genzken, Phys.Rev. A **41**, 5568 (1990).
25. D.J. Thouless, Nucl. Phys. **21**, 225 (1960).
26. E. Lipparini and S. Stringari, Nucl. Phys. **A371**, 430 (1981).
27. T.Suzuki and H. Sagava, Prog. Theor. Phys.**65**, 565 (1981).
28. T. Kubo, H. Sakamoto, T. Kammuri and T. Kishimoto, Phys. Rev. C**54**, 2331 (1996).
29. N. van Giai, Ch. Stoyanov and V.V. Voronov, Phys. Rev. C**57**, 1204 (1998).
30. C. Yannouleas and R.A. Broglia, Ann. Phys. (N.Y.), **217**, 105 (1992).
31. J. Babst, P.-G. Reinhard, *Z. Phys.* D**42**, 209 (1997).
32. R.J. Barlett, in "Modern Electronic Structure Theory", ed. by D.R. Yakorny (World Scientific, Singapure, 1995) **1** p.1047.
33. J. Paldus and X. Li, Adv. Chem. Phys. **110**, 1 (1999).
34. P. Piecuch, K. Kowalski, I.S.O. Pimienta, and M.J. McGuire, Int. Rev. Phys. Chem. **21**, 527 (2002).
35. P. Piecuch, K. Kowalski, P.-D. fan, and I.S.O. Pimienta, in "Progress in Theoretical Chemistry and Physics", eds. J. Maruani, R. Lefebvre, and E. Brändas (Kluwer, Dordrecht, 2003), **12**, 119.
36. P.-G. Reinhard, Ann. Phys. (Leipzig) **1**, 632 (1992).
37. J. Dobaczewski and J. Dudek, Phys. Rev. C**52**, 1827 (1995).
38. E. Runge and E.K.U. Gross, Phys. Rev. Lett., **52**, 997 (1984).
39. H. Haberland and M. Schmidt, Eur. Phys. J. D**6**, 109 (1999).
40. D. Gogny, in *Nuclear Self-Consistent Fields*, eds. G. Ripka and M. Porneuf (North-Holland, Amsterdam, 1975).
41. A.B. Migdal, *Theory of Finite Fermi Systems and Nuclei (Nauka, Moscow, 1983).*

INEQUALITIES RELATING THE ELEMENTS OF THE SECOND-ORDER REDUCED DENSITY MATRIX

G. DEZSŐ [1,2], I. BÁLINT [1,2,3] AND I. GYÉMÁNT [1]

1. Department of Theoretical Physics, University of Szeged, Szeged, Hungary, H-6720 Tisza L. krt. 84-86
2. Department of Technology and Product Engineering, College of Nyíregyháza, Nyíregyháza, Hungary, H-4401 Sóstói út 31/b
3. Department of Pharmaceutical Analysis, University of Szeged, Szeged, Hungary, H-6720 Somogyi u. 4

e-mails: dezsog@nyf.hu, ibalint@physx.u-szeged.hu, gyemant@physx.u-szeged.hu

Abstract. The elements of the second-order reduced density matrix are pointed out to be written exactly as scalar products of specially defined vectors. Our considerations work in an arbitrarily large, but finite orthonormal basis, and the underlying wave function is a full-CI type wave function. Using basic rules of vector operations, inequalities are formulated without the use of wave function, including only elements of density matrix.

1. Introduction

The question, what conditions are to be fulfilled by a density matrix to be the image of a wave function, that is, to describe a real physical system is opened till today. The contracted Schrödinger-equations derived for different order reduced density matrices by H. Nakatsui [1] give opportunity to determine density matrices by a non-variational way. The equations contain density matrices of different order, and the relationships needed for the exact solutions are not yet known in spite of the intensive research activity [2, 3]. Recently perturbation theory corrections were published for correcting the error of the energy obtained by minimizing the density matrix directly applying the known conditions of N-representability [4], and

J.-P. Julien et al. (eds.),
Recent Advances in the Theory of Chemical and Physical Systems, 151–157.

variational calculations were performed for density matrices of bosonic systems including harmonic interactions showing that two-positivity may be exact for them [5].

In this paper a class of inequalities are derived for the elements of second-order reduced density matrices of fermion systems.

2. The second-order reduced density matrix in geminal basis

Let be $B_M = \{\varphi_i(1)\}_{i=1\ldots M}$ an M-dimensional one-electron function basis. Slater-determinants constructed over B_M span an orthonormal, $\mu = \binom{M}{N}$ dimensional subspace of the N-electron Hilbert space. The projection of the exact wave function in this subspace (Ψ) can be given as a linear combination of Slater-determinants (Φ) :

$$\Psi = \sum_{\alpha=1}^{\mu} c_\alpha \Phi_\alpha, \quad \mu = \binom{M}{N}. \tag{1}$$

This is the well-known full-CI scheme. The two-electron density matrix ($\Gamma^{(2)}$) is defined by the formula

$$\Gamma^{(2)}(1,2;1',2') = \int \Psi(1,2,3,\ldots,N)\Psi^*(1',2',3,\ldots,N)\; d3\ldots dN. \tag{2}$$

Inserting the linear combination (1) into (2), after the Laplace-expansion of the determinants the two-matrix has the form:

$$\Gamma^{(2)}(1,2;1',2') = \sum_{i<j,k<l}^{M} g_{i,j}(1,2)\; \Theta_{i,j;k,l}\; g^*_{k,l}(1',2'), \tag{3}$$

where $g_{i,j}(1,2) = \psi_i(1)\psi_j(2) - \psi_i(2)\psi_j(1), \quad i<j$ is an anti-symmetrized two-electron function (geminal), and

$$\Theta_{i,j;k,l} = \frac{1}{N!} \sum_{\alpha,\beta=1}^{\mu} c_\alpha c^*_\beta \int {}^{\alpha}g^{+}_{i,j}(3,\ldots,N)\; {}^{\beta}g^{+*}_{k,l}(3,\ldots,N)\, d3\ldots dN. \tag{4}$$

The ${}^{\alpha}g^{+}_{i,j}(3,\ldots,N)$ denotes the adjoint geminal of $g_{i,j}(1,2)$ in Slater-determinant Φ_α. One can introduce the so-called structure matrix with elements

$$V^{i,j;k,l}_{\alpha,\beta} = \frac{1}{(N-2)!} \int {}^{\alpha}g^{+}_{i,j}(3,\ldots,N)\; {}^{\beta}g^{+*}_{k,l}(3,\ldots,N)\, d3\ldots dN. \tag{5}$$

The density matrix can be written as:

$$\Theta_{i,j;k,l} = \frac{(N-2)!}{N!} \sum_{\alpha,\beta=1}^{\mu} c_\alpha c^*_\beta\; V^{i,j;k,l}_{\alpha,\beta} \tag{6}$$

The second-order reduced density matrix in geminal basis is expressed by the parameters of the wave function [6–9]. The second-order reduced density matrix (3) is the kernel of the second-order reduced density operator. Quantities Θ are matrix elements of the second-order reduced density operator in the basis of geminals. In spite of this, the expression "element of density matrix" is usual. In this sense, in the followings Θ is called as element of second-order reduced density matrix.

3. Density matrix elements as scalar products

We return to the expression (4), and rearrange it by changing the position of coefficients c_α and c_β:

$$\Theta_{i,j;k,l} = \frac{1}{N!} \sum_{\alpha,\beta=1}^{\mu} \int c_\alpha \; {}^{\alpha}g^{+}_{i,j}(3,\ldots,N) \;\; c^{*}_{\beta} \; {}^{\beta}g^{+*}_{k,l}(3,\ldots,N)\, d3\ldots dN.. \quad (7)$$

In this expression the products $c_\alpha \; {}^{\alpha}g^{+}_{i,j}(3,\ldots,N)$ and $c^{*}_{\beta} \; {}^{\beta}g^{+*}_{k,l}(3,\ldots,N)$ suggests the suspicion that elements Θ can be considered as scalar products of vectors being element of the vector space spanned by adjoint geminals. We will rewrite the formula (7) so it will contain summation over adjoint geminals (N-2 electron functions) instead of Slater-determinants (N-electron functions). To demonstrate it, first we have to briefly summarize properties of the index-sets of determinants, geminals and adjoint geminals.

While determinants Φ_α are N-electron functions, we can identify them by an index-set I_α containing ordered indices of one-electron functions from which the determinant is built up. In the set I_α there are N piece of integers between 1 and M, $I_\alpha = \{\alpha_1, \alpha_2 \ldots \alpha_N\}$. Similarly, the adjoint geminals can be identified with index sets I_λ containing N-2 piece of integers sequentially. Really, the denomination "adjoint geminal" is for the relationship with the N-electron Slater determinant, but one can handle adjoint geminals as N-2-electron functions. We number adjoint geminals, and in the followings they will be noted as $\{g^{+}_{\lambda}\}_{\lambda=1\ldots\binom{M}{N-2}}$. Eventually, geminal $g_{i,j}$ can be considered as a "mini-determinant" (2 by 2 determinant) identified by the index-set $I_\kappa = \{i, j\}$ so we will write g_κ instead of $g_{i,j}$.

If one starts with the determinant Φ_α , then select a geminal g_κ from it, and the adjoint geminal is g^{+}_{λ}, then

$$I_\alpha \setminus I_\kappa = I_\lambda \quad (8)$$

is true. Two of α, κ and λ determines the third one. In other words if we know the Slater-determinant, and the geminal selected from it, we can tell the adjoint geminal too, or if the geminal and the adjoint geminal is known, one can tell the Slater-determinant. This relationship let be denoted

by $\alpha(\kappa,\lambda)$. Of course this is defined only if $I\kappa \cap I_\lambda$ is empty set, that is the geminal and its adjoint must be constructed from different one-electron functions because of mathematical properties of determinants. For the sake of consistency let be $\alpha(\kappa,\lambda)=0$ if $I_\kappa \cap I_\lambda$ is not empty, and the vector of configuration coefficients (c) augmented by an element $c_0=0$.

The adjoint geminals have a sign depending on that which rows and columns they contain from the original determinant. This sign can be determined from the index-sets I_κ and I_λ, because the union of this two gives I_α, and so we can determine the ordinal number of the rows and columns of the geminal and the adjoint geminal in the original Slater-determinant. Signs are substantially important, because they determines the sign of the integral, and the coefficients c are multiplied with them in a large summation. The notation ${}^{\alpha}g^{+}_{i,j}(3,\ldots,N)$ carries the sign, because it refers both the determinant from which it is derived, and the geminal. Although $g^{+}_{\lambda}(3\ldots N)$ may note the same N-2-electron function, but without the sign! Of course, signs are defined while N-2 electron functions (adjoint geminals) are considered in connection with a certain Slater-determinant and a certain geminal. In other words index sets I_κ and I_λ determines not only the set I_α and the Slater determinant, but the sign of g^{+}_{λ} in Φ_α too. In the followings signs of adjoint determinants are denoted as: $\omega(\kappa,\lambda)$. For mathematical consistency : $\omega(\kappa,\lambda)=0$ if $I_\kappa \cap I_\lambda$ is not the empty set .

Now we return to formula (7), and rewrite it using $\{i,j\}=\kappa$ and $\{k,l\}=\kappa'$ notations:

$$\Theta_{\kappa,\kappa'}=\frac{1}{N!}\sum_{\alpha,\beta=1}^{\mu}\int c_\alpha\ {}^{\alpha}g^{+}_{\kappa}(3,\ldots,N)\ \ c^{*}_{\beta}\ {}^{\beta}g^{+*}_{\kappa'}(3,\ldots,N)\,d3\ldots dN.. \qquad (9)$$

At this point applying the rules of indices described above, we can write $\omega(\kappa,\lambda)g^{+}_{\lambda}(3\ldots N)$ instead of ${}^{\alpha}g^{+}_{\kappa}(3,\ldots,N)$, where $I_\lambda = I_\alpha \setminus I_\kappa$, and $c_{\kappa,\lambda}$ can be written instead of c_α (where $I_\lambda = I_\alpha \setminus I_\kappa$ again). The number of N-2 electron functions is $\nu=\binom{M}{N-2}$. At this point we can convert the summation indices and write (9) as follows:

$$\Theta_{\kappa,\kappa'}=\frac{1}{N!}\sum_{\lambda,\lambda'=1}^{\nu}\int \underbrace{c_{\alpha(\kappa,\lambda)}\ \omega(\kappa,\lambda)}_{D^{\kappa}_{\lambda}}\, g^{+}_{\lambda}(3,\ldots,N)\cdot$$

$$\cdot\underbrace{c_{\beta(\kappa',\lambda')}\ \omega(\kappa'\lambda')}_{D^{\kappa'}_{\lambda'}}\, g^{+}_{\lambda'}(3,\ldots,N)\ d3\ldots dN. \qquad (10)$$

The following notations are introduced:

$$D^{\kappa}_{\lambda}=c_{\alpha(\kappa,\lambda)}\ \omega(\kappa,\lambda) \qquad (11)$$

$$D^{\kappa'}_{\lambda'} = c_{\alpha(\kappa',\lambda')}\ \omega(\kappa',\lambda') \tag{12}$$

With these notations we can rearrange the formula (10) of Θ:

$$\Theta_{\kappa,\kappa'} = \frac{1}{N!}\sum_{\lambda,\lambda'=1}^{\nu} D^{\kappa}_{\lambda} D^{\kappa'}_{\lambda'} \int \underbrace{g^{+}_{\lambda}(3,\ldots,N) g^{+}_{\lambda'}(3,\ldots,N) d3\ldots dN}_{\delta_{\lambda,\lambda'}\cdot\ (N-2)!} \tag{13}$$

Because of the orthogonality of N-2 electron functions (N-2 by N-2 determinant functions constructed over an orthonormal one-electron basis set) the summation indices λ and λ' can be set to be equal:

$$\Theta_{\kappa,\kappa'} = \frac{(N-2)!}{N!}\sum_{\lambda} D^{\kappa}_{\lambda} D^{\kappa'}_{\lambda}. \tag{14}$$

Eventually, quantities D^{κ}_{λ} can be considered as the λth element of vector $\vec{D}^{\kappa}$, so we can write the element of two-electron density matrix Θ as a scalar product of two vectors:

$$\Theta_{\kappa,\kappa'} = \frac{(N-2)!}{N!}\vec{D}^{\kappa}\cdot\vec{D}^{\kappa'}. \tag{15}$$

The components of vectors $\{\vec{D}^{\kappa}\}_{\kappa=1\ldots\nu}$ are completely defined by the parameters of the underlying full-CI type wave function, and the index sets of Slater-determinants and their subdeterminants according to (13). The number of vectors $\vec{D}^{\kappa}$ is $\binom{M}{2}$, and this is of course equal to the number of geminals g_{κ} constructed over the M-dimensional one-particle basis B_M.

We can word the results up to this point: for an N-particle fermion system, using M-dimensional one-particle function basis, the elements of the second-order reduced density matrix in geminal basis are scalar products of $\binom{M}{2}$ piece of $\binom{M}{N-2}$ dimensional vectors.

4. Inequalities fulfilled by the density matrix elements

The most interesting corollary of the results of the previous chapter is, that using basic vector operations and features of vectors, inequalities relating the elements of density matrix can be formulated. Vectors $\vec{D}^{\kappa}$ are completely determined by the configurational coefficients of the underlying full-CI type wave function, *but we do not need the knowledge of these coefficients* when deriving the inequalities.

From the basic property of the scalar product

$$|\vec{D}^{\kappa}||\vec{D}^{\kappa'}| \geq \vec{D}^{\kappa}\cdot\vec{D}^{\kappa'}$$

we get

$$\Theta_{\kappa\kappa}\Theta_{\kappa'\kappa'} \geq (\Theta_{\kappa\kappa'})^2 \quad \forall\kappa,\kappa'. \tag{16}$$

Writing the sum of two vectors (cosine theorem), and employing that the norm of a vector is non-negative, that is $(\vec{D}^{\kappa}+\vec{D}^{\kappa'})^2 = |\vec{D}^{\kappa}|^2+|\vec{D}^{\kappa'}|^2+2\vec{D}^{\kappa}\cdot\vec{D}^{\kappa'} \geq 0$ we obtain

$$\frac{1}{2}(\Theta_{\kappa\kappa}+\Theta_{\kappa'\kappa'}) \geq \Theta_{\kappa\kappa'} \quad \forall\kappa,\kappa'. \tag{17}$$

This inequality can be easily generalized, while the non-negativity of the norm is valid for an arbitrary vector, for example:

$$(\vec{D}^{\kappa}+\vec{D}^{\kappa'}+\vec{D}^{\kappa"})^2 \geq 0,$$

and in general:

$$(\sum_{i=1}^{k}\vec{D}^{\kappa_i})^2 \geq 0. \tag{18}$$

Here κ_i is an element of an index set containing k integer of possible values of geminal indices κ.

$$\{\kappa_1,\kappa_2\ldots\kappa_k\} \subseteq \{1,2\ldots\binom{M}{2}\} \tag{19}$$

Evaluating the square of the sum of k piece of vectors for all possible value of k, a hierarchy of inequalities can be formulated:

$$\frac{1}{2}\sum_{i=1}^{k}\Theta_{\kappa_i\kappa_i} \geq \sum_{i,j=1,i<j}^{k}|\Theta_{\kappa_i\kappa_j}| \quad \forall k \; and \; \forall\{\kappa_1,\kappa_2\ldots\kappa_k\}. \tag{20}$$

For the formula (20) contains several inequality, it can be interesting to study the number of them. The values of k can be $2,3\ldots\binom{M}{2}$, remember, that $\binom{M}{2}$ is the number of vectors $\vec{D}^{\kappa}$. For a certain value of k there is $\binom{\binom{M}{2}}{k}$ possibility to pick out κ_i indices from the set of numbers $\{1,2\ldots\binom{M}{2}\}$. Taking into account all possible selections, the number of inequalities (20) can be calculated as:

$$\binom{\binom{M}{2}}{2}+\binom{\binom{M}{2}}{3}+\ldots+\binom{\binom{M}{2}}{\binom{M}{2}} = \sum_{k=2}^{\binom{M}{2}}\binom{\binom{M}{2}}{k}. \tag{21}$$

5. Conclusions

Elements of second order reduced density matrix of a fermion system are written in geminal basis. Matrix elements are pointed out to be scalar product of special vectors. Based on elementary vector operations inequalities are formulated relating the density matrix elements. While the inequalities are based only on the features of scalar product, not the full information is exploited carried by the vectors $\vec{D}^{\kappa}$. Recently there are two object of research. The first is theoretical investigation of inequalities, reducibility of the large system of them. Further work may have the chance for reaching deeper insight of the so-called N-representability problem. The second object is a practical one: examine the possibility of computational applications, associate conditions above with known methods and conditions for calculating density matrices.

6. Acknowledgements

G.D. acknowledges the Ministry of Education of Hungary for supporting by the Békési György fellowship (BÖ 92/2003), the National Office for Research and Technology of Hungarian Government for the grant (MEC-01180/2004), the Faculty of Engineering and Agriculture, and the International Relations Center of College of Nyíregyháza for financial support.

References

1. H. Nakatsui, Phys.Rev. A **14**, 41-50 (1976)
2. H. Nakatsui, K. Yashuda, Phys. Rev. Lett. **76** 1039-1042 (1996)
3. F. Colmenero, C. Valdemoro, Int. J. Quant. Chem. **62** 369 (1994)
4. T. Juhász, D. A. Mazziotti, J. Chem. Phys. **121/3** 1201-1205 (2004)
5. G. Gidofalvi, D. A. Mazziotti, Phys. Rev. A **69** 042511 (2004)
6. I.Bálint, G.Dezső, I.Gyémánt, Journal of Molecular Structure, THEOCHEM **501-502** 125-132 (2000)
7. I.Bálint, G.Dezső, I.Gyémánt, J.Chem.Inf.Comp.Sci. **41** 806-810 (2001)
8. G.Dezső, I.Bálint, I.Gyémánt, Journal of Molecular Structure, THEOCHEM **542** 21-23 (2001)
9. I.Bálint, G.Dezső, I.Gyémánt, Int.J.Quant.Chem **84**(1) 32-38 (2001)

STRUTINSKY'S SHELL-CORRECTION METHOD IN THE EXTENDED KOHN-SHAM SCHEME: APPLICATION TO THE IONIZATION POTENTIAL, ELECTRON AFFINITY, ELECTRONEGATIVITY AND CHEMICAL HARDNESS OF ATOMS

YA. I. DELCHEV, A. I. KULEFF
Institute for Nuclear Research and Nuclear Energy, BAS, 72 Tzarigradsko Chaussee, 1784 Sofia, Bulgaria
ydelchev@inrne.bas.bg

J. MARUANI
Laboratoire de Chimie Physique, CNRS and UPMC, 11 rue Pierre et Marie Curie, 75005 Paris, France
maruani@ccr.jussieu.fr

TZ. MINEVA
Institute for Catalysis, BAS, Acad. G. Bonchev ul., bl. 11, 1113 Sofia, Bulgaria
tmineva@ic.bas.bg

AND

F. ZAHARIEV
Department of Chemistry, University of British Columbia, Vancouver, BC, Canada V6T 1Z1
fzahari@chem.ubc.ca

Abstract. Calculations of the first-order shell corrections of the ionization potential, $\delta_1 I$, electron affinity, $\delta_1 A$, electronegativity, $\delta_1 \chi$, and chemical hardness, $\delta_1 \eta$ are performed for elements from B to Ca, using the previously described Strutinsky averaging procedure in the frame of the extended Kohn-Sham scheme. A good agreement with the experimental results is obtained, and the discrepancies appearing are discussed in terms of the approximations made.

J.-P. Julien et al. (eds.),
Recent Advances in the Theory of Chemical and Physical Systems, 159–176.

1. Introduction

Because the total energy $E(N)$ of an N-electron system is not much informative, intuitive concepts have been introduced in chemistry to allow the properties of a molecule (or an aggregate) to be rationalized in terms of properties of the constitutive fragments. Some of these, such as electronegativity (χ) [1] and chemical hardness (η) [2], have been strictly defined in the frame of density functional theory (DFT): both electronegativity and its first derivative are key concepts in making this theory chemically descriptive [3, 4]. The derivative of electronegativity with respect to the charge of a system is related to their dipole polarizability [5, 6]. Similarly the electronegativity helps to understand various molecular properties: electron distribution [7], charge transfer, dipole moments, bond energies, force constants, as well as NMR and XAS / XPS chemical shifts [8] or the work function in metals. According to Pearson (Ref. [9], p. 34), in the making of a molecule from constitutive fragments, "the difference in electronegativity drives the process while the sum of hardness parameters acts as a resistance".

In previous papers [10, 11] we have formulated a procedure for splitting the ground-state energy of a multifermionic system into an averaged, structure-less part, $\tilde{E}$, and a residual, shell-structure part, δE. The latter originates from quantum interference effects of the one-particle motion in the confining potential [12] and has the form of a shell-correction expansion: $\delta E = \sum_i \delta_i E$. It was also shown [11] that the first-order corrective term, $\delta_1 E$, not only governs the oscillating behavior of the residual part, δE, but also is a good quantitative estimate for both neutral atoms and positive ions. This first-order shell-correction term, $\delta_1 E$, is the weighted sum of ground-state one-particle energies, ε_i^0, with the occupation probabilities δn_i.

The variation of δE and $\delta_1 E$ as a function of the atomic number Z manifests the saw-tooth pattern, well-known in atomic nuclei and metal clusters [13]- [15], having sharp minima at atoms with filled or half-filled shells in accordance with the shell-filling process.

The splitting of the energy was achieved using the so-called Strutinsky averaging procedure (SAP) [16]- [18], based on the concept that the oscillating part of the total energy originates from irregularities in the one-particle energy-level distribution. It introduces new occupation numbers that are not necessarily integer and positive while preserving the total number of particles. In practice the occupancies of only few orbitals are involved in the "redistribution process" taking place in the SAP. The SAP automatically leads to a consistent core-valence division in both the energy and coordinate spaces [19]. This procedure distinguishes a "core" region, where the

ground-state occupancy is preserved, and a "valence" region, where outer (sub)shell orbitals are involved.

In the next section we shall recall the definitions of the chemical concepts relevant to this paper in the framework of DFT. In Section 3 we briefly review Strutinsky's averaging procedure and its formulation in the extended Kohn-Sham (EKS) scheme. The following section is devoted to the presentation and discussion of our results for the residual, shell-structure part of the ionization potential, electron affinity, electronegativity, and chemical hardness for the series of atoms from B to Ca. The last section will present some conclusions.

2. Electronegativity and chemical hardness in EKS-DFT

For a fixed external potential $v(\vec{r})$, the ground-state electron density ρ_0 satisfies the variational equation:

$$\left.\frac{\delta\left\{E_v[\rho]-\mu N[\rho]\right\}}{\delta\rho(\vec{r})}\right|_{\rho=\rho_0}=0, \tag{1}$$

where $E_v[\rho]$ is the energy density functional and the chemical potential μ appears as a Lagrange multiplier enforcing the fulfillment of the normalization condition:

$$N[\rho]=\int\rho(\vec{r})d\vec{r}=n.$$

Enlarging the domain of definition of Eqn (1) to all positive n, one could assume the minimum of the density functional $E_v[\rho]$, i.e. the ground-state energy $E_0(n)$ for a given external potential $v(\vec{r})$, to be a continuous and even a differentiable function of the number of electrons n. From the Lagrange multiplier theory, it would further follow that

$$\mu=\left(\frac{\partial E_0}{\partial n}\right)_v, \tag{2}$$

thus linking with the standard understanding of chemical potential μ as a sensitivity of the ground-state energy E_0 to a change in the number of electrons n or alternatively as an escaping tendency of electrons from an equilibrium system [3].

Indeed, there is such an approach to DFT that gives a physical justification to the above assumption of continuity with the only complication involved being the non-differentiability of $E_0(n)$ at an integer number of electrons $n=N$, a phenomenon known as 'DFT derivative discontinuity'. The approach is based on an extension of the original Hohenberg-Kohn theorem [20] to the grand canonical ensemble first given by Mermin [21]. It

describes an open system at a temperature T with a chemical potential μ. The number of electrons of such a system can fluctuate around a generally speaking non-integer average value n. Perdew *et al.* [22, 23] reformulated Mermin's theory in the $T \to 0$ limit following the "constrained search" method of Levy [24]. The zero-temperature ensemble reduces to a simple statistical mixture of an N-electron pure state, Ψ_N, and an $(N+1)$-electron pure state, Ψ_{N+1}, with the respective weights $(1-f)$ and f, thus giving a concrete physical realization to the fractional electron number $n = N + f$ $(0 \leq f \leq 1)$. The universal density functional is defined as:

$$F_n[\rho] = \min_{(1-f)\Psi_N + f\Psi_{N+1} \to \rho} \left\{ (1-f)\langle \Psi_N | \hat{H}_N | \Psi_N \rangle + f \langle \Psi_{N+1} | \hat{H}_{N+1} | \Psi_{N+1} \rangle \right\} \tag{3}$$

and if degeneracies are present this definition could be further extended by replacing the pure-states Ψ_N, Ψ_{N+1} with the density matrices $\hat{D}_N = \sum_i c_i |\Psi_{N,i}\rangle\langle\Psi_{N,i}|$, $\hat{D}_{N+1} = \sum_i c_i |\Psi_{N+1,i}\rangle\langle\Psi_{N+1,i}|$ and the energy components with $Tr_N(\hat{H}_N \hat{D}_N)$, $Tr_{N+1}(\hat{H}_{N+1}\hat{D}_{N+1})$. There is a Kohn-Sham version of the above zero-temperature DFT (see [22, 23, 25] for details).

In fact, there is another approach to DFT that allows fractional electron numbers, namely the extended Kohn-Sham (EKS) scheme [23, 26, 27]. It allows the use of fractional occupation numbers $f_i : \{0 \leq f_i \leq 1\}$, hence the energy functional $E[\{\phi_i^{(\vec{f})}\}; \{f_i\}]$ depends on $\vec{f} \equiv \{f_i\}$ and in addition to the orbitals $\{\phi_i^{(\vec{f})}\}$. The density is given by $\rho(\vec{r}) = \sum_i f_i |\phi_i(\vec{r})|^2$. Assuming a stationary point of the functional exists for any given set $\{f_i\}$, one can consider the energy as a function of f_i's and whose partial derivatives with respect to the occupation numbers give the respective Kohn-Sham eigenvalues

$$\frac{\partial}{\partial f_i} E(f_1, f_2, \ldots) = \varepsilon_i, \tag{4}$$

the so-called Janak's theorem [28]. The very definition of the derivative $\frac{\partial E}{\partial f_i}$ implies that the function $E(f_1, f_2, \ldots)$ can be varied freely in the neighborhood of f_i's without conserving the total number of particles $\sum_i f_i$ (see the Appendix of [11] where the validity of Janak's theorem is discussed). That is why, making use of Eqn (4), one should precise the condition of its application.

The two approaches described above, namely the zero-temperature DFT and EKS, are generally speaking non-equivalent, the main difference being in the valid range of occupation numbers below that of the highest occupied orbital (HOMO). On the one hand the more physically grounded zero-temperature DFT approach completely fills in all the states below HOMO of the ground state according to the Fermi statistics, i.e. $f_i = 1$ $(i = 1, \ldots, N-1)$, assuming non-degeneracy. On the other hand the

EKS approach, based on the more formal Janak's type of argumentation, doesn't put these restrictions on the ground-state occupation numbers below HOMO. In what follows in this chapter we will use the fractional occupation of HOMO only, in which case both approaches agree. Using Eqn (4) for HOMO energy ε_N with respect to $(N-1+f)$ electrons, and for HOMO energy ε_{N+1} with respect to $(N+f)$ electrons, one can express I and A in the following form:

$$I(N) = E(N-1) - E(N) = -\int_0^1 \varepsilon_N(N-1+f)df, \tag{5}$$

$$A(N) = I(N+1) = E(N) - E(N+1) = -\int_0^1 \varepsilon_{N+1}(N+f)df. \tag{6}$$

The analysis of the asymptotic density profile of HOMO's in Kohn-Sham theory [29] allows one to make the identification [30]:

$$\varepsilon_N = -I, \tag{7}$$

$$\varepsilon_{N+1}(N+f) = -A, \tag{8}$$

where

$$I = E(N-1) - E(N) \equiv E^{cation} - E^{atom} \tag{9}$$

is the ionization potential (I) and

$$A = E(N) - E(N+1) \equiv E^{atom} - E^{anion} \tag{10}$$

is the electron affinity (A) of an N-electron system. The above gives a clear physical interpretation of the highest occupied (or partially occupied) orbital. Expressing the values of I and A through orbital energies, Eqs (5-8), give a possibility to avoid their determination as differences of two large numbers.

A differential analog of Eqs (5-6) could be obtained based on Eq. (3), Eq. (1) and Eq. (2) (see [22, 23]):

$$\mu(N^+) = \left(\frac{\partial E}{\partial n}\right)^+_{v,n=N} = -A(N), \tag{11}$$

$$\mu(N^-) = \left(\frac{\partial E}{\partial n}\right)^-_{v,n=N} = -I(N), \tag{12}$$

where the superscripts $(\pm)$ denote if the derivative is taken from the left or from the right, i.e. $n \to N \pm 0$. Equations (11) and (12) show that in ensemble theory the chemical potential μ is a step function for each

integer number of electrons. The functional derivative discontinuity has two components:

$$\left(\frac{\partial E}{\partial N}\right)_v^+ - \left(\frac{\partial E}{\partial N}\right)_v^- = (\varepsilon_N(N) - \varepsilon_{N+1}(N)) + \Delta_{xc}, \tag{13}$$

a Kohn-Sham's component $(\varepsilon_N(N)-\varepsilon_{N+1}(N))$ involving HOMO and LUMO energies and an exchange-correlation component [23, 31]:

$$\Delta_{xc} = \left(\frac{\delta E_{xc}}{\delta\rho(\vec{r})}\right)_{n=N^+} - \left(\frac{\delta E_{xc}}{\delta\rho(\vec{r})}\right)_{n=N^-} \equiv v_{xc}^+(\vec{r}) - v_{xc}^-(\vec{r}). \tag{14}$$

In a recent paper [25] $\Delta_{xc} = 0$ was claimed, meaning that the overall derivative discontinuity is entirely due to its Kohn-Sham component but this issue is still under intense debate.

As for the value of the chemical potential at the mere point of $n = N$ there are at least four if not more existing definitions in the literature (see [25] for more details on this).

The first [32]- [34] identifies the chemical potential with the mean total electronic energy

$$\mu(N) = \frac{E_0(N)}{N}. \tag{15}$$

The second [35], with the highest occupied Kohn-Sham orbital energy $\epsilon_N(N)$ and is identified to be the negative of the first ionization potential

$$\mu(N) = \epsilon_N(N) = -I. \tag{16}$$

The third [36, 37], with the negative of Mulliken's electronegativity

$$\mu(N) = -\chi = -\frac{I + A}{2}. \tag{17}$$

The fourth [3, 38], with a value that could lie between two limits

$$-I \leq \mu(N) \leq -A. \tag{18}$$

We will not be concerned with the subtleties of chemical potential expressions in this work but simply use Eqn (17) as a definition of electronegativity [1].

The next property of substantial importance is chemical hardness [2]:

$$\eta = \frac{1}{2}\left(\frac{\partial^2 E}{\partial N^2}\right)_v = \frac{1}{2}\left(\frac{\partial \mu}{\partial N}\right)_v. \tag{19}$$

Its inverse $S = \frac{1}{2\eta}$ is naturally called chemical softness.

The approximate expression

$$\eta \approx \frac{I - A}{2} = \frac{E^{cation} - 2E^{atom} + E^{anion}}{2} \tag{20}$$

can be interpreted as a three-point approximation to Eq. (2) based on Eqs (9) and (10) in the last equation. Note that if Eqs (11) and (12) were used instead in the case that there was no derivative discontinuity, i.e. if the energy dependence on the electron number was smooth, the second equation in Eq. (20) would be zero.

The above quantities are very useful tools in the theoretical analysis of chemical reactivity by means of the following three guiding principles.

The crudest one is Sanderson's electronegativity equalization principle [39, 40] according to which "atoms-in-molecule" make electron transfers from lower to higher electronegative parts thus achieving equilibrium in electronegativity.

A more refined but still debated in the literature notion is Pearson's Hard and Soft Acids and Bases (HSAB) principle [9, 41], which quantifies energy changes to second order according to which hard (soft) acids (electron pair acceptors) prefer to interact with hard (soft) bases (electron pair donors). "Soft likes soft" relates to covalent bonds being facilitated by high polarizabilities, while "hard likes hard" relates to a creation of predominantly electrostatic interactions.

The Maximum Hardness principle [41] further extends HSAB principle by stating that "molecules try to arrange themselves to be as hard as possible".

A theoretical account from the point of view of DFT could be found in [1, 42, 43]. For a good review of chemical applications of the above principles as described by quantum chemical methods in general and density functional methods in particular see the papers of Geerlings and De Proft [4, 44, 45].

3. Strutinsky's shell-correction method

In what follows we briefly recall the essentials of Strutinsky's shell-correction method and its formulation in the EKS DFT frame, referring to Refs [10,11] for details.

The Strutinsky method is a receipt for exact splitting of the total energy of a fermionic system into a smooth part and small shell corrections. It is based on the assumption that the irregular (oscillating) term in all energetic properties is due to the non-uniformities in the shell structure of the one-particle energy level distribution. Then, the smoothing of the one-particle energy spectrum yields the smoothing of the energy.

This smoothing of the level density, $g(E) = \sum_i \delta(E-\varepsilon_i)$, can be obtained through the convolution of $g(E)$ with an appropriate smoothing (averaging) function $f(x)$:

$$\tilde{g}(E) = \frac{1}{\gamma} \int_{-\infty}^{+\infty} g(E') f\left(\frac{E-E'}{\gamma}\right) dE' = \frac{1}{\gamma} \sum_i f\left(\frac{E-\varepsilon_i}{\gamma}\right), \qquad (21)$$

where γ is the width of the averaging function. The choice of this function is a widely discussed in the literature problem (see for example Refs [17, 18]), the most used form being the modified Gaussian of order M:

$$f_M(x) = \frac{1}{\sqrt{\pi}} \sum_{n=0}^{M} \frac{(-1)^n}{2^{2n} n!} \frac{d^{2n}}{dx^{2n}} e^{-x^2}, \qquad x = \left(\frac{E-E'}{\gamma}\right). \qquad (22)$$

This expression includes the so-called curvature corrections to the Gaussian function which ensures that the smooth density $\tilde{g}(E)$ does not change after its own averaging through the same procedure.

Imposing the particle conservation condition, which introduces a new Fermi level $\tilde{\lambda}$, we can define the so-called generalized occupation numbers $\tilde{n}_i$:

$$N \equiv \int_{-\infty}^{\tilde{\lambda}} \tilde{g}(E) dE = \sum_i \int_{-\infty}^{\tilde{\lambda}} \tilde{g}_i(E) dE \equiv \sum_i \tilde{n}_i. \qquad (23)$$

Combining Eqs (21) and (23), one obtains the explicit form of these occupation numbers:

$$\tilde{n}_i = \int_{-\infty}^{t_i} f(x) dx, \qquad t_i = \frac{\tilde{\lambda} - \varepsilon_i}{\gamma}. \qquad (24)$$

By analogy with the expression for the total energy Σ in a shell model frames:

$$\Sigma = \sum_i \varepsilon_i n_i = \int_{-\infty}^{\lambda} E\, g(E) dE, \qquad (25)$$

one can define the smooth energy $\tilde{\Sigma}$, substituting in Eqn (25) the one-particle energy distribution $g(E)$ with the smooth density $\tilde{g}(E)$ and the Fermi level λ with $\tilde{\lambda}$. The result is:

$$\tilde{\Sigma} = \int_{-\infty}^{\tilde{\lambda}} E\, \tilde{g}(E)\, dE = \sum_i (\varepsilon_i\, \tilde{n}_i + \gamma\, s_i) = \sum_i \varepsilon_i\, \tilde{n}_i + \gamma\, S, \qquad (26)$$

where the functions s_i have the form:

$$s_i = \int_{-\infty}^{t_i} x\, f(x)\, dx = s(t_i),$$

and their sum $S = \sum_i s_i$ ensures the satisfaction of the so-called plateau condition [18]:

$$\left.\frac{d\tilde{\Sigma}}{d\gamma}\right|_{\gamma=\gamma_0} = S = 0. \tag{27}$$

This condition should be fulfilled, at least approximately, for a given range of the smearing width $\gamma = \{\gamma_0\}$ and a given order M of the correction polynomial, in order to obtain an independent of the averaging procedure and of the formal parameter γ smooth energy.

The elimination of the other parameter, M, can be done imposing a saturation condition with respect to M calculating the root γ_0, i.e.:

$$\tilde{\Sigma}(\gamma_0, M) = \tilde{\Sigma}(\gamma_0, M+1). \tag{28}$$

In that way the averaging procedure is closed which allows us to determine the generalized occupation numbers $\tilde{n}_i$ and δn_i connected with standard occupation numbers n_i through the relation:

$$n_i = \tilde{n}_i + \delta n_i. \tag{29}$$

These numbers allows the splitting of the density $\rho(\vec{r})$ into a smooth $\tilde{\rho}(\vec{r})$ and irregular $\delta\rho(\vec{r})$ part yielding in that way the splitting of all energetic properties.

This procedure leads directly to the determination of the first-order shell correction:

$$\delta_1 E = \sum_i \varepsilon_i \delta n_i, \tag{30}$$

according to the so-called Strutinsky's energy theorem, proven within the Hartree-Fock scheme:

$$E[\rho] = E[\tilde{\rho}] + \sum_i \varepsilon_i \delta n_i + \vartheta[(\delta\rho)^2]. \tag{31}$$

In Refs [10, 11] we have shown that Eqn (30) is an expression for the first-order shell correction term in the EKS-DFT frame. As we pointed it out, the extended version [26, 27] of the Kohn-Sham scheme [46] is appropriate because it allows fractional occupation numbers, thus permitting the treatment of unequally weighted states.

According to this scheme, the ground-state energy E_0 of the system is the minimum of the energy functional:

$$\mathcal{E}\left[\{\phi_i\};\{n_i\}\right] = \sum_{i=1}^{\infty} n_i \int \phi_i^*(\vec{r})\hat{h}(\vec{r})\phi_i(\vec{r})\,d\vec{r} + \frac{1}{2}\int V(\vec{r},\vec{r}\,')\rho(\vec{r})\rho(\vec{r}\,')\,d\vec{r}d\vec{r}\,' + E_{xc}[\rho], \qquad (32)$$

and hence is:

$$E_0 = \sum_{i=1}^{\infty} n_i^0\varepsilon_i^0 - \frac{1}{2}\int V(\vec{r},\vec{r}\,')\rho_0(\vec{r})\rho_0(\vec{r}\,')\,d\vec{r}d\vec{r}\,' + E_{xc}[\rho_0] - \int V_{xc}([\rho_0];\vec{r})\rho_0(\vec{r})\,d\vec{r}. \qquad (33)$$

Let us denote with $\bar{E}(\{n_i\})$ the stationary value of the functional (32) with respect to arbitrary occupation numbers $\{n_i\} \equiv (n_1, n_2, ...) \equiv \vec{n}$ for the orbitals $\{\phi_i\}$, satisfying the particle conservation condition, i.e.:

$$\bar{E}(\{n_i\}) = \mathcal{E}[\{\phi_i^{(\vec{n})}\};\{n_i\}], \qquad \sum_i n_i = N. \qquad (34)$$

Such occupation numbers can be the $\tilde{n}_i$'s obtained within the smoothing procedure described above. Since these numbers are very close to the ground-state occupation numbers n_i^0, i.e the increments $\delta n_i = n_i^0 - \widetilde{n}_i$ are very small, we can expand Eqn (34) in a Taylor series with respect to the δn_i's. The result is:

$$\bar{E}(\vec{\tilde{n}}) = \bar{E}(\vec{n}_0 - \delta\vec{n}) = \bar{E}(\vec{n}_1) - \sum_i \delta n_i \left.\frac{\partial\bar{E}}{\partial n_i}\right|_{\vec{n}_0} + \frac{1}{2!}\sum_{i,j}\delta n_i\delta n_j \left.\frac{\partial^2\bar{E}}{\partial n_i\partial n_j}\right|_{\vec{n}_0} - \frac{1}{3!}\sum_{i,j,k}\delta n_i\delta n_j\delta n_k \left.\frac{\partial^3\bar{E}}{\partial n_i\partial n_j\partial n_k}\right|_{\vec{n}_0} + \ldots . \qquad (35)$$

The first term in this expansion is the ground-state energy: $E_0 \equiv \bar{E}(\vec{n}_0)$. For the second term we use Janak's theorem, Eqn (4):

$$\left.\frac{\partial\bar{E}(n_1,n_2,...)}{\partial n_i}\right|_{\vec{n}} = \varepsilon_i^{(\vec{n})}, \quad i = 1, 2, ... \qquad (36)$$

Thus we obtain for the second term in Eqn (35) the shell-model form of the shell correction, Eqn (30):

$$\sum_i \delta n_i \left.\frac{\partial\bar{E}}{\partial n_i}\right|_{\vec{n}_0} = \sum_i \delta n_i \varepsilon_i^{(\vec{n}_0)}. \qquad (37)$$

The ground-state energy can then be written in the form:

$$E_0 = \widetilde{E} + \delta_1 E + \delta_2 E + \delta_3 E + ..., \tag{38}$$

where

$$\widetilde{E} = \bar{E}(\widetilde{n}_1, \widetilde{n}_2, ...) \qquad \text{and} \qquad \delta_1 E = \sum_i \delta n_i \varepsilon_i^0 \tag{39}$$

are the leading (uniform) and first-order shell-correction terms, other $\delta_i E$ terms contributing higher-order shell effects.

The first derivatives in a Taylor expansion, similar to Eqn (28), of the energy E with respect to the occupation numbers n_i provide the KS-eigenvalues, as stated by Janak's theorem, and the second derivatives:

$$\frac{\partial^2 E}{\partial n_i \partial n_j} = \eta_{ij} \tag{40}$$

give the hardness matrix, as defined by Liu and Parr [47].

Since the KS-eigenvalues are defined through Janak's theorem as first derivatives of the total DF-energy, the ij-th element of the hardness matrix can be obtained as the first derivative of ε_i with respect to n_j:

$$\eta_{ij} = \frac{\partial \varepsilon_i}{\partial n_j} \tag{41}$$

and be approximated numerically using the finite difference formula:

$$\eta_{ij} = \frac{\varepsilon_i(n_j - \Delta n_j) - \varepsilon_i(n_j)}{\Delta n_j}. \tag{42}$$

The expression (42) takes into account the response of the i-th orbital to the change of occupation number of the j-th orbital, i.e., the variation of energy of the i-th orbital due to the variation of the j-th occupation number [48].

The use of the extended DFT in these reactivity indices has two advantages: 1) the functional can be expanded over non-integer occupation numbers, and 2) in the calculation of hardness matrix elements one can use first derivatives only, cf. Eqn (41), thus reducing numerical errors.

The Strutinsky average energy component $\widetilde{E}(N)$ is considered to be varying smoothly with the electron number N (see [16] for many concrete examples and [49] for a more general account on this).

SAP produces a set of virtual excitations from the fully occupied to the unoccupied Kohn-Sham orbitals thus producing a fictitious statistical ensemble. A thermodynamic interpretation of SAP is presented in [50] (see [51, 52] as well), where two main observations are given. First, "the redistribution of single particle states in the smoothing procedure leads to

the creation of entropy". Second, "the corresponding change in energy is very small and the statistical temperature defined by $T^{-1} = \partial S/\partial E$ is very low." Nevertheless the fictitious temperature is low, it should be enough in order to smooth out the derivative discontinuities of the energy at an integer N according to the general thermodynamic argument of Gyftopoulos and Hatsopoulos [36] often used in the context of DFT [22, 23, 25].

4. Results and Discussion

The interpretation of the Kohn-Sham one-orbital energies as orbital electronegativities [47], following from Janak's expression of the ε_i's as first derivatives with respect to the occupation numbers (Eqn (4)), shows that a definition of δA through $\delta_1 A$ is physically relevant. That is why an improvement in the results for δA could be achieved only by using some approximation for the exchange-correlation potential more precise than GGA. On the contrary, the neglect of the off-diagonal elements of the hardness tensor (see below Eqs (40) and (41)) and thus of the corresponding second-order correction term in the hardness expression, leads to a disregard of the response of the i-th orbital to a change in the occupation number of the j-th orbital. In Refs [48, 53] there is given a finite-difference method for calculating the second derivatives of the energy with respect to the occupation numbers, i.e., the elements of the hardness tensor.

In refs [10, 11] we have proposed a procedure for splitting the ground-state energy of a multifermionic system into averaged and shell-correction parts in the framework of the EKS scheme. We have also shown that the first-order term of the shell-correction series yields practically identical results to that obtained through the self-consistent application of the procedure. That is why in the present paper we deal only with the first-order shell-correction term of the energy, Eqn (30), obtained through the application of Strutinsky's averaging procedure, recalled in Section 3, on the single-particle KS spectrum.

The calculation of the atomic and ionic spectra were performed through the spin-dependent KS-DFT code *deMon* [54], using for the exchange-correlation functional the form proposed by Perdew and Yue (PW GGA-I) [55] and for basis orbitals the standard DZVP basis set. The solution of the stationary condition (27) was fulfilled by minimizing the function $\delta E(\gamma, M)$ expressed by Eqs (30), (24) and (22) while maintaining the particle conservation constraint (23) determining the new Fermi level. The resulting system was solved using the package *Mathematica* [56].

In Fig. 1 there is presented the first-order shell correction of the total binding energy of atoms, cations, and anions from beryllium to calcium. As expected, the oscillating part of the energy displays minima for the atoms

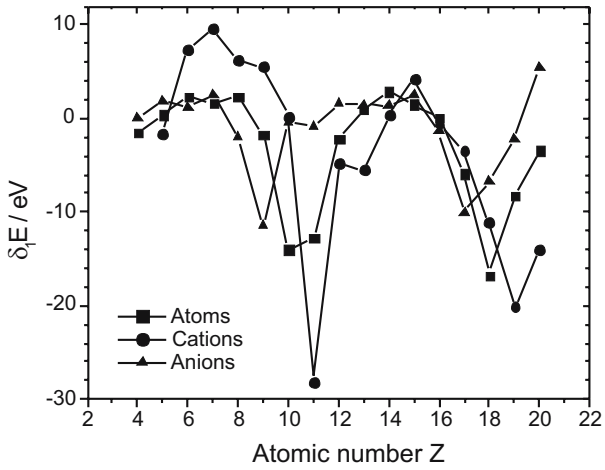

Figure 1. The first-order shell correction $\delta_1 E$ of the total binding energy of atoms (squares), cations (circles) and anions (triangles) from beryllium to calcium, as a function of the atomic number Z.

with closed shells, Ne and Ar, as well as for the corresponding isoelectronic ions, Na^+ and K^+, and F^- and Cl^-. It is also seen that the oscillations for the cations are amplified with respect to those for the atoms. This is due to the decreased screening and hence increased bonding of the electrons in cations compared to that in the isoelectronic atoms, shell effects being stronger for strongly bound systems. This latter finding is confirmed from the results for anions, for which the shell corrections are, on the opposite, smaller than for the isoelectronic atoms.

Making the difference between the results for cations and atoms and for atoms and anions we can obtain the shell-correction part of the ionization potential and electron affinity, respectively (see Eqs (9) and (10)). These results are presented in Figs 2 and 3 together with experimental data taken from [57] and [58], respectively. It is seen on Fig. 2 that the behavior of the oscillating component of the ionization potential, $\delta I \approx \delta_1 I(N)$, as a discrete function of N, closely follows the experimental variation, $I(N)$, reproducing local maxima at atoms with filled and half-filled shells. Furthermore, these singularities are enhanced in the variations of the oscillating part, confirming that the properties of these systems are determined by the valence electrons, since the SAP deals mostly with valence electrons. All this shows that the SAP applied within the KS-DFT scheme using GGA for v_{xc} allows to be extracted a component of I which contains practically all shell effects for that property.

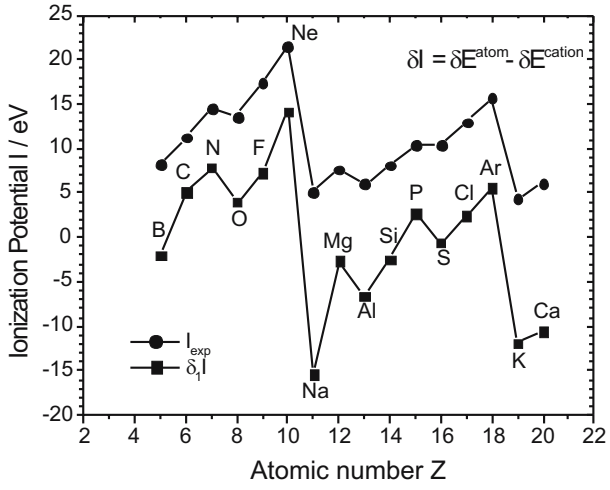

Figure 2. The shell-correction part of the ionization potential $\delta_1 I$ (squares), as a function of the atomic number Z, and experimental data for the total ionization potential I_{exp} (circles), taken from Ref. [57].

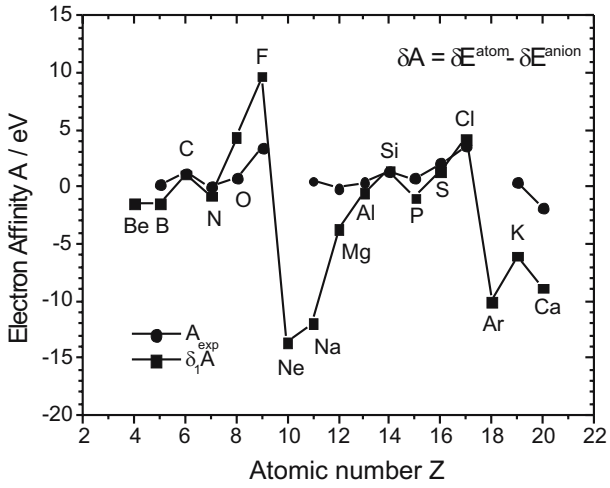

Figure 3. The shell-correction part of the electron affinity $\delta_1 A$ (squares), as a function of the atomic number Z, and experimental data for the total electron affinity A_{exp} (circles), taken from Ref. [58].

The same holds for the electron affinity, depicted in Fig. 3, where the slopes in the graphic for $\delta A \approx \delta_1 A$ have the same sign as those in the

experimental one, $A(N)$, with a single exception between Na and Mg. But since the GGA's fail to reproduce the correct long-range behavior of $v_{xc}(\vec{r})$, one could not expect a more precise estimate of the oscillating part of the electron affinities.

In Figs 4 and 5 there are given the oscillating components of the electronegativity, $\delta\chi \approx \delta_1\chi$, and chemical hardness, $\delta\eta \approx \delta_1\eta$, respectively. We observe the same trends as for the previously discussed quantities: the oscillating parts closely follow the experimental results (where available) with an amplified sensitivity to all peculiarities. The only opposite trends occur in the P-S interval for electronegativity, and O-F for chemical hardness. These imperfections in the description of shell effects in chemical hardness and electronegativity are due to their reduced occurrence in the results for electron affinity as well as to the neglect of the second-order corrections especially for chemical hardness.

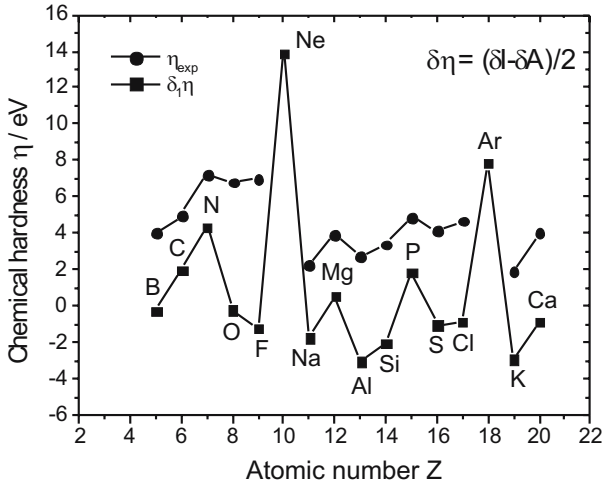

Figure 4. The shell-correction part of the chemical hardness $\delta_1\eta$ (squares), as a function of the atomic number Z, and experimental data for the total chemical hardness η_{exp} (circles), taken from Ref. [58].

5. Conclusion

Summarizing the results obtained for neutral atoms and positive and negative ions we can conclude that Strutinsky's shell-correction procedure in the EKS-DFT scheme is a helpful tool for investigating such important properties for the chemistry of atomic systems as the ionization potential,

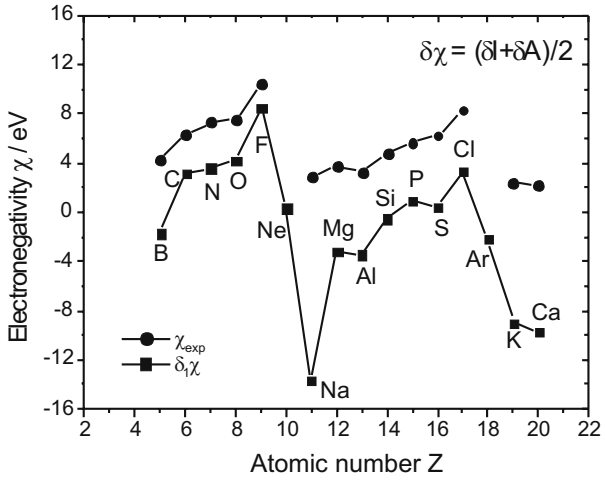

Figure 5. The shell-correction part of the electronegativity $\delta_1\chi$ (squares), as a function of the atomic number Z, and experimental data for the total electronegativity χ_{exp} (circles), taken from Ref. [58].

electron affinity, electronegativity and chemical hardness. Separated from the smooth part, the shell correction, in fact, contains all peculiarities of a given energetic property, the variations of that property being significantly amplified. Thus, the first-order shell-correction term appears to be very sensitive such variations and can serve as a "microscope" in the investigation of the properties.

Being formally a strict approach, the SAP, based on the idea that the smearing of the orbital energy spectrum of a finite system, allows to separate the effects in the energetic properties due to the shell structure of the energy level distribution. The realization of this concept leads to a consistent core-valence division of the spectrum and, in this way, of all energetic properties. Performing the presented calculations, using PW-GGA-I for exchange-correlation KS potential, we obtain that such a continuous approximation (which does not reproduce derivative discontinuity) gives a satisfactory description of δI but modest one of δA. Nevertheless, it allows to obtain an, in general, correct extraction of the shell effects in the electronegativity and chemical hardness.

DFT schemes, which allow to calculate the electron affinities of atoms are based on the exact [59, 60] and generalized (local) [61, 62] exchange self-interaction-corrected (SIC) density functionals, treating the correlation separately in some approximation. Having better asymptotic behavior than GGA's, like in the improved SIC-LSD methods, one should obtain more

precise results than the reported in this work. Nevertheless, these methods are considerably harder to be implemented in the Strutinsky scheme.

Acknowledgements

This work was partly supported by a twinning convention between Universities Pierre et Marie Curie (Paris) and Saint Kliment Ohridski (Sofia). Two of us (Ya.I.D. and A.I.K.) thank Laboratoire de Chimie Physique (UPMC and CNRS) and CMOA for financial support.

References

1. R. G. Parr, R. A. Donnelly, M. Levy and W. E. Palke, J. Chem. Phys. **68** (1978) 3801.
2. R. G. Parr and R. G. Pearson, J. Am. Chem. Soc. **105** (1983) 7512.
3. R. G. Parr and W. Yang, *Density Functional Theory of Atoms and Molecules* (Oxford University Press, New York, 1989), chapter 5.
4. F. De Proft and P. Geerlings, Chem. Rev **101** (2001) 1451.
5. K. D. Sen, P. C. Schmidt and M. C. Bohm, Struct. Bond. **66** (1987) 99.
6. P. Politzer, J. Chem. Phys. **86** (1987) 1072.
7. P. Politzer and H. Weinstein, J. Chem. Phys. **71** (1979) 4218.
8. J. Maruani, A. Khoudir and M. Tronc, Progr. Theor. Chem. Phys. **B3** (2000) 123.
9. R. G. Pearson, *Chemical Hardness* (Wiley, New York, 1997).
10. A. I. Kuleff, Ya. I. Delchev, P. Tz. Yotov, Tz. Mineva and J. Maruani, Int. J. Quantum Chem. **89** (2002) 217.
11. Ya. I. Delchev, A. I. Kuleff, Tz. Mineva, F. Zakhariev and J. Maruani, Int. J. Quantum Chem. **99** (2004) 265.
12. D. Ullmo, T. Nagano, S. Tomsovic and H. U. Baranger, Phys. Rev. B **63** (2001) 125339.
13. M. Reimann, M. Brack and K. Z. Hansen, Z. Phys. D **28** (1993) 235.
14. C. Yannouleas and U. Landman, Phys. Rev. B **51** (1995) 1902.
15. D. Bonatsos, A. I. Kuleff, J. Maruani, P. P. Raychev and P. A. Terziev, Int. J. Quantum Chem. **89** (2002) 377.
16. V. M. Strutinsky, Yad. Phys. **3** (1966) 614 [Sov. J. Nucl. Phys. **3** (1966) 449]; Nucl. Phys. A **95** (1967) 420-442; ibid. **122** (1968) 1.
17. M. Brack, J. Damgaard, A. S. Nilsen, H. S. Pauli, V. M. Strutinsky and C. Y. Wong, Rev. Mod. Phys. **44** (1973) 320.
18. M. Brack and H. C. Pauli, Nucl. Phys. A **207** (1973) 401.
19. Ya. I. Delchev, A. I. Kuleff, J. Maruani and R. L. Pavlov, Adv. Quantum Chem. **31** (1999) 53.
20. P. Hohenberg and W. Kohn, Phys. Rev. B **136** (1964) 864.
21. N. D. Mermin, Phys. Rev. **137** (1965) A1141.
22. J. P. Perdew, R. G. Parr, M. Levy and J. L. Balduz, Phys. Rev. Lett. **49** (1982) 1691.
23. J. P. Perdew, in *Density-Functional Methods in Physics*, vol. 123 of NATO Advanced Study Institute, Series B, R. M. Diezler and J. da Providencia (Eds) (Plenum, New York, 1985).
24. M. Levy, Proc. Natl. Acad. Sci. USA **76** (1972) 6062.
25. F. E. Zahariev and Y. A. Wang, Phys. Rev. A **70** (2004) 042503.
26. E. K. U. Gross, L. N. Oliveira and W. Kohn, Phys. Rev. A **37** (1988) 2805; *idem* 2809; *idem* 2821.
27. R. M. Dreizler and E. K. U. Gross, *Density Functional Theory* (Springer-Verlag, Berlin, 1990).

28. F. J. Janak, Phys. Rev. B **18** (1978) 7165.
29. J. P. Perdew and M. Levy, Phys. Rev. B **56** (1997) 16021.
30. C.-O. Almbladh and U. von Barth, Phys. Rev. B **31** (1985) 3231.
31. J. P. Perdew and M. Levy, Phys. Rev. Lett. **51** (1983) 1884.
32. I. Lindgren and S. Salomonson, Phys. Rev. A **67** (2003) 56501; I. Lindgren and S. Salomonson, Adv. Quantum Chem. **43** (2003) 95.
33. S. Liu and R. G. Parr, Phys. Rev. A **53** (1996) 2211; S. Liu and R. G. Parr, *ibid.* **55** (1997) 1792; N. H. March, *ibid.* **56** (1997) 1025; R. G. Parr and S. Liu, Chem. Phys. Lett. **276** (1997) 164; S. Liu and R. G. Parr, *ibid.* **278** (1997) 341; R. G. Parr and S. Liu, *ibid.* **280** (1997) 159.
34. T. T. Nguyen-Dang, R. F. W. Bader and H. Essen, Int. J. Quantum Chem. **22** (1982) 1049; D. Bergmann and J. Hinze, in *Electronegativity, Structure and Bonding*, Vol. 66, K. D. Sen and C. K. Jorgensen (eds) (Springer-Verlag, Berlin, 1987), p. 145.
35. M. Levy, J. P. Perdew and V. Sahni, Phys. Rev. A **30** (1984) 2745.
36. E. P. Gyftopoulos and G. N. Hatsopoulos, Proc. Natl. Acad. Sci. U.S.A. **60** (1968) 786.
37. R. S. Mulliken, J. Chem. Phys. **2** (1934) 782.
38. R. G. Parr and L. J. Bartolotti, J. Phys. Chem. **87** (1983) 2810.
39. R. T. Sanderson, Science **121** (1955) 207.
40. R. T. Sanderson, *Polar Covalence* (Academic Press, New York, 1983).
41. R. G. Pearson, J. Am. Chem. Soc. **85** (1963) 3533.
42. P. K. Chattaraj, P. K. Lee, and R. G. Parr, J. Am. Chem. Soc. **113** (1991) 1855.
43. R. G. Parr and P. K. Chattaraj, J. Am. Chem. Soc. **113** (1991) 1854.
44. P. Geerlings and F. De Proft, Int. J. Mol. Sci. **3** (2002) 276.
45. P. Geerlings and F. De Proft, Int. J. Quant. Chem. **80** (2000) 227.
46. W. Kohn and L. S. Sham, Phys. Rev. A **140** (1965) 1133.
47. G. H. Liu and R. G. Parr, J. Am. Chem. Soc. **117** (1995) 3179.
48. N. Neshev and T. Mineva, in *Metal-Ligand Interactions: Structure and Reactivity*, N. Russo and D. R. Salahub (eds) (Kluwer, Dordrecht, 1996) pp. 361.
49. K. Pomorski, arXiv:nucl-th/0403082 v1 (2004).
50. M. Rajasekaran, D. Caleb Chanthi Raj, R. Premanand and V. Devanathan, Phys. Rev. **41** (1990) 394.
51. C. Yannouleas and U. Landman, Phys. Rev. Lett. **78** (1997) 1424.
52. M. Brack and P. Quentin, Nucl. Phys. A **361** (1981) 35.
53. T. Mineva, N. Neshev, N. Russo, E. Sicilia, and M. Toscano, Adv. Quantum Chem. **33** (1999) 273; T. Mineva, N. Russo and E. Sicilia, J. Am. Chem. Soc. **120** (1998) 9053.
54. A. St-Amant and D. R. Salahub, Chem. Phys. Lett. **169** (1990) 387; KS-DFT deMon package (version 3.5): M. E. Casida, C. Daul, A. Goursot, A. Koester, L. G. M. Pettersson, E. Proynov, A. St-Amant, and D. R. Salahub are principal authors; S. Chrétien, H. Duarte, N. Godbout, J. Guan, C. Jamorski, M. Leboeuf, V. Malkin, O. Malkina, M. Nyberg, L. Pedocchi, F. Sim and A. Vela are contributing authors (deMon Software, Montreal, 1998).
55. J. P. Perdew, Phys. Rev. B **33** (1986) 8822; J. P. Perdew and W. Yue, Phys. Rev. B **33** (1986) 8800.
56. For information about this package, see http://www.wolfram.com.
57. C. E. Moore, Nat. Stand. Ref. Data Ser., Nat. Bur. Stand. (U.S.) **34** (1970).
58. R. G. Pearson, Inorg. Chem. **27** (1988) 734.
59. S. Baroni and E. Tuncel, J. Chem. Phys. **79** (1983) 6140.
60. S. Baroni, J. Chem. Phys. **80** (1984) 5703.
61. S. Manoli and M. A. Whitehead, Phys. Rev. A **34** (1986) 4629.
62. Y. Guo, S. Manoli and M. A. Whitehead, Phys. Rev. A **38** (1988) 1120.

GENERALIZED DIABATIC STUDY OF ETHYLENE "ISOMERISM"

O. TAPIA

Department of Physical Chemistry, Uppsala University, Box 579, 75123 Uppsala, Sweden

& Department of Physical Chemistry, Valencia University, Burjassot, Spain

AND

V. POLO AND J. ANDRES

Department of Experimental Sciences, Jaume I University, Box 224, 12080 Castelló, Spain

Abstract. The generalized electronic diabatic (GED) approach is used to study a cis-trans isomerization process. At variance with standard Born-Oppenheimer approach, where a unique adiabatic potential energy function depending of a dihedral angle connects both isomers, a configuration interaction model permits describing isomerization process with four diabatic electronic states. These GED states form a minimal CI space; each state conserves local symmetry properties along a properly defined reaction coordinate. The diabatic states diagonalize the Coulomb Hamiltonian. The state mixing obtains via kinematic couplings, electron-phonon and spin-orbit operators. The process is mapped to a full quantum mechanical linear superposition of diabatic states.

1. Introduction

Ethylene electronic isomerism is introduced as a new concept and examined from the perspective of the generalized electronic diabatic (GED) scheme. In chemistry isomerism is related to distributions in space of atomic nucleus in one and the same adiabatic potential energy surface. Therefore, in this case cis and trans isomers would be indistinguishable when the four hydrogen atoms are identical. Nevertheless, in this paper we show that isomerism is an electronic

J.-P. Julien et al. (eds.),
Recent Advances in the Theory of Chemical and Physical Systems, 177–196.

chattel, where cis and trans are different diabatic electronic base states clearly distinguishable via nodal plane properties.

To accomplish the action, it is necessary to use an approach going beyond the standard Born-Oppenheimer (BO) model [1,2]. This one is the GED scheme that is capable to yield a rigorous mapping between the algorithmic approach in mixed real/Hilbert space and exact molecular quantum mechanics in full Hilbert space. This model has been constructed and reported in previous publications [3-9]. The key to it stands on a careful separation from the exact quantum mech-anical electro-nuclear description of the electronic Hilbert space and a model of a mass-less positive charge background in real space that is mapped to the nuc-lear charges. While quantum state wavefunctions of the global system are not separable, molecular base states can be separable, each base state being direct products of diabatic electronic and nuclear base states. These base functions are used to represent quantum states as linear superpositions. These aspects are ex-amined in sections 2 and 3 where a summary of the fundamental ideas and new ideas on the formalism is presented.

Real space algorithms (section 4) allow for mappings between present day computer programs and strict molecular quantum mechanics [10,11]. It is the separability of base molecular states that permits characterizing molecular states in electronic Hilbert space and molecular species in real space. This feature eliminates one of the shortcomings of the standard BO scheme [6,7,12]. Confining and asymptotic GED states are introduced. In section 5 the concept of conformation states in electronic Hilbert space is qualitatively presented.

Isomerization in ethylene is used to illustrate the ideas. This example is not a theoretical toy. In fact, it helps understanding the reactivity correlated to the electronic quantum mechanical cis-trans isomerization. The varied chemistry and physical chemistry of diene fragments is highlighted in a new quantum mechanical perspective. It is shown that isomerism (conformational change) can be seen as a pure electronic process. Inclusion of the massless positive background leads to diabatic potential energy hypersurfaces and localization. The attractor in real space leads to the chemical concept of rigid molecular structure; reintroducing atomic masses a standard vibration analysis can be implemented.

In section 6, chemical reactivity of ethylene-like species is discussed. A post-BO scheme recently proposed by us [11] is presented and used to examine the conformational change process. A check to the general properties discussed here is presented in section 7. In section 8 connections to the standard diabatic and adiabatic methods are examined. Section 9 presents a general discussion.

2. Basic state quantum mechanics

The concept of quantum states is the basic element of quantum mechanics; the set of quantum states $\{|\Psi>\}$ and the field of complex numbers, C, define a Hilbert space as being a linear vector space; the mapping $<\Psi|\Psi>$ introduces the dual conjugate space (bra-space) to the ket-space; the number $C(\Psi)=<\Psi|\Psi>$ is a

functional of the quantum state; in the projective space used in quantum mechanics; $C(\Psi)=1$ [13]. The infinite variety of quantum states is elicited with a complete set of denumerable orthonormal quantum states $\{|jk\rangle\}$, j and k being integers. The complex number amplitudes $\langle jk|\Psi\rangle = C_{jk}(\Psi)$ are "direction cosines" of the quantum state in the complete base set.

Special relativity space-time inertial frames are used. A real arbitrary space vector **x** relates to base states $|\mathbf{x}\rangle$ in a rigged Hilbert space [14]; this is invariant to an origin displacement of the inertial frame, i.e. $T_{\mathbf{a}}|\mathbf{x}\rangle = |\mathbf{x}+\mathbf{a}\rangle$, the operator $T_{\mathbf{a}}$ is unitary. Using the reciprocal space **k**, one gets $T_{\mathbf{a}} = \exp(-i\mathbf{k}\cdot\mathbf{a})$ and $\langle\mathbf{x}+\mathbf{a}|\mathbf{x}+\mathbf{a}\rangle = \langle \mathbf{x}|T_{\mathbf{a}}^{\dagger}T_{\mathbf{a}}|\mathbf{x}\rangle = \langle\mathbf{x}|\mathbf{x}\rangle$; the symbol † stands for transpose complex conjugation. The projection in configuration space is $|\Psi\rangle \leftrightarrow \int d\mathbf{x}\ |\mathbf{x}\rangle\langle\mathbf{x}|\Psi\rangle$. The symbol $\leftrightarrow$ is used to emphasize the difference in nature of the selected spaces. The direction cosine along the axis $|\mathbf{x}\rangle$ is the wave function $\langle\mathbf{x}|\Psi\rangle \equiv \Psi(\mathbf{x})$, i.e. a mathematical function with a domain covering all the configuration space **x** referred to a fixed (inertial) I-frame; the I-frame belongs to <u>real space</u>. Comparisons between I-frames permit a natural introduction of classical physics concepts when appropriate. A reference to a particle model is not done here. Using now the denumerable base set, the quantum state is given by:

$$|\Psi\rangle <\!\!-\!\!> \int d\mathbf{x}\ |\mathbf{x}\rangle \Sigma_{jk}\, \Phi_{jk}(\mathbf{x})C_{jk}(\Psi) = \int d\mathbf{x}\ |\mathbf{x}\rangle\langle\mathbf{x}|\Psi\rangle. \qquad (1)$$

From eq. (1), eq. (2) trivially follows:

$$\langle\mathbf{x}|\Psi\rangle \equiv \Psi(\mathbf{x}) = \Sigma_{jk}\, \Phi_{jk}(\mathbf{x})C_{jk}(\Psi) = (C_{10}(\Psi)\ldots C_{jk}(\Psi)\ldots)\cdot[\Phi_{10}(\mathbf{x})\ldots\Phi_{jk}(\mathbf{x})\ldots] \quad (2)$$

The column vector is indicated by square brackets, a row vector by round brackets. The quantum numbers may be determined by the complete set of hermitian operators commuting with the generator of time evolution. Invariance of the quantum state to frame rotation, origin displacement, parity and other symmetry operations determine quantum numbers for the corresponding irreducible representations. Frame related symmetry operations translate into unitary operator acting on Hilbert space (rigged), e.g. $T_{\mathbf{a}}$.

Once the base states are found for a given material system (to be defined later on), it is the quantum state that is susceptible of (laboratory) preparation, manipulation and/or measurement.

From eq. (1) follows that picking up the wave function only at one point does not make sense; it has to be defined in a neighborhood to such a point; it is by adding the products of the measure $d\mathbf{x}$ and $\Psi(\mathbf{x})$ that produce a "portrait" of the corresponding quantum state. Given a set $\{C_{jk}(\Psi)\}$, this fully determines the quantum state $|\Psi\rangle$ in the corresponding basis set. Contemporary computing techniques can be adapted to take advantage of this property and generate more or less definite portraits of specific quantum states.

Because the base states are time independent, any change of the physical state of the system in time $|\Psi,t\rangle$ is elicited by variation of amplitudes C_{jk} from, say, $(C_{10}(\Psi,t_o)\ldots C_{jk}(\Psi,t_o)\ldots)$ to a new set $(C_{10}(\Psi,t)\ldots C_{jk}(\Psi,t)\ldots)$.

An eigenstate corresponds to a row vector with zero amplitude everywhere except at the base state function that is the case. It is then defined in Hilbert space and does not stand for an individual "molecular" state. The corresponding base state cannot be a dynamically unstable state as it is time independent. This is an important difference with standard approaches [15].

Time evolution in Hilbert space is done by a unitary operator $U(t,t_o)$. The corresponding generator of the unitary transformation is a total Hamiltonian $\mathtt{H}$. Henceforward, $h/2\pi=1$; h is Planck's constant. The operator $U(t,t_o)$ fulfils the differential equation: $-i\partial U(t,t_o)/\partial t = \mathtt{H}U(t,t_o)$ [16]. A quantum state prepared at time t_o, say $|t_o\rangle$, is propagated in time as usual: $U(t,t_o)|t_o\rangle = |t\rangle$.

The time-dependent Schrödinger (3), relates Hamiltonian and quantum states in a unique manner:

$$i\,\partial\langle \mathbf{x}|\Psi,t\rangle/\partial t = \mathtt{H}(\mathbf{x})\langle \mathbf{x}\,|\Psi,t\rangle \tag{3}$$

Observe that eq. (3) engenders a true change so long $\mathtt{H}(\mathbf{x})$ is the generator of time translations; i.e. a change in the direction cosines can be experimentally detectable as for instance in a pump-probe experiment or in electron photodetachments measurements.

For an isolated system, $\mathtt{H}(\mathbf{x})$ is time independent, eq. (3) is separated as usual leading to the time independent equation: $\mathtt{H}(\mathbf{x}) < \mathbf{x}| \Phi\rangle = E < \mathbf{x}\,|\Phi\rangle$. The structure of $\mathtt{H}$ is not known in detail. So far, it is just a symbol, but if this is a hermitian and self-adjoint operator, there exists a complete denumerable set of eigenfunctions.

Let us focus on molecular systems for which we know molecular Hamiltonian models, $H(\mathbf{q},\mathbf{Q})$. Electronic and nuclear configuration coordinates are designated with the vectors $\mathbf{q}$ and $\mathbf{Q}$, respectively; $\mathbf{x} = (\mathbf{q},\mathbf{Q}) = (\mathbf{q}_1,\ldots, \mathbf{q}_n, \mathbf{Q}_1,\ldots, \mathbf{Q}_m$. For an n-electron system, $\mathbf{q}$ has dimension 3n; $\mathbf{Q}$ has dimension 3m for an m-nuclei system. The wave function is the projection in configuration space of a particular abstract quantum state, namely $\Psi(\mathbf{x}) \rightarrow \Psi(\mathbf{q},\mathbf{Q})$, and base state functions $\Omega_{jk}(\mathbf{q},\mathbf{Q})$ with two quantum labels, nothing more. This implies a first-level separability when the first label refers to an electronic state and the second to nuclear base function subsidiary to the electronic one. This statement represents the crux of the ansatz proposed by Born and Oppenheimer; the nuclear parametric dependence of the electronic base function is a second-level separability hierarchy.

In rigorous quantum mechanics, something like an electronic base function parametrically dependent on nuclear configuration space cannot be. Such dependence would imply that the electronic quantum number of the base function depends upon the particular selected region of nuclear configuration space.

The proof comes with the scrutiny of the exact electro-nuclear base function $\Omega_{jk}(\mathbf{q},\mathbf{Q})$. We assume the existence of eq. (4) exists because $H(\mathbf{q},\mathbf{Q})$ is self-adjoint:

$$H(\mathbf{q},\mathbf{Q})\Omega_{jk}(\mathbf{q},\mathbf{Q}) = E_{jk}\Omega_{jk}(\mathbf{q},\mathbf{Q}) \tag{4}$$

The equation is defined in an I-frame and no rotation and translation base states are present yet; these latter appear after translating the origin to an I-frame in uniform motion with (classical) velocity **v**, a **v**-frame. This aspect is not examined in this paper; but observe that global angular momentum of the system is described with the invariances to rotation of the **v**-frame and will apply to all internal electronuclear state of the I-frame [10].

The important result is that an electronic quantum number doesn't depend at all on the domain of **Q** that we might have selected to look at; equation (4) is valid for all **Q**-values; the quantum number results from boundary conditions and general frame-invariance.

3. Molecular quantum mechanics

Consider the extreme case where H is diagonal in the base set $\{\Omega_{jk}(\mathbf{q},\mathbf{Q})\}$. Accordingly, in absence of external fields, no time evolution is to be expected except for changes in time-phases. But, by hypothesis, we took H to be the generator of time displacement in Hilbert space. Such a situation is not useful in molecular physics because one search after a Hamiltonian that is able to generate the time evolution. This suggests the idea that the time generator $\mathtt{H}$ of interest contains two classes of operators: $\mathtt{H} = \mathtt{H}_o + V$. The Hamiltonian $\mathtt{H}_o$ is assumed to generate a complete set of molecular base states. The operator V would couple the base states of $\mathtt{H}_o$. It is the intermediate base set that has a meaning in interpreting the base states as molecular base states.

The $\mathtt{H}_o$ operator is mapped on to the well-known molecular Hamiltonian $H(\mathbf{q},\mathbf{Q})$ because this one can be rigorously diagonalized in a particular separable base state set [7,12], cf. eq. (4). We briefly review this point. Now, we write:

$$\mathtt{H}(\mathbf{q},\mathbf{Q}) = \mathtt{H}_o(\mathbf{q},\mathbf{Q}) + V(\mathbf{q},\mathbf{Q}) = H(\mathbf{q},\mathbf{Q}) + V(\mathbf{q},\mathbf{Q}) \tag{5}$$

The symbol $V(\mathbf{q},\mathbf{Q})$ stands for a kinematic operator containing spin-orbit terms, electron-phonon couplings and, eventually, a coupling to external fields. The molecular Hamiltonian is given by:

$$H(\mathbf{q},\mathbf{Q}) = K_N(\mathbf{Q}) + H_C(\mathbf{q},\mathbf{Q}) = K_N(\mathbf{Q}) + K_e(\mathbf{q}) + V_C(\mathbf{q},\mathbf{Q}) \tag{6}$$

$K_N(\mathbf{Q})$ and $K_e(\mathbf{q})$ are the kinetic energy operators for m-nuclei and n-electrons. The operator $V_C(\mathbf{q},\mathbf{Q})$ represents the total Coulomb interaction: electron-electron (V_{ee}), electron-nuclei (V_{eN}) and nuclei-nuclei (V_{NN}).

In principle, the time evolution of a particular linear superposition on the molecular base states will reflect a chemical process via the changes shown by the amplitudes. This represents a complete quantum mechanical representation of the chemical processes in Hilbert space. The problem is that the separability cannot be achieved in a complete and exact manner. One way to introduce a model that is able to keep as much as possible of the linear superposition principle is to use generalized electronic diabatic base functions.

Separability between electronic and nuclear states is fundamental to get a description in terms of a hierarchy of electronic and subsidiary nuclear quantum numbers. Physical quantum states, i.e. wavefunctions $\Phi(\mathbf{q},\mathbf{Q})$, are non-separable. On the contrary, there is a special base set of functions $\{\Psi_{jk}(\mathbf{q},\mathbf{Q})\}$ that can be separable in a well defined mode, and used to represent quantum states as linear superpositions over the base of separable molecular states. For the electronic part, the symmetric group offers a way to assign quantum numbers in terms of irreducible representations [17]. Space base functions can hence be either symmetric or anti-symmetric to odd label permutations. The spin part can be treated in a similar fashion [17]. The concept of molecular species can be introduced; this is done at a later stage [10]. Molecular states and molecular species are not the same things. The latter belong to classical chemistry, the former are base function in molecular Hilbert space.

For the electro-nuclear model, it is the charge the only homogeneous element between electron and nuclear states. The electronic part corresponds to fermion states, each one represented by a 2-spinor and a space part. Thus, it has always been natural to use the Coulomb Hamiltonian $H_C(\mathbf{q},\mathbf{Q})$ as an entity to work with. The operator includes the electronic kinetic energy (K_e) and all electrostatic interaction operators ($V_{ee} + V_{eN} + V_{NN}$). In fact this is a key operator for describing molecular physics events [1-3]. Let us consider the electronic space problem first; exact solutions exist for this problem; the wavefunctions are defined as $\psi(\mathbf{q})$; do not mix up these functions with the previous electro-nuclear wavefunctions. At this level, H_C and **S** (total electronic spin operator) commute; the spin operator appears in the kinematic operator V and H commute with the total angular momentum **J**=**L**+**S** in the I-frame; **L** is the total orbital angular momentum, the system is referred to a unique origin.

Define the functional $U(\mathbf{Q};[\psi])=\langle\psi(\mathbf{q})|H_C(\mathbf{q},\mathbf{Q})|\psi(\mathbf{q})\rangle_{\mathbf{q}}$; integration over the electronic configuration space is indicated as a sub-index. The variational principle applied [6] to the (spin-free) function space $\psi(\mathbf{q})$ leads to the Euler-Lagrange equation:

$$H_C(\mathbf{q},\mathbf{Q})\ \psi(\mathbf{q})= E(\mathbf{Q})\ \psi(\mathbf{q}) \qquad (7)$$

Observe that eq. (7) is fundamentally different from eq. (4). Albeit, for a self-adjoint $H_C(\mathbf{q},\mathbf{Q})$, Kato's theorem ensures existence of a complete set of base functions, $\{\phi_j(\mathbf{q})\}$ [18]. Thus, $E_i(\mathbf{Q}) \equiv U(\mathbf{Q};[\phi_j])$. The number and type of nodal planes, permutation properties, parity and general topologic properties characterize the diabatic base functions. The wavefunctions here are not defined as in the standard BO approach; they are independent from the nuclear configuration space. It is the energy $E(\mathbf{Q})$ that depends upon such coordinates. Note that such an equation is not an eigenvalue equation it only has the form. Given a nuclear configuration domain, the energy ordering $E_i(\mathbf{Q})$ may differ from one point to another; nevertheless, the nature of the electronic base function is an invariant. This is a key point to understand the role of GED functions would play in electronic structure studies. Longuet-Higgins and Herzberg-Teller proposed an approach based on one fixed $\mathbf{Q}^o$ point [19,20]. They did not hint at the completeness of the base shown by us. We retain, however, this one-point hypothesis and consequently the complete electronic spectrum is determined from one and only one fixed electronic Hamiltonian. The algorithm now consider any excited state $E_i(\mathbf{Q}^o)$ and calculate the nearest stationary point by following the steepest descent path in $\mathbf{Q}$-space; if there is one, we name it as $E_i(\mathbf{Q}^j)$. In principle, this procedure must be carry on for all energies $E_k(\mathbf{Q}^o)$.

The problem still is to finding a complete set of solutions to the molecular Hamiltonian H that contains nuclear kinetic energy operators:

$$H(\mathbf{q},\mathbf{Q})\,\Phi(\mathbf{q},\mathbf{Q}) = (H_C(\mathbf{q},\mathbf{Q}) + K_N(\mathbf{Q}))\,\Phi(\mathbf{q},\mathbf{Q}) = E\,\Phi(\mathbf{q},\mathbf{Q}) \tag{8}$$

Constructing a linearly independent set of factored functions solves the problem in the sense that eq. (8) is diagonal. The diabatic potential is used to define equations for the nuclear wavefunctions leading to a product set $\{\phi_k(\mathbf{q})\zeta_{km}(\mathbf{Q})\}$ by solving for each electronic diabatic potential the corresponding equation (9):

$$\{K_N + U(\mathbf{Q};[\phi_k]) - E_{km}\}\zeta_{km}(\mathbf{Q}) = 0 \tag{9}$$

The problem with these equations is that they correspond to infinite different Hamiltonians so that the solutions for different electronic quantum numbers are incommensurate. To do away with these objections, use instead the complete set of functions rendering the kinetic energy operator K_N diagonal. The set, within normalization factors, is $\{f_{\mathbf{k}}(\mathbf{Q}) \approx \exp(i\mathbf{k}\bullet\mathbf{Q})\}$; $\mathbf{k}$ is a vector in nuclear reciprocal space. Including the system in a box of volume $\mathcal{V}$, the reciprocal vectors are discrete, k_i, and the functions $f_i(\mathbf{Q}) = (1/\sqrt{\mathcal{V}})\exp(i\mathbf{k}_i\bullet\mathbf{Q})$ form an orthonormal set with the completeness relation $\delta(\mathbf{Q}-\mathbf{Q}') = \Sigma_i\, f_i(\mathbf{Q})\, f_i(\mathbf{Q}')$. The direct product set $\{\phi_j(\mathbf{q})f_{ki}(\mathbf{Q})\}$ is complete. The matrix elements of eq. (8) reads:

$$\begin{aligned}&\langle\phi_j(\mathbf{q})f_{\mathbf{k}'}(\mathbf{Q})|(H_C(\mathbf{q},\mathbf{Q})+K_N(\mathbf{Q}))|\phi_g(\mathbf{q})f_{\mathbf{k}}(\mathbf{Q})\rangle = \\ &\qquad\qquad \langle f_{\mathbf{k}'}(\mathbf{Q})|(K_N+U(\mathbf{Q};[\phi_j])|f_{\mathbf{k}}(\mathbf{Q})\rangle\delta_{jg}\end{aligned} \tag{10}$$

Eq. (10) is block diagonalized as a function of an electronic quantum number, δ_{jg} (Kronecker symbol) factor. Equations (9) and (10) are related. These equations for each electronic subspace differ only by a local linear transformation, then, one may write:

$$\zeta_{jm}(\mathbf{Q}) = \Sigma_{k'} A_{k'}(\zeta_{jm}) f_{\mathbf{k}'}(\mathbf{Q}) \tag{11}$$

The coefficients $A_{k'}(\zeta_{jm})$ are fixed for each jm-index. And, as it is implied by eq. (10), the connection between different electronic states is absent.

The $\{\phi_j(\mathbf{q})\zeta_{jm}(\mathbf{Q})\}$ is a set of linearly independent functions; the $\zeta_{jm}(\mathbf{Q})$ functions are not orthogonal in **Q**-space for arbitrary electronic states; the overlap integrals $\int d^{3m}\mathbf{Q}\ \zeta_{jm}(\mathbf{Q})\ \zeta_{j'm'}(\mathbf{Q})$ are the well known Franck-Condon factors. The hypothesis is that an arbitrary quantum molecular state is given by the linear superposition jus as in the general case:

$$\Gamma(\mathbf{q},\mathbf{Q},t) = \Sigma_{jm} C_{jm}(\Gamma,t)\ \phi_j(\mathbf{q})\zeta_{jm}(\mathbf{Q}) \tag{12}$$

The caveat is that integration over electronic configuration space is performed first. Any physical base quantum state with respect to the Coulomb Hamiltonian is a robust species. Observe that no structural features are implied yet. Thus, separability via electronic quantum numbers is achieved although the general quantum states $\{\Gamma(\mathbf{q},\mathbf{Q},t)\}$ are not separable.

As a consequence of eq. (10), the molecular Hamiltonian H cannot by itself be a generator of time evolution in Hilbert space, for this reason it was assigned to H_o in eq. (5).

Consider now the equality $H_{oj'm',jm}=<\zeta_{\mathbf{j'm'}}(\mathbf{Q})|(K_N+U(\mathbf{Q};[\phi_j])|\ \zeta_{\mathbf{jm}}(\mathbf{Q})>\delta_{j'j}$. Thus, in this model, preparing the system in the ground state of the Coulomb Hamiltonian, no time evolution can be expected if we do not switch on the kinematic couplings. We take a simple case where the electron-phonon coupling is on. The matrix elements of H in this base set look like:

$$\{\int dQ\ \zeta^*_{j'm'}(\mathbf{Q})\ \{(K_N+ U(\mathbf{Q};[\phi_j]))\ \delta_{jk'}+ <\phi_{j'}|V_{e\otimes ph}(\mathbf{q},\mathbf{Q})|\phi_j>_{\mathbf{q}}\}\zeta_{km}(\mathbf{Q})\}= H_{o\ j'm',jm}\ \delta_{jj'}\ \ \delta_{mm'}+ V_{e\otimes ph\ j'm',jm} \tag{13}$$

The time evolution operator propagates an arbitrary quantum state thanks to the non-zero matrix elements $(V_{e\otimes ph})_{j'm',jm}$. The set $\{\phi_j(\mathbf{q})\zeta_{jm}(\mathbf{Q})\}$ has all electronic base states corresponding to all possible chemical species in the sense discussed above only because the generalized electronic diabatic set is complete.

The amplitudes integrated in time and general V reinstated read:

$$C_{jk}(\Gamma,t) = \Sigma_{j'k'} C_{j'k'}(\Gamma,t_o)\ \delta_{j',j}\ \delta_{k',k} - i\Sigma_{j'k'} \int_{to}^{t} dt'\ C_{j'k'}(\Gamma,t_o)V_{j'k',jk}(t') + i^2\ \Sigma_{j'k'}\ \Sigma_{j''k''} \int_{t'}^{t} dt' \int_{to}^{t'} dt''\ C_{j'k'}(\Gamma,t_o)\ V_{j'k',j''k''}(t')V_{j''k'',jk}(t'') - \ldots \tag{14}$$

The amplitude $C_{jk}(\Gamma,t)$ is the one multiplying the fixed base state $\phi_j(\mathbf{q})\zeta_{jk}(\mathbf{Q})$. The relative simplicity of this type of equation is due to the fact that the base set ordering is maintained fixed and all changes are performed on the space of amplitudes; it is the quantum state that is changing. The energy spectra appears explicitly because the operators in the interaction representation are given by $V(t) = \exp(iH_o t)V\exp(-iH_o t)$ in atomic units. Furthermore, contributions to the $C_{jk}(\Gamma,t)$ amplitude can only originate from those base states found in the initial quantum state with amplitudes different from zero if no measurement is effected on the system in the time gap $t\text{-}t_o$. In this case, measuring the complete set $\{C_{jk}(\Gamma,t)\}$ at time t would provide a determination of the initial state, $\{C_{j'k'}(\Gamma,t_o)\}$. An amplitude different from zero at time t_o opens a possibility for the model sys-tem to respond under the perturbing source reflected by the operator V. Note that possibility has nothing to do with probability. The kinematic operator V effects the linear superposition of molecular quantum states.

The difficulty eq. (14) may put to a chemist is that the amplitude's time dependence is given in a closed form; integration over the whole electronic and nuclear configuration space must be carried out [10-12].

Albeit a number of conclusions can be gained from parity considerations, chemistry is described in terms of real space variables and particle ideology. Reaction coordinate, molecular species, molecular structure and properties are to be related to the present approach. This cannot be made rigorously because quantum mechanics is about quantum states and not objects in real space. This confusion has been fatal to a correct understanding of molecular phenomena in spite of the effort made by Primas [15].

A manner to do away with the problem is to introduce appropriate algorithms in the sense that mappings from real space to Hilbert space can be defined. The generalized electronic diabatic, GED approach fulfils this constraint while the BO scheme as given by Meyer [2] does not due to an early introduction of center-of-mass coordinates and rotating frame. The standard BO takes a typical molecule as an object description. Similarly, the wave function is taken to describe the electrons and nuclei. Thus, the adiabatic picture follows. The electrons instantaneously follow the position of the nuclei. This picture requires the system to be always in the ground state.

We summarize below the GED approach. The reader may sense the difference.

4. Real-space algorithms

The diabatic potential-energy hypersurfaces $U(\mathbf{Q};[\phi_j])$ are of use to examine the energy reshuffling in neighborhoods of a crossing point $\mathbf{Q}\#$, where $U(\mathbf{Q}\#;[\phi_j]) = U(\mathbf{Q}\#;[\phi_{j'}])$. This may look like a conic intersection but it should not be confused with that; the domain where this condition holds can be named a seam as it is common practice in the adiabatic scheme, see vol.127 of Faraday Discussions

[21]; the crux of the matter is the degeneracy involved at crossings. The contributions to $H_{j'm',jm}$ would then be determined by such neighborhoods. For a quantum state having $C_{j'm'}(t_o)\neq 0$ and $C_{jm}(t_o)=0$, equation (14) tells that $C_{jm}(t)$ will become different from zero if some matrix element $V_{j'm',jm}$ is different from zero. The integral responsible for the process will be peaked in the region around the intersection as defined here. We see the mapping $U(\mathbf{Q};[\phi_j])$ may induce structural-like features onto the nuclear configuration space.

The construction of pictures leading to structural appearance requires a mapping assigning some physical meaning to the nuclear configuration space. Up till now, this space sustains the nuclear electronic wave function only; some hints concerning structural features have been elicited via the diabatic potential energy hypersurface and asymptotic Hamiltonians. The point is the calculation of the positive source (nuclear) dynamics using numerical methods in real space.

Confining and asymptotic GED states: A hint at molecular structure. The change from a configuration space where the nuclear wave function is defined to a special role as the positive source (nuclear) configuration space **Q** in eq. (7), is achieved by an isometry mapping; the distances are invariant but the ideology is changed.

The isometry mapping helps describing classes of diabatic base functions with diabatic potential energy hypersurface $U(\mathbf{Q};[\phi_j])$. The properties of confinement and asymptotic states induce a picture of nuclear charges as if they could be seen in real 3D space, each one of them. A diabatic electronic state may embody an attractor towards the positive charge background. This attractor in real space would permit defining one fixed point at which the gradient of $U(\mathbf{Q};[\phi_j])$ is zero along any direction. This is the nearest one can get to the structure concept without lose a rigorous QM basis.

To emphasize the nature of the algorithm, and avoid misunderstandings, the vector **Q** is replaced by the symbol $\boldsymbol{\xi}=(\xi_1,\xi_2,\ldots,\xi_m)$ representing a set of positive charges in real space. The methodology can hence be applied to nanosystems, and all sorts man-made devices such as molecular meccanos.

The model corresponds to a quantum electronic system interacting with a PCB, represented by a charge vector $\mathbf{Z} = (z_1,\ldots z_m)$, mass $\mathbf{M} = (M_1,\ldots M_m)$ and nuclear spin $\mathbf{I}=(I_1,\ldots I_m)$.

The gradient can hence be calculated: $\partial U(\boldsymbol{\xi};[\phi_j])/\partial\boldsymbol{\xi}$. For a given confining diabatic electronic state, there is a PCB for which the gradient is zero along any direction in real space; this point is identified as $\boldsymbol{\xi}^j$. The second order tensor $G_{kk'} = \partial^2 U(\boldsymbol{\xi};[\phi_j])/\partial\boldsymbol{\xi}_k\partial\boldsymbol{\xi}_{k'}$ at $\boldsymbol{\xi}^j$ is the Hessian having all the eigenvalues positive with some of them possibly being zero (I-frame).

An attractor does not necessarily correspond to a confined state. By taking the limit where the external potential tends to zero, with zero $\boldsymbol{\xi}$–kinetic energy, equation (6) with **Q** replaced by $\boldsymbol{\xi}$ has the limit of an interacting n free-electron state system. The system does not dissociate into fragments by manipulations of the PCB. The limit is one of the free electron quantum states. This is a positive

number located above the limit of full ionization. For this reason, an attractor state has as an upper energy bound the fully ionized state; all electron states belong to the continuum.

For confined systems one can solve the quadratic approximation to eq. (9) in $\boldsymbol{\xi}$-space. All non-harmonic terms are operators acting in $\boldsymbol{\xi}$-space. The concept of molecular structure can hence be introduced at this level. The configuration $\boldsymbol{\xi}^j$ would stand as a rigid model to the confined system referred to the inertial frame used from the beginning. A change of origin can hence be performed, a center-of-mass defined for each confined electronic state. The inertial character of the frame remains; this makes a big difference with the BO scheme. The concept of topologic graph can also be used with much of its chemical flavor [6].

Once the electronic diabatic base set is obtained, the quantum state is a linear superposition where the PCB configuration enters parametrically as $C_k(\boldsymbol{\xi})$ amplitudes:

$$\Phi(\mathbf{q};\boldsymbol{\xi}) = \Sigma_k \, C_k(\boldsymbol{\xi})\phi_k(\mathbf{q}) \tag{15}$$

This is a post Born-Oppenheimer scheme. It retains the essential idea of separability but the electronic base functions are diabatic functions. These functions are obtained from one Hamiltonian operator, namely the electronic operator defined in eq. (5).

The analyses given for the set of equations (8) to (13) are valid once the isometric change of $\mathbf{Q}$ by $\boldsymbol{\xi}$ is completed. Once approximate solutions have been worked out with the algorithms (BO or GED), only the GED scheme can be reverted to an exact quantum mechanical description in terms of quantum states.

5. Ethylene conformational "isomerism"

All diabatic electronic states are described in one and the same inertial frame. Irrespectively from the point in nuclear configuration space chosen, the electronic base function for the cis "conformer" must differ from the trans "conformer" in their relative phase; this is related to the characteristic nodal planes (NPs) that define what we use to call π-orbitals. Thus, selecting cis-NP perpendicular to x-axis and trans-NP perpendicular to z-axis, the angle between the corresponding normal vectors is π/2 coinciding with standard group character tables, i.e. C_{2v} and C_{2h}, respectively [22]. By symmetry argument, the overlap between them yields zero. In Figure 1, a schematic representation is shown to help visualizing the state of affairs.

Moreover, there are two diradical states of symmetry C_s constructed on the basis of 1-electron base states. To help visualizing the analysis we use the planes associated to the CH_2 groups. At π/4 the planes defining each CH_2 sigma base states at opposite sites have normal vectors making a π/2 angle. The local π-axis serve to identify new 1-e-base states: $\gamma_1 + \gamma_2$ and $\gamma_1 - \gamma_2$. The + state has two local NPs; the minus (–) state increases the number of nodes by one unit. The

dis-rotatory displacements of hydrogen-related positive charges cannot break such symmetry in the electronic space.

Put together in one frame, the "reaction coordinate" is a dis-rotatory displacement of "local" π-base functions (π-like orbitals). These topologic properties are independent of ξ for this matter.

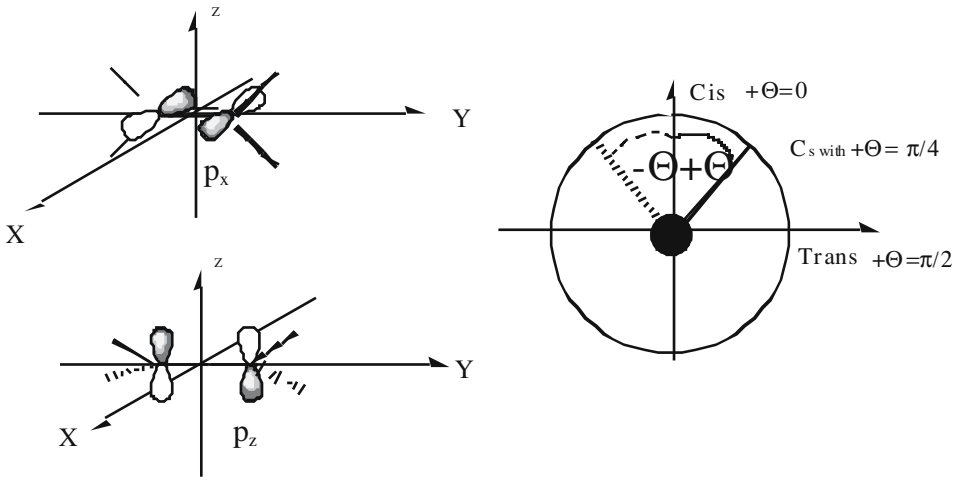

Figure 1. Schematic indication of nodal planes for cis and trans conformers in ethylene.

The key to get a diabatic electronic state is a strict constraint: i.e. keep local symmetry elements invariant. For ethylene, let us start from the cis conformer case. The nuclear geometry of the attractor must be on the (y,z)-plane according to Fig.1. The reaction coordinate must be the dis-rotatory displacement. Due to the nature of the LCAO-MO model in quantum computing chemistry, the closed shell filling of the HOMO must change into a closed shell of the LUMO beyond Θ=π/4. The symmetry of the diabatic wave function is hence respected. *Mutatis mutandis*, the trans conformer wave function before π/4 corresponds to a double filling of the LUMO; beyond the π/4 point on fills the HOMO twice. At π/4 there is the diradical singlet and triplet base wavefunctions.

Quasi-diabatic electronic calculations can be performed with any atomic basis set by controlling the symmetry elements of the wavefunction. In this work calculations were performed with Gaussian 98 [23] at the HF level, using the cc-pvtz Dunning basis set, and by means of density functional theory (DFT), under the popular B3LYP approximation for the exchange-correlation, together with three basis sets of different quality: STO-3G, 6-31++G, and the cc-pvtz. At each point geometries were optimized, for the AA-state (0-π/2) and BB-state (π/2-π). Upper energy curves were calculated with controlled occupancy and not self-consistently. Closed shell calculations (AA and BB curves) were carried out using the restricted formalism while open shell systems (curves AB and Triplet)

were calculated with the unrestricted methodology. We report in Figure 2 only one significant result because the symmetry made the difference, not the quality of the basis set.

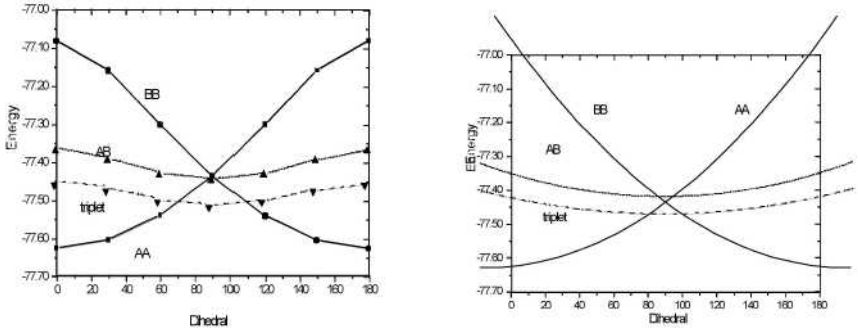

Figure 2. To the left, quasi-diabatic potential energy surfaces in the B3LYP/cc-pvtz Dunning's basis set. AA represents a cis state (solid line); BB a trans state (solid line); AB is the excited diradical state spin singlet (dashed line); Triplet is the diradical state S=1 (dotted line). To the right, extrapolated diabatic potential energy surfaces for the same states. The angle used to plot energy entries is $\alpha = 2\,|\Theta|$. All calculations were done with Gaussian 98 [23].

The cis, trans and singlet diradical cross at $\alpha = 90^{\bullet}$. The nature of the technology used makes a change on the slope. This is why we name these curves as quasi-diabatic. The triplet and the singlet diradical states have an attractor character at $\alpha =$ /2. The triplet potential energy cross the ground state cis and trans states at lower energy than the diradical singlet. This trend is the same for all basis functions used.

To take into account confinement, diabatic potential energy hypersurfaces are extrapolated with a curve-fitting program using a polynomial function of third order; all curves present a r^2 better than 0.999 (in AA (BB) curve the point $\alpha = \pi/2$ has not been considered in the fitting). Now, the system looks like the Marcus approach to electron transfer reactions. The reorganization energy is the energy difference between the ground state attractor geometry and the energy extrapolated from the second ground state attractor geometry.

6. Isomerism and quantum reactivity

The electronic structure analysis given so far can be used to examine chemical reactivity features of this important subsystem. In real space, eqs. (7) and (13) can be adapted to study the change in amplitudes for the electronic states by diagonalizing the matrix equation over a finite number of diabatic states [11]:

$$\Sigma_j \{ \langle \phi_{j'} | (H_c(\mathbf{q},\xi) + V(\mathbf{q},\xi)) | \phi_j \rangle_{\mathbf{q}} - E(\xi)\, \delta_{j'j} \} C_{j'j}(\xi) = 0 \quad \text{for } j'=1 \text{ to } 4 \qquad (16)$$

The row vector ($C_1(\xi)$ $C_2(\xi)$ $C_3(\xi)$ $C_4(\xi)$) corresponds to labels 1=AA, 2=Triplet, 3=AB and 4=BB in Fig.2. The local quantum state is given by the linear superpositions:

$$\chi_k(\mathbf{q};\xi) = C_{k_1}(\xi)\phi_1(\mathbf{q}) + C_{k_2}(\xi)\phi_2(\mathbf{q}) + \phi_3(\mathbf{q})C_{k_3}(\xi) + \phi_4(\mathbf{q})C_{k_4}(\xi) \qquad (17)$$

The index k identifies the roots of the secular equation (16).

In a neighborhood of the cis-attractor, the energy gaps between cis and other states is the largest for the diabatic case; the amplitude $C_{1_1}(\xi^1)$ is maximal; $C_{1_4}(\xi^1)$ being negligible. For the trans attractor, the amplitude $C_{1_4}(\xi^4)$ is maximal; $C_{1_1}(\xi^4)$ being negligible; the energy state values change place.

Observe that the matrix element V_{14} is zero by parity. This implies that V_{12}, V_{13}, V_{42} and V_{43} will produce non-zero amplitudes as the energy gaps decrease; these matrix elements being independent from the reaction coordinate. Only the energy gaps as a function of ξ control the relative amplitudes. That is, when the reaction coordinate is in a neighborhood of the crossing point the mixing with the triplet becomes sizable as the system approaches the crossing point and the energy gaps decrease. $V(\mathbf{q},\xi)$ will mix the states of different spin before coming to $\alpha = /2$. Here, a linear superposition of singlet and triplet states represents a stationary quantum state. The quantum state is not an eigenstate of S^2.

Amplitudes different from zero are interpreted in terms of possibilities (propensities) the system will show whenever external interactions probing the spectral response related to the base states are switched on. The maximal mixing of states takes place in a neighborhood of $\alpha = \pi/2$. Any external constraint forcing the system to this crossing zone will enhance the response of the triplet-state. In this context, changes of amplitudes are meaningful; the potential energy functions are auxiliary devices and the concept of avoided crossing does not make sense.

The access to different ξ-regions is controlled by the vibration spectra. In particular, it is the anti-symmetric vibration mode that may shift the geometry towards the point of maximal mixing. The other way round, freezing this mode will trap the quantum system at the initial state, cis or trans as the case may be. Now, a vibration excitation along this anti-symmetric mode will be prompting the electronic activity of the system. For example, a perpendicular symmetric attack of carbene can only proceed if non-zero amplitude develops at the diradical states. This concept includes the elementary orbital considerations and overcome them.

The electron-phonon operator is a tensor product between the electronic dipole and the nuclear dipole operators. A mixing between the AA and BB via the singlet-spin diradical AB state is possible now. A linear superposition of identical vibration states in AA and BB is performed by the excited state diradical AB. If the system started at cis state, after coupling may decohere by emission of a vibration photon in the trans state; furthermore, relaxation to the trans

conformer would follow by the emission of another photon until getting to the ground vibration state. Decoherence appears to be a mechanism in Hilbert space to accomplish conformational change measured as a radical change in the amplitude pattern. We are far from wanderings on potential energy hypersurfaces. Still, the concept may be useful as a communication tool.

7. Nodal planes and the ELF function

The question remains whether the nodal planes, essential for the qualitative analysis, remain in the more advanced calculations of wavefunctions. To test this point, the electronic localization function (ELF) as implemented by B. Silvi and A. Savin [24] is used. In Figure 3 we summarize the results.

The nodal planes used qualitatively to discuss cis/trans isomerization clearly appear in the ELF profiles. For AA and BB at the crossing point, the picture reveals the numerical artifact of the adiabatic calculations. At the respective attractors, AA and BB show the expected nodal plane distribution. The method is not capable to distinguish between singlet and triplet spin-state ELF. This issue was discussed during the meeting. The reader may find appropriate discussions in this volume.

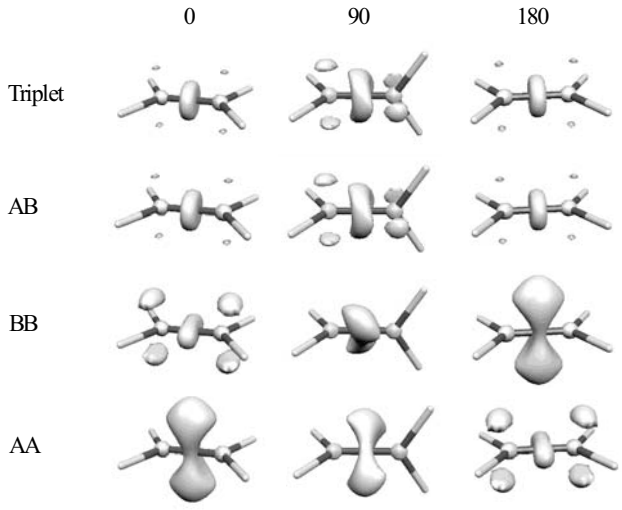

Figure 3. ELF isocontours (0.78) for the four states: AA, BB, AB and Triplet at points in the quasi-diabatic curves $\alpha = 0$, $\pi/2$ and π. ELF basins involving hydrogen atoms are not displayed for clarity.

Not shown to the quasi-diabatic potential energy surfaces in Fig. (3) there is a adiabatic potential energy surface. This is distinguished by the maximum at the crossing point $\pi/2$. The system has a saddle-point structure. In the regions about the cis and trans attractors there is no difference between them. Between $2\pi/3$

and 2π-$2\pi/3$ the curves start differ in curvature. The LCAO model mixes the states AA and BB for the ground doubly occupied states. The BO scheme does not respect symmetry properties because doubly occupancy wipes out the basic differences. At the crossing point there is no correct electronic solution to the BO scheme. This is translated into the saddle-point nature of the PES at the crossing point.

The import of diabatic electronic states for dynamical treatments of conical intersecting BO potential energy surfaces is well acknowledged. This intersection is characterized by the non-existence of symmetry element determining its location in nuclear space [25]. This problem is absent in the GED approach. Because the symmetries of the cis and trans conformer are irreducible to each other, a regularization method without a correct reaction coordinate does not make sense. The slope at the (conic) intersection is well defined in the GED scheme. Observe, however, that for closed shell structures, the direct coupling of both states is zero. A configuration interaction is necessary to obtain an appropriate description; in other words, correlation states such as diradical ones and the full "excited" BB state in the AA local minimum cannot be left out the scheme.

The method discussed so far originates from an analysis of n-electrons quantum states based on general mathematical theorems such as Kato's [18]. The particle model is not an element of the theory. In this sense, no direct relation to orbital methods including diabatic ones can be found at the present level of development. The diabaticity is related to a global conservation of the nodal planes. And the calculations reported here have been monitored to keep up to this level.

The problem of electronic correlation is akin to particle representations. The present approach can be mapped to some of the practical ways to treat correlation. A thorough discussion of this matter will be done elsewhere.

8. Comparison with other schemes

An important question concerns the relation of the present method with the one using diabatic orbitals. Such methods are implemented in standard *ab initio* packages such as MOLPRO [27] with emphasis in multiconfiguration-reference CI and related methods. These methods are based on the particle model.

The GED approach is a general procedure based on the exact solutions to the n-electron system. Only one Hamiltonian is required at variance with the infinite Hamiltonian approach (defined on the parametric ξ-space) characteristic of the BO scheme. All the base functions are expanded from a unique origin of the I-frame. The characteristics of the n-electrons diabatic base functions are independent from the positions taken by the sources of the external potential.

The concept of correlation enters via the inclusion of asymptotic base states. Translated into the particle model, one type of asymptotic state is given by a doubly occupancy of an anti-bonding state; the fragments show a repulsive

potential energy function with zero gradient along specific directions in ξ-space at infinite distance from the origin. The crossing between this anti-bonding state with the confining state locate the domain in ξ-space where the amplitudes in eq. (15) will change. Diabatic base electronic states are intrinsic properties of the system that, in principle, do not derive from adiabatic models via diabatization procedures.

Once the diabatic potential energy surfaces relevant to describing a process, the integration of the sources of external potential (nuclear dynamics) can be done in real space using numerical integration methods.

No one of the equations introduced here are defined as in the standard Born-Oppenheimer approach. The reason is that electronic base functions that depend parametrically on the geometry of the sources of external potential are not used. The concept of a quantum state with parametric dependence is different. This latter is a linear superposition; the other are objects gathered in column vectors.

Still, one can use standard packages for attractor states by actually finding a stationary geometry. The problem is that the standard theory does not conceive of confined states. This element is new. It qualitatively simplifies the analyses. But it is not a practical tool yet. However, confinement underlies a severe limitation of the LCAO bonding orbitals as they dissociate in a manner inconsistent with the general confinement property. Barrier less profiles for radical association process can be traced back to a numerical artifact.

If one had a complete basis set then, for the stationary geometry, the corresponding electronic wavefunctions obtained by actual calculation would be models for the diabatic base functions. The latter statement has to be understood in the sense that the set of nodal planes so obtained must be kept fixed. This was the procedure used to extract diabatic base states for cis and trans ethylene.

Finally, the rules of angular momentum construction can be made as if the system had spherical symmetry. The reason is that the invariance to rotation of the I-frame leads to angular momentum conservation. Once all base states have been constructed, the dynamics is reflected on the quantum state that is a linear superposition on that base. As the amplitudes change in time, motion of different kinds result.

For reactivity studies where intersystem crossings are important, it is the total angular momentum of the electronic system J that is conserved: $\mathbf{J}=\mathbf{L}+\mathbf{S}$ and the coupling operator $\mathbf{L}\cdot\mathbf{S}$ permits mixing. The linear superposition includes electronic states that are space symmetric with spin anti-symmetric and vice versa. For ethylene, vibration activation would bring the system at the domain where the energy gaps are small enough between singlet and triplet. Amplitudes different from zero appear before the crossing point as the matrix elements of $\mathbf{L}\cdot\mathbf{S}$ are different from zero in the "product" channel. Propagation to the trans singlet will achieve an internal fluctuation with variation of the electronic structure. There is no wandering on potential energy surfaces. These latter are useful devices to visualize things.

9. Discussion

A rigorous electro-nuclear separability scheme has been examined. Therein, an equivalent positive charge background replaces the nuclear configuration space; the coordinates of which form, in real space, the $\boldsymbol{\xi}$-space. Diabatic potential energy hypersurfaces for isomers of ethylene in $\boldsymbol{\xi}$ -space were calculated by adapting standard quantum chemical packages.

The model defined by eqs.(15)-(17) looks similar to the BO scheme. This is true but similarity is not equality. The parametric dependence is induced by the kinematic operator $V(\mathbf{q},\boldsymbol{\xi})$. As pointed out by Prof. Berrondo (personal communication) it is the $\boldsymbol{\xi}$-space, used in parametric form that eliminates the dynamical Coulomb interactions of nuclear with electronic subspaces; this is the reason justifying inclusion of an electron-phonon term. This operator mixes states in a neighborhood of energy degeneracy. The transition integrals between two vibration states with different electronic label connect states of different parity. These two factors can be mapped on to a real space representation by using the diabatic potential surfaces introduced here. Yet, the description retains its quantum mechanical flavor; at each point all the amplitudes involved can be calculated. The process is not to be described as a population of any of the base states used for. Present trends in chemical dynamics calculations go in the direction of non-BO trajectories calculations [26]. Still, propagation is done only on one electronic state at a time; this is a classical mechanical paradigm. In our case, two attitudes are possible. One consists in the full quantum mechanical calculation once the significant regions in real space have been determined. The other consists in using the collections of amplitudes to determine the behavior of the system with wave packets propagation; constraints imposed by external sources (e.g. active sites) can easily be represented [8]; model correlation functions can be obtained that can be directly related to experimental data.

The principle of conservation of local symmetries is an important result. This permit patching asymptotic fragments to bonded supermolecules. The former states are prepared in real space; they do not belong to the electronic Hilbert space yet. It is clear that incorporation in the appropriate Hilbert space requires the presence of a nodal plane between the fragment centers. This simply translates into a potential energy hypersurface where the associated LUMO is to be double filled. The potential is repulsive. This is a logical result. The improper use of molecular orbital technology fill the bonding orbital thereby leading to a barrierless process; that is, from the present standpoint, a numerical artifact.

Real space systems calculations are algorithmic schemes in nature; GED and BO are two of them. The former can be mapped to rigorous quantum mechanics the latter does not. This is the fundamental difference between them.

Acknowledgements

Orlando Tapia is much indebted to Profs. M. Berrondo (Utha, USA) and O. Goscinski (Uppsala University) for invaluable discussions on the methodology. J.A. and V.P would like to thank Universitat Jaume I-Fundacio Bancaixa Project P1B99-02 for financial support. J.A. also thanks Generalitat Valenciana for a post-doctoral stay of three months at Uppsala. Discussions with O. Roncero from CSIC (Madrid) have been illuminating. The final version was completed while O.T. was visiting Valencia University; this author is most grateful to Rector F. Tomas Vert and other authorities that made possible and agreeable this visit.

References

1. M. Born; K. Huang *Dynamical theory of crystal lattices*; Clarendon: Oxford (1954).
2. H. Meyer *Ann.Rev.Phys.Chem.* **53**, 141 (2002).
3. O. Tapia, in *Quantum systems in chemistry and physics,* Vol II*: Advanced problems and complex systems*; A. Hernandez-Laguna, J. Maruani, R. McWeeny, S. Wilson, eds; Kluwer: Dordrecht; pp 193-212 (2000).
4. O. Tapia, in *New Trends in Quantum Systems in Chemistry and Physics*; J. Maruani, S. Wilson, Y. G. Smeyers, eds.; Kluwer: Dordrecht, Vol. II; pp 23-47 (2000).
5. O. Tapia *Adv.Quantum Chem.* **40**, 103 (2001).
6. O. Tapia; G. A. Arteca *Internet Electron.J.Mol.Des.* **2**, 454 (2003).
7. G. A. Arteca; O. Tapia *J.Math.Chem.* **35**, 1 (2004).
8. O. Tapia *Int.J.Quantum Chem.* **97**, 637 (2004).
9. O. Tapia *Int.J.Quantum Chem.* **99**, 373 (2004).
10. O. Tapia *TN-10* **Sept. 14**, Submitted (2004).
11. O. Tapia; G. A. Arteca *Adv.Quantum Chem.* **47**, 273 (2004).
12. G. A. Arteca; O. Tapia *J.Math.Chem.* **35**, 159 (2004).
13. S. Weinberg *The quantum theory of fields*; Cambridge University Press: New York, Vol. 1 (1995).
14. L. E. Ballantine *Quantum Mechanics: A modern development*; World Scientific: Singapore (1998).
15. H. Primas *Chemistry, quantum mechanics and reductionism*; Springer-Verlag: Berlin, Vol. 24 (1981).
16. J. J. Sakurai *Modern Quantum Mechanics*; Benjamin / Cummings: Menlo Park (1994).
17. R. Pauncz *Spin eigenfunctions*; Plenum Press: New York (1979).
18. T. Kato *Trans.Am.Math.Soc.* **70**, 195 (1951).
19. G. Herzberg; E. Teller *Z.Physik.Chem.* **B21**, 410 (1933).
20. H. C. Longuet-Higgins *Adv.Spectry.* **2**, 429 (1961).
21. *Faraday Discussions* (Royal Society of Chemistry) **127** (2004).
22. L. D. Landau; E. M. Lifshitz *Quantum mechanics*; Pergamon Press (1962).
23. M. J. Frisch; G. W. Trucks; H. B. Schlegel; G. E. Scuseria; M. A. Robb; J. R. Cheeseman; V. G. Zakrzewski; J. A. Montgomery Jr.; R. E. Stratmann; J. C. Burant; S. Dapprich; J. M. Millam; A. D. Daniels; K. N. Kudin; M. C. Strain; O. Farkas; J. Tomasi; V. Barone; M. Cossi; R. Cammi; B. Mennucci; C. Pomelli; C. Adamo; S. Clifford;

J.Ochterski; G. A. Petersson; P. Y. Ayala; Q. Cui; K. Morokuma; D. K. Malick; A. D. Rabuck; K. Raghavachari; J. B. Foresman; J. Cioslowski; J. V. Ortiz; A. G. Baboul; B. B. Stefanov; G. Liu; A. Liashenko; P. Piskorz; I. Komaromi; R. Gomperts; R. L. Martin; D. J. Fox; T. Keith; M. A. Al-Laham; C. Y. Peng; A. Nanayakkara; C. Gonzalez; M. Challacombe; P. M. W. Gill; B. Johnson; W. Chen; M. W. Wong; J. L. Andres; C. Gonzalez; M. Head-Gordon; E. S. Replogle; J. A. Pople; Revision A.7 ed.; Gaussian, Inc.: Pittsburgh P. A. (1998).
24. B. Silvi; A. Savin *Nature* **371**, 683 (1994).
25. H. Köppel *Faraday Discuss.* **127**, 35 (2004).
26. A. W. Jasper; C. Zhu; S. Nangia; D. G. Truhlar *Faraday Discuss.* **127**, 1 (2004).
27. H.-J. Werner; P.J. Knowles *http://www.molpro.net*.

PART II

RELATIVISTIC AND HEAVY-ELEMENT SYSTEMS

PROGRESS WITH BERTHA: A RELATIVISTIC ATOMIC AND MOLECULAR STRUCTURE PACKAGE

I. P. GRANT
Mathematical Institute,
24/29 St. Giles,
Oxford OX1 3LB, U.K. ‡

AND

H. M. QUINEY
School of Physics,
University of Melbourne,
Victoria 3010, Australia §

Abstract. BERTHA is a 4-component relativistic molecular structure program based on relativistic Gaussian (G-spinor) basis sets which is intended to make affordable studies of atomic and molecular electronic structure, particularly of systems containing high-Z elements. This paper reviews some of the novel technical features embodied in the code, and assesses its current status, its potential and its prospects.

1. Introduction

The need for reliable methods to study the electronic structure of atoms, molecules and condensed matter using relativistic quantum theory has been evident in the number of presentations at this Workshop which have noted the importance of relativistic effects. These ranged from astrochemistry, involving mainly molecules containing only light elements, to complicated systems containing transition metals or high-Z elements. Whilst most studies to date have been performed with approximate relativistic Hamiltonians or effective core potentials, these schemes make approximations whose errors are usually unquantifiable. Our objective is to design a well-constructed

‡email: ipg@maths.ox.ac.uk
§email: quiney@unimelb.edu.au

J.-P. Julien et al. (eds.),
Recent Advances in the Theory of Chemical and Physical Systems, 199–215.

tool for physicists and chemists based on clearly understood relativistic quantum mechanical principles which will have the potential to make fully relativistic studies which are both accurate and affordable.

This paper outlines the current status of the BERTHA program. This has been named (with her approval) after Lady Jefferies (1902-1999) (*née* Bertha Swirles), a colleague of D.R. Hartree at Cambridge University and a distinguished applied mathematician who, amongst other achievements, wrote the earliest paper on "relativistic self-consistent fields" for atoms [1].

2. The BERTHA program

At the time of writing, the program has the following capabilities:

- Dirac-Hartree-Fock-Breit (DHFB) calculations of atoms and molecules across the Periodic Table.
- Relativistic charge-current densities expressed in terms of G-spinor basis sets for stable and economical numerical calculations [2].
- Relativistic generalization for G-spinor basis functions of the well-known McMurchie-Davidson algorithm [3] for direct evaluation of interaction integrals.
- Calculation of electromagnetic properties within the formalism of relativistic quantum electrodynamics (QED).
- Relativistic density functional theory (RDFT), including relativistic exchange-correlation functionals [4, Chapter 4].
- Reformulation of electronic structure theory in terms of interaction between internal electric and magnetic fields [5].
- Representation of orbital spinors of symmetric molecules in terms of relativistic double groups [6].
- Correlation corrections using standard many-body theory.

3. Elements of the theory

A full account of the theory of relativistic molecular structure based on standard QED in the Furry picture will be found in a number of publications such as [7, Chapter 22], [8, Chapter 3]. These accounts use a relativistic second quantized formalism. For present purposes, it is sufficient to present the structure of BERTHA in terms of the *unquantized* effective Dirac-Coulomb-Breit (DCB) N-electron Hamiltonian:

$$H_{DCB} = \sum_{i=1}^{N} h_i + \sum_{i>j=1}^{N} g_{ij} \tag{1}$$

(Hartree atomic units will be used throughout.) Here h_i is a Dirac Hamiltonian for the i-th electron in the frame of K fixed nuclei

$$h_i = c\,\boldsymbol{\alpha}_i{\cdot}\boldsymbol{p}_i + \beta_i c^2 + \sum_K V_{iK}. \tag{2}$$

where c is the speed of light ($c = \alpha^{-1} \approx 137$, where α is the fine structure constant) and $\boldsymbol{p}$ is the particle momentum. The symbols $\boldsymbol{\alpha}$ and β denote 4×4 Dirac matrices with the standard representation

$$\boldsymbol{\alpha} = \begin{pmatrix} 0 & \boldsymbol{\sigma} \\ \boldsymbol{\sigma} & 0 \end{pmatrix}, \quad \beta = \begin{pmatrix} \boldsymbol{I} & 0 \\ 0 & \boldsymbol{I} \end{pmatrix}$$

in terms of the usual 2×2 Pauli matrices $\boldsymbol{\sigma} = (\sigma_x, \sigma_y, \sigma_z)$ and the identity matrix $\boldsymbol{I}$. We shall sometimes write $\sigma_0 = \boldsymbol{I}$ when convenient. V_{iK} is the electron-nucleus interaction; we shall use finite size nuclear model charge distributions which support the G-spinor boundary conditions near the origin so that $V_{iK}(\boldsymbol{r}) = -Z_K(\boldsymbol{r}_{iK})/r_{iK}$. The form of $Z_K(\boldsymbol{r}_{iK})$ ensures that V_{iK} is Coulombic outside the K-th nucleus, where $Z_K(\boldsymbol{r}_{iK}) \to Z_K$, and is roughly parabolic inside. The symbol g_{ij} denotes the Coulomb-Breit effective interaction

$$g_{ij} = \frac{1}{r_{ij}} + \frac{1}{2}\left(\frac{\boldsymbol{\alpha}_i{\cdot}\boldsymbol{\alpha}_j}{r_{ij}} + \frac{(\boldsymbol{\alpha}_i{\cdot}\boldsymbol{r}_{ij})(\boldsymbol{\alpha}_j{\cdot}\boldsymbol{r}_{ij})}{r_{ij}^3} \right). \tag{3}$$

The two parts of this formula are derived from the *same* QED Feynman diagram for interaction of two electrons in the Coulomb gauge. The first term is the Coulomb potential and the second part, the Breit interaction, represents the mutual energy of the electron currents on the assumption that the virtual photon responsible for the interaction has a wavelength long compared with system dimensions. The DCB hamiltonian reduces to the complete standard Breit-Pauli Hamiltonian [9, §21.1], including all the relativistic and spin-dependent correction terms, when the electrons move nonrelativistically.

4. Electromagnetic interactions in QED

Using Einstein's summation convention, the formula for the interaction of a charge-current distribution $j^\nu(x)$ at a space-time point $x = (x^0, x^1, x^2, x^3) \equiv (ct, \boldsymbol{x})$ with the local electromagnetic four-potential $A^\nu(x)$,

$$\frac{1}{c}\int j^\nu(x) A_\nu(x)\, d\boldsymbol{x}$$

is central to QED. It is therefore necessary to find a way to represent the charge-current four-vector

$$j^\nu(x) = (c\rho(x), \boldsymbol{j}(x)), \tag{4}$$

where $\rho(x)$ is the electric charge density and $\boldsymbol{j}(x)$ is the current density vector in electronic structure theory. If $\psi(x)$ is a Dirac spinor, with adjoint $\widetilde{\psi}(x) = \psi^\dagger(x)\gamma^0$, then the electron charge-current four-vector is

$$j^\nu(x) = -ec\,\widetilde{\psi}(x)\,\gamma^\nu\,\psi(x) \tag{5}$$

so that

$$\rho(x) = j^0(x)/c = -e\,\psi^\dagger(x)\,\psi(x), \quad \boldsymbol{j}(x) = -ec\,\psi^\dagger(x)\,\boldsymbol{\alpha}\,\psi(x) \tag{6}$$

where $\gamma^0 = \beta$, and $\boldsymbol{\alpha} = \gamma^0\boldsymbol{\gamma}$ with components $\boldsymbol{\alpha} = (\alpha_1, \alpha_2, \alpha_3)$. In the quantized theory, $\psi(x)$ is an operator with components from all parts of the one-body Dirac spectrum, including electron bound and continuum states (described loosely as "positive energy") and positron states ("negative energy"). Both "positive energy" and "negative energy" states appear in our numerical calculation, although the latter normally play a passive role. For chemical purposes, they can usually be regarded as "deep core" states, which can only be accessed in processes requiring energies greater than $2mc^2$, enough to create a real electron-positron pair, and it is usually safe to ignore them in correlation calculations (the *no virtual-pair* (NVP) approximation). On the other hand, some electromagnetic interaction operators, for example those involved in NMR shielding, introduce interactions with negative energy virtual states that dominate the calculation in the relativistic theory. Nor can negative energy contributions to vacuum polarization and the self-energy of the electron (Lamb shift) be ignored. There are clear advantages to a formulation in which the negative energy states are easily accessed when necessary.

5. G-spinor expansion of Dirac amplitudes

The stationary states of a one-body Dirac operator h, (2), in the presence of a central-field potential have the spatial form

$$\psi(\boldsymbol{x}) = \begin{pmatrix} P(r)\;\chi_{\kappa,m}(\theta,\phi) \\ iQ(r)\chi_{-\kappa,m}(\theta,\phi) \end{pmatrix} \tag{7}$$

where $P(r), Q(r)$ are radial amplitudes and

$$\chi_{\kappa,m}(\theta,\phi) = \sum_{\sigma=\pm 1/2} \langle l, m-\sigma, 1/2, \sigma \,|\, j, m\rangle\, Y_{l,m-\sigma}(\theta,\phi)\,\varphi_\sigma \tag{8}$$

is an eigenfunction of $\boldsymbol{j}^2$, $\boldsymbol{l}^2$, $\boldsymbol{s}^2$ and j_z, where $\boldsymbol{j} = \boldsymbol{l} + \boldsymbol{s}$. $Y_{l,m-\sigma}(\theta,\phi)$ is a normalized spherical harmonic [10, Appendix IV], [11, §2.2] with the standard Condon-Shortley choice of phase factors [12] and $\langle l, m-\sigma, 1/2, \sigma \,|\, j, m\rangle$ is a Clebsch-Gordon coefficient [10, Appendix I], [11, §2.8]. The index κ,

defined by $\kappa = (j+1/2)\eta$ with $\eta = \pm 1$ and $l = j+\eta/2$, covers both possible couplings. Thus if $\varphi^t_{1/2} = (1,0)$ and $\varphi^t_{-1/2} = (0,1)$ (where the superscript t denotes column-row transposition), we have the 2-spinor

$$\chi_{\kappa,m}(\theta,\phi) = \begin{pmatrix} \langle l, m-1/2, 1/2, 1/2 \,|\, j, m\rangle \, Y_{l,m-1/2}(\theta,\phi) \\ \langle l, m+1/2, 1/2, -1/2 \,|\, j, m\rangle \, Y_{l,m+1/2}(\theta,\phi) \end{pmatrix}. \tag{9}$$

We define a spherical Gaussian function (SGTF) centred at the origin by

$$S[a, \boldsymbol{r}; \boldsymbol{n}] = r^{2n+l}\, e^{-a\boldsymbol{r}^2}\, Y_{l,m}(\theta,\phi) \;\equiv\; r^{2n} \mathcal{Y}_{l,m}(\boldsymbol{r})\, e^{-a\boldsymbol{r}^2} \tag{10}$$

where $a > 0$ and $\boldsymbol{n}$ denotes the integer triplet (n, l, m). As usual, $l \geq 0$, $-l \leq m \leq l$, and we only need the values $n = 0, 1$. The solid harmonic $\mathcal{Y}_{l,m}(\boldsymbol{r})$ can be regarded as a homogeneous polynomial in the Cartesian coordinates x, y, z of order l. We shall expand $\psi(\boldsymbol{x})$ in terms of G-spinors $M[\beta, \mu; \boldsymbol{r}]$ defined by

$$\begin{aligned} M(\beta,\mu;\boldsymbol{r}_\mu) := & \\ N^\beta_\mu \begin{bmatrix} -(\beta\eta_\mu)\mathcal{C}^{-(\beta\eta_\mu)}_{l_\mu m_\mu} \Big\{ t^\beta_\mu \, S[a_\mu, \boldsymbol{r}_\mu; (0, l_\mu, m^-_\mu)] \\ \qquad -(1-\beta) a_\mu S[a_\mu, \boldsymbol{r}_\mu; (1, l_\mu, m^+_\mu)] \Big\} \\ \mathcal{C}^{(\beta\eta_\mu)}_{l_\mu m_\mu} \Big\{ t^\beta_\mu \, S[a_\mu, \boldsymbol{r}_\mu; (0, l_\mu, m^-_\mu)] \\ \qquad -(1-\beta) a_\mu S[a_\mu, \boldsymbol{r}_\mu; (1, l_\mu, m^+_\mu)] \Big\} \end{bmatrix} \end{aligned} \tag{11}$$

so that

$$\psi(\boldsymbol{x}) = \sum_{\mu=1}^{N} \begin{bmatrix} {c_\mu}^{+1} \; M(+1, \mu, x) \\ i{c_\mu}^{-1} \; M(-1, \mu, x) \end{bmatrix} \tag{12}$$

where the index β of (11) takes the value $\beta = +1$ for the *upper* pair of components and $\beta = -1$ for the *lower* pair. (For brevity we shall often label parameters using only the sign of β.) The upper pair reduce to a Schrödinger-Pauli spin-orbital in the nonrelativistic limit $c \to \infty$ whilst the lower pair vanish like $1/c$. The upper and lower pair are often called "large" (L) and "small" (S) components respectively, but it is important to realize that this description applies only to electron states; the roles reverse for positron states.

Four-spinor angular momentum labels: κ_μ, j_μ, l_μ, etc. are those of the *upper* components. Basis set elements are indexed by $\mu = 1, \ldots, N$. The primary G-spinor parameters are

- a_μ: Gaussian exponent.
- $\boldsymbol{A}_\mu$: nuclear centre position vector.
- The position vector of an electron relative to the origin is denoted by $\boldsymbol{r}$: its relative position vector is $\boldsymbol{r}_\mu = \boldsymbol{r} - \boldsymbol{A}_\mu$.

– j_μ, m_μ : total angular momentum quantum number and projection on the axis of quantization.
– $m_\mu^\pm = m_\mu \pm 1/2$

Other G-spinor parameters depend on the component index β. Thus

– $l_\mu = j_\mu + \beta\eta_\mu/2$.
– $t_\mu^+ = 1;\ \ t_\mu^- = (2l_\mu + 1)(1 + \eta_\mu)/2$

The remaining symbols in (11) are the normalization constants

$$N_\mu^\beta = \left(\frac{2(2a_\mu)^{l_\mu+1+\beta/2}}{\Gamma(l_\mu + 2 - \beta/2)} \right)^{1/2} \tag{13}$$

and the spin-orbit coupling coefficients

$$\mathcal{C}^\eta_{l_\mu m_\mu} = s_{l_\mu m_\mu} \left(\frac{l_\mu + 1/2 + \eta m_\mu}{2l_\mu + 1} \right)^{1/2} \tag{14}$$

in which we have combined specific Clebsch-Gordon coefficients from (9) with the spherical harmonic normalization and phase factors

$$s_{l_\mu m_\mu} := (-1)^{(m_\mu+|m_\mu|)/2} \left[\frac{2l_\mu + 1}{4\pi} \frac{(l_\mu - |m_\mu|)!}{(l_\mu + |m_\mu|)!} \right]^{1/2} \tag{15}$$

The appearance of the general expression (11) is at first sight far from obvious, although its construction can be described quite transparently [7, §22.6]; see also [8, §3]. Here we just highlight key elements. For the upper 2-spinor, $\beta = +1$, the term with the factor $(1 - \beta)$ vanishes; what remains is equivalent to a radial function $r_\mu^{2n+l_\mu} \exp(-a_\mu \boldsymbol{r}_\mu^2)$ multiplied by a single spin-orbital (9), giving the corresponding Schrödinger-Pauli SGTF basis function in the nonrelativistic limit. The main issue is the choice of exponents a_μ, for which any of the methods used in nonrelativistic electronic structure can be used. It is usually possible to adapt exponent sets from related nonrelativistic calculations which will provide a good description of the electron distribution for much of the radial range. One or two additional large exponents may be needed to improve the radial density distribution in the region near the nuclei where the relativistic effects originate. This is especially important for the description of nuclear spin-dependent effects [13].

The lower 2-spinor components, $\beta = -1$, are related to the upper components by the *kinetic matching* relation.

$$M(-1, \mu; \boldsymbol{r}_A) = \text{const.}\ \boldsymbol{\sigma} \cdot \boldsymbol{p}\ M(+1, \mu; \boldsymbol{r}_A). \tag{16}$$

When $\eta_\mu < 0$, so that the upper component has $l_\mu = j_\mu - 1/2$, the factor t_μ^- vanishes, leaving one SGTF in each component with the same radial

factor and the orbital index $\bar{l}_\mu = l_\mu + 1$. When $\eta_\mu > 0$, there are two SGTF in each component and the orbital index is $\bar{l}_\mu = l_\mu - 1$. The use of (16) is vital for computational economy and ensures that the Gram matrices for both upper and lower basis sets have almost the same condition number. The *kinetic balance* prescription adopted in other codes, advocated first by Lee and McLean [14], notes that the lower components have a different radial dependence from the upper components, and suggests introducing additional basis functions in order to "balance the set kinetically". Unfortunately the additional functions make the lower component Gram matrix more singular because of *practical* linear dependence. Basis sets which are kinetically balanced in the sense of Lee and McLean [14] are therefore best avoided; the algebraic system generated with kinetic balance is numerically much less stable than with our kinetic matching procedure and generates spurious eigenvalues and eigenstates with no physical meaning.

6. Overlap densities and the McMurchie-Davidson algorithm

The evaluation of relativistic Fock matrix elements depends on an efficient way to evaluate interaction integrals following the McMurchie-Davidson scheme [3]. The key step is the recognition that the product of two Gaussian functions on different nuclear centres $\boldsymbol{A}_\mu, \boldsymbol{A}_\nu$ is proportional to a third Gaussian on some intermediate centre $\boldsymbol{A}_{\mu\nu}$. It is thus easy to see that the product of two SGTF (10) can be put in the form

$$S[a_\mu, \boldsymbol{r}_\mu; \boldsymbol{n}]\, S[a_\nu, \boldsymbol{r}_\nu; \boldsymbol{n}'] = K_{\mu\nu} \sum_{\boldsymbol{\gamma} \in \mathcal{T}_\Lambda} E[\boldsymbol{n}; \boldsymbol{n}'; \boldsymbol{\gamma}]\, H(a_{\mu\nu}, \boldsymbol{r}_{A_{\mu\nu}}; \boldsymbol{\gamma}) \qquad (17)$$

where $\boldsymbol{n} = (n, l, m)$, $\boldsymbol{n}' = (n', l', m')$, $\boldsymbol{r}_{A_{\mu\nu}} = \boldsymbol{r} - \boldsymbol{A}_{\mu\nu}$,

$$\begin{aligned} a_{\mu\nu} &= a_\mu + a_\nu, \\ \boldsymbol{A}_{\mu\nu} &= \frac{a_\mu \boldsymbol{A}_\mu + a_\nu \boldsymbol{A}_\nu}{a_\mu + a_\nu}, \\ K_{\mu\nu} &= \exp\{-\frac{a_\mu a_\nu}{a_\mu + a_\nu} (\boldsymbol{A}_\mu - \boldsymbol{A}_\nu)^2\}, \end{aligned}$$

and

$$H(a, \boldsymbol{r}_A; \boldsymbol{\gamma}) = D_x^\rho D_y^\sigma D_z^\tau \exp[-a\, \boldsymbol{r}_A^2] \qquad (18)$$

where $D_i := \partial / \partial A_i$, $i == x, y, z$ and $\boldsymbol{\gamma} = (\rho, \sigma, \tau)$ is an Hermite Gaussian type function (HGTF), a product of a Gaussian with a homogeneous polynomial of degree $\Lambda = \rho + \sigma + \tau$ in the Cartesian components of $\boldsymbol{r}_A$. The numerical coefficients $E[\boldsymbol{n}; \boldsymbol{n}'; \boldsymbol{\gamma}]$ result from the expansion of the polynomial parts of the two SGTF about the centre $\boldsymbol{A}_{\mu\nu}$ and therefore carry information about the geometry. The symbol $\mathcal{T}_\Lambda$ represents the exponent set

$$\mathcal{T}_\Lambda := \{\boldsymbol{\gamma} := (\rho, \sigma, \tau) \,|\, 0 \le \rho + \sigma + \tau \le \Lambda\}\,. \qquad (19)$$

The G-spinor representation (12), when substituted into (5), results in a time-dependent charge-current density

$$j^\nu(x) \;=\; \sum_{\mu\mu'}\sum_{\beta\beta'} c_\mu^{\beta\,*} c_{\mu'}^{\beta'} \left[j^\nu_{\mu\mu'}(x)\right]^{\beta\beta'}\; e^{-itE_{\mu\mu'}} \tag{20}$$

with overlap charge densities ($\nu = 0$ component)

$$\rho_{\mu\mu'}(\boldsymbol{x}) = -e \sum_{\beta=\pm1} M^\dagger(\beta,\mu,\boldsymbol{x})\, M(\beta,\mu',\boldsymbol{x}) \tag{21}$$

and the overlap current densities ($\nu = 1,2,3$)

$$\boldsymbol{j}^{+-}_{\mu\mu'}(\boldsymbol{x}) = \left[\boldsymbol{j}^{-+}_{\mu'\mu}(\boldsymbol{x})\right]^* = -iecM^\dagger(+1,\mu,\boldsymbol{x})\,\boldsymbol{\sigma}\, M(-1,\mu',\boldsymbol{x}) \tag{22}$$

which are linear combinations of SGTF products of the type of (17). It follows that the G-spinor overlaps in (21) and (22) can be expressed in a similar form

$$M^\dagger[\beta,\mu;\boldsymbol{r}_\mu]\;\sigma_q\, M[\beta',\nu;\boldsymbol{r}_\nu] = K_{\mu\nu} \sum_{\boldsymbol{\gamma}\in\mathcal{T}_\Lambda} E_q^{\beta,\beta'}[\mu,\nu;\boldsymbol{\gamma}]\, H(a_{\mu\nu},\boldsymbol{r}_{A_{\mu\nu}};\boldsymbol{\gamma}) \tag{23}$$

where the expansion coefficients $E_q^{\beta,\beta'}[\mu,\nu;\boldsymbol{\gamma}]$ are simple linear combinations of the nonrelativistic $E[\boldsymbol{n};\boldsymbol{n}';\boldsymbol{\gamma}]$ coefficients, incorporating both geometrical and spinor properties. Thus for charge densities and overlap matrices we require only

$$\begin{aligned}
E_0^{++}[\mu,\nu;\boldsymbol{\gamma}] &= N_\mu^+ N_\nu^+ \\
&\times\big\{\eta_\mu\eta_\nu \mathcal{C}^{-\eta_\mu}_{l_\mu m_\mu}\mathcal{C}^{-\eta_\nu}_{l_\nu m_\nu}(-1)^{m_\mu^-} E[0,l_\mu,-m_\mu^-;0,l_\nu,m_\nu^-;\boldsymbol{\gamma}] \\
&\qquad + \mathcal{C}^{\eta_\mu}_{l_\mu m_\mu}\mathcal{C}^{\eta_\nu}_{l_\nu m_\nu}(-1)^{m_\mu^+} E[0,l_\mu,-m_\mu^+;0,l_\nu,m_\nu^+;\boldsymbol{\gamma}]\big\}
\end{aligned} \tag{24}$$

$$\begin{aligned}
E_0^{--}[\mu,\nu;\boldsymbol{\gamma}] &= N_\mu^- N_\nu^-\Big\{\eta_\mu\eta_\nu \mathcal{C}^{\eta_\mu}_{l_\mu m_\mu}\mathcal{C}^{\eta_\nu}_{l_\nu m_\nu}(-1)^{m_\mu^-} \\
&\times\Big[t_\mu^- t_\nu^-\, E[0,\bar{l}_\mu,-m_\mu^-;0,\bar{l}_\nu,m_\nu^-;\boldsymbol{\gamma}] - 2t_\mu^- a_\nu\, E[0,\bar{l}_\mu,-m_\mu^-;1,\bar{l}_\nu,m_\nu^-;\boldsymbol{\gamma}] \\
&\quad - 2t_\nu^- a_\mu\, E[1,\bar{l}_\mu,-m_\mu^-;0,\bar{l}_\nu,m_\nu^-;\boldsymbol{\gamma}] + 4a_\mu a_\nu\, E[1,\bar{l}_\mu,-m_\mu^-;1,\bar{l}_\nu,m_\nu^-;\boldsymbol{\gamma}]\Big] \\
&\qquad + \mathcal{C}^{-\eta_\mu}_{l_\mu m_\mu}\mathcal{C}^{-\eta_\nu}_{l_\nu m_\nu}(-1)^{m_\mu^+} \\
&\times\Big[t_\mu^- t_\nu^-\, E[0,\bar{l}_\mu,-m_\mu^+;0,\bar{l}_\nu,m_\nu^+;\boldsymbol{\gamma}] - 2t_\mu^- a_\nu\, E[0,\bar{l}_\mu,-m_\mu^+;1,\bar{l}_\nu,m_\nu^+;\boldsymbol{\gamma}] \\
&\quad - 2t_\nu^- a_\mu\, E[1,\bar{l}_\mu,-m_\mu^+;0,\bar{l}_\nu,m_\nu^+;\boldsymbol{\gamma}] + 4a_\mu a_\nu\, E[1,\bar{l}_\mu,-m_\mu^+;1,\bar{l}_\nu,m_\nu^+;\boldsymbol{\gamma}]\Big]\Big\}
\end{aligned} \tag{25}$$

The current density components are overlap products

$$\begin{aligned}
\left[\boldsymbol{j}^{+-}_{\mu\nu}\right]_x &= -i\,ec\left\{M^\dagger[+1,\mu^+]\,M[-1,\nu^-] + M^\dagger[+1,\mu^-]\,M[-1,\nu^+]\right\} \\
\left[\boldsymbol{j}^{+-}_{\mu\nu}\right]_y &= -ec\left\{M^\dagger[+1,\mu^+]\,M[-1,\nu^-] - M^\dagger[+1,\mu^-]\,M[-1,\nu^+]\right\} \\
\left[\boldsymbol{j}^{+-}_{\mu\nu}\right]_z &= -i\,ec\left\{M^\dagger[+1,\mu^-]\,M[-1,\nu^-] - M^\dagger[+1,\mu^+]\,M[-1,\nu^+]\right\}
\end{aligned} \tag{26}$$

where $\mu^\pm$ denotes the upper/lower element of the two-spinor. The full expressions can be constructed using

$$\begin{aligned}
M^\dagger[-1,\nu^+]\,M[+1,\mu^-] &= N^-_\mu N^+_\nu(-\eta_\nu)\mathcal{C}^{-\eta_\mu}_{l_\mu m_\mu}\mathcal{C}^{-\eta_\nu}_{\bar{l}_\nu m_\nu}K_{\mu\nu}(-1)^{m^+_\mu} \\
&\times\sum_{\mathcal{T}_\Lambda}\left\{t_\mu E[0,l_\mu,-m^+_\mu;0,\bar{l}_\nu,m^-_\nu;\boldsymbol{\gamma}] - 2a_\mu E[1,l_\mu,-m^+_\mu;0,\bar{l}_\nu,m^-_\nu;\boldsymbol{\gamma}]\right\} \\
&\times H(a_{\mu\nu},\boldsymbol{r}_{A_{\mu\nu}};\boldsymbol{\gamma})
\end{aligned} \tag{27}$$

where $l_\mu = j_\mu + \eta_\mu/2, \bar{l}_\mu = j_\mu - \eta_\mu/2$ and exploiting the symmetries of (22).

The construction of relativistic and nonrelativistic E-coefficients is therefore at the centre of an efficient electronic structure program; a paper describing how to organize this on modern multi-node computers is nearly finished [15]. Relativistic symmetry relations can be exploited to reduce the number of independent coefficients which need to be calculated.

7. G-spinor representation of operators

The application of G-spinor basis sets can be illustrated most conveniently by constructing the matrix operators needed for DCB calculations. The DCB equations can be derived from a variational principle along familiar nonrelativistic lines [7], [8, Chapter 3]. It has usually been assumed that the absence of a global lower bound to the Dirac spectrum invalidates this procedure; it has now been established [16] that *the upper spectrum has a lower bound* when the trial functions lie in an appropriate domain. This theorem covers the variational derivation of G-spinor matrix DCB equations. Sucher's repeated assertions [17] that the DCB Hamiltonian is fatally diseased and that the operators must be surrounded with energy projection operators can be safely forgotten.

7.1. THE DCB FOCK MATRIX

The Fock equations take the familiar form

$$\boldsymbol{F}\,\boldsymbol{c} = \boldsymbol{\varepsilon}\,\boldsymbol{S}\,\boldsymbol{c} \tag{28}$$

where $\boldsymbol{S}$ is the Gram (overlap) matrix for the $2N$-dimensional G-spinor basis set, and the $2N \times 2N$-dimensional Fock matrix is

$$\boldsymbol{F} := \boldsymbol{h} + \boldsymbol{J} - \boldsymbol{K} + \boldsymbol{B} \tag{29}$$

The Dirac Hamiltonian matrix $\boldsymbol{h}$ can be written in terms of $N \times N$ submatrices

$$\boldsymbol{h} = \begin{bmatrix} \boldsymbol{V}_{nuc}^{++} & \boldsymbol{h}^{+-} \\ \boldsymbol{h}^{-+} & \boldsymbol{V}_{nuc}^{--} - 2mc^2\boldsymbol{S}^{--} \end{bmatrix} \tag{30}$$

Since the nuclear potential is a multiplicative function, the nuclear potential matrix elements are defined by

$$[\boldsymbol{V}_{nuc}]_{\mu\nu}^{\beta\beta'} = \delta_{\beta\beta'} \int \rho_{\mu\nu}^{\beta\beta}(\boldsymbol{x})\, V_{nuc}(\boldsymbol{x})\, d\boldsymbol{x} \tag{31}$$

The Gram matrix $\boldsymbol{S}$ is also block diagonal, and

$$S_{\mu\nu}^{\beta\beta'} = \delta_{\beta\beta'} \left(\frac{\pi}{a_{\mu\nu}}\right)^{3/2} E_0^{\beta\beta}[\mu, \nu; \boldsymbol{0}]. \tag{32}$$

Finally, the kinetic matrices $\boldsymbol{h}^{\beta,-\beta}$, which are matrix representations of the operator $\boldsymbol{\sigma} \cdot \boldsymbol{p}$, are simply proportional to elements of $\boldsymbol{S}^{--}$:

$$h_{\mu\nu}^{-+} = \left[h_{\nu\mu}^{+-}\right]^* = S_{\mu\nu}^{--} \cdot \frac{N_\nu^-}{N_\nu^+} \tag{33}$$

This elegant result has the consequence that the operator equivalence $\boldsymbol{p}^2 = (\boldsymbol{\sigma} \cdot \boldsymbol{p})^2$ is reproduced exactly in the matrix form [18], [19, Equation (28)]

$$\boldsymbol{h}^{+-}[\boldsymbol{S}^{--}]^{-1}\boldsymbol{h}^{-+} = [\boldsymbol{p}^2]^{++}, \tag{34}$$

ensuring that the correct nonrelativistic Schrödinger equation in the upper basis set results in the limit $c \to \infty$.

The matrices $\boldsymbol{J}$, $\boldsymbol{K}$ and $\boldsymbol{B}$ are direct, exchange and Breit interaction matrices, of which only the first is block diagonal. Their matrix elements are linear combinations of interaction integrals over G-spinors.

7.2. TWO-BODY INTERACTIONS WITH G-SPINORS

Coulomb interaction integrals over molecular orbitals can be written as a sum of similar interaction integrals with G-spinor overlap densities $\rho_{\mu\nu}^{\beta\beta}$ and $\rho_{\sigma\tau}^{\beta'\beta'}$:

$$(AB|CD) = \sum_{\mu\nu\sigma\tau} \sum_{\beta\beta'} c_{\mu A}^{\beta *}\, c_{\nu B}^{\beta}\, c_{\rho C}^{\beta *\prime}\, c_{\sigma D}^{\beta'}\, (\mu\beta, \nu\beta|\sigma\beta', \tau\beta'), \tag{35}$$

where

$$\begin{aligned} (\mu\beta, \nu\beta|\sigma\beta', \tau\beta') &= \iint \frac{\rho_{\mu\nu}^{\beta\beta}(\boldsymbol{x})\rho_{\sigma\tau}^{\beta'\beta'}(\boldsymbol{y})}{|\boldsymbol{x} - \boldsymbol{y}|} \\ &= \sum_{\boldsymbol{\gamma},\boldsymbol{\gamma}'} E_0^{\beta\beta}[\mu, \nu; \boldsymbol{\gamma}]\, E_0^{\beta'\beta'}[\sigma, \tau; \boldsymbol{\gamma}']\, (a_{\mu\nu}, \boldsymbol{r}_{A_{\mu\nu}}; \boldsymbol{\gamma}|a_{\sigma\tau}, \boldsymbol{r}_{A_{\sigma\tau}}; \boldsymbol{\gamma}') \end{aligned} \tag{36}$$

The auxiliary integrals over HGTF,

$$(a_{\mu\nu}, \boldsymbol{r}_{A_{\mu\nu}}; \boldsymbol{\gamma} | a_{\sigma\tau}, \boldsymbol{r}_{A_{\sigma\tau}}; \boldsymbol{\gamma}') = \iint \frac{H(a_{\mu\nu}, \boldsymbol{r}_{A_{\mu\nu}}; \boldsymbol{\gamma})\, H(a_{\sigma\tau}, \boldsymbol{r}_{A_{\sigma\tau}}; \boldsymbol{\gamma}')}{|\boldsymbol{x} - \boldsymbol{y}|}, \quad (37)$$

are well-known from nonrelativistic calculations and there are efficient algorithms for their construction.

The $J_{\mu\nu}^{\beta\beta}$ matrix elements represent the classical interaction energy of the overlap density $\rho_{\mu\nu}^{\beta\beta}$ with the electron distribution. Following Almlöf [20], we can write this in the form

$$J_{\mu\nu}^{\beta\beta'} = \delta_{\beta\beta'} \sum_{\boldsymbol{k}} E_0^{\beta\beta}[\mu\nu; \boldsymbol{\gamma}]\, U_{\{\mu\},\{\nu\}}(\boldsymbol{\gamma}) \quad (38)$$

where

$$U_{\{\mu\},\{\nu\}}(\boldsymbol{\gamma}) = \sum_{\boldsymbol{\gamma}'} \sum_{\{\sigma\}\{\tau\}} (a_{\mu\nu}, \boldsymbol{r}_{A_{\mu\nu}}; \boldsymbol{\gamma} | a_{\sigma\tau}, \boldsymbol{r}_{|_{\sigma\tau}}; \boldsymbol{\gamma}') D_{\{\sigma\}\{\tau\}}(\boldsymbol{\gamma}') \quad (39)$$

with

$$D_{\{\sigma\}\{\tau\}}(\boldsymbol{\gamma}) = \sum_{\{\sigma\}\{\tau\}} \sum_{\boldsymbol{\gamma}} \sum_{\beta} E_0^{\beta\beta}[\sigma\tau; \boldsymbol{\gamma}]\, D_{\sigma\tau}^{\beta\beta}, \quad D_{\sigma\tau}^{\beta\beta'} = \sum_{A} c_{\sigma A}^{\beta *} c_{\tau A}^{\beta'},$$

where $\{\mu\} = \{\mu^{(1)}, \ldots, \mu^{(n_\mu)}\}$ denotes the set of all basis functions

$$\mu^{(i)} = (\boldsymbol{A}_\mu, a_\mu, \kappa_\mu^{(i)}, m_\mu^{(i)})$$

on the same centre $\boldsymbol{A}_\mu$ with the same exponent a_μ. The cost of this construction is comparable with that of the electron-nucleus interaction matrix. However, no such simplification is available for the exchange matrices $\boldsymbol{K}^{\beta\beta'}$:

$$K_{\mu\nu}^{\beta\beta'} = \sum_{\boldsymbol{\gamma}} E_0^{\beta\beta}[\mu\nu; \boldsymbol{\gamma}] \sum_{\boldsymbol{\gamma}'} \sum_{\sigma\tau} (a_{\mu\nu}, \boldsymbol{r}_{A_{\mu\nu}}; \boldsymbol{\gamma} | a_{\sigma\tau}, \boldsymbol{r}_{A_{\sigma\tau}}; \boldsymbol{\gamma}')\, . E_0^{\beta'\beta'}[\sigma\tau; \boldsymbol{\gamma}'] D_{\sigma\tau}^{\beta'\beta} \quad (40)$$

and the Breit matrices $\boldsymbol{B}^{\beta\beta'}$ are still more complicated [8, §5.4].

8. Energy of the internal electromagnetic fields

We have recently shown that considerable economies can result from noting the well-known equivalence of the energy of a system of interacting charges and currents with the energy of the electric and magnetic fields that they generate [5]. In the case of the G-spinor Coulomb interaction integral (36), we showed that

$$(\mu\beta, \nu\beta | \sigma\beta', \tau\beta') = \epsilon_0 \sum_{\beta\beta'} \int d\boldsymbol{x}\; \boldsymbol{E}_{\mu\nu}^{\beta\beta}(\boldsymbol{x}) \cdot \boldsymbol{E}_{\sigma\tau}^{\beta'\beta'}(\boldsymbol{x}) \quad (41)$$

where $\boldsymbol{E}^{\beta\beta}_{\mu\nu}(\boldsymbol{x})$ is the electric field at the point $\boldsymbol{x}$ generated by the overlap charge distribution $\rho^{\beta\beta}_{\mu\nu}(\boldsymbol{x})$. The equivalence of (36) and (41) requires a standard result of electrostatics used, for example, by Slater [21, Appendix 19] to prove the positivity of exhange integrals. Thus, writing $G^{\beta\beta'}_{\mu\nu} = J^{\beta\beta'}_{\mu\nu} - K^{\beta\beta'}_{\mu\nu}$, we have

$$G^{\beta\beta'}_{\mu\nu} = \epsilon_0 \int d\boldsymbol{x} \left\{ \delta_{\beta\beta'}\, \boldsymbol{E}(\boldsymbol{x}) \cdot \boldsymbol{E}^{\beta\beta}_{\mu\nu}(\boldsymbol{x}) - \sum_{\sigma\tau} \boldsymbol{E}^{\beta\beta}_{\mu\tau}(\boldsymbol{x}) \cdot \boldsymbol{E}^{\beta'\beta'}_{\sigma\nu}(\boldsymbol{x}) D^{\beta'\beta}_{\sigma\tau} \right\} \quad (42)$$

where

$$\boldsymbol{E}(\boldsymbol{x}) = \sum_{\sigma\tau} \sum_{\beta} \boldsymbol{E}^{\beta\beta}_{\sigma\tau}(\boldsymbol{x})\, D^{\beta\beta}_{\sigma\tau} \quad (43)$$

is the $\boldsymbol{E}$-field due to the whole electronic charge distribution. The structure of the first (direct) term is reminiscent of the Almlöf $\boldsymbol{J}$-matrix scheme and the second part is the exchange field contribution. Note that the interaction of $\rho^{\beta\beta}_{\mu\nu}(\boldsymbol{x})$ with itself contained in the direct term cancels exactly with a corresponding term in the exchange sum. The $\boldsymbol{E}$-fields are constructed from the same components as the interaction integrals: the r-th component ($r = 1, 2, 3$) is

$$\left[\boldsymbol{E}^{\beta\beta'}_{\mu\nu}(\boldsymbol{x})\right]_r = \frac{e}{4\pi\epsilon_0} \delta_{\beta\beta'} \sum_{\boldsymbol{\gamma}} E^{\beta\beta}_0(\mu, \nu; \boldsymbol{\gamma})\, (a_{\mu\nu}, \boldsymbol{A}_{\mu\nu}; \boldsymbol{\gamma} + \boldsymbol{e}_r | \boldsymbol{x}_{A_{\mu\nu}}) \quad (44)$$

where $\boldsymbol{e}_r = (\delta_{r1}, \delta_{r2}, \delta_{r3})$ and

$$(a_{\mu\nu}, \boldsymbol{A}_{\mu\nu}; \boldsymbol{\gamma} | \boldsymbol{x}_{A_{\mu\nu}}) = \int \frac{H(a_{\mu\nu}, \boldsymbol{y}_{A_{\mu\nu}}; \boldsymbol{\gamma})}{|\boldsymbol{x} - \boldsymbol{y}|} \quad (45)$$

is a special case of (37). The electron nuclear interaction matrix elements are given by

$$V^{\beta\beta}_{nuc} = \epsilon_0 \int d\boldsymbol{x}\; \boldsymbol{E}_{nuc}(\boldsymbol{x}) \cdot \boldsymbol{E}^{\beta\beta}_{\mu\nu}(\boldsymbol{x}) \quad (46)$$

where $\boldsymbol{E}_{nuc}(\boldsymbol{x})$ is the classical electric field due to the nuclei.

The Breit interaction matrix can be treated in a similar way. The off-diagonal blocks can be written in terms of the magnetic fields using

$$B^{\beta,-\beta}_{\mu\nu} = \frac{1}{\mu_0} \int d\boldsymbol{x} \left\{ \boldsymbol{B}(\boldsymbol{x}) \cdot \boldsymbol{B}^{\beta,-\beta}_{\mu\nu}(\boldsymbol{x}) - \sum_{\sigma\tau} \boldsymbol{B}^{\beta,-\beta}_{\mu\tau}(\boldsymbol{x}) \cdot \boldsymbol{B}^{\beta,-\beta}_{\sigma\nu}(\boldsymbol{x})\, D^{\beta,-\beta}_{\sigma\tau} \right\} \quad (47)$$

where the total $\boldsymbol{B}$-field is

$$\boldsymbol{B}(\boldsymbol{x}) = \sum_{\sigma\nu} \sum_{\beta} D^{\beta,-\beta}_{\sigma\tau}\, \boldsymbol{B}^{\beta,-\beta}_{\sigma\nu}$$

and the diagonal blocks have elements

$$B_{\mu\nu}^{\beta,\beta} = -\frac{1}{\mu_0}\int d\boldsymbol{x} \sum_{\sigma\tau} \boldsymbol{B}_{\mu\tau}^{\beta,-\beta}(\boldsymbol{x}) \cdot \boldsymbol{B}_{\sigma\nu}^{-\beta,\beta}(\boldsymbol{x})\, D_{\sigma\tau}^{-\beta,-\beta}. \tag{48}$$

The magnetic field Cartesian components can be expressed in a form analogous to (44)

$$\left[\boldsymbol{B}_{\mu\nu}^{\beta,-\beta}(\boldsymbol{x})\right]_r = +i\,\epsilon_{rst}\,\frac{ec\mu_0}{4\pi}\sum_{\boldsymbol{\gamma}}\Big\{E_s^{\beta,-\beta}(\mu,\nu;\boldsymbol{\gamma})\,(a_{\mu\nu},\boldsymbol{A}_{\mu\nu};\boldsymbol{\gamma}+\boldsymbol{e}_t|\boldsymbol{x}_{A_{\mu\nu}}) - E_t^{\beta,-\beta}(\mu,\nu;\boldsymbol{\gamma})\,(a_{\mu\nu},\boldsymbol{A}_{\mu\nu};\boldsymbol{\gamma}+\boldsymbol{e}_s|\boldsymbol{x}_{A_{\mu\nu}})\Big\} \tag{49}$$

where the Levi-Civita density ϵ_{rst} takes the value $+1$ if rst is an even permutation of 123, -1 if it is an odd permutation of 123, and vanishes otherwise.

The usefulness of this reformulation rests upon the fact that it requires $O(3N^2)$ field components to be evaluated at, say M, integration points $\boldsymbol{x}_i$ distributed over the region occupied by the molecule rather than $O(N^4)$ interaction integrals, a substantial saving when N is large. We have adapted [5] the Becke cell integration scheme [22] from density functional theory for this purpose; clearly there is considerable scope for exploiting the independence of the calculation at different points $\boldsymbol{x}_i$ on modern vector and parallel machines. Integrands close to the nuclei can be evaluated using radial-angular decomposition, whilst multipole expansions can be used for large radii.

9. Applications

Relativistic DCB atomic structure calculations using the present formalism but with S-spinors (based on exponential rather than Gaussian functions) have been performed since 1987 [23–25], starting with He-like ions up to U^{90+}. Argon-like atoms were studied in [26] along with some experiments including negative energy intermediate states in second order MBPT for He-like ions, which were extended to Ar in [27] and to Hg in [28].

The experience gained in these studies has been invaluable for the development of the BERTHA molecular code; much of the material of the present article was first presented in [29] and [30], together with applications to the study of magnetic and hyperfine interactions in atoms and small molecules, NMR shielding constants for H_2O and NH_3, and P-odd interactions in chiral molecules such as CHBrClF. A detailed study of the water molecule [31] examined the convergence of the DHF and DHFB calculations with a series of uncontracted correlation consistent basis sets due

to Dunning [32], augmented by a triple-zeta quality basis set developed to represent the spinor amplitudes better near the nucleus. The paper also threw light on the mechanism of pair correlation in relativistic MBPT2 calculations, and presented values of NMR shielding constants which compare well with those calculated by completely different methods. The noteworthy element of the ^{17}O shielding calculation is the dominant contribution of intermediate virtual states of negative energy to the final figure [31, Table 1]. The calculations for NH_3 in [29] show the same effect.

The water calculations showed an unsuspected relativistic geometry correction to the ground state potential energy surface and led to further collaborative work in which the potential energy surface was determined as a function of geometry at over 300 points [34]. The calculations combined corections including the two-electron Darwin term of the Coulomb-Pauli Hamiltonian at the cc-pVQZ CCSD(T) level of theory, Gaunt and Breit corrections calculated perturbationally, together with DHF calculations using two different basis sets. Finally a fitted correction surface was used together with a high-accuracy *ab initio* Born-Oppenheimer PE hypersurface to calculate vibrational band origins and rotational term values for $H_2{}^{16}O$. The calculations suggested that the previously neglected two-electron relativistic corrections have a substantial influence on the rotation-vibrational levels of water, and gave a detailed analysis. Similar results were later obtained for $H_2{}^{32}S$ [35].

Whilst this demonstrates that calculations using the methods of this paper may prove very useful in studies of molecules containing only low-Z atoms, a major objective has been to study systems containing heavier atoms. So far, only a limited number of molecular calculations have been carried out with BERTHA at the DHF level, mainly in connection with studies of hyperfine and PT-odd effects in heavy polar molecules such as YbF [33] and TlF [13]. The reader is referred to the literature for an assessment of these calculations and for technical details on the construction of basis sets which must not only describe molecular bonding properly but also give a good representation of spinors close to the heavy nuclei to handle the short-range electron-nuclear electroweak interactions.

Finally the BERTHA technology has been applied to relativistic density functional theory by Quiney and Belanzoni [36]. This showed that the method works well for closed shell atoms as compared with benchmark calculations using finite difference methods, and there have been promising parallelization studies [37] which should in future greatly extend the range of application of the code.

10. Conclusion and outlook

Although the framework of many-electron atomic physics was settled in the 1930s, widespread *ab initio* implementations only became feasible some

thirty years later as the first electronic computers were introduced at national and university laboratories. Many current developments in non-relativistic quantum chemistry implement ideas that were first proposed decades ago but had to await the widespread diffusion of affordable computing power. The desirability of a fully relativistic formulation of quantum chemistry to extend traditional quantum chemistry to the lower rows of the Periodic Table and to interpret high precision experimental data has been recognized for at least twenty years. Our project, building upon both the extensive experience of using relativistic methods in atomic physics and recent technical progress in computational molecular sciences, is another step in the same direction.

BERTHA, whose methods were outlined in [29,30], is the first quantum chemistry package in which the spinor character of the G-spinor basis set has played a central role, although a related approach has been adopted by Yanai *et al.* [38–40]. This paper has tried to show that our formalism simplifies the equations and makes their physical interpretation easier. The approach used in most other four component quantum chemistry packages such as MOLFDIR [41] or DIRAC [42] utilizes standard nonrelativistic integral packages. This forces one to treat the "large" and "small" basis functions as if each component were a scalar Cartesian Gaussian spin-orbital. Fægri and Dyall [43, pp. 259–290] have recently outlined practical solutions to the problems that arise as a result of the decision to use integral codes for scalar functions. We have avoided these difficulties at the expense of devising our own efficient integral evaluation package [15].

Our approach retains as much as possible of the physics of relativistic interactions and dynamics while minimizing the computational cost. In practice this cost depends both on the choice of algorithms and on the way they are implemented on the available computers. As in other codes, we employ symmetry and screening methods [29, §6.4] to reduce the labour of calculating interaction integrals, and we have also looked for savings from a reformulation, §8, based on standard electromagnetic theory. We can also take advantage of the way in which interaction integrals simplify when all wavefunctions are centred on the same nucleus. Since the largest relativistic effects are due to one-centre integrals, this makes it possible to do direct DHF calculations for atomic cores and to optimize basis sets directly for each atom of interest. One-centre algorithms can also be exploited in polyatomic systems to reduce the computational burden. It is then straightforward to build up more complex systems cheaply from converged atomic or molecular fragments [29, §6.4]. The technology is applicable to DFT models as well as DHF and can be extended straightforwardly to permit correlation calculations along familiar lines.

Many-body effects play a leading role in the description of chemical phenomena, and there is little point advancing detailed relativistic theories which cannot treat the electron correlation problem. A major advan-

tage of our approach is that almost all of the computational technology of many-electron quantum chemistry may be interfaced to BERTHA with little change. Current trends towards the $O(N)$ evaluation of the Coulomb interaction within complex extended systems, the use of density functional or high-order response theories to describe the interaction with external fields may all be generalized with little effort within the relativistic formulation. The similarity of nonrelativistic and relativistic theories of correlation becomes more transparent when the interactions are written in terms of the charge-current densities. This can suggest surprising economies. Examples are the strong localization of direct relativistic effects to the neighbourhood of nuclei, the equivalence of expressions for the electron-electron interaction energy, either represented in terms of conventional interaction integrals or as the energy associated with the corresponding internal electromagnetic fields, and the relativistic generalization of the Hohenberg-Kohn theorem.

We believe that our relativistic methods should be seen as part of mainstream quantum chemistry, and not as some exotic offshoot. We have described a relativistic molecular structure scheme that is built on the analytical evaluation of some standard integrals, the solution of generalized matrix eigenvalue equations, numerical quadratures and cubatures, and repeated linear transformations using standard computational methods. While our physical point of view is, perhaps, unfamiliar to some of our readers, we wish to emphasize that its implementation is very much a case of "business as usual". We hope that wider understanding of its advantages will encourage more quantum chemists to consider if BERTHA and similar programs can be used to advantage in their research.

References

1. B. Swirles, Proc. Roy. Soc. A **152**, 625 (1935); Proc. Roy. Soc. A **157**, 680 (1936).
2. H. M. Quiney, H. Skaane and I. P. Grant, J. Phys. B: At. Mol. Opt Phys. **30**, L829 (1997).
3. L. E. McMurchie and E. R. Davidson, J. Comput. Phys. **26**, 218 (1978).
4. E. Engel, R. M. Dreizler, S. Varga and B. Fricke, in *Relativistic Effects in Heavy-element Chemistry and Physics* (ed. B. A. Hess) (John Wiley and Sons Ltd, Chichester 2003).
5. H. M. Quiney and I. P. Grant, Int. J. Quant. Chem. **99**, 198 (2004).
6. J. Meyer, W.-D. Sepp, B. Fricke and A. Rosén, Comput. Phys. Commun. **96**, 263 (1996).
7. I. P. Grant, in *Atomic, Molecular and Optical Physics Handbook* (ed. G. W. F. Drake) (American Institute of Physics, Woodberry, New York, 1996).
8. I. P. Grant and H. M. Quiney in *Relativistic Electronic Structure Theory, Part I: Fundamentals* (ed. P. Schwerdtfeger). Theoretical and Computational Chemistry, Vol. 11. (Elsevier Science B. V., Amsterdam 2002).
9. C. Froese Fischer, in *Atomic, Molecular and Optical Physics Handbook* (ed. G. W. F. Drake) (American Institute of Physics, Woodberry, New York, 1996).
10. D. M. Brink and G. R. Satchler, *Angular Momentum* (2nd edition) (Clarendon Press, Oxford, 1968).

11. J. D. Louck, in *Atomic, Molecular and Optical Physics Handbook* (ed. G. W. F. Drake) (American Institute of Physics, Woodberry, New York, 1996).
12. E. U. Condon and G. H. Shortley, *Theory of Atomic Spectra* (Cambridge University Press, 1935).
13. H. M. Quiney, J. K. Laerdahl, K. Fægri jr., and T. Saue, Phys. Rev. A **57** 920 (1998).
14. Y. S. Lee and A. D. McLean, J. Chem. Phys. **76**, 735 (1982).
15. H. M. Quiney and I. P. Grant, to be published (2005).
16. I. P. Grant and H. M. Quiney, Phys. Rev. A **62**, 22508 (2000).
17. J. Sucher, Phys. Rev. A **22**, 348 (1980); Int, J, Quant. Chem. **25**, 3 (1982).
18. K. G. Dyall, I. P. Grant and S. Wilson, J. Phys. B.: At. Mol. Phys. **17**, 493 (1984).
19. I. P. Grant, J. Phys. B.: At. Mol. Phys. **19**, 3187 (1986).
20. A. Almlöf, J. Chem. Phys. **104**, 4685 (1966); G. R. Ahmadi and A. Almlöf, Chem. Phys. Lett. **246**, 364 (1966).
21. J. C. Slater, *Quantum Theory of Atomic Structure* Volume 1 (McGraw-Hill, New York 1960).
22. A. D,. Becke, J. Chem. Phys. **88**, 2547 (1988).
23. H. M. Quiney, I. P. Grant and S. Wilson, J. Phys. B.: At. Mol. Phys. **20**, 1413 (1987).
24. H. M. Quiney, I. P. Grant and S. Wilson, Physica Scripta **36**, 460 (1987).
25. I. P. Grant and H. M. Quiney, Adv. At. Mol. Phys. **23**, 37 (1988)
26. H. M. Quiney, I. P. Grant and S. Wilson, in *Many-Body Methods in Quantum Chemistry* (Lecture Notes in Chemistry No. 52) (ed. U. Kaldor), p. 307 (Springer-Verlag, Berlin 1989).
27. H. M. Quiney, I. P. Grant and S. Wilson, J. Phys. B.: At. Mol. Phys. **23**, L271 (1990).
28. I. P. Grant in *The effects of relativity in atoms, molecules and solids* (ed. S. Wilson, I. P. Grant and B. L. Gyorffy), p. 17 (Plenum Press, New York 1991); and in *Proceedings of the 15the International Conference on X-ray and inner-shell processes* (X-90) (ed. T. A. Carlson), p. 46 (AIP Conference Series No. 215, 1990).
29. H. M. Quiney, H. Skaane and I. P. Grant, Adv. Quant. Chem.. **32**,1 (1998).
30. I. P. Grant and H. M. Quiney, Int. J. Quant. Chem. **80**, 283 (2000).
31. H. M. Quiney, H. Skaane and I. P. Grant, Chem. Phys. Lett. **290**, 473 (1998).
32. T. H. Dunning jr., J. Chem. Phys. **90**, 1007 (1989); R. A. Kendall, T. H. Dunning jr. and R. J. Harrison J. Chem. Phys. **96**, 6796 (1992).
33. H. M. Quiney, H. Skaane and I. P. Grant, J. Phys. B.: At. Mol. Opt. Phys. **31**, L85 (1998)
34. H. M. Quiney, P. Barletta, G. Tarczay, A. G. Császár, O. L. Polyansky and J. Tennyson, Chem. Phys. Lett. **344**, 413 (2001).
35. P. Barletta, A. G. Császár, H. M. Quiney and J. Tennyson, Chem. Phys. Lett. **361**, 121 (2002).
36. H. M. Quiney and P. Belanzoni, J. Chem. Phys. **117**, 5550 (2002)
37. L. Belpassi, L. Storchi, F. Tarantelli, A. Sgamellotti and H. M. Quiney, Future Generation Computer Systems **20**, 739 (2004).
38. T. Yanai, T. Nakajima, Y. Ishikawa amd K. Hirao, J. Chem. Phys. **114**, 6526 (2001).
39. T. Yanai, H. Iikura, T. Nakajima, Y. Ishikawa amd K. Hirao, J. Chem. Phys. **115** 8267 (2001).
40. T. Yanai, T. Nakajima, Y. Ishikawa amd K. Hirao, J. Chem. Phys. **116**, 10122 (2002).
41. L. Visscher, O. Visser, H. Aerts, H. Merenga and W. C. Nieuwpoort, Comput. Phys. Commun. **81**, 120 (1994).
42. T. Saue, K. Fægri, T. Helgaker and O. Gropen, Mol. Phys. **91**, 937 (1997).
43. K. Fægri and K. G. Dyall in *Relativistic Electronic Structure Theory, Part I: Fundamentals* (ed. P. Schwerdtfeger). Theoretical and Computational Chemistry, Vol. 11. (Elsevier Science B. V., Amsterdam 2002).

NON-STANDARD REPRESENTATIONS OF THE DIRAC EQUATION AND THE VARIATIONAL METHOD

MONIKA STANKE AND JACEK KARWOWSKI

Instytut Fizyki,
Uniwersytet Mikołaja Kopernika,
Grudziądzka 5, PL-87-100 Toruń, Poland

Abstract. An application of the Rayleigh-Ritz variational method to solving the Dirac-Coulomb equation, although resulted in many successful implementations, is far from being trivial and there are still many unresolved questions. Usually, the variational principle is applied to this equation in the standard, Dirac-Pauli, representation. All observables derived from the Dirac equation are invariant with respect to the choice of the representation (i.e. to a similarity transformation in the four-dimensional spinor space). However, in order to control the behavior of the variational energy, the trial functions are subjected to several conditions, as for example the kinetic balance condition. These conditions are usually representation-dependent. The aim of this work is an analysis of some consequences of this dependence.

Apart of historical reasons, there are several features of the Dirac-Pauli representation which make its choice rather natural. In particular, it is the only representation in which, in a spherically-symmetric case, large and small components of the wavefunction are eigenfunctions of the orbital angular momentum operator. However, this advantage of the Dirac-Pauli representation is irrelevant if we study non-spherical systems. It appears that the representation of Weyl has several very interesting properties which make attractive its use in variational calculations. Also several other representations seem to be worth of attention. Usefulness of these ideas is illustrated by an example.

J.-P. Julien et al. (eds.),
Recent Advances in the Theory of Chemical and Physical Systems, 217–228.

1. Introduction

The Dirac equation for an electron in the field of a stationary potential V reads

$$\Big[c\,(\boldsymbol{\alpha}\cdot\boldsymbol{p}) + (\beta - I)\mu c^2 + \mathsf{V}\Big]\,\Psi = E\Psi, \tag{1}$$

where Ψ is the four-component Dirac spinor, $\boldsymbol{\alpha}$, β and I are 4×4 Dirac matrices, c is the velocity of light and E is the energy relative to μc^2. Usually the variational principle is applied to Eq. (1) in the Dirac-Pauli representation

$$\begin{pmatrix} \mathsf{V} - E, & c(\boldsymbol{\sigma}\cdot\boldsymbol{p}) \\ c(\boldsymbol{\sigma}\cdot\boldsymbol{p}), & \mathsf{V} - E - 2\mu c^2 \end{pmatrix} \begin{pmatrix} \Psi^L \\ \Psi^S \end{pmatrix} = 0, \tag{2}$$

where $\boldsymbol{\sigma}$ are 2×2 Pauli matrices, and Ψ^L, Ψ^S are two-component spinors, respectively large and small components of the Dirac wavefunction. In the variational procedure Ψ^L and Ψ^S are expanded in predefined basis sets $\{\phi^L_m\}_{m=1}^{N_L}$ and $\{\phi^S_m\}_{m=1}^{N_S}$, respectively. Thus,

$$\Psi^L = \sum_{m=1}^{N_L} C^L_m \phi^L_m, \quad \Psi^S = \sum_{m=1}^{N_S} C^S_m \phi^S_m, \tag{3}$$

where $\{C^L_m\}_{m=1}^{N_L}$ and $\{C^S_m\}_{m=1}^{N_S}$ are variational parameters. The basis functions are usually taken in the form $\phi \sim r^g\, e^{-\alpha r^q}$, where g and α may be treated as non-linear variational parameters, and $q = 1, 2$ depending on whether a Slater-type or a Gauss-type basis sets are used. The basis functions are usually centered on the nuclei and, in some cases, on other properly selected points, as e.g. on the geometric center of the molecule or the middle of a bond. The pattern of convergence of the variational energies $\mathcal{E}_j$, $j = 1, 2, \ldots, N^L$, derived from the resulting algebraic Dirac equation

$$\begin{pmatrix} \boldsymbol{H}^{LL} - \mathcal{E}\boldsymbol{S}^{LL}, & \boldsymbol{H}^{LS} \\ \boldsymbol{H}^{SL}, & \boldsymbol{H}^{SS} - \mathcal{E}\boldsymbol{S}^{SS} \end{pmatrix} \begin{pmatrix} \boldsymbol{C}^L \\ \boldsymbol{C}^S \end{pmatrix} = 0, \tag{4}$$

where

$$H^{LL}_{mn} = \langle \phi^L_m | \mathsf{V} | \phi^L_n \rangle, \quad H^{SS}_{mn} = \langle \phi^S_m | \mathsf{V} - 2\mu c^2 | \phi^S_n \rangle,$$
$$H^{LS}_{mn} = c\,\langle \phi^L_m | (\boldsymbol{\sigma}\cdot\boldsymbol{p}) | \phi^S_n \rangle,$$
$$S^{aa}_{mn} = \langle \phi^a_m | \phi^a_n \rangle, \quad a = L, S,$$

to the corresponding exact eigenvalues E_j of the Dirac Hamiltonian has been studied by many authors (see e.g. [1–3] and references therein). It has been demonstrated that the relations between spaces $\mathcal{H}^L$ and $\mathcal{H}^S$ spanned by the basis functions $\{\phi^L_m\}_{m=1}^{N_L}$ and $\{\phi^S_m\}_{m=1}^{N_S}$ respectively, are crucial for the correct behavior of the variational solutions of Eq. (4). In particular,

the solutions of Eq. (4) converge to their non-relativistic counterparts while $c \to \infty$ if

$$\mathcal{H}^S = (\boldsymbol{\sigma} \cdot \boldsymbol{p})\, \mathcal{H}^L. \tag{5}$$

Besides, condition (5) is necessary for $\mathcal{E}$ to be an upper bound to the corresponding eigenvalue E. The question how to control the behavior of the variational energy by using rather weakly constrained variational trial functions, motivated the formulation of a number of minimax principles [4–6]. A detailed discussion and classification of these approaches has been given in ref. [7]. In most general terms, they are based on the following condition:

$$E = \min_{\{L\}} \left[\max_{\{S\}} \frac{\langle \Psi | H | \Psi \rangle}{\langle \Psi | \Psi \rangle} \right], \tag{6}$$

where E is the ground state of a Dirac electron and $\{L\}$, $\{S\}$ refer, respectively, to the spaces in which large and small components of the Dirac-Pauli wavefunction are represented.

It is easy to see that Eq. (1) is invariant with respect to a similarity transformation in the four-dimensional spinor space. If Ψ and E are solutions of Eq. (1) then

$$\left[c\,(\tilde{\boldsymbol{\alpha}} \cdot \boldsymbol{p}) + (\tilde{\beta} - I)\mu c^2 + \mathsf{V} \right] \tilde{\Psi} = E \tilde{\Psi}, \tag{7}$$

where $\tilde{\boldsymbol{\alpha}} = A \boldsymbol{\alpha} A^{-1}$, $\tilde{\beta} = A \beta A^{-1}$, $\tilde{\Psi} = A\Psi$, and A is a non-singular 4×4 matrix. However, conditions (5) and (6) are not invariant with respect to such a transformation. Therefore, the performance of a variational procedure applied to the Dirac equation depends on the selected representation. The aim of the present work is to study this dependence.

Hartree atomic units are used in this paper, however in some places the mass μ of the electron is written explicitly in order to make the presentation more clear.

2. The Dirac-Pauli representation

The Dirac-Pauli representation is most commonly used in all applications of the Dirac theory to studies on electronic structure of atoms and molecules. Apart of historical reasons, there are several features of this representation which make its choice quite natural. Probably the most important is a well defined symmetry of Ψ^L and Ψ^S in the case of spherically-symmetric potentials V. The Dirac Hamiltonian

$$\mathsf{H} = c\,(\boldsymbol{\alpha} \cdot \boldsymbol{p}) + (\beta - I)\mu c^2 + \mathsf{V} \tag{8}$$

does not commute with the orbital angular momentum operators L^2 and L_z, however it does commute with the total angular momentum

$$\mathsf{J} = \mathsf{L} + \tfrac{1}{2}\boldsymbol{\Sigma}, \tag{9}$$

where, in the Dirac-Pauli representation,

$$\mathbf{\Sigma} = \begin{pmatrix} \boldsymbol{\sigma}, & 0 \\ 0, & \boldsymbol{\sigma} \end{pmatrix}. \tag{10}$$

Also, both H and J commute with an operator K defined as

$$\mathsf{K} = \beta \left(\mathbf{\Sigma} \cdot \mathsf{L} + \mathsf{I} \right), \tag{11}$$

where I is a 2×2 unit matrix. Explicitly K is given by

$$\mathsf{K} = \begin{pmatrix} \mathsf{k}, & 0 \\ 0, & -\mathsf{k} \end{pmatrix}, \tag{12}$$

where $\mathsf{k} = (\boldsymbol{\sigma} \cdot \mathsf{L}) + \mathsf{I}$ acts in the two-dimensional spinor space. Thus, a four-component eigenfunction of H may be chosen to be a simultaneous eigenfunction of J^2, J_z and K. The corresponding eigenvalues are $j(j+1)$, m_j and $k = \pm(j + 1/2)$. Then, for a spherically-symmetric potential V, we can write $\Psi = \Psi_{nkm_j}$, where n is the quantum number associated with the radial variable. Eq. (12) implies

$$\begin{array}{rcl} \left[(\boldsymbol{\sigma} \cdot \mathsf{L}) + \mathsf{I} \right] \Psi^L_{nkm_j} & = & k \, \Psi^L_{nkm_j}, \\ \left[(\boldsymbol{\sigma} \cdot \mathsf{L}) + \mathsf{I} \right] \Psi^S_{nkm_j} & = & -k \, \Psi^S_{nkm_j} \end{array} \tag{13}$$

Since $\mathsf{L}^2 = \mathsf{J}^2 - (\boldsymbol{\sigma} \cdot \mathsf{L}) - 3/4$, we can rewrite Eqs. (13) as

$$\begin{array}{rcccl} \mathsf{L}^2 \Psi^L_{nkm_j} & = & k(k-1) \Psi^L_{nkm_j} & = & l^L(l^L+1) \Psi^L_{nkm_j}, \\ \mathsf{L}^2 \Psi^S_{nkm_j} & = & k(k+1) \Psi^S_{nkm_j} & = & l^S(l^S+1) \Psi^S_{nkm_j}. \end{array} \tag{14}$$

The orbital angular momentum quantum numbers, $l^L \equiv l$ and l^S, corresponding, respectively, to the large and to the small components of the Dirac spinor are equal to

$$l = l^L = \begin{cases} k - 1 = j - 1/2, & \text{if} \quad k > 0, \\ -k = j + 1/2, & \text{if} \quad k < 0, \end{cases}$$

and

$$l^S = \begin{cases} k = j + 1/2, & \text{if} \quad k > 0, \\ -k - 1 = j - 1/2, & \text{if} \quad k < 0. \end{cases} \tag{15}$$

Hence, $l^S = l + 1$ if $k > 0$ and $l^S = l - 1$ if $k < 0$. Consequently, in the Dirac-Pauli representation Ψ^L and Ψ^S have definite parity, $(-1)^{l^L}$ and $(-1)^{l^S}$ respectively. It is customary in atomic physics to assign the orbital angular momentum label l to the state Ψ_{nkm_j}. Then, we have states $1s_{1/2}$, $2s_{1/2}$, $2p_{1/2}$, $2p_{3/2}$, ..., if the large component orbital angular momentum quantum numbers are, respectively, $0, 0, 1, 1, \ldots$ while the corresponding small components are eigenfunctions of L^2 to the eigenvalues $1, 1, 0, 2, \ldots$.

According to Eqs. (2) and (13) the Hamiltonian eigenfunction in the Dirac-Pauli representation may be written as

$$\Psi_{nkm_j} = \begin{pmatrix} \Psi^L_{nkm_j} \\ \Psi^S_{nkm_j} \end{pmatrix} = \frac{1}{r} \begin{pmatrix} \Theta_{km_j} R^L_{nk} \\ i\Theta_{-km_j} R^S_{nk} \end{pmatrix}, \tag{16}$$

where Θ_{km_j}, Θ_{-km_j} are the spin-angular functions and R^L_{nk}, R^S_{nk} are radial amplitudes. As one can easily check (see e.g [8]),

$$\begin{aligned} (\boldsymbol{\sigma}\cdot\boldsymbol{p})\Psi^L_{nkm_j} &= i\Theta_{-km_j}\frac{1}{r}\left(\frac{d}{dr}-\frac{k}{r}\right)R^L_{nk} \\ (\boldsymbol{\sigma}\cdot\boldsymbol{p})\Psi^S_{nkm_j} &= \Theta_{km_j}\frac{1}{r}\left(-\frac{d}{dr}-\frac{k}{r}\right)R^S_{nk} \end{aligned} \tag{17}$$

Consequently, the angular dependence may be removed from Eq. (2) reducing the Dirac equation to

$$\begin{pmatrix} \mathsf{V}-E, & c\,(-d/dr-k/r) \\ c\,(d/dr-k/r)\,, & \mathsf{V}-E-2\mu c^2 \end{pmatrix} \begin{pmatrix} R^L_{nk} \\ R^S_{nk} \end{pmatrix} = 0. \tag{18}$$

Changing the representation, i.e. taking

$$\tilde{\Psi} = \begin{pmatrix} \tilde{\Psi}^{\,u} \\ \tilde{\Psi}^{l}, \end{pmatrix} = \begin{pmatrix} a_{LL}\Psi^L + a_{LS}\Psi^S \\ a_{SL}\Psi^L + a_{SS}\Psi^S \end{pmatrix},$$

where

$$A = \begin{pmatrix} a_{LL}, & a_{LS} \\ a_{SL}, & a_{SS} \end{pmatrix},$$

and a_{LL}, a_{LS}, a_{SL}, a_{SS} are 2×2 matrices, destroys the symmetry relations between the components of the Dirac spinor. If we restrict our considerations to the case of $a_{LS}a_{SL} \neq 0$, then the Dirac-Pauli representation is the only one in which, for spherically-symmetric potentials, the components of the Dirac spinor are eigenfunctions of L^2.

Another important feature of the Dirac-Pauli representation is its natural adaptation to the non-relativistic limit. If $|\mathsf{V}-E| << \mu c^2$, then Eq. (2) transforms directly to its non-relativistic counterpart known as the Lévy-Leblond equation:

$$\begin{pmatrix} \mathsf{V}-E, & (\boldsymbol{\sigma}\cdot\boldsymbol{p}) \\ (\boldsymbol{\sigma}\cdot\boldsymbol{p}), & 2\mu \end{pmatrix} \begin{pmatrix} \Psi^L \\ c\,\Psi^S \end{pmatrix} = 0.$$

From here, after the elimination of Ψ^S, one obtains the Schrödinger equation

$$\left[\frac{(\boldsymbol{\sigma}\cdot\boldsymbol{p})^2}{2\mu} + \mathsf{V} - E\right]\Psi^L = 0$$

with Ψ^L transformed to the Schrödinger wavefunction.

The elimination of Ψ^S from Eq. (2) results in

$$\left\{\mathsf{V} - E + (\boldsymbol{\sigma}\cdot\boldsymbol{p})\left[2\mu - (\mathsf{V}-E)/c^2\right]^{-1}(\boldsymbol{\sigma}\cdot\boldsymbol{p})\right\}\Psi^L = 0. \tag{19}$$

From here, expanding the operator acting on Ψ^L in terms of powers of c^{-2}, one obtains the familiar Pauli approximation as well as numerous two-component quasi-relativistic approximations.

3. The Weyl representation

The Weyl representation corresponds to the transformation matrix

$$A_{\mathrm{w}} = \frac{1}{\sqrt{2}}\begin{pmatrix} \mathsf{I} & \mathsf{I} \\ \mathsf{I} & -\mathsf{I} \end{pmatrix} = A_{\mathrm{w}}^{-1}.$$

In this representation Eq. (1) reads

$$\begin{pmatrix} \mathsf{V} - E + c(\boldsymbol{\sigma}\cdot\boldsymbol{p}) - \mu c^2, & \mu c^2 \\ \mu c^2, & \mathsf{V} - E - c(\boldsymbol{\sigma}\cdot\boldsymbol{p}) - \mu c^2 \end{pmatrix}\begin{pmatrix} \Psi^u \\ \Psi^l \end{pmatrix} = 0, \tag{20}$$

and $\Psi^u = (\Psi^L + \Psi^S)/\sqrt{2}$, $\Psi^l = (\Psi^L - \Psi^S)/\sqrt{2}$. Equation (20) may be rewritten as a pair of Dirac-Weyl equations

$$\left[\mathsf{V} - E + c(\boldsymbol{\sigma}\cdot\boldsymbol{p}) - \mu c^2\right]\Psi^u = -\mu c^2\Psi^l, \tag{21}$$

$$\left[\mathsf{V} - E - c(\boldsymbol{\sigma}\cdot\boldsymbol{p}) - \mu c^2\right]\Psi^l = -\mu c^2\Psi^u. \tag{22}$$

As it is seen, the equations are decoupled if $\mu = 0$. As a consequence we obtain the two-component model of mass-less neutrino with Ψ^u corresponding to the *right* and Ψ^l – to the *left* neutrino [8].

If $\mu \neq 0$ Eqs. (21) and (22) are coupled, but the relations between components of the wavefunction are much simpler than in the standard Dirac-Pauli representation. By the elimination of Ψ^u and Ψ^l, respectively from Eq. (21) and from Eq. (22), we get two *decoupled* second-order equations for Ψ^u and Ψ^l:

$$\left[\frac{(\boldsymbol{\sigma}\cdot\boldsymbol{p})^2}{2\mu} + \mathsf{V} - E + \frac{(\mathsf{V}-E)^2}{2\mu c^2} + \frac{\boldsymbol{\sigma}(\boldsymbol{p}\mathsf{V})}{2\mu c}\right]\Psi^u = 0, \tag{23}$$

$$\left[\frac{(\boldsymbol{\sigma}\cdot\boldsymbol{p})^2}{2\mu} + \mathsf{V} - E + \frac{(\mathsf{V}-E)^2}{2\mu c^2} - \frac{\boldsymbol{\sigma}(\boldsymbol{p}\mathsf{V})}{2\mu c}\right]\Psi^l = 0. \tag{24}$$

The spin-independent part of these equations is identical to the Klein-Gordon equation. If the singularity of V is not stronger than $1/r$ then,

contrary to the Pauli corrections derived from Eq. (19), no irregular terms appear. However, the components of the Dirac-Weyl spinor, Ψ^u and Ψ^l, do not have any definite parity and a procedure of the elimination of the angular dependence from the Dirac-Weyl equation, similar to the one described in Eqs. (16) - (18) cannot be performed.

The solutions of the second-order equations should fulfill the normalization condition $\langle\Psi|\Psi\rangle = 1$. Since in Eqs. (23) and (24) the components of Ψ are determined independently, in order to secure the correct normalization one can use the following procedure

- Determine Ψ^u from the second-order equation
- Find $\Psi^l = -\left(\mu c^2\right)^{-1}\left[\mathsf{V} - E + c(\boldsymbol{\sigma}\cdot\boldsymbol{p}) - \mu c^2\right]\Psi^u$
- Determine the normalization constant as $\left(\langle\Psi^u|\Psi^u\rangle + \langle\Psi^l|\Psi^l\rangle\right)^{-1/2}$.

The Dirac-Weyl equations (21), (22) are known since the early days of quantum mechanics (see e.g. [9]) but, to our knowledge, were never used in numerical calculations for many-electron systems. Contrary to the standard representation, where Ψ^L and Ψ^S are eigenfunctions of L^2, here neither Ψ^u nor Ψ^l corresponds to a specific value of l. The space inversion applied to Ψ^u gives Ψ^l and *vice versa*. As a consequence, in the case of spherical symmetry, the two-component functions cannot be represented as products of a radial part and a spin-angular part. This disadvantage makes applications of the Weyl representation in atomic calculations rather inconvenient. However, in the case of molecules, it may offer an interesting alternative to the standard approach. Equation (23) may be solved using basis-set expansion methods developed for the Schrödinger equation with spin-dependent terms. For example, the spin-dependent formalism within symmetric group approach [10] is ideally suited for computer implementations of this equation.

4. Spherical symmetry and the representation of Biedenharn

Let us assume that $\mathsf{V} = \mathsf{V}(r)$. Then Eq. (23) may be rewritten as

$$\left(\mathsf{H}_r - \frac{1}{2\mu r^2}\Omega\right)\Psi_{njm_j} = E_{nj}\Psi_{njm_j}, \tag{25}$$

where

$$\mathsf{H}_r = -\frac{\triangle_r}{2\mu} + \mathsf{V} + \frac{1}{2\mu c^2}(\mathsf{V} - E)^2 \tag{26}$$

is the energy-dependent radial part of the Hamiltonian,

$$\Omega = \mathsf{L}^2 - \frac{r^2}{c}\frac{d\mathsf{V}}{dr}\,\pi \tag{27}$$

and

$$\pi = i\frac{(\boldsymbol{\sigma}\cdot\boldsymbol{r})}{r}, \quad \pi^2 = -1 \tag{28}$$

is the spin and angular part of the total Hamilton operator and we used the total angular momentum quantum number j instead of k. Let us try to separate the radial part of Ψ, i.e. to express the two-component wavefunction as

$$\Psi(r,\vartheta,\varphi)_{njm_j} = \chi_{jm_j}(\vartheta,\varphi)\, R_{nj}(r)/r \tag{29}$$

If the wavefunction (29) is to fulfill Eq. (25), then $\chi_{jm_j}(\vartheta,\varphi)$ has to be an eigenfunction of Ω, i.e.

$$\Omega\, \chi_{jm_j}(\vartheta,\varphi) = \lambda\, \chi_{jm_j}(\vartheta,\varphi). \tag{30}$$

Since the space of two-component eigenfunctions of J, J_z and k corresponding to a given set $\{j, m_j\}$ is spanned by Θ_{km_j} and Θ_{-km_j}, we have

$$\chi_{jm_j} = a\, \Theta_{km_j} + b\, \Theta_{-km_j}, \tag{31}$$

where a and b are numerical coefficients. Due to Eq. (14) and relations

$$\pi\ \Theta_{km_j} = -\Theta_{-km_j}, \quad \pi\ \Theta_{-km_j} = \Theta_{km_j},$$

Eq. (30) results in

$$\begin{vmatrix} k(k-1)-\lambda, & -c^{-1}\, r^2\, d\mathsf{V}/dr \\ c^{-1}\, r^2\, d\mathsf{V}/dr, & k(k+1)-\lambda \end{vmatrix} = 0. \tag{32}$$

Then

$$\lambda_\pm = k^2 \pm \sqrt{k^2 - (c^{-1}\, r^2\, dV/dr)^2}.$$

The coefficients a and b are r-independent only if $r^2\, dV/dr = Z = const$, i.e if $V = -Z/r$ is the Coulomb potential. In such a case

$$\lambda_\pm = k^2 \pm |s|, \quad s = k\sqrt{1 - Z^2/(kc)^2}. \tag{33}$$

Now, after the elimination of the spin and angular part from Eq. (25) and substitution of the explicit form of the potential we get the following second-order radial equation

$$\left[-\frac{d^2}{dr^2} + \frac{s(s-1)}{r^2} - \frac{2Z\Lambda}{r}\right] R_{nk}(r) = E_{nj}(1+\Lambda) R_{nk}(r), \tag{34}$$

where, $\Lambda = 1 + E_{nj}/c^2$ and we set $\mu = 1$. By substitution $\rho = \Lambda r$ and

$$e_{nj} = \frac{1+\Lambda}{2\Lambda^2}\, E_{nj} \tag{35}$$

we get

$$\left[-\frac{d^2}{d\rho^2} + \frac{s(s-1)}{\rho^2} - \frac{2Z}{\rho}\right] R_{nk}(\rho) = 2e_{nj} R_{nk}(\rho). \tag{36}$$

The last equation is formally identical to the radial Schrödinger equation with a non-integer value of the angular momentum quantum number. Its spectrum is bounded from below and the discrete eigenvalues are given by

$$e_{nj} = -\frac{Z^2}{2\tilde{n}^2}, \tag{37}$$

where $\tilde{n} = n - |k| + |s|$. By combining Eqs. (35) and (37) one can readily get the Sommerfeld formula for E_{nj}. Eq. (36) is known as the Biedenharn equation [11]. Among other applications, it was used to the construction of quasi-relativistic methods [12] and to deriving formulas for matrix elements between hydrogenic Dirac wavefunctions [13].

Eq. (36) may also be expressed as a system of two first-order equations, i.e. as the radial Dirac equation in the representation of Biedenharn. Let us rewrite the radial Dirac-Pauli equation (18) with $V = -Z/r$ in the form

$$\left[\frac{d}{dr}\begin{pmatrix} 1 & 0 \\ 0 & 1 \end{pmatrix} + \frac{1}{r}\begin{pmatrix} -k & -Z/c \\ Z/c & k \end{pmatrix} + \begin{pmatrix} 0 & -t_+ \\ t_- & 0 \end{pmatrix}\right]\begin{pmatrix} R^L_{nk} \\ R^S_{nk} \end{pmatrix} = 0, \tag{38}$$

where $t_\pm = c(\Lambda \pm 1)$. A similarity transformation defined by the matrix

$$A_{\mathrm{b}} = \begin{pmatrix} q_+, & q_- \\ q_-, & q_+ \end{pmatrix}, \qquad A^{-1}_{\mathrm{b}} = \begin{pmatrix} q_+, & -q_- \\ -q_-, & q_+ \end{pmatrix} \tag{39}$$

where $q_\pm = \sqrt{(k \pm s)/2s}$, diagonalizes the matrix of coefficients of $1/r$ in Eq. (38) and, consequently, yields

$$\begin{pmatrix} -c\left(\dfrac{k\Lambda}{s} - 1\right), & -\dfrac{d}{dr} - \dfrac{s}{r} + \dfrac{Z}{s}\Lambda \\ \dfrac{d}{dr} - \dfrac{s}{r} + \dfrac{Z}{s}\Lambda, & -c\left(\dfrac{k\Lambda}{s} + 1\right) \end{pmatrix}\begin{pmatrix} R^A \\ R^B \end{pmatrix} = 0, \tag{40}$$

where $R^A = q_+R^L + q_-R^S$ and $R^B = q_-R^L + q_+R^S$. Eqs. (40) may be easily decoupled giving as the result Eq. (34) with $R^A, R^B = R_{nk}$.

Transformation (39) applied to the case of a non-Coulomb spherically-symmetric potential results in an equation in which residual terms proportional to $\mathsf{W} = \mathsf{V} + Z/r$ would appear. Its algebraic representation reads:

$$\begin{pmatrix} \boldsymbol{H}^{AA} - \mathcal{E}\boldsymbol{S}^{AA}, & \boldsymbol{H}^{AB} - \mathcal{E}\boldsymbol{S}^{AB} \\ \boldsymbol{H}^{BA} - \mathcal{E}\boldsymbol{S}^{BA}, & \boldsymbol{H}^{BB} - \mathcal{E}\boldsymbol{S}^{BB} \end{pmatrix}\begin{pmatrix} \boldsymbol{C}^A \\ \boldsymbol{C}^B \end{pmatrix} = 0, \tag{41}$$

where

$$H^{AA}_{mn} = -\langle\phi^A_m|k\,\mathsf{W} + kc^2 - sc|\phi^A_n\rangle/(sc),$$
$$H^{BB}_{mn} = -\langle\phi^B_m|k\,\mathsf{W} + kc^2 + sc|\phi^B_n\rangle/(sc),$$

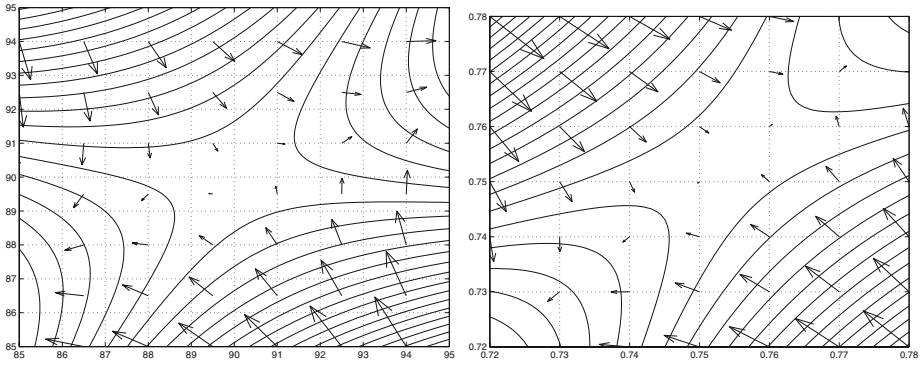

Figure 1. Variational ground state energy $\mathcal{E}$ of a $Z = 90$ hydrogen-like atom obtained from the Dirac-Pauli equation as a function of α (abscissa) and β (ordinate) while $a = b = s$ (left figure) and as a function of a (abscissa) and b while $\alpha = \beta = Z$ (right figure). The arrows are proportional to the gradient of $\mathcal{E}$. The saddle points correspond to the exact eigenvalues of the Dirac Hamiltonian.

$$H_{mn}^{AB} = -\left\langle \phi_m^A \left| \frac{d}{dr} + \frac{s}{r} - \frac{Z\mathsf{W}}{sc^2} \right| \phi_n^B \right\rangle,$$

$$S_{mn}^{aa} = k\langle \phi_m^a | \phi_n^a \rangle / (sc), \quad S_{mn}^{ab} = -Z\langle \phi_m^a | \phi_n^a \rangle / (sc^2), \quad a = A, B, \quad b = A, B,$$

and ϕ_m^A, $(m = 1, 2, \ldots, N_A)$, ϕ_n^B, $(n = 1, 2, \ldots, N_B)$ are, respectively, the basis function R^A and R^B are expanded in.

5. Minimax principle and structure of the energy surfaces

Relativistic variational principles are usually formulated as prescriptions for reaching a saddle point on the energy hypersurface in the space of variational parameters. The results of the variational calculations depend upon the orientation of the saddle in the space of the nonlinear parameters. The structure of the energy hypersurface may be very complicated and reaching the correct saddle point may be difficult [14, 15]. If each component of the wavefunction is associated with an independent set of nonlinear parameters, then changing the representation of the Dirac equation results in a transformation of the energy hypersurface. As a consequence, the numerical stability of the variational procedure depends on the chosen representation.

As an example we apply the variational principle to the evaluation of the ground state energy of a hydrogen-like atom using a minimum basis set of two-component radial functions:

$$R^A(r) \sim \phi^A(r) = r^a \mathrm{e}^{-\alpha r}, \quad R^B(r) \sim \phi^B(r) = r^b \mathrm{e}^{-\beta r}.$$

The exact wavefunction corresponds to $a = b = s$ and $\alpha = \beta = Z$. The variational ground state energy of $Z = 90$ hydrogen-like ion in the Dirac-Pauli

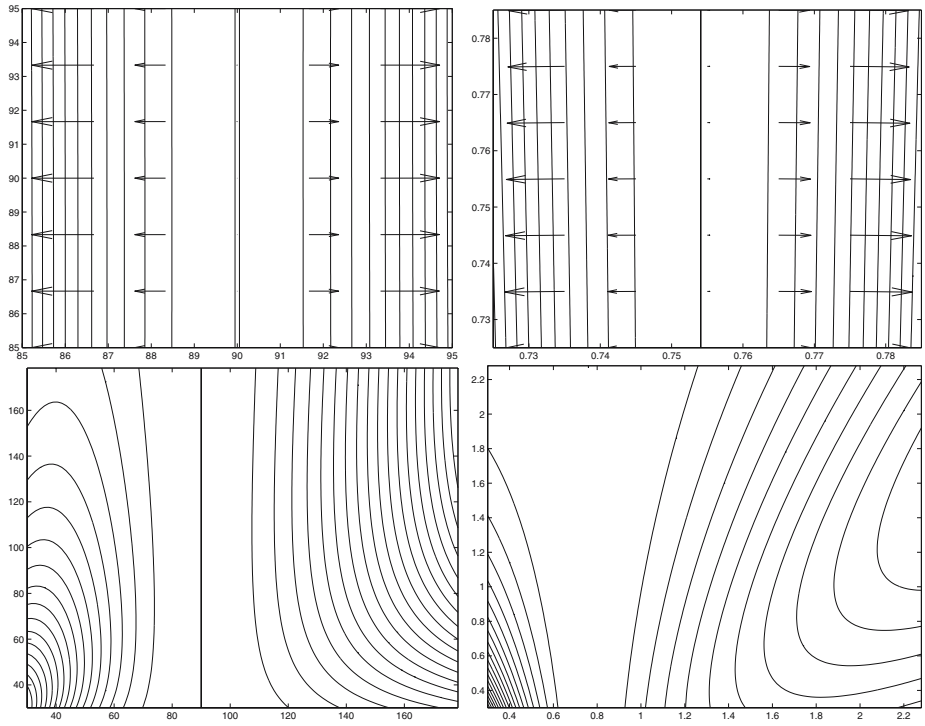

Figure 2. The same as in Fig. 1 but the variational energies are derived from the algebraic Dirac equation in the Biedenharn representation (41). The bottoms of the valleys at $\beta = 90$ (left figures) and at $b = 0.754$ (right figures) correspond to the exact eigenvalues of the Dirac Hamiltonian. The lower figures show the same function as the upper ones, but over a wider range of parameters.

representation, i.e. derived from the algebraic representation of Eq. (18), as a function of $\{\alpha, \beta\}$ while $a = b = s$ (the left-hand-side diagram), and as a function of $\{a, b\}$ while $\alpha = \beta = Z$ (the right-hand-side diagram), is plotted in Fig. 1. Analogous diagrams, but in the Biedenharn representation, i.e. derived from Eq. (41), are presented in Fig. 2. As one can see, the structure of the energy surfaces changes dramatically with the change of the representation. Typical saddles of the Dirac-Pauli representation transform to valleys, bounded from below by the exact ground state energy, when the representation is changed to the Biedenharn one. The bottom of the valley corresponds to the exact energy regardless of the values of the nonlinear parameters characterizing R^B. Consequently, the variational energy reaches its minimum equal to the exact ground state energy for all values of b and β as long as $a = s$ and $\alpha = Z$.

As we can see, the choice of the representation is relevant for the performance of the variational principle. However, in order to draw some general

conclusions concerning usefulness of this or another representation, further studies on this subject are necessary.

6. Final remarks

We demonstrated that by the selection of a representation of the Dirac Hamiltonian in the spinor space one may strongly influence the performance of the variational principle. In a vast majority of implementations the standard Pauli representation has been used. Consequently, computational algorithms developed in relativistic theory of many-electron systems have been constructed so that they are applicable in this representation only. The conditions, under which the results of these implementations are reliable, are very well understood and efficient numerical codes are available for both atomic and molecular calculations (see e.g. [16]). However, the representation of Weyl, if the external potential is non-spherical, or the representation of Biedenharn, in spherically-symmetric cases, seem to be attractive and, so far, hardly explored options.

References

1. G. W. F. Drake and S. P. Goldman, Phys. Rev. A **23**, 2093 (1981).
2. I. P. Grant and H. M. Quiney, Phys. Rev. A **62**, 022508 (2000).
3. G. Pestka, Physica Scripta, **68**, 254 (2003); **69**, 203 (2004).
4. J. Wood, I. P. Grant and S. Wilson, J. Phys. B: At. Mol. Phys. **18**, 3027 (1985).
5. J. D. Talman, Phys. Rev. Letters **57**, 1091 (1986).
6. S. N. Datta and G. Deviah, Pramana **30**, 387 (1988).
7. W. Kutzelnigg, Chem. Phys. **225**, 203 (1997).
8. J. J. Sakurai, *Advanced Quantum Mechanics* (Addison-Wesley, Redwood City, 1987).
9. A. I. Akhiezer and V. B. Beresteckij, *Quantum Electrodynamics* (Interscience Publishers, New York, 1965) Chapter 2.
10. J. Karwowski, J. Mol. Structure (Theochem) **547** (2001) 245.
11. L. C. Biedenharn, Phys. Rev. **126**, 845 (1962).
12. J. Karwowski and J. Kobus, Int. J. Quantum Chem. **30**, 808 (1986).
13. J. Kobus, J. Karwowski and W Jaskólski, J. Phys. A: Math. Gen. **20**, 3347 (1987).
14. J. Karwowski, G. Pestka and M. Stanke, in "Quantum Systems in Chemistry and Physics, Vol. I: Basic Problems and Model Systems", A. Hernandez-Laguna *et al.* editors, Kluwer Academic Publishers, Dordrecht, 2000, pp 179-193.
15. M. Stanke and J. Karwowski, in "New Trends in Quantum Systems in Chemistry and Physics", Vol. I, J. Maruani *et al.* editors, Kluwer Academic Publishers, Dordrecht, 2001, pp 175-190.
16. I. P. Grant and H. M. Quiney, *Progress with BERTHA: A relativistic atomic and molecular structure package*, this Volume.

GENERALIZED RECP ACCOUNTING FOR BREIT EFFECTS: URANIUM, PLUTONIUM AND SUPERHEAVY ELEMENTS 112, 113, 114

N. S. MOSYAGIN, A. N. PETROV AND A. V. TITOV
Petersburg Nuclear Physics Institute, Gatchina, St-Petersburg district 188300, Russia; mosyagin@pnpi.spb.ru; http://www.qchem.pnpi.spb.ru

AND

I. I. TUPITSYN
Physics Department, St-Petersburg State University, Starii Petergoff, St-Petersburg 198904, Russia

Abstract. The Generalized Relativistic Effective Core Potential (GRECP) method is described, which allows to simulate Breit interaction and finite nuclear models by an economic way with high accuracy. The corresponding GRECPs for the uranium, plutonium, eka-mercury (E112), eka-thallium (E113) and eka-lead (E114) atoms are generated. The accuracy of these GRECPs and of the RECPs of other groups is estimated in atomic numerical SCF calculations with Coulomb two-electron interactions and point nucleus as compared to the corresponding all-electron Hartree-Fock-Dirac-Breit calculations with the Fermi nuclear charge distribution. Different nuclear models and contributions of the Breit interaction between different shells are studied employing all-electron four-component methods.

1. Introduction

Investigation of physical and chemical properties of recently synthesized, relatively long-living isotopes of superheavy elements (SHEs) with nuclear charges Z=105 to 116 [1, 2, 3, 4] and their compounds is of fundamental importance. Their measured lifetimes may reach several hours and the nuclei near the top of the "island of stability" are predicted to exist for many years. The experimental study of the SHE properties is very difficult be-

J.-P. Julien et al. (eds.),
Recent Advances in the Theory of Chemical and Physical Systems, 229–251.

cause of their extremely small quantities: only single atoms are available for research. Accurate calculations for SHEs and their compounds are needed in order to better understand their physical and chemical properties, that often differ from those of the lighter homologs in the chemical groups, due to very strong relativistic effects in their electronic shells. Besides, for elements decaying by spontaneous fission, the chemical identification is the only way to prove their Z number.

Experimental investigations of spectroscopic and other physical-chemical properties of actinides are severely hampered by their radioactive decay and radiation which lead to chemical modifications of the systems under study. The diversity of properties of lanthanide and actinide compounds is unique due to the multitude of their valency forms (which can vary over a wide range) and because of the particular importance of relativistic effects. They are, therefore, of great interest, both for fundamental research and for the development of new technologies and materials. The most important practical problems involve storage and processing of radioactive waste and nuclear fuel, as well as pollution of the environment by radioactive waste, where most of the decayed elements are actinides.

From a formal point of view, four-component correlation calculations [5, 6] based on the Dirac-Coulomb-Breit (DCB) Hamiltonian (see [7, 8, 9, 10, 11] and references therein) can provide with very high accuracy the physical and chemical properties of molecules containing heavy atoms. However, such calculations were not widely used for such systems during last decade because of the following theoretical and technical complications [12]:

- too many electrons are treated explicitly in heavy-atom systems and too large number of Gaussians is required for accurate description of the large number of oscillations, which valence spinors have in heavy atoms;
- the necessity to work with four-component Dirac spinors leads to serious complication of calculations as compared to the nonrelativistic case:

  (a) the number of kinetically-balanced two-component ("2c") uncontracted Gaussian basis spinors for the Small components, N_S^{2c}, can be estimated as $2N_L^{2c}$, where N_L^{2c} is the number of basis spinors for Large components; so the total number of uncontracted Gaussian basis spinors in the relativistic four-component ("4c") calculations $N_{bas}^{4c} \sim 3N_L^{2c}$ and the number of two-electron integrals as [12]

  $$N_{2eInt}^{4c} \sim (1{+}2{\cdot}2^2{+}2^4)N_{2eInt}^{2c} \equiv 25{\cdot}N_{2eInt}^{2c} \ ;$$

  Note, however, that the situation is seriously improved here during last years, see [13, 14, 5, 6].

(b) the number of basis $2c$-spinors, N^{2c}_{bas}, is twice more than the number of nonrelativistic basis one-component ("$1c$") orbitals, N^{1c}_{bas}, therefore

$$N^{2c}_{2eInt} \sim 2^4/2 \cdot N^{1c}_{2eInt} \equiv 8 \cdot N^{1c}_{2eInt} \ ,$$

The minimal number of two-electron integrals in the spin-orbit basis set, which are required to be saved coincides, obviously, with N^{1c}_{2eInt}.

The Relativistic Effective Core Potential (RECP) method is most widely used in calculations on molecules containing heavy atoms [15, 16] because it reduces drastically the computational cost at the integral generation, SCF and integral transformation stages. In our papers [17, 18, 19], the conventional radially-local (semi-local) form of the RECP operator (used by many groups up to now but suggested and first applied about 40 years ago [20, 21, 22]) was shown to be limited by accuracy and some nonlocal corrections to the RECP operator were suggested [17, 23, 19, 24], which have already allowed us to improve significantly the RECP accuracy [18, 19, 25, 26].

It is known that the Breit interaction can give contributions in excess of one thousand wave numbers even to energies of transitions between lowest-lying states of very heavy elements (see, e.g., tables 7 and 8). It is also clear that the point nuclear model becomes less appropriate when the nuclear charge is increased. Therefore, the RECPs designed for accurate calculations of actinide and SHE compounds should allow one to take into account the Breit interaction and the finite size of nuclei. The most economic way is to incorporate the corresponding contributions into the RECP operator.

2. Generalized RECP method

In a series of papers (see [17, 18, 19, 24, 27] and references), we introduced and developed the Generalized RECP (GRECP) method. Its main features are:

- The inner core (IC), outer core (OC) and valence (V) electrons are first treated employing different approximations for each (including relaxation of the IC shells which are explicitly excluded from GRECP calculations).
- GRECP involves both radially-local, separable and Huzinaga-type potentials as its components and particular cases.
- The GRECP operator includes terms of other types for economical treatment of transition metals, lanthanides and actinides (see sections 2.1–2.2).

– The outer core pseudospinors (nodeless) together with valence pseudospinors (nodal) are used for constructing the GRECP components [28].
– Quantum electrodynamics effects (see [29] and section 2.3), arbitrary nuclear models, and correlation with IC shells [30] can be efficiently treated within GRECPs.

The GRECP method is described in detail in the above papers and we only add here that it allows one to avoid the complications of the four-component calculations described in the introduction (see also [30]) and to attain very high accuracy, limited in practice by possibilities of the correlation methods, while requiring moderate computational efforts when the IC, OC and V subspaces are appropriately chosen.

The contributions of different nuclear models which are described by local potentials can be easily taken into account in the framework of the (G)RECP method. The situation is more complicated in the case of the Breit interaction because it is represented by a two-electron operator. General justification of the possibility to simulate the Breit effects by means of an one-electron (G)RECP operator with good accuracy and the scheme of such GRECP generation are presented in [29] (see also section 2.3). This scheme is applied in the present work to generate GRECPs for the uranium, plutonium, eka-mercury (E112), eka-thallium (E113) and eka-lead (E114) atoms. The 32, 34, 20, 21 and 22 electrons are explicitly treated in calculations with these GRECPs, correspondingly. Moreover, the 52 electron GRECP (52e-GRECP) version for E112 was also generated. The conventional Coulomb operator for two-electron interactions and the point nuclear model should be used in these GRECP calculations. However, they will account for the Fermi nuclear charge model that is close to the experimental distribution. Moreover, the Breit interactions of the electrons from the state used for the GRECP generation with the electrons explicitly treated in the subsequent calculations are simulated by the GRECP (in some sense, the Breit interaction is "frozen" here).

2.1. SELF-CONSISTENT GRECP VERSION FOR *D*- AND *F*-ELEMENTS

The Self-Consistent (SfC) (G)RECP version [23, 19, 24, 27] allows one to minimize errors for energies of transitions with the change of the occupation numbers for the OuterMost Core (OMC) shells without extension of space of explicitly treated electrons. It allows one to take account of relaxation of those core shells, which are explicitly excluded from the GRECP calculations, thus going beyond the frozen core approximation. This method is most optimal for studying compounds of transition metals, lanthanides, and actinides. Features of constructing the self-consistent GRECP are:

1. The all-electron HFDB calculations of two generator states with different occupation numbers N
   carried out for an d- or f-element.
2. The GRECP versions with separable correction $\mathbf{U}^{N_1}$ and $\mathbf{U}^{N_2}$ are constructed for these generator states employing the standard scheme [17, 18, 19, 24]. The GRECP operator with the separable correction has the form

$$\begin{aligned}
\mathbf{U}^{N_i} &= E^{N_i}_{\rm core} + U^{N_i}_{n_v LJ}(r) \\
&+ \sum_{l=0}^{L} \sum_{j=|l-1/2|}^{l+1/2} \Big\{ \big[U^{N_i}_{n_v lj}(r) - U^{N_i}_{n_v LJ}(r)\big] \mathbf{P}_{lj} \\
&+ \sum_{n_c} \big[U^{N_i}_{n_c lj}(r) - U^{N_i}_{n_v lj}(r)\big] \widetilde{\mathbf{P}}^{N_i}_{n_c lj} \\
&+ \sum_{n_c} \widetilde{\mathbf{P}}^{N_i}_{n_c lj} \big[U^{N_i}_{n_c lj}(r) - U^{N_i}_{n_v lj}(r)\big] \\
&- \sum_{n_c, n_{c'}} \widetilde{\mathbf{P}}^{N_i}_{n_c lj} \left[\frac{U^{N_i}_{n_c lj}(r) + U^{N_i}_{n_{c'} lj}(r)}{2} - U^{N_i}_{n_v lj}(r) \right] \widetilde{\mathbf{P}}^{N_i}_{n_{c'} lj} \Big\},
\end{aligned} \tag{2.1}$$

   where

$$\mathbf{P}_{lj} = \sum_{m=-j}^{j} \big| ljm \big\rangle \big\langle ljm \big|,$$

$$\widetilde{\mathbf{P}}^{N_i}_{n_c lj} = \sum_{m=-j}^{j} \big| (\widetilde{n_c ljm})^{N_i} \big\rangle \big\langle (\widetilde{n_c ljm})^{N_i} \big|,$$

   $\big| ljm \big\rangle \big\langle ljm \big|$ is the projector on the two-component spin-angular function χ_{ljm}, $\big| (\widetilde{n_c ljm})^{N_i} \big\rangle \big\langle (\widetilde{n_c ljm})^{N_i} \big|$ is the projector on the outer core pseudospinor $\widetilde{\varphi}^{N_i}_{n_c lj} \chi_{ljm}$, $U^{N_i}_{n_v lj}$ and $U^{N_i}_{n_c lj}$ are the radial components of the GRECP derived for valence $\widetilde{\varphi}^{N_i}_{n_v lj}$ and outer core $\widetilde{\varphi}^{N_i}_{n_c lj}$ pseudospinors for the OMC d or f shell occupation number N_i (i=1, 2), $E^{N_i}_{\rm core}$ is the core energy, L is one more than the highest orbital angular momentum of the inner core spinors and $J = L + 1/2$. The separable terms (lines 3–5 in Eq. (2.1)) are added to the conventional radially-local RECP operator. These terms take into account the difference between the potentials acting on the outer core and valence electrons with the same l and j.

3. The self-consistent GRECP, $\mathbf{U}^{\mathrm{SfC}}$, with the quadratic correction writes as

$$\begin{aligned}\mathbf{U}^{\mathrm{SfC}} &= \frac{\mathbf{U}^{N_1}+\mathbf{U}^{N_2}}{2} + \frac{\mathbf{U}^{N_1}-\mathbf{U}^{N_2}}{N_1-N_2}\left(N_{\mathrm{omc}} - \frac{N_1+N_2}{2}\right) \\ &+ B\left(N_{\mathrm{omc}} - \frac{N_1+N_2}{2}\right)^2 , \end{aligned} \tag{2.2}$$

where B is some adjustable parameter, $N_{\mathrm{omc}}=\langle\tilde{\Psi}|\mathbf{N}_{\mathrm{omc}}|\tilde{\Psi}\rangle$, $\tilde{\Psi}$ is the many-electron wavefunction for the calculated state, and $\mathbf{N}_{\mathrm{omc}}$ is the occupation number operator of the considered d (f) shell that is written as

$$\mathbf{N}_{\mathrm{omc}} = \sum_{j=|l-1/2|}^{l+1/2} \sum_{m=-j}^{j} \tilde{\mathbf{a}}^{\dagger}_{n_{\mathrm{omc}}l_{\mathrm{omc}}jm}\tilde{\mathbf{a}}_{n_{\mathrm{omc}}l_{\mathrm{omc}}jm} , \tag{2.3}$$

$\tilde{\mathbf{a}}^{\dagger}_{n_{\mathrm{omc}}l_{\mathrm{omc}}jm}$ ($\tilde{\mathbf{a}}_{n_{\mathrm{omc}}l_{\mathrm{omc}}jm}$) is the creation (annihilation) operator for the electron in the pseudostate $|\widetilde{n_{\mathrm{omc}}l_{\mathrm{omc}}}jm\rangle$ corresponding the original one-electron state $|n_{\mathrm{omc}}l_{\mathrm{omc}}jm\rangle$, n_{omc} and l_{omc} are the principal and orbital quantum numbers of the OMC shell.

4. The $\widetilde{\mathbf{P}}^{N_i}_{n_clj}$ projectors in $\mathbf{U}^{N_i}$ from Eq. (2.2) are replaced by the projectors

$$\widetilde{\mathbf{P}}^{\mathrm{av}}_{n_clj} = \sum_{m=-j}^{j} \left|(\widetilde{n_cljm})^{\mathrm{av}}\right\rangle\left\langle(\widetilde{n_cljm})^{\mathrm{av}}\right|$$

for simplicity, where $\left|(\widetilde{n_cljm})^{\mathrm{av}}\right\rangle\left\langle(\widetilde{n_cljm})^{\mathrm{av}}\right|$ is the projector on the outer core pseudospinor $\widetilde{\varphi}^{\mathrm{av}}_{n_clj}\chi_{ljm}$,

$$\widetilde{\varphi}^{\mathrm{av}}_{n_clj}(r) = C_{\mathrm{norm}}\left[\widetilde{\varphi}^{\mathrm{N}_1}_{n_clj}(r) + \widetilde{\varphi}^{\mathrm{N}_2}_{n_clj}(r)\right] , \tag{2.4}$$

and C_{norm} is the normalizing factor.

The comparison of self-consistent and conventional GRECP versions by accuracy in calculations on the uranium and plutonium atoms can be found in paper [29].

2.2. TERM-SPLITTING CORRECTION FOR D, F-ELEMENTS

The self-consistent (G)RECP correction gives no improvement in description of splittings to terms, e.g., of the configuration $5f^3_{5/2}6d^1_{3/2}7s^2_{1/2}$ of uranium as compared to the parent (G)RECPs [19, 24]. Analysis of the corresponding errors shows that the main contribution (about 90 %) is due

to smoothing the original OMC spinors in the core region. The simplest way to minimize these errors is to use such (G)RECPs, in which the $5f$ shell is described by nodal pseudospinors, whereas the $4f$ pseudospinors are nodeless. To reduce computational efforts, the $4f$ shell can be treated as "frozen" using the level-shift technique [19, 31].

If the small magnitude of the OMC shell ($5f$ here) relaxation is taken into account, there is another way out that can be optimal for the low-lying states. It was suggested in [19] to add the Term-Splitting (TS) correction (see also [24]) to the (G)RECP operator

$$\begin{aligned}\mathbf{U}^{\mathrm{TS}} &= \sum_{x_1,x_2,x_3,x_4} \lambda_{x_1x_2,x_3x_4} \widetilde{|x_1\rangle}\widetilde{|x_3\rangle}\widetilde{\langle x_2|}\widetilde{\langle x_4|} \\ &- 2\sum_{w}\sum_{x_1,x_2,x_3} (\lambda_{x_1x_2,x_3x_3} - \lambda_{x_1x_3,x_3x_2})\delta_{wx_3}\widetilde{|x_1\rangle}\widetilde{\langle x_2|}\ , \quad (2.5)\end{aligned}$$

where $\lambda_{x_1x_2,x_3x_4}$ is the difference between the two-electron integrals calculated with original spinors and pseudospinors for the generator state, the indices $w \equiv (n_{\mathrm{occ}}l_{\mathrm{occ}}j_{\mathrm{occ}}m_{\mathrm{occ}})$ correspond to the occupied spinors for the calculated state, the indices $x \equiv (n_{\mathrm{omc}}l_{\mathrm{omc}}jm)$ run over all possible $j = |l_{\mathrm{omc}} \pm 1/2|$ and $m = -j, -j+1, \ldots j$ for the given OMC shell. These terms correct the one- and two-electron integrals containing only the $5f$ pseudospinors of uranium in the considered case.

2.3. ACCOUNTING FOR THE BREIT INTERACTION BETWEEN DIFFERENT SHELLS

Let us analyze contributions of the Breit interaction between electrons from different shells to the energy of a heavy atom [27]. We will use the estimate (e.g., see [32])

$$\langle P, P'|(\vec{\alpha}_i \cdot \vec{\alpha}_{i'})|P, P'\rangle \sim \frac{1}{c^2}\langle(\vec{v}_P \cdot \vec{v}_{P'})\rangle\ ;$$

for an uncoupled one-electron state P: $\langle P|\vec{\alpha}|P\rangle \sim \frac{\langle\vec{v}\rangle_P}{c}$, $\frac{|\langle\vec{v}\rangle_P|}{c} \sim \alpha Z_P^*$, where $\vec{\alpha}_i$ are 4×4 Dirac matrices for the i-th electron, c and $\vec{v}$ are velocities of light and electron, $\alpha \approx \frac{1}{137}$ is the fine structure constant. In the above expression a "pseudocharge", Z_P^*, is introduced which can be most naturally defined in our consideration as [29]

$$Z_P^* = \langle P|\frac{1}{r}|P\rangle\ , \quad (2.6)$$

that coincides with the nuclear charges only for nonrelativistic electrons occupying the ground states in hydrogen-like ions. Besides, $\langle\frac{1}{r_{12}}\rangle$ can be estimated as $\langle\frac{1}{r}\rangle$ for the outermost of the one-electron states P, P' [27]:

$$\langle P,P'|\frac{1}{r_{12}}|P,P'\rangle \sim \min\left[\langle P|\frac{1}{r}|P\rangle,\langle P'|\frac{1}{r}|P'\rangle\right] = \min\left[Z^*_P, Z^*_{P'}\right] \ .$$

As a result, the Breit interaction between the one-electron states P and P' can be estimated as

$$B_{PP'} \approx \alpha^2 Z^*_P Z^*_{P'} \cdot \min\left[Z^*_P, Z^*_{P'}\right] \cdot \mathcal{F}$$

where the correcting factor $\mathcal{F} \sim [0.1 \div 1]$ is introduced, which depends on $\Delta l{=}|l_P{-}l_{P'}|$, $\Delta j{=}|j_P{-}j_{P'}|$, etc.

Applying Eq. (2.6) for inner core ($P{\equiv}f$), outer core ($P{\equiv}c$) and valence ($P{\equiv}v$) electrons one has $Z^*_f{\sim}100$, $Z^*_c{\sim}3$, $Z^*_v{\sim}1$ by the order of magnitude (Z^*_P differs from an "effective charge" of the core with respect to the electron in the P-th state, $Z^{\rm Ef}_P{=}Z{-}N^P_c$, that is usually used in RECP calculations, where Z is the nuclear charge, N^P_c is the number of core electrons with respect to the P-th state). Therefore, $\mathcal{B}_{PP'}{\equiv}\mathcal{F}^{-1}B_{PP'}$ is as

$$\begin{array}{lll}
\mathcal{B}_{ff'} \sim 10\,000\,000\,{\rm cm}^{-1}\,, & \mathcal{B}_{fc} \sim 9\,000\,{\rm cm}^{-1}\,, & \mathcal{B}_{fv} \sim 1000\,{\rm cm}^{-1}\,, \\
\mathcal{B}_{cf} \sim 9\,000\,{\rm cm}^{-1}\,, & \mathcal{B}_{cc'} \sim 270\,{\rm cm}^{-1}\,, & \mathcal{B}_{cv} \sim 30\,{\rm cm}^{-1}\,, \\
\mathcal{B}_{vf} \sim 1000\,{\rm cm}^{-1}\,, & \mathcal{B}_{vc} \sim 30\,{\rm cm}^{-1}\,, & \mathcal{B}_{vv'} \sim 10\,{\rm cm}^{-1}\,.
\end{array}$$

Let us consider approximations in accounting for the Breit interaction, that we made when outer core and valence electrons are included in GRECP calculations with Coulomb two-electron interactions, but inner core electrons are absorbed into the GRECP. When both electrons belong to the inner core shells, the Breit effect is of the same order as the Coulomb interaction between them. Though $B_{ff'}$ does not contribute to "differential" (valence) properties directly, it can lead to essential relaxation of both core and valence shells. This relaxation is taken into account when the Breit interaction is treated by self-consistent way in the framework of the HFDB method [33, 34].

The inner core electrons occupy closed shells. The only exchange part of the two-electron Breit interaction between the valence, outer core and inner core electrons, B_{fv} and B_{fc}, gives non-zero contribution. The contributions from B_{fv} and B_{fc}, are quite essential for calculation at the level of "chemical accuracy" (about 1 kcal/mol or 350 cm^{-1} for transition energies). This accuracy level is, in general, determined by the possibilities of modern correlation methods and computers already for compounds of light elements. Note, that the contribution from the exchange interaction is not smaller than that from the Coulomb part [29]. The inner core electrons can be considered as "frozen" in most physical-chemical processes of interest. Therefore, the effective operators for B_{fv} and B_{fc} acting on the valence and

TABLE 1. Transition energies (TE) between states averaged over the relativistic configurations of E112 derived from HFDB calculations with Fermi nuclear model and the corresponding absolute errors of other all-electron calculations (in cm^{-1}).

Method	HFDB	HFDB	HFDB	HFDB	HFD+B	HFD
Nuclear model	Fermi	Ball	Fermi	Point	Fermi	Fermi
A=	296	296	285		296	296
	(a)	(b)	(a)	(c)	(d)	(e)
Configuration	TE	Absolute errors				
$6d^4_{3/2}6d^6_{5/2}7s^2_{1/2} \rightarrow$						
$6d^4_{3/2}6d^6_{5/2}7s^1_{1/2}7p^1_{1/2}$	46406	-3	22	1768	1	-27
$6d^4_{3/2}6d^6_{5/2}7s^1_{1/2}7p^1_{3/2}$	64559	-4	25	1964	-1	239
$6d^4_{3/2}6d^6_{5/2}7s^1_{1/2}8s^1_{1/2}$	72571	-3	22	1760	-1	257
$6d^4_{3/2}6d^6_{5/2}7s^1_{1/2}7d^1_{3/2}$	81845	-4	23	1879	-1	277
$6d^4_{3/2}6d^5_{5/2}7s^2_{1/2}7p^1_{1/2}$	28701	1	-8	-644	2	-576
$6d^4_{3/2}6d^5_{5/2}7s^2_{1/2}7p^1_{3/2}$	52595	1	-6	-464	0	-267
$6d^4_{3/2}6d^5_{5/2}7s^2_{1/2}8s^1_{1/2}$	62635	2	-10	-776	0	-252
$6d^4_{3/2}6d^5_{5/2}7s^2_{1/2}7d^1_{3/2}$	72443	1	-9	-666	0	-234
$6d^4_{3/2}6d^5_{5/2}7s^2_{1/2}$	84449	1	-9	-672	0	-234
$6d^3_{3/2}6d^6_{5/2}7s^2_{1/2}7p^1_{1/2}$	53581	2	-10	-765	2	-281
$6d^3_{3/2}6d^6_{5/2}7s^2_{1/2}7p^1_{3/2}$	75273	1	-8	-600	0	7
$6d^3_{3/2}6d^6_{5/2}7s^2_{1/2}8s^1_{1/2}$	85677	2	-12	-915	-1	25
$6d^3_{3/2}6d^6_{5/2}7s^2_{1/2}7d^1_{3/2}$	95546	2	-10	-805	-1	43

(a,c) All-electron Hartree-Fock-Dirac-Breit (HFDB) calculations with Fermi and point nuclear charge distributions, accordingly.
(b) All-electron HFDB calculation with the uniform nuclear charge distribution within a sphere.
(d) All-electron HFD calculation with accounting for the Breit interaction within PT-1 (HFD+B) and with Fermi nuclear model.
(e) All-electron HFD calculation without accounting for the Breit interaction (HFD) and with Fermi nuclear model.

outercore shells, $B^{\rm Ef}_{fv}$ and $B^{\rm Ef}_{fc}$, are of the same kind as the exchange $f-v$ and $f-c$ contributions of the SCF field in the Huzinaga-type potential, i.e. these terms can be well approximated by the spin-dependent potential of the form:

$$B^{\rm Ef}_{fv} + B^{\rm Ef}_{fc} = \sum_{lj} V^{Br}_{lj}(r)\mathbf{P}_{lj} \; + \sum_{n_c lj} \big[V^{Br}_{n_c lj}(r) - V^{Br}_{lj}(r)\big]\widetilde{\mathbf{P}}_{n_c lj},$$

which has basically the same spin-angular structure as the GRECP has.

TABLE 2. Transition energies (TE) between states averaged over the relativistic configurations of E112 derived from HFDB calculations with Fermi nuclear model for A=296 and the corresponding absolute errors of (G)RECP calculations (in cm^{-1}).

	HFDB Fermi 296 (a)	52e-GRECP (f)	20e-GRECP (f)	Ionic 20e-RECP (g)	20e-RECP of Nash *et al.* (h)	20e-PP of Seth *et al.* (i)
Configuration	TE			Absolute errors		
$6d^4_{3/2}6d^6_{5/2}7s^2_{1/2} \rightarrow$						
$6d^4_{3/2}6d^6_{5/2}7s^1_{1/2}7p^1_{1/2}$	46406	1	-17	588	3198	153
$6d^4_{3/2}6d^6_{5/2}7s^1_{1/2}7p^1_{3/2}$	64559	4	-29	820	5480	27
$6d^4_{3/2}6d^6_{5/2}7s^1_{1/2}8s^1_{1/2}$	72571	6	-25	719	5085	105
$6d^4_{3/2}6d^6_{5/2}7s^1_{1/2}7d^1_{3/2}$	81845	6	-18	809	5465	99
$6d^4_{3/2}6d^5_{5/2}7s^2_{1/2}7p^1_{1/2}$	28701	31	305	-422	-3723	380
$6d^4_{3/2}6d^5_{5/2}7s^2_{1/2}7p^1_{3/2}$	52595	37	277	-181	-1254	189
$6d^4_{3/2}6d^5_{5/2}7s^2_{1/2}8s^1_{1/2}$	62635	43	314	-315	-1879	326
$6d^4_{3/2}6d^5_{5/2}7s^2_{1/2}7d^1_{3/2}$	72443	43	322	-220	-1514	314
$6d^4_{3/2}6d^5_{5/2}7s^2_{1/2}$	84449	43	322	-224	-1531	308
$6d^3_{3/2}6d^6_{5/2}7s^2_{1/2}7p^1_{1/2}$	53581	45	387	-376	-3903	22
$6d^3_{3/2}6d^6_{5/2}7s^2_{1/2}7p^1_{3/2}$	75273	52	437	-84	-1515	-126
$6d^3_{3/2}6d^6_{5/2}7s^2_{1/2}8s^1_{1/2}$	85677	60	477	-213	-2126	22
$6d^3_{3/2}6d^6_{5/2}7s^2_{1/2}7d^1_{3/2}$	95546	60	484	-119	-1760	7

(a) All-electron Hartree-Fock-Dirac-Breit (HFDB) calculations with Fermi nuclear charge distribution.
(f) GRECP generated in the present work from HFDB calculation with Fermi nuclear model.
(g) Semi-local RECP generated here from HFDB calculation with Fermi nuclear model on the ionic closed-shell generator-state.
(h) RECP from [37] generated from HFD calculation.
(i) PP from M. Seth *et al.* to be published (P. Schwerdtfeger, private communication, 2003) generated from HFD+B calculation.

Thus, it can be taken into account directly when the HFDB (not HFD) calculation [8] is performed to generate outer core and valence bispinors but in the inversion procedure of the HF equations for generating the components of GRECP, the conventional interelectronic Coulomb interaction should be used instead of the Coulomb-Breit one. Then, in the GRECP calculations one should consider only the Coulomb interaction between the explicitly treated electrons.

TABLE 3. Transition Energies (TE) between states averaged over the relativistic configurations of E113 (in cm^{-1}). See Table 1.

Method	HFDB	HFDB	HFDB	HFDB	HFD+B	HFD
Nuclear model	Fermi	Ball	Fermi	Point	Fermi	Fermi
A=	297	297	284		297	297
Configuration	TE		Absolute errors			
$6d^4_{3/2}6d^6_{5/2}7s^2_{1/2}7p^1_{1/2} \rightarrow$						
$6d^4_{3/2}6d^6_{5/2}7s^2_{1/2}7p^1_{3/2}$	25106	0	3	221	-2	339
$6d^4_{3/2}6d^6_{5/2}7s^2_{1/2}8s^1_{1/2}$	34981	0	-2	-128	-3	354
$6d^4_{3/2}6d^6_{5/2}7s^2_{1/2}7d^1_{3/2}$	45172	0	0	-4	-3	374
$6d^4_{3/2}6d^6_{5/2}7s^2_{1/2}6f^1_{5/2}$	50338	0	0	-10	-3	374
$6d^4_{3/2}6d^6_{5/2}7s^2_{1/2}5g^1_{7/2}$	52811	0	0	-10	-3	374
$6d^4_{3/2}6d^6_{5/2}7s^2_{1/2}$	57201	0	0	-10	-3	374
$6d^4_{3/2}6d^6_{5/2}7s^1_{1/2}7p^2_{1/2}$	61500	-4	32	2220	2	-60
$6d^4_{3/2}6d^6_{5/2}7s^1_{1/2}7p^1_{1/2}7p^1_{3/2}$	83184	-5	36	2485	-1	241
$6d^4_{3/2}6d^6_{5/2}7s^1_{1/2}7p^2_{3/2}$	112678	-6	41	2843	-3	612
$6d^4_{3/2}6d^6_{5/2}7s^1_{1/2}7p^1_{1/2}$	115758	-5	34	2344	-1	250
$6d^4_{3/2}6d^6_{5/2}7s^1_{1/2}7p^1_{3/2}$	149550	-5	40	2739	-3	654
$6d^4_{3/2}6d^6_{5/2}7s^1_{1/2}$	234435	-5	37	2583	-4	747
$6d^4_{3/2}6d^5_{5/2}7s^2_{1/2}7p^2_{1/2}$	47371	2	-13	-864	3	-739
$6d^4_{3/2}6d^5_{5/2}7s^2_{1/2}7p^1_{1/2}7p^1_{3/2}$	74898	1	-9	-606	1	-391
$6d^4_{3/2}6d^5_{5/2}7s^2_{1/2}7p^2_{3/2}$	110406	1	-4	-244	-2	22
$6d^4_{3/2}6d^5_{5/2}7s^2_{1/2}7p^1_{1/2}$	110120	2	-13	-882	0	-388
$6d^4_{3/2}6d^5_{5/2}7s^2_{1/2}7p^1_{3/2}$	150102	1	-7	-477	-2	59
$6d^4_{3/2}6d^5_{5/2}7s^2_{1/2}$	239523	2	-12	-807	-2	144
$6d^3_{3/2}6d^6_{5/2}7s^2_{1/2}7p^2_{1/2}$	78821	2	-15	-983	2	-375
$6d^3_{3/2}6d^6_{5/2}7s^2_{1/2}7p^1_{1/2}7p^1_{3/2}$	104059	1	-11	-742	0	-49
$6d^3_{3/2}6d^6_{5/2}7s^2_{1/2}7p^2_{3/2}$	137048	1	-6	-403	-2	341
$6d^3_{3/2}6d^6_{5/2}7s^2_{1/2}7p^1_{1/2}$	139819	2	-15	-1021	0	-42
$6d^3_{3/2}6d^6_{5/2}7s^2_{1/2}7p^1_{3/2}$	177137	1	-9	-638	-3	381

Due to small relaxation of outer core shells in most processes of interest, these shells can be also considered as "frozen" when analyzing the Breit contributions and the $B_{cc'}$ and B_{cv} terms can be taken into account similarly to the B_{fc} and B_{fv} ones. The error of this approximation will be additionally suppressed by relative weakness of the Breit interaction with the outer core electrons as compared to the inner core ones. We note here, that the estimates for Z_c^*, Z_v^* and, therefore, for $B_{cc'}$, B_{cv} and $B_{vv'}$

TABLE 4. Transition Energies (TE) between states averaged over the relativistic configurations of E113 (in cm^{-1}). See Table 2.

	HFDB Fermi 297	21e-GRECP	Ionic 21e-RECP	21e-RECP of Nash *et al.*	21e-PP of Seth *et al.*
Configuration	TE		Absolute errors		
$6d^4_{3/2}6d^6_{5/2}7s^2_{1/2}7p^1_{1/2} \rightarrow$					
$6d^4_{3/2}6d^6_{5/2}7s^2_{1/2}7p^1_{3/2}$	25106	-21	233	275	-349
$6d^4_{3/2}6d^6_{5/2}7s^2_{1/2}8s^1_{1/2}$	34981	5	112	-205	-307
$6d^4_{3/2}6d^6_{5/2}7s^2_{1/2}7d^1_{3/2}$	45172	9	200	140	-275
$6d^4_{3/2}6d^6_{5/2}7s^2_{1/2}6f^1_{5/2}$	50338	9	196	127	-276
$6d^4_{3/2}6d^6_{5/2}7s^2_{1/2}5g^1_{7/2}$	52811	9	196	127	-276
$6d^4_{3/2}6d^6_{5/2}7s^2_{1/2}$	57201	9	196	127	-276
$6d^4_{3/2}6d^6_{5/2}7s^1_{1/2}7p^2_{1/2}$	61500	28	610	4830	148
$6d^4_{3/2}6d^6_{5/2}7s^1_{1/2}7p^1_{1/2}7p^1_{3/2}$	83184	-6	833	5170	-172
$6d^4_{3/2}6d^6_{5/2}7s^1_{1/2}7p^2_{3/2}$	112678	-10	1171	5717	-504
$6d^4_{3/2}6d^6_{5/2}7s^1_{1/2}7p^1_{1/2}$	115758	-3	784	5143	-105
$6d^4_{3/2}6d^6_{5/2}7s^1_{1/2}7p^1_{3/2}$	149550	-9	1163	5784	-454
$6d^4_{3/2}6d^6_{5/2}7s^1_{1/2}$	234435	-2	1221	6102	-336
$6d^4_{3/2}6d^5_{5/2}7s^2_{1/2}7p^2_{1/2}$	47371	404	-597	-2349	322
$6d^4_{3/2}6d^5_{5/2}7s^2_{1/2}7p^1_{1/2}7p^1_{3/2}$	74898	344	-378	-2055	-44
$6d^4_{3/2}6d^5_{5/2}7s^2_{1/2}7p^2_{3/2}$	110406	310	-47	-1528	-407
$6d^4_{3/2}6d^5_{5/2}7s^2_{1/2}7p^1_{1/2}$	110120	386	-451	-2298	41
$6d^4_{3/2}6d^5_{5/2}7s^2_{1/2}7p^1_{3/2}$	150102	344	-82	-1667	-339
$6d^4_{3/2}6d^5_{5/2}7s^2_{1/2}$	239523	416	-39	-1617	-188
$6d^3_{3/2}6d^6_{5/2}7s^2_{1/2}7p^2_{1/2}$	78821	380	-649	-2230	-270
$6d^3_{3/2}6d^6_{5/2}7s^2_{1/2}7p^1_{1/2}7p^1_{3/2}$	104059	412	-364	-1931	-544
$6d^3_{3/2}6d^6_{5/2}7s^2_{1/2}7p^2_{3/2}$	137048	481	38	-1402	-804
$6d^3_{3/2}6d^6_{5/2}7s^2_{1/2}7p^1_{1/2}$	139819	447	-439	-2161	-466
$6d^3_{3/2}6d^6_{5/2}7s^2_{1/2}7p^1_{3/2}$	177137	516	9	-1523	-736

given above are rather the upper limits. For heavy atoms these Breit contributions are smaller approximately by one–two orders of magnitude. This decrease is due to enlarged radii of the valence and outer core shells and other effects in heavy atoms [29]. For example, for uranium ($Z = 92$) one has Z^*_{1s}[nonrel. SCF]$\sim$92.4, Z^*_{1s}[DHFB]$\sim$122.4 (starting from $Z \sim 30$, Z^*_{1s} grows faster than Z due to relativistic effects, whereas Z^*_{nl} is essentially

TABLE 5. Transition Energies (TE) between states averaged over the relativistic configurations of E114 (in cm^{-1}). See Table 1.

Method	HFDB	HFDB	HFDB	HFDB	HFD+B	HFD
Nuclear model	Fermi	Ball	Fermi	Point	Fermi	Fermi
A=	298	298	289		298	298
Configuration	TE			Absolute errors		
$6d^4_{3/2}6d^6_{5/2}7s^2_{1/2}7p^2_{1/2} \rightarrow$						
$6d^4_{3/2}6d^6_{5/2}7s^2_{1/2}7p^1_{1/2}7p^1_{3/2}$	29093	-1	3	314	-2	380
$6d^4_{3/2}6d^6_{5/2}7s^2_{1/2}7p^1_{1/2}8s^1_{1/2}$	41211	0	-1	-135	-3	370
$6d^4_{3/2}6d^6_{5/2}7s^2_{1/2}7p^1_{1/2}8p^1_{1/2}$	48149	0	0	-5	-3	360
$6d^4_{3/2}6d^6_{5/2}7s^2_{1/2}7p^1_{1/2}7d^1_{3/2}$	52230	0	0	16	-3	387
$6d^4_{3/2}6d^6_{5/2}7s^2_{1/2}7p^1_{1/2}6f^1_{5/2}$	57618	0	0	7	-3	384
$6d^4_{3/2}6d^6_{5/2}7s^2_{1/2}7p^1_{1/2}5g^1_{7/2}$	60094	0	0	7	-3	384
$6d^4_{3/2}6d^6_{5/2}7s^2_{1/2}7p^1_{1/2}$	64483	0	0	7	-3	384
$6d^4_{3/2}6d^6_{5/2}7s^2_{1/2}7p^2_{3/2}$	66669	-2	6	755	-5	833
$6d^4_{3/2}6d^6_{5/2}7s^2_{1/2}7p^1_{3/2}8s^1_{1/2}$	81879	-1	3	277	-5	850
$6d^4_{3/2}6d^6_{5/2}7s^2_{1/2}7p^1_{3/2}$	106776	-1	4	497	-5	872
$6d^4_{3/2}6d^6_{5/2}7s^2_{1/2}8s^2_{1/2}$	108893	1	-3	-361	-6	883
$6d^4_{3/2}6d^6_{5/2}7s^2_{1/2}8s^1_{1/2}$	136567	0	-1	-207	-6	907
$6d^4_{3/2}6d^6_{5/2}7s^2_{1/2}$	197486	0	1	128	-6	961
$6d^4_{3/2}6d^6_{5/2}7s^1_{1/2}7p^2_{1/2}7p^1_{3/2}$	102896	-6	24	3110	0	256
$6d^4_{3/2}6d^6_{5/2}7s^1_{1/2}7p^2_{1/2}8s^1_{1/2}$	115405	-5	21	2745	-1	224
$6d^4_{3/2}6d^6_{5/2}7s^1_{1/2}7p^2_{1/2}$	138842	-6	23	2905	-1	233
$6d^4_{3/2}6d^5_{5/2}7s^2_{1/2}7p^2_{1/2}7p^1_{3/2}$	97736	2	-6	-771	1	-506
$6d^4_{3/2}6d^5_{5/2}7s^2_{1/2}7p^2_{1/2}8s^1_{1/2}$	112486	3	-10	-1277	1	-543
$6d^4_{3/2}6d^5_{5/2}7s^2_{1/2}7p^2_{1/2}$	136356	2	-9	-1129	1	-534
$6d^3_{3/2}6d^6_{5/2}7s^2_{1/2}7p^2_{1/2}7p^1_{3/2}$	133837	2	-7	-904	0	-91
$6d^3_{3/2}6d^6_{5/2}7s^2_{1/2}7p^2_{1/2}8s^1_{1/2}$	149162	3	-11	-1415	0	-126
$6d^3_{3/2}6d^6_{5/2}7s^2_{1/2}7p^2_{1/2}$	173108	3	-10	-1265	0	-117

smaller than the corresponding effective charge $Z^{\rm Ef}_{nl}$ for all other nl), $Z^*_{5f}\sim1$, $Z^*_{6s}\sim1$, $Z^*_{6p}\sim0.7$, $Z^*_{6d}\sim0.4$, $Z^*_{7s}\sim0.3$. Thus, $B_{cc'}$, B_{cv}, and $B_{vv'}$ contributions are negligible for the "chemical accuracy" of calculation. Therefore, the above made estimates provide us a good background for approximating the Breit interaction by a one-electron GRECP operator that should work well both for actinides and for superheavy elements. The numerical tests of the GRECPs accounting for the Breit effects are discussed in the next section.

TABLE 6. Transition Energies (TE) between states averaged over the relativistic configurations of E114 (in cm^{-1}). See Table 2.

	HFDB Fermi 298	22e-GRECP	Ionic 22e-RECP	22e-RECP of Nash *et al.*	22e-PP of Seth *et al.*
Configuration	TE		Absolute errors		
$6d^4_{3/2}6d^6_{5/2}7s^2_{1/2}7p^2_{1/2} \rightarrow$					
$6d^4_{3/2}6d^6_{5/2}7s^2_{1/2}7p^1_{1/2}7p^1_{3/2}$	29093	-46	211	449	-457
$6d^4_{3/2}6d^6_{5/2}7s^2_{1/2}7p^1_{1/2}8s^1_{1/2}$	41211	-51	53	-333	-348
$6d^4_{3/2}6d^6_{5/2}7s^2_{1/2}7p^1_{1/2}8p^1_{1/2}$	48149	-44	114	11	-318
$6d^4_{3/2}6d^6_{5/2}7s^2_{1/2}7p^1_{1/2}7d^1_{3/2}$	52230	-44	149	115	-320
$6d^4_{3/2}6d^6_{5/2}7s^2_{1/2}7p^1_{1/2}6f^1_{5/2}$	57618	-43	143	86	-318
$6d^4_{3/2}6d^6_{5/2}7s^2_{1/2}7p^1_{1/2}5g^1_{7/2}$	60094	-43	143	86	-317
$6d^4_{3/2}6d^6_{5/2}7s^2_{1/2}7p^1_{1/2}$	64483	-43	143	86	-317
$6d^4_{3/2}6d^6_{5/2}7s^2_{1/2}7p^2_{3/2}$	66669	-52	535	1209	-926
$6d^4_{3/2}6d^6_{5/2}7s^2_{1/2}7p^1_{3/2}8s^1_{1/2}$	81879	-64	377	374	-834
$6d^4_{3/2}6d^6_{5/2}7s^2_{1/2}7p^1_{3/2}$	106776	-53	503	969	-808
$6d^4_{3/2}6d^6_{5/2}7s^2_{1/2}8s^2_{1/2}$	108893	-82	174	-725	-718
$6d^4_{3/2}6d^6_{5/2}7s^2_{1/2}8s^1_{1/2}$	136567	-72	285	-241	-680
$6d^4_{3/2}6d^6_{5/2}7s^2_{1/2}$	197486	-45	547	853	-584
$6d^4_{3/2}6d^6_{5/2}7s^1_{1/2}7p^2_{1/2}7p^1_{3/2}$	102896	96	929	6650	-327
$6d^4_{3/2}6d^6_{5/2}7s^1_{1/2}7p^2_{1/2}8s^1_{1/2}$	115405	59	754	5987	-243
$6d^4_{3/2}6d^6_{5/2}7s^1_{1/2}7p^2_{1/2}$	138842	73	848	6439	-206
$6d^4_{3/2}6d^5_{5/2}7s^2_{1/2}7p^2_{1/2}7p^1_{3/2}$	97736	472	-631	-3156	-28
$6d^4_{3/2}6d^5_{5/2}7s^2_{1/2}7p^2_{1/2}8s^1_{1/2}$	112486	473	-830	-4091	83
$6d^4_{3/2}6d^5_{5/2}7s^2_{1/2}7p^2_{1/2}$	136356	487	-732	-3647	122
$6d^3_{3/2}6d^6_{5/2}7s^2_{1/2}7p^2_{1/2}7p^1_{3/2}$	133837	391	-746	-2821	-675
$6d^3_{3/2}6d^6_{5/2}7s^2_{1/2}7p^2_{1/2}8s^1_{1/2}$	149162	380	-952	-3758	-579
$6d^3_{3/2}6d^6_{5/2}7s^2_{1/2}7p^2_{1/2}$	173108	391	-855	-3309	-541

3. Results and Discussion

For all-electron calculations, we used the atomic HFDB code [35, 36] which allows one to account for the Breit interactions both in the framework of the first-order perturbation theory (PT-1) and by the self-consistent way as well as to account for different models of nuclear charge distribution. For test calculations with (G)RECPs, the atomic Hartree-Fock code in the jj-coupling scheme (HFJ) [17] was used (that was quite sufficient for

TABLE 7. Transition Energies (TE) between states averaged over the nonrelativistic configurations of uranium (in cm^{-1}). See footnotes in Tables 1 and 2.

		HFDB Fermi 238	HFDB Point	HFD+B Fermi 238	HFD Fermi 238	32e-GRECP
Transition		TE		Absolute errors		
$5f^3 7s^2 6d^1 \rightarrow$	$5f^3 7s^2 7p^1$	7516	-40	0	-93	5
	$5f^3 7s^2$	36289	-68	0	-62	9
	$5f^3 7s^1 6d^2$	13124	97	0	78	-7
	$5f^3 7s^1 6d^1 7p^1$	17200	75	0	14	-1
	$5f^3 7s^1 6d^1$	42328	63	0	44	0
	$5f^3 6d^2$	54576	177	0	138	-6
$5f^3 7s^2 6d^1 \rightarrow$	$5f^4 7s^2$	15780	76	2	627	-363
$5f^4 7s^2 \rightarrow$	$5f^4 7s^1 6d^1$	15010	78	0	43	3
	$5f^4 7s^1 7p^1$	14932	62	0	21	-3
	$5f^4 7s^1$	38813	50	-1	50	-3
	$5f^4 6d^2$	33792	147	1	82	6
	$5f^4 6d^1 7p^1$	32115	146	0	79	2
	$5f^4 6d^1$	53379	148	0	108	1
$5f^3 7s^2 6d^1 \rightarrow$	$5f^2 7s^2 6d^2$	4640	-85	-1	-779	362
$5f^2 7s^2 6d^2 \rightarrow$	$5f^2 7s^2 6d^1 7p^1$	12809	-44	0	-118	11
	$5f^2 7s^2 6d^1$	42793	-71	0	-83	15
	$5f^2 7s^1 6d^3$	10480	113	0	104	-12
	$5f^2 7s^1 6d^2 7p^1$	19217	87	0	15	-1
	$5f^2 7s^1 6d^2$	45352	75	0	50	0
	$5f^2 6d^3$	54611	204	0	168	-12
$5f^3 7s^2 6d^1 \rightarrow$	$5f^1 7s^2 6d^3$	31450	-176	-2	-1673	680
$5f^1 7s^2 6d^3 \rightarrow$	$5f^1 7s^2 6d^2 7p^1$	18326	-48	0	-137	11
	$5f^1 7s^2 6d^2$	49329	-75	0	-96	16
	$5f^1 7s^1 6d^4$	7331	127	0	124	-15
	$5f^1 7s^1 6d^3 7p^1$	21038	98	0	18	-1
	$5f^1 7s^1 6d^3$	48001	87	0	57	0
	$5f^1 6d^4$	53806	230	0	196	-15
$5f^3 7s^2 6d^1 \rightarrow$	$5f^5$	99459	252	4	1126	-671

TABLE 8. Transition Energies (TE) between states averaged over the nonrelativistic configurations of plutonium (in cm^{-1}). See footnotes in Tables 1 and 2.

		HFDB Fermi 244	HFDB Point	HFD+B Fermi 244	HFD Fermi 244	34e-GRECP
Transition		TE		Absolute errors		
$5f^6 7s^2 \rightarrow$	$5f^6 7s^1 6d^1$	17164	96	0	53	-2
	$5f^6 7s^1 7p^1$	15678	76	0	19	-1
	$5f^6 7s^1$	39853	61	0	47	-1
	$5f^6 6d^1$	56794	183	0	114	-2
	$5f^6 7p^1$	66677	172	-1	71	1
$5f^6 7s^2 \rightarrow$	$5f^7 7s^1$	43691	159	4	504	-377
$5f^7 7s^1 \rightarrow$	$5f^7 6d^1$	19877	67	0	54	-1
	$5f^7 7p^1$	14816	68	-1	62	-6
	$5f^7$	34957	70	-1	96	-9
$5f^6 7s^2 \rightarrow$	$5f^5 7s^2 6d^1$	-3099	-103	-2	-704	414
$5f^5 7s^2 6d^1 \rightarrow$	$5f^5 7s^2 7p^1$	6743	-50	0	-93	10
	$5f^5 7s^1 6d^2$	15044	120	0	82	-10
	$5f^5 7s^1 6d^1 7p^1$	18246	94	0	17	0
	$5f^5 7s^2$	35910	-84	0	-61	14
	$5f^5 7s^1 6d^1$	43764	80	0	48	1
$5f^6 7s^2 \rightarrow$	$5f^4 7s^2 6d^2$	17425	-213	-2	-1545	807
$5f^4 7s^2 6d^2 \rightarrow$	$5f^4 7s^2 6d^1 7p^1$	12434	-55	0	-116	16
	$5f^4 7s^1 6d^3$	12221	141	0	105	-16
	$5f^4 7s^1 6d^2 7p^1$	20405	109	0	18	-1
	$5f^4 7s^2 6d^1$	42841	-88	0	-77	19
	$5f^4 7s^1 6d^2$	46949	95	0	55	0
$5f^6 7s^2 \rightarrow$	$5f^3 7s^2 6d^3$	62648	-328	-3	-2496	1136
$5f^3 7s^2 6d^3 \rightarrow$	$5f^3 7s^1 6d^4$	8926	159	0	124	-20
	$5f^3 7s^2 6d^2 7p^1$	18247	-59	0	-133	18
	$5f^3 7s^1 6d^3 7p^1$	22323	123	0	21	-1
	$5f^3 6d^5$	24140	295	0	231	-36
	$5f^3 7s^2 6d^2$	49677	-92	0	-89	22
	$5f^3 7s^1 6d^3$	49694	109	0	63	0

TABLE 9. Transition Energies (TE) between terms of E112 (in cm^{-1}). See footnotes in Tables 1 and 2.

	HFDB Fermi 296	HFD+B Fermi 296	HFD Fermi 296	52e-GRECP	20e-GRECP	Ionic 20e-RECP	20e-RECP of Nash *et al.*	20e-PP of Seth *et al.*
Term	TE			Absolute errors				
$6d^4_{3/2}6d^6_{5/2}7s^1_{1/2}7p^1_{1/2}$ J=0 →								
J=1	9468	0	54	9	42	59	288	27
$6d^4_{3/2}6d^5_{5/2}7s^2_{1/2}7p^1_{1/2}$ J=2 →								
J=3	1958	0	25	6	16	43	165	11
$6d^3_{3/2}6d^6_{5/2}7s^2_{1/2}7p^1_{1/2}$ J=1 →								
J=2	-8145	1	-92	3	172	40	-558	100
$6d^4_{3/2}6d^5_{5/2}7s^2_{1/2}7p^1_{3/2}$ J=1 →								
J=2	-1919	0	-24	-5	34	14	-42	16
J=3	39	0	-17	0	74	56	4	78
J=4	-3166	0	-27	-6	9	-13	-69	-23

studying errors of the one-electron (G)RECP operators). Both the codes are numerical that allows us to exclude the errors due to the incompleteness of basis sets when estimating accuracy of different RECPs and GRECPs.

The transition energies between states averaged over the low-lying configurations of SHEs 112, 113, 114 and actinides U, Pu are presented in tables 1, 3, 5 and 7, 8, respectively. One can see that the errors due to the point nuclear model reach a few thousand wave numbers for the SHEs and several hundred wave numbers for the actinides. The considered small variations in the nuclear charge distribution (including the nuclear size) in the framework of finite-size nuclei lead to change of the transition energies for the studied SHEs less than on 60 cm^{-1}. The differences between the results with the PT-1 and self-consistent ways of accounting for the Breit interaction are within 7 cm^{-1} for SHEs and actinides whereas neglecting the Breit effects leads to the errors up to a few thousand wave numbers for the studied actinides and several hundred wave numbers for the SHEs.

The GRECP errors in reproducing the results of the all-electron HFDB calculations with the Fermi nuclear model are collected into two groups. First, the GRECP errors for transitions without change in the occupation

TABLE 10. Transition Energies (TE) between terms of uranium (in cm^{-1}). See footnotes in Tables 1 and 2.

	HFDB Fermi 238	HFD+B Fermi 238	HFD Fermi 238	32e-GRECP	32e-GRECP TS-corr. (j)	24e-SfC GRECP (k)	24e-SfC GRECP TS-corr. (j,k)
Term	TE			Absolute errors			
$5f^3_{5/2}6d^1_{3/2}7s^2_{1/2}$ J=0 →							
J=1	18576	0	74	137	-15	67	-102
J=2	9710	0	22	140	-12	117	-53
J=3	7749	0	66	-57	-9	-103	-49
J=4	6691	0	69	-77	-5	-121	-40
J=5	-8005	0	83	-439	8	-470	31
J=6	-10767	0	69	-416	31	-431	69
$5f^3_{5/2}5f^1_{7/2}7s^2_{1/2}$ J=1 →							
J=2	4399	0	-5	159	-35	165	-51
J=3	2840	0	4	109	-23	113	-33
J=4	3468	0	11	134	-29	139	-42
J=5	2785	0	22	117	-24	121	-36
J=6	4606	1	29	181	-42	188	-62
J=7	-6030	1	78	-176	12	-186	26
J=8	-5542	1	90	-149	6	-158	17
$5f^2_{5/2}6d^2_{3/2}7s^2_{1/2}$ J=0 →							
J=1	-19109	0	23	-432	-61	-426	-8
J=2	-15310	0	1	-304	-45	-288	5
J=3	-23656	0	41	-598	-77	-593	-8
J=4	-26013	0	21	-638	-69	-618	23
J=5	-32544	0	36	-754	-86	-732	21
J=6	-39562	0	-2	-724	-57	-671	82

(j) Term-Splitting (TS) correction generated in the present work from HFDB calculation with Fermi nuclear charge distribution.
(k) Self-Consistent Generalized Relativistic Effective Core Potential (SfC GRECP) generated in [29] from HFDB calculation with Fermi nuclear charge distribution.

number of the $6d$ shell for the SHEs (tables 2, 4 and 6) and the $5f$ shell for the actinides (tables 7 and 8) are relatively small whereas the corresponding errors of the other tested RECPs for the SHEs are significantly higher. The same number of electrons is explicitly treated in calculations with different (G)RECP versions for a given atom. Here and further, we do not discuss the particular case of the 52e-GRECP for E112 if the opposite is not explicitly

TABLE 11. Matrix Elements (ME) of $< r^2 >$ for some spinors from states averaged over the relativistic configurations of E112 (in a.u.). See footnotes in Tables 1 and 2.

	HFDB Fermi 296	HFD Fermi 296	52e-GRECP	20e-GRECP	Ionic 20e-RECP	20e-RECP of Nash *et al.*	20e-PP of Seth *et al.*
Conf., spinor	ME			Absolute errors			
$6d^4_{3/2}6d^6_{5/2}7s^2_{1/2}$							
$6d_{3/2}$	3.150	-0.005	0.001	0.024	0.030	0.066	0.072
$6d_{5/2}$	3.781	0.002	0.001	0.024	0.032	0.074	0.057
$7s_{1/2}$	7.157	-0.023	0.000	0.005	-0.099	-0.425	0.024
$6d^4_{3/2}6d^6_{5/2}7s^1_{1/2}7p^1_{1/2}$							
$6d_{3/2}$	3.144	-0.004	0.001	0.023	0.028	0.064	0.071
$6d_{5/2}$	3.648	0.002	0.001	0.024	0.031	0.069	0.057
$7s_{1/2}$	6.898	-0.020	0.000	0.002	-0.097	-0.394	0.022
$7p_{1/2}$	13.023	-0.116	-0.001	0.005	-0.131	-0.841	0.055
$6d^4_{3/2}6d^5_{5/2}7s^2_{1/2}7p^1_{1/2}$							
$6d_{3/2}$	3.057	-0.004	0.001	0.023	0.030	0.071	0.071
$6d_{5/2}$	3.522	0.002	0.001	0.025	0.035	0.080	0.059
$7s_{1/2}$	6.739	-0.019	0.000	0.001	-0.092	-0.361	0.025
$7p_{1/2}$	11.259	-0.087	-0.002	-0.001	-0.105	-0.597	0.049

stated. The RECPs of other groups for uranium were tested in paper [19]. It should be noted that they do not take into account the large contribution from the Breit interaction. The Breit effects were also not considered at the generation stage of the RECP of Nash *et al.* [37]. However, it can not explain the large errors for this RECP in tables 2, 4 and 6. It is not clear from paper [37] which nuclear model was used there. The Breit interaction was taken into account only in the PT-1 approximation at the generation stage of the PseudoPotential (PP) of Seth *et al.* However, the corresponding changes in the transition energies are negligible in comparison with the PP errors.

Second, the GRECP errors for transitions with excitation of one $6d$ electron for the SHEs or one $5f$ electron for the actinides are about 400 cm^{-1}. These errors have a systematic nature (unlike the corresponding errors for the tested RECPs of other groups) and are connected with the fact that the OMC $6d$ shell for the SHEs and the OMC $5f$ shell for the actinides in the present GRECP versions are described with the help of nodeless pseudospinors. Obviously, these errors can be reduced significantly if one

TABLE 12. Radial integrals $2\int_{R_n}^{\infty} |\, f_{n_v lj}(r)[f_{n_v lj}(r) - \widetilde{\varphi}_{n_v lj}(r)]\,| \, dr$ for valence spinors from states averaged over the relativistic configurations of E112 (in a.u.) where $f_{n_v lj}$ is the large component of the Dirac spinor from HFDB calculation with the Fermi nuclear charge distribution for $A = 296$, $\widetilde{\varphi}_{n_v lj}$ is the radial part of the corresponding pseudospinor (or the large component of the Dirac spinor), R_n is the radius of the last node for the spinor. See footnotes in Tables 1 and 2.

	HFD Fermi 296	52e-GRECP	20e-GRECP	Ionic 20e-RECP	20e-RECP of Nash *et al.*	20e-PP of Seth *et al.*
Conf., spinor				Integrals		
$6d^4_{3/2}6d^6_{5/2}7s^2_{1/2}$						
$7s_{1/2}$	0.0037	0.0000	0.0006	0.0131	0.0590	0.0024
$6d^4_{3/2}6d^6_{5/2}7s^1_{1/2}7p^1_{1/2}$						
$7s_{1/2}$	0.0036	0.0001	0.0002	0.0137	0.0581	0.0022
$7p_{1/2}$	0.0087	0.0001	0.0004	0.0091	0.0610	0.0047
$6d^4_{3/2}6d^5_{5/2}7s^2_{1/2}7p^1_{1/2}$						
$7s_{1/2}$	0.0034	0.0001	0.0003	0.0134	0.0546	0.0026
$7p_{1/2}$	0.0079	0.0002	0.0002	0.0088	0.0514	0.0050

includes the $5d, 5f$ electrons for the SHEs and the $4f$ electrons for the actinides explicitly in the GRECP calculations (see the 52e-GRECP results for E112 in table 2). The corresponding pseudospinors can be then "frozen" in these GRECP calculations with the help of the level-shift technique [19, 31] to reduce the computational efforts. Alternatively, the self-consistent GRECP method described in section 2.1 can be used.

The energies of splittings between terms are considered in table 9 for E112 and table 10 for U. The errors of the RECP and GRECP approximations and the errors caused by neglecting the Breit effects are within 200 cm^{-1} for E112 (except for the RECP of Nash *et al.*). The Breit contributions to the term-splitting energies for U are within 100 cm^{-1} whereas the GRECP errors are up to 750 cm^{-1}. The latter can be reduced drastically by applying the term-splitting correction (see section 2.2 and table 10). The results show that addition of the term-splitting correction allows one to reduce the most serious errors up to 10 times for the splittings into terms, thus reducing the errors for the energies of transition between terms to the same order of magnitude as the errors for transitions between the states averaged over the configurations (when only the self-consistent GRECP is applied). Obviously, any transition between two different terms having different occupation numbers of the OMC shell, $\mathbf{N}^1_{\rm omc}$ and $\mathbf{N}^2_{\rm omc}$,

TABLE 13. One-electron energies, ε, for some spinors from states averaged over the relativistic configurations of E112 (in a.u.). See footnotes in Tables 1 and 2.

	HFDB Fermi 296	HFD Fermi 296	52e-GRECP	20e-GRECP	Ionic 20e-RECP	20e-RECP of Nash *et al.*	20e-PP of Seth *et al.*
Conf., spinor	ε	Absolute errors					
$6d^4_{3/2}6d^6_{5/2}7s^2_{1/2}$							
$6d_{3/2}$	0.5624	0.0003	0.0000	0.0001	-0.0026	-0.0112	-0.0037
$6d_{5/2}$	0.4432	-0.0011	0.0000	-0.0001	-0.0026	-0.0095	-0.0009
$7s_{1/2}$	0.4497	0.0014	0.0000	-0.0003	0.0042	0.0272	0.0001
$6d^4_{3/2}6d^6_{5/2}7s^1_{1/2}7p^1_{1/2}$							
$6d_{3/2}$	0.6148	-0.0001	0.0000	-0.0001	-0.0025	-0.0118	-0.0039
$6d_{5/2}$	0.4870	-0.0017	0.0000	0.0000	-0.0024	-0.0108	-0.0009
$7s_{1/2}$	0.5217	0.0011	0.0000	0.0000	0.0048	0.0278	0.0004
$7p_{1/2}$	0.2248	0.0015	0.0000	-0.0001	0.0012	0.0114	-0.0004
$6d^4_{3/2}6d^5_{5/2}7s^2_{1/2}7p^1_{1/2}$							
$6d_{3/2}$	0.6663	-0.0002	0.0000	-0.0002	-0.0042	-0.0173	-0.0043
$6d_{5/2}$	0.5314	-0.0018	0.0000	-0.0001	-0.0040	-0.0159	-0.0014
$7s_{1/2}$	0.5253	0.0010	0.0000	0.0000	0.0044	0.0258	0.0001
$7p_{1/2}$	0.2653	0.0017	0.0000	0.0000	0.0011	0.0110	-0.0005

can be presented as a combination of three consequent transitions: transiton from the first term to the average over the configuration with the same $\mathbf{N}^1_{\text{omc}}$, transition between averages over configurations with $\mathbf{N}^1_{\text{omc}}$ and $\mathbf{N}^2_{\text{omc}}$ and transition from the latter to the second term with $\mathbf{N}^2_{\text{omc}}$. Therefore, applying of both the self-consistent and term-spitting GRECP corrections to treatment of transitions between any terms allows one to reduce dramatically the (G)RECP approximation errors without increasing the number of explicitly treated core electrons of a considered d, f-element.

In tables 11 and 12, the matrix elements of $< r^2 >$ and radial integrals $2\int_{R_n}^{\infty} \mid f_{n_v lj}(r)[f_{n_v lj}(r) - \widetilde{\varphi}_{n_v lj}(r)] \mid dr$ (where $f_{n_v lj}$ is the large component of the Dirac spinor, $\widetilde{\varphi}_{n_v lj}$ is the radial part of the corresponding pseudospinor and R_n is the radius of the last spinor node) are considered for the cases of spinors from different configurations of E112. The errors in these matrix elements and integrals characterize the quality of reproducing the electronic density in outer core and valence regions of the atom. One can see that the GRECP allows one to reproduce the electronic density in the valence region

(the $7s_{1/2}$ and $7p_{1/2}$ spinors) with very high accuracy. The one-electron energies for spinors from different configurations of E112 are presented in table 13. Similar conclusion can be made in the latter case.

4. Conclusions

Different nuclear models and contributions of the Breit interaction between valence, inner and outer core shells of uranium, plutonium and superheavy elements E112, E113, and E114 are considered in the framework of all-electron four-component and (G)RECP methods. It is concluded on the basis of the performed calculations and theoretical analysis that the Breit contributions with inner core shells must be taken into account in calculations of actinide and SHE compounds with "chemical accuracy" whereas those between valence and outer core shells can be omitted.

The differences in the atomic energies between the cases of the PT-1 and self-consistent ways of treating the Breit interaction as well as small variations in the nuclear charge distribution in the framework of finite-size nuclei are not essential for the considered accuracy of calculations. However, the difference between the point and finite nuclear models is important for the valence (transition) energies. The effects of accounting for the Breit interaction and finite nuclear model can be simulated by GRECPs with very good accuracy when only Coulomb interaction between the explicitly treated electrons is taken into account. Thus, the GRECP method allows one to carry out reliable calculations of actinides, SHEs and their compounds at the level of "chemical accuracy".

Acknowledgements

The present work is supported by the U.S. CRDF grant RP2–2339–GA–02 and the RFBR grant 03–03–32335. N.M. is also supported by grants of the Russian Science Support Foundation and of the governor of Leningrad district. A.P. is grateful to the Ministry of Education of the Russian Federation (grant PD 02–1.3–236).

References

1. Hofmann, S. and Münzenberg, G. *Rev. Mod. Phys.* **2000**, *72*, 733.
2. Oganessian, Y. T. *et al*. *Nature* **1999**, *400*, 242.
3. Oganessian, Y. T. *Nature* **2001**, *413*, 122.
4. Schädel, M. (ed.). *The Chemistry of Superheavy Elements* (Kluwer, Dordrecht, 2003). 318 pp.
5. Hirao, K. and Ishikawa, Y. (eds.). *Recent Advances in Relativistic Molecular Theory* (World Scientific, Singapore, 2004). 328 pp.
6. Schwerdtfeger, P. (ed.). *Relativistic Electronic Structure Theory. Part 2. Applications*, vol. 14 of *Theoretical and Computational Chemistry* (Elsevier, Amsterdam, 2004). xv + 787 pp.

7. Mohr, P. J. *Phys. Rep.* **1997**, *293*, 227.
8. Grant, I. P. and Quiney, H. M. *Int. J. Quantum Chem.* **2000**, *80*, 283.
9. Reiher, M. and Hess, B. A. In: J. Grotendorst (ed.) *Modern Methods and Algorithms of Quantum Chemistry*, vol. 1, pp. 451–477 (Jülich, 2000). [http://www.fz-juelich.de/nic-series].
10. Shabaev, V. M. *Phys. Rep.* **2002**, *356*, 119.
11. Labzowsky, L. N. and Goidenko, I. In: P. Schwerdtfeger (ed.) *Relativistic Electronic Structure Theory. Part I. Fundamentals*, pp. 401–467 (Elsevier, Amsterdam, 2002).
12. Visscher, L. *Chem. Phys. Lett.* **1996**, *253*, 20.
13. Dyall, K. G. *J. Comput. Chem.* **2002**, *23*, 786.
14. Visscher, L. *J. Comput. Chem.* **2002**, *23*, 759.
15. Ermler, W. C., Ross, R. B., and Christiansen, P. A. *Adv. Quantum Chem.* **1988**, *19*, 139.
16. Titov, A. V. *et al*. Study of parity violation effects .... This issue.
17. Tupitsyn, I. I., Mosyagin, N. S., and Titov, A. V. *J. Chem. Phys.* **1995**, *103*, 6548.
18. Mosyagin, N. S., Titov, A. V., and Latajka, Z. *Int. J. Quantum Chem.* **1997**, *63*, 1107.
19. Titov, A. V. and Mosyagin, N. S. *Int. J. Quantum Chem.* **1999**, *71*, 359.
20. Phillips, J. C. and Kleinman, L. *Phys. Rev.* **1959**, *116*, 287.
21. Abarenkov, I. V. and Heine, V. *Philos. Mag.* **1965**, *12*, 529.
22. Heine, V. and Abarenkov, I. V. *Philos. Mag.* **1964**, *9*, 451.
23. Titov, A. V. and Mosyagin, N. S. *Structural Chem.* **1995**, *6*, 317.
24. Titov, A. V. and Mosyagin, N. S. *Russ. J. Phys. Chem.* **2000**, *74,* Suppl. 2, S376. [arXiv: physics/0008160].
25. Mosyagin, N. S., Eliav, E., Titov, A. V., and Kaldor, U. *J. Phys. B* **2000**, *33*, 667.
26. Isaev, T. A., Mosyagin, N. S., Kozlov, M. G., Titov, A. V., Eliav, E., and Kaldor, U. *J. Phys. B* **2000**, *33*, 5139.
27. Titov, A. V. *Doctorate Thesis* (Petersburg Nuclear Physics Institute, RAS, Russia, 2002).
28. Titov, A. V., Mitrushenkov, A. O., and Tupitsyn, I. I. *Chem. Phys. Lett.* **1991**, *185*, 330.
29. Petrov, A. N., Mosyagin, N. S., Titov, A. V., and Tupitsyn, I. I. *J. Phys. B* **2004**, *37*, 4621.
30. Mosyagin, N. S. and Titov, A. V. *J. Chem. Phys.* **2005**, *122*, 234106.
31. Titov, A. V., Mosyagin, N. S., Alekseyev, A. B., and Buenker, R. J. *Int. J. Quantum Chem.* **2001**, *81*, 409.
32. Labzowsky, L. N., Klimchitskaya, G. L., and Dmitriev, Y. Y. *Relativistic Effects in the Spectra of Atomic Systems* (Institute of Physics Publishing, Bristol and Philadelphia, 1993). 340 pp.
33. Quiney, H. M., Grant, I. P., and Wilson, S. *J. Phys. B* **1987**, *20*, 1413.
34. Lindroth, E., Mårtensson-Pendrill, A.-M., Ynnerman, A., and Öster, P. *J. Phys. B* **1989**, *22*, 2447.
35. Bratzev, V. F., Deyneka, G. B., and Tupitsyn, I. I. *Bull. Acad. Sci. USSR, Phys. Ser.* **1977**, *41*, 173.
36. Tupitsyn, I. I. and Petrov, A. N. in *5th Session of the V.A. Fock School on Quantum and Computational Chemistry*, p. 62 (Novgorod the Great, 2002).
37. Nash, C. S., Bursten, B. E., and Ermler, W. C. *J. Chem. Phys.* **1997**, *106*, 5133. [Erratum: JCP *111* (1999) 2347].

P,T-PARITY VIOLATION EFFECTS IN POLAR HEAVY-ATOM MOLECULES

A. V. TITOV, N. S. MOSYAGIN, A. N. PETROV AND T. A. ISAEV
Petersburg Nuclear Physics Institute, Gatchina, St.-Petersburg district 188300, Russia; titov@pnpi.spb.ru;
http://www.qchem.pnpi.spb.ru

AND

D. P. DEMILLE
Physics Department, Yale University, New Haven, Connecticut 06520, USA

Abstract. Investigation of P,T-parity nonconservation (PNC) phenomena is of fundamental importance for physics. Experiments to search for PNC effects have been performed on TlF and YbF molecules and are in progress for PbO and PbF molecules. For interpretation of molecular PNC experiments it is necessary to calculate those needed molecular properties which cannot be measured. In particular, electronic densities in heavy-atom cores are required for interpretation of the measured data in terms of the P,T-odd properties of elementary particles or P,T-odd interactions between them. Reliable calculations of the core properties (PNC effect, hyperfine structure etc., which are described by the operators heavily concentrated in atomic cores or on nuclei) usually require accurate accounting for both relativistic and correlation effects in heavy-atom systems. In this paper, some basic aspects of the experimental search for PNC effects in heavy-atom molecules and the computational methods used in their electronic structure calculations are discussed. The latter include the generalized relativistic effective core potential (GRECP) approach and the methods of nonvariational and variational one-center restoration of correct shapes of four-component spinors in atomic cores after a two-component GRECP calculation of a molecule. Their efficiency is illustrated with calculations of parameters of the effective P,T-odd spin-rotational Hamiltonians in the molecules PbF, HgF, YbF, BaF, TlF, and PbO.

J.-P. Julien et al. (eds.),
Recent Advances in the Theory of Chemical and Physical Systems, 253–283.

1. Introduction

It is well recognized that polar diatomics containing heavy elements are very promising objects for the search of a break of inversion symmetry (P) and time-reversal invariance (T). Although the search for P,T-parity non-conservation (PNC) effects in heavy atoms (and molecules) has produced no results so far, there are serious reasons to search for them with the presently accessible (or expected) level of experimental sensitivity. The observation of non-zero P,T-odd effects at this level would indicate the presence of so-called "new physics"[1] beyond the Standard Model (SM) of electroweak and strong interactions [2, 3, 4, 5] that is certainly of fundamental importance. Despite well known drawbacks and unresolved problems of the Standard Model (radiative corrections to the Higgs mass are quadratically divergent; rather artifiial Higgs mechanism of symmetry breaking is not yet verified in experiment; the problem of CP-violation is not well understood, where "C" is charge conjugation symmetry etc.) there are no experimental data available which would be in direct contradiction with this theory (see section 3 and papers [6, 1] for more details and references). In turn, some popular extensions of the Standard Model, which allow one to overcome its disadvantages, are not confirmed experimentally.

A crucial feature of PNC experiments in atoms, molecules, liquids or solids is that for interpretation of measured data in terms of fundamental constants of the P,T-odd interactions, one must calculate those properties of the systems, which establish a connection between the measured data and studied fundamental constants (see section 4). These properties are described by operators heavily concentrated near or on heavy nuclei; they cannot be measured and their theoretical study is not a trivial task. During the last several years the significance of (and requirement for) *ab initio* calculation of electronic structure providing a high level of reliability and accuracy in accounting for both relativistic and correlation effects has only increased (see sections 3 and 10).

The main goal of the paper is to discuss the present status of relativistic calculations of P,T-odd properties in heavy-atom molecules, the two-step methodology used in these calculations, and the accuracy of this method. The historical background of the PNC study in atoms and molecules, its current status and some general remarks on the PNC experiments are presented in sections 2, 3 and 4, correspondingly. The *ab initio* relativistic methods and the two-step techniques of calculation designed for studying PNC properties in heavy-atom molecules are discussed in sections 5 and 6. The calculations of PNC properties and hyperfine structure in molecules PbF, HgF, YbF, BaF, TlF and PbO are presented in sections 7–10. Concluding remarks are outlined in section 11.

2. Study of P- and T-parity nonconservation effects in heavy-atom molecules: Historical background

After discovery of the combined charge and space parity violation, or CP-violation, in K_L^0-meson decay [7], the search for the electric dipole moments (EDMs) of elementary particles has become one of the most fundamental problems in physics [6, 8, 9, 10, 1]. A permanent EDM is induced by the weak interaction that breaks both the space symmetry inversion and time-reversal invariance [11]. Considerable experimental effort has been invested in probing for atomic EDMs induced by EDMs of the proton, neutron and electron, and by P,T-odd interactions between them. The best available restriction for the electron EDM, d_e, was obtained in the atomic Tl experiment [12], which established an upper limit of $|d_e| < 1.6 \times 10^{-27}$ e·cm, where e is the charge of the electron. The benchmark upper limit on a nuclear EDM is obtained in atomic experiment on ^{199}Hg [13], $|d_{\rm Hg}| < 2.1 \times 10^{-28}$ e·cm, from which the best restriction on the proton EDM, $|d_p| < 5.4 \times 10^{-24}$ e·cm, was also recently obtained by Dmitriev & Sen'kov [14] (the previous upper limit on the proton EDM was obtained in the TlF experiment, see below).

Since 1967, when Sandars suggested the use of polar heavy-atom molecules in the experimental search for the proton EDM [15], molecules have been considered the most promising objects for such experiments. Sandars also noticed earlier [16] that the P- and P,T-parity nonconservation effects are strongly enhanced in heavy atoms due to relativistic and other effects. For example, in paramagnetic atoms the enhancement factor for an electron EDM, $d_{\rm atom}/d_e$, is roughly proportional to $\alpha^2 Z^3 \alpha_D$, where $\alpha \approx 1/137$ is the fine structure constant, Z is the nuclear charge and α_D is the atomic polarisability. It can be of order 100 or greater for highly polarizable heavy atoms ($Z \geq 50$). Furthermore, the effective intramolecular electric field acting on electrons in polar molecules can be five or more orders of magnitude higher than the maximal field accessible in a laboratory. The first molecular EDM experiment was performed on TlF by Sandars *et al.* [17] (Oxford, UK); it was interpreted as a search for the proton EDM and other nuclear P,T-odd effects. In 1991, in the last series of the ^{205}TlF experiments by Hinds *et al.* [18] (Yale, USA), the restriction $d_p = (-4 \pm 6) \times 10^{-23}$ e·cm was obtained (this was recalculated in 2002 by Petrov *et al.* [19] as $d_p = (-1.7 \pm 2.8) \times 10^{-23}$ e·cm).

In 1978 the experimental investigation of the electron EDM and other PNC effects was further stimulated by Labzowsky *et al.* [20, 21] and Sushkov & Flambaum [22] who clarified the possibilities of additional enhancement of these effects in diatomic radicals like BiS and PbF due to the closeness of levels of opposite parity in Ω-doublets having a $^2\Pi_{1/2}$ ground state. Then Sushkov *et al.* [23] and Flambaum & Khriplovich [24] suggested the

use of Ω-doubling in diatomic radicals with a $^2\Sigma_{1/2}$ ground state for such experiments and the HgF, HgH and BaF molecules were first studied semi-empirically by Kozlov [25]. At the same time, the first two-step *ab initio* calculation of PNC effects in PbF initiated by Labzowsky was finished by Titov *et al.* [26, 27]. A few years later, Hinds started an experimental search for the electron EDM in the YbF molecule, on which the first result was obtained by his group in 2002 (Sussex, UK) [28], $d_e=(-0.2\pm3.2)\times10^{-26}e\cdot$cm. Though that restriction is worse than the best current d_e datum (from the Tl experiment, see above), nevertheless, it is limited by only counting statistics, as Hinds *et al.* pointed out in [28].

A new series of electron EDM experiments on YbF by Hinds' group (Imperial College, UK) are in progress and a new generation of electron EDM experiments using a vapor cell, on the metastable $a(1)$ state of PbO, is being prepared by the group of DeMille (Yale, USA). The unique suitability of PbO for searching for the elusive d_e is demonstrated by the very high projected statistical sensitivity of the Yale experiment to the electron EDM. In prospect, it allows one to detect d_e of order of $10^{-29} \div 10^{-31}$ $e\cdot$cm [29], two–four orders of magnitude lower than the current limit quoted above. Some other candidates for the EDM experiments, in particular, HgH, HgF, TeO^*, and HI^+ are being discussed and an experiment on PbF is planned (Oklahoma Univ., USA).

3. Present status of the electron EDM search

As is mentioned in the introduction, the observation of a non-zero EDM would point out the presence of so called "new physics" (see [30, 1] and references) beyond the Standard Model [2, 3, 4, 5, 31] or CP violation in the QCD sector of SM, $SU(3)_C$. The discovery of a lepton EDM (electron EDM in our case) would have an advantage as compared to the cases of neutron or proton EDMs because the latter are not considered as elementary particles within the SM and its extensions.

In Table 1 some estimates for the electron EDM predicted by different theoretical models are given (e.g., see [6] for more details). One can see from the table that the most conservative estimate is given by the Standard Model. This is explained by severe cancellations and suppressions of the contributions producing the electron EDM within the SM. In turn, the "new physics" (extensions of the Standard Model: supersymmetry (SUSY) [32, 33, 1] multi-Higgs [34, 35, 36], left-right symmetry [37, 35, 33], lepton flavor-changing [38, 39] etc.) is very sensitive to the EDMs of elementary particles. This is especially true for the minimal ("naive") SUSY model, which predicts an electron EDM already at the level of $10^{-25}e\cdot$cm. However, the best experimental estimate on the electron EDM, $1.6\times10^{-27}e\cdot$cm,

TABLE 1. Prediction for the electron EDM, $|d_e|$, in popular theoretical models

Model	$\lvert d_e\rvert$ (in e·cm)
Standard Model	$< 10^{-38}$
Left-right symmetric	$10^{-28} - 10^{-26}$
Lepton flavor-changing	$10^{-29} - 10^{-26}$
Multi-Higgs	$10^{-28} - 10^{-27}$
Supersymmetric	$\leq 10^{-25}$
Experimental limit[12]	$< 1.6{\times}10^{-27}$

obtained in the experiment on the Tl atom [12], is almost two orders of magnitude smaller. More sophisticated SUSY models (which are extremely popular among theorists because they allow one to overcome serious theoretical drawbacks of SM, explain the "gauge hierarchy problem", solve the problem of dark matter in astrophysics etc.) still predict the electron EDM at the level of $10^{-27}e$·cm or somewhat smaller. Since the Tl experiment is finished now, an intriguing expectation is connected with the ongoing experiment on the $a(1)$ state of the PbO molecule, which is expected to be sensitive to the electron EDM at least two orders of magnitude smaller. Thus, the most popular extensions of SM can be severely examined by this experiment, i.e. even the result compatible with zero will dramatically influence their status.

4. General remarks on experimental search for EDMs in atoms and molecules

The experiments to search for EDMs in atoms and molecules are carried out using different approaches [40, 6]. The experimental technique depends on the properties of the atoms and molecules used in such an experiment. These properties influence the atomic and molecular sources, resonance region and detector. For example, for diatomic radicals like YbF or PbF the

experiments on molecular beams are most reasonable, while for molecules with closed electronic shells in the ground state like PbO the EDM measurements can be carried out in optical cells.

Nevertheless, the statistical sensitivity of the experiments to the electron or proton EDM usually depends on some parameters common for all such EDM experiments. The easiest way to see this is to apply the Heisenberg uncertainty principle to evaluate the sensitivity of the EDM measurement. Suppose that the EDM of a molecule is measured in some electric field, $\vec{E}$. (Do not confuse the *EDM of a polar molecule* with the large conventional *dipole moment* of the molecule, which averages to zero in the absence of external electric field in the laboratory coordinate system. In contrast to the latter, the (vanishingly small) molecular EDM can exist only due to P,T-odd interactions; it is *permanent* and its direction depends on the sign of the projection of the total electronic momentum on the molecular axis. See [6] for more details.) Thus the energy of interaction of the molecular EDM, $\vec{d} = d\vec{\sigma}$ (where $\vec{\sigma}$ is a unit vector along the total angular momentum of the molecule), with the electric field is $\vec{d} \cdot \vec{E}$ (linear Stark effect) and the energy difference between the levels with opposite directions of the total angular momentum (leading to the contributions of different signs) is $2\vec{d} \cdot \vec{E}$. If a measurement is carried out by detecting the energy shift during a time T, the uncertainty in the d determination is $\delta d = \hbar/(2T\vec{E} \cdot \vec{\sigma})$. For such measurement on N uncorrelated molecules one, obviously, has

$$\delta d = \hbar/(2T\sqrt{N}\vec{E} \cdot \vec{\sigma}) = \hbar/(2TE_\sigma\sqrt{\tau dN/dt}) \ ,$$

where dN/dt is the counting rate, $E_\sigma = \vec{E} \cdot \vec{\sigma}$, and τ is the total measurement time (usually $\tau \gg T$ and T is limited by the *coherence time* of the considered system). Up to now we deal with the molecular EDM $\vec{d}$. Let us write $d = Gd_e$, where d_e is the value of the *electron EDM* (the same is valid, of course, for the proton EDM) and G is the proportionality coefficient (usually called the *enhancement factor*). Thus, the final expression for δd_e is

$$\delta d_e = \frac{\hbar}{2TGE_\sigma\sqrt{\tau dN/dt}} = \frac{\hbar}{2TW\sqrt{\tau dN/dt}}, \tag{4.1}$$

where the value $W = GE_\sigma$ is the *effective electric field* in the molecule, which can be interpreted as the field that should be applied along the EDM of a free electron to give the energy shift $2Wd_e \equiv 2E_\sigma d$.

From expression (4.1), the basic conditions which should be met in any prospective EDM experiment can be derived:

1. The counting rate (dN/dt) should be made as high as possible. From this point of view the experiments on vapor cells, like that planned for PbO, have a clear advantage as compared to beam experiments

because molecular vapor density can be usually made much higher than molecular beam density. Thus, in the experiment on the PbO cell the counting rate is estimated to be of order 10^{11}–10^{15} Hz [29], while in the experiment on the YbF molecular beam the counting rate was of order 10^3—10^4 Hz [28].

2. It is crucial to attain high coherence time T. In the beam experiments that time is just the time of flight through the region with the electric field. For a gas-dynamic molecular source the typical time of flight is $1-10$ ms. On the other hand, for the PbO experiment in vapor cell T is close to the lifetime of the excited (metastable) state $a(1)$, $T \approx 0.1$ ms. So, the beam experiments have advantage in the coherence time.
3. It is also critical to have a high value of the effective electric field W, acting on the electron. The only way to know that parameter is to perform relativistic calculations. It is notable that the first semiempirical estimates of this kind were performed by Sandars in [16, 15] for Cs and TlF, correspondingly. In these papers the importance of accounting for relativistic effects and using heavy atoms and heavy-atom molecules in EDM experiments was first understood.

The expected energy difference, $2\vec{d}\cdot\vec{E}$ is extremely small even for completely polarized heavy-atom molecules. Thus, in practice, the EDM experiment is usually carried out in parallel and antiparallel electric and magnetic ($\vec{B}$) fields. Interaction energy of the molecular magnetic moment, $\vec{\mu}$, with the magnetic field is much higher than that of the EDM with the electric field and the energy differences are

$$2\vec{\mu}\cdot\vec{B} + 2\vec{d}\cdot\vec{E}$$

and

$$2\vec{\mu}\cdot\vec{B} - 2\vec{d}\cdot\vec{E}$$

for parallel and antiparallel fields, respectively (in practice, the atomic or molecular spin precession is usually studied instead of direct measurement of the energy shift, see [40]). When the electric field is reversed, the energy shift, $4\vec{d}\cdot\vec{E} = 4d_eW$, points to the existence of the permanent molecular EDM. The same measurement technique is applicable to studying other P,T-odd interactions in atoms and molecules.

The electronic structure parameters describing the P,T-odd interactions of electrons (sections 7, 8, and 10) and nucleons (section 9) including the interactions with their EDMs should be *reliably* calculated for interpretation of the experimental data. Moreover, *ab initio* calculations of some molecular properties are usually required even for the stage of preparation of the experimental setup. Thus, electronic structure calculations suppose a high level of accounting for both correlations and relativistic effects (see below). Modern methods of relativistic *ab initio* calculations (including very

recently developed approaches) allow one to achieve the required high accuracy. These approaches will be outlined and discussed in the following sections.

5. Heavy-atom molecules: Computational strategies

The most straightforward method for electronic structure calculation of heavy-atom molecules is solution of the eigenvalue problem using the Dirac-Coulomb (DC) or Dirac-Coulomb-Breit (DCB) Hamiltonians [41, 42, 43] when some approximation for the four-component wave function is chosen.

However, even applying the four-component single configuration (SCF) approximation, Dirac-Fock (DF) or Dirac-Fock-Breit (DFB), to calculation of heavy-atom molecules (followed by transformation of two-electron integrals to the basis of molecular spinors is not always an easy task) because a very large set of primitive atomic basis functions can be required for such all-electron four-component SCF calculations (see [44]). Starting from the Pauli approximation and Foldy–Wouthuysen transformation, many different two-component approaches were developed in which only large components are treated explicitly (e.g., see [45, 46, 47, 48] and references). In addition, the approaches with perturbative treatment of relativistic effects [49] have been developed in which a nonrelativistic wavefunction is used as reference. During the last few years, good progress was also attained in four-component techniques [50, 51, 52, 41] which allowed one to reduce efforts in calculation and transformation of two-electron matrix elements with small components of four-component molecular spinors. These developments are applied, in particular, in the DIRAC [53] and BERTHA [54, 55] molecular programs. Thus, accurate DC(B) calculations of relatively simple heavy-atom molecules can be performed on modern computers now.

The greatest computational savings are achieved when the two-component relativistic effective core potential (RECP) approximation suggested originally by Lee *et al.* [56] is used (e.g., see reviews [57, 58, 59]). There are several reasons for using RECPs (including model potentials and pseudopotentials) in calculations of complicated heavy-atom molecules, clusters and solids. The RECP approaches allow one to exclude the large number of chemically inactive electrons from molecular calculations and to treat explicitly only valence and outermost core electrons from the beginning. Then, the oscillations of the valence spinors are usually smoothed in heavy-atom cores simultaneously with excluding small components from the explicit treatment. As a result the number of primitive basis functions can be reduced dramatically; this is especially important for calculation and transformation of two-electron integrals when studying many-atomic systems and compounds of very heavy elements including actinides and superheav-

ies. The RECP method is based on a well-developed nonrelativistic technique of calculations; however, an effective spin-orbit interaction and other scalar-relativistic effects are taken into account usually by means of radially-local [57, 58, 59, 60], separable [61, 62, 63] or Huzinaga-type [64, 65, 66] operators.

Correlation molecular calculations with RECPs are naturally performed in the basis of spin-orbitals (and not of spinors as is in all-electron four-component calculations) even for the cases when quantum electrodynamics (two-electron Breit etc.) effects are taken into account [67, 44]. Note, however, that the DCB technique with the separated spin-free and spin-dependent terms also has been developed [68], but it can be efficiently applied only in the cases when spin-dependent effects can be neglected both for valence and for core shells. In the RECP method, the interactions with the excluded inner core shells (spinors!) are described by spin-dependent potentials whereas the explicitly treated valence and outer core shells are usually described by spin-orbitals in molecular calculations. It means that some "soft" way of accounting for the core-valence orthogonality constraints is applied in the latter case [69] (note, meantime, that the strict core-valence orthogonality can be retrieved after the RECP calculation by using the restoration procedures described below). Another merit of the RECP method is in its natural ability to account for correlations with the explicitly excluded inner core electrons [70] (this direction is actively developed during last years). The use of the molecular spin-orbitals and the "correlated" RECPs allows one to reduce dramatically the expenses at the stage of correlation calculation of heavy-atom molecules. These are important advantages when a very high level of accounting for correlations is required even in studying diatomics (e.g., see calculations of PbO described in section 10). Thus, many complications of the DC(B) molecular calculations are avoided when employing RECPs.

The "shape-consistent" (or "norm-conserving") RECP approaches are most widely employed in calculations of heavy-atom molecules though "energy-adjusted/consistent" pseudopotentials [58] by Stuttgart team are also actively used as well as the Huzinaga-type "*ab initio* model potentials" [66]. In plane wave calculations of many-atom systems and in molecular dynamics, the separable pseudopotentials [61, 62, 63] are more popular now because they provide linear scaling of computational effort with the basis set size in contrast to the radially-local RECPs. The nonrelativistic shape-consistent effective core potential was first proposed by Durand & Barthelat [71] and then a modified scheme of the pseudoorbital construction was suggested by Christiansen *et al.* [72] and by Hamann *et al.* [73].

In a series of papers (see [69, 74, 75, 67, 70] and references) a generalized RECP approach was developed that involves both radially-local, separable

and Huzinaga-type potentials as its components in particular cases. It allows one to attain very high accuracy of calculation of valence properties and electronic densities in the valence region when treating outermost core shells in calculations explicitly (see section 6 for more details).

Nevertheless, calculation of such properties as spin-dependent electronic densities near nuclei, hyperfine constants, P,T-parity nonconservation effects, chemical shifts etc. with the help of the two-component pseudospinors smoothed in cores is impossible. We should notice, however, that the above core properties (and the majority of other properties of practical interest which are described by the operators heavily concentrated within inner cores or on nuclei) are mainly determined by electronic densities of the valence and outer core shells near to, or on, nuclei. The valence shells can be open or easily perturbed by external fields, chemical bonding etc., whereas outer core shells are noticeably polarized (relaxed) in contrast to the inner core shells. Therefore, accurate calculation of electronic structure in the valence and outer core region is of primary interest for such properties.

For evaluation of the matrix elements of the operators concentrated on (or close to) nuclei, proper shapes of the valence molecular four-component spinors must be restored in atomic core regions after performing the RECP calculation of that molecule. In 1959, a nonrelativistic procedure of restoration of the orbitals from smoothed Phillips–Kleinman pseudoorbitals was proposed [76] based on the orthogonalization of the latter to the original atomic core orbitals. In 1985, Pacios & Christiansen [77] suggested a modified orthogonalization scheme in the case of shape-consistent pseudospinors. At the same time, a simple procedure of "nonvariational" one-center restoration (NOCR, see below) employing the idea of generation of equivalent basis sets in four-component Dirac-Fock and two-component RECP/SCF calculations was proposed and first applied in [26] to evaluation of the P,T-odd spin-rotational Hamiltonian parameters in the PbF molecule. In 1994, a similar procedure was used by Blöchl inside the augmentation regions [78] in solids to construct the transformation operator between pseudoorbitals ("PS") and original orbitals ("AE") in his projector augmented-wave method.

All the above restoration schemes are called "nonvariational" as compared to the "variational" one-center restoration (VOCR, see below) procedure proposed in [79, 80]. Proper behavior of the molecular orbitals (four-component spinors) in atomic cores of molecules can be restored in the scope of a variational procedure if the molecular pseudoorbitals (two-component pseudospinors) match correctly the original orbitals (large components of bispinors) in the valence region after the molecular RECP calculation. As is demonstrated in [69, 44], this condition is rather correct when the shape-consistent RECP is involved to the molecular calculation with explicitly

treated outermost core orbitals and, especially, when the generalized RECP operator is used since the above matching condition is implemented at their generation.

At the restoration stage, a one-center expansion in the spherical harmonics with numerical radial parts is most appropriate both for orbitals (spinors) and for the description of "external" interactions with respect to the core regions of a considered molecule. In the scope of the discussed two-step methods for the electronic structure calculation of a molecule, finite nucleus models and quantum electrodynamic terms including, in particular, two-electron Breit interaction may be taken into account without problems [67].

One-center expansion was first applied to whole molecules by Desclaux & Pyykkö in relativistic and nonrelativistic Hartree-Fock calculations for the series CH_4 to PbH_4 [81] and then in the Dirac-Fock calculations of CuH, AgH and AuH [82] and other molecules [83]. A large bond length contraction due to the relativistic effects was estimated. However, the accuracy of such calculations is limited in practice because the orbitals of the hydrogen atom are reexpanded on a heavy nucleus in the entire coordinate space. It is notable that the RECP and one-center expansion approaches were considered earlier as alternatives to each other [84, 85].

The applicability of the discussed two-step algorithms for calculation of wavefunctions of molecules with heavy atoms is a consequence of the fact that the valence and core electrons may be considered as two subsystems, interaction between which is described mainly by some integrated properties of these subsystems. The methods for consequent calculation of the valence and core parts of electronic structure of molecules give us a way to combine the relative simplicity and accessibility both of molecular RECP calculations in gaussian basis set, and of relativistic finite-difference one-center calculations inside a sphere with the atomic core radius.

The first two-step calculations of the P,T-odd spin-rotational Hamiltonian parameters were performed for the PbF radical about 20 years ago [26, 27], with a semiempirical accounting for the spin-orbit interaction. Before, only nonrelativistic SCF calculation of the TlF molecule using the relativistic scaling was carried out [86, 87]; here the P,T-odd values were underestimated by almost a factor of three as compared to the later relativistic Dirac-Fock calculations. The latter were first performed only in 1997 by Laerdahl *et al.* [88] and by Parpia [89]. The next two-step calculation, for PbF and HgF molecules [90], was carried out with the spin-orbit RECP part taken into account using the method suggested in [91].

Later we performed correlation GRECP/NOCR calculations of the core properties in YbF [92], BaF [93], again in YbF [94] and in TlF [19]. In 1998, first all-electron Dirac-Fock calculations of the YbF molecule were also

performed by Quiney *et al.* [95] and by Parpia [96]. Recently we finished extensive two-step calculations of the P,T-odd properties and hyperfine structure of the excited states of the PbO molecule [97, 98]. One more two-step calculation of the electron EDM enhancement effect was performed very recently for the molecular ion HI^+ [99].

We would like to emphasize here that the all-electron Dirac-Fock calculations on TlF and YbF are, in particular, important for checking the quality of the approximations made in the two-step method. The comparison of appropriate results, Dirac-Fock vs. RECP/SCF/NOCR, is, therefore, performed in papers [94, 19] and discussed in the present paper.

In this paper, the main features of the two-step method are presented and PNC calculations are discussed, both those without accounting for correlation effects (PbF and HgF) and those in which electron correlations are taken into account by a combined method of the second-order perturbation theory (PT2) and configuration interaction (CI), or "PT2/CI" [100] (for BaF and YbF), by the relativistic coupled cluster (RCC) method [101, 102] (for TlF, PbO, and HI^+), and by the spin-orbit direct-CI method [103, 104, 105] (for PbO). In the *ab initio* calculations discussed here, the best accuracy of any current method has been attained for the hyperfine constants and P,T-odd parameters regarding the molecules containing heavy atoms.

6. Two-step method of calculation of core properties

The two-step method consists of a two-component molecular RECP calculation at the first step, followed by restoration of the proper four-component wave function in atomic cores at the second step. Though the method was developed originally for studying core properties in heavy-atom molecules, it can be efficiently applied to studying the properties described by the operators heavily concentrated in cores or on nuclei of light atoms in other computationally difficult cases, e.g., in many-atom molecules and solids. The details of these steps are described below.

Generalized RECP When core electrons of a heavy-atom molecule do not play an active role, the effective Hamiltonian with RECP can be presented in the form

$$\mathbf{H}^{\mathrm{Ef}} = \sum_{i_v} [\mathbf{h}^{\mathrm{Schr}}(i_v) + \mathbf{U}^{\mathrm{Ef}}(i_v)] + \sum_{i_v > j_v} \frac{1}{r_{i_v j_v}} \,. \tag{6.1}$$

This Hamiltonian is written only for a valence subspace of electrons which are treated explicitly and denoted by indices i_v and j_v. In practice, this subspace is often extended by inclusion of some outermost core shells for better

accuracy but we will consider them as the valence shells below if these outermost core and valence shells are not treated using different approximations. In Eq. (6.1), $\mathbf{h}^{\mathrm{Schr}}$ is the one-electron Schrödinger Hamiltonian

$$\mathbf{h}^{\mathrm{Schr}} = -\frac{1}{2}\vec{\nabla}^2 - \frac{Z_{ic}}{r} , \tag{6.2}$$

where Z_{ic} is the charge of the nucleus decreased by the number of inner core electrons. $\mathbf{U}^{\mathrm{Ef}}$ in (6.1) is an RECP (relativistic pseudopotential) operator that is usually written in the radially-local (semi-local) [57] or separable (e.g., see [63] and references) approximations when the valence pseudospinors are smoothed in the heavy-atom cores. Contrary to the four-component wave function used in Dirac-Coulomb(-Breit) calculations, the pseudo-wave function in the RECP case can be both two- and one-component. The use of the effective Hamiltonian (6.1) instead of all-electron four-component Hamiltonians leads to the question about its accuracy. It was shown both theoretically and in many calculations (see [69, 75] and references) that the typical accuracy of the radially-local RECPs is within 1000–3000 cm^{-1} for transition energies between low-lying states though otherwise is sometime stated (see [106, 107]).

In our two-step calculations the generalized RECP operator [69, 74] is used that includes the operators of radially-local shape-consistent RECP, separable pseudopotential and Huzinaga-type model potential as its components. Additionally, the GRECP operator can include terms of other types, known as "self-consistent" and two-electron "term-splitting" corrections [108, 69, 74], which are important particularly for economical (but precise!) treatment of transition metals, lanthanides and actinides. With these terms, the accuracy provided by GRECPs can be even higher than the accuracy of the frozen core approximation (employing the same number of explicitly treated electrons) because they can account for relaxation of explicitly excluded (inner core) electrons [69, 75]. The theoretical background of the GRECP concept is developed in a series of papers [69, 74, 75, 67, 44, 70]. In contrast to other RECP methods, GRECP employs the idea of separating the space around a heavy atom into three regions: inner core, outer core and valence, which are first treated employing different approximations for each. It allows one to attain practically any desired accuracy, while requiring moderate computational efforts since the overall accuracy is limited in practice by possibilities of correlation methods.

When innermost core shells must be treated explicitly, the four-component versions of the GRECP operator can be used, in principle, together with the all-electron relativistic Hamiltonians. The GRECP can describe here some quantum electrodynamics effects (self-energy, vacuum polarization etc.) thus avoiding their direct treatment. One more remark is that the

two-component GRECP operator can be applied even to very light atoms when smoothing the large components of the four-component spinors only in the vicinity of the nucleus just to account for relativistic effects (the GRECP for hydrogen provides accuracy of treatment of very small relativistic contributions within 5%).

Nonvariational one-center restoration. The electronic densities evaluated from the two-component pseudo-wave function very accurately reproduce the corresponding all-electron four-component densities in the valence and outer core regions not only for the state used in the GRECP generation but also for other states which differ by excitations of valence electrons. This is illustrated in figure 1 (see also tables 8 and 9 in [44]), where the radial parts of the large components of the thallium bispinor and the corresponding pseudospinor are compared for the state averaged over the relativistic $6s^2_{1/2}6p^1_{1/2}$ configuration, whereas the 21-electron GRECP is generated for the state averaged over the nonrelativistic $6s^16p^16d^1$ configuration. That is true also for the electronic densities obtained in the corresponding Dirac-Coulomb(-Breit) and GRECP calculations accounting for correlation.

In the inner core region, the pseudospinors are smoothed, so that the electronic density with the pseudo-wave function is not correct. When operators describing properties of interest are heavily concentrated near or on nuclei, their mean values are strongly affected by the wave function in the inner region. The four-component molecular spinors must, therefore, be restored in the heavy-atom cores.

All molecular spinors ϕ_p can be restored as one-center expansions in the cores using the nonvariational one-center restoration (NOCR) scheme [26, 27, 90, 92, 93, 94, 19, 97, 98] that consists of the following steps:

- Generation of *equivalent* basis sets of one-center four-component spinors $\begin{pmatrix} f_{nlj}(r)\chi_{ljm} \\ g_{nlj}(r)\chi_{2j-l,jm} \end{pmatrix}$ and smoothed two-component pseudospinors $\tilde{f}_{nlj}(r)\chi_{ljm}$ in finite-difference all-electron Dirac-Fock(-Breit) and GRECP/SCF calculations of the same configurations of a considered atom and its ions. The nucleus is usually modeled by a uniform charge distribution within a sphere. The all-electron four-component HFDB [109, 110, 111] and two-component GRECP/HFJ [112, 113] codes are employed to generate two equivalent numerical basis sets used at the restoration. These sets, describing mainly the atomic core region, are generated independently of the basis set used for the molecular GRECP calculations.
- The molecular *pseudospinorbitals* are then expanded in the basis set of one-center two-component atomic *pseudospinors* (for $r \leq R_{\mathrm{nocr}}$, where

$R_{\rm nocr}$ is the radius of restoration that should be sufficiently large for calculating core properties with required accuracy),

$$\tilde{\phi}_p(\mathbf{x}) \approx \sum_{l=0}^{L_{max}} \sum_{j=|l-1/2|}^{j=|l+1/2|} \sum_{n,m} c^p_{nljm} \tilde{f}_{nlj}(r)\chi_{ljm} \ , \tag{6.3}$$

where $\mathbf{x}$ denotes spatial and spin variables. Note that for linear molecules only one value of m survives in the sum for each ϕ_p.

– Finally, the atomic two-component pseudospinors in the molecular basis are replaced by equivalent four-component spinors and the expansion coefficients from Eq. (6.3) are preserved:

$$\phi_p(\mathbf{x}) \approx \sum_{l=0}^{L_{\rm max}} \sum_{j=|l-1/2|}^{j=|l+1/2|} \sum_{n,m} c^p_{nljm} \begin{pmatrix} f_{nlj}(r)\chi_{ljm} \\ g_{nlj}(r)\chi_{2j-l,jm} \end{pmatrix} . \tag{6.4}$$

The molecular four-component spinors constructed this way are orthogonal to the inner core spinors of the atom, because the atomic basis functions used in Eq. (6.4) are generated with the inner core shells treated as frozen.

Variational one-center restoration. In the variational technique of one-center restoration (VOCR) [79, 80], the proper behavior of the four-component molecular spinors in the core regions of heavy atoms can be restored as an expansion in spherical harmonics inside the sphere with a restoration radius, $R_{\rm vocr}$, that should not be smaller than the matching radius, R_c, used at the RECP generation. The outer parts of spinors are treated as frozen after the RECP calculation of a considered molecule. This method enables one to combine the advantages of two well-developed approaches, molecular RECP calculation in a gaussian basis set and atomic-type one-center calculation in numerical basis functions, in the most optimal way. This technique is considered theoretically in [80] and some results concerning the efficiency of the one-center reexpansion of orbitals on another atom can be found in [75].

The VOCR scheme can be used for constructing the core parts of the molecular spinors (orbitals) instead of using equivalent basis sets as in the NOCR technique. A disadvantage of the NOCR scheme is that molecular pseudoorbitals are usually computed in a spin-averaged GRECP/SCF molecular calculation (i.e. without accounting for the effective spin-orbit interaction) and the reexpansion of molecular pseudospinorbitals on one-center atomic pseudospinors can be restricted in accuracy, as was noticed in the GRECP/RCC/NOCR calculations [19] of the TlF molecule (see below).

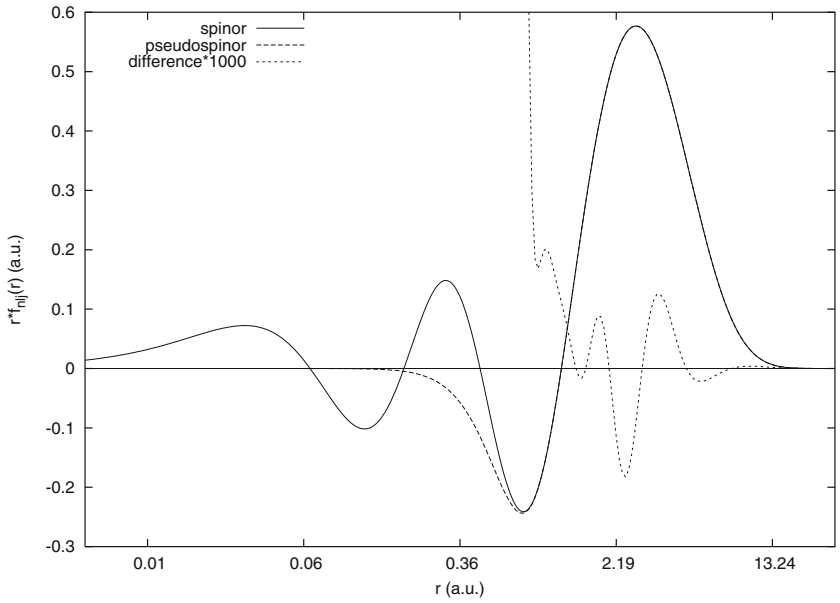

Figure 1. The radial parts of the large component of the $6p_{1/2}$ bispinor and the corresponding pseudospinor obtained in equivalent Dirac-Fock and 21-electron GRECP/SCF calculations for the state averaged over the relativistic $6s^2_{1/2}6p^1_{1/2}$ configuration of thallium. Their difference is multiplied by 1000. The GRECP is generated for the state averaged over the nonrelativistic $6s^16p^16d^1$ configuration.

With the restored molecular bispinors, the two-electron integrals on them can be easily calculated. Thus, the four-component transfomation from the atomic basis that is a time-consuming stage of four-component calculations of heavy-atom molecules can be avoided. Besides, the VOCR technique developed in [92] for molecular *pseudospinors* can be reformulated for the case of molecular *pseudospinorbitals* to reduce the complexity of the molecular GRECP calculation as is discussed in section 5.

However, the most interesting direction in the development of the two-step method is the possibility to "split" the correlation structure calculation of a molecule into two sequential correlation calculations: first, in the valence region, where the *outer core and valence* electrons are explicitly involved in the GRECP calculation; and then, in the core region, when the *outer and inner core* space regions are only treated at the restoration stage. Correlation effects in the valence and outer core regions (not only valence parts of molecular orbitals but also configuration coefficients) can be calculated, for example, by a combination of RCC and CI methods (see section 10) with very high accuracy. Then correlation effects in

the inner and outer core regions (including the dipole-type relaxation of atomic inner core shells in a molecule) can be taken into account using the Dirac-Coulomb(-Breit) Hamiltonian and the one-center expansion. By increasing the one-center restoration radius $R_{\rm vocr}$, one can take into account correlation effects in the intermediate region (outer core in our case) with the required accuracy. Roughly speaking, the computational efforts for the correlation structure calculations in the core and valence regions are added when using the two-step approach, whereas in the conventional one-step scheme, they have multiplicative nature.

Two-step calculation of molecular properties. To evaluate one-electron core properties (hyperfine structure, P,T-odd effects etc.) employing the above restoraton schemes it is sufficient to obtain the one-particle density matrix, $\{\widetilde{D_{pq}}\}$, after the molecular RECP calculation in the basis of pseudospinors $\{\widetilde{\phi}_p\}$. At the same time, the matrix elements $\{W_{pq}\}$ of a property operator $\mathbf{W}(\mathbf{x})$ should be calculated in the basis of equivalent four-component spinors $\{\phi_p\}$. The mean value for this operator can be then evaluated as

$$\langle \mathbf{W} \rangle \;=\; \sum_{pq} \widetilde{D_{pq}} W_{pq} \;. \tag{6.5}$$

Only the explicitly treated valence shells are used for evaluating a core property when applying Eq. (6.5) since the atomic frozen core (closed) shells do not usually contibute to the properties of practical interest. However, correlations with the core electrons explicitly excluded from the RECP calculation can be also taken into account if the effective operator technique [114] is applied to calculate the property matrix elements $\{W^{\rm Ef}_{pq}\}$ in the basis set of bispinors $\{\phi_p\}$. Then, in expression (6.5) one should only replace $\{W_{pq}\}$ by $\{W^{\rm Ef}_{pq}\}$. Alternatively, the correlations with the inner core electrons can be, in principle, considered within the variational restoration scheme for electronic structure in the heavy atom cores. Strictly speaking, the use of the effective operators is correct when the molecular calculation is carried out with the "correlated" GRECP (see [70]), in which the same correlations with the excluded core electrons are taken into account at the GRECP generation as they are in constructing $\{W^{\rm Ef}_{pq}\}$. Nevertheless, the use of the (G)RECP that does not account for the core correlations at the molecular calculation stage can be justified if these correlations do not influence dramatically the electronic structure in the valence region. The latter approximation was applied in the calculations of YbF and BaF molecules described in the following section.

When contributions to $\langle \mathbf{W} \rangle$ are important both in the core and valence regions, the scheme for evaluating the mean value of $\mathbf{W}(\mathbf{x})$ can be as follows:

– calculation of matrix elements with the molecular pseudospinorbitals (which are usually linear combinations of atomic gaussians) over the entire space region using conventional codes for molecular RECP calculations (although the operator $\mathbf{W}$ can be presented in different forms in calculations with the RECP and Dirac-Coulomb(-Breit) Hamiltonians),

$$\widetilde{\langle \mathbf{W} \rangle} \;=\; \sum_{pq} \widetilde{D_{pq}} \int\limits_{r<\infty} \widetilde{\phi}_p(\mathbf{x})\; \mathbf{W}(\mathbf{x})\; \widetilde{\phi}_q(\mathbf{x})\; d\mathbf{x}\;; \tag{6.6}$$

– calculation of the inner part of the matrix element of the operator with the same molecular pseudospinorbitals using the one-center expansion for $\{\widetilde{\phi}_p\}$ ($R_{\rm ocr}$ stands for $R_{\rm nocr}$ or $R_{\rm vocr}$ below, $R_{\rm ocr} \geq R_c$):

$$\widetilde{\langle \mathbf{W} \rangle}^{<} \;=\; \sum_{pq} \widetilde{D_{pq}} \int\limits_{r<R_{\rm ocr}} \widetilde{\phi}_p(\mathbf{x})\; \mathbf{W}(\mathbf{x})\; \widetilde{\phi}_q(\mathbf{x})\; d\mathbf{x}\;; \tag{6.7}$$

– calculation of the inner part of the matrix element of the operator with the restored molecular four-component spinors using the one-center expansion for $\{\phi_p\}$:

$$\langle \mathbf{W} \rangle^{<} \;=\; \sum_{pq} \widetilde{D_{pq}} \int\limits_{r<R_{\rm ocr}} \phi_p^{<}(\mathbf{x})\; \mathbf{W}(\mathbf{x})\; \phi_{\mathbf{q}}^{<}(\mathbf{x})\; \mathbf{dx}\;. \tag{6.8}$$

The matrix element $\langle \mathbf{W} \rangle$ of the $\mathbf{W}(\mathbf{x})$ operator is evaluated as

$$\langle \mathbf{W} \rangle \;=\; \widetilde{\langle \mathbf{W} \rangle} \;-\; \widetilde{\langle \mathbf{W} \rangle}^{<} \;+\; \langle \mathbf{W} \rangle^{<}\;. \tag{6.9}$$

Obviously, the one-center basis functions can be numerical (finite-difference) for better flexibility.

The mean values of the majority of operators for the valence properties can be calculated with good accuracy without accounting for the inner parts of the matrix elements (6.7) and (6.8). As discussed above, for calculating the mean values of the operators heavily concentrated on or near nuclei it is sufficient to account only for the inner parts (6.8) of the matrix elements of $\mathbf{W}(\mathbf{x})$ on the restored functions $\phi_p^{<}(\mathbf{x})$, whereas the other contributions, (6.6) and (6.7), can be neglected.

Calculation of properties using the finite-field method [115, 116] and Eq. (6.5) within the coupled-cluster approach is described in section 9.

7. Calculation of PbF and HgF

The ground states of the diatomic radicals PbF and HgF are $^2\Pi_{1/2}$ and $^2\Sigma_{1/2}$, respectively. Here the superscript denotes spin multiplicity, Π and

Σ are the projections of the electron orbital angular momentum on the molecular axis and the subscript is the projection of the total electron angular momentum on the molecular axis directed from the heavy atom to fluorine. It is convenient to describe the spin-rotational spectrum of the ground electronic state in terms of the effective spin-rotational Hamiltonian $\mathbf{H}^{sr}_{\rm eff}$, following [90, 117]:

$$\begin{aligned}\mathbf{H}^{sr}_{\rm eff} &= B\vec{J}^2 + \Delta\vec{S}'\cdot\vec{J} + \vec{S}'\cdot\mathbf{A}\cdot\vec{I} \\ &+ \mu_0\vec{S}'\cdot\mathbf{G}\cdot\vec{B} - D\vec{\lambda}\cdot\vec{E} \\ &+ W_{\rm A}k_{\rm A}\vec{\lambda}\times\vec{S}'\cdot\vec{I} + (W_d d_e + W_{\rm S}k_{\rm S})\vec{S}'\cdot\vec{\lambda}\end{aligned} \tag{7.1}$$

The first line in this expression describes the rotational structure with ω- or spin-doubling and the hyperfine interaction of the effective electron spin $\vec{S}'$ with the nuclear spin $\vec{I}$. B is the rotational constant, $\vec{J}$ is the electron-rotational angular momentum, Δ is the ω-doubling constant. The second line describes the interaction of the molecule with the external fields $\vec{B}$ and $\vec{E}$, ($\vec{\lambda}$ is the unit vector directed from the heavy nucleus to the light one). The last line corresponds to the P-odd electromagnetic interaction of the electrons with the anapole moment of the nucleus described by the constant $k_{\rm A}$ [40], P,T-odd interaction of the electron EDM d_e with the interamolecular field, and P,T-odd scalar interactions of the electrons with the heavy nucleus [90].

The parameter Δ, tensors $\mathbf{A}$ and $\mathbf{G}$, molecular dipole moment D and the constants W_i are expressed in terms of one-electron matrix elements; concrete expressions for the above parameters can be found in [90], and for W_d and $A_\parallel$ they are also given in the next sections. The results of the calculations are presented in Table 2.

In [90] the conclusion was made, that the accuracy in calculations of the parameters of the effective spin-rotational Hamiltonian is close to 20%. However, further *ab initio* calculations showed the situation is more complicated.

As was understood in calculations of YbF [92], a fortuitous cancellation of effects of different types took place in the above calculations. Accounting for the polarization of the $5s, 5p$-shells leads to an enhancement of the contributions of the valence shells to the $A_\parallel$, $A_\perp$ and PNC constants on the level of 50% of magnitude. A contribution of comparable magnitude but of opposite sign takes place when the relaxation-correlation effects of the $5d$-shell are taken into account. This was confirmed in [120] when accounting for electron correlation both in the valence and core regions of HgF as compared to the YbF case.

TABLE 2. Parameters of the spin-rotational Hamiltonian for the ground states of ^{199}HgF and ^{207}PbF ($\vec{I}$=1/2); (a) experimental data [118]; (b) semiempirical results from [25]; (c) *ab initio* calculations [90]; (d),(e) *ab initio* calculations [27] with semiempirical accounting for the "minimal" and "maximal" spin-orbit mixing models, respectively, and $\Delta/2B$ from [119] (the W_i values in [27] have wrong sign).

		$A_\parallel$ (MHz)	$A_\perp$ (MHz)	$G_\parallel$	$G_\perp$	W_S (kHz)	W_d ($10^{25}\frac{\text{Hz}}{\text{e cm}}$)
HgF	(a)	22621	21880	1.993	1.961		
	(b)					−191	−4.8
	(c)	24150	23310	1.996	1.960	−185	−4.8
PbF	(d)	8690	-7460	0.034	−0.269	51	1.0
	(e)	9550	-8240	0.114	−0.438	99	1.8
	(c)	10990	-8990	0.040	−0.326	55	1.4

8. Calculation of YbF and BaF

The results of two-step calculations for the YbF molecule (1996,1998) [92, 94] and for the BaF molecule (1997) [93] are presented in Table 3, where they are compared with other semiempirical and four-component results. For the isotropic hyperfine constant $A = (A_\parallel + 2A_\perp)/3$, the accuracy of our calculation is about 3%, as determined by comparison to the experimental datum. The dipole constant $A_\mathrm{d} = (A_\parallel - A_\perp)/3$ (which is much smaller in magnitude), though better than in all previous calculations known from the literature, is still underestimated by almost 23%. After a semiemprical correction for a perturbation of $4f$-shell in the core of Yb due to the bond making, this error is reduced to 8%. Our value for the effective electric field on the unpaired electron is $W = W_d|\vec{S}'\cdot\vec{\lambda}| = 4.9$ a.u.$= 2.5\times10^{10}$ V cm^{-1} (see section 4 and Eq. (7.1)).

In Table 3 the values of the W_d constant

$$W_d d_\mathrm{e} = 2W d_\mathrm{e} = 2\langle {}^2\Sigma_{1/2}|\sum_i H_d(i)|{}^2\Sigma_{1/2}\rangle, \tag{8.1}$$

where H_d describes interaction of the electron EDM d_e with the internal molecular electric field $\mathbf{E}^\mathrm{mol}$:

$$H_d = 2d_\mathrm{e}\begin{pmatrix} 0 & 0 \\ 0 & \sigma \end{pmatrix}\cdot\mathbf{E}^\mathrm{mol},$$

from various calculations are tabulated. These include the unrestricted Dirac-Fock calculation of Parpia (1998) [96], four-component calculations of Quiney *et al.* (1998) [95] accounting for correlation, the most recent semi-empirical calculation of Kozlov (1997) [121] and our latest GRECP/RAS-SCF/EO calculation (EO stands for the effective operator technique in the framework of the second-order perturbation theory; see section 6 and paper [100] for more details). All results are in very close agreement now. It should be noted that the valence electron contribution to W_d in [96] differs by only 7.4% from the corresponding RECP-based calculation of Titov *et al.* (1996) [92].

A similar increase in the values for the hyperfine constants and parameters of the P,T-odd interactions when the correlations with the core shells (primarily, $5s, 5p$) are taken into account is also observed for the BaF molecule [93], as one can see in Table 3. Of course, the corrections from the $4f$-electron excitations are not required for this molecule. The enhancement factor for the P,T-odd effects in BaF is three times smaller than in YbF mainly because of the smaller nuclear charge of Ba.

9. Calculation of the ^{205}TlF molecule

Effective Hamiltonian. Here we consider the P,T-odd interaction of the ^{205}Tl nucleus (which has one unpaired proton) with the electromagnetic field of the electrons in the ^{205}TlF molecule [19]. This molecule is one of the best objects for measurements of the proton EDM. The effective interaction with the EDM of the Tl nucleus in TlF is written in the form

$$H^{\rm eff} = (d^V + d^M)\vec{I}/I \cdot \vec{\lambda} \ , \tag{9.1}$$

where $\vec{I}$ is the Tl nuclear spin operator; $\vec{\lambda}$ is the unit vector along z (from Tl to F); d^V and d^M are the *volume* and *magnetic* constants [126]:

$$d^V = 6SX = (-d_p R + Q)X \ , \tag{9.2}$$

where S is the nuclear Schiff moment; d_p is the proton EDM; R and Q are the factors determined by the nuclear structure of ^{205}Tl (see [19]);

$$X = \frac{2\pi}{3}\left[\frac{\partial}{\partial z}\rho_\psi(\vec{r})\right]_{x,y,z=0} \ ; \tag{9.3}$$

$\rho_\psi(\vec{r})$ is the electronic density calculated from the electronic wavefunction ψ,

$$d^M = 2\sqrt{2}(d_p + d_N)\left(\frac{\mu}{Z} + \frac{1}{2mc}\right)M \ , \tag{9.4}$$

TABLE 3. The hyperfine structure constants $A = (A_\parallel + 2A_\perp)/3$ (isotropic) and $A_d = (A_\parallel - A_\perp)/3$ (dipole) and PNC parameters W_i (i.e. W_d, W_A, and W_S) described in Eqs. (7.1) and (8.1) for the ^{171}YbF and ^{137}BaF molecules.

	A (MHz)	A_d (MHz)	W_d ($10^{25}\frac{\text{Hz}}{\text{e cm}}$)	W_A (Hz)	W_S (kHz)
The ^{171}YbF molecule					
Experiment [122]	7617	102			
Semiempirical [121]			−1.5	730	−48
Semiempirical [123] (with $4f$-correction)			−1.26		−43
GRECP/SCF/NOCR [92]	4932	59	−0.91	484	−33
GRECP/RASSCF/NOCR [92]	4854	60	−0.91	486	−33
Restricted DF (Quiney, 1998) [95][1]	5918	35	−0.62	326	−22
Rescaled[1,2] restricted DF			−1.24	652	−44
Restricted DF + core polarization[1]	7865	60	−1.20	620	−42
Unrestricted DF (Parpia, 1998) [96] (unpaired valence electron)			−0.962		
Unrestricted DF [96]			−1.203		−44[1]
GRECP/RASSCF/NOCR/EO [94]	7842	79	−1.206	634	
GRECP/RASSCF/NOCR/EO [94] (with $4f$-correction)	7839	94	−1.206	634	
The ^{137}BaF molecule					
Experiment [124][3]	2326	25			
Semiempirical [25]			−0.41	240	−13
Experiment [125][4]	2418	17			
Semiempirical [25]			−0.35	210	−11
GRECP/SCF/NOCR [93]	1457	11	−0.230	111	−6.1
GRECP/RASSCF/NOCR [93]	1466	11	−0.224	107	−5.9
GRECP/SCF/NOCR/EO [93]	2212	26	−0.375	181	
GRECP/RASSCF/NOCR/EO [93]	2224	24	−0.364	175	

[1] The results of Quiney *et al.* and Parpia have been adjusted by a factor of two to be consistent with the definition of W_i used here, see Eqs. (7.1) and (8.1).

[2] The W_i values are rescaled from the "restricted DF" results employing the calculated and experimental A and A_d values by the factor $\sqrt{(A^{\text{expt}} \cdot A_d^{\text{expt}})/(A^{\text{calc}} \cdot A_d^{\text{calc}})}$, which are in good agreement with the "restricted DF + core polarization" values.

[3] The hyperfine constants are measured in an inert gas matrix [124] and the semiempirical W_i values [25] are based on these data.

[4] The hyperfine constants are measured in a molecular beam [125].

where d_N is the nuclear EDM arising due to P,T-odd forces between the nucleons; μ, m and Z are the magnetic moment, mass and charge of the Tl nucleus; c is the velocity of light;

$$M = \frac{1}{\sqrt{2}}\langle\psi| \sum_i \left(\frac{\vec{\alpha}_i \times \vec{\mathbf{l}}_i}{r_i^3} \right)_z |\psi\rangle \ ; \tag{9.5}$$

$\vec{\mathbf{l}}_\mathbf{i}$ is the orbital momentum of i-th electron; $\vec{\alpha}_i$ are its Dirac matrices. Accounting for H_{eff} leads to a difference in the hyperfine splitting of TlF in parallel and antiparallel electric and magnetic fields. The level shift $h\nu = 4(d^V + d^M)\langle\vec{I}\cdot\vec{\lambda}\rangle/\mathrm{I}$ is measured experimentally (for the latest results see [18]).

The parameters X of Eq. (9.3) and M of Eq. (9.5) are determined by the electronic structure of the molecule. They were calculated in 1997 for the ground 0^+ state of TlF by Parpia [89] and by Laerdahl, Saue, Faegri Jr., and Quiney [88] using the Dirac–Fock method with gaussian basis sets of large sizes (see Table 4). Below we refer to paper [127] with the calculations presented in details and not to the brief communication [88] of the same authors. There was also a preliminary calculation of electronic structure in TlF performed by Wilson *et al.* in [128]. In paper [19] the first calculation of ^{205}TlF that accounts for correlation effects was performed (see also [129] where the limit on the Schiff moment of ^{205}Tl was recalculated).

Results. Calculations were carried out at two internuclear separations, the equilibrium $R_e = 2.0844$ Å as in Ref. [89], and 2.1 Å, for comparison with Ref. [127]. The relativistic coupled cluster (RCC) method [130, 131] with only single (RCC-S) or with single and double (RCC-SD) cluster amplitudes is used (for review of different coupled cluster approaches see also [132, 133] and references). The RCC-S calculations with the spin-dependent GRECP operator take into account effects of the spin-orbit interaction at the level of the one-configurational SCF-type method. The RCC-SD calculations include, in addition, the most important electron correlation effects.

The results obtained with the one-center expansion of the molecular spinors in the Tl core in either $s; p$, $s; p; d$ or $s; p; d; f$ partial waves are collected in Table 4. The first point to notice is the difference between spin-averaged SCF values and RCC-S values; the latter include spin-orbit interaction effects. These effects increase X by 9% and decrease M by 21%. The RCC-S function can be written as a single determinant, and results may therefore be compared with DF values, even though the RCC-S function is not variational. The GRECP/RCC-S values of M indeed differ only by 1–3% from the corresponding DF values [89, 127] (see Table 4).

TABLE 4. Calculated X (9.3) and M (9.5) parameters (in a.u.) for the ^{205}TlF ground state, compared with DF values [89, 127]. GRECP/RCC-S results include spin-orbit interaction, and GRECP/RCC-SD values also account for electron correlation.

	$R_e = 2.0844$ Å				$R = 2.1$ Å		
Expansion	s,p	s,p,d	s,p,d,f	s,p	s,p	s,p,d,f	s,p
		M		X		M	X
SCF(spin-averaged)	19.67	17.56	17.51	8967	19.52	17.43	8897
GRECP/RCC-S	16.12		13.84	9813	16.02	13.82	9726
DF [89]	15.61			7743			
DF [127]						13.64[1]	8747
GRECP/RCC-SD			11.50	7635			

[1] M is calculated in Ref. [127] using two-center molecular spinors, corresponding to infinite L_{max} in Eq. (6.4).

Much larger differences occur for the X parameter. There are also large differences between the two DF calculations for X, which cannot be explained by the small change in internuclear separation. The value of X may be expected to be less stable than M [127]. The conclusion in [19] is that the RCC-S value for X, which is higher than that of [89, 127], is more correct. The electron correlation effects are calculated by the RCC-SD method at the molecular equilibrium internuclear distance R_e. A major correlation contribution is observed, decreasing M by 17% and X by 22%.

The hyperfine structure constants of Tl $6p^1_{1/2}$ and Tl^{2+} $6s^1$, which (like X and M) depend on operators concentrated near the Tl nucleus, were also calculated. The errors in the DF values are 10–15% with respect to experiment and the RCC-SD results are within 1–4% of experiment. The improvement in X and M upon inclusion of correlation is expected to be similar.

10. Calculation of the ^{207}PbO molecule

As is noted in section 2, experiments on the excited $a(1)$ [29] or $B(1)$ [134] states of PbO having nonzero projection of total electronic momentum on the internuclear axis can be, in principle, sensitive enough to detect d_e two or even four orders of magnitude lower than the current limit. Knowl-

edge of the effective electric field, W, is required for extracting d_e from the measurements (see section 4). In papers [97, 98], W for the $a(1)$ ($^3\Sigma^+$ $\sigma_1^2\sigma_2^2\sigma_3^2\pi_1^3\pi_2^1$) and $B(1)$ ($^3\Pi_1$ $\sigma_1^2\sigma_2^2\sigma_3^1\pi_1^4\pi_2^1$) states of the PbO molecule was calculated by the RCC-SD [101, 102] and configuration interaction (CI) [135, 103, 104, 105] methods. To provide an accuracy check for the calculation of the electronic structure near the Pb nucleus the hyperfine constant, $A_\parallel$, was also calculated.

Results. CI calculations [98] were performed at two internuclear distances: $R = 3.8$ a.u. (as in RCC calculations), and $R = 4.0$ a.u. (which is close to the equilibrium distances of the $a(1)$ and $B(1)$ states). In the RCC calculations [97] the internuclear distance $R = 3.8$ a.u. was used because of problems with convergence at larger distances. The calculated values with the one-center expansion of the molecular spinors in the Pb core in either $s; p$ or $s; p; d$ partial waves are collected in Table 5.

Let us consider the $5s, 5p, 5d$ orbitals of lead and $1s$ orbital of oxygen as the outercore and the σ_1, σ_2, σ_3, π_1, π_2 orbitals of PbO (consisting mainly of $6s, 6p$ orbitals of Pb and $2s, 2p$ orbitals of O) as valence. Although in the CI calculations we take into account only the correlation between valence electrons, the accuracy attained in the CI calculation of $A_\parallel$ is much better than in the RCC-SD calculation. The main problem with the RCC calculation was that the Fock-space RCC-SD version used there was not optimal in accounting for nondynamic correlations (see [136] for details of RCC-SD and CI calculations of the Pb atom). Nevertheless, the potential of the RCC approach for electronic structure calculations is very high, especially in the framework of the intermediate Hamiltonian formulation [102, 131].

Next we estimate the contribution from correlations of valence electrons with outercore ones (which also account for correlations between outercore electrons) as the difference between the results of the corresponding 10- and 30-electron GRECP/RCC calculations (see also [136] where this correction is applied to the Pb atom). We designate such correlations in Table 5 as "outercore correlations". When taking into account outercore contributions at the point $R = 4.0$ a.u. we used the results of the RCC calculation at the point $R = 3.8$ a.u. Since these contributions are relatively small and because the correlations with the outercore electrons are more stable than correlations in the valence region when the internuclear distance is changed, this approximation seems reasonable. Finally, we have linearly extrapolated the results of the calculations to the experimental equilibrium distances, $R_e = 4.06$ a.u. for $a(1)$ [137] and $R_e = 3.91$ a.u. for $B(1)$ [119]. The final results are: $A_\parallel = -3826$ MHz, $W = -6.1{\cdot}10^{24}\mathrm{Hz}/(e \cdot \mathrm{cm})$ for $a(1)$ and $A_\parallel = 4887$ MHz, $W = -8.0{\cdot}10^{24}\mathrm{Hz}/(e \cdot \mathrm{cm})$ for $B(1)$. The estimated error for the final W value is 20% for the $B(1)$ state. For $a(1)$ the estimated error

TABLE 5. Calculated parameters $A_\parallel$ (in MHz) and W (in 10^{24}Hz/$(e\cdot$cm), see section 4 and Eq. (8.1)) for the $a(1)$ and $B(1)$ states of ^{207}PbO at the internuclear distances 3.8 and 4.0 a.u. The experimental value of $A_\parallel$ in $a(1)$ is -4113 MHz [138]. The preliminary experimental value of $A_\parallel$ for $B(1)$ is 5000 ± 200 MHz [139].

State	$a(1)$	$\sigma_1^2\sigma_2^2\sigma_3^2\pi_1^3\pi_2^1$	$^3\Sigma_1$	$B(1)$	$\sigma_1^2\sigma_2^2\sigma_3^1\pi_1^4\pi_2^1$	$^3\Pi_1$
Parameters	$A_\parallel$	W		$A_\parallel$	W	
Expansion	s,p,d	s,p	s,p,d	s,p,d	s,p	s,p,d
Internuclear distance $R = 3.8$ a.u.						
10e-RCC-SD [97]	-2635	-2.93	-3.05	3878	-11.10	-10.10
30e-RCC-SD [97]	-2698		-4.10	4081	-9.10	-9.70
outercore:						
(30e-10e)-RCC-SD	*-63*		*-1.05*	*203*		*0.40*
10e-CI [98]	-3446		-4.13	4582		-10.64
FINAL [98]						
(10e-CI + outercore)	**-3509**		**-5.18**	**4785**		**-10.24**
Internuclear distance $R = 4.0$ a.u.						
10e-CI [98]	-3689		-4.81	4762		-7.18
FINAL [98]						
(10e-CI + outercore)[1]	**-3752**		**-5.86**	**4965**		**-6.78**

[1] It is assumed that the outercore contribution at the internuclear distance R=4.0 a.u. is approximately the same as is at R=3.8 a.u.

bounds put the actual W value between 90% and 130% of our final value (for details see [98]).

11. Conclusions

The P,T-parity nonconservation parameters and hyperfine constants have been calculated for the particular heavy-atom molecules which are of primary interest for modern experiments to search for PNC effects. It is found that a high level of accounting for electron correlations is necessary for reliable calculation of these properties with the required accuracy. The applied two-step (GRECP/NOCR) scheme of calculation of the properties described by the operators heavily concentrated in atomic cores and on nuclei has proved to be a very efficient way to take account of these correlations with moderate efforts. The results of the two-step calculations for hyperfine constants differ by less than 10% from the corresponding exper-

imental data. A comparable level of accuracy is expected for the P,T-odd spin-rotational Hamiltonian parameters, which can not be obtained experimentally.

The precision of the discussed calculations is limited by the current possibilities of the correlation methods and codes and not by the GRECP and NOCR approximations, despite the fact that the GRECP/NOCR method allows one to reduce seriously the computational expenses of the correlation treatment as compared to conventional Dirac-Coulomb(-Breit) approaches when *(1)* using molecular spin-orbitals instead of spinors in (G)RECP calculation; *(2)* employing "correlated" GRECP versions [70] to account for correlations with the core electrons explicitly excluded from (G)RECP calculations; *(3)* combining gaussian basis functions at the molecular (G)RECP calculation with numerical functions at the one-center restoration; and *(4)* splitting the correlation treatment of a molecule into two sequential steps, first in valence and then in core regions.

In turn, the accuracy attained in the calculations presented above is sufficient for a reliable interpretation of the measurements in PNC experiments on these molecules.

Acknowledgements

We are very grateful to L.N. Labzowsky for initiating and supporting our activity in studying PNC properties in heavy-atom molecules over many years. We would like to thank also our colleagues I.V. Abarenkov, A.B. Alekseyev, R.J. Buenker, E. Eliav, U. Kaldor, M.G. Kozlov, A.I. Panin, A.V. Tulub, and I.I. Tupitsyn for stimulating discussions and fruitful collaboration on the relevant research.

The present work is supported by U.S. CRDF grant RP2–2339–GA–02 and RFBR grant 03–03–32335. A.P. is also grateful to the Ministry of Education of the Russian Federation (grant PD 02–1.3–236) and to the St.-Petersburg Committee for Science (grant PD 03-1.3-60). N.M. is supported by grants from the Russian Science Support Foundation and from the Governor of Leningrad district. D.D. acknowledges additional support from NSF (grant PHY-0244927) and from the David and Lucile Packard Foundation. Part of the calculations on PbO was performed on the computers of Boston University in the framework of the MARINER project.

References

1. Erler, J. and Ramsey-Musolf, M. J. Low energy tests of the weak interaction **2004** . Eprint http:// arXiv.org/ hep-ph/0404291.
2. Glashow, S. L. *Nuclear Physics* **1961**, *22*, 579.
3. Weinberg, S. *Phys. Rev. Lett.* **1967**, *19*, 1264.

4. Salam, A. In: N. Svartholm (ed.) *Elementary particle theory, relativistic groups, and analyticity*, pp. 367–377 (Almqvist and Wiksells, Stockholm, Sweden, 1968).
5. Weinberg, S. *Phys. Rev. D* **1972**, *5*, 1412.
6. Commins, E. D. *Adv. At. Mol. Opt. Phys.* **1999**, *40*, 1.
7. Christenson, J. H., Cronin, J. W., Fitch, V. L., and Turlay, R. *Phys. Rev. Lett.* **1964**, *13*, 138.
8. Sapirstein, J. In: Schwerdtfeger [41], pp. 468–522.
9. Berger, R. In: Schwerdtfeger [42], pp. 188–288.
10. Ginges, J. S. M. and Flambaum, V. V. *Phys. Rep.* **2004**, *397*, 63.
11. Landau, L. D. *Sov. Phys.–JETP* **1957**, *5*, 336.
12. Regan, B. C., Commins, E. D., Schmidt, C. J., and DeMille, D. *Phys. Rev. Lett.* **2002**, *88*, 071805/1.
13. Romalis, M. V., Griffith, W. C., Jacobs, J. P., and Fortson, E. N. *Phys. Rev. Lett.* **2001**, *86*, 2505.
14. Dmitriev, V. F. and Sen'kov, R. A. *Phys. Rev. Lett.* **2003**, *91*, 212303/1.
15. Sandars, P. G. H. *Phys. Rev. Lett.* **1967**, *19*, 1396.
16. Sandars, P. G. H. *Phys. Lett.* **1965**, *14*, 194.
17. Hinds, E. A., Loving, C. E., and Sandars, P. G. H. *Phys. Lett. B* **1976**, *62*, 97.
18. Cho, D., Sangster, K., and Hinds, E. A. *Phys. Rev. A* **1991**, *44*, 2783.
19. Petrov, A. N., Mosyagin, N. S., Isaev, T. A., Titov, A. V., Ezhov, V. F., Eliav, E., and Kaldor, U. *Phys. Rev. Lett.* **2002**, *88*, 073001.
20. Labzowsky, L. N. *Sov. Phys.–JETP* **1978**, *48*, 434.
21. Gorshkow, V. G., Labzovsky, L. N., and Moskalyov, A. N. *Sov. Phys.–JETP* **1979**, *49*, 209.
22. Sushkov, O. P. and Flambaum, V. V. *Sov. Phys.–JETP* **1978**, *48*, 608.
23. Sushkov, O. P., Flambaum, V. V., and Khriplovich, I. B. *Sov. Phys.–JETP* **1984**, *87*, 1521.
24. Flambaum, V. V. and Khriplovich, I. B. *Phys. Lett. A* **1985**, *110*, 121.
25. Kozlov, M. G. *Sov. Phys.–JETP* **1985**, *62*, 1114.
26. Titov, A. V. *PhD Thesis*, (St.-Petersburg (former Leningrad) State University, Russia, 1985).
27. Kozlov, M. G., Fomichev, V. I., Dmitriev, Y. Y., Labzovsky, L. N., and Titov, A. V. *J. Phys. B* **1987**, *20*, 4939.
28. Hudson, J. J., Sauer, B. E., Tarbutt, M. R., and Hinds, E. A. *Phys. Rev. Lett.* **2002**, *89*, 023003.
29. DeMille, D., Bay, F., Bickman, S., Kawall, D., Krause, Jr., D., Maxwell, S. E., and Hunter, L. R. *Phys. Rev. A* **2000**, *61*, 052507.
30. Okun', L. B. *Leptons and quarks* (North Holland, Amsterdam, 1982).
31. Kobayashi, M. and Maskawa, T. *Progr. Theor. Phys.* **1973**, *49*, 652.
32. Kazakov, D. I. Beyond the standard model (In search of supersymmetry) **2000**. ArXiv: hep-ph/0012288.
33. Mohapatra, R. N. *Unification and Supersymmetry. The Frontiers of Quark-Lepton Physics* (Springer, New-York, U.S.A., 2003). 421 pp.
34. Barr, S. M. *Phys. Rev. Lett.* **1992**, *68*, 1822.
35. Barr, S. M. *Int. J. Mod. Phys. A* **1993**, *8*, 209.
36. Ginzburg, I. F. and Krawczyk, M. Symmetries of two Higgs doublet model and CP violation **2004**. ArXiv: hep-ph/0408011.
37. Pati, J. C. and Salam, A. *Phys. Rev. D* **1974**, *10*, 275.
38. Liu, J. T. and Ng, D. Lepton flavor changing processes and CP violation in the 331 model **1994**. ArXiv: hep-ph/9401228.
39. Masina, I. and Savoy, C. A. Changed lepton flavour and CP violation: Theoretical impact of present and future experiments **2004**. ArXiv: hep-ph/0410382.
40. Khriplovich, I. B. and Lamoraux, S. K. *CP Violation without Strangeness. The Electric Dipole Moments of Particles, Atoms, and Molecules* (Springer-Verlag, Berlin, 1997).

41. Schwerdtfeger, P. (ed.). *Relativistic Electronic Structure Theory. Part I. Fundamentals*, vol. 11 of *Theoretical and Computational Chemistry* (Elsevier, Amsterdam, 2002). xx + 926 pp.
42. Schwerdtfeger, P. (ed.). *Relativistic Electronic Structure Theory. Part 2. Applications*, vol. 14 of *Theoretical and Computational Chemistry* (Elsevier, Amsterdam, 2004). xv + 787 pp.
43. Hirao, K. and Ishikawa, Y. (eds.). *Recent Advances in Relativistic Molecular Theory* (World Scientific, Singapore, 2004). 328 pp.
44. Mosyagin, N. S. *et al*. GRECPs accounting for Breit effects .... This issue.
45. Wood, J. H. and Boring, A. M. *Phys. Rev. B* **1978**, *18*, 2701.
46. Barthelat, J. C., Pelissier, M., and Durand, P. *Phys. Rev. A* **1980**, *21*, 1773.
47. van Lenthe, E., Baerends, E. J., and Snijders, J. G. *J. Chem. Phys.* **1993**, *99*, 4597.
48. Wolf, A., Reiher, M., and Hess, B. A. In: Schwerdtfeger [41], pp. 622–663.
49. Kutzelnigg, W. *Z. Phys. D* **1990**, *15*, 27.
50. Dyall, K. G. *J. Comput. Chem.* **2002**, *23*, 786.
51. Visscher, L. *J. Comput. Chem.* **2002**, *23*, 759.
52. Grant, I. P. and Quiney, H. (Les Houches, France, 2004). Conference "Quantum Systems in Chemistry and Physics: QSCP-IX", oral and poster reports.
53. Saue, T., Jensen, H. J. A., Visscher, L., *et al*. "DIRAC04" **2004**. A relativistic *ab initio* electronic structure program.
54. Quiney, H. M., Skaane, H., and Grant, I. P. *Adv. Quantum Chem.* **1999**, *32*, 1.
55. Grant, I. P., Quiney, H. M., and Skaane, H. "BERTHA" **1998**. An ab initio relativistic molecular electronic structure program [54].
56. Lee, Y. S., Ermler, W. C., and Pitzer, K. S. *J. Chem. Phys.* **1977**, *67*, 5861.
57. Ermler, W. C., Ross, R. B., and Christiansen, P. A. *Adv. Quantum Chem.* **1988**, *19*, 139.
58. Schwerdtfeger, P. In: U. Kaldor and S. Wilson (eds.) *Theoretical chemistry and physics of heavy and superheavy elements*, pp. 399–438 (Kluwer academic publishers, Dordrecht, The Netherlands, 2003).
59. Lee, Y. S. In: Schwerdtfeger [42], pp. 352–416.
60. Teichteil, C., Maron, L., and Vallet, V. In: Schwerdtfeger [42], pp. 476–551.
61. Blöchl, P. E. *Phys. Rev. B* **1990**, *41*, 5414.
62. Vanderbilt, D. *Phys. Rev. B* **1990**, *41*, 7892.
63. Theurich, G. and Hill, N. A. *Phys. Rev. B* **2001**, *64*, 073106, 1.
64. Bonifacic, V. and Huzinaga, S. *J. Chem. Phys.* **1974**, *60*, 2779.
65. Katsuki, S. and Huzinaga, S. *Chem. Phys. Lett.* **1988**, *152*, 203.
66. Seijo, L. and Barandiarán, Z. In: Schwerdtfeger [42], pp. 417–475.
67. Petrov, A. N., Mosyagin, N. S., Titov, A. V., and Tupitsyn, I. I. *J. Phys. B* **2004**, *37*, 4621.
68. Dyall, K. G. *J. Chem. Phys.* **1994**, *100*, 2118.
69. Titov, A. V. and Mosyagin, N. S. *Int. J. Quantum Chem.* **1999**, *71*, 359.
70. Mosyagin, N. S. and Titov, A. V. *J. Chem. Phys.* **2005**, *122*, 234106.
71. Durand, P. and Barthelat, J.-C. *Theor. Chim. Acta* **1975**, *38*, 283.
72. Christiansen, P. A., Lee, Y. S., and Pitzer, K. S. *J. Chem. Phys.* **1979**, *71*, 4445.
73. Hamann, D. R., Schlüter, M., and Chiang, C. *Phys. Rev. Lett.* **1979**, *43*, 1494.
74. Titov, A. V. and Mosyagin, N. S. *Russ. J. Phys. Chem.* **2000**, *74,* Suppl. 2, S376. [arXiv: physics/0008160].
75. Titov, A. V. *Doctorate Thesis*, (Petersburg Nuclear Physics Institute, RAS, Russia, 2002).
76. Phillips, J. C. and Kleinman, L. *Phys. Rev.* **1959**, *116*, 287.
77. Pacios, L. F. and Christiansen, P. A. *J. Chem. Phys.* **1985**, *82*, 2664.
78. Blöchl, P. E. *Phys. Rev. B* **1994**, *50*, 17953.
79. Titov, A. V. In: *Theses of reports of the 4th European Conf. on Atomic and Mol. Physics*, p. 299 (Riga, Latvia, 1992).

80. Titov, A. V. *Int. J. Quantum Chem.* **1996**, *57*, 453.
81. Desclaux, J. P. and Pyykkö, P. *Chem. Phys. Lett.* **1974**, *29*, 534.
82. Desclaux, J. P. and Pyykkö, P. *Chem. Phys. Lett.* **1976**, *39*, 300.
83. Desclaux, J.-P. In: Schwerdtfeger [41], pp. 1–22.
84. Pitzer, K. S. *Acc. Chem. Res.* **1979**, *12*, 271.
85. Pyykkö, P. and Desclaux, J.-P. *Acc. Chem. Res.* **1979**, *12*, 276.
86. Hinds, E. A. and Sandars, P. G. H. *Phys. Rev. A* **1980**, *21*, 471.
87. Coveney, P. V. and Sandars, P. G. H. *J. Phys. B* **1983**, *16*, 3727.
88. Laerdahl, J. K., Saue, T., Faegri, Jr, K., and Quiney, H. M. *Phys. Rev. Lett.* **1997**, *79*, 1642.
89. Parpia, F. A. *J. Phys. B* **1997**, *30*, 3983.
90. Dmitriev, Y. Y., Khait, Y. G., Kozlov, M. G., Labzovsky, L. N., Mitrushenkov, A. O., Shtoff, A. V., and Titov, A. V. *Phys. Lett. A* **1992**, *167*, 280.
91. Titov, A. V. *Int. J. Quantum Chem.* **1992**, *42*, 1711.
92. Titov, A. V., Mosyagin, N. S., and Ezhov, V. F. *Phys. Rev. Lett.* **1996**, *77*, 5346.
93. Kozlov, M. G., Titov, A. V., Mosyagin, N. S., and Souchko, P. V. *Phys. Rev. A* **1997**, *56*, R3326.
94. Mosyagin, N. S., Kozlov, M. G., and Titov, A. V. *J. Phys. B* **1998**, *31*, L763.
95. Quiney, H. M., Skaane, H., and Grant, I. P. *J. Phys. B* **1998**, *31*, L85.
96. Parpia, F. *J. Phys. B* **1998**, *31*, 1409.
97. Isaev, T. A., Petrov, A. N., Mosyagin, N. S., Titov, A. V., Eliav, E., and Kaldor, U. *Phys. Rev. A* **2004**, *69*, 030501(R).
98. Petrov, A. N., Titov, A. V., Isaev, T. A., Mosyagin, N. S., and DeMille, D. P. *Phys. Rev. A* **2005**, *72*, 022505.
99. Isaev, T. A., Mosyagin, N. S., Petrov, A. N., and Titov, A. V. *Phys. Rev. Lett.* **2005**. In press; arXiv: physics/0412177.
100. Dzuba, V. A., Flambaum, V. V., and Kozlov, M. G. *JETP Lett.* **1996**, *63*, 882.
101. Kaldor, U. In: R. J. Bartlett (ed.) *Recent Advances in Coupled-Cluster Methods*, pp. 125–153 (World Scientific, Singapore, 1997).
102. Landau, A., Eliav, E., and Kaldor, U. *Adv. Quantum Chem.* **2001**, *39*, 171.
103. Buenker, R. J. and Krebs, S. In: K. Hirao (ed.) *Recent Advances in Multireference Methods*, pp. 1–29 (World Scientific, Singapore, 1999).
104. Alekseyev, A. B., Liebermann, H.-P., and Buenker, R. J. In: Hirao and Ishikawa [43], pp. 65–105.
105. Titov, A. V., Mosyagin, N. S., Alekseyev, A. B., and Buenker, R. J. *Int. J. Quantum Chem.* **2001**, *81*, 409.
106. Dolg, M. In: J. Grotendorst (ed.) *Modern Methods and Algorithms of Quantum Chemistry*, vol. 1 of *NIC Series*, pp. 479–508 (Jülich, 2000). [http://www.fz-juelich.de].
107. Titov, A. V. and Mosyagin, N. S. Comments on "Effective Core Potentials" by M.Dolg [106]. ArXiv.org/ physics/0008239 (2000).
108. Titov, A. V. and Mosyagin, N. S. *Structural Chem.* **1995**, *6*, 317.
109. Tupitsyn, I. I. "HFDB" **2003**. Program for atomic finite-difference four-component Dirac-Hartree-Fock-Breit calculations written on the base of the HFD code [110].
110. Bratzev, V. F., Deyneka, G. B., and Tupitsyn, I. I. *Bull. Acad. Sci. USSR, Phys. Ser.* **1977**, *41*, 173.
111. Tupitsyn, I. I. and Petrov, A. N. In: *5-th Session of the V.A. Fock School on Quantum and Computational Chemistry*, p. 62 (Novgorod the Great, 2002).
112. Tupitsyn, I. I. and Mosyagin, N. S. "GRECP/HFJ" **1995**. Program for atomic finite-difference two-component Hartree-Fock calculations with the generalized RECP in the jj-coupling scheme.
113. Tupitsyn, I. I., Mosyagin, N. S., and Titov, A. V. *J. Chem. Phys.* **1995**, *103*, 6548.
114. Lindgren, I. *Rep. Prog. Phys.* **1984**, *47*, 345.
115. Kunik, D. and Kaldor, U. *J. Chem. Phys.* **1971**, *55*, 4127.
116. Monkhorst, H. J. *Int. J. Quantum Chem.: Quantum Chem. Symp.* **1977**, *11*, 421.

117. Kozlov, M. and Labzowsky, L. *J. Phys. B* **1995**, *28*, 1931.
118. Knight, Jr., L. B., Fisher, T. A., and Wise, M. B. *J. Chem. Phys.* **1981**, *74*, 6009.
119. Huber, K. P. and Herzberg, G. *Constants of Diatomic Molecules* (Van Nostrand-Reinhold, New York, 1979).
120. Mosyagin, N. S. *et al*. GRECP/NOCR calculations of hyperfine structure and parity violation effects in YbF, HgF and HgH **2002**. Unpublished.
121. Kozlov, M. G. and Ezhov, V. F. *Phys. Rev. A* **1994**, *49*, 4502.
122. Knight, Jr., L. B. and Weltner, Jr., W. *J. Chem. Phys.* **1970**, *53*, L4111.
123. Kozlov, M. G. *J. Phys. B* **1997**, *30*, L607.
124. Knight, L. B., Easley, W. C., and Weltner, W. *J. Chem. Phys.* **1971**, *54*, 322.
125. Ryzlewicz, C., Schütze-Pahlmann, H. U., Hoeft, J., and Törring, T. *Chem. Phys.* **1982**, *71*, 389.
126. Schiff, L. I. *Phys. Rev.* **1963**, *132*, 2194.
127. Quiney, H. M., Laerdahl, J. K., Faegri, Jr, K., and Saue, T. *Phys. Rev. A* **1998**, *57*, 920.
128. Wilson, S., Moncrieff, D., and Kobus, J. TlF ($^1\Sigma^+$): Some preliminary electronic structure calculations **1994**. RAL-94-082 Report.
129. Dzuba, V. A., Flambaum, V. V., Ginges, J. S. M., and Kozlov, M. G. *Phys. Rev. A* **2002**, *66*, 012111.
130. Kaldor, U. and Eliav, E. *Adv. Quantum Chem.* **1999**, *31*, 313.
131. Kaldor, U., Eliav, E., and Landau, A. In: Hirao and Ishikawa [43], pp. 283–327.
132. Paldus, J. and Li, X. *Adv. Chem. Phys.* **1999**, *110*, 1.
133. Paldus, J. In: S. Wilson (ed.) *Handbook of Molecular Physics and Quantum Chemistry*, vol. 2, pp. 272–313 (John Wiley & Sons, Ltd, Chichester, 2003).
134. Egorov, D., Weinstein, J. D., Patterson, D., Friedrich, B., and Doyle, J. M. *Phys. Rev. A* **2001**, *63*, 030501(R).
135. Buenker, R. J. and Peyerimhoff, S. D. *Theor. Chim. Acta* **1974**, *35*, 33.
136. Isaev, T. A., Mosyagin, N. S., Kozlov, M. G., Titov, A. V., Eliav, E., and Kaldor, U. *J. Phys. B* **2000**, *33*, 5139.
137. Martin, F., Bacis, R., Verges, J., Bachar, J., and Rosenwaks, S. *Spectrochim. Acta* **1988**, *44A*, 889.
138. Hunter, L. R., Maxwell, S. E., Ulmer, K. A., Charney, N. D., Peck, S. K., Krause, D., Ter-Avetisyan, S., and DeMille, D. *Phys. Rev. A* **2002**, *65*, 030501(R).
139. Kawall, D., Gurevich, Y., and DeMille, D. To be published.

QED CALCULATION OF HEAVY MULTICHARGED IONS WITH ACCOUNT FOR CORRELATION, RADIATIVE AND NUCLEAR EFFECTS

A.-V. GLUSHKOV, S.-V. AMBROSOV, A.-V. LOBODA,
E.-P.GURNITSKAYA AND O.-Y. KHETSELIUS

Latom.-Nucl.-Laser Spectroscopy Centre and
Institute for Applied Mathematics, Odessa OSE University,
P.O. Box 24A, Odessa-9, 65009, Ukraine
glushkov@paco.net

Abstract. A highly accurate, ab-initio approach to the relativistic calculation of spectra of multi-electron, super-heavy ions, accounting for correlation, nuclear, radiative, and relativistic effects is developed. The method is based on quantum electrodynamics (QED) perturbation theory (PT). Zeroth approximation is generated by an effective ab-initio model functional constructed on the basis of the comprehensive gauge-invariant procedure. The wave-function zeroth-order basis set is found from the Dirac equation with a potential including the core ab-initio potential and the electric and polarization potentials of the nucleus (a Gaussian form is used for the charge distribution in the nucleus). The magnetic interelectronic interaction is included in the lowest $(\alpha)^2$ term, and the Lamb shift polarization effect, in the Uehling-Serber approximation (self-energy part of the Lamb shift), is accounted for within the Ivanov-Ivanova non-perturbative procedure. Results of the calculations are presented for the energy levels, dielectronic satellite wavelengths, hyperfine structure constants, and QED corrections for $1s^2nlj$- states of Li-like ions.

1. Introduction

During the last few years the study of spectra of heavy and superheavy elements (atoms and ions) has been of great interest for further development in atomic and nuclear theories [1-12]. Theoretical methods used to calculate the spectroscopic characteristics of heavy and superheavy ions may be divided into

J.-P. Julien et al. (eds.),
Recent Advances in the Theory of Chemical and Physical Systems, 285–299.

three main groups. a) The multi-configuration Hartree-Fock method, in which relativistic effects are taken into account in the Pauli approximation, gives a rather rough approximation, which makes it possible to get only a qualitative idea of the spectra of heavy ions. b) The multi-configuration Dirac-Fock (MCDF) approximation (e.g., Desclaux' program) has been, many years, the most reliable method for calculations on multi-electronic systems with large nuclear charge; in these calculations one- and two-particle relativistic effects are taken into account rather precisely. Desclaux' program takes proper account of the finiteness of the nucleus; however, a detailed investigation of the role of the nucleus size is lacking. In the region of small nuclear charge Z the calculation error in the MCDF approximation is related mainly to the incomplete inclusion of correlation and exchange effects, which are only weakly dependent on Z. c) In the study of lower states for ions with $Z \leq 40$, an expansion in a double series of the parameters 1/Z and αZ (α being the fine structure constant) turns out to be quite useful. It allows an evaluation of the relative contributions of the various expansion terms, non-relativistic, relativistic, QED, as functions of Z. Nevertheless, serious problems in the calculation of spectra of heavy elements have led to developing new, highly accurate methods accounting for QED effects, particularly the Lamb shift (LS), the self-energy part (SE), vacuum polarization (VP), and corrections for nuclear finite size [1-10].

In the present paper, a new ab initio approach to the calculation of spectra of multi-electron, super-heavy ions, accounting for relativistic, correlation, nuclear, and radiative effects, is developed. This method is based on quantum electrodynamics (QED) perturbation theory (PT). Zeroth approximation is generated by an effective ab initio model functional constructed on the basis of the comprehensive gauge-invariant procedure [12, 13]. The wave-function zeroth-order basis set is found from the Dirac equation with a potential that includes the core ab-initio potential and the electric and polarization potentials of the nucleus (a Gaussian form is used for the charge distribution in the nucleus) [11, 12]. The correlation corrections of higher orders are taken into account using the Green functions method with the Feynman diagrams technique. There are taken into account all correlation corrections of the second order and dominant classes of higher-order diagrams (electrons screening, particle-hole interaction, mass-operator iterations). The magnetic interelectronic interaction is included in the lowest (α^2) term, and the Lamb shift polarization effect, in the Uehling-Serber approximation (self-energy part of the Lamb shift), is accounted for within the Ivanov-Ivanova non-perturbative procedure [11]. We have performed calculations of the spectra of *nlj* (n = 2, 3, 4) states of *Li*-like ions with nuclear charge Z=20-100.

We have made a detailed analysis of the relation between the various corrections and shown the important role of radiative corrections for ions with high Z. The wavelengths of the *Li*-like bielectronic satellite lines to the $1s^{21}S_0$-$1s3p^1P_1$ line of radiation in K plasma are also calculated. The values calculated

for the hyperfine (electric quadruple and magnetic dipole) constants for a few Li-like ions are presented.

2. QED perturbation theory for the calculation of heavy and superheavy ions

Let us describe the key moments of the new, ab initio approach to relativistic calculation of the spectra for multi-electron superheavy ions with an account of relativistic, correlation, nuclear, radiative effects.

2.1. Definition of the basis for the relativistic orbitals

One-particle wave-functions in a central field are obtained as solutions of the relativistic Dirac equation, which can be written in the two-component form:

$$\frac{\partial F}{\partial r} + (1+\chi)\frac{F}{r} - (\varepsilon + m - v)G = 0\,,$$
$$\frac{\partial G}{\partial r} + (1-\chi)\frac{G}{r} + (\varepsilon - m - v)F = 0\,. \qquad (1)$$

Here we put the fine structure constant α=1. The moment number writes as:

$$\chi = \begin{cases} -(1+1), & j > 1 \\ 1, & j < 1 \end{cases} \qquad (2)$$

At large χ the radial functions F and G vary rapidly at the origin of coordinates:

$$F(r), G(r) \approx r^{\gamma - 1}$$
$$\gamma = \sqrt{\chi^2 - \alpha^2 z^2} \qquad (3)$$

This involves difficulties in the numerical integration of the equations in the region $r \to 0$. To prevent the integration step from becoming too small it is convenient to turn to some new functions isolating the main power dependence: $f = Fr^{1-|\chi|}$, $g = Gr^{1-|\chi|}$. The Dirac equation for the *F* and *G* components is transformed into:

$$f' = -(\chi + |\chi|) f/r - \alpha Z V g - (\alpha Z E_{n\chi} + 2/\alpha Z) g$$
$$g' == (\chi - |\chi|) g/r - \alpha Z V f + \alpha Z E_{n\chi} f \quad (4)$$

Here the Coulomb units (C.u.) are used: 1 C.u. of length = 1 a.u. Z; 1 C.u. of energy = 1 a.u. Z^2. In Coulomb units, atomic characteristics vary weakly with Z. $E_{n\chi}$ is the one-electron energy without the rest energy.

The system of equations (4) has two fundamental solutions. We are interested in the solution regular at $r \to 0$. Boundary values of the correct solution are found from the first terms of the expansion into a Taylor series:

$$g = (V(0) - E_{n\chi}) r\alpha\, Z/(2\chi + 1); \quad f = 1 \text{ at } \chi < 0$$
$$f = (V(0) - E_{n\chi} - 2/\alpha^2 Z^2) \alpha Z; \quad g = 1 \text{ at } \chi > 0 \quad (5)$$

The condition $f, g \to 0$ at $r \to \infty$ determines the quantified energies of the state $E_{n\chi}$. At a correctly determined energy $E_{n\chi}$ the asymptotic f and g at $r \to \infty$ are:

$$f, g \sim \exp(-r/n^*) \quad (6)$$

where $n^* = \sqrt{1/2|E_{n\chi}|}$ is the effective main quantum number. Equations (4) were solved using the Runge-Kutta method. The initial integration point (where R is the nucleus radius), $r_0 = R/10^6$, and the end of the integration interval is determined as $r_k \approx 30 n^*$.

2.2. The nuclear potential

Earlier we calculated some characteristics of hydrogen-like ions with the nucleus in the form of a uniformly charged sphere; analogous calculations using an improved model were also made: here a smooth Gaussian function is used for the charge distribution in the nucleus. Using a smooth distribution function (ins-tead of a discontinuous one) permits a flexible simulation of the real distribution of the charge in the nucleus and simplifies the calculation process. As in ref. [12] we represent the charge distribution in the nucleus by the normalized Gaussian function:

$$\rho(r|R) = (4\gamma^{3/2}/\sqrt{\pi}) \exp(-\gamma r^2) \quad (7)$$

$$\int_0^\infty dr r^2 \rho(r|R) = 1; \quad \int_0^\infty dr r^3 \rho(r|R) = R$$

where $\gamma = 4/\pi R^2$, R being the effective nuclear radius. The following simple dependence of R on Z is assumed:

$$R = 1.60 \times 10^{-13} z^{1/3} \ (cm) \tag{8}$$

Such a definition of R is rather conventional: we assume it as some zeroth-order approximation. Further, the derivatives of various characteristics with respect to R are calculated. They describe the interaction of the nucleus with the outer elec-tron and this permits the recalculation of results when R varies within reasonable limits. The Coulomb potential for the spherically symmetric density $\rho(r|R)$ is:

$$V_{nucl}(r|R) = -((1/r)\int_0^r dr' r'^2 \rho(r'|R) + \int_r^\infty dr' r' \rho(r'|R) \tag{9}$$

It is determined by the following system of differential equations:

$$V'nucl(r,R) = (1/r^2)\int_0^r dr' r'^2 \rho(r',R) \equiv (1/r^2) y(r,R)$$

$$y'(r,R) = r^2 \rho(r,R) \tag{10}$$

$$\rho'(r,R) = -8\gamma^{5/2} r/\sqrt{\pi} \exp(-\gamma r^2) = -2\gamma r \rho(r,R) = -\frac{8r}{\pi r^2} \rho(r,R)$$

with the boundary conditions:

$$V_{nucl}(0,R) = -4/(\pi r)$$

$$y(0,R) = 0,$$

$$\rho(0,R) = 4\gamma^{3/2}/\sqrt{\pi} = 32/R^3 \tag{11}$$

2.3. General scheme of calculation

Consider the Dirac-Fock equations for a three-electron system $1s^2nlj$. Formally they fall into one-electron Dirac equations for the orbitals $1s$ and nlj with the potential:

$$V(r) = 2V(r|1s) + V(r|nlj) + V_{ex}(r) + V(r|R) \tag{12}$$

$V(r|R)$ includes the electrical and the polarization potentials of the nucleus; the components of the Hartree potential:

$$V(r|i) = \frac{1}{Z}\int d\vec{r}\,'\rho(r|i)/|\vec{r} - \vec{r}\,'| \tag{13}$$

Here $\rho(r|i)$ is the distribution of the electron density in the state $|\ i\ >$, V_{ex} is the exchange interelectron interaction. The main exchange effect will be taken into account if, in the equation for the $1s$ orbital, we assume

$$V(r) = V(r|1s) + V(r|nlj) \tag{14}$$

and, in the equation for the nlj orbital,

$$V(r) = 2V(r|1s) \tag{15}$$

The rest of the exchange and correlation effects will be taken into account to the first two orders of PT by the total interelectron interaction [13-19]. The electron density is determined by an iteration algorithm [11, 14]. In the first iteration we assume

$$\rho^{(1)}(r|nlj) = 0$$

$$\rho^{(1)}(r|1s) = N\exp(-2Br)r^{2A-2};\quad A = \sqrt{1-(\alpha Z)^2} \tag{16}$$

$$B = \sqrt{2|E_{1s}|};\quad N = 1\Big/\int_0^\infty dr\exp(-2Br)r^{2A}$$

Respectively:

$$V^{(1)}(r|nlj) = 0 \tag{17}$$

$$V^{(1)}(r|1s)=\frac{N}{Z}\left(\frac{1}{r}\int_0^r dr'\exp(-Br')r'^{2A}+\int_r^\infty dr'\exp(-2Br')r'^{2A-1}\right)$$

The expression (16) of $\rho(r|1s)$ coincides with the precise one for a one-electron relativistic atom with a point nucleus. The finiteness of the nucleus and the presence of the second *1s* electron are included effectively into the energy E_{1s}. Actually, for the determination of the properties of the outer *nlj* electron, one iteration is sufficient. Refinements resulting from the second iteration do not exceed the correlation corrections of higher orders omitted in the present calculation. The relativistic potential of the core: $2V^{(1)}(r|1s)=V_{scr}$, has correct asymptotic behaviour at zero and at infinity; at $\alpha\to 0$ it changes to an appropriate potential constructed on the basis of the non-relativistic hydrogen-like functions. Details of the calculation are given in the refs. [11-19].

2.4. Vacuum polarization

This effect is usually taken into account to first order in PT by means of the Uehling potential. This potential is usually written as follows [1, 11]:

$$U(r)=-\frac{2\alpha}{3\pi r}\int_1^\infty dt\exp(-2rt/\alpha Z)\left(1+1/2t^2\right)\frac{\sqrt{t^2-1}}{t^2}\equiv-\frac{2\alpha}{3\pi r}C(g), \qquad (18)$$

where $g=\frac{r}{\alpha Z}$. In the present section we shall show that the Uehling potential determined as a quadrature (18) may be approximated with high precision by a simple analytical function. For its derivation, the same as in [11, 14], we determine the asymptote of the function *C(g)* in two limiting cases:

$$\begin{aligned} C(g)&\to\widetilde{C}_1(g)=\ln(g/2)+1.410548-1.037845g \\ &\quad g\to 0 \\ C(g)&\to\widetilde{C}_2(g)=-1.8800\exp(-g)/g^{3/2} \\ &\quad g\to\infty \end{aligned} \qquad (19)$$

In Eq. (19) a matching of the two limiting expressions for C(g) was made as follows [11]:

$$\widetilde{C}(g) = \widetilde{C}_1(g)\widetilde{C}_2(g)/\left(\widetilde{C}_1(g) + \widetilde{C}_2(g)\right) \quad (20)$$

Here, for more precise approximation of the Uehling potential, we make a complete numerical calculation of the function *C(g)* in Eq. (18). This procedure is described in detail in refs [11, 17]. Using the precise values obtained for *C(g)* we perform the matching of $\widetilde{C}_1(g)$ with the function $\widetilde{C}_2(g)$, which is corrected by multiplying it with a polynomial *f(g)*. The coefficients of this polynomial are determined in such a way that the result of the matching gives the best coincidence with the precise function *C (g)*. Thus, the corrected matching is:

$$\widetilde{\widetilde{C}}(g) = \widetilde{C}_1(g)\widetilde{\widetilde{C}}_2(g)/\left(\widetilde{C}_1(g) + \widetilde{\widetilde{C}}_2(g)\right) \quad (21)$$

$$\widetilde{\widetilde{C}}_2(g) = \widetilde{C}_2(g) f(g) \quad (22)$$

$$f(g) = \left((1.1022/g - 1.3362)/g + 0.8028\right) \quad (23)$$

The use of the new approximation for the Uehling potential permits to decrease the computation errors for this term down to 0.5– 1%. Besides, using such a simple analytical expression for approximating the Uehling potential allows its easy inclusion into the general system of differential equations. This system includes also the Dirac equation and the equations for the matrix elements.

2.5. Calculation of the self-energy part of the Lamb shift

Our method of calculation is based on an idea by Ivanov-Ivanova [11]. In an atomic system, the radiative shift and the relativistic part of the energy are, in principle, determined by one and the same physical field. It may be assumed that there exists some universal function that connects the self-energy correction and the relativistic energy. The self-energy correction for the states of a hydrogen-like ion was presented by Mohr [1] as:

$$E_{SE}\left(H|Z,nlj\right) = 0.027148\frac{Z^4}{n^3}F\left(H|Z,nlj\right) \quad (24)$$

The values of *F* are given at $Z = 10-110$, $nlj = 1s, 2s, 2p_{1/2}, 2p_{3/2}$. These results are here modified for the $1s^2$ *nlj* states of Li-like ions. It is assumed that for any ion with an *nlj* electron over the core of closed shells the searched value may be presented in the form:

$$E_{SE}(Z,nlj)=0.027148\frac{\xi^4}{n^3}f(\xi,nlj)\left(cm^{-1}\right) \qquad (25)$$

The parameter $\xi=(E_R)^{1/4}$, E_R is the relativistic part of the binding energy of the outer electron; and the universal function $f(\xi,nlj)$ does not depend on the composition of the closed shells or on the actual potential of the nucleus. The procedure of generalization for Li-like ions with finite nucleus consists in the following steps [11]:

1) Calculation of the values E_R and ξ for the states *nlj* of *H*-like ions with a point nucleus (in accordance with the Zommerfeld formula);

2) Construction of an approximating function $f(\xi,nlj)$ by the determined reference *Z* and the appropriate $F(H|Z,nlj)$ [1, 11];

3) Calculation of E_R and ξ for the states *nlj* of *Li*-like ions with a finite nucleus;

4) Calculation of E_{SE} for the searched states by Eq. (25). The approximating function is determined as:

$$f(\xi,nlj)=X_0+X_1/\xi+X_2/\xi^2+X_3/\xi^3 \qquad (26)$$

The parameters X_0,X_1,X_2,X_3 are determined by four especially chosen reference points. The energies of the states of Li-like ions were calculated twice: with the real value of the fine structure constant $\alpha=1/137$ and with the smaller value $\widetilde{\alpha}=\alpha/1000$. The results of these latter calculations were considered as non-relativistic. This helped the isolation of E_R and ξ. A detailed evaluation of their accuracy may be made only after a complete calculation of $E_{SE}^{n}(Li\ Z,nlj)$. It may be stated that the above extrapolation method is more justified than using expansions on the parameter αZ.

2.6. Calculation of the hyperfine structure parameters

The energies of the electric quadrupole (W_q) and magnetic dipole (W_μ) interactions, which determine the hyperfine structure, are calculated as follows [11, 20]:

$$W_q=[\Delta+C(C+1)]B,\quad W_\mu=0{,}5\ AC,$$
$$\Delta=-(4/3)(4\chi-1)(I+1)/[i(I-1)(2I-1)],$$
$$C=F(F+1)-J(J+1)-I(I+1). \qquad (27)$$

Here I is a nuclear spin, F is the full momentum of the system, and J is the full electron momentum. The hyperfine splitting constants are expressed through the standard radial integrals:

$$A=\{[(4,32587)10^{-4}Z^2\chi g_I]/(4\chi^2-1)\}(RA)_{-2},$$
$$B=\{7.2878\ 10^{-7}\ Z^3Q/[(4\chi^2-1)I(I-1)\}\ (RA)_{-3}, \tag{28}$$

Here g_I is the Landé factor and Q, the quadruple momentum of the nucleus, and the radial integrals are defined as follows:

$$(RA)_{-2,}=\int_0^\infty drr^2F(r)G(r)U(1/r^2,R),$$
$$(RA)_{-3,}=\int_0^\infty drr^2[F^2(r)+G^2(r)U(1/r^2,R), \tag{29}$$

and calculated in Coulomb units ($3.57\ 10^{20}\ Z^2\ m^{-2}$; $6.174\ 10^{30}\ Z^3\ m^{-3}$ for variables of the corresponding dimension). The radial parts F and G of the components of the Dirac function for the electron, which moves in the potential $V(r,R)+U(r,R)$, are determined by the solution of the Dirac equation [see above, system (1)]. For the calculation of the hyperfine interaction potentials $U(1/r^n,R)$ we solve the fol-lowing differential equations:

$$U(1/r^n,R)=-ny(r,R)/r^{n+1}.$$

These are analogous to Eqs (9) and (10). The functions $dU(1/r^n,R)/dR$ are calculated using an analogous procedure. The details of the calculations are presented in refs [11, 14, 17, 18].

3. Results and Conclusion

Now we shall present the results of some of our computations. In Table 1 there are given the different energy contributions to the energy of the $2s_{1/2}$-$2p_{1/2}$ transition in the spectrun of U^{89+} calculated within different theoretical schemes: our approach (column F); MCDF (Cheng-Kim-Desclaux, A); PT model in the Dirac-Fock "0" approximation (Ivanov et al., B); relativistic multiparticle PT with zeroth-order Hartree-Fock-Slater potential (Persson-Lindgren-Salomonson, C); multiparticle PT in the Dirac-Fock "0" approximation (Blundell, D) [4-8, 11, 14]. Alhough the overall agreement between all theoretical and experimental data is quite good, more exact results are obtained in the columns (C) and (F). In Table 2 there are given the results of

our calculations for the contributions to the energy due to the VP and SE parts of the Lamb shift in Li-like ions (account from core $1s^2$ energy).

TABLE 1. Different contributions (in eV) to the energy of the $2s_{1/2}$-$2p_{1/2}$ transition in the spectrum of the Li-like ion of uranium U^{89+}.

Values	A	B	C	D	F
Relativistic PT	324.10	319.67	322.31	322.41	322.33
SE	-56.08	-52.09	-54.34	-54.24	-54.16
VP	14.61	13.08	12.56	12.56	12.35
RC	---	---	0.1	0.1	0.1
HOPT	---	---	---	0.01	---
Full energy	282.63	280.66	280.63	280.83	280.62
Experiment		280.59(9)			

VP: vacuum polarization; SE: self-energy part of the Lamb shift; LS = VP + SEB: Lamb shift; RC: nucleus recoil correction, polarization; Relativistic PT: accounts for the main relativistic and correlation effects; HOPT: higher-order PT contributions. Data are from refs [1-10].

TABLE 2. QED corrections (in cm^{-1}) to the energy of Li-like ions in $1s^2nlj$- states.

Z	$2s_{1/2}$		$2p_{1/2}$		$2s_{3/2}$	
	-VP	SE	-VP	SE	-VP	SE
20	108	1567	0.7	32	0.2	31
30	553	6940	11	-134	1.4	269
41	2154	21032	65	-215	13	1164
59	11022	77078	695	1380	77	7034
69	24085	142470	2103	6264	173	14710
79	50191	243595	6115	18178	425	27087
92	122837	497245	23230	60425	1035	55063

Detailed analysis of the VP and SE energy contributions shows that for ions with small Z the QED contribution is not significant, but with growth of Z ($Z > 40$) the QED contribution becomes very important. Moreover, for heavy and superheavy ions its role is of main importance. Now let us consider the role of the nuclear finite-size effect. As calculations show, for multicharged ions with $Z < 20$ its contribution is very small, but for ions with $Z > 70$ it can equal the vacuum polarization contribution. In Table 3 there are displayed the results of calculations for the nuclear correction to the energy of low transitions for Li-like ions. Our calculations also show that a variation of the nuclear radius by a

few per cent may lead to a change in the transition energy by tens of thousands of cm^{-1} !

TABLE 3. Nuclear finite-size correction to the energy (in cm^{-1}) for the low transitions of Li-like ions, and values of the effective nuclear radius (in 10^{-13} cm).

Z	$2s_{1/2} - 2p_{1/2}$	$2s_{1/2} - 2p_{3/2}$	R
20	- 15.1	- 15.5	3.26
30	- 117.5	- 118.0	3.73
41	- 659.0	- 670.0	4.14
59	- 6 610.0	- 6 845.0	4.68
69	- 20 690.0	- 21 712.0	4.93
79	- 62 315.0	- 66 931.0	5.15
92	- 267 325.0	- 288 312.0	5.42

Further we present the results of our calculations of the *Li*-like *K*-plasma satellite lines on the basis of QED PT with ab initio zeroth-order approximation for three-quasiparticle systems, together with the optimized Dirac-Fock results and experimental data for comparison. In Table 4 there are displayed the experimental value: (A) for wavelength (in Å) of the *Li*-like lines dielectron satellites to the $1s^{21}S_0$-$1s3p^1P_1$ line of radiation in the K plasma, and the corresponding theoretical results: (B) PT on 1/Z; (C) QED PT (our data); (D) calculation by the AUTOJOLS method, and (E) MCDF [12, 21].

TABLE 4. The wavelength (in Å) of the *Li*-like lines dielectronic satellites to the $1s^{21}S_0$-$1s3p^1P_1$ line of radiation in the K plasma (see text).

Transitions	Wavelength				Wl
	B	C	D	E	A
$1s^2 2p^2 P_{1/2} - 1s2p3p^2 D_{3/2}$	3.0613	3.0608	3.0607	3.0610	
$1s^2 2p^2 P_{3/2} - 1s2p3p^2 D_{5/2}$	3.0613	3.0614	3.0615	3.0616	3.0608±
$1s^2 2p^2 P_{1/2} - 1s2s3d^4 D_{3/2}$	3.0608	3.0611	3.0612	3.0614	0.0019
$1s^2 2p^2 P_{3/2} - 1s2p3p^4 P_{3/2}$	-----	3.0623	------	3.0625	
$1s^2 2p^2 P_{3/2} - 1s2p3p^4 P_{5/2}$	------	3.0626	------	3.0629	

We have also performed the calculation of hyperfine coupling constants: the electric quadrupole constant B and magnetic dipole constant A, with inclusion of nuclear finiteness and the Uehling potential for Li-like ions. Analogous calculations of the constant A for ns states of hydrogen-, lithium- and sodium-like ions were made in refs [11, 22]. In those papers other bases were used for the relativistic orbitals, another model was adopted for the charge distribution in the nuclei, and another method of numerical calculation was used for the Uehling potential.

In Tables 5 and 6 there are displayed the results for the hyperfine coupling constants in the lowest excited states of Li-like ions. In Table 5 we compare the results of our calculations with those from papers [11, 22] for magnetic dipole coupling constants in the ground state $1s^2 2s$ of a few lithium-like ions.

TABLE 5. Theoretical results for the magnetic dipole coupling constant. For the nuclear magnetic dipole, bulk distribution (present paper and [11]) and surface distribution [22].

Z	$\overline{A}$ (present)	$\overline{A}$ [11]	$\overline{A}$ [22]
25	988–03	1002–02	9872–03
28	1031–02	1034–02	1020–02
34	1094–02	1099–02	1087–02
37	1131–02	1135–02	1123–02
43	1210–02	1214–02	1203–02
53	1379–02	1381–02	1370–02

TABLE 6. Constants of the hyperfine electron-nuclear interaction: $A=Z^3 g_I \overline{A}$ cm^{-1}, $B=\dfrac{Z^3 Q}{I(2I-1)}\overline{B}$ cm^{-1}.

nlj	Z	20	69	79	92
$2s$	$\overline{A}$	93–03	176–02	215–02	314–02
$3s$	$\overline{A}$	26–03	51–03	63–03	90–03
$4s$	$\overline{A}$	15–03	19–03	24–03	36–03
$2p_{1/2}$	$\overline{A}$	25–03	56–03	71–03	105–02
$3p_{1/2}$	$\overline{A}$	81–04	16–03	20–03	31–03

$4p_{1/2}$	$\overline{A}$	32–04	72–04	91–04	11–03
$2p_{3/2}$	$\overline{A}$	50–04	67–04	71–04	72–04
	$\overline{B}$	9–04	13–04	15–04	17–04
$3p_{3/2}$	$\overline{A}$	13–04	19–04	21–04	22–04
	$\overline{B}$	31–05	51–05	55–05	62–05
$4p_{3/2}$	$\overline{A}$	62–05	89–05	92–05	8–04
	$\overline{B}$	10–05	20–05	22–05	26–05
$3d_{3/2}$	$\overline{A}$	88–05	10–04	11–04	12–04
	$\overline{B}$	51–06	9–05	10–05	11–05
$4d_{3/2}$	$\overline{A}$	35–05	51–05	55–05	58–05
	$\overline{B}$	12–06	44–06	50–06	56–06
$3d_{5/2}$	$\overline{A}$	36–05	48–05	50–05	52–05
	$\overline{B}$	21–06	38–06	39–06	40–06
$4d_{5/2}$	$\overline{A}$	15–05	19–05	20–05	21–05
	$\overline{B}$	59–07	15–06	16–06	17–06

The main difference between the quoted papers lies in the modeling of the magnetic moment distribution in the nucleus: a bulk distribution is assumed in the present paper and in paper [11] and a surface distribution is adopted in ref. [22]. A systematic ~1% difference is observed, which cannot be explained by the uncertainty in the nuclear radius. However, it is known that variations of the nuclear size within reasonable limits can lead to variations in the value of A of several orders of magnitude [11, 14]. This question will be analysed in a separ-ate paper.

Acknowledgements

One of us (A.V.G.) would like to thank Profs Leonid Ivanov and Elena Ivanova for their help and for the possibility of using the atomic numerical code used in this work, and Profs Walter Kohn, Ilya Kaplan, and Andreas Theophilou for helpful comments.

References

1. P.J. Mohr, Phys. Scr. **46**, 44 (1993); At. Data & Nucl. Data Tabs **24**, 453 (1983).
2. J.F. Seely, J.O. Ekberg, C.M. Brown et al., Phys. Rev. Lett. **57**, 2924 (1996).

3. H. Gould, Phys. Scr. **46**, 61 (1993).
4. K. Cheng, Y. Kim, J. Desclaux, At. Data & Nucl. Data Tabs **24**, 11 (1979).
5. S. Blundell, Phys. Scr. **46**, 144 (1993).
6. G. Drake, Phys. Scr. **46**, 116 (1993).
7. H. Persson, I. Lindgren, S. Salomonson, Phys. Rev. Lett. **76**, 204 (1996).
8. W.R. Johnson, J. Sapirstein, S.A. Blundell, Phys. Scr. **46**, 184 (1993).
9. V. Dzuba, V. Flambaum, P. Silvestrov, O. Sushkov, Phys. Rev. A **44**, 2828 (1991).
10. P. Pyykkö, L.-B. Zhao, J. Phys. B **36**, 1469 (2003).
11. L.N. Ivanov, E.P. Ivanova, E.V. Aglitsky, Phys. Rep. **164**, 317 (1988).
12. A.V. Glushkov et al., Nucl. Phys. A **734**, E21 (2004).
13. L.N. Ivanov, E.P. Ivanova, L.N. Knight, Phys. Rev. A **48**, 4365 (1993).
14. A. Glushkov, L. Ivanov, Phys. Lett. A **170**, 33 (1992).
15. L.N. Ivanov, E.P. Ivanova, A.V. Glushkov, A.E. Kramida, Phys. Scr. **32**, 514 (1985).
16. A.V. Glushkov, JETP Lett. **55**, 97 (1992).
17. L.N. Ivanov, A.V. Glushkov, S.V. Malinovskaya, S.V. Ambrosov, Preprint of the Institute for Spectroscopy AN, № AS-5, ISAN, Troitsk, 1991.
18. A.V. Glushkov, V.D. Rusov, S.V. Ambrosov, A.V. Loboda, in: New projects and new lines of research in nuclear physics, eds. G. Fazio & F. Hanappe, World Scientific, Singapore, 146 (2003).
19. A.V. Glushkov, L.N. Ivanov, J. Phys. B **26**, L376 (1993).
20. I. I. Sobel'man, Introduction to the theory of atomic spectra, Nauka, Moscow (1977).
21. E.V. Aglitskii, A.S. Panin, U.I. Safronova et al., J. de Phys. **49**, 267 (1988).
22. I.M. Band, M.A. Listengarten, M.B. Trzhaskovskaya, Izv. Acad. Nauk SSSR, Ser. Phys. **49**, 2202 (1985); **50**, 2440 (1986).

QUANTUM CALCULATION OF COOPERATIVE MUON-NUCLEAR PROCESSES: DISCHARGE OF METASTABLE NUCLEI DURING NEGATIVE MUON CAPTURE

S.-V. MALINOVSKAYA, A.-V. GLUSHKOV,
Y.-V. DUBROVSKAYA AND L.-A.VITAVETSKAYA

Department of Quantum Optics and Nuclear Physics, Odessa University, P.O. Box 24A, Odessa-9, 65009, Ukraine
glushkov@paco.net

Abstract. There is presented a consistent energy approach to the quantum electrodynamics (QED) theory of the discharge of a nucleus with emission of a γ radiation and further muon conversion, which initiates this discharge. A numerical calculation is carried out for nucleus ${}^{49}_{21}Sc_{28}$.

1. Introduction

A negative muon μ capture by a metastable nucleus may accelerate the discharge of the latter by many orders of magnitude [1-3]. Principal possibility of storage of significant quantities of metastable nuclei in processes of nuclear technology and their concentrating by chemical and laser methods lead to questions regarding methods of governing the velocity of their decay. It has been studied [1] a possibility of action on processes of decay of nuclei with a participation of the electrons of atomic shells (K-capture and internal conversion) by means of their ionization [1]. It has been considered a possibility of accelerating the discharge of a metastable nucleus by means of the angular momentum part of the electron shells of atoms [3]. A comprehensive QED theory of cooperative laser-electron-nucleus processes is developed in refs. [4-6]. Electron shell effect is quite small, as the parameter r_n/r_a is small (r_n being the radius of the nucleus and r_a that of the atom). In this respect, a meso-atomic system differs advantageously of a usual atom, as the ratio r_n/r_a may vary in wide limits depending on the nuclear charge. For a certain ratio between the energy range of the nuclear and muonic levels the

J.-P. Julien et al. (eds.),
Recent Advances in the Theory of Chemical and Physical Systems, 301–307.

discharge may be followed by the ejection of a muon, which may then participate in the discharge of other nuclei.

In this paper we present a consistent energy approach to the QED theory of the discharge of a nucleus with emission of γ radiation and further muon conversion, which initiates this discharge. Traditional processes of muon capture are studied in fundamental papers [7-9, 10-13] and are not considered here. Within the QED energy approach [4-6, 14-19], a decay probability is presented as the imaginary part of the energy shift. In our situation the probability of the corresponding process (decay) is linked to the imaginary part of the "nucleus core + proton + muon" system. For radiative decays it is manifested as an effect of the retardation in interaction and self-action.

2. Model and channels of decay for meso-atomic system: Energy approach

We consider a simple one-particle system of nucleus. It is supposed that the system consists of a twice-magic core. A single proton and single muon moves in the core field. The proton and muon interact through the Coulomb potential. This interaction will be accounted for in the first order of the atomic perturbation theory (PT) or second order of the QED PT. Surely a majority of known excited nuclear states have the multi-particle character and it is hardly possible to describe their structure within one-particle model. Nevertheless, the studied effects of muon-proton interaction are not connected with one-particle character of the model. In principle it is possible to consider also a dynamical interaction of two particles through the core. It accounts for the mass finiteness of the core. However, this interaction may decrease the multipolity of nuclear transitions only by unit. Indeed, an interest attracts strongly forbidden transitions of high multipolity. We will calculate probabilities of decay to different channels of the system, which consists of a proton (in an excited state $\Phi_{N_1 J_1}$) and a muon (in the ground state Ψ^{μ}_{1s}).

Three channels should be taken into account [3]: i) a radiative, purely nuclear 2^j-pole transition (probability P_1); ii) a non-radiative decay, when the proton transits to the ground state and the muon leaves the nucleus with the following energy: $E = \Delta E^{p}_{N_1 J_1} - E^{i}_{\mu}$; here $\Delta E^{p}_{N_1 J_1}$ is the energy of the nuclear transition and E^{i}_{μ} is the bond energy of the muon in the *1s* state (P_2); iii) a transition of the proton to the ground state with muon excitation and emission of γ radiation with energy $h\omega = \Delta E^{p}_{N_1 J_1} - \Delta E^{\mu}_{nl}$ (P_3). Corresponding Feynman diagrams are given in Figure 1.

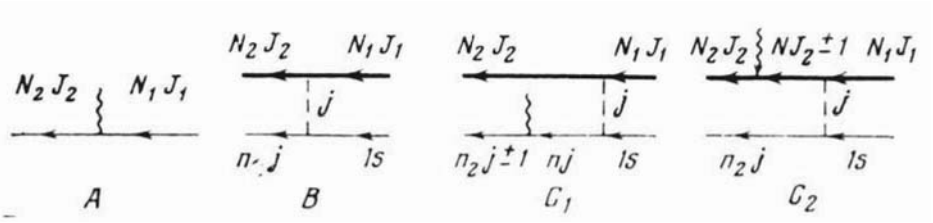

Figure 1. Feynman diagrams corresponding to different channels of decay of the meso-atom (see text).

The diagram A (Fig.1) corresponds to the first channel, diagram B, to the second channel, and diagrams C_1 and C_2, to the third channel. The thin line on the diagrams corresponds to the muon state and the bold line, to the proton state. The indexes on the lines correspond to the initial and final states of the proton and the muon. The dashed line with index j represents the Coulomb interaction between muon and proton with the exchange of 2^j-pole quanta. The waved line corresponds to the operator of radiative dipole transition. This effect is due to muon-proton interaction. Diagram A is of zero order in the muon-proton interaction, while other diagrams are of first order.

A probability of purely radiative nuclear 2^j-pole transition is defined as follows (r_n=5·10^{-13} cm):

$$P_1 = 2\cdot 10^{20}\cdot\frac{j+1}{j[(2j+1)!!]^2}\left(\frac{3}{j+3}\right)^2\left(\frac{\Delta E[MeV]}{40}\right)^{2j+1} \qquad (1)$$

The diagrams C_1 and C_2 account for the effects of the interaction of the particles in the initial state. Surely there are other versions of these diagrams, but their contributions to the probabilities of the studied processes is significantly less important than the contributions of the diagrams C_1 and C_2 [3].

Within QED PT [5-7], a full probability is divided into a sum of partial contributions connected with decays to definite final states. These contributions are equal to the corresponding transition probabilities (P_i). For example, under the condition $\Delta E^{p}_{N_1J_1} > E^{i}_{\mu}$ a probability definition reduces the QED calculation of the probability of autoionization decay of the two-particle system. The imaginary part of the energy of the excited state of the system at the lowest QED PT order can be written in the standard form [14-18]:

$$\mathrm{Im}\,E = e^2\,\mathrm{Im}\,i\lim\iint d^4x_1 d^4x_2 e^{\gamma(t_1+t_2)} \bullet\{D(r_{c1t1}, r_{c2t2})\cdot$$
$$< \Phi_I \mid (j_{cv}(x_1) j_{cv}(x_2)) \mid \Phi_I > + D(r_{p1t1}, r_{p2t2}) < \Phi_I \mid (j_{pv}(x_1) j_{pv}(x_2)) \mid \Phi_I >$$
$$+ D(r_{\mu 1t1}, r_{\mu 2t2}) < \Phi_I \mid (j_{\mu v}(x_1) j_{\mu v}(x_2)) \mid \Phi_I >\} \tag{2}$$

Here $D(r_1t_1,r_2t_2)$ is the photon propagator; j_{cv}, j_{pv}, $j_{\mu v}$ are the four-dimensional components of the operator of current for the considered particles: core, proton, muon; $x = (r_c, r_p, r_\mu, t)$ includes the space coordinates of the three particles plus time (equal for all particles); and γ is the adiabatic parameter. For the photon propagator, it is possible to use the exact electrodynamical expression. Below we are limited by the lowest order of QED PT, i.e., the next QED corrections to *Im E* will not be considered. After some algebraic manipulation we arrive at the following expression for the imaginary part of the excited state energy as a sum of contributions:

$$\mathrm{Im}\,E = \mathrm{Im}\,Ec + \mathrm{Im}\,Ep + \mathrm{Im}\,E\mu,$$

$$\mathrm{Im}\,Ea = -Z_a^2 / 4\pi \sum_F \iint dr_{c1} dr_{c2} \iint dr_{p1} dr_{p2} \iint dr_{+1\mu 1} dr_{\mu 2} \Phi_I^*(1) \Phi_F^*(2) \cdot$$

$$\cdot T_a(1,2) \Phi_F(1) \Phi_I(2),$$

$$T_a(1,2) = \exp(w_{IF} r_{a12}) / r_{a12} \{1 - \alpha_1 \alpha_2\},$$

(3)

in which $r_{a12} = \mid r_{a1} - r_{aa2} \mid$; Φ_c, Φ_p, Φ_e are the secondly quantified operators of the fields of the core particles, proton and muon. The sum on F designates a summation on the final states of the system. To the second QED PT order, the full width of a level is divided into a sum of partial contributions connected with the effective radiation decays of the states of system. The contributions are proportional to the probabilities of the corresponding transitions.

Let us consider a case where the energy of excitation of the nucleus is larger than the energy of ionization of the meso-atomic system, E_μ^i. It is obvious that $P_3 << P_2$ as P_3 has an additional small parameter in the interaction with the electromagnetic field [3]. Calculation of the probability P_2 can lead to the calculation of the probability of autoionization decay for the state of the two-particle system, i.e., $P_2 = 2ImE/\hbar$, where *ImE* is defined by Eq. (2). We have carried out a precise numerical calculation of different decay probabilities for effective states of the nucleus ${}^{49}_{21}Sc_{28}$ with the model nuclear potential.

3. Calculation for the nucleus $^{49}_{21}Sc_{28}$

The nucleus of $^{49}_{21}Sc_{28}$ contains one proton above the twice magic core of $^{49}_{20}Ca_{28}$. A scheme of the energy levels for this nucleus is presented in Figure 2. The level $p_{1/2}$ is connected with the ground level $f_{7/2}$ by an E4 transition and with the low-lying level $p_{3/2}$ by an E2 transition. The levels $p_{3/2}$ and $f_{7/2}$ are connected by the E2 transition. One could also consider the magnetic transitions between these levels. The life-time for the isolated nucleus in the excited states is of the order of 10^{-11}. Following papers [3, 20], let us assume that a proton moves in an effective field of the core:

$$V - 25 \cdot f(l, j) \cdot V' / r \tag{4}$$

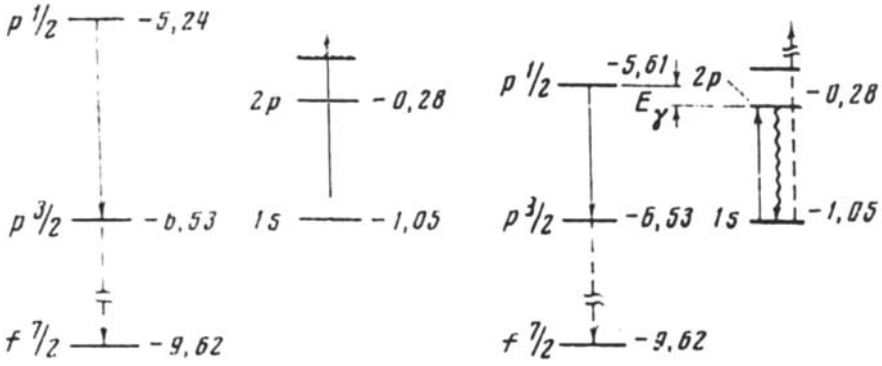

Figure 2. Schemes of energy levels for proton (left part of the figure) and muon (right) in $^{49}_{21}Sc_{28}$. Transitions of proton and muon in 1 and 2 stages are denoted by solid and dotted lines.

We adopt for the self-nuclear part of the interaction V the following form (displayed in Figure 3):

$$\begin{aligned} &V_0 - a[r^4/4 - r^3(R_1 + R_2)/3 + r^2 R_1 R_2/2], \ldots\ldots r < R_2 \\ &0, \ldots\ldots\ldots\ldots\ldots\ldots\ldots\ldots\ldots\ldots\ldots\ldots\ldots\ldots\ldots\ldots r > R_2 \end{aligned} \tag{5}$$

As it was shown in ref. [3], this potential is more suitable in the numerical computation because it does not lead to divergence (under $r \to 0$) of the spin-orbit interaction $-25f(l,j)V'/r_i$. In this respect, it differs advantageously from the well-known Woods-Saxon potential.

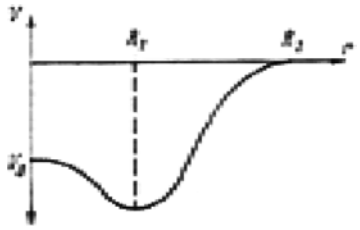

Figure 3. Nuclear potential *V(r)* (Eq. 5).

The electric core potential was taken as the potential of a charged sphere (the upper sign is for the proton and the lower sign, for the muon):

$$U(r) = \pm Z \cdot e^2 \cdot \begin{cases} 3/2 \cdot R - r^2 / 2R^3, ...r < R \\ 1/r, ...r > R. \end{cases} \quad (6)$$

Parameters are defined from the fitting condition for calculated and theoretical energies of the ground and first excited states. With V_0 = -47.6, R_1=2, R_2=7.65, R=4.75, it was obtained for the proton states: *E(f7/2)*=-9.62, *E(p3/2)*=-6.53, *E(p1/2)*=-5.24; and for the muon states*: E(1s)*=-1.05, *E(2s)* =-0.27, and *E(2p)* =-0.281 (units of energy: 1 MeV, and of length: 10^{-13} cm). To calculate the corresponding integrals in Eq. (2), we use the effective Ivanov-Ivanova technique [16-19]. The probabilities of the meso-atomic decay (in s^{-1}) for different nuclear transitions are as follows:

$$P_2(p_{1/2}\text{-}p_{3/2})=3.93\cdot10^{15},\ P_2(p_{1/2}\text{-}f_{7/2})=3.15\cdot10^{12},\ P_2(p_{3/2}\text{--}f_{7/2})=8.83\cdot10^{14}.$$

Let us note that these values are significantly higher that the corresponding non-relativistic estimates [3], e.g.: $P_2(p_{1/2}\text{-}p_{3/2})=3.30\cdot10^{15}$. For the above indicated transitions, the nucleus must give a momentum ΔJ no less than 2.4 and 2, according to the momentum and parity rules. If a meso-atomic system is in the initial state $p_{1/2}$ then the cascade discharge occurs with ejection of the muon in the first stage and the γ quantum emission in the second stage.

To consider a case where the second channel is closed and the third one is opened, let us assume that $E^p(p_{1/2})\text{-}E^p(p_{3/2})$ = 0.92 MeV (Fig. 2). The energy of the nuclear transition is not sufficient for a transition of the muon to the continuum. However, it is sufficient for an excitation to the *2p* state. It is important to note that this energy is not lying in the resonant range. The diagram C_1 (Fig. 1) describes the proton transition $p_{1/2}\text{-}p_{3/2}$ with a virtual excitation of the muon to states of the series *nd* with a γ quantum emission of energy:

$$h\omega=E^{p}(p_{1/2})+E^{\mu}(1s)-E^{p}(p_{3/2})-E^{\mu}(2p).$$

Furthermore the dipole transition *2p-1s* can occur. The calculated value for the probability of this transition is $P_3=1.9\cdot10^{13}$ s^{-1}. This value is significantly higher than the corresponding non-relativistic value [3]. It is important to note that the value P_3 is larger than the probability of the radiation transition $p_{1/2}$-$p_{3/2}$ and that of the non-radiative transition $p_{1/2} - f_{7/2}$. The next transition $p_{3/2} - f_{7/2}$ occurs without radiation during the time 10^{-15}s, with ejection of the muon.

Acknowledgements

One of us (A.V.G.) would like to thank Professors V.S. Letokhov and L.I. Ivanov for helpful comments.

References

1. V.I. Gol'dansky, V.S. Letokhov, JETP **67**, 513 (1974).
2. D.F. Zaretsky, V. Novikov, Nucl. Phys. **14**, 540 (1960).
3. L.N. Ivanov, V.S. Letokhov, JETP **70**, 19 (1976).
4. A.V. Glushkov, S.V. Malinovskaya, in: New projects and new lines of research in nuclear physics, eds G.Fazio & F.Hanappe, World Scientific, Singapore, 242 (2003).
5. A.V. Glushkov, S.V. Malinovskaya, Y.G. Chernyakova, A.A. Svinarenko, Int. J. Quant. Chem. **99**, 889 (2004).
6. S.V. Malinovskaya, Int. J. Quant. Chem. **104**, 531 (2005).
7. J. J. Tiomno, J.A. Weller, Rev. Mod. Phys. **21**, 153 (1949).
8. J. S. Bell, J. Loves, Nuovo Cimento **34**, 433 (1964).
9. L.L. Foldi, J.D. Walecka, Nuovo. Cimento **34**, 1026 (1964).
10. L.I. Ponomarev, G. Fiorentini, Muon Catal. Fusion **1**, 3 (1987).
11. S.S. Gerstain, Yu.V. Petrov, L.I. Ponomarev, Usp. Phys. Nauk **160**, 3 (1990).
12. L.I. Men'shikov, L.N. Somov, Usp. Phys. Nauk **160**, 47 (1990).
13. A.V. Kravtsov, A.I. Mikhailov, Phys. Rev. A **49**, 3566 (1994).
14. A.V. Glushkov, L.N. Ivanov, Phys. Lett. A **170**, 33 (1992).
15. A.V. Glushkov, JETP Lett. **55**, 97 (1992).
16. L.N. Ivanov, E.P. Ivanova, L.N. Knight, Phys. Rev. A **48**, 4365 (1993).
17. A.V. Glushkov, S.V. Ambrosov, A.V. Loboda, E.P. Gurnitskaya, G.P. Prepelitsa, Int. J. Quant. Chem. **104**, 537 (2005).
18. A.V. Glushkov, S.V. Ambrosov, A.V. Loboda, et al., Nucl. Phys. A **734**, E21 (2004).
19. A.V. Glushkov, V.D. Rusov, S.V. Ambrosov, A.V. Loboda, in: New projects and new lines of research in nuclear physics, eds G.Fazio & F.Hanappe, World Scientific, Singapore, 146 (2003).
20. J. Blomkvist, S. Wahlborn, Ark. Fys. **16**, 545 (1960).

COMPUTER SIMULATIONS IN HEAVY PARTICLE COLLISIONS

FRANCESCA O'ROURKE
Department of Applied Mathematics & Theoretical Physics
Queen's University Belfast
Belfast, BT7 1NN, N.Ireland

RUTH PEDLOW
Department of Applied Mathematics & Theoretical Physics
Queen's University Belfast
Belfast, BT7 1NN, N.Ireland

AND

DERRICK CROTHERS
Department of Applied Mathematics & Theoretical Physics
Queen's University Belfast
Belfast, BT7 1NN, N.Ireland

Abstract. One area in atomic and molecular physics that computer modelling and its applications are extensively used is in ion-atom collisions. In this paper we consider computer simulations for various theoretical continuum-distorted-wave eikonal-initial-state (CDW-EIS) models used in the study of single ionization of neutral target atoms by fast highly charged ions. In our first study we examine ultra-low energy electrons for 3.6 MeV amu^{-1} Au^{53+} on helium, neon and argon. Doubly differential cross sections as a function of the longitudinal electron velocity for various transverse velocity cuts are obtained using the CDW-EIS model. A sharp asymmetric peak centred at a longitudinal velocity of zero is observed to emerge at ultra-low energies in all of the collisions studied. The shape of this target cusp which is very sensitive to the details of the two-centre potential, is shown to be in excellent accord with the experimental measurements. In our second study we explore fully differential cross sections for 3.6 MeV amu^{-1} $Au^{24+,53+}$ + He collisions. Different versions of the CDW-EIS model are used and compared with recent experimental data for fully differential cross sections involving the collisions 3.6 MeV amu^{-1} $Au^{24+,53+}$ on helium. One CDW-EIS model in this study is seen to give better agreement with experiment at high projectile charges, low electron energy and high

J.-P. Julien et al. (eds.),
Recent Advances in the Theory of Chemical and Physical Systems, 309–333.

momentum transfer than other models. This approximation is based on a model potential with physically appropriate short-range and long-range behaviour.

1. Introduction

The subject of single ionization of neutral target atoms by charged particle impact has been the focus of intense interest for decades by both theoretical and experimental physicists due to its practical applications in various fields such as fusion research and astrophysics. In recent years advances in experimental techniques have made it possible to make measurements of a large variety of processes, in different energy regimes, for different targets and projectile charge states. For example ejected electron spectroscopy has been very successful at reproducing measurements of double differential cross sections as a function of ionized electron energy and angle.[1] More recently the advent of reaction microscopy enables measurements to be made simultaneously the momenta of the emitted electrons and the recoiling residual target ion which gives direct evidence of the momentum transferred in the collision. For fast heavy ions Moshammer et al[2] measured the momentum vectors of the ejected electron and recoil ion and obtained the scattered projectile momentum from the momentum consevation law. However in the analysis of this and subsequent experiments Schmitt et al [3] focused on differential and recoil ion momentum distributions. More recently Schulz et al and Fischer et al[4,5] have used reaction microscopy to examine triply and fully differential cross sections respectively for fast ion-atom collisions at large perturbations.

On the theoretical side ionization of multielectron targets has been studied using a wide variety of distorted wave models. The simplest model for the ionization process involves a three-particle system interacting through long range Coulomb potentials. From a theoretical perspective the main problem is the representation of the final electronic state, where the ionized electron travels under the influence of the Coulomb potential due to both the projectile and target nuclei. Due to the long range behaviour of the Coulomb interaction this cannot be represented by a plane wave. An exact analytical solution of the three-body problem is not possible although its asymptotic form may be found.[6–10] One useful perturbative method which accounts for long range Coulomb potentials at intermediate and high energies is continuum distorted wave theory (CDW). It was originally introduced by Cheshire[11] to model the process of charge transfer during the collision of an atom/ion with an ion and later applied to single ionization for ion-atom collisions by Belkić.[12] However one major defect of the CDW ionization theory developed by Belkić[12] was that it led to spurious results due to

the fact that the initial state was not normalized. This flaw was corrected by the continuum distorted wave theory first introduced by Crothers and McCann.[6] They first both presented and applied it to the ionization of a hydrogen atom by H^+, He^{2+}, Li^{3+}, Be^4+ and C^{6+}. The CDW-EIS model differs from the original continuum distorted wave (CDW) ionization theory of Belkić[12] in that it describes the distortion in the initial state by an eikonal phase factor rather than by a full continuum wave. The phase factor originates from the asymptotic expansion of the CDW. Since it is not possible to solve the Schrödinger equation for three mutually interacting particles in closed analytic form a comprehensive description of the entire collision necessitates a numerical approach.

Theoretical CDW-EIS models and computer simulations developed during the last decade have been very successful in reproducing experimental data of doubly differential cross sections as a function of ejected electron energy and angle.[7,8,13–17] These studies have enabled us to understand the main characteristics of electron emission spectra and the nature of two centre effects which may be observed in the double differential cross section spectrum.

It was also found that the CDW-EIS theory was successful in describing the experimental results for longitudinal momentum distributions of fast highly charged projectile ions by neutral target atoms produced with reaction microscopy technique.[9,10,18–20]

The main aim of this paper is to review the CDW-EIS model used commonly in the decription of heavy particle collisions. A theoretical description of the CDW-EIS model is presented in section 2. In section 3 we discuss the suitablity of the CDW-EIS model to study the characteristics of ultra-low and low energy electrons ejected from fast heavy-ion helium, neon and argon atom collisions. There are some distinct characteristics based on two-centre electron emission that may be identified in this spectrum. This study also allows us to examine the dependence of the cross sections on the initial state wave function of multi-electron targets and as such is important in aiding our understanding of the ionization process.

Recently Schulz et al and Fischer et al[4,5] have had some difficulty in applying the CDW-EIS theory successfully for fully differential cross sections in fast ion-atom collisions at large perturbations. These ionization cross sections are expected to be sensitive to the quality of the target wave function and therefore accurate wave functions are needed to calculate these cross sections. Thus one purpose of this paper is to address this problem theoretically by re-examining the CDW-EIS model and the assumptions on which it is based. We will explore this by employing different potentials to represent the interaction between the ionized electron, projectile ion and residual target ion. For other recent work carried out on fully differential cross sections see[21–23] and references therein. This discussion is presented in section 4.

Finally we summarize our results in section 5. Atomic units are used throughout unless otherwise stated.

2. Continuum Distorted Wave Eikonal Initial State Method

2.1. PERTURBATION THEORY

In the present section we present a theoretical description for the continuum-distorted-wave eikonal-initial-state (CDW-EIS) model. This model is one of the most advanced and complete perturbative theories of heavy particle collisions which has been formulated to date. The reasons for the success of this model particularly in describing ionization at high energies in the MeV/amu range are that:
a) the ionized electron sees the Coulomb field from both the target and projectile ion
b) the wave function satisfies the correct asymptotic boundary conditions
c) the initial and final wave states are normalised at all times and all impact parameters.

In this paper we restrict our discussion to the processes of single ionization by charged particle impact for the neutral target atoms helium, neon and argon. In our work we adopt the independent electron model to treat the neutral target atom. Our analysis is within the semiclassical rectilinear impact parameter ($\boldsymbol{\rho}$), time-dependent (t) formalism. We consider the problem of three charged particles where an ion of nuclear charge Z_P and mass M_P impinges with a collision velocity $\mathbf{v}$ on a neutral target atom with nuclear charge Z_T and mass M_T. As $M_{T,P} \gg 1$, the motion of the nuclei can be uncoupled from that of the electron. The trajectory of the heavy particle is then characterized by two parameters $\boldsymbol{\rho}$ and the impact velocity $\mathbf{v}$ such that $\boldsymbol{\rho}.\mathbf{v} = 0$.

The internuclear coordinate is defined by

$$\mathbf{R} = \mathbf{r_T} - \mathbf{r_P} = \boldsymbol{\rho} + \mathbf{v}t \tag{1}$$

and

$$\mathbf{r} = \frac{1}{2}(\mathbf{r_T} + \mathbf{r_P}) \tag{2}$$

where $\mathbf{r_T}$, $\mathbf{r_P}$ and $\mathbf{r}$ are the position vectors of the electron relative to the target nucleus, projectile nucleus and their midpoint respectively. The impact parameter picture of the collision is equivalent to the full quantal or wave treatment when the eikonal criterion for small angle scattering is satisfied.[24] It has become standard to work in a generalised nonorthogonal coordinate system in which the vectors $\mathbf{r_T}(\mathbf{r_P})$ from the target (projectile) to the electron are treated, along with $\mathbf{R}$, as independent variables.[25] Working in the frame centred on the target nucleus and using atomic units, the

transition amplitude, in post form, may be given by:

$$\tilde{a}_{if}(\boldsymbol{\rho}) = -\mathrm{i}\int_{-\infty}^{\infty} dt \left\langle \tilde{\chi}_i^+ \right| \left(\tilde{H}_e - i\frac{\partial}{\partial t_{\mathbf{r}}} \right) \left| \chi_k^- \right\rangle. \tag{3}$$

where

$$H_e = -\frac{1}{2}\nabla_{\mathbf{r}}^2 - \frac{Z_T}{r_T} - \frac{Z_P}{r_P}. \tag{4}$$

The superscripts plus and minus refer to outgoing and incoming Coulomb boundary conditions respectively. Of course χ_i^+ and χ_k^- are not exact solutions of the three-body Schrödinger equation, but in fact are the asymptotic forms of the wave functions. It should be noted that since the potentials appearing in equation 4 are pure Coulomb potentials, they continue to affect the relevant wave functions even at infinity. We adopt an independent electron model to approximate the neutral target atom, therefore as in any independent electron model, no explicit electron correlation in the initial state is considered. As such, the electronic Hamiltonian for the projectile/neutral target atom collision system is modified from that of the original monoelectronic CDW-EIS approximation,[6] in that the electron residual target interaction $-\frac{Z_T}{r_T}$ is replaced by a Coulombic potential with an effective charge $-\tilde{Z}_T$ to account for passive electron screening. The influence of the passive electrons is to add a short range potential to the long range Coulomb potential given by the electron-residual ion interaction. We follow the approach of Belkić et al[26] to describe how the effective charge should be chosen. Thus we make the assumption that the emitted electron, ionized from an orbital of Roothan-Hartree-Fock (RHF) energy ε_i, moves in a residual target potential of the form

$$V_T(\mathbf{r}_T) = -\frac{\tilde{Z}_T}{r_T}. \tag{5}$$

The effective target charge is given by

$$\tilde{Z}_T = \sqrt{-2n^2\varepsilon_i}, \tag{6}$$

where ε_i is the binding energy of the neutral target atom, and n is the principal quantum number. The initial and final CDW-EIS wave functions may be expressed explicitly as

$$\begin{aligned} |\chi_i^+\rangle &= \varphi_i(\mathbf{r}_T)\exp(-\frac{1}{2}\mathrm{i}\mathbf{v}.\mathbf{r} - \frac{1}{8}\mathrm{i}v^2t - \mathrm{i}\varepsilon_i t) \\ &\quad \exp(-\mathrm{i}\nu\ln(vr_P + \mathbf{v}.\mathbf{r_P})) \end{aligned} \tag{7}$$

$$\begin{aligned} |\chi_k^-\rangle &= (2\pi)^{-3/2}N^*(\varepsilon)N^*(\zeta)\exp(\mathrm{i}\mathbf{k}.\mathbf{r_T} - \frac{1}{2}\mathrm{i}\mathbf{v}.\mathbf{r} - \frac{1}{8}\mathrm{i}v^2t - \mathrm{i}E_k t) \\ &\quad {}_1F_1(-\mathrm{i}\varepsilon;1;-\mathrm{i}kr_T - \mathrm{i}\mathbf{k}.\mathbf{r_T}){}_1F_1(-\mathrm{i}\zeta;1;-\mathrm{i}pr_P - \mathrm{i}\mathbf{p}\cdot\mathbf{r_P}). \end{aligned} \tag{8}$$

Here,

$$E_k = \frac{1}{2}k^2. \tag{9}$$

is the electron energy in the final continuum state. The momentum $\mathbf{p}$ of the ejected electron relative to the projectile is given by

$$\mathbf{p} = \mathbf{k} - \mathbf{v} \tag{10}$$

where $\mathbf{k}$ is the momentum of the ejected electron with respect to a reference frame fixed on the target nucleus. We note that the polar axis for reference is taken along the incident beam direction so that

$$d\mathbf{k} = k^2 dk \sin\theta d\theta d\phi. \tag{11}$$

The spherical coordinates of the ejected electron momentum $\mathbf{k}$ are k, θ, and ϕ, where $\theta = \cos^{-1}(\hat{\mathbf{k}}.\hat{\mathbf{v}})$. Because the impact velocity lies along the Z axis, then $\mathbf{v}$=v $\hat{\mathbf{Z}}$. The three Sommerfeld parameters are defined by

$$\varepsilon = \frac{\tilde{Z_T}}{k} \tag{12}$$

$$\nu = \frac{Z_P}{v} \tag{13}$$

$$\zeta = \frac{Z_P}{p} \tag{14}$$

and

$$N(a) = \exp(\frac{1}{2}\pi a)\Gamma(1 - \mathrm{i}a) \tag{15}$$

represents the Coulomb density of states factor. Equations 7 and 8 model the electron moving within the continuum of both the projectile and target. In the CDW-EIS approximation the residual post-interaction is the nonorthogonal kinetic energy term,

$$\begin{aligned}\left(H_e - \mathrm{i}\frac{\partial}{\partial t_{\mathbf{r}}}\right)|\chi_k^-\rangle \quad &= [-\boldsymbol{\nabla}_{\mathbf{r_T}} \ln {}_1F_1(-\mathrm{i}\varepsilon; 1; -\mathrm{i}kr_T - \mathrm{i}\mathbf{k}\cdot\mathbf{r_T}) \\ &\cdot \boldsymbol{\nabla}_{\mathbf{r_P}} \ln {}_1F_1(-\mathrm{i}\zeta; 1; -\mathrm{i}pr_P - \mathrm{i}\mathbf{p}\cdot\mathbf{r_P})]\,|\chi_k^-\rangle. \end{aligned} \tag{16}$$

The active electron bound state $\varphi_i(\mathbf{r_T})$ satisfies the Schrödinger equation

$$\left(\frac{1}{2}\nabla^2_{\mathbf{r_T}} + \frac{Z_T}{r_T} + \varepsilon_i\right)|\varphi_i(\mathbf{r_T})\rangle = 0 \tag{17}$$

The ground state $\varphi_i(\mathbf{r_T})$ of the neutral target atom is represented by a Roothan-Hartree-Fock wavefunction that may be expanded in terms of Slater orbitals.[27] Denoting the triply differential cross section by

$$\frac{d^3\sigma}{d\mathbf{k}} = \alpha(\mathbf{k}) = \int d\boldsymbol{\rho}|a_{if}(\boldsymbol{\rho})|^2 \tag{18}$$

with

$$a_{if}(\boldsymbol{\rho}) = \mathrm{i}(\rho v)^{\frac{2\mathrm{i}Z_T^{\sim} z_P}{v}} \tilde{a}_{if}(\boldsymbol{\rho}) \tag{19}$$

we obtain for the CDW-EIS model

$$\begin{aligned}\tilde{a}_{if}(\boldsymbol{\rho}) = -\mathrm{i}\frac{N(\varepsilon)N(\zeta)}{(2\pi)^{3/2}} \int_{-\infty}^{\infty} dt \int d\mathbf{r} \varphi_i(\mathbf{r_T}) \exp(\mathrm{i}\Delta\epsilon t - \mathrm{i}\mathbf{k}.\mathbf{r_T}) \\ \exp(-\mathrm{i}\nu \ln(vr_P + \mathbf{v}.\mathbf{r_P}))[\boldsymbol{\nabla}_{\mathbf{r_T}} {}_1F_1(\mathrm{i}\varepsilon; 1; \mathrm{i}kr_T + \mathrm{i}\mathbf{k}.\mathbf{r_T}) \\ .\boldsymbol{\nabla}_{\mathbf{r_P}} {}_1F_1(\mathrm{i}\zeta; 1; \mathrm{i}pr_P + \mathrm{i}\mathbf{p}.\mathbf{r_P})]\end{aligned} \tag{20}$$

where $\Delta\epsilon = E_k - \varepsilon_i$. Instead of $\tilde{a}_{if}(\boldsymbol{\rho})$ it is easier to calculate its two dimensional Fourier transform $R_{if}(\boldsymbol{\eta})$ as a function of the transverse heavy-particle relative momentum transfer $\boldsymbol{\eta}$; thus the scattering amplitude is

$$R_{if}(\boldsymbol{\eta}) = \frac{1}{2\pi} \int d\boldsymbol{\rho} \exp(\mathrm{i}\boldsymbol{\eta}.\boldsymbol{\rho}) \tilde{a}_{if}^{*}(\boldsymbol{\rho}) \tag{21}$$

where $\boldsymbol{\eta}.\mathbf{v}$=0.

Closed analytical expressions for the squares of the moduli of the scattering amplitudes $|R_{if}(\boldsymbol{\eta})|^2$ are given in the next section for neutral target atoms ranging from hydrogen up to and including argon. From the scattering amplitude $R_{if}(\boldsymbol{\eta})$ as a function of the transverse momentum $\boldsymbol{\eta}$ we may obtain the probability that for a certain fixed value of $\boldsymbol{\eta}$, the electron initially in a bound state of the target will be emitted to a continuum state with momentum $\mathbf{k}$. The integration over ϕ gives the double differential cross section as a function of the ejected electron energy E_k and angle θ:

$$\frac{d^2\sigma}{dE_k d(\cos\theta)} = k \int_0^{2\pi} \alpha(\mathbf{k}) d\phi. \tag{22}$$

2.2. CDW AND CDW-EIS SCATTERING AMPLITUDES

In this section we consider a generalization of the original CDW-EIS model, which was orginally designed to calculate the single ionization from a $1s$ orbital for the monoelectronic case of hydrogen to consider single ionization of any ground-state multielectron atom ranging from helium up to and including argon by charged particle impact. The scattering amplitudes considered here are obtained in closed analytical form. The advantage of our analytical method is that the extension to multielectron targets in the frozen core approximation is straightforward, and computation of the various cross sections is very fast. Numerical models of the CDW-EIS theory, requiring greater computational effort than the analytical model, have been considered by Gulyas et al (1995)[8] using Hartree Fock Slater target potentials and more recently by Gulyas et al (2000)[28] using target potentials

obtained from the optimized potential method Engel et al.[29] The drawback of the numerical approach is that no closed forms are possible for the wavefunctions or the transition amplitudes. On the otherhand it is possible using the numerical approach to get initial and final states that are completely orthogonal.

The validity of our analytical model for the multielectron targets lies in the description of the bound and continuum states of the target atom. The analytical form of the scattering amplitudes is derived by representing the initial-target bound state by a linear combination of Slater-type orbitals. The coefficients of these expansions are obtained using the tables of Clementi and Roetti.[27] The continuum states of the target atom are represented by a hydrogenic wavefunction with an effective charge chosen from the energy of the initial bound state in accord with equation (6). This of course means that the initial and the final states correspond to different potentials and hence are not orthogonal. Let us first consider the single ionization of the argon atom by ion impact. The electronic configuration of argon is $1s^2\ 2s^2\ 2p^6\ 3s^2\ 3p^6$. Thus to provide a description of the target wavefunctions for all the atoms ranging from the monoelectronic case of hydrogen to the multielectronic atoms from helium to argon, we first require the post form of the CDW-EIS scattering amplitudes for the $1s$, $2s$ and $3s$ orbitals in the K, L, and M shells (corresponding to the values $n = 1, 2$, and 3 of the principal quantum number, respectively). Secondly, we require post forms of the CDW-EIS scattering amplitudes for the $2p$ and $3p$ orbitals in the L and M shells (corresponding to the principal quantum numbers $n = 2$ and 3, respectively). The post form of the square of the CDW-EIS scattering amplitudes for the $1s$, $2s$, and $3s$ orbitals is given by

$$\begin{aligned} |R_{if}(\boldsymbol{\eta})|^2 &= \frac{|N(\varepsilon)N(\zeta)N(\nu)|^2}{2\pi^2\alpha^2\gamma^2 v^2} {Z_P}^2 {\tilde{Z}_T}^2 A \\ &\times \left| {}^{\mathrm{s}}A_I\ {}_2F_1(\mathrm{i}\nu;\mathrm{i}\zeta;1;\tau) - \mathrm{i}\nu\, {}^{\mathrm{s}}A_{II}\ {}_2F_1(\mathrm{i}\nu+1;\mathrm{i}\zeta+1;2;\tau)\right|^2, \end{aligned} \tag{23}$$

where ${}^{S}A_I$ and ${}^{S}A_{II}$ have different values depending on the atom selected. For the case of atoms from sodium through to Argon

$${}^{\mathrm{s}}A_I = \sum_{\lambda=1} b_\lambda Z_\lambda^{3/2} G_\lambda B_\lambda + \sum_{\lambda=2}^{8} \frac{2}{\sqrt{90}} b_\lambda Z_\lambda^{7/2} G_\lambda (A_\lambda B_\lambda + \mathrm{i} L_\lambda \hat{\mathbf{k}}.\mathbf{q}), \tag{24}$$

and

$${}^{\mathrm{s}}A_{II} = \sum_{\lambda=1} b_\lambda Z_\lambda^{3/2} G_\lambda B_\lambda \Omega_\lambda + \sum_{\lambda=2}^{8} \frac{2}{\sqrt{90}} b_\lambda Z_\lambda^{7/2} G_\lambda (A_\lambda B_\lambda \Omega_\lambda + \mathrm{i}\Omega_\lambda L_\lambda \mathbf{q}.\hat{\mathbf{k}}), \tag{25}$$

where

$$\begin{aligned} A_\lambda &= \frac{2(\mathrm{i}\varepsilon-1)(-1-\mathrm{i}\varepsilon)Z_\lambda(Z_\lambda-\mathrm{i}k)}{\alpha_\lambda(\alpha_\lambda+\beta_\lambda)} \\ &+ \frac{(\mathrm{i}\varepsilon-2)(\mathrm{i}\varepsilon-1)Z_\lambda^2}{\alpha_\lambda^2}+\frac{(\mathrm{i}\varepsilon-1)}{\alpha_\lambda}+\frac{(-1-\mathrm{i}\varepsilon)}{(\alpha_\lambda+\beta_\lambda)} \\ &+ \frac{(-1-\mathrm{i}\varepsilon)(-2-\mathrm{i}\varepsilon)(Z_\lambda-\mathrm{i}k)^2}{(\alpha_\lambda+\beta_\lambda)^2}, \end{aligned} \tag{26}$$

and

$$L_\lambda = \frac{2Z_\lambda(\mathrm{i}\varepsilon-1)}{\alpha_\lambda}+\frac{2(-1-\mathrm{i}\varepsilon)(Z_\lambda-\mathrm{i}k)}{\alpha_\lambda+\beta_\lambda}. \tag{27}$$

Physical quantities related to the final continuum target state are:

$$\mathbf{q} = -\boldsymbol{\eta} - \frac{\Delta\epsilon}{v}\hat{\mathbf{v}}, \tag{28}$$

$$G_\lambda = \frac{1}{{\alpha_\lambda}^2}\left(\frac{\alpha_\lambda}{\alpha_\lambda+\beta_\lambda}\right)^{1+\mathrm{i}\varepsilon}, \tag{29}$$

$$B_\lambda = \mathbf{q}.(\mathrm{i}\hat{\mathbf{k}}Z_\lambda+\mathbf{k}+\mathbf{q}), \tag{30}$$

$$C_\lambda = (\hat{\mathbf{p}}v-\mathbf{v}).(\mathrm{i}\hat{\mathbf{k}}Z_\lambda+\mathbf{k}+\mathbf{q}), \tag{31}$$

$$\alpha_\lambda = \frac{1}{2}[Z_\lambda^2+(\mathbf{q}+\mathbf{k})^2], \tag{32}$$

$$\beta_\lambda = -[\mathbf{q}.\mathbf{k}+k^2(1+\mathrm{i}\varepsilon_\lambda)], \tag{33}$$

$$\varepsilon_\lambda = \frac{Z_\lambda}{k}, \tag{34}$$

$$\alpha = \frac{1}{2}q^2, \tag{35}$$

$$\beta = \mathbf{q}.\mathbf{v}, \tag{36}$$

$$\gamma = \mathbf{p}.\mathbf{q}+\alpha, \tag{37}$$

$$\delta = \mathbf{p}.\mathbf{v}-pv+\beta. \tag{38}$$

The coefficients Z_λ and b_λ in the above expressions come from the description of the Roothan-Hartree-Fock wave functions of the particular atom which may range from hydrogen to argon inclusively.[27] The values of A, Ω_λ and τ are common to both the p shell and the s shell in all atoms yet have specific values for the two theories. For the CDW-EIS model we have

$$A = \exp(-2\pi\nu), \tag{39}$$

$$\Omega_\lambda = \frac{\alpha}{\beta\gamma B_\lambda}(\gamma C_\lambda+\delta B_\lambda), \tag{40}$$

$$\tau = 1 - \frac{\alpha\delta}{\beta\gamma}. \tag{41}$$

Expressions for ${}^{s}A_I$ and ${}^{s}A_{II}$ for ionization from the 1s and 2s states of target atoms ranging from lithium to neon are given by

$${}^{\mathrm{s}}A_I = \sum_{\lambda=1}^{2} b_\lambda Z_\lambda^{3/2} G_\lambda B_\lambda + \sum_{\lambda=3}^{6} \frac{1}{\sqrt{3}} b_\lambda Z_\lambda^{5/2} G_\lambda (A_\lambda B_\lambda - \mathrm{i}\hat{\mathbf{k}}.\mathbf{q}), \tag{42}$$

$${}^{\mathrm{s}}A_{II} = \sum_{\lambda=1}^{2} b_\lambda Z_\lambda^{3/2} G_\lambda B_\lambda \Omega_\lambda + \sum_{\lambda=3}^{6} \frac{1}{\sqrt{3}} b_\lambda Z_\lambda^{5/2} G_\lambda (A_\lambda B_\lambda \Omega_\lambda - \mathrm{i}\Omega_\lambda \mathbf{q}.\hat{\mathbf{k}}), \tag{43}$$

and

$$A_\lambda = \frac{(1-\mathrm{i}\varepsilon)Z_\lambda}{\alpha_\lambda} + \frac{(1+\mathrm{i}\varepsilon)(Z_\lambda - \mathrm{i}k)}{\alpha_\lambda + \beta_\lambda}. \tag{44}$$

For ionization from the 1s states of helium the value of ${}^{s}A_I$ and ${}^{s}A_{II}$ are given by

$${}^{\mathrm{s}}A_I = \sum_{\lambda=1}^{5} b_\lambda Z_\lambda^{3/2} G_\lambda B_\lambda, \tag{45}$$

and

$${}^{\mathrm{s}}A_{II} = \sum_{\lambda=1}^{5} b_\lambda Z_\lambda^{3/2} G_\lambda B_\lambda \Omega_\lambda. \tag{46}$$

The values of ${}^{\mathrm{s}}A_I$ and ${}^{\mathrm{s}}A_{II}$ for hydrogen can be found from this by taking the value of $Z_\lambda = \tilde{Z}_T = 1 = Z_T$ and $b_\lambda = 1$. Since our theoretical treatment is based on the independent electron model we can also easily obtain an analytical expression for the molecular hydrogen wave function. This may be derived by simplifying the H_2 target to an effective one-electron hydrogenic target with charge $\tilde{Z}_T = 1.064$, where $\frac{1}{2}\tilde{Z}_T^2$ is the single ionization energy of H_2. This approximation is valid for intermediate-to-high energy collisions where the cross sections for the H_2 target are essentially similar to twice the atomic-hydrogen cross sections.

Next turning to the 2p and 3p Roothan-Hartree-Fock orbitals, the post form of the square of the CDW-EIS scattering amplitudes may be given as

$$\begin{aligned} |R_{if}(\boldsymbol{\eta})|^2 \;=\; & \frac{|N(\varepsilon)N(\zeta)N(\nu)|^2}{2\pi^2 v^2 \alpha^2 \gamma^2} {Z_P}^2 \tilde{Z}_T^2 A \\ & \times |{}^{\mathrm{p}}A_I \;\; {}_2F_1(\mathrm{i}\nu; \mathrm{i}\zeta; 1; \tau) - \mathrm{i}\nu \;\; {}^{\mathrm{p}}A_{II} \;\; {}_2F_1(\mathrm{i}\nu + 1; \mathrm{i}\zeta + 1; 2; \tau)|^2. \end{aligned} \tag{47}$$

Again as in the s shells ${}^{\mathrm{p}}A_I$ and ${}^{\mathrm{p}}A_{II}$ have different values depending on the atom selected. Thus to calculate the various ionization cross sections

the contributions from the 2p and 3p spectra depend on the values of ${}^{\mathrm{p}}A_I$ and ${}^{\mathrm{p}}A_{II}$ which are given by

$$\begin{aligned} {}^{\mathrm{p}}A_I &= \sum_{\lambda=1} b_\lambda Z_\lambda^{3/2} G_\lambda [A_\lambda^{\hat{\mathbf{n}}} B_\lambda - Z_\lambda \hat{\mathbf{n}}.\mathbf{q}] \\ &+ \sum_{\lambda=2}^{8} \frac{b_\lambda Z_\lambda^{3/2}}{\sqrt{105}} [(-\frac{\mathrm{d}^3}{\mathrm{d}\mu^3}(G_\lambda)|_{\mu=0}) B_\lambda + 3(\frac{\mathrm{d}^2}{\mathrm{d}\mu^2}(G_\lambda)|_{\mu=0}) Z_\lambda \hat{\mathbf{n}}.\mathbf{q}], \end{aligned} \tag{48}$$

$$\begin{aligned} {}^{\mathrm{p}}A_{II} &= \sum_{\lambda=1} b_\lambda Z_\lambda^{3/2} G_\lambda [A_\lambda^{\hat{\mathbf{n}}} B_\lambda \Omega_\lambda - Z_\lambda \hat{\mathbf{n}}.\mathbf{q} \Omega_\lambda] \\ &+ \sum_{\lambda=2}^{8} \frac{b_\lambda Z_\lambda^{3/2}}{\sqrt{105}} [(-\frac{\mathrm{d}^3}{\mathrm{d}\mu^3}(G_\lambda)|_{\mu=0}) B_\lambda \Omega_\lambda + 3(\frac{\mathrm{d}^2}{\mathrm{d}\mu^2}(G_\lambda)|_{\mu=0}) Z_\lambda \hat{\mathbf{n}}.\mathbf{q} \Omega_\lambda], \end{aligned} \tag{49}$$

where

$$A_\lambda^{\hat{\mathbf{n}}} = \frac{(1-\mathrm{i}\varepsilon)}{\alpha_\lambda} Z_\lambda \hat{\mathbf{n}}.(\mathbf{q}+\mathbf{k}) + \frac{(1+\mathrm{i}\varepsilon)}{(\alpha_\lambda+\beta_\lambda)} Z_\lambda \hat{\mathbf{n}}.\mathbf{q}, \tag{50}$$

with

$$\hat{\mathbf{n}} = \begin{cases} \mathbf{i} & \text{for } 2\mathrm{p}_x \text{ state,} \\ \mathbf{j} & \text{for } 2\mathrm{p}_y \text{ state,} \\ \mathbf{k} & \text{for } 2\mathrm{p}_z \text{ state.} \end{cases} \tag{51}$$

Here

$$\begin{aligned} \frac{d^2}{d\mu^2}(G_\lambda)|_{\mu=0} &= \alpha_\lambda^{\mathrm{i}\varepsilon-1} (\alpha_\lambda+\beta_\lambda)^{-1-\mathrm{i}\varepsilon} \\ &[\frac{(1-\mathrm{i}\varepsilon)(2-\mathrm{i}\varepsilon)}{\alpha_\lambda^2} (\hat{\mathbf{n}}.\mathbf{q} + \hat{\mathbf{n}}.\mathbf{k})^2 Z_\lambda^2 + \frac{(\mathrm{i}\varepsilon-1) Z_\lambda^2}{\alpha_\lambda} \\ &+ \frac{2(1-\mathrm{i}\varepsilon)(1+\mathrm{i}\varepsilon) Z_\lambda^2 (\hat{\mathbf{n}}.\mathbf{q} + \hat{\mathbf{n}}.\mathbf{k}) \hat{\mathbf{n}}.\mathbf{q}}{\alpha_\lambda(\alpha_\lambda+\beta_\lambda)} \\ &+ \frac{(1+\mathrm{i}\varepsilon)(-Z_\lambda^2)}{(\alpha_\lambda+\beta_\lambda)} + \frac{(1+\mathrm{i}\varepsilon)(2+\mathrm{i}\varepsilon) Z_\lambda^2 (\hat{\mathbf{n}}.\mathbf{q})^2}{(\alpha_\lambda+\beta_\lambda)^2}], \end{aligned} \tag{52}$$

and

$$\begin{aligned} \frac{d^3}{d\mu^3}(G_\lambda)|_{\mu=0} &= \alpha_\lambda^{\mathrm{i}\varepsilon-1} (\alpha_\lambda+\beta_\lambda)^{-1-\mathrm{i}\varepsilon} Z_\lambda^3 [\frac{1}{\alpha_\lambda^3} (\hat{\mathbf{n}}.\mathbf{q} + \hat{\mathbf{n}}.\mathbf{k})^3 (1-\mathrm{i}\varepsilon)(2-\mathrm{i}\varepsilon)(3-\mathrm{i}\varepsilon) \\ &+ \frac{1}{(\alpha_\lambda+\beta_\lambda)^3} (\hat{\mathbf{n}}.\mathbf{q})^3 (1+\mathrm{i}\varepsilon)(2+\mathrm{i}\varepsilon)(3+\mathrm{i}\varepsilon) \\ &+ \frac{1}{\alpha_\lambda^2} (\hat{\mathbf{n}}.\mathbf{q} + \hat{\mathbf{n}}.\mathbf{k})(-3(1-\mathrm{i}\varepsilon)(2-\mathrm{i}\varepsilon)) \end{aligned}$$

$$
\begin{aligned}
&+ \quad \frac{1}{(\alpha_\lambda+\beta_\lambda)^2}(\hat{\mathbf{n}}.\mathbf{q})(-3(1+\mathrm{i}\varepsilon)(2+\mathrm{i}\varepsilon)) \\
&+ \quad \frac{1}{\alpha_\lambda^2(\alpha_\lambda+\beta_\lambda)}(\hat{\mathbf{n}}.\mathbf{q}+\hat{\mathbf{n}}.\mathbf{k})^2(\hat{\mathbf{n}}.\mathbf{q})(3(1-\mathrm{i}\varepsilon)(2-\mathrm{i}\varepsilon)(1+\mathrm{i}\varepsilon)) \\
&+ \quad \frac{1}{\alpha_\lambda(\alpha_\lambda+\beta_\lambda)}(\hat{\mathbf{n}}.\mathbf{q})(-3(1-\mathrm{i}\varepsilon)(1+\mathrm{i}\varepsilon)) \\
&+ \quad \frac{1}{\alpha_\lambda(\alpha_\lambda+\beta_\lambda)}(\hat{\mathbf{n}}.\mathbf{q}+\hat{\mathbf{n}}.\mathbf{k})(-3(1-\mathrm{i}\varepsilon)(1+\mathrm{i}\varepsilon)) \\
&+ \quad \frac{1}{\alpha_\lambda(\alpha_\lambda+\beta_\lambda)^2}(\hat{\mathbf{n}}.\mathbf{q}+\hat{\mathbf{n}}.\mathbf{k})(\hat{\mathbf{n}}.\mathbf{q})^2(3(1-\mathrm{i}\varepsilon)(1+\mathrm{i}\varepsilon)(2+\mathrm{i}\varepsilon))].
\end{aligned}
\tag{53}
$$

Partial contributions to the cross sections for atoms from boron to neon from the outer L shell depend on the values of ${}^{p}A_I$ and ${}^{p}A_{II}$ which are given by

$$
{}^{\mathrm{p}}A_I = \sum_{\lambda=1}^{4} b_\lambda Z_\lambda^{3/2} G_\lambda [A_\lambda^{\hat{\mathbf{n}}} B_\lambda - Z_\lambda \hat{\mathbf{n}}.\mathbf{q}], \tag{54}
$$

and

$$
{}^{\mathrm{p}}A_{II} = \sum_{\lambda=1}^{4} b_\lambda Z_\lambda^{3/2} G_\lambda [A_\lambda^{\hat{\mathbf{n}}} B_\lambda \Omega_\lambda - Z_\lambda \hat{\mathbf{n}}.\mathbf{q} \Omega_\lambda], \tag{55}
$$

where $A_\lambda^{\hat{\mathbf{n}}}$ and $\hat{\mathbf{n}}$ are defined as above in equation (50) and (51) respectively.

3. Longitudinal electron velocity distributions

In this section we apply the theory developed in the preceding sections to a series of experiments carried out by Schmitt et al[3] using the so-called reaction microscope for ultra-low energy electrons emitted from neutral target atoms. This state of the art experimental technique has enabled experimentalists to measure simultaneously the momenta of the emitted electrons and the recoiling residual-target ion and many new striking features have been found.

Details of the emission of ultra-low and low energy electrons can be seen in the cross sections doubly differential in the longitudinal and transverse momenta. The formula for the double differential cross section as a function of the longitudinal electron velocity $v_{e||}$ for various transverse electron velocity $v_{e\perp}$ cuts can be obtained from equation (57) by noting that

$$
E_k = \frac{1}{2}(p_{e||}^2 + p_{e\perp}^2) \tag{56}
$$

where $p_{e\perp}$ is the transverse momentum of the ejected electron. Hence

$$
\frac{1}{2\pi v_{e\perp}} \frac{d^2\sigma}{dv_{e||} dv_{e\perp}} = \frac{1}{2\pi} \int_0^{2\pi} \alpha(\mathbf{k}) d\phi. \tag{57}
$$

The doubly differential cross sections are defined in this manner in order to correct for the increasing volume element with increasing $v_{e\perp}$. We have adopted cylindrical coordinates in velocity space with the axis along the beam propagation direction. This choice of coordinate system is well adapted to the azimuthal symmetry of the electron emission if no scattering plane is defined. Thus the cross sections will have the shape and dimension of the triply differential cross sections assuming azimuthal symmetry. The experimental single ionization data have been normalised to the total CDW-EIS cross sections for each target considered. In figure 1 the doubly differential cross section is shown as a function of the longitudinal electron velocity for various transverse velocity cuts in singly ionizing 3.6 MeV/u Au^{53+} on helium collisions.

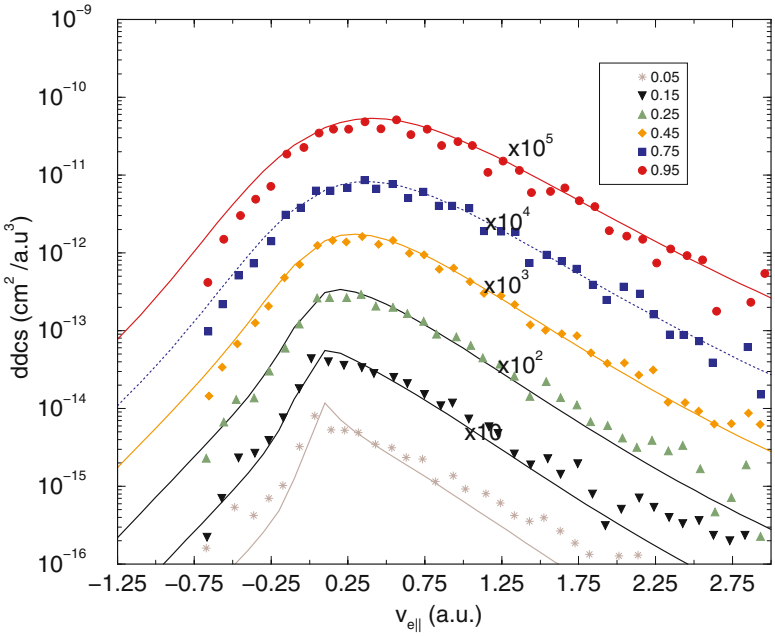

Figure 1. Double differential cross sections (ddcs $= \frac{1}{2\pi v_{e\perp}} \frac{d^2\sigma}{dv_{e||}dv_{e\perp}}$) as a function of the longitudinal electron velocity for various transverse velocity cuts in singly ionizing collisions of 3.6 MeV/u Au^{53+} ions on He. CDW-EIS results (solid lines: Schulz et al[3]) are shown along with the experimental data from Schmitt et al.[3] Cross sections at different $v_{e\perp}$ are multiplied by factors of 10 respectively.

There is excellent agreement between the CDW-EIS theory and measurement. This is observed in both shape and in absolute magnitude. A strong

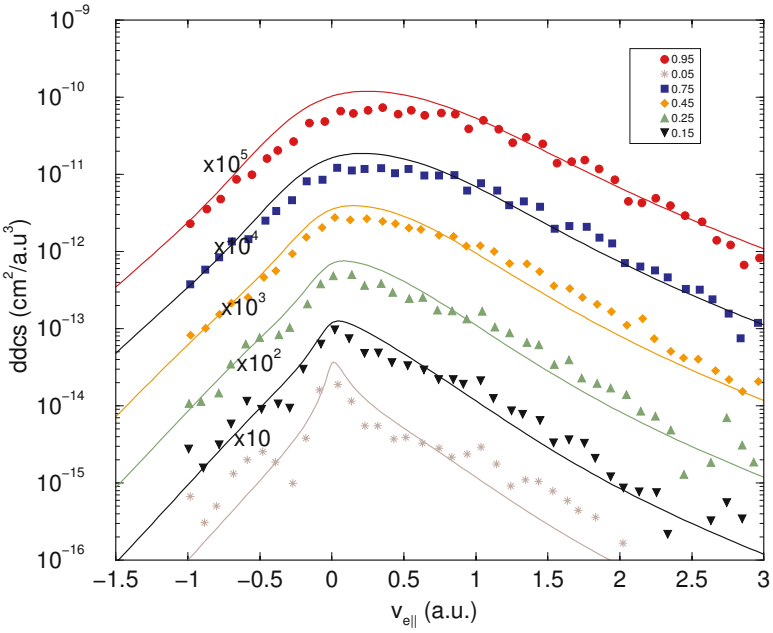

Figure 2. Double differential cross sections (ddcs = $\frac{1}{2\pi v_{e\perp}} \frac{d^2\sigma}{dv_{e||} dv_{e\perp}}$) as a function of the longitudinal electron velocity for various transverse velocity cuts in singly ionizing collisions of 3.6 MeV/u Au^{53+} ions on Ne. CDW-EIS results (solid lines: McSherry et al[30]) are shown along with the experimental data from Moshammer et al.[20] Cross sections at different $v_{e\perp}$ are multiplied by factors of 10 respectively.

forward-backward asymmetry is found. All the longitudinal velocity distributions for different transverse velocities including their maxima are shifted towards positive velocities. These asymmetrical distributions are attributed to the two-centre effects i.e. the post collision interaction effect. The CDW-EIS model predicts these features since it is adapted to take account of the long-range Coulomb interaction of the projectile and target field. The emerging long-range potential of the Au^{53+} projectile ion provides a large perturbation strength of Z_p/v_p (where Z_p and v_p are the charge and velocity of the projectile). This attracts the emitted electron pulling it into the forward direction. With increasing $v_{e\perp}$ the electron distributions are shifted to higher values of $v_{e||}$ while the electrons with very small $v_{e\perp}$ =0.05 a.u. show a maximum close to $v_{e||} = 0$ a.u..

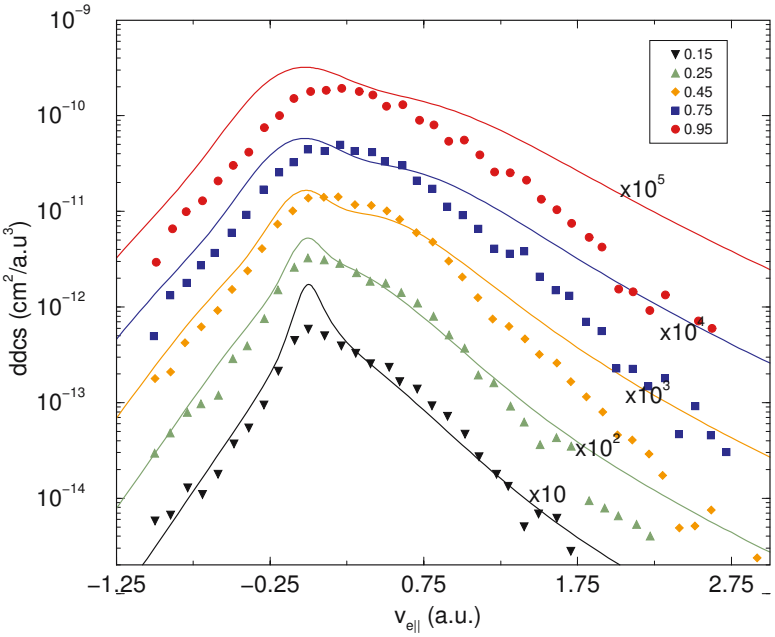

Figure 3. Double differential cross sections (ddcs = $\frac{1}{2\pi v_{e\perp}} \frac{d^2\sigma}{dv_{e||} dv_{e\perp}}$) as a function of the longitudinal electron velocity for various transverse velocity cuts in singly ionizing collisions of 3.6 MeV/u Au^{53+} ions on Ar. CDW-EIS results (solid lines: McSherry et al[30]) are shown along with the experimental data from Moshammer et al.[20] Cross sections at different $v_{e\perp}$ are multiplied by factors of 10 respectively.

In figures 2, 3 and 4 the experimental longitudinal electron velocity distributions for different transverse electron velocities are shown for singly ionizing 3.6 MeV/u Au^{53+} on neon and argon respectively. As in the case of helium the theoretical CDW-EIS and experimental distributions show the characteristic features of single target ionization by fast heavy ions and most of these features have been discussed above. In particular both neon and argon show the sharp maximum at $v_{e||} = 0$ as was shown in figure 1 for helium. This feature is closely analogous to the one observed for $v_e = v_p$ for electron capture to the continuum mechanism or to electron loss to the continuum which is often referred to as the cusp. The electrons with $v_e = v_T = 0$ in the low lying continuum states of the target ion also form a sharp peak known as the 'target cusp'.

Beyond these well established characteristic features however the total width of the electron distributions is much narrower for the argon target than for neon or helium. These patterns are due to the signatures of the initial state wave function. In figure 3, a systematic discrepancy between experiment and theory appears at higher electron energies. This discrepancy occurs due to one of the basic postulates of the CDW-EIS model, namely that it is based on the independent electron model which considers there

to be only one active electron. Within this model it is assumed that the entire impact parameter range contributes only to single ionization. However, particularly at low impact parameters, single ionization competes with double and multiple ionization. By plotting the summation of differential cross sections irrespective of the degree of ionization as measured by conventional spectroscopy, this extra contribution can be included. Figure 4 shows that this considerably improves the accord between the CDW-EIS theory and experimental data for the complete range of energies considered. This demonstrates that reliable ionization data can be obtained only when the charge state of the remaining target ion is known in the experiment.

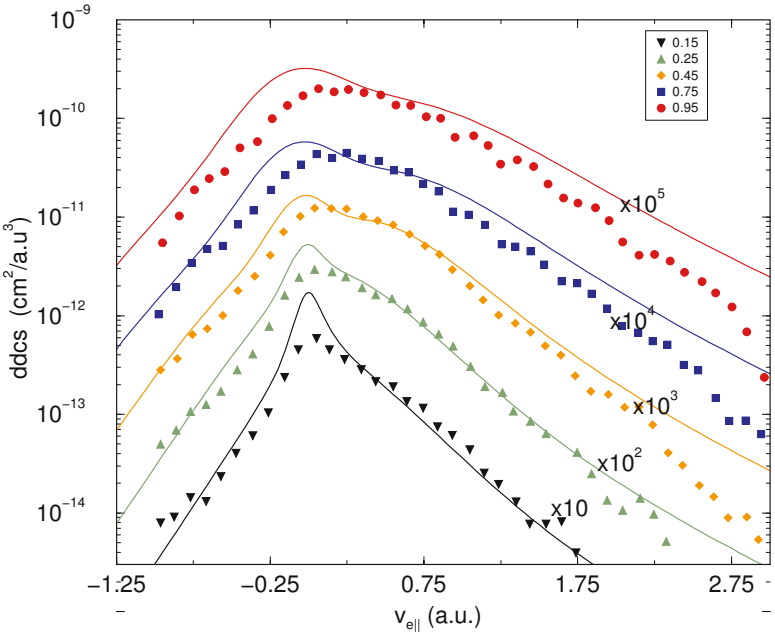

Figure 4. Double differential cross sections (ddcs $= \frac{1}{2\pi v_{e\perp}} \frac{d^2\sigma}{dv_{e||} dv_{e\perp}}$) for electron emission due to single, double or triple ionization of Ar by 3.6 MeV/u Au^{53+} ions. The DDCS for the specified recoil-ion charge states are added according to their relative contribution to the total cross section. CDW-EIS results (solid lines: McSherry et al[30]) are shown along with the experimental data from Moshammer et al.[20] The experimental data are divided by 1.4. Cross sections at different $v_{e\perp}$ are multiplied by factors of 10 respectively.

Similar theoretical calculations using the CDW-EIS approximation for neon and argon have been carried out by Moshammer et al.[20] Their calculations are based on using a generalised version of the CDW-EIS model which differs from our model by solving the stationary Schrödinger equation with Hartree-Fock-Slater model potentials for the target atoms. In the case of argon their theoretical CDW-EIS results showed a shoulder effect at

lower transverse velocity cuts which they attributed to the nodal structure of the initial argon $3p_0$ orbital whose contribution dominates in this region. This effect does not appear in our model as shown in figures 3 and 4. This shoulder effect has also been analysed recently by Gulyás et al[28] using the CDW-EIS model approximation with a target potential obtained from the optimized potential method. They concluded that the shoulder effect was an artefact caused by a deficiency of the Hartree-Fock-Slater model. Both our work and the recent work of Gulyás et al[28] suggest that it is better to avoid using the Hartree-Fock-Slater model[20] in calculations for ion-atom collisions since it can produce artificial structures in the low energy continuum wave functions especially for the heavier targets such as argon. However all three studies[20, 28, 30] confirm that the target wave function is sensitive to the initial state.

4. Fully Differential cross sections for highly charged ions

The calculations in the previous section show that CDW-EIS is valid if the parameter $\frac{Z_P}{v_P^2}$ is small compared with 1 a.u.. The CDW-EIS model is thus generally viewed as the state of the art approximation for heavy ion impact. Given the success of the CDW-EIS model in describing the electron spectra for highly charged ions in collision with neutral target atoms it was a suprise to discover that the CDW-EIS model had difficulty in reproducing the experimental results of Schulz et al[4] involving fully differential cross sections for 3.6 MeV amu^{-1} $Au^{24+,53+}$ on helium. Thus in this section we seek to examine the possible causes of the discrepancies between theory and experiment.

In particular it was considered initially[4] that the above discrepancy was due to the lack of orthogonality between the EIS and the CDW state wavefunctions. However, Bubelev and Madison[31] reported that orthogonality was not required as the interaction potential was already included in the wavefunctions. Therefore, it was concluded that the missing projectile-target internuclear potential might account for the lack of the recoil peak. Ciappina et al[38] have pointed out that when dealing with multielectronic targets, initial and final states become a source of concern, as exact wavefunctions are not available in these cases. Slater orbital expansions of Roothan-Hartree-Fock wavefunctions are usually employed for the initial bound state.[27] In order to circumvent this problem in the final continuum, the system is reduced to that of one active electron in a model potential. In that scheme the remaining target electrons provide a partial screening of the nuclear charge. The simplest approach is to represent the continuum by hydrogenic wavefunctions with an effective nuclear charge accounting for the screening effects. This allows us to obtain an analytical expression for both the wavefunctions and the transition amplitude. Although Gulyas et al[8] have extended the CDW-EIS model to include both initial and final numerically calculated

wavefunctions, we feel it is still desirable to study further improvements to the simple and successful CDW-EIS approximation which still allows us to obtain an analytical expression for the transition amplitude to calculate the fully differential cross sections.

Recently in the literature a number of authors[36–38] have examined the ionization and excitation of targets by ion impact using different potentials within theoretical models very similiar to the CDW-EIS model. In particular Bhattacharya et al[37] studied the ionization of argon by proton impact in the energy range 10-300 keV. In their study they used the Born initial-state wave function and the final state was described using the product of two continuum distorted waves involving distinct electron nucleus interaction. Charge screening was also included in their model via a model potential which included both short and long range effects. In our present work we adopt this model with the exception that we employ an eikonal phase in the initial channel. This model we will refer to as "CDW-EIS Bhattacharya".[37] Olivera et al[36] studied the electronic excitation of dielectronic targets by ion impact. Their model used an independent-electron approximation where one electron, the passive one remains frozen during the collision. The interaction in Olivera's model[36] between the projectile and passive electron along with the internuclear potential is accounted for by a static potential. Distorted initial and final wave functions are described in Olivera's model by the symmetrical eikonal model. In our present work we also adopt Olivera's model with the exception that the distortion in our initial wavefunction is accounted for by an eikonal phase and the distortion in the final wave function is accounted for by a continuum-distorted-wave. This model we will refer to as "CDW-EIS Olivera".

This section brings all of that work together and compares with our own versions of the CDW-EIS model used here to see if any particular version of the CDW-EIS model is more effective than the others so far as the parameters considered are concerned. In particular our present model focuses on discussing the effect which including the internuclear potential has on the results of fully differential cross sections for highly charged ions. Furthermore we consider the effect of eliminating the RHF wavefunction. This latter is considered as we feel that care ought to be taken when considering RHF wavefunctions, which can lead to unphysical components.[32]

The case of ionization of the projectile may be neglected due to its large charge which means that the electrons will be tightly bound and therefore very unlikely to be ionized.

The fully differential cross section (FDCS) is given by

$$\frac{d^5\sigma}{d^3\mathbf{k}d^2\boldsymbol{\eta}} = \left|R_{if}(\boldsymbol{\eta})\right|^2, \tag{58}$$

where $\mathbf{k}$ is the ejected-electron wave number, $\boldsymbol{\eta}$ is the transverse component of the change in the relative momentum of the nuclei and R_{if} is the

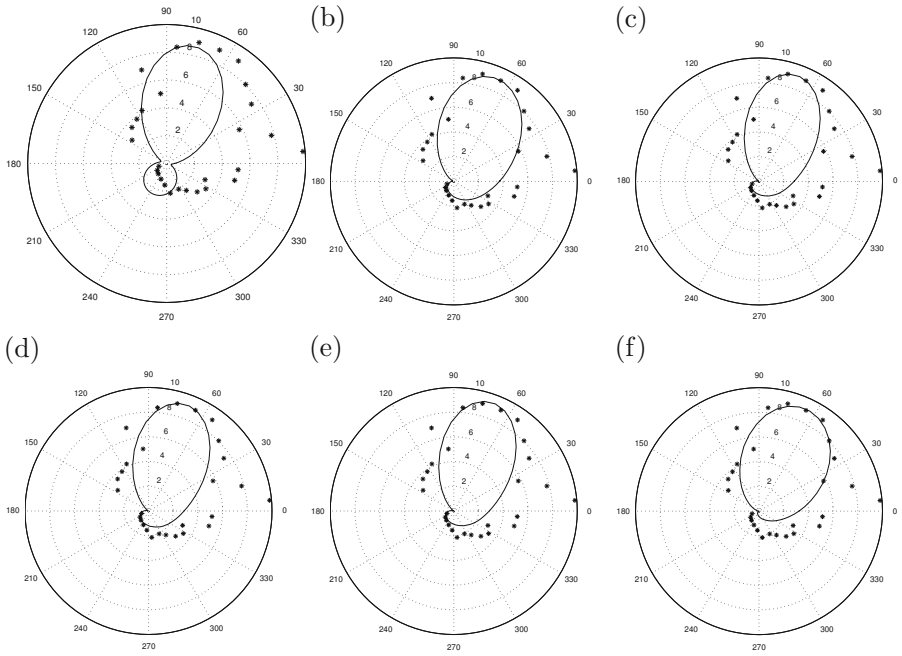

Figure 5. FDCS for electrons emitted into the scattering plane for a fixed electron energy, $E_k = 4\ eV$, and fixed magnitude of the momentum transfer (see eqn (6)) $q = 0.65$ $a.u.$, as a function of the polar electron emission angle for 3.6 MeV amu^{-1} Au^{24+}+ He collisions. The following notation is used: * experimental data of Fischer et al,[5] — theoretical results. The six diagrams above represent the following models: (a) FBA, (b) CDW-EIS, (c) CDW-EIS+nn, (d) CDW-EIS+RHF, (e) CDW-EIS Olivera, (f) CDW-EIS Bhattacharya. The polar radius of figures (a) to (f) is $10a.u.$.

scattering amplitude.[6] The scattering amplitude may be given by:

$$\tilde{R}_{if}(\boldsymbol{\eta}) = \frac{1}{2\pi}\int d\boldsymbol{\rho}\exp(i\boldsymbol{\eta}.\boldsymbol{\rho})\tilde{a}_{if}(\boldsymbol{\rho}), \tag{59}$$

where $\boldsymbol{\rho}$ is the impact parameter and $\mathbf{v}$ is the impact velocity, with $\boldsymbol{\eta}\cdot\mathbf{v} = 0$ and $\boldsymbol{\rho}\cdot\mathbf{v} = 0$. $\tilde{a}_{if}(\boldsymbol{\rho})$ is the transition amplitude without the internuclear potential and the tilde so indicates.

From McCann,[33] the transition amplitude including the internuclear potential is given by:

$$a_{if}(\boldsymbol{\rho}) = (\rho v)^{\frac{2iZ_TZ_P}{v}}\tilde{a}_{if}(\boldsymbol{\rho}), \tag{60}$$

where Z_T and Z_P are the target and projectile-nucleus charges respectively.

This means that the scattering amplitude including the internuclear potential is given by:

$$R_{if}(\boldsymbol{\eta}) = \int_0^\infty \rho d\rho \mathrm{J}_0(\eta\rho)(\rho v)^{2i\overline{\gamma}}\int_0^\infty \tilde{R}_{if}(\boldsymbol{\eta}')\mathrm{J}_0(\eta'\rho)\eta' d\eta', \tag{61}$$

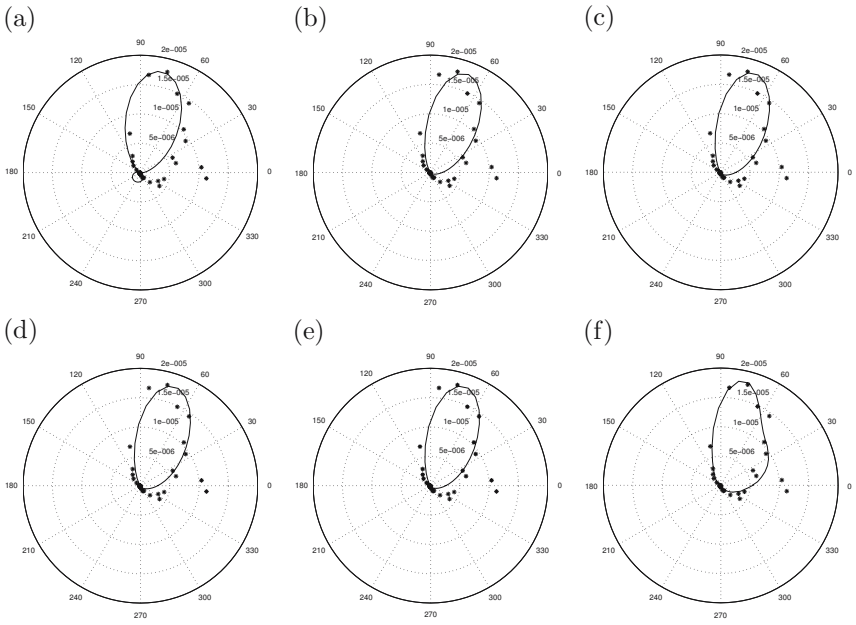

Figure 6. Same as figure 4.1 but for singly ionizing collisions of 3.6 MeV amu^{-1} Au^{53+}+ He collisions with electron energy, $E_k = 17.5\ eV$, and momentum transfer $q = 1.5\ a.u.$ and except for * which now represents the experimental data of Schulz et al.[4] The polar radius of figures (a) to (f) is 2E-5 $a.u.$.

where $\overline{\gamma} = \frac{Z_T Z_P}{v}$, as in McSherry et al.[34] The authors call CDW-EIS including this term CDW-EIS+nn.

The ground state wavefunction, $\varphi_i(\mathbf{r_T})$, for the outer electron orbital of the neutral target was obtained from Crothers,[35] with $He^+(1s)$ taken as the inner-electron orbital and with

$$\varphi(\mathbf{r_T}, z_0) = z_0^{3/2}\pi^{-1/2}\exp(-z_0 r_T) \tag{62}$$

where the value of z_0 is $(1.8072)^{1/2}$. This is essentially an open shell Shull-Löwdin wavefunction, suitably normalized and symmetrized.

Figures 5, 6 and 7 represent various computer simulations pertaining to the FDCS for electrons emitted into the scattering plane in 3.6 MeV amu^{-1} Au$^{24+,53+}$+ He collisions. The experimental results are absolute with the theoretical data normalized to them. The results are shown in the form of polar plots with the FDCS plotted as polar radial functions of the scattering (polar) angle. The figures contain six different models, each of which has been labelled for discussion. The top left (a) is FBA, top middle (b) is CDW-EIS, without internuclear potential, top right (c) CDW-EIS+nn. The bottom left (d) is CDW-EIS with RHF wavefunctions (CDW-EIS+RHF),

bottom middle (e) is CDW-EIS with the internuclear potential given by[36] (CDW-EIS Olivera) as described earlier in this section. This model is shown bottom right (f) is CDW-EIS with the model potential of[37] (CDW-EIS Bhattacharya) as described earlier in this section. All the models except for (d) CDW-EIS+RHF, have used the modified wavefunction of (62); also the internuclear potential has been included in all models except for (a) the FBA and (b) the CDW-EIS models.

Figure 5 shows the FDCS for electrons emitted into the scattering plane in 3.6 MeV amu^{-1} Au^{24+}+ He collisions at momentum transfer of $q = 0.65$ a.u. and electron energy $E_k = 4\ eV$, where the momentum transfer q is defined by

$$q^2 = \eta^2 + (\Delta\epsilon/v)^2 \tag{63}$$

given $\Delta\epsilon$ is the resonance defect. The perturbation parameter is quite large at 2.0. The experimental data are from.[5] The theoretical data for (a) is scaled down by 909, while the theoretical data for (b) to (f) have been scaled up by factors of 1.2, 3.8, 4.1, 3.9 and 8.2 respectively. The FBA gives a poor approximation as expected, due to the large perturbation but has been included for reference. The models indicate that the best method for producing qualitative results is CDW-EIS (b) in this case. All the simulations reproduce the upper lobe about 60° but do not reproduce the lobe in the forward direction. All the CDW-EIS variations give a 'bottom' lobe, currently thought to be the recoil peak.[5] It is a concern that the magnitude of the different theoretical models varies widely with the FBA overestimating the experimental data while the others underestimate it. The PCI ought to be more effective for a stronger perturbation.

To see this consider 3.6 MeV amu^{-1} Au $^{53+}$+ He collisions at the momentum transfer of $q = 1.5\ a.u.$ and electron energy $E_k = 17.5\ eV$. In this regime the perturbation is 4.4, which is considered to be a large perturbation. Figure 6 shows the FDCS for this collision, with experimental data from Schulz et al.[4] The theoretical data for figures (a) to (f) have been scaled down by factors of 2.3E7, 2.0E5, 1.8E4, 1.6E4, 1.8E4 and 185 respectively. The PCI is seen to influence the models including the internuclear potential and leads to slightly better results for them. However, the model that gives the best qualitative agreement is the CDW-EIS Bhattacharya simulation. In this model the FDCS is starting to peak in the forward direction and is closer to the two results nearest 0° than any other model. It gives good agreement for FDCS between 270° and 360°, which is not achieved in any of the other models. In this case all models overestimate the experimental data, with (f) being closest.

In figure 7 the FDCS for 3.6 MeV amu^{-1} Au^{53+}+ He collisions with electron energy $E_k = 4.0\ eV$, and momentum transfer $q = 1.0\ a.u.$ have been presented with experimental data from Fischer et al.[5] This is a high-perturbation regime as in figure 6. The theoretical data for (a) and (b) was

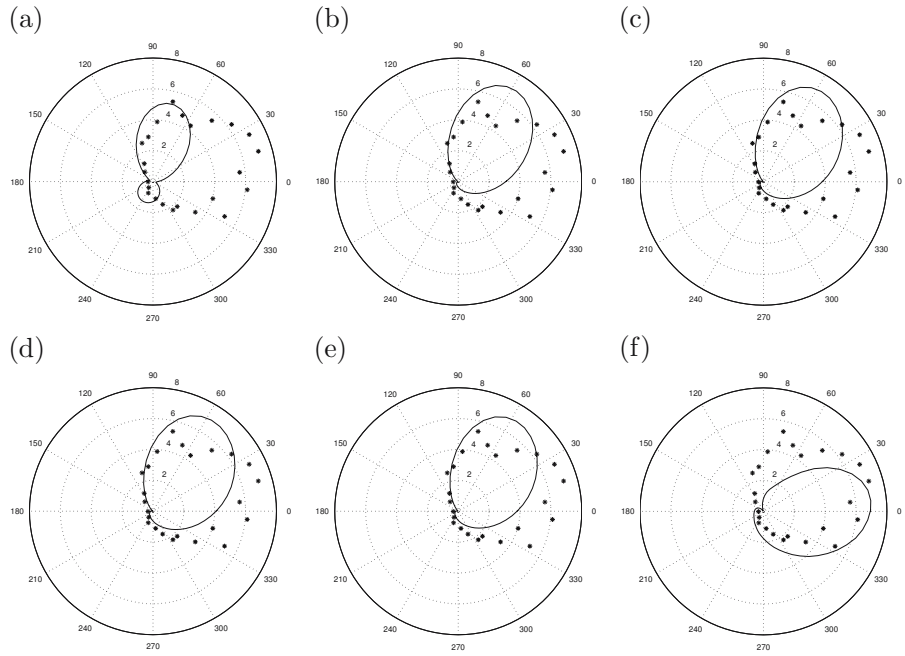

Figure 7. Same as figure 4.1 but for the singly ionization collisions of 3.6 MeV amu^{-1} Au^{53+}+ He collisions with electron energy, $E_k = 4.0\ eV$, and momentum transfer $q = 1.0$ *a.u.* and except for * which represents the experimental data of Fischer et al.[5] The polar radius of figures (a) to (f) is 8 *a.u.* .

scaled down by factors of 5.3E3 and 1.9, while the theoretical data for (c) to (f) was scaled up by factors of 4.6, 5.0, 4.6 and 146 respectively. Models (b) to (e) all appear to reproduce the upper lobe about 60°, and the recoil peak to a lesser extent, but fail to reproduce the peak in the forward direction. Conversely, the CDW-EIS Bhattacharya simulation provides the best agreement with the peak in the forward direction but does not appear to have picked up the upper lobe about 60°.

If we take the same parameters as in figure 7 namely $q = 1.0$ *a.u.*, but for the Au^{24+}+ case, no pattern emerges.
Using a different target wavefunction instead of RHF wavefunctions has made very little difference in this case. In a recent paper by Ciappina et al,[38] results are presented to illustrate post-prior discrepancies in the CDW-EIS simulation for ion-helium ionization. It suggests that using the prior version gives better results than the post version due to the prior version being less sensitive to the choice of the final state. This would be of benefit as the final state, CDW, cannot be computed exactly due to the 3-body problem and normally it is modelled with a hydrogenic continuum state for the electron-residual target state. Using the prior version may lead

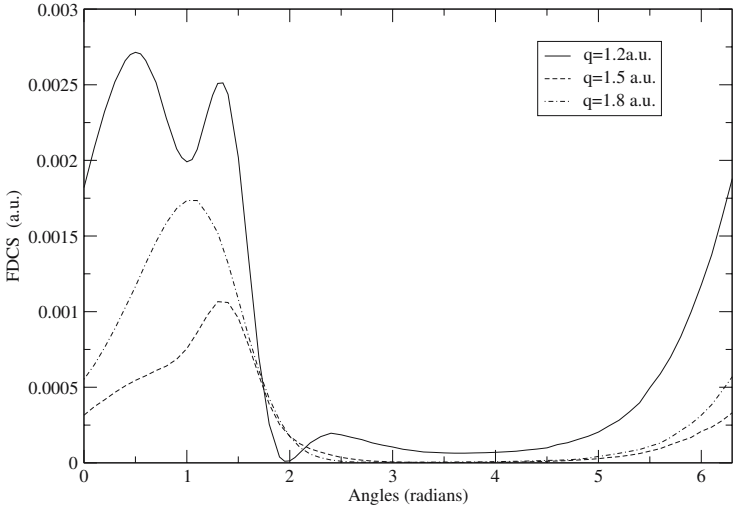

Figure 8. Same as figure 6(f), except, for clarity, linear plot instead of polar plot, and theoretical FDCS for $q = 1.5 \pm 0.3$ a.u. contrasted with the theoretical FDCS for $q = 1.5$ a.u. of figure 6(f).

to better agreement between theory and experiment. The discord may be due to omitting the out of collision plane events caused by rotational coupling.[39, 40] In reference[4] the electron energies and the momentum transfer have a degree of uncertainity which strongly influences results of theoretical calculations. For example, when considering 3.6 MeV amu^{-1} Au^{53+}+ He collisions, with $E_k = 17.5\ eV$ and $q = 1.5\ a.u$ the degree of error associated with q is 0.3. This degree of error changes the shape of the theoretical data for model (f), CDW-EIS Bhattacharya, depending heavily on the actual value of q, see figure 8. This degree of error may be expected in the experimental results[5] accordingly.

For our study on fully differential cross sections for highly charged ions using different variations of the CDW-EIS model, it has been concluded that, for the single ionization of 3.6 MeV amu^{-1} Au^{24+}+ He collisions, the standard CDW-EIS model, (b), provides a slightly better approximation than the other variations considered in this paper. It is apparent from this study for 3.6 MeV amu^{-1} Au^{53+}+ He collisions, that the model which yields the best qualitative results is CDW-EIS with the model potential from Bhattacharya et al,[37] (f). A 'bulge' in the forward direction is starting to appear for $E_k = 17.5\ eV$ but for $E_k = 4\ eV$ only the peak in the forward direction appears. It may indicate that the standard CDW-EIS model is more appropriate at lower projectile charges and lower perturbations and that the CDW-EIS Bhattacharya is best suited to higher projectile charges and stronger perturbations. Clearly these processes require further theoretical and experimental study.

5. Summary

To conclude we have examined the applicability of the continuum-distorted-wave theory to experiments carried out using the reaction microscopy technique for both doubly differential cross sections for longitudinal electron velocities and fully differential cross sections applied to the single ionization of 3.6 MeV amu^{-1} Au$^{24+,53+}$ on neutral target atoms. For the case of the longitudinal electron velocity distributions discussed in section 3 we found that overall good agreement was obtained between theory and experiment. In particular it was noted that a strong forward-backward asymmetry was found for the ultra-low and low energy electron emission. It was also found that the DDCS are extremely sensitive to the initial state target wave function.

In our second study of fully differential cross sections applied to the single ionization of 3.6 MeV amu^{-1} Au$^{24+,53+}$ on helium in section 4 we used different versions of the CDW-EIS model and compared with the experimental data of Schulz et al[4] and Fischer et al[5] for fully differential cross sections. The model that overall gave the best agreement with experiment at high projectile charges, low electron velocity and high momentum transfer is the CDW-EIS model which employs the potential from Bhattacharya et al. This particular version of the CDW-EIS approximation is based on a model potential which has physically appropriate short and long range behaviour. It is hoped that further calculations using the CDW-EIS model to simulate fully differential cross sections, both qualitatively and quantitatively may lead to a fuller understanding of single ionization by highly charged ion impact.

Acknowledgements

One of the authors (R.T. Pedlow) wishes to thank the Department of Employment and Learning, Northern Ireland, for financial support.

References

1. N. Stolterfoht, R.D. DuBois, R.D. Rivarola *Electron Emission in Heavy-Ion Atom Collsions*, Vol 20, Toennies, ed., Springer-Verlag, Berlin, 1997.
2. R. Moshammer, J. Ullrich, M. Unverzagt, W. Schmidt, P. Jardin, R. E. Olson, R. Mann, R. Dörner, V. Mergel, U. Buck, H. Schmidt-Böcking Phys. Rev. Lett. **73**, 3371 (1994).
3. W. Schmitt, R. Moshammer, S.F.C. O'Rourke, H. Kollmus, L. Sarkadi, R. Mann, S. Hagmann, R.E. Olson, J. Ullrich Phys. Rev. Lett. **81**, 4337 (1998).
4. M. Schulz, R. Moshammer, A.N. Perumal, J. Ullrich J. Phys. B: At. Mol. Opt. Phys. **35**, L161 (2002).
5. D. Fischer, R. Moshammer, M. Schulz, J. Ullrich J. Phys. B: At. Mol. Opt. Phys. **36**, 3555 (2003).

6. D.S.F. Crothers, J.F. McCann J. Phys. B: At. Mol. Phys. **16**, 3229 (1983).
7. P.D. Fainstein, V.H. Ponce, R.D. Rivarola J. Phys. B: At. Mol. Opt. Phys. **21**, 287 (1988).
8. L. Gulyás, P.D. Fainstein, A. Salin J. Phys. B: At. Mol. Opt. Phys. **28**, 245 (1995).
9. S.F.C. O'Rourke, I. Shimamura, D.S.F. Crothers Proc. R. Soc. Lond. A **452**, 175 (1996).
10. S.F.C. O'Rourke, R. Moshammer, J. Ullrich, J. Phys. B: At. Mol. Opt. Phys. **30**, 5281 (1997).
11. I.M. Cheshire, Proc. Phys. Soc. **84**, 89 (1964).
12. Dž. Belkič J. Phys. B: At. Mol. Phys. **11**, 3529 (1978).
13. P.D Fainstein, R.D. Rivarola Phys. Lett. A **150**, 23 (1990).
14. M. McCartney, D.S.F. Crothers J. Phys. B: At. Mol. Opt. Phys. **26**, 4561 (1993).
15. S.F.C O'Rourke, W. Schmitt, R. Moshammer, J. Ullrich, B.S. Nesbitt, D.S.F. Crothers *New Directions in Atomic Physics* edited by Whelan et al., Kluwer Academic/Plenum Publishers, New York, p223 (1999).
16. C. McGrath, D.M. McSherry, M.B. Shah, S.F.C. O'Rourke, D.S.F. Crothers, G. Montgomery, H.B. Gilbody, C. Illescas, A. Riera (2000) J. Phys. B: At. Mol. Phys. **33**, 3693 (2000).
17. B.S. Nesbitt, M.B. Shah, S.F.C. O'Rourke, C. McGrath, J. Geddes, D.S.F. Crothers J. Phys. B: At. Mol. Opt. Phys. **33**, 637 (2000).
18. S.F.C. O'Rourke, D.S.F. Crothers J. Phys. B: At. Mol. Opt. Phys. **30**, 2443 (1997).
19. W. Schmitt, R. Moshammer, H. Kollmus, S. Hagmann, R. Mann, R.E. Olson, S.F.C. O'Rourke, J. Ullrich Physica Scripta **T80**, 335 (1999).
20. R. Moshammer, P.D. Fainstein, M. Schultz, W. Schmitt, H. Kollmus, R. Mann, S. Hagmann, J. Ullrich Phys. Rev. Lett. **83**, 4721 (1999).
21. J. Fiol, R.E. Olson J. Phys. B: At. Mol. Opt. Phys. **37**, 3947 (2004).
22. M. Foster, D.H. Madison, J.L. Peacher, J. Ullrich J. Phys. B: At. Mol. Opt. Phys. **37**, 3797 (2004).
23. M. Schulz, R. Moshammer, D. Fischer, J. Ullrich J. Phys. B: At. Mol. Opt. Phys. **37**, 4055 (2004).
24. B.H. Bransden, M.R.C. McDowell, *Charge Exchange and The Theory of Ion-Atom Collisions* (Oxford, Claredon, 1990).
25. D.S.F. Crothers J. Phys. B: At. Mol. Phys. **15**, 2061 (1982).
26. Belkič, Dž., Gayet, R., Salin, A., Phys. Rep. **56**, 279 (1979).
27. E. Clementi, C. Roetti At. Data. Nucl. Data. Tables **14**, 177 (1974).
28. L. Gulyás, T. Kirchner, T. Shirai, M. Horbatsch Phys. Rev. A **62**, 022702, (2000).
29. E. Engel, S.H. Vosko Phys. Rev. A **47**, 2800 (1993).
30. D.M. McSherry, S.F.C. O'Rourke, R Moshammer and J. Ullrich Applications of Accelerators in Research and Industry, Edited by J.L. Duggan and L.L. Morgan The American Institute of Physics, 133 (2001).
31. V.E. Bubelev, D.H. Madison J. Phys. B: At. Mol. Opt. Phys. **26**, 3541 (1993).
32. P. Knowles, M. Schütz, H.J. Werner, Ab initio Methods for Electron Correlation in Molecules in Modern Methods and Algorithms of Quantum Chemistry, Edited by Grotendorst, John von Neumann, Institute for computing, NIC series **88**, 69 (2002).
33. J.F. McCann Thesis, Queen's University Belfast (1984).
34. D.M. McSherry Thesis, Queen's University Belfast (2001).
35. D.S.F. Crothers J. Phys. B: At. Mol. Opt. Phys. **19**, 463 (1986).
36. G.H. Olivera, C.A. Ramirez, R.D. Rivarola Phys. Rev. A. **47**, 1000 (1993).
37. S. Bhattacharya, R. Das, N.C. Deb, K. Roy, D.S.F. Crothers Phys. Rev. A. **68**, 052702 (2003).
38. M.F. Ciappina, W.R. Cravero, C.R. Garibotti J. Phys. B: At. Mol. Opt. Phys. **36**, 3775 (2003).
39. D.S.F. Crothers, D.M. McSherry, S.F.C. O'Rourke, M.B. Shah, C.McGrath, H.B. Gilbody Phys. Rev. Lett. **88**, 053201 (2002).
40. S.F.C. O'Rourke, D.M. McSherry, D.S.F. Crothers J. Phys. B: At. Mol. Opt. Phys. **36**, 341 (2003).

PART III

COMPLEXES AND CLUSTERS

STUDY OF INTERACTION ABILITIES USING AN ENERGY PARTITIONING SCHEME IN SOME WATER CLUSTERS

C. KOZMUTZA, E. TFIRST, F. BARTHA* AND O. KAPUY

Institute of Physics, Budapest University of Technology and Economics, Budafoki út 8. H-1111 Budapest, Hungary
kozmutza@phy.bme.hu

Abstract. The separation of the total energy into one- and two-body terms for interacting molecules at the HF-SCF level has already been proved to provide useful information. Several energy contributions for the linear water dimer molecule and for some hexamer water clusters were calculated using various basis sets in the present work. The results suggest that some partitioned energy terms derived separately for each contributing monomer (using the method of Separated Molecular Orbitals) show significant differences for the proton donor and the proton acceptor molecules in the linear structured water dimer. The sum of these terms per each subunit corresponds to a (partitioned) total energy quantity for the given subsystem. This energy contribution allows characterizing the proton donor / acceptor ability of the monomers. In this way the identification of the monomers by their proton donor / acceptor nature in some water hexamers was also investigated.

1. Introduction

The independent particle model is a well-defined basic strategy for quantum chemistry. In cases of closed shell systems the electronic structure can be well described by using a single determinant built from one-particle functions. Applying the variation procedure, the ab initio method provides the Hartree-Fock-Roothaan equations, and solving them the canonical molecular orbitals can be obtained. The advantage of the HF method is its conceptual simplicity: nowadays molecular systems with many hundreds of electrons can be treated by this procedure. As the HF model describes the static status of electrons, certain effects (related to dynamical electron correlation) cannot be investigated by this method alone. More sophisticated models are needed for analyzing dispersion

J.-P. Julien et al. (eds.),
Recent Advances in the Theory of Chemical and Physical Systems, 337–345.

forces, e.g. in weakly interacting molecular structures [1]. The HF method gives quite acceptable values for one-electron quantities. This holds also for some energetic terms, like the kinetic energy.

The hydrogen bond is often regarded as a special case of interaction. The H-bond in the linear water dimer structure may also be called donor-acceptor interaction [2]. Due to its importance in life, a tremendous number of investigations, both experimental and theoretical, refer to the water dimer and larger clusters [3-9]. Several solvation approaches have been elaborated, including some considering explicitly the solvent molecules [10, and refs. therein]. The possibility of using localized orbitals in these alternative methods has also been investigated [11-15].

It is known that the conformation of a given molecular structure is one of its main characteristics. The geometrical parameters of the molecules can in a large number of cases be calculated, to a good approximation, by using the HF method. The local minima on the potential energy surface can be assessed by using the virial theorem. The analysis of isolated molecules indicates that the virial theorem holds at equilibrium geometries: the ratio of the total (E) and kinetic (T) energies with opposite signs (-E/T) is (nearly) one. The ratio of the potential (V) and kinetic (T) energies with opposite signs (-V/T) is also often taken as a characteristic feature of the system, and equals nearly two at equilibrium. Such terms are useful for checking the quality of the basis set actually used.

2. The SMO method

The Separated Molecular Orbitals (SMO) method has been described earlier in details in refs. [16, 17]. At the Hartree-Fock SCF level the closed shell total energy has the following form:

$$E_{HF} = E_{nuc} + 2\sum_{i} T_i + V_i + \sum_{i,j}\left(2J_{ij} - K_{ij}\right)$$

where

$$E_{nuc} = \sum_{\substack{a,b \\ a>b}} Z_a Z_b R_{ab}^{-1},$$

$$T_i = -\frac{1}{2}\int \psi_i^*(\mathbf{r})\,\Delta\psi(\mathbf{r})\,d^3\mathbf{r},$$

$$V_i = -\sum_{a} Z_a \int \psi_i^*(\mathbf{r})\,\left|\mathbf{r}-\mathbf{R}_a\right|^{-1}\psi_i(\mathbf{r})\,d^3\mathbf{r},$$

$$J_{ij} = \iint \psi_i^*(\mathbf{r}_1)\,\psi_j^*(\mathbf{r}_2)\,\left|\mathbf{r}_1-\mathbf{r}_2\right|^{-1}\psi_i(\mathbf{r}_1)\,\psi_j(\mathbf{r}_2)\,d^3\mathbf{r}_1 d^3\mathbf{r}_2,$$

$$K_{ij} = \iint \psi_i^*(r_1)\,\psi_j^*(r_2)\,|r_1 - r_2|^{-1}\,\psi_j(r_1)\,\psi_i(r_2)\,d^3r_1 d^3r_2 .$$

Using SMO's this expression can be separated into one- and two-body terms by

$$E_{HF} = \sum_{A} E_{HF}^{A} + \sum_{\substack{A,B \\ A>B}} E_{HF}^{AB},$$

where

$$E_{HF}^{A} = E_{nuc}^{A} + 2\sum_{i\in O_A} T_i + V_i^A + \sum_{i,j\in O_A} (2J_{ij} - K_{ij})$$

and

$$E_{HF}^{AB} = E_{nuc}^{AB} + 2\left(\sum_{i\in O_A} V_i^B + \sum_{i\in O_B} V_i^A\right) + 2\sum_{\substack{i\in O_A \\ j\in O_B}} 2J_{ij} - K_{ij} .$$

A and *B* label the monomers, *O*-s are sets of occupied orbitals counted to monomer *A* or *B*, respectively, and

$$E_{nuc}^{A} = \sum_{\substack{a,b\in N_A \\ a>b}} Z_a Z_b R_{ab}^{-1},$$

$$E_{nuc}^{AB} = \sum_{\substack{a\in N_A \\ b\in N_B}} Z_a Z_b R_{ab}^{-1},$$

$$V_i^A = -\sum_{a\in N_A} Z_a \int \psi_i^*(r)\,|r - R_a|^{-1}\,\psi_i(r)\,d^3r .$$

The partitioned energy terms can thus be derived separately for each contributing monomer (M). The sum of these terms per each subunit corresponds to a (partitioned) total energy quantity for the given subsystem (EM).

Various energy terms calculated for the linear water dimer molecule and for some hexamer water clusters at the HF level in both the canonical and the "separated" representations, using various basis sets are given in the present work. This study is twofold. First, the differences between the proton donor and proton acceptor molecules have been assessed in the linear water dimer. The EM energy contributions (obtained in the separated representation) are expected to characterize the proton donor / acceptor ability of the monomers. Secondly, a possibility of identification of a proton donor or acceptor character of the monomers in some water hexamers was tested.

3. Results obtained for a linear water dimer structure

Let us first discuss the results obtained in canonical representation. The energy quantities calculated by using eight different basis sets for a water monomer are given in Table I.

Certain regularities in basis set dependence could be found as comparing the values obtained for the energy quantities. The extension of the 6-31G and 6-311G basis sets, e.g., lead to similar changes in the kinetic energy and the two-electron energy. It does not hold the same, however, for the potential energy terms. As to the more extended basis sets, the VDZ and VTZ (and their augmented sets, too) show remarkable similarities regarding the one-electron potential, the kinetic and the two-electron energy contributions.

It is worthwhile analyzing whether the same conclusion holds when the water dimer structure is considered. A series of calculations have been performed for a linear structured water dimer, the values are listed in Table II.

TABLE I. Canonical energy components in a water monomer.

Basis sets	Energies (given in hartree)				-V/T
	Total	One-electron potential	Kinetic	Two-electron	
6-31G	-75.9839	-198.9791	75.9839	37.8015	1.9998
6-31G/d	-76.0105	-198.8796	75.8229	37.8503	2.0025
6-311G	-76.0093	-199.1120	76.0858	37.8205	1.9990
6-311G/d	-76.0315	-199.1859	76.0856	37.8723	1.9993
VDZ	-76.0268	-199.1421	75.9897	37.9303	2.0005
Aug VDZ	-76.0414	-198.9072	75.9282	37.7412	2.0015
VTZ	-76.0572	-199.1280	76.0067	37.8678	2.0007
Aug VTZ	-76.0606	-199.0141	75.9599	37.7972	2.0013

TABLE II. Canonical energy components in a water dimmer.

Basis sets	Energies (given in hartree)				-V/T
	Total	One-electron potential	Kinetic	Two-electron	
6-31G	-151.9798	- 434.5822	152.0020	93.9209	1.9990
6-31G/d	-152.0300	- 434.3686	151.6528	94.0064	2.0025
6-311G	-152.0309	- 434.8239	152.1702	93.9434	1.9991
6-311G/d	-152.0735	- 434.9622	152.1718	94.0376	1.9994
VDZ	-152.0628	- 434.8696	151.9850	94.1425	2.0005
Aug VDZ	-152.0889	- 434.4469	151.8873	93.7915	2.0013
VTZ	-152.1213	- 434.8466	152.0233	94.0226	2.0006
Aug VTZ	-152.1269	- 434.6558	151.9475	93.9019	2.0012

The quantities in Table II unambiguously show that for the water dimer the terms follow similar regulations as found for the water monomer. The problem, however, is that the analysis of the water dimer does not provide information on the monomers behavior: donor or acceptor, when using the canonical representtation. Let us consider smaller or larger basis sets; the results do not provide any characteristic feature on the monomers although (due to a sub-symmetric relationship of the monomers in the dimer) the electron structures of the monomers are different.

A question arises, whether the various energy quantities derived by the SMO method could yield useful information on the monomer's role (proton donor or acceptor) in the weakly interacting water dimer system.

The energy values obtained for the proton donor and acceptor subsystems in a linear water dimmer, calculated in the separated representation, are given in Table III.

The basis sets are selected from those presented in the previous Tables. First it can be stated that using the SMO method the kinetic energy / partitioned total energy ratios calculated according to the monomers are close to -1. It is found by using other basis sets, too [18, 19]. The results presented here also support that the separator of the SMO method works adequately.

TABLE III. Separated energy terms in a water dimmer.

	Basis sets	Energies (given in hartree)			
		Partitioned total	One-electron potential	Kinetic	Two-electron
Proton donor	6-31G/d	-76.0013	-198.9298	75.8340	37.8980
	6-311G	-75.9998	-199.1431	76.0790	37.8679
	6-311G/d	-76.0224	-199.1843	76.0527	37.9128
	VTZ	-76.0432	-199.1546	75.9907	37.9014
Proton acceptor	6-31G/d	-75.9873	-198.8732	75.8369	37.8525
	6-311G	-75.9863	-199.1016	76.0910	37.8276
	6-311G/d	-76.0095	-199.1414	76.0622	37.8733
	VTZ	-76.0296	-199.1222	76.0013	37.8665

Let us now compare the partitioned total energy (EM) for the different monomers (acceptor and donor). The results show that the separation conserves the relative difference for this energy term vs. the variation of the basis set when comparing them to the non-interacting monomers values (Table I). This holds both for proton donor and acceptor-type monomers. It is also remarkable that the EM's are regularly higher for the proton acceptor subsystems than for the proton donor ones. In other words, the electron structure of the proton donor subsystem is significantly more compact for any of the basis sets used. Going to the partitioned one-electron potential energy terms, a similar conclusion can be

found: the values are systematically different for the proton donor and acceptor monomers. This holds for the two-electron energy as well. These results suggest that the proton donor / acceptor behavior can be definitively (and in a simple way) characterized by certain energy terms decomposed using the separation procedure. The values presented in the Tables show that basis sets of rather different size and quality produce similar results in characterizing a donor or acceptor molecule in a standard H-bond. Comparing the partitioned kinetic energy quantities calculated for the proton donor and acceptor molecules, however, the values are rather close to each other. This result suggests that the kinetic energy quantities play some special role in interacting systems consisting of similar monomers such as water aggregates.

Following the analysis of the characteristic features determined for the proton donor and acceptor molecules in a linear water dimer, we performed the same study for some water hexamer clusters. The structures considered are representative of those published in a previous paper [18].

4. Study of the energetic contributions in water hexamer molecules

Five different structures were investigated in separated representation, using two basis sets. The results are given in Table IV.

TABLE IV. Energy terms in two basis sets for some water hexamer clusters (separated representation). Values are given in hartree.

	Boat	Chair	Prism	W6t	W6q
Basis set 6-31G/d	-75.9821	-75.9814	-75.9880	-75.9845	-75.9842
	-75.9837	-75.9814	-75.9817	-75.9853	-75.9850
	-75.9816	-75.9814	-75.9932	-75.9676	-75.9692
	-75.9802	-75.9814	-76.0034	-75.9684	-75.9701
	-75.9797	-75.9814	-75.9875	-75.9927	-75.9914
	-75.9735	-75.9814	-75.9798	-75.9811	-75.9807
Basis set VTZ	-76.0179	-76.0171	-76.0252	-76.0237	-76.0229
	-76.0186	-76.0171	-76.0183	-76.0241	-76.0234
	-76.0174	-76.0171	-76.0367	-76.0189	-76.0195
	-76.0165	-76.0171	-76.0451	-76.0197	-76.0208
	-76.0164	-76.0171	-76.0260	-76.0433	-76.0419
	-76.0158	-76.0171	-76.0164	-76.0228	-76.0196

The selected structures are the followings: the boat and chair denote well-known configurations (structural parameters and figures can be found in ref. 18), the prism refers to the structure producing the lowest total energy. The w6t and w6q (as proposed by one of the authors [E. K.] of ref. 18) correspond to two cage structures. In this study these five water hexamer structures could be

considered as "sample" configurations. The EM total energy was determined for each contributing monomer in the given hexamer structure. This (partitioned) total energy is important at the HF level and proves useful for characterizing the water molecules in the separated representation (see previous section).

The results can be summarized as follows. First, where the symmetry allows, the monomers EM quantities are quite different. Taking the reference values from the chair structure (ch/EM), it can be noticed that the EM values resulting for the boat structures are nearby the same: three are slightly above and three below. It is remarkable, however, that in the prism structure there are two EM values rather low, namely those obtained for monomers 3 and 4. The partitioned total energy values calculated for monomers 1 to 6 in the boat, chair and prism hexamer structures using basis set 6-31G/d are depicted on Figure I. Looking at the (partitioned) total energies obtained for the other two hexamers, it can be noticed that the EM value calculated for monomer 5 is relatively low in both the w6t and w6q structures. This can be seen on Figure II, where the EM values calculated for the monomers in the w6t and w6q systems are presented. The results suggest that in the prism, w6t and w6q structures there are some monomers in certain specific positions. The EM results predict extra proton donor or proton acceptor ability in these structures. It should be emphasized, that the results are in good agreement with those presented in our earlier work [18].

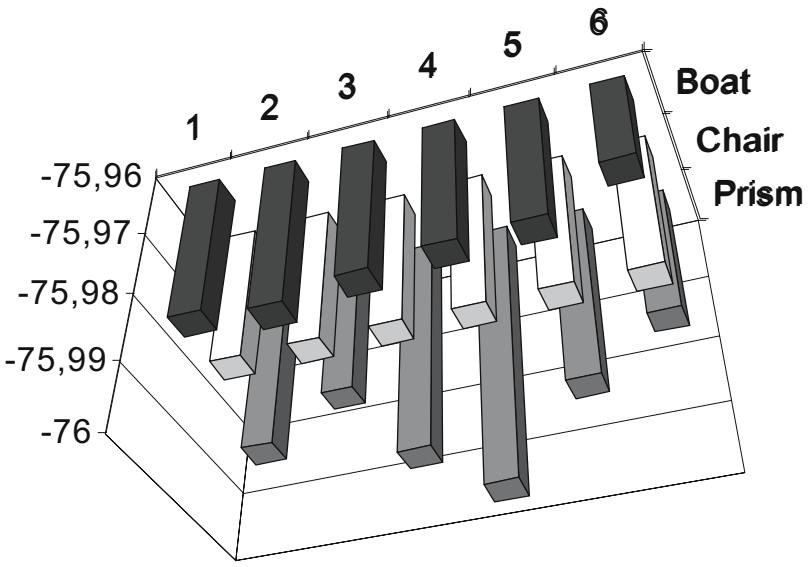

Figure I. Partitioned total energy values (in hartree) calculated for three different water hexamer using basis set 6-31G/d.

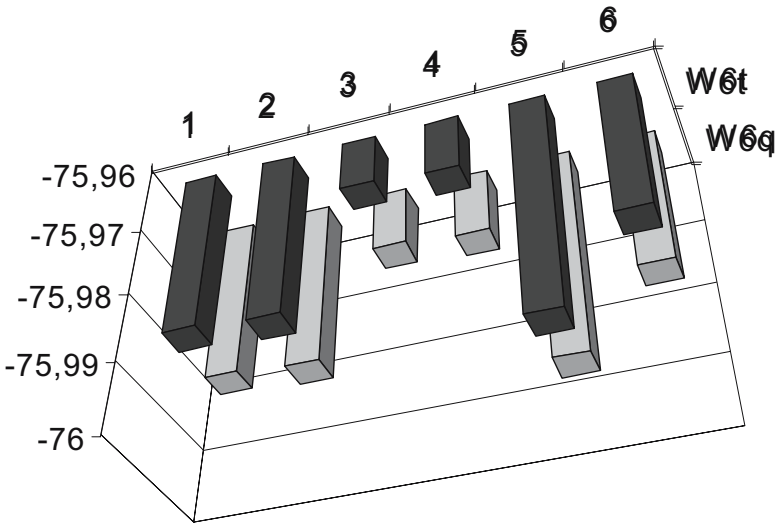

Figure II. Partitioned total energy values (in hartree) calculated for two different water hexamer using basis set 6-31G/d.

5. Conclusion and suggestion

The results presented in this work show that in the linear structured water dimer the partitioned energy terms calculated for the proton donor and acceptor molecules are significantly different (except the kinetic energy). The electron structure of the proton donor molecule was found more compact than that of the acceptor subsystem, when compared their (partitioned) total energy EM values. This result is in an excellent agreement with our pre-vious results obtained on the separated molecular orbital energies [17].

In this work the separated representation was used to determine the energetic quantities for each contributing monomer in some water hexamer systems, too. On one hand, the results obtained for the monomers in these structures did not suggest to identify the same proton donor or acceptor nature as it was found for the linear water dimer. On the other hand, in three of the water hexamer structures that were investigated, some monomers showed a specific nature. These results confirm previous results [18] that there are extra interaction abilities in these hexamer structures (prism, w6t and w6q).

Acknowledgements

C. K. is thankful to the Office of Project Research (Hungary) for financial support. She is also indebted to Dr. J. H. van Lenthe for valuable discussions.

(*) F. Bartha is an independent scientist.

References

1. J.H. van Lenthe, J.G.C.M. van Duijneveldt-van de Rijdt and F.B. van Duijneveldt, Weakly bonded systems, Ab initio methods in Quantum Chemistry, vol. II, in Advances in Chemical Physics, vol. LXIX, Wiley, 1987.
2. W.G. Schneider, J. Chem. Phys. **23**, 26 (1955).
3. E.D. Isaacs, A. Shukla, P.M. Platzman, D.R. Hamann, B. Barbielini and C.A. Tulk, Phys. Rev. Lett. **82***,* 600 (1999).
4. A.H. Romero, P.L. Silvestrelli and M. Parinello, J. Chem. Phys. **115**, 115 (2001).
5. M.J. Tubergen, Ch.R. Torok, and R.J. Lavrich, J. Chem. Phys. **119**, 8397 (2003).
6. A. Hamza and I. Mayer, Int. J. Quant. Chem. **82**, 53 (2001).
7. E.S. Kryachko and M.T. Nguyen, J. Phys. Chem. **A 106**, 4267 (2002).
8. B. Silvi, E.S. Kryachko, O. Tischchenko, F. Fuster and M.T. Nguyen, Mol. Phys. **100**, 1659 (2002).
9. A.M. Saitta, T. Strässle, G. Rousse, G. Harnel, S. Klotz, R.J. Nelmes and J.S. Loveday, J. Chem. Phys. **121**, 8430 (2004).
10. P. Bandyopadhyay, M.S. Gordon, B. Mennucci and J. Tomasi, J. Chem. Phys. **116**, 5023 (2002).
11. J. Langlet, J. Caillet, J. Bergès and P. Reinhardt, J. Chem. Phys. **118,** 8157 (2003).
12. C. Kozmutza and E. Kapuy, Int. J. Quant. Chem. **38**, 665 (1990).
13. C. Humpel and H.-J. Werner, J. Chem. Phys. **104**, 6286 (1996).
14. P. Reinhardt and J.-P. Malrieu, J. Chem. Phys. **109**, 7632 (1998).
15. C. Kozmutza and E. Kapuy, Chem. Phys. Lett. **226**, 484 (1994).
    C. Kozmutza and E. Tfirst, J. Mol. Struct. (Theochem) **671**, 67 (2004).
16. C. Kozmutza and E. Tfirst, Advances in Quantum Chemistry **31**, 231 (1998).
17. C. Kozmutza and E. Tfirst, in "Recent Research Developments in Quantum Chemistry" (Transworld Research Network, Trivandrum, India), vol. **3**, 169 (2002).
18. C. Kozmutza, E. Kryachko and E. Tfirst, J. Mol. Struct. (Theochem) **501-502**, 435 (2000).
19. F. Bartha, O. Kapuy, C. Kozmutza and C. van Alsenoy, J. Mol. Struct. (Theochem) **666-667**, 117 (2003).

AB INITIO VAN DER WAALS POTENTIAL ENERGY SURFACES APPLICATION TO COMPLEXES OF BROMINE MOLECULE WITH HELIUM ATOMS

ÁLVARO VALDÉS, RITA PROSMITI, PABLO VILLARREAL AND GERARDO DELGADO-BARRIO
Instituto de Matemáticas y Física Fundamental, C.S.I.C., Serrano 123, 28006 Madrid, Spain

Abstract. The additivity of the two and three-body potential energy surfaces (PES) is studied for the van der Waals (vdW) complex formed by Br_2 and two Helium atoms. First, the three-dimensional interaction potential for $HeBr_2$ molecule is calculated using a coupled-cluster (CCSD(T)) method. This surface shows a double-minimum topology in agreement with the available experimental data. In turn, an intermolecular potential energy surface for He_2Br_2 complex in the ground state is calculated at the levels of fourth-order (MP4) Møller-Plesset and coupled-cluster [CCSD(T)] approximations. It is found that results obtained by summing the above [CCSD(T)] three-body parameterized $HeBr_2$ interactions and the He–He interaction are in very good accord with the corresponding MP4/CSSD(T) configuration energies. Variational calculations using the above potential form are performed to calculate the bound states of the vdW complex and these results are compared with available experimental data.

1. Introduction

Until recently, most models of vdW interactions were based on additive atom-atom forces. However, during recent years *ab initio* methods have progressed sufficiently and interaction potentials between rare-gas atoms and dihalogen molecule have been computed with high accuracy,[1,2] predicting the existence of two minima on the potential energy surface at linear and T-shaped configurations. A linear structure is not consistent with an additive pair potential form used for describing the intermolecular forces and, it became clear that even in the well region of a vdW bond such models do not

J.-P. Julien et al. (eds.),
Recent Advances in the Theory of Chemical and Physical Systems, 347–369.

work.[1,2] Linear species have been determined by microwave spectroscopy for several interhalogen complexes (Ar–ClF,[3] Kr–ClF,[4] He–ClF,[1] Ar–ICl[5]) and for Ar–Cl_2,[6] Ar–I_2.[7] Further, recent experimental studies by Loomis and coworkers in the B ← X spectrum have shown that spectral features are associated with transitions of the linear complexes of He–ICl,[8] Ne–ICl[9] and He–Br_2.[10] Also, recent *ab initio* calculations confirm the existence of two isomers for Rg–F_2,[11] Rg–Cl_2,[12] Rg–Br_2[13] and Ar–I_2[14] in accord with available experimental data.

Van der Waals (vdW) complexes of dihalogen molecule surrounded by several rare gas atoms have been intensely studied over the past decades by high resolution spectroscopy techniques. Such experimental investigations have covered a large number of vdW complexes including He_nI_n (n=1-3),[15] Ne_nI_2 (n=1-6),[16,17] Ne_nBr_2,[18] Rg_2Cl_2 (Rg=He,Ne,Ar)[19–21] and Ar_nHX (X=Cl or F and n=1-3 or 4).[22–24] The objective of these studies has been to elucidate the structure, spectroscopy and dynamics of vdW complexes and thus providing direct information on intermolecular forces.

An interesting example is the experimental studies by Janda and coworkers[19–21] on Rg_2Cl_2 clusters. In their attempt[19] to characterize the structure of the He_2Cl_2 complex they failed in fitting the rotationally resolved excitation spectrum using a rigid rotor tetrahedral structural model, which results from pairwise additive potentials. Such structure has been successful in the cases of Ne_2Cl_2 and Ar_2Cl_2. Several similar rigid rotor geometries have also failed to fit their observed data. This led them to conclude that He_2Cl_2 is an extremely floppy, liquidlike cluster without any average structure and the dynamics of He_nCl_2 complexes will be quite different from their Rg_nCl_2 analogs. In situations like these, theoretical calculations on energetics and dynamics of such systems become indispensable for the quantitative modeling and interpretation of the experimental spectra.[25–30] Several theoretical studies based on a sum of atom-atom pairwise interactions and using quantum Monte Carlo[29] or variational[30] calculations have been carried out. Both results, in agreement with the experimental analysis, suggest the floppiness of the ground vdW state of He_nCl_2 (n=2,3) and emphasize the importance of performing exact calculations for such liquid-like systems.

Studies of larger species are more complex and the difficulty in the evaluation of their potential surfaces increases with their size. Up to now accurate potentials have been obtained by inversion of spectroscopic data[31,32] or through high level *ab initio* calculations[33–40] for several triatomic vdW systems. Thus, the interactions for such clusters are available with satisfactory accuracy, which permits the testing of various models of nonadditivity for their ability to reproduce a number of experimental observations. These facts made complexes composed of two rare-gas atoms and a dihalogen molecule especially attractive targets for the study of nonadditive forces. The first attempt to extract information on nonadditive interactions from

spectroscopic data has been undertaken by Hutson *et al.*[41] in similar vdW systems. They have used the microwave spectroscopic data of Klots *et al.*[42] to calculate a number of spectroscopic constants of Ar_2HCl cluster, concluding that the data from the microwave spectra was not sufficient to reconstruct the three-body potential uniquely and more extensive regions of the potential surface should be measured. *Ab initio* studies have been also carried out[43,44] and the three-body effects in the Ar_2HF and Ar_2HCl clusters have been studied using Møller-Plesset pertubation theory, where the nonadditivite interactions have been found to be large and repulsive around the equilibrium geometries for both systems. Later, Hutson and coworkers have presented nonadditive potentials for Ar_2HF[45] and Ar_2HCl[46] incorporating different contributions to the three-body forces arising from the interaction between the permanent multipoles of the HF molecule and the exchange quadrupole caused by distortion of the two Ar atoms as they overlap.

The aim of the present study is to investigate the validity of the pairwise additivity of two-body and three-body potentials for He_2Br_2. These results are compared with *ab initio* calculations[47] and a simple model of the three-body potential is proposed to determine well depths and equilibrium structures for different isomeric configurations of the complex, as well as the minimum energy pathways through them. Additionally, variational methods are used to calculate the vibrational states of He_2Br_2. The wavefunctions of the lower states are analyzed in terms of probability distributions of the internal coordinates and the zero-point energy of the vdW cluster is evaluated.

The paper is organized as follows. In the next section we present first results of a CCSD(T) PES for the $HeBr_2$ complex, together with bound states calculations. The purpose of this study is to construct a reliable three-dimensional surface reproducing available experimental data for the ground state of $HeBr_2$. In turn, in order to analyze the additivity of the van der Waals potentials *ab initio* calculations are performed for the tetraatomic cluster He_2Br_2 and compared with results obtained using an additive model of two-body and three-body $HeBr_2$ potentials. Bound state calculations using the above model surface are then reported and discussed in terms of available experimental data for similar systems. Conclusions constitute the closing section.

2. Methods and results

2.1. TRIATOMIC COMPLEX

2.1.1. *Ab initio* calculations

All computations are carried out at the CCSD(T) level of theory. *Ab initio* calculations are performed using the *Gaussian 98* program.[48] For bromine

atoms, the Stuttgart group (SDD) effective core potential[49] (ECP) is employed. The valence electrons are described using the SDD basis set augmented with (sp) diffusion and (3df) polarization functions, denoted as SDD+G(3df). The exponents of diffusion and polarization functions used for bromine, associated with the SDD ECP were those specified in the literature.[50–52] Such ECPs basis sets tend to be computationally more effective than their all-electron counterparts and have been used[50,51,53] in calculations of halogen-containing molecules. In particular, CCSD(T) calculations for the Br_2 molecule using the SDD+G(3df) basis set[52] are in very good agreement with experimental data and with recent CCSD(T) *ab initio* calculations using the extended SDB-cc-pVQZ basis set.[54]

For the He atom we use augmented correlation consistent aug-cc-pV5Z basis sets incorporated in the *Gaussian 98* programs. For a better description of the long range interactions an additional set $(3s3p2d2f1g)$ of mid-bond functions[55] is employed, improving the interactions energies by 5% in such dispersion-bound complexes.[56–58] We denote the above basis set as aug-cc-pV5Z+$(3s3p2d2f1g)$ and we use in all calculations 6d and 10f Cartesian functions.

The potential energy surface for $HeBr_2$ complex is examined using the supermolecular approach. In a supermolecular calculation, the interaction energy between a pair of atoms or molecules, is given by

$$\Delta E = E_{HeBr_2} - E_{BSSE} - E_{He} - E_{Br_2}, \tag{1}$$

where E_{HeBr_2} is the energy of the complex and the E_{He}, E_{Br_2} are the energies of the monomers. Basis-set superposition error (E_{BSSE}) is corrected by using the standard counterpoise method.[59]

We use Jacobi coordinates (r, R, θ) to describe the PES of $HeBr_2$ complex, where R is the intermolecular distance of He atom from the center of mass of Br_2, r is the bond length of Br_2, and θ is the angle between the $\mathbf{R}$ and $\mathbf{r}$ vectors. Intermolecular energies are calculated for several R distances ranging from R=3 to 9 Å, while the angle θ is set to 0°,30°,45°,60°,75°, and 90°, considering five different Br_2 bond-lengths of r =2.1, 2.19, 2.28, 2.37, and 2.46 Å. The r values are chosen around the equilibrium distance r_e = 2.28 Å in a range that is enough to describe some of the first few excited vibrational levels, v, of Br_2(X). We should mention that changes of r influence the overall energy of the complex much more than the changes of the intermolecular distance R. The results of the interaction energies for the different Br–Br bond-lengths are qualitatively similar. For all the r values the linear configuration is found to be lower in energy than the T-shaped one. The supermolecular interaction energies of the T-shaped structures are found to be more sensitive to small changes of the Br–Br bond length than the ones for the linear configuration. In Figure 1 we plot the dependence of the interaction energies around their minimum values

for θ=0 and 90°, as r value changes. As can be seen the interaction for the T-shaped configurations is predicted to become less attractive as r increases, while the interaction at linear configurations is much less affected. This produces an increasing in the energy difference between the linear and T-shaped configurations, when the Br–Br bond is lengthened.

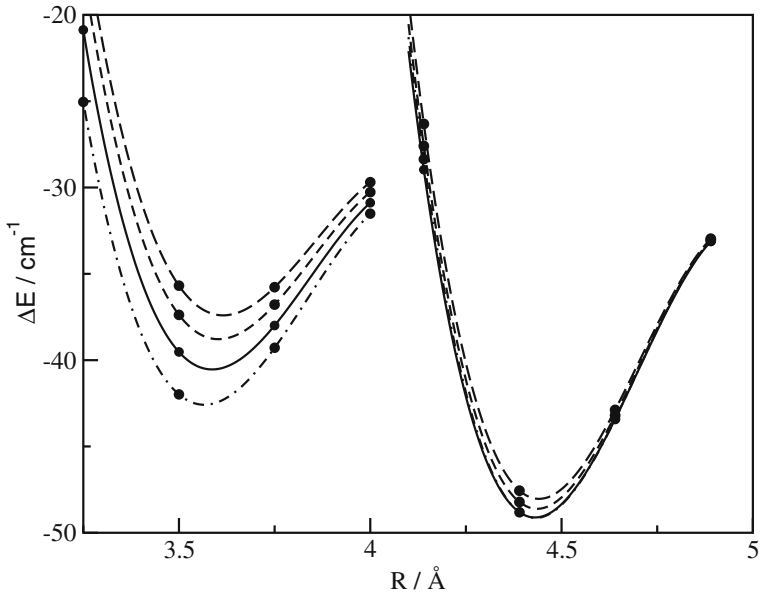

Figure 1. Dependence of the interaction energies for the linear and T-shaped configurations as r bond increases. Dot-dashed, solid, dotted, long-dashed type of lines correspond to r= 2.19, 2.28, 2.37 and 2.46 Å, respectively

2.1.2. *Potential Energy Surface Representation*

In order to represent the PES for the $HeBr_2$ complex we used an analytical functional form to fit the CCSD(T) *ab initio* points. We used an expansion in Legendre polynomials, $P_\lambda(\cos\theta)$, to describe the two-dimensional He...Br_2 interaction potential,

$$V(R,\theta;r_k) = \sum_\lambda V_{k\lambda}(R) P_\lambda(\cos\theta),\ k = 1-5 \tag{2}$$

with $\lambda = 0, 2, 4, 6, 8, 10$, due to the symmetry of the system with respect to $\theta = 90°$. The $V_{k\lambda}(R)$ coefficients are obtained by a collocation method applying the following procedure. For each of the six values of angle θ, we

fitted the CCSD(T) data to a Morse-vdW function,

$$V(R;\theta_i;r_k) = \alpha_0^{ik}(\exp(-2\alpha_1^{ik}(R-\alpha_2^{ik}))-2\exp(-\alpha_1^{ik}(R-\alpha_2^{ik})))-\frac{\alpha_3^{ik}}{R^6}-\frac{\alpha_4^{ik}}{R^8}, \tag{3}$$

with parameters α_0^{ik}, α_1^{ik}, α_2^{ik}, α_3^{ik} and α_4^{ik}, where $i = 1-6$ and $k = 1-5$. These parameters are fitted to the *ab initio* points using a nonlinear least square technique. Finally, for a 3D representation of the potential a one dimensional cubic spline interpolation is employed for the r coordinate.

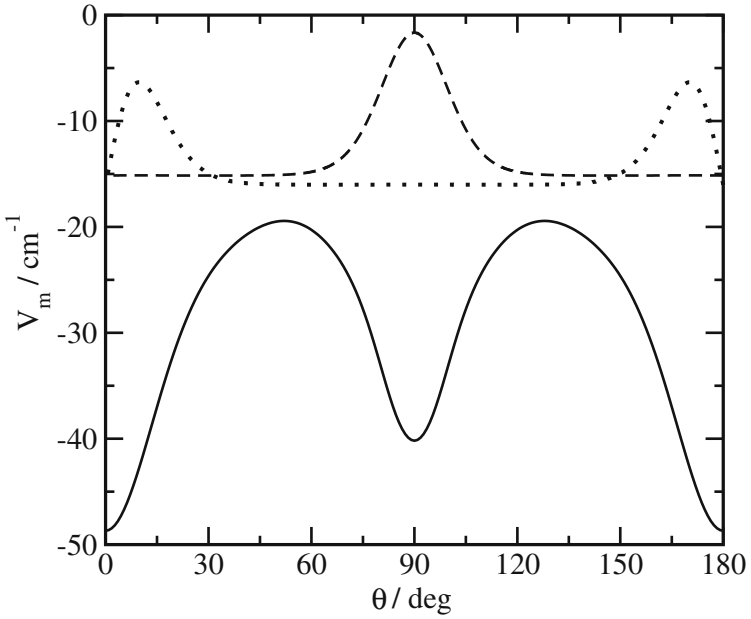

Figure 2. Minimum energy path, V_m in cm^{-1}, as a function of θ for r=2.28 Å together with the n=0,1 (collinear) and n=2 (T-shaped) angular probability distributions for $J = 0$ vdW levels of $HeBr_2$.

The $HeBr_2$ potential energy surface exhibits two minima. In the r range studied, the global minimum with an energy of -48.70 cm^{-1} at R = 4.42 Å and r=2.28 Å corresponds to a linear ($\theta = 0°$) configuration. The second minimum, with energy of -44.92 cm^{-1}, is at R = 3.55 Å and r=2.1 Å corresponding to a T-shaped ($\theta = 90°$) configuration of the complex. This latter result compares very well with the corresponding experimental distance of 3.7±0.2 Å.[60] The isomerization barrier between the two wells is found at an energy of -19.16 cm^{-1} (29.54 cm^{-1} above the global linear minimum), with $R \sim 4.5$ Å and $\theta \sim 51°$. These potential minima and the corresponding barrier are displayed in Figure 2, where the minimum energy path, V_m, of the minimum energy for r=2.1 and 2.28 Å are plotted as a function of the angle θ. These results are in agreement with previous

ab initio calculations,[13,61] although the present calculations give lower interaction energies by 5.7 cm^{-1} for linear isomer and by 5.9 cm^{-1} for the T-shaped one than in the MP4 study,[61] whereas a lower interaction energy by 4.6 cm^{-1} is obtained for the T-shaped structure than the previous two-dimensional CCSD(T) one[13] (see Table 1). As it has been mentioned above, the T-shaped minimum is displaced to $r \sim 2.1$ Å, while the linear one is remaining close to $r{=}r_e{=}2.28$ Å in the 3D surface. Furthermore, the present calculations predict a smaller (by 3.8 cm^{-1}) difference between the energies of the two structures than the two-dimensional CCSD(T) results.[13] In Table 1 we also present results on the D_e and R_e values given by a IDIM PT1 semiempirical model.[63] This model also predicts double minimum topology for the ground He–Br_2 state with almost similar energies for the two isomers; 38.0 cm^{-1} for the linear and 37.9 cm^{-1} for the T-shaped.

2.1.3. *Bound state calculations*

The rovibrational Hamiltonian in the Jacobi coordinate system has the form

$$\hat{H} = -\frac{\hbar^2}{2\mu_1}\frac{\partial^2}{\partial R^2} + \frac{\hat{j}^2}{2\mu_2 r^2} + \frac{\hat{l}^2}{2\mu_1 R^2} + V(R,\theta,r) + \hat{H}_{Br_2}, \qquad (4)$$

where $\hat{H}_{Br_2} = -\frac{\hbar^2}{2\mu_2}\frac{\partial^2}{\partial r^2} + V_{Br_2}(r)$ is the vibrational Hamiltonian for a free Br_2 molecule. $\mu_1 = \frac{m_{\mathrm{He}} 2m_{\mathrm{Br}}}{m_{\mathrm{He}}+2m_{\mathrm{Br}}}$ and $\mu_2 = \frac{m_{\mathrm{Br}}}{2}$ are the reduced masses, m_{He}=4.00260 and m_{Br}=78.9183361 amu are the atomic masses of ^{4}He and ^{79}Br Isotopes, $\hat{l}$ and $\hat{j}$ are the angular momentum operators associated with the vectors **R** and **r**, respectively, leading to a total angular momentum $\hat{J} = \hat{l} + \hat{j}$. Here all calculations are performed for J=0. Starting from the $V(R,\theta;r_k)$ potential of (Eq. 2), 1D cubic-spline interpolation is used to compute the value of $V(R,\theta,r)$ at 21 Gauss-Legendre points in the interval of $2.1 < r < 2.46$ Å. $V_{Br_2}(r)$ is the one-dimensional Br_2 ground state potential function and a cubic-spline interpolation to CCSD(T) *ab initio* data (see Table 2 of Ref.[52]) is used to reproduce the V_{Br_2} potential at any r point. The eigenvalues and eigenfunctions of diatomic $\hat{H}_{Br_2}$ Hamiltonian are denoted as $E_{Br_2}(v)$ and $\chi_v(r)$, respectively, and are evaluated by solving the 1D Schrdinger equation using a combined Truhlar-Numerov algorithm.[65] The vdW levels and corresponding wave functions are calculated variationally by diagonalizing the vibrationally averaged Hamiltonian

$$H_v = <\chi_v|H|\chi_v> = -\frac{\hbar^2}{2\mu_1}\frac{\partial^2}{\partial R^2} + \frac{\hat{l}^2}{2\mu_1 R^2} + V_{v,v}(R,\theta) + E_{Br_2}(v) + \frac{B_v \hat{j}^2}{\hbar^2}, \qquad (5)$$

where, $V_{v,v}(R,\theta) = <\chi_v|V(R,\theta,r)|\chi_v>$ is the intermolecular vdW potential of $HeBr_2$ averaged over the Br_2 $v = 0$ vibrational eigenfunction and B_v is the Br_2 rotational constant averaged over the $v = 0$ eigenstate. The Hamiltonian is represented on a finite three-dimensional basis set. The $V_{v,v}$

TABLE 1. Experimental and theoretical binding energies (D_e and D_0 in cm^{-1}), equilibrium distances (R_e and R_0 in Å), for the linear and T-shaped isomers together with the theoretical predictions for the isomerization barrier of the $HeBr_2$ complex.

	Collinear ($\theta_e = 0°$)		Isomerization Barrier			T-shaped	
	D_e / D_0	R_e / R_0	E^*	θ^*	R^*	D_e / D_0	R_e / R_0
This work	48.70 / 16.02	4.42 / 4.88	29.54	51	4.50	44.92 / 14.90	3.55 / 4.14
CCSD(T) 2D[13]	48.8 /17.2	4.42 / ...	30.7	...	...	40.3 / 17.7	3.58 / ...
MP4 *ab initio* value[61,62]	43.0 / ...	4.50 / ...	...	...	...	39.0 / ...	3.70 / ...
Semiempirical value[63]	38.0 / 16.8	4.93 / ...	...	...	...	37.9 / 17.3	3.63 / ...
Experimental value[60,62,64]	... / ...	... / ...	...	...	...	... / 17.0±1.5	3.7±0.2 / ...
Experimental value (LIF)[10]	... / 17.6(2)	... / ...	...	...	...	... / 16.9(2)	... / ...

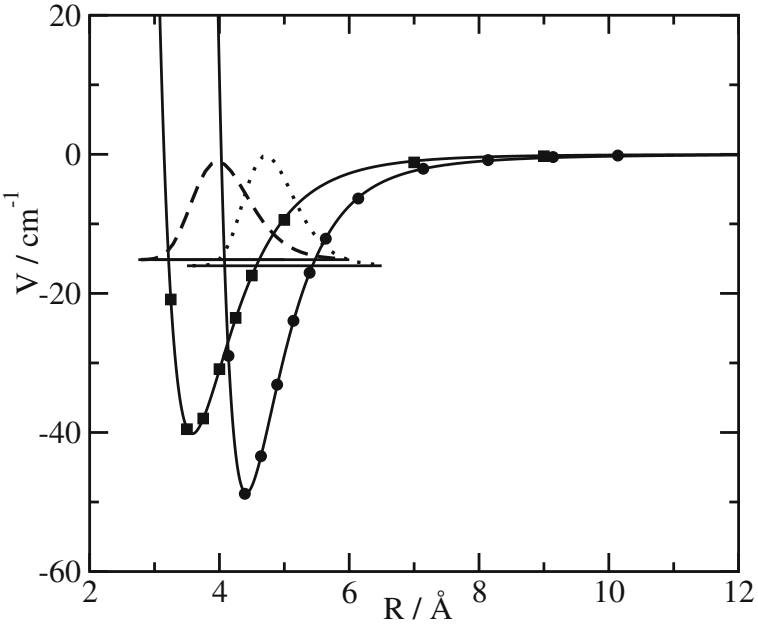

Figure 3. Analytical potential curves $V(R, \theta, r_e)$ for $HeBr_2$ complex with $\theta = 0°$ (squares) and $\theta = 90°$ (circles). The eigenvalues and radial probability distributions corresponding to the $J = 0$ lowest vibrational vdW level at each configuration, $n = 0$ (dotted line) and $n = 2$ (dashed line) respectively, are also included.

potential matrix elements are calculated using Gaussian quadrature in the r coordinate, while for the angular coordinate we used orthonormalized Legendre polynomials $\{P_j(\cos\theta)\}$ as basis functions, with up to 40 values (even and odd) of the diatomic rotation j. For the radial R coordinate, a discrete variable representation (DVR) basis set is used based on the particle in a box eigenfunctions.[66] A basis set of 100 DVR functions over the range from $R = 1.75$ to 15 Å are used. In this way, a convergence of 0.0001 cm^{-1} is achieved in bound state calculations.

The results of the bound state calculations for the $HeBr_2(X)$ potential show that the lowest three vdW vibrational levels ($n = 0, 1, 2$) are at energies of -16.0167, -16.0159 and -14.9030 cm^{-1}. The angular and radial probability distributions of the associated wave functions are shown in Figures 2 and 3. As can be seen the first two states correspond to linear configurations and the last one to T-shaped ones. The next four bound vibrational states are found at energies of -7.9204, -6.9803, -4.9400 and -2.7761 cm^{-1} and are spreading all over θ values. All calculated vdW vibrational levels are located above the potential isomerization barrier (-19.16 cm^{-1}). The small energy difference between $n = 0$ and $n = 2$ states (only 1.1 cm^{-1}) provides indications for coexistence of the two isomers even at low temperatures. Vibrationally averaged structures with R_0^L=4.88 Å and R_0^T=4.14 Å are obtained for the linear and T-shaped isomers, respectively.

The experimental value for binding energy of the X state of $HeBr_2$ has been determined to be in the range between 15.5 and 18.5 cm^{-1}[62,64] for a T-shaped structure. The corresponding values obtained here are 16.02 and 14.90 cm^{-1} for the linear and T-shaped isomers, and are very closed to the ones predicted experimentally. Further, recent LIF experimental studies[10] have determined the binding energy (D_0) for both isomers (linear and T-shaped) to be 17.6(2) and 16.9(2) cm^{-1}, respectively. These findings are in excellent agreement with the present calculations, confirming our theoretical predictions.

We should mention that the binding energies obtained from the 2D CCSD(T) and semiempirical surfaces contrary to the 3D CCSD(T) results predict that a T-shaped structure is slightly more stable than the linear one. This finding can be partially attributed in the lack of the r dependence. However, we have found that this is the case for the linear configurations, while for the T-shaped ones the difference obtained in the D_0 value is mainly due to the inadequate description of the 2D CCSD(T) potential in the region of the T-shaped well. It was found that more angular points are necessary to describe its anharmonicity. Note that, as it was expected for $r = r_e$, the properties (D_0 and R_0) of the linear well, and the the well-depths (D_e) and equilibrium distances (R_e) for both linear and T-shaped configurations are not affected (see Table 1).

2.2. TETRA-ATOMIC COMPLEX

2.2.1. *Ab initio* calculations

The *ab initio* calculations are performed also using the *Gaussian 98* package.[48] Computations are carried out at the MP4 and CCSD(T) levels of theory. The He_2–Br_2 system is described using the $(r, R_1, R_2, \theta_1, \theta_2, \gamma)$ coordinate system. r is the bond length of Br_2; R_1, R_2 are the intermolecular distances of each He atom from the center of mass of Br–Br, θ_1 is the angle between the $\mathbf{R_1}$ and $\mathbf{r}$ vectors, while θ_2 is the one between $\mathbf{R_2}$ and $\mathbf{r}$, and γ is the angle between the $\mathbf{R_1}$ and $\mathbf{R_2}$ vectors.

For the present calculation we used for Br atoms the Stuttgart-Dresden-Bonn (SDB) large-core energy-consistent pseudopotential[49] in conjunction with the augmented correlation consistent triple zeta (SDB-aug-cc-pVTZ) valence basis set.[54] This basis set is of cc-pVTZ quality and has been optimized for use with the SDB pseudopotential. For the He atoms we employed different basis sets such as the aug-cc-pV5Z and d-aug-cc-pV5Z from EMSL library.[67] Some convergence problems arised from the use of the double augmented basis sets imposing the use of the single augmented ones. In addition, the role of using bond functions, such as the $(3s3p2d2f1g)$ ones[55] is investigated. Test runs are carried out for a few specific configurations, e.g. for the tetrahedral structure, where a set of the $(3s3p2d2f1g)$ bond

functions are located in the middle of the intermolecular distance R, which connects the center of masses of He_2 and Br_2 molecules. Similar differences are obtained in the interaction energies at both levels of theory. It was found that their efficiency to saturate the dispersion energy, accounts for an improvement of about 10%, around the equilibrium geometry. The effect of the use of bond functions has been found to be $\approx 5\%$ in other studies on triatomic dispersion-bound complexes.[56,57] Although, as the effect of their location for other configurations is still ambiguous, we choose to use for the He atoms the augmented correlation consistent (aug-cc-pV5Z) basis sets without the additional set of bond functions. In all calculations here 6d and 10f Cartesian functions are used.

The supermolecular approach is used for the determination of the intermolecular energies, ΔE:

$$\Delta E = E_{He_2Br_2} - E_{BSSE} - E_{He_2} - E_{Br_2}, \tag{6}$$

where $E_{He_2Br_2}$, E_{He_2}, and E_{Br_2} are the energies of He_2–Br_2, He_2 and Br_2, respectively. The correction, (E_{BSSE}), for the basis-set superposition error is calculated using the standard counterpoise method.[59]

We performed MP4/CCSD(T) calculations for several configurations fixing the Br_2 bondlength at its equilibrium value r_e=2.281 Å. The linear configuration has the lowest energy -90.39/-89.18 cm^{-1} at MP4/CCSD(T) levels with $R_1 = R_2$ =4.44 Å. The next two equlibrium structures are found at energies of -81.23/-80.78 cm^{-1} and -74.40/-74.02 cm^{-1}, respectively, and correspond to a 'police-nightstick' (R_1=4.44 and R_2 =3.58 Å) and tetrahedral (R =3.33 Å) configurations (see Figure 4). We should note that the equilibrium distances of the above structures are very close to the ones obtained by CCSD(T) calculations for the optimized linear and T-shaped geometries for the triatomic $HeBr_2$ complex.[40]

In order to extract information on nonadditive interactions in He_2Br_2 we examine the above equilibrium structures based on the *ab initio* calculations and partitioning the interaction energy into components, as given in Ref.[44] Therefore, we show in Table 2 the summary of supermolecular calculations of the entire nonadditivity in the three He_2Br_2 equilibrium structures using the results of the MPPT (Møller-Plesset Perturbation theory) up to fourth order along with the ones of the CCSD(T) method. As can be seen in Table 2 the total three-body interaction for the three different equilibrium geometries computed through the MP3 amounts -77.76, -70.06 and -62.88 cm^{-1}, respectively. These energies neglect completely the effects of intramonomer correlation on three-body dispersion. The major effect of the intrasystem correlation on dispersion appears in MP4 level and is especially sensitive to the presence of triple excitations. For all configurations studied the MP4(SDQ) level reduce this effect to -71.29, -65.35 and -59.09 cm^{-1}, respectively, while the inclusion of triples enhances

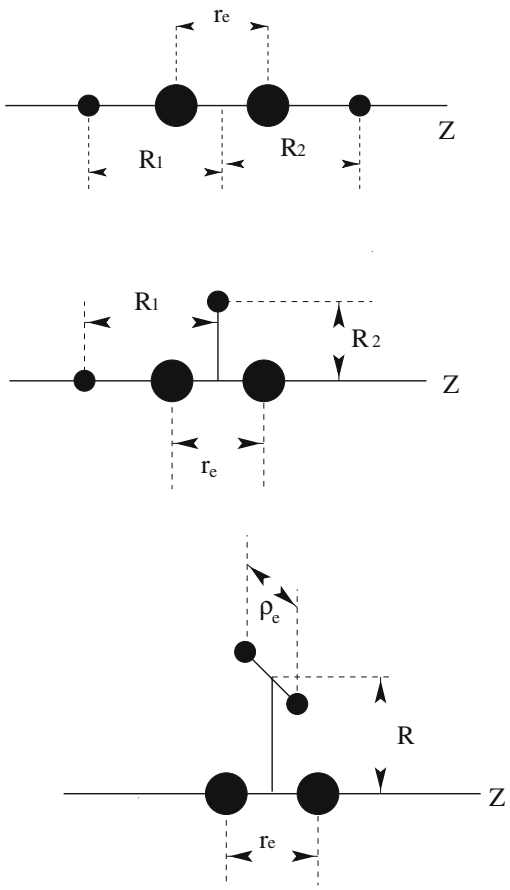

Figure 4. Optimal MP4/CCSD(T) structures for He_2Br_2. Coordinates are defined in the text, and ρ_e is the He-He distance.

both MP4(SDQ) and CCSD interaction energies (see MP4(SDTQ) and CCSD(T) values in Table 2). The MP4(SDQ) results seem to be well converged with respect to the CCSD calculations, For a consistent treatment of two and three-body correlation effects, the three-body potentials should be summed to a level one order higher than the corresponding two-body ones. The MP4(SDTQ) reproduces quantitatively the dominant contributions to the two-body interaction energy, while to achieve a similar level of correlation for the three-body terms one needs to advance to next order of theory, practically more accurate to turn to the CCSD(T) theory. Our calculations indicate that the total nonadditive effect in He_2Br_2 originating from supermolecular CCSD(T) calculations amounts to -88.49, -80.44 and

TABLE 1. Summary of the supermolecular calculations of the nonadditive effects around the three equilibrium He_2Br_2 structures. Energy is in cm^{-1} and distances in Å.

Linear structure

$R_{1,2}$/Method	HF	MP2	MP3	MP4(SDQ)	MP4(SDTQ)	CCSD	CCSD(T)
4.3	125.57	-75.57	-69.09	-61.26	-83.14	-59.87	-81.67
4.4	84.41	-83.42	-77.76	-71.29	-89.77	-70.23	-88.49
4.5	56.45	-83.91	-78.88	-73.50	-89.15	-72.69	-88.01

Police-nightstick structure

$R_{1,2}$/Method	HF	MP2	MP3	MP4(SDQ)	MP4(SDTQ)	CCSD	CCSD(T)
4.3	97.10	-70.21	-65.76	-60.38	-77.67	-59.41	-77.06
4.4	76.49	-74.12	-70.06	-65.36	-80.94	-64.57	-80.44
4.5	62.53	-74.34	-70.58	-66.48	-80.59	-65.80	-80.20

Tetrahedral structure

R/Method	HF	MP2	MP3	MP4(SDQ)	MP4(SDTQ)	CCSD	CCSD(T)
3.0	154.18	-42.58	-39.53	-35.31	-53.14	-34.26	-53.57
3.25	70.80	-65.71	-62.88	-59.94	-72.87	-59.43	-73.24
3.5	31.87	-63.58	-61.06	-58.10	-68.41	-58.69	-68.59

-73.24 cm^{-1} for configurations nearby its equilibrium structures. We should mention that the same behaviour were observed in the results of the MPPT energies for the $HeBr_2$ complex[40] around its linear and T-shaped equilibrium configurations. This finding indicates a similar nature of binding in triatomic and tetratomic complexes of such type, and thus information on intermolecular interactions available for triatomic species might serve to study larger systems.

2.2.2. *Potential Energy Surface Representation*

Two functional forms are checked for the He_2–Br_2 potential energy function. One is based on the pairwise atom-atom interaction, which has been widely used in all previous calculations on triatomic and tetratomic, Rg_n–X_2 with n=1,2, complexes.[29,30,63,68,69] The parameters for the two-body He–He interactions are taken from Ref.[70] The second one is given by summing up three-body $HeBr_2$ interactions and the He–He one,

$$V(r_e, R_1, R_2, \theta_1, \theta_2, \gamma) = \sum_i V_{He_iBr_2}(r_e, R_i, \theta_i) + V_{HeHe}(R_1, R_2, \gamma) \quad (7)$$

where the corresponding $V_{He_iBr_2}(r_e, R_i, \theta_i)$ terms with $i = 1$ and 2, are the CCSD(T) parameterized potential of the $HeBr_2$ complex[40] and $V_{HeHe}(R_1, R_2, \gamma)$ term is the potential function for He_2 given in Ref.[71]

Configuration energies are determined by optimizing different structures with respect to atomic positions using the above mentioned functional expressions. In Fig.5 we compare the two different potential functional forms with the MP4 *ab initio* results. Solid lines are for the sum of the three-body

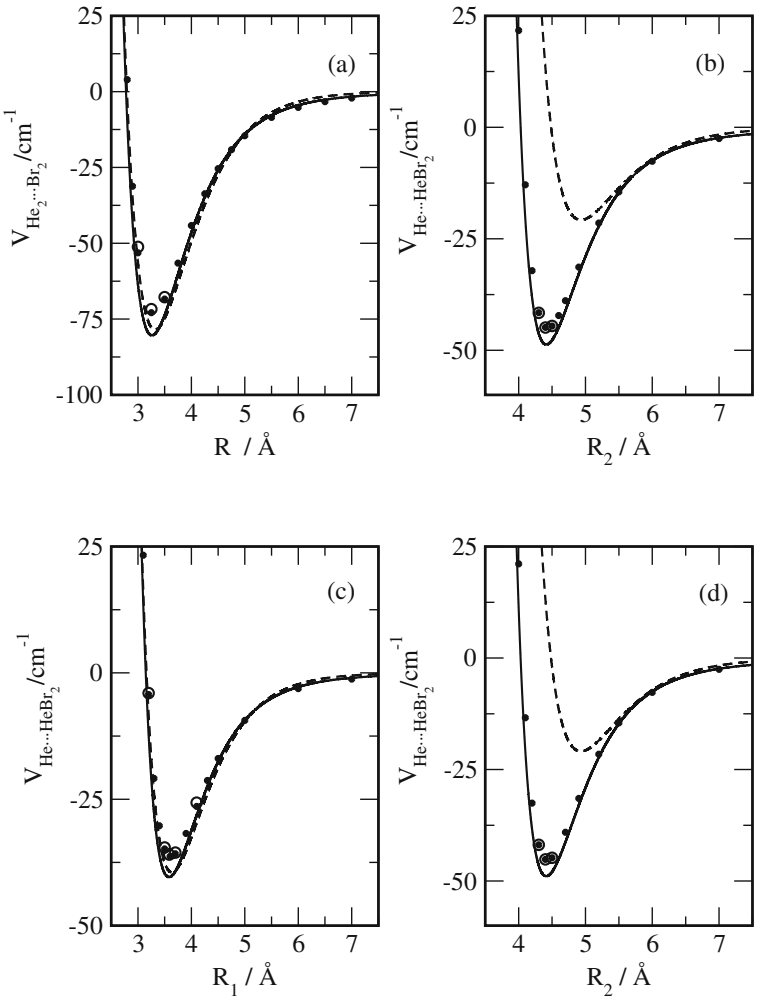

Figure 5. Comparison of two different potential energy curves for tetrahedron (a), linear (b) and police-nightstick (c,d) orientations of He_2Br_2. Solid lines are for the sum of three-body CCSD(T) interaction potential, while dotted lines correspond to the pairwise atom-atom form. The MP4 *ab initio* values are also indicated by filled circles, whereas potential values obtained using the sum of three-body MP4 interaction $HeBr_2$ potential are shown by open circles.

CCSD(T) $HeBr_2$ interaction potential, dashed lines correspond to the pairwise atom-atom form, while filled circles indicate the MP4 *ab initio* values. Open circles are for the potential values obtained using the sum of the three-body MP4 potential for $HeBr_2$, at the specific geometries with the same basis set as in the He_2Br_2 calculations. Fig.5a represents the potential energy curves as a function of the distance R between the center of masses of Br_2 and He_2 in the tetrahedron structure. As can be seen both forms represent well the *ab initio* data at this configuration. In Fig. 5b an one-

dimensional plot for the linear geometry is shown, while in Fig. 5c and 5d representations of the potential energy are given for the 'police-nightstick' structure as a function of R_1 and R_2 distances, respectively. The additive atom-atom interactions form predicts the overall minimum of the well for a distorted tetrahedron, while the sum of the three-body $HeBr_2$ interactions evaluates a linear structure as the global minimum, and two other ones, 'police-nightstick' and tetrahedral, as local minima of the He_2Br_2 surface. As can be seen results obtained using the sum of the three-body $HeBr_2$ interactions are in very good accord with the corresponding *ab initio* values. In contrast, large deviations of the *ab initio* results from the values predicted by the pairwise atom-atom interactions form, particularly for linear configurations are found. Thus, we choose the sum of the three-body CCSD(T) $HeBr_2$ interactions henceforth to represent the potential surface of He_2Br_2 and to check further its validity in comparison with *ab initio* data.

The potential has three wells at energies of -97.39, -88.88 and -80.38 cm^{-1}, with the collinear well to be the deeper than the 'police-nightstick' and tetrahedral ones. The equilibrium distances and angles are at $R_1^e = R_2^e = 4.41$ Å for the linear well, R_1^e=4.41, R_2^e=3.58 Å for the 'police-nightstick' one and R^e=3.27 Å for the tetrahedral well. The isomerization barrier between the collinear $\leftrightarrow$ police-nightstick wells is found at energy of -68.15 cm^{-1} and an angle of 127°. One-dimensional representations of the potential are shown in Figure 6, where minimum energy paths are plotted as a function of the angle γ=$\theta_1 - \theta_2$ for planar (see Figure 6a) and non-planar with $\theta_1 = \theta_2 = 90°$ and $\gamma = \phi_1 - \phi_2$ (see Figure 6b) configurations.

In Table 3 we present for the indicated geometries, selected along to a minimum energy path ($HeBr_2$ molecule is fixed at linear configuration, $\theta_1 =$ 180, while the R_1 and R_2 distances are optimized for each θ_2 value), the *ab initio* MP4 and CCSD(T) values and compare them with the corresponding $V(r_e, R_1, R_2, \theta_1, \theta_2, \gamma)$ ones, given by the Eq. (7). For sake of comparison the potential values using the two-body potential form are also listed in the last column. As can be seen, the differences obtained in the CCSD(T) results are fully justified due to the different basis sets used, including or not bond functions, in the *ab initio* calculations of the triatomic and tetratomic complexes, respectively. We should note that CCSD(T) results are within the difference of 10% in the interaction energies attributed from the test runs to the use of bond functions.

2.2.3. *Bound state calculations*

The Hamiltonian operator has the form

$$\hat{H} = -\frac{\hbar^2}{2\mu_1}\left(\frac{\partial^2}{\partial R_1^2} + \frac{2}{R_1}\frac{\partial}{\partial R_1}\right) - \frac{\hbar^2}{2\mu_2}\left(\frac{\partial^2}{\partial R_2^2} + \frac{2}{R_2}\frac{\partial}{\partial R_2}\right) \quad (8)$$

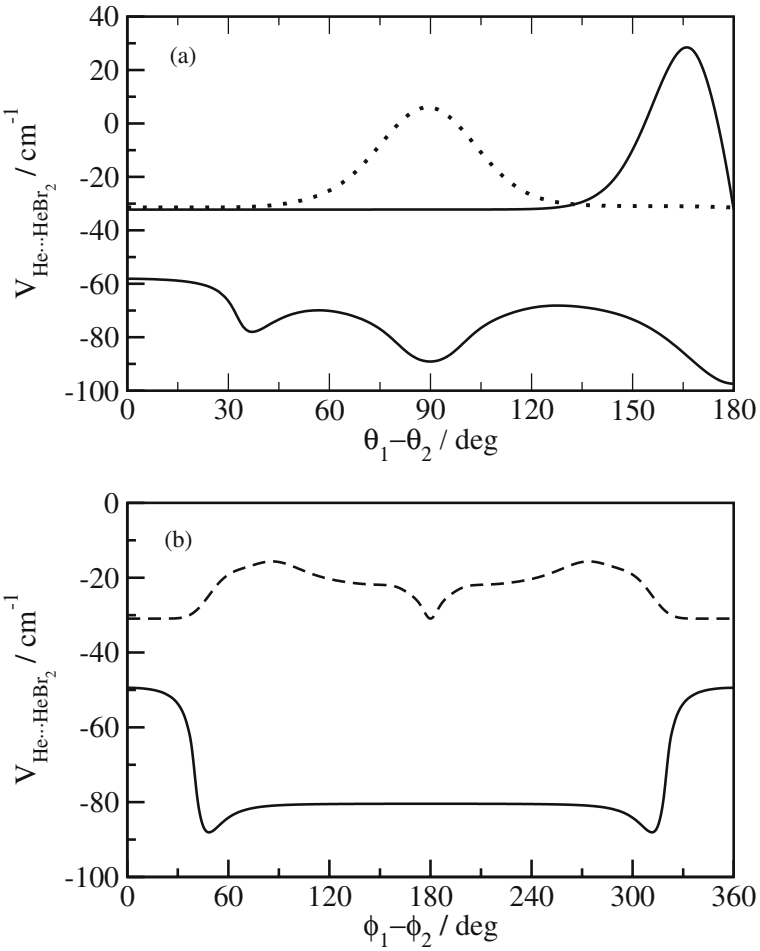

Figure 6. Minimum energy path, V_m in cm^{-1} as a function of angle γ, for planar γ=($\theta_1 - \theta_2$) (a) and no-planar with $\theta_1 = \theta_2 = 90^\circ$, γ=($\phi_1 - \phi_2$) with $\theta_1 = \theta_2 = 90^\circ$ (b) configurations. The probability $\int |\Psi|^2 \sin\gamma dR$ distributions for n=0(collinear), n=1(police-nightstick) and n=2(tetrahedral) vdW levels of He_2Br_2 are also depicted.

$$+\frac{\hat{j}^2}{2\mu_3 r_e^2} + \frac{\hat{l_1}^2}{2\mu_1 R_1^2} + \frac{\hat{l_2}^2}{2\mu_2 R_2^2} - \frac{\hbar^2}{2m_{Br}}\nabla_1 \cdot \nabla_2 + V(\mathbf{r}, \mathbf{R_1}, \mathbf{R_2})$$

where $\mu_1 = \mu_2 = \frac{m_{\rm He} 2m_{\rm Br}}{m_{\rm He}+2m_{\rm Br}}$ and $\mu_3 = \frac{m_{\rm Br}}{2}$ are the reduced masses, $\hat{l_1}$, $\hat{l_2}$ and $\hat{j}$ are the angular momenta associated with the vectors $\mathbf{R_1}$ $\mathbf{R_2}$ and $\mathbf{r}$, respectively, leading to a total angular momentum $\hat{J} = \hat{l_1} + \hat{l_2} + \hat{j} = \hat{L} + \hat{j}$. r is fixed at the equilibrium Br–Br bond length (r_e), and the potential for He_2Br_2 complex is given by the expansion in Eq. (7).

For a total angular momentum J, the Hamiltonian of Eq. (8) is represented in a set of basis functions consisting of linear combinations of

TABLE 2. MP4 and CCSD(T) interaction energies, ΔE [Eq. (6)], and potential values obtained from Eq. (7) using three-body (3B) MP4, CCSD(T) and CCSD(T)+bf $HeBr_2$ interaction potentials for the He_2–Br_2 complex at the indicated (θ_2, R_1, R_2) points. The potential values based on the two-body (2B) sum are also listed. Energies in cm^{-1}, angles in degrees and distances in Å.

$(\theta_2,\ R_1,\ R_2)$	MP4	CCSD(T)	V^{3B}_{MP4}	$V^{3B}_{CCSD(T)}$	$V^{3B}_{CCSD(T)+bf}$	V_{2B}
(0,4.41,4.41)	-90.01	-88.80	-90.03	-88.71	-97.39	22.11
(15,4.41,4.52)	-78.95	-77.87	-78.95	-77.80	-85.67	1.45
(30,4.41,4.65)	-67.36	-66.48	-67.33	-66.41	-73.32	-10.10
(45,4.41,4.60)	-63.06	-62.29	-63.03	-62.26	-68.69	-11.23
(60,4.41,4.34)	-63.01	-62.62	-62.99	-62.57	-68.97	-13.83
(75,4.41,3.92)	-69.99	-69.40	-69.95	-69.35	-76.38	-21.81
(90,4.41,3.58)	-81.03	-80.59	-80.96	-80.46	-88.88	-27.95
(105,4.41,3.92)	-69.99	-69.51	-69.95	-69.35	-76.38	-21.82
(120,4.41,4.33)	-63.19	-62.57	-63.21	-62.53	-68.96	-13.99
(135,4.41,4.57)	-64.04	-62.29	-62.90	-62.16	-68.65	-11.49
(150,4.40,5.48)	-56.54	-55.77	-56.34	-55.68	-60.54	1.72
(165,4.40,6.92)	-47.82	-47.03	-47.49	-46.92	-52.94	11.39
(180,4.41,7.34)	-47.01	-46.33	-46.79	-46.11	-50.43	10.08

products of bidimensional radial functions by angular functions, which incorporate the whole symmetry of the system.[30] For the R_1 and R_2 coordinates numerical $\{\xi_n(R_i)\}$, with $i = 1, 2$ and $n = 1, ..., N_R$ functions are used. We evaluate them as follows: First, the two-dimensional Schrdinger equation is solved in (R, θ, r_e) variables for a triatomic He–Br_2 system at total angular momentum zero. The employed PES was the CCSD(T) *ab initio* surface given in Ref.,[40] and a discrete variable representation (DVR) basis seti[66] is used. It consists of functions given by

$$f_l(R) = \frac{2}{\sqrt{\mathcal{L}(N+1)}} \sum_{k=1}^{N} \sin \frac{k\pi(R-R^{min})}{\mathcal{L}} \sin \frac{k\pi l}{N+1}$$

where N is the total number of DVR points, $\mathcal{L}$ is $R_i^{max} - R_i^{min}$, and the DVR points in the R coordinate are $R^l = \frac{l\mathcal{L}}{N+1} + R^{min}$ for $l = 1, ..., N$. Second, consindering a set of the N_R lowest eigenstates, their corresponding radial distributions are orthonormalized through a Gram-Schmidt procedure, and constitute the radial basis set, $\{\xi_n(R_i)\}$, for the tetraatomic calculations.

For the angular basis functions, we consider the following linear combinations, which are eigenfunctions of the parity of total nuclear coordinates inversion p,

$$\mathcal{F}^{(JMp)}_{l_1 l_2 L|\Omega|} = \sqrt{\frac{1}{2(1+\delta_{|\Omega|0})}} [\mathcal{W}^{(JM)}_{l_1 l_2 L\Omega} + p(-1)^{J+l_1+l_2+L} \mathcal{W}^{(JM)}_{l_1 l_2 L-\Omega}] \qquad (9)$$

with

$$\mathcal{W}^{(JM)}_{l_1 l_2 L\Omega} = \sqrt{\frac{2J+1}{4\pi}} \mathcal{D}^{J*}_{M\Omega}(\phi_r, \theta_r, 0) \mathcal{Y}^{L\Omega}_{l_1 l_2}(\mathbf{R_1}, \mathbf{R_2}) \tag{10}$$

M is the projection of J on the space-fixed z-axis, Ω its projection on the body-fixed z-axis, which is chosen here along the $\mathbf{r}$ vector. The $\mathcal{D}^{J}_{M\Omega}$ are Wigner matrices[72] and $\mathcal{Y}^{L\Omega}_{l_1 l_2}$ are angular functions[73] in the coupled BF representation.

In turn, taking into account that in case of He_2Br_2 the Hamiltonian is also invariant under $\mathbf{R_1} \leftrightarrow \mathbf{R_2}$ inversion, then a well-defined parity,p_{12}, basis set is built up as follows:

$$\Phi^{JMpp_{12}}_{l_1 l_2 L|\Omega|nm} = \sqrt{\frac{1}{2(1+\delta_{nm}\delta_{l_1 l_2})}} [\Phi^{JMp}_{l_1 l_2 L|\Omega|nm} + p_{12}(-1)^{l_1+l_2+L} \Phi^{JMp}_{l_1 l_2 L|\Omega|mn}], \tag{11}$$

where $\Phi^{JMp}_{l_1 l_2 L|\Omega|nm} = \phi_{nm} \mathcal{F}^{(JMp)}_{l_1 l_2 L|\Omega|}$ and $\phi_{nm}(R_1, R_2) = \xi_n(R_1)\xi_m(R_2)/R_1 R_2$.

For the evaluation of the Hamiltonian matrix elements, the numerical set of the radial basis functions $\{\xi_n(R_i)\}$ mentioned above, are represented as linear combinations of the f_l DVR functions, $\xi_n(R_i) = \sum_{l=1}^{N} < \xi_n | f_l > f_l(R_i) = \sum \xi_n(R_i^l) f_l(R_i)$, $i = 1, 2$ and $n = 1, ..., N_R$. The matrix elements of the Hamiltonian are given in Ref.[30]

In our calculations at J=,0 N_R =7 radial numerical functions, represented at 50 DVR points over the range of 2.5 to 8 Å, for each R_1 and R_2 coordinate are used. In turn, values of $L = j = 0 - 12$ (even) with $l_1^{max} = l_2^{max} = 12$ for even ($p_{12} = (-1)^{l_1+l_2+L} = +1$) and $p = (-1)^{J+L+l_1+l_2}$ parity symmetries, were enough to achieve convergence in the variational calculation.

The three lowest vibrational states of He_2Br_2 are found at energies of -32.240, -31.437 and -30.930 cm^{-1} (see Fig. 6 and 7). In Figure 6, together with the minimum energy path, we plot the angular probability density of the angle γ for the $n = 0$ (solid line), $n = 1$ (dotted line) (see Fig. 6a) and $n = 2$ (dashed line) (see Fig. 6b) eigenfunctions, while in Fig. 7 the radial $R_{i=1,2}$ and angular $\theta_{i=1,2}$ distributions for these states are shown. As can be seen, the $n = 0$ state is localized in the linear well and its distribution is peaked at $\theta_{1,2} = 0, 180°$, $R_{1,2}$=4.722 Å and γ=180°. The $n = 1$ state corresponds to 'police-nightstick' configurations, with two maxima at $\theta_{1,2} = 90$ and 0/180°, and at $R_{1,2}$=3.98 and 4.631 Å, and only one peak at $\gamma = 90°$ (see Fig. 6a), while the $n = 2$ state exhibits a tetrahedral structure with a maximum value at $\theta_{1,2} = 90°$ and $R_{1,2}$=3.940 Å and a broad distribution in γ, except a small peak at $\gamma \approx 60°$, where the He–He attractive interaction is maximum. There is a forbidden area around γ=0 where the two atoms are collided (see Fig.5b). The radial expectation values for each of the above structures, R_i^0, are obtained by averaging R_i over the corresponding distributions. To our knowledge, for first time such results on the vibrationally averaged structures of He_2Br_2 are presented.

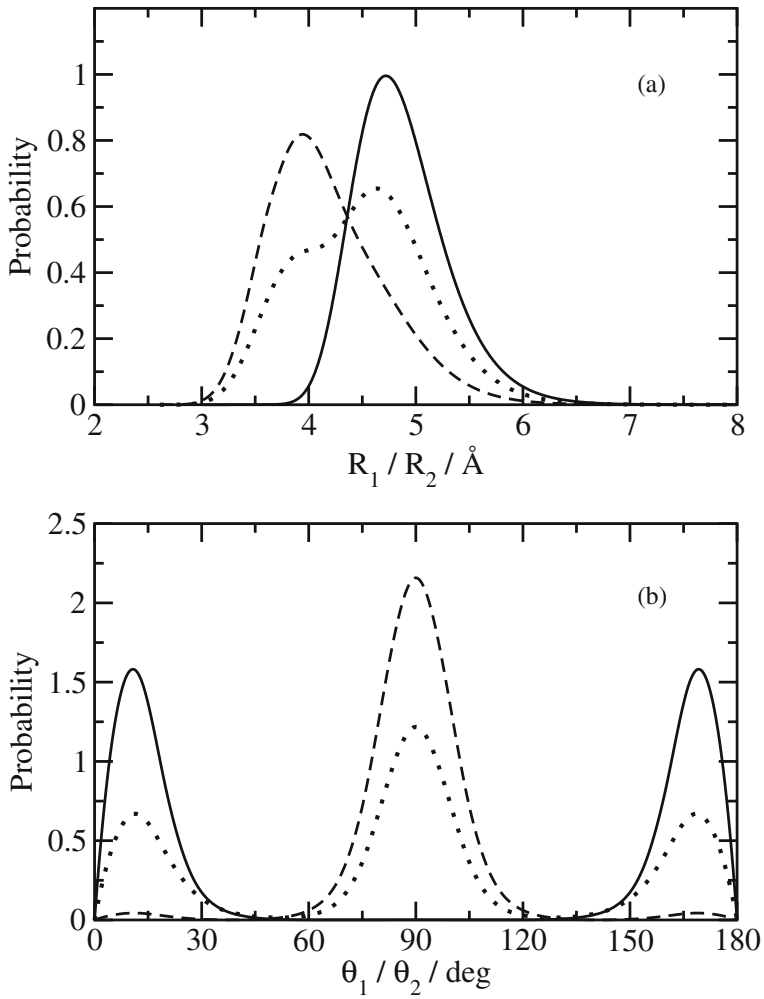

Figure 7. Radial (a) and angular (b) probability densities for the indicated vdW levels of He_2Br_2 for $J = 0$ calculated using the $V(r_e, R_1, R_2, \theta_1, \theta_2, \gamma)$ PES.

In contrast with previous studies[19,29,30] on He_2Cl_2 cluster, in the present work localized structures are determined for the lower He_2Br_2 vdW states. Traditional models based on a He_2Cl_2 tetrahedron frozen stucture have failed to reproduce the experimental absorption spectrum, suggesting a quite delocalized structure for its vibrationally ground state.[19] Here, based on *ab initio* calculations we propose different structural models, like linear or 'police-nightstick', in order to fit the rotationally resolved excitation spectrum of He_2Cl_2 or similar species.

We should note that the energy difference between the above mentioned isomers is small, and the lack of the r dependence in the potential form might influence their relative stability. For the triatomic vdW complexes

of He atom with homopolar/heteropolar halogens has been found[2,11,12,40] that the energy difference between the linear and T-shaped wells increases when the r bond is lengthened, and a similar behaviour should be expected for the tetratomic complexes. However, in order to justify our assertions for such tetratomic species, comparison with experimental measurements is needed, which would finally contribute to evaluate the present CCSD(T) potential.

3. Conclusions

A three-dimensional potential energy surface is calculated for the $HeBr_2(X)$ complex at the CCSD(T) level of theory. As in other studies on such complexes, the existence of two minima for both linear and T-shaped configurations is established. The dependence of the binding energy on the Br–Br bond length, r, is examined for distances in the range between 2.19 and 2.46 Å. The elongation of the Br–Br bond makes the interaction for both linear and T-shaped structures weaker, with that in the linear structure showing a smaller sensitivity to the r changes. For linear structures, the energies of the well-depths vary from 47.5 to 48.7 cm^{-1}, while for T-shaped structures the well depth changes from 37.0 to 44.9 cm^{-1} for the range of the r values studied.

Bound state calculations with $J = 0$ are carried out for the above CCSD(T) surface. The linear He–Br–Br structure is found to be the most stable isomer with a binding energy of D_0=16.02 cm^{-1}, while the T-shaped isomer is predicted to lie only 1.1 cm^{-1} above, indicates the coexistence of them even at low temperatures. The vibrationally averaged structures for these isomers are determined to be (R=4.88 Å, θ= 0°) and (R=4.14 Å, θ=90°), respectively. The above values are in good accordance with earlier experimental observations[62,64] and in excellent agreement with recent LIF experimental data available.[10]

In order to study larger clusters we investigate the additivity of the potential energy surface in the He_2Br_2. In general, such model surfaces are useful for studying the relaxation dynamics of impurities embedded in He nanodroplets.[74] Therefore, analytical representations based on a sum of pairwise atom-atom interactions and a sum of three-body $HeBr_2$ CCSD(T) potentials and He–He interaction are checked in comparison with the tetratomic MP4/CCSD(T) *ab initio* results for He_2Br_2. The sum of the three-body interactions form is found to accurately represent the *ab initio* data. For first time an analytical expression in accord with high level *ab initio* studies is proposed for describing the intermolecular interactions for such two atoms rare gas–dihalogen complexes. The existence of three (linear, 'police-nightstick' and tetrahedral) minima is established for the He_2Br_2 ground PES. This finding may permit the fitting of the rotationally resolved excitation spectrum of He_2Cl_2 or similar species, where the traditional tetrahedral structural models, based on pairwise additive potentials, have failed.

Variational bound state calculation is carried out for the above surface and vdW energy levels and eigenfunctions for $J = 0$ are evaluated for He_2Br_2. Radial and angular distributions are calculated for the three lower vdW states. All of them are well localized in configuration space, with an exception of the broad distribution of the angle γ for the $n = 2$ state, due to the weak He-He interaction. The ground state corresponds to a linear isomer and the next two excited vdW levels are assigned to 'police-nightstick' and tetrahedral ones. The binding energies and the average structures for these species are determined to be D_0=32.240 cm^{-1} with $R^0_{1,2}$=4.867 Å, D_0=31.437 cm^{-1} with $R^0_{1,2}$=4.491 Å, and D_0=30.930 cm^{-1} with $R^0_{1,2}$=4.171 Å, respectively.

Whether the properties of the weak bonding in such systems can be predicted by the sum of atom-diatom interactions deserve further investigation. Such model should be applicable to a broad class of Rg_2XY, with Rg=rare-gas and X,Y=halogen atoms, vdW clusters. It is particularly interesting to investigate the intermolecular interactions and structural properties of similar clusters consist of heteropolar halogens, evaluating the importance of additional effects (e.g. introducing electric dipole moment, changing the reduced mass of the complex, etc..) Work in this line is in progress.

Acknowledgements

We would like to thank Dr Richard Loomis for providing us his experimental results prior to publication. The authors also wish to thank the Centro de Cálculo de IMAFF, the Centro Técnico de Informática (CTI), CSIC, the Centro de Supercomputación de Galicia (CESGA) and the Grupo de SuperComputación del CIEMAT (GSC) for allocation of computer time. This work has been supported by CICYT, Spain, Grant No. FIS2004-02461 and by a European TMR network, Grant No. HPRN-CT-1999-00005. R.P. acknowledges a contract from the Comunidad Autónoma de Madrid, Spain.

References

1. K. Higgins, F-M. Tao and W. Klemprerer, *J. Chem. Phys.*, **109**, 3048 (1998).
2. R. Prosmiti, C. Cunha, P. Villarreal, G. Delgado-Barrio, *J. Chem. Phys.* **119**, 4216 (2003).
3. S.J. Harris, S.E. Novick, W. Klemperer and W.E. Falconer, *J. Chem. Phys.*, **61**, 193 (1974).
4. S.E. Novick, S.J. Harris, K.C. Janda and W. Klemperer, *Can. J. Phys.*, **53**, 2007 (1975).
5. J.B. Davey, A.C. Legon and Waclawicki, *Chem. Phys. Lett.*, **306**, 133 (1999).
6. Y. Xu, W. Jäger, I. Ozier and M.C.L. Gerry, *J. Chem. Phys.*, **98**, 3726 (1993).
7. A. E. Stevens Miller, C-C. Chuang, H.C. Fu, K.J. Higgins and W. Klemperer, *J. Chem. Phys.*, **111**, 7844 (1999).
8. J.P. Darr, R.A. Loomis and A.B. McCoy, *J. Chem. Phys.*, **120**, 2677 (2004).
9. D.B. Strasfeld, J.P. Darr, and R.A. Loomis *Chem. Phys. Lett.*, **397**, 116 (2004).

10. R.A. Loomis (private communication).
11. K.W. Chan, T.D. Power, J. Jai-nhuknan and S.M. Cybulski, *J. Chem. Phys.*, **110**, 860 (1999)
12. S.M. Cybulski and J.S. Holt, *J. Chem. Phys.*, **110**, 7745 (1999).
13. R. Prosmiti, C. Cunha, P. Villarreal, and G. Delgado-Barrio, *J. Chem. Phys.*, **116**, 9249 (2002).
14. R. Prosmiti, P. Villarreal, and G. Delgado-Barrio, *Chem. Phys. Lett.*, **359**, 473 (2002).
15. W. Sharfin, K.E. Johnson, L. Wharton and D.H. Levy, *J. Chem. Phys.*, **71**, 1292 (1979).
16. J.E. Kenny, K.E. Johnson, W. Sharfin and D.H. Levy, *J. Chem. Phys.*, **72**, 1109 (1980).
17. M. Gutmann, D.M. Willberg and A.H. Zewail, *J. Chem. Phys.*, **97**, 8048 (1992).
18. B.A. Swartz, D.E. Brinza, C.M. Western and K.C. Janda, *J. Phys. Chem.*, **88**, 6272 (1984).
19. W.D. Sands, C.R. Bieler and K.C. Janda, *J. Chem. Phys.*, **95**, 729 (1991).
20. S.R. Hair, J.I. Cline, C.R. Bieler and K.C. Janda, *J. Chem. Phys.*, **90**, 2935 (1989).
21. C.R. Bieler, D.D. Edvard and K.C. Janda, *J. Chem. Phys.*, **94**, 7452 (1990).
22. H.S. Gutowsky, T.D. Klots, C. Chuang, J.D. Keen, C.A. Schmuttenmaer and T. Emilsson, *J. Am. Chem. Soc.* , **109**, 5653 (1987).
23. A. McIlroy, R. Lascola, C.M. Lovejoy and D.J. Nesbitt, *J. Chem. Phys.*, **95**, 2636 (1991).
24. M.J. Elrod, D.W. Steyert and R.J. Saykally, *J. Chem. Phys.*, **95**, 3182 (1991).
25. P. Villarreal, A. Varad and G. Delgado-Barrio, *J. Chem. Phys.*, **90**, 2684 (1989).
26. P. Villarreal, S. Miret-Arts, O. Roncero, S. Serna, J. Campos-Martnez and G. Delgado-Barrio, *J. Chem. Phys.*, **93**, 4016 (1990).
27. A. Garca-Vela, P. Villarreal and G. Delgado-Barrio, *J. Chem. Phys.*, **92**, 496 (1990).
28. E. Le Qur and S.K. Gray , *J. Chem. Phys.*, **98**, 5396 (1993).
29. Z. Bacic, M. Kennedy-Mandziuk, J.W. Moskowitz and K.E. Schmidt, *J. Chem. Phys.*, **97**, 6472 (1992).
30. P. Villarreal, O. Roncero and G. Delgado-Barrio, *J. Chem. Phys.* **101**, 2217 (1994).
31. J.M. Hutson, *J. Chem. Phys.*, **96**, 6752 (1992).
32. J.M. Hutson, *J. Chem. Phys.*, **89**, 4550 (1988).
33. S.M. Cybulski, J.S. Holt, *J. Chem. Phys.* **110**, 7745 (1999).
34. F.Y. Naumikin, *Chem. Phys. Chem.* **2**, 121 (2001).
35. G. Chalasinski, M.M. Szczesniak, *Chem. Rev.* **100**, 4227 (2000).
36. A. Rohrbacher, J. Williams, K.C. Janda, S.M. Cybulski, R. Burcl, M.M. Szcześniak, G. Chalasiński, N. Halberstadt, *J. Chem. Phys.* **106**, 2685 (1997).
37. R. Prosmiti, C. Cunha, P. Villarreal, G. Delgado-Barrio, *J. Chem. Phys.* **117**, 7017 (2002).
38. A. Valds, R. Prosmiti, P. Villarreal, G. Delgado-Barrio, *Chem. Phys. Lett.* **357**, 328 (2003).
39. R. Prosmiti, P. Villarreal, G. Delgado-Barrio, *Israel. J. Chem.* **43**, 297 (2003).
40. A. Valds, R. Prosmiti, P. Villarreal, G. Delgado-Barrio, *Mol. Phys.* in press (2004).
41. J.M. Hutson, J.A. Beswick and N. Halberstadt, *J. Chem. Phys.*, **90**, 1337 (1989).
42. T.D. Klots, C. Chuang, R.S. Ruoff, T. Emilsson and H.S. Gutowsky, *J. Chem. Phys.*, **86**, 5315 (1987); *ibid* **87**, 4383 (1987). , 5315 (1987)
43. G. Chalasinski, M.M. Szcześniak and B. Kukawska-Tarnawska, *J. Chem. Phys.*, **94**, 6677 (1991).
44. M.M. Szcześniak, G. Chalasinski and P. Piecuch, *J. Chem. Phys.* **99**, 6732 (1993).
45. A. Ernesti and J.M. Hutson, *Phys. Rev. A* **51**, 239 (1995).
46. A.R. Cooper and J.M. Hutson, *J. Chem. Phys.* **98**, 5337 (1993).
47. A. Valds, R. Prosmiti, P. Villarreal, G. Delgado-Barrio, *J. Chem. Phys.* **122**, XX1-XX10 (2005).
48. Gaussian 98, Revision A.7, M. J. Frisch, G. W. Trucks, H. B. Schlegel, G. E. Scuseria, M. A. Robb, J. R. Cheeseman, V. G. Zakrzewski, J. A. Montgomery, Jr.,

R. E. Stratmann, J. C. Burant, S. Dapprich, J. M. Millam, A. D. Daniels, K. N. Kudin, M. C. Strain, O. Farkas, J. Tomasi, V. Barone, M. Cossi, R. Cammi, B. Mennucci, C. Pomelli, C. Adamo, S. Clifford, J. Ochterski, G. A. Petersson, P. Y. Ayala, Q. Cui, K. Morokuma, D. K. Malick, A. D. Rabuck, K. Raghavachari, J. B. Foresman, J. Cioslowski, J. V. Ortiz, A. G. Baboul, B. B. Stefanov, G. Liu, A. Liashenko, P. Piskorz, I. Komaromi, R. Gomperts, R. L. Martin, D. J. Fox, T. Keith, M. A. Al-Laham, C. Y. Peng, A. Nanayakkara, C. Gonzalez, M. Challacombe, P. M. W. Gill, B. Johnson, W. Chen, M. W. Wong, J. L. Andres, C. Gonzalez, M. Head-Gordon, E. S. Replogle, and J. A. Pople, Gaussian, Inc., Pittsburgh PA, (1998).

49. A. Bergner, M. Dolg, W. Kuechle, H. Stoll and H. Preuss, *Mol. Phys.* **80**, 1431 (1993).
50. M.N. Glukhovtsev, A. Pross, M.P. McGrath and L. Radom, *J. Chem. Phys.*, **103**, 1878 (1995).
51. Y.G. Lazarou, A.V. Prosmitis, V.C. Papadimitriou and P. Papagiannakopoulos, *J. Phys. Chem.*, **105**, 6729 (2001).
52. C. Cunha, R. Prosmiti, P. Villareal and G. Delgado-Barrio, *Mol. Phys.*, **100** 3231 (2002).
53. W.R. Wadt and P.J. Hay, *J. Chem. Phys.*, **82**, 284 (1985).
54. J.M.L. Martin and A. Sundermann, *J. Chem. Phys.* **114**, 3408 (2001).
55. S.M. Cybulski and R.R. Toczylowski, *J. Chem. Phys.* **111**, 10520 (1999).
56. F.-M. Tao and W. Klemperer, *J. Chem. Phys.*, **97**, 440 (1992).
57. G. Chalasinski and M.M. Szczesniak, *Chem. Rev.*, **94**, 1723 (1994).
58. R. Prosmiti, A. Valds, P. Villarreal and G. Delgado-Barrio, *J. Phys. Chem. A*, **108**, 6065 (2004).
59. S.F. Boys and F. Bernardi, *Mol. Phys.* **19**, 553 (1970).
60. L.J. van de Burgt, J.-P. Nicolai and M.C. Heaven, *J. Chem. Phys.*, **81**, 5514 (1984).
61. J. Williams, *PhD Thesis*, University of California, Irvine, USA (1998).
62. A. Rohrbacher, N. Halberstadt and K.C. Janda, *Annu. Rev. Phys. Chem.*, **51**, 405 (2000).
63. M.I. Hernndez, T. Gonzlez-Lezana, G. Delgado-Barrio, P. Villarreal and A. Buchachenko, *J. Chem. Phys.*, **113**, 4620 (2000).
64. D.G. Jahn, S.G. Clement and K.C. Janda, *J. Chem. Phys.*, **101**, 283 (1996).
65. G. Delgado-Barrio, A.M. Cortina, A. Varad, P. Mareca, P. Villarreal and S. Miret-Arts, *J. Comp. Chem.*, **7** 208 (1986).
66. J.T. Muckerman, *Chem. Phys. Lett.*, **173** 200 (1990).
67. Enviromental Molecular Sciences Laboratory, *http://www.emsl.pnl.gov/*.
68. A. Rohrbacher, J. Williams and K.C. Janda, *Phys. Chem. Chem. Phys.*, **1**, 5263 (1999).
69. M.I. Hernndez, A. Garcia-Vela, J. Campos-Martnez, O. Roncero, P. Villarreal and G. Delgado-Barrio, *Comp. Phys. Comm.* **145**, 97 (2002).
70. T. Gonzlez-Lezana, M.I. Hernndez, G. Delgado-Barrio, A.A. Buchachenko and P. Villarreal, *J. Chem. Phys.*, **105**, 7454 (1996).
71. R.A. Aziz and M.J. Slaman, *J. Chem. Phys.*, **94**, 8047 (1991).
72. R.N. Zare, *Angular Momentum*, Wiley, New York (1988).
73. G. Danby, *J. Phys. B* **16**, 3393 (1983).
74. K. Nauta and R.E. Miller, *J. Chem. Phys.*, **117**, 4846 (2002).

ONE-ELECTRON PSEUDO-POTENTIAL INVESTIGATION OF $Na(3p^2P)Ar_n$ CLUSTERS: ELECTRONICALLY EXCITED ISOMERS AND EMISSION SPECTRA

M. BEN EL HADJ RHOUMA[a], Z. BEN LAKHDAR [b] AND F. SPIEGELMAN [c]

[a]*Laboratoire d'Etude des Milieux Ionisés et Réactifs (EMIR), Institut Préparatoire aux Etudes d'Ingénieur, Monastir, Tunisie*

[b]*Laboratoire de Spectroscopie Atomique et Moléculaire et Applications (LSAMA), Faculté des Sciences de Tunis, Tunisie*

[c]*Laboratoire de Physique Quantique (UMR 5626 du CNRS), IRSAMC, Université Paul-Sabatier, 118 route de Narbonne, 31065 Toulouse Cedex, France*

Abstract. We present a quantum-classical determination of stable isomers of Na^*Ar_n clusters with an electronically excited sodium atom in $3p^2P$ states. The excited states of Na perturbed by the argon atoms are obtained as the eigenfunctions of a single-electron operator describing the electron in the field of a Na^+ Ar_n core, the Na^+ and Ar atoms being substituted by pseudo-potentials. These pseudo-potentials include core-polarization operators to account for polarization and correlation of the inert part with the excited electron [1, 2]. The geometry optimization of the excited states is carried out via the basin-hopping method of Wales et al. [2, 3]. The present study confirms the trend for small Na^*Ar_n clusters in 3p states to form planar structures, as proposed earlier by Tutein and Mayne [4] within the framework of a first order perturbation theory on a "Diatomics in Molecules" type model.

1. Introduction

The spectroscopy of elementary systems such as atoms / molecules trapped in the volume or at the surface of small rare-gas clusters is a subject of continuous investigation [2, 5-9]. This is due to the fact that they may be considered as prototypes for the description of chromophores interacting with molecular clusters or inert solvents. From a theoretical point of view, the *ab-initio* determination of

J.-P. Julien et al. (eds.),
Recent Advances in the Theory of Chemical and Physical Systems, 371–383.

the excited states and electronic spectroscopic properties of such systems still remains a challenge, due to the number of electrons carried by the inert atoms, even when only valence electrons are considered. Experimental studies of such clusters have increased in the past decade with the development of formation and characterization techniques. An appealing application is that inert clusters can be used as trapping media to study the reactivity of isolated species [10]. In many studies, spectroscopy is an especially convenient tool to get information on the electronic structure, geometrical properties and even dynamical motion. Absorption spectra may, in particular, provide information on the structure of the first solvation shell [2].

There have been a number of theoretical investigations of the structure and dynamics of heterogeneous clusters in which a single atom or molecule interacts with a rare-gas cluster [11-14]. Pair potentials are often a good candidate for providing a simplified treatment for the ground state of extended systems such as small van der Waals clusters like $NaAr_n$ [2, 15, 16], $HgAr_n$ [17] or Li^+Ar_n [9], or impurities in rare-gas liquids [18] or rare-gas matrices [19]. Whenever excited states are involved, for instance in the np states of alkali atoms or ns-np states of alkaline earth atoms [10, 17, 20], pair potentials must be generalized in order to take into account the anisotropic perturbation mixing of initially degenerate states. Such extensions, parameterized on the excited states of the diatomic constituents, can be viewed as a particular case of the more general *Diatomics in Molecules* (DIM) picture [21]. They provide simple matrix schemes widely used for atoms solvated / trapped in inert clusters / matrices. The DIM picture relies on the assumption that the excited states of a polyatomic system can be spanned by combinations of wavefunctions localized on atomic or diatomic fragments.

Though such expansions are exact in principle, their practical application requires their truncation to a limited subspace, usually spanned by the minimal relevant fragment-states qualitatively involved in the description of the global system wavefunction. While extremely appealing for its simplicity and efficiency, the relevance of the DIM picture, namely the transferability of the diatomic interactions, remains to be confirmed, because truncation limits the inclusion of many-body effects. This may turn out to be critical whenever the excited states are diffuse and, therefore, not necessarily localizable on the atomic or diatomic fragments. Actually, first order perturbative schemes do no take into account the wavefunction relaxation, which would require higher configurations to be included. In a recent study of $Na(3p)Ar_n$ cluster geometries, Tutein and Mayne [4] used a perturbation approach involving combinations of Σ and Π type NaAr potentials to model the clusters. Due to the fact that the 3p orbitals are directional and favor anisotropic interactions, Tutein and Mayne obtained minimal energy isomers for the lowest 3p excited state very different from those known for the ground state. Indeed, because of the size and isotropic character of the 3s orbital the sodium atom in the ground state sits at the surface of the argon clusters [2].

For clusters in the range n =3-8 with 3p excited states, Tutein and Mayne actually observed a predominance of planar or quasi-planar structures. This was interpreted, in terms of diatomic interactions, as due to the strongest binding of

the Π potential (D_e=565 cm^{-1}, R_e=5.73 bohr) with respect to the Σ one (D_e=32 cm^{-1}, R_e=12.95 bohr), favoring an arrangement of the inert atoms in a plane perpendicular to the 3p orbital. This stimulated us to undertake a study of the electronically excited clusters Na(3p)Ar_n with a hybrid Hamiltonian, not relying on the DIM approximation for the excited electron and based on a pseudo-potential description of the rare-gas atoms closer to the *ab initio* approaches. This work extends our previous investigation [2] of the ground-state Na(3s)-Ar_n geometries and absorption spectroscopy to that of stable isomers on the Na(3p)Ar_n potential energy surface. Following photon absorption, the 3p states are expected to relax into configurations possibly responsible for fluorescence. Although fluorescence has not yet been observed in these clusters, it has been investigated in Na /Ar matrices [22, 23], yielding valuable information about isolation sites.

In Section 2 we briefly present the theoretical framework and schemes of the hybrid method used to compute the electronic states of clusters and the algorithm used for structure optimizations. Section 3 is devoted to the presentation and discussion of our results and a comparison with the DIM computations of Tutein and Mayne [4]. The emission lines originating from Na(3p)Ar_n excited states are also calculated and discussed.

2. Potential-energy surface calculations and optimization methods

A - Pseudo-potential calculation

The pseudo-potentials used here are of the l-dependent semi-local type, according to the expression of Barthelat and Durand [24]. The single valence electron pseudo-potential for the [Na^+] core has been widely used in accurate standard valence calculations [25, 26]. The argon atoms are represented via [Ar] atomic pseudo-potentials operators already used in the investigation of the absorption spectroscopy of atoms or molecules interacting with argon clusters or matrices [1, 2, 27, 28]. The pseudo-potentials also incorporate core polarization operators using a stepwise cut-off adaptation by Foucrault and coworkers [29] of the formulation proposed by Müller and Meyer [30]. These operators account for the polarization of the alkali ionic core as well as of the argon atoms considered as a core entities. The core-polarization operator reads

$$W^{pol} = -\frac{1}{2}\sum_{\lambda} \alpha_{\lambda}\, \vec{f}_{\lambda}\, \vec{f}_{\lambda}$$

The sum in W^{pol} runs over all polarizable cores (λ=Na^+, Ar); α_λ is the dipole polarizability of core λ, namely 0.9947 a_0^3 and 11.08 a_0^3 for sodium and argon respectively; $\boldsymbol{f}_\lambda$ is the electrostatic field at center λ, produced by the ion [Na^+] and the single valence electron at relative distance r_λ of core λ . The electronic field is truncated by a stepwise cut-off function F_λ, in order to avoid integral divergencies:

$$\vec{f}_\lambda = \frac{\vec{r}_\lambda}{r_\lambda^3} F_\lambda(r_\lambda) - \frac{\vec{R}_{\lambda Na'}}{R^3_{\lambda Na'}} \delta_{\lambda Na}$$

The electronic part of the Hamiltonian is thus given by the single-electron operator

$$h = -\frac{1}{2}\Delta - \frac{1}{r_{Na}} + W_{Na} + \sum_{\lambda}^{Ar} W_{Ar}$$

in which W_{Na} and W_{Ar} include both the averaged and core polarization operators. The total Hamiltonian also includes classical pair contributions V_{NaAr^+} between the sodium core and the argon atoms, taken from the work of Ahmadi et al [31], and pair potentials between argon atoms V_{ArAr}, taken from the multiproperty fit of Aziz et al [32]. This hybrid Hamiltonian has been shown to yield an accuracy comparable to (or even better than) that of existing all-electron calculations for free diatomics: LiAr, NaAr and KAr [1], where comparison with high resolution spectroscopic data is available. Using such pseudo-potential techniques, we restrict the number of active electrons to a single one for the whole system. The ground and excited states are readily obtained through simple diagonalization within a Gaussian-type orbital basis set (6s5p3d on sodium, 5s4p on each argon atom). The computational cost is strongly reduced and it becomes possible to implement the electronic calculation with global optimization techniques for exploring the potential energy surface (PES) and find the geometry of the lowest energy isomers of $Na(3p)Ar_n$.

B - Global optimization

Several optimization methods can be employed to find cluster isomers. Here we use the powerful global optimization method of Wales and Doye [3], called basin-hopping. This algorithm has proven to be especially efficient [33, 34] to locate global minima (GM) as well other low-lying minima even in pathologic situations. This algorithm essentially converts the potential energy surface into a series of terraces by quenching the structures generated in the Monte-Carlo moves, using gradient minimization. The energy at any point in the configuration space is associated with that of the closest local minimum found by local optimization started at that point. The transformed energy is given by

$$E'(X) = \min_l \left[E(X) \right]$$

where X is the vector representing a point in the nuclear configuration space and min_l indicates that local energy minimization has been completed starting form X. A Monte-Carlo sampling is actually carried out “on the fly” on the transformed potential energy surface. The removal of the potential energy barriers accelerates the dynamics and broadens the transition temperature regions.

This increases the probability of sampling the global minimum at a temperature where the free energy barriers between the funnel leading to the global minima and other funnels may be crossed.

3. Results and Discussion

A - Structure of Na(3p)Ar_n

As shown in previous publications relative to absorption spectroscopy and ground-state equilibrium geometries, the sodium atom in a 3s state prefers to bind on the "surface" of a rare-gas cluster. This stems from the fact that the NaAr diatomics have a smaller bonding energy at a longer internuclear distance than ArAr, in concordance with the rather large size of the isotropic 3s orbital.

The 3p manifold of sodium generates three potential energy surfaces for the cluster. These may undergo adiabatically avoided crossings or possibly meet degeneracy situations such as Jahn-Teller or Renner-Teller configurations, the former being frequently associated with conical intersections at points of high symmetry. The optimization procedure was carried out individually for the three adiabatic surfaces a, b and c (alphabetic labeling according to increasing energy), generating isomers associated with these surfaces (and correspondingly labeled a, b and c).

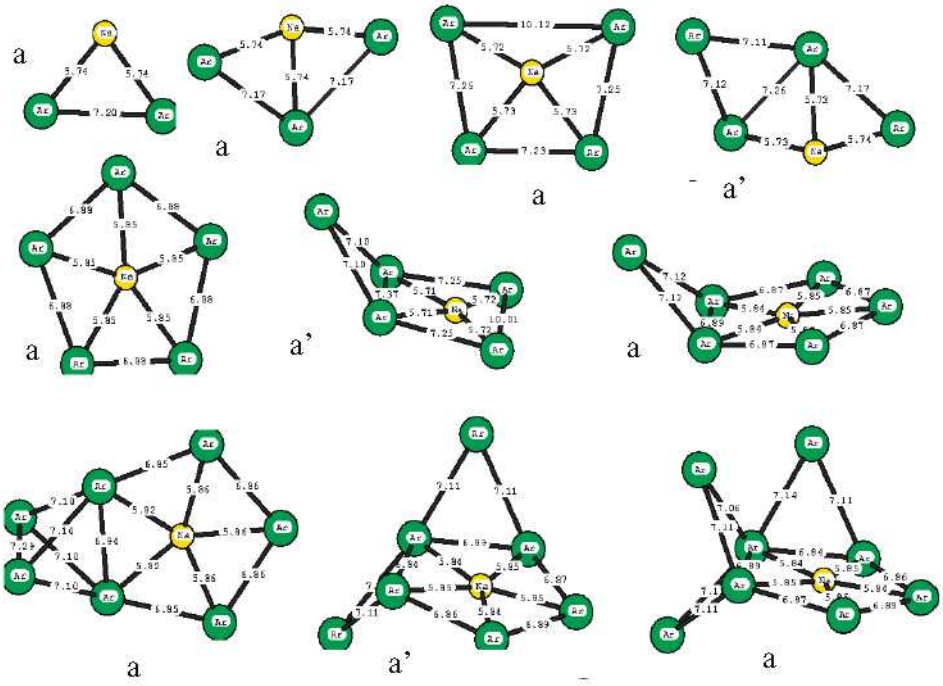

Figure 1. Low-energy isomers of Na(3p)Ar_n clusters, obtained on the lowest 3p PES. Isomers labeled (a) are global minima, isomers (a') have higher energies.

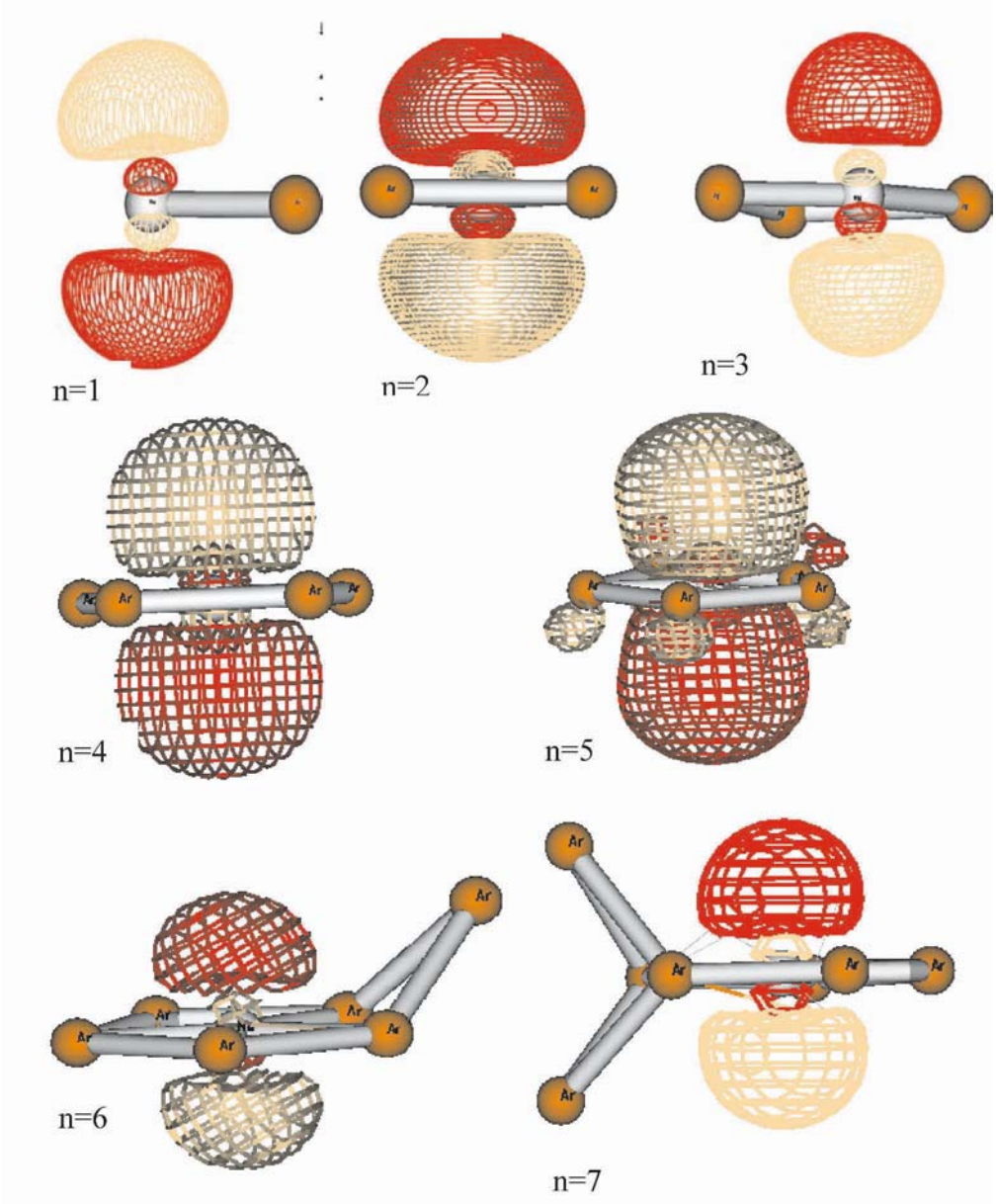

Figure 2. Orbital contour plots for the global minima isomers (a) of $Na(3p)Ar_n$ clusters.

We start with the minima obtained on the lowest 3p PES (labeled a). The global minimum (GM) energy geometries of Na^*Ar_n clusters with n=2-8 are illustrated in Fig. 1, with a few other energetically nearby isomers. For n=2-8, the calculated GM equilibrium structures on the lowest 3p PES are in good agreement with the results of Tutein and Mayne [4]. One advantage of the present mo-

del is that it actually provides a true orbital density for the excited electron. The contour plots of the 3p orbitals for the lowest isomers are given in Fig. 2. These plots clearly confirm, for all global minima, the role of Π oriented interactions to stabilize planar shapes, favoring the ring arrangement of the nearest neighbor argon atoms in the nodal plane of the 3p orbital. The number of possible nearest neighbors around the sodium atom saturates at n=5, since the argon atoms tend to form bonds with geometry as close as possible to the equilibrium distance of the ArAr diatomics (Re = 7.11 bohr). As first stated by Tutein and Mayne, the 5-atom ring in $NaAr_5$ clusters is particularly stable and occurs to be a structural seed: the growth mechanism for larger sizes indeed consists of bonding extra argon atoms (n = 6, 7 and 8) to the ring. The positions of the added atoms depart from the plane so as to maximize their bonding energy with the central sodium, achieving in this intermediate bent position a more favorable balance between Π and Σ interactions along the NaAr axes: NaAr bond lengths are in the range 9.5-10.5 bohr, and the angle with the plane in the range 20-28 degree. For n=7 and 8 the added argon atoms mutually rearrange in neighboring locations (symmetrically with respect to the ring plane for n=7), in order to form ArAr bonds bringing extra stabilization.

Table 1 lists the atomization energies of the $Na(3p)Ar_n$ clusters. The atomization energies found in the present work and those obtained by Tutein and Mayne are in very good agreement within 200 cm^{-1}, whatever the cluster size. The size dependence of stabilities observed by Tutein and Mayne is confirmed.

Up to the saturation of the 5-atom ring, the energy gained by each argon atom addition corresponds to the addition of a new Π–like interaction with sodium, plus the formation of an extra weak ArAr dispersion bond (two in $NaAr_5$). Beyond this size, the addition of argon atoms mainly involves the formation of ArAr bonds, and the stabilization is found to be weaker. In this respect, the stability of $Na(3p)Ar_5$ is enhanced with respect to its immediate size neighbors and this cluster can be considered as an excited magic size cluster.

Isomers different from the global minima on the lowest PES have also been found. Some of them are reported in Fig. 1. Up to n=5, the isomers consist of structures characterized by a number of argon atoms in the ring which is not maximal and the extra argon atom weakly binds to the others ones in the ring and to the central sodium atom. Their structural excitation energy essentially corresponds to the removal of one Π type interaction. Beyond n=6 the lowest structurally excited isomers are still based on 5-atom rings but they exhibit less favorable arrangements of the argon atoms weakly attached to the ring. These arrangements do not maximize the number of ArAr nearest-neighbor bonds and therefore lie a few 100 cm^{-1} only above the global minimum. Interestingly, Tutein and Mayne have achieved optimization for larger clusters in the range n=9-12 and for n=17 within the DIM approximation. They observed that the stable structures are obtained mainly via the growth of a segregated, purely rare-gas sub-cluster based on tetrahedral units, and sharing argon atoms with the 5-atom ring of the $NaAr_5$ unit.

TABLE 1. Symmetry, atomization energies (e_a) with respect to Na(3p) + nAr, transition energies corresponding to absorption (ν_{abs}) and emission (ν_{em}), and emission line intensities (A) of Na(3p)Ar_n clusters. The atomization energies of Tutein and Mayne [4] are given in parentheses. The labeling a, b, c of the states corresponds to the increasing energy ordering of the three adiabatic 3p PES. The primed structures (a') are higher energy isomers on the lowest energy surface.

Cluster	Isomer	Sym.	e_a (cm^{-1})	ν_{abs} (cm^{-1})	ν_{em}(cm^{-1})	A_{k0}(10^6 s^{-1})
Na				16969	16969	61.49
NaAr	3s	$C_{\infty v}$		16916, 16916, 17175		
	ab 3pΠ	$C_{\infty v}$	565 (563*)		15943	49.48
	c 3p Σ	$C_{\infty v}$	32		16940	62.61
$NaAr_2$	3s	C_{2v}		16874, 16961, 17315		
	a 3p	C_{2v}	1184 (1227)		14981	41.13
	b 3p	C_1	704		15943	49.50
	c 3p	C_s	126		16946	62.82
$NaAr_3$	3s	C_{3v}		16922, 16922, 17450		
	a 3p	C_{2v}	1790 (1900)		13840	32.77
	b 3p	C_1	1141		14779	41.45
	c 3p	C_{3v}	401		16941	64.71
$NaAr_4$	3s	C_{3v}		16917, 16917, 17450		
	a 3p	C_{2v}	2414 (2604)		12390	24.63
	a' 3p	C_1	2018		13794	32.09
	c 3p	C_{3v}	660		16939	66.57
$NaAr_5$	3s	C_{4v}		16960, 16960, 17557		
	a 3p	D_{5h}	3048 (3189)		11792	20.99
	a' 3p	C_{2v}	2045		12329	24.01
	b 3p	C_{2v}	925		14204	33.71
	c 3p	C_s	788		16935	59.08
$NaAr_6$	3s	C_{2v}		16863, 17053, 17553		
	a 3p	C_s	3276 (3402)		11770	20.56
	b 3p	C_s	1292		11701	21.69
	c 3p	C_s	788		16931	60.27
$NaAr_7$	3s	C_s		16882, 16908, 17526		
	a 3p	C_{2v}	3578 (3714)		11739	20.18
	a' 3p	C_2	3262		11759	20.43
	b 3p	C_{2v}	1771		9617	19.15
$NaAr_8$	3s	C_1		16851, 17304, 17856		
	a 3p	C_1	3774 (4027)		11767	20.29

For n = 17, this growth results in an icosaedral argon sub-cluster attached to the ring. However, from the results obtained here this building pattern could come in competition with another architecture, completing the formation of two external argon rings respectively above and below the 5-atom central ring plane. This would result in a second shell completion at n = 15. Such a pattern was not discussed by Tutein and Mayne.

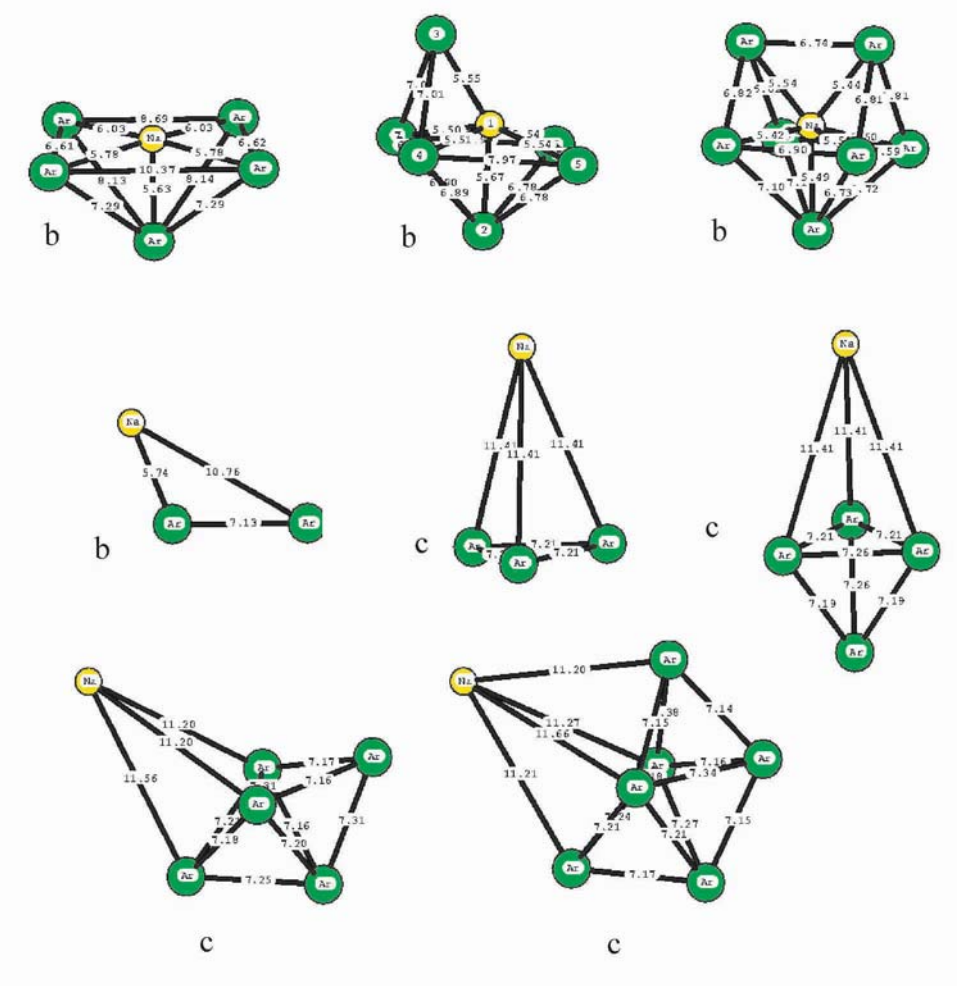

Figure 3. Low-energy isomers of Na(3p)Ar_n clusters obtained on the second (b) and third (c) 3p potential energy surfaces.

We have also achieved optimization for the second and third excited PES originating from the 3p configuration. It is not quite obvious that, depending on the excitation mechanism, a cluster may stabilize with a significant lifetime on those PES due to the proximity of the others and the various possibilities of surface hopping induced by non-adiabatic couplings. Such transition may combine with intra-cluster vibrational relaxation, as investigated by Gerber et al. [20] on $BaAr_n$ clusters. Nevertheless, some representative structures were systematically studied and are reported here. Starting from the second excited PES, we obtain a few non-planar isomers of size n = 5. For instance, the $NaAr_5$ (b) isomer is built from a distorted square 4-argon atom basis with the sodium atom in the middle capped by an extra argon atom. The basis is not exactly planar, the sodium atom being pushed off the plane. This structure is also a seed for the isomers of larger clusters such as $NaAr_6$ (b) and $NaAr_7$ (b), where extra atoms complete the first solvation shell (Fig.3).

Starting from the third PES (c), we found another series of clusters that can easily be identified as consisting of a sodium atom weakly attached to a stable argon cluster keeping its isolated geometry, closer to ground-state 3s-type structures where the alkali atom remains on the surface [2]. The bonding energy is weak and the bond length slightly shorter than the equilibrium distance in the Σ state of NaAr diatomics (about 11.5 bohr instead of R_e=12.95 bohr), meaning that the bond is dominated by a Σ type interaction with a small admixture of Π component. These clusters should be considered as pure van der Waals clusters in an excited state. At smaller atom-cluster distance, the Σ interaction becomes strongly repulsive.

B - Emission lines

Whereas absorption spectra can be obtained at a given temperature via Monte-Carlo type simulations, the reach of equilibrium in an excited state of an isolated cluster is less obvious, and even less is the definition of a relevant temperature. In any case, the final state may be strongly dependent on the excitation process. Here we will ignore the vibrations of the $Na(3p)Ar_n$ cluster. We assume a Franck-Condon type approximation and that emission takes place from relaxed equilibrium geometry structures on the $Na(3p)Ar_n$ excited PES. The Einstein coefficients of the lines of emission towards the ground state at energy ΔE are given by

$$A_{k0} = \frac{4}{3}\frac{\Delta E^3}{\hbar^4 c^3}\left(\frac{e^2}{4\pi\varepsilon_0}\right)\langle\phi_k \mid \vec{r} \mid \phi_0\rangle^2$$

They are listed in Table 1 for the various electronically excited stable isomers The transition dipole moments from these electronic excited states ϕ_k at equilib-

.

rium geometry towards the cluster ground state ϕ_0 at the same geometry are explicitly computed using the cluster wavefunctions provided by the single electron model. They take into account the orbital deformation and relaxation in the upper and ground states, whereas first-order perturbation theory would assume frozen atomic wavefunctions and therefore only describe their mixing within the 3p manifold. For the sake of comparison, we also provide the transition energies corresponding to absorption from the $Na(3s)Ar_n$ clusters in the ground-state equilibrium geometries towards the 3p states.

In clusters, the 3p states are split into two or three components depending on symmetry. The resonance transition energy of the free sodium atom is 16969 cm^{-1}. In the case of ring planar or quasi-planar clusters (a), the emission transition is systematically red-shifted, due to the fact that the upper state is stabilized whereas the ground state is conversely destabilized. Since the minimum of the Π interaction in the NaAr molecule occurs with a binding energy of 565 cm^{-1}, whereas at this internuclear distance the ground state is accordingly repulsive by 580 cm^{-1}, one can roughly estimate that up to n = 5 each addition of a extra argon atom increases the red shift by 1150 cm^{-1}. This is clearly observed in Table 1. From 15943 in NaAr, the emission transition energy decreases successively down to 14981 cm^{-1} in $NaAr_2$, 13840 cm^{-1} in $NaAr_3$, 12390 cm^{-1} in $NaAr_4$, and down to 11792 cm^{-1} in $NaAr_5$. Afterwards, the addition of second neighbor argon atoms does not alter the situation, and the lines for $NaAr_6$ (a), $NaAr_7$ (a,b), and $NaAr_8$ (a) also lie close to 11700 cm^{-1}. This means it will be almost impossible to discriminate emission spectra of isomers based on the same 5-ring pattern like $NaAr_7$ (a, b), and differing only by the positions of the external argon atoms.

The incomplete $NaAr_2$ (b), $NaAr_3$ (b), $NaAr_4$ (b) and $NaAr_5$ (b) isomers follow the same logic, namely their emission line is larger by roughly 1150 cm^{-1} than that of the ring isomers discussed above. Some modulations with respect to this rule naturally occur due to distance relaxation: in $NaAr_5$ (b), the axial NaAr distances are smaller than those in $NaAr_5$ (a).

The emission in compact clusters such as $NaAr_5$ (c), $NaAr_6$ (b) and $NaAr_7$ (c) are calculated to be 14204 cm^{-1}, 11700 cm^{-1} and 9617 cm^{-1}, respectively (see Table 1). The increase of the red-shift and its particularly large value in $NaAr_7$ (c) is mostly attributable to an increase of the repulsive character of the ground state for more and more compact geometries.

Obviously, the clusters $NaAr_2$ (c), $NaAr_3$ (c), $NaAr_4$ (c), $NaAr_5$ (d), and $NaAr_6$ (c), which correspond to the simple van der Waals long distance addition of a excited sodium atom to an argon cluster, are characterized by 3p states and 3s states only weakly shifted with respect to the isolated atom limit. Their emission lines are therefore very close to the atomic line.

4. Conclusion

We have investigated the minimal energy isomers of excited $Na(3p)Ar_n$ clusters using a hybrid pseudo-potential model where a single electron quantum descrip-

tion is combined with classical argon-argon and Na^+-argon pair potentials. The global minima obtained via the basin-hopping algorithm are in agreement with those obtained via DIM type first-order perturbation calculations by Tutein and Mayne, evidencing the importance of ring-type planar geometries induced by the more favorable NaAr Π- type interaction. Geometrical and energetic size effects have been discussed, together with possible construction patterns for larger clusters. The atomization energies are also in very close agreement with the DIM values. Since the DIM and pseudo-potential schemes are completely independent methods, this agreement gives credit to both of them. It seems to confirm the relevance of the DIM model to address the lowest excited configurations of alkali rare-gas clusters. It also validates the present pseudo-potential formulation, which may be used in future studies to address higher (Rydberg) excited states. Emission lines and oscillator strengths are shown to exhibit size effects. Obviously experimental data on clusters are needed. Excited state dynamics could also be investigated with the present model. Experimental results on similar systems do exist but mass-selected experiments have not yet been achieved on the species investigated here. Time-resolved pump-probe techniques are now available. They allow for real-time investigation of excited-state dynamics (following the pump laser pulse) and size selection through ionization (probe laser pulse). We hope that the present theoretical results will motivate further research in this direction.

References

1. Ben El Hadj Rhouma M., Berriche H., Ben Lakhdar Z., Spiegelman F., J. Chem. Phys. **116**, 1839 (2002).
2. Ben El Hadj Rhouma M., Berriche H., Ben Lakhdar Z., Spiegelman F., Int. J. Quant. Chem. **99**, 495 (2004).
3. Tutein A. B., Mayne H. R., J. Chem. Phys. **108**, 308 (1998).
4. Wales D. J., Doyle J. P. K., J. Phys. Chem. A **101**, 5111 (1997).
5. Böhmer W., Haensel R., Schwentner N., Boursey E., Chergui M., Chem. Phys. Lett. **59**, 2752 (1973).
6. Gedanken A., Raz B., Jortner J., J. Chem. Phys. **59**, 2752 (1973).
7. Chergui M., Schwentner N., Chem. Phys. Lett. **219**, 237 (1994).
8. Resta L., Resta R., Phys. Rev. **19**, 16833 (1979).
9. Froudakis G. E., Farantos S. C., Velegrakis M., J. Chem. Phys. **258**, 13 (2000).
10. Gaveau M. A., Briand M., Fournier P. R., Mestdagh J. M., Visticot J. P., Calvo F., Spiegelman F., Eur. Phys. J. D **21**, 153 (2002).
11. Perera L., Amar F. G., J. Chem. Phys. **93**, 4884 (1990).
12. Fried L. E., Mukamel S., J. Chem. Phys. **96**, 116 (1992).
13. Hahn M. Y., Whetten R. L., Phys. Rev. Lett. **61**, 1190 (1988).
14. Tsoo C., Estrin D. A., Singer S. J., J. Chem. Phys. **96**, 7977 (1992).
15. Balling L. C., Wright J. J., J. Chem. Phys. **79**, 2941(1983); **81**, 675 (1984).
16. Boatz J. A., Fajardo M. E., J. Chem. Phys. **101**, 3472 (1994).
17. Roncero O., Beswick J. A., Halberstadt N., Soep B., NATO ASI Series B **227**, 471 (1990).
18. Batista V. S., Coker D. F., J Chem. Phys. **105**, 2033 (1996).
19. McCaffrey J. G., Kerins P. N., J. Chem. Phys. **106**, 7885 (1997).

20. Jungwirth P., Gerber R. B., J. Chem. Phys. **104**, 5803 (1996).
21. Kuntz P. J., in "Atom-Molecule Collision Theory" (Bernstein R.B. edr), Plenum Press, New York, 1979, p. 79; Kendrick B., Pack T., J. Chem. Phys. **102**, 194 (1995).
22. Balling L. C., Harvey M. D., Dawson J. F., J. Chem. Phys. **69**, 1670 (1978).
23. Tam S., Fajardo M. E., J. Chem. Phys. **99**, 854 (1993).
24. Barthelat J.C., Durand Ph., Theor. Chim. Acta **38**, 283 (1975).
25. Jeung G. H., Phys. Rev. A **35**, 26 (1987).
26. Magnier S., Millié Ph., Dulieu O., Masnou-Seuuws F., J. Chem. Phys. **98**, 7113 (1993).
27. Gross M., Spiegelman F., J. Chem. Phys. **108**, 4148 (1998).
28. Durand G., Duplan P., Spiegelman F., Z. Phys. D: At. Mol. Clusters **40**, 177 (1997).
29. Foucrault M., Millié Ph., Daudey J. P., J. Chem. Phys. **96**, 1257 (1992).
30. Müller W., Flesch J., Meyer W., J. Chem. Phys. **80**, 3297 (1984).
31. Ahmadi R., Røggen G., J. Phys. B: At. Mol. Opt. Phys. **27**, 5603 (1994).
32. Aziz R. A., J. Chem. Phys. **99**, 4518 (1993).
33. Wales D. J., Scheraga H., Science **285**, 1368 (1999).
34. Wales D. J., Doye J. P. K., J. Chem. Phys. **101**, 5111 (1997).
35. Northby J. A., J. Chem. Phys. **87**, 6166 (1987).

UNDERSTANDING CHEMICAL REACTIONS INVOLVING NON-ADIABATIC TRANSITIONS: PREDISSOCIATION OF THE ELECTRONICALLY EXCITED Li-HF COMPLEX

A. AGUADO, M. PANIAGUA
Unidad Asociada UAM-CSIC, Departamento de Qu´mica F´sica, Facultad de Ciencias C–XIV, Universidad Autónoma de Madrid, 28049 Madrid, Spain.

AND

CRISTINA SANZ, OCTAVIO RONCERO
Unidad Asociada UAM-CSIC, Instituto de Matemáticas y F´sica Fundamental, C.S.I.C., Serrano 123, 28006 Madrid, Spain.

Abstract. The electronic predissociation from several excited electronic states of LiHF is studied using a time dependent Golden rule treatment, in an adiabatic representation. The potential energy surfaces used are those developed recently [J. Chem. Phys. **119** (2003) 10088] to simulate the experimental spectrum. The non-adiabatic couplings are calculated using highly correlated electronic functions and a finite difference method. It is found that the electronic predissociation process towards the ground electronic state yields to the formation of LiF products, with a large probability, $> 90\%$. Also, the lifetimes associated to the A states are much shorter than for the B state. It is inferred that the electronic predissociation from the B and B' electronic states should take place through the A electronic state, which acts as a doorway. Such process is explained by important $\Sigma - \Pi$ vibronic couplings appearing between the A, B and B's.

1. Introduction

In chemical reactions there is an electronic reordering in which some bonds are broken to form new ones. A full description of a chemical process thus requires the understanding of the electronic change involved since it will determine the main forces appearing along the process. Using the electronic states of reactants and products as a "diabatic" basis set representation, the reactions take place when

J.-P. Julien et al. (eds.),
Recent Advances in the Theory of Chemical and Physical Systems, 385–405.

those states cross. The main features of the resulting adiabatic states, and their potential energy surfaces (PES's), are determined by these crossings and the nature of the diabatic states involved, as for example the reaction barriers appearing in the transition state region. If the resulting adiabatic PES's are well separated at the crossing, the reaction dynamics can be reasonably well described in the Born-Oppenheimer approach in a single adiabatic state. In general, however, it is important to study the role of non-adiabatic effects to understand the electronic reordering.

One textbook example of such situation is provided by the harpoon-like mechanism[1], where "covalent" diabatic states, correlating to reactants, cross with "ionic" diabatic states of products. The crossings take place at precise nuclear configurations, where an electron "jumps" forming the products, giving rise in general to reaction barriers. Typical model systems of this situation is provided by metal atoms (M) with hydrogen halides (HX): the electron jumps from M forming HX^- transient, which is unstable and dissociates rapidly, leaving the M^+X^- ionic products. This is the so-called Direct Interaction with Product Repulsion (DIPR) mechanism, recently reviewed[2]. The collision reaction dynamics in the ground as well as in the excited electronic states has been widely studied in these systems[3, 4, 5, 6, 7, 8, 9, 10, 11, 12, 13] and permits the study of non-adiabatic effects occurring in the electronic transitions.

Moreover, these systems present van der Waals wells from which the system can be promoted to electronic states correlating to excited metal atoms [14, 15, 16, 17, 18, 19, 20, 21, 22, 23, 24, 25, 26, 27, 28]. After the excitation, the system evolves towards products in several electronic states, thus involving one or several electronic transitions and providing very valuable information of the electronic correlations.

Reactions involving alkali metal atoms are particularly interesting because their relative simplicity: the cations are closed shell leading to a single final M^+X^- ionic electronic state in the energy interval of interest, and this state cross, in the entrance channel, with the covalent states correlating to the excited metal atom M(^2P). The photon excitation from the van der Waals well in the ground electronic state reaches this manifold of states, thus allowing the monitoring of the excited states reaction dynamics.

Among them, Li+HF can be considered a benchmark model system[29, 30] because its low number of electrons makes possible to calculate accurate PES's. Its electronic spectrum has been meassured by Polanyi and coworkers[22], and has been recently very nicely reproduced using purely adiabatic PES's [31]. In the simulation of the spectrum[31], the transition lines were artificially "dressed" by lorentzians which widths were fitted to better reproduce the experimental envelop. The physical origin of such widths is the decay of the quasibound states of the excited electronic states through electronic predissociation (EP) towards the ground electronic state. This EP process is the result of the non-adiabatic cou-

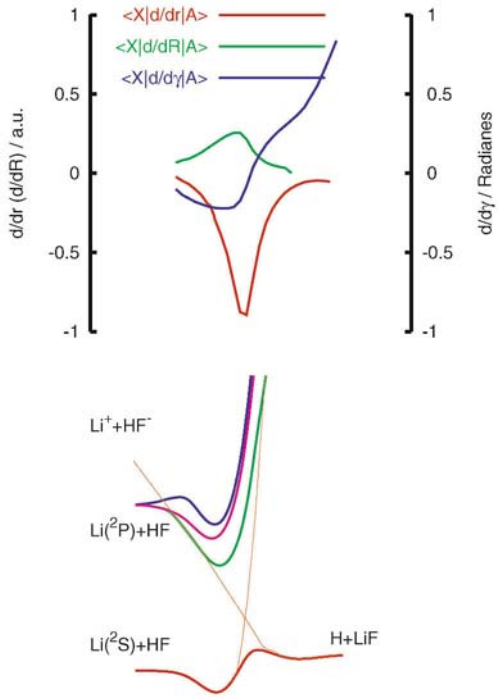

Figure 1. Lower panel: Minimum energy path of the four lower adiabatic states, correlating to Li(^2S)+HF($^1\Sigma^+$) and Li(^2P)+HF($^1\Sigma^+$). Also, the ionic diabatic state has been qualitatively shown. Upper panel: non-adiabatic couplings between the ground and first excited electronic states along the minimum energy path, as a function the internal Jacobi coordinates describing the Li+HF entrance channel.

plings among the excited and the ground electronic states, which becomes very important in the transition state region because of the crossing of the "diabatic" states, as it is shown in Fig.1. The wells in the excited electronic states are close to the transition state region of the ground electronic state, and therefore the EP of their associated quasibound states can be used as a trace of the "diabatic" curve crossing.

The purpose of this work is to study the electronic predissociation from the bound states of the excited A and B adiabatic electronic states, using a time dependent Golden rule (TDGR) method, as previously used to study vibrational predissociation[32, 33] as well as electronic predissociation[34, 35]. The only difference with previous treatments[34, 35] is the use of an adiabatic representation, what requires the calculation of non-adiabatic couplings. The method used is described in section II, while the corresponding results are discussed in section III. Finally, some conclusions are extracted in section IV.

2. Time-dependent Golden-rule treatment for Electronic predissociation

Let's consider an initial quasibound state $\Psi^{\alpha,k}(\mathbf{r},\mathbf{R})\xi_\alpha$, corresponding to a rovibrational level k in an excited electronic state α, which decays on dissociative states in the electronic state β, $\Psi^{\beta,v,j,E_{\alpha,k}}(\mathbf{r},\mathbf{R})\xi_\beta$, where v,j labels the quantum states of the fragments obtained at the energy of the initial state, $E_{\alpha,k}$. The $\mathbf{r},\mathbf{R}$ Jacobi vectors are defined below. This electronic predissociation process is governed by the coupling between different electronic states. The total Hamiltonian operator factorized as

$$\hat{H} = \hat{T}_N + \hat{H}^e, \tag{1}$$

where $\hat{T}_N$ is the kinetic energy operator associated to the nuclei while $\hat{H}^e$ is the electronic Hamiltonian. When this Hamiltonian is represented in the electronic subspace formed by the initial and final electronic states, the resulting Hamiltonian matrix becomes

$$\mathbf{H}^e = \begin{pmatrix} H^e_{\alpha,\alpha} & H^e_{\alpha,\beta} \\ H^e_{\beta,\alpha} & H^e_{\beta,\beta} \end{pmatrix} \tag{2}$$

with $H^e_{\alpha,\beta} = \langle\xi_\alpha|\hat{H}^e|\xi_\beta\rangle$. If the coupling between different electronic states is weak enough, the decay of the initial state is slow, following an exponential law characterized by a lifetime τ, or equivalently a width $\Gamma_{\alpha,k} = \hbar/2\tau$. Thus, using a first-order perturbation treatment, the width can be calculated using the well known Golden rule approach as[36]

$$\Gamma_{\alpha,k} = \pi \sum_{v,j} \left| \left\langle \Psi^{\alpha,k} | H^e_{\alpha,\beta} | \Psi^{\beta,v,j,E_{\alpha,k}} \right\rangle \right|^2 . \tag{3}$$

The reaction dynamics in the final electronic state ξ_β will be described within a time dependent approach. To transform Eq.(3) to its time dependent analog, the integral representation of the $\delta(E_{\alpha,k} - E')$ function is introduced in Eq.(3), thus obtaining[32]

$$\Gamma_{\alpha,k} = \frac{1}{2\hbar} \sum_{v,j} \int dE' \int dt\, e^{i(E_{\alpha,k}-E')t/\hbar} \left| \left\langle \Psi^{\beta,v,j,E'} | H^e_{\alpha,\beta} | \Psi^{\alpha,k} \right\rangle \right|^2 . \tag{4}$$

Using $e^{-iE't/\hbar}\,\Psi^{\beta,v,j,E'} \equiv e^{-iH_{\beta,\beta}t/\hbar}\,\Psi^{\beta,v,j,E'}$, considering the closure relationship in the subspace of the β electronic state,

$$\mathbf{1}_{\beta,\beta} = \sum_{v,j} \int dE \left| \Psi^{\beta,v,j,E} \right\rangle \left\langle \Psi^{\beta,v,j,E} \right| + \sum_k \left| \Psi^{\beta,k} \right\rangle \left\langle \Psi^{\beta,k} \right| , \tag{5}$$

(where $\Psi^{\beta,k}$ are rovibrational bound states on the isolated β electronic state) and rearranging terms, we arrive to the time dependent version of the Golden Rule expression[32, 33, 34],

$$\Gamma_{\alpha,k}(E) = \frac{1}{2\hbar}\int_{-\infty}^{\infty} dt\, e^{iEt/\hbar} \left\langle \Phi^{\alpha,k}(\mathbf{r},\mathbf{R},t=0)|\Phi^{\alpha,k}(\mathbf{r},\mathbf{R},t)\right\rangle \tag{6}$$

similar to the most commonly used for photodissociation[37, 38]. Here, however, the only energy of interest is $E = E_{\alpha,k}$. Also,

$$\left\langle \Phi^{\alpha,k}(\mathbf{r},\mathbf{R},t=0)|\Phi^{\alpha,k}(\mathbf{r},\mathbf{R},-t)\right\rangle = \left\langle \Phi^{\alpha,k}(\mathbf{r},\mathbf{R},t=0)|\Phi^{\alpha,k}(\mathbf{r},\mathbf{R},t)\right\rangle^{*}.$$

In Eq.(6), the initial wavepackets are defined as

$$\Phi^{\alpha,k}(\mathbf{r},\mathbf{R},t=0) = H_{\beta,\alpha}\Psi^{\alpha,k}(\mathbf{r},\mathbf{R}) \tag{7}$$

and its evolution in time as

$$\Phi^{\alpha,k}(\mathbf{r},\mathbf{R},t) = e^{-iH_{\beta,\beta}t/\hbar}\,\Phi^{\alpha,k}(\mathbf{r},\mathbf{R},t=0) \tag{8}$$

where the contributions of the bound states of the β electronic states has been neglected.

The initial states are bound eigensolutions in the isolated α electronic subspace, and $\Phi^{\alpha,k}(\mathbf{r},\mathbf{R},t)$ is propagated in the β electronic state. Thus the calculations involved are similar to the usual calculations in the Born-Oppenheimer approach, and will be briefly described below.

The non-adiabatic character of the process under study is included in the present approach in the evaluation of the initial wavepacket in Eq.(7). In an electronic diabatic representation, the electronic wavefunctions are considered to do not depend on the nuclear coordinates, so that the coupling between different states is only given by the electronic Hamiltonian, being of potential-type character.

In an electronic adiabatic representation, however, the electronic Hamiltonian becomes diagonal,$i.e.$ $\langle\xi_\alpha|H_e|\xi_\beta\rangle = \delta_{\alpha,\beta}\,V_\alpha$, where the adiabatic V_α potentials for initial (A,B,B') and final (X) electronic states were described in Ref.[31]. The couplings between different electronic states arises from the matrix elements of the nuclear kinetic operator $\hat{T}_N$, giving rise to the so-called non-adiabatic coupling matrix elements (NACME) and are due to the dependence of the electronic functions on the nuclear coordinates. The actual form of these matrix elements depends on the choice of the coordinates.

In this work we use an adiabatic electronic representation, and Jacobi nuclear coordinates are chosen: $\mathbf{r}$, the HF internuclear vector, and $\mathbf{R}$, the vector joining the HF center-of-mass to the Li atom, in a body-fixed frame in which the three atoms lie on the $x-z$ body-fixed plane, with $\mathbf{R}$ being parallel to the body-fixed

z-axis. Thus the coordinates are separated in internal, r, R, γ (with $\cos\gamma = \mathbf{r}\cdot\mathbf{R}$), specifying the relative position of the nuclei, and external, ϕ, θ, χ, the three Euler angles specifying the orientation of the body-fixed axis. The potential term V_α only depends on the internal coordinates, while the nuclear kinetic operator takes the form

$$\begin{aligned}\hat{T}_N &= -\frac{\hbar^2}{2\mu}\left(\frac{2}{R}\frac{\partial}{\partial R}+\frac{\partial^2}{\partial R^2}\right)+\frac{\mathbf{J}^2+\mathbf{j}^2-2\mathbf{J}\cdot\mathbf{j}}{2\mu R^2}\\ &\quad -\frac{\hbar^2}{2m}\left(\frac{2}{r}\frac{\partial}{\partial r}+\frac{\partial^2}{\partial r^2}\right)+\frac{\mathbf{j}^2}{2mr^2}\end{aligned} \tag{9}$$

where

$$\mathbf{j^2} = -\hbar^2\left\{\cot\gamma\frac{\partial}{\partial\gamma}+\frac{\partial^2}{\partial\gamma^2}+\frac{1}{\sin^2\gamma}\frac{\partial^2}{\partial\chi^2}\right\} \tag{10}$$

$$\mathbf{J}^2 = -\hbar^2\left\{\frac{\partial^2}{\partial\theta^2}+\cot\theta\frac{\partial}{\partial\theta}+\frac{1}{\sin^2\theta}\left(\frac{\partial^2}{\partial\phi^2}+\frac{\partial^2}{\partial\chi^2}-2\cos\theta\frac{\partial^2}{\partial\chi\partial\phi}\right)\right\}$$

$$\begin{aligned}\mathbf{J}\cdot\mathbf{j} &= -\hbar^2\left\{(1-\cot\gamma\cot\theta\cos\chi)\frac{\partial^2}{\partial\chi^2}-\cot\theta\sin\chi\frac{\partial^2}{\partial\chi\partial\gamma}+\cos\chi\frac{\partial^2}{\partial\theta\partial\gamma}\right.\\ &\quad \left.+\frac{\cot\gamma\cos\chi}{\sin\theta}\frac{\partial^2}{\partial\phi\partial\chi}+\frac{\sin\chi}{\sin\theta}\frac{\partial^2}{\partial\phi\partial\gamma}-\cot\gamma\sin\chi\frac{\partial^2}{\partial\theta\partial\chi}\right\}.\end{aligned}$$

The initial bound states are eigensolutions of the Hamiltonian in the α electronic subspace, and are expanded as

$$\Psi^{\alpha,k}(\mathbf{r},\mathbf{R})\,\xi_\alpha = \sum_{\Omega,j,v,n} C^{\alpha,k}_{\Omega,j,v,n}\frac{\varphi_v(r)H_n(R)}{rR}Y_{j\Omega}(\gamma,0)\,W^{JM\epsilon}_\Omega(\phi,\theta,\chi)\,\xi_\alpha \tag{11}$$

where $Y_{j\Omega}(\gamma,0)$ are normalized associated Legendre functions and

$$\begin{aligned}W^{JM\epsilon}_\Omega(\phi,\theta,\chi) &= \sqrt{\frac{2J+1}{16\pi^2(1+\delta_{\Omega,0})}}\Big[D^{J*}_{M\Omega}(\phi,\theta,\chi)\\ &+ \epsilon\sigma(-1)^{J+\Omega}D^{J*}_{M-\Omega}(\phi,\theta,\chi)\Big]\end{aligned} \tag{12}$$

where $D^{J*}_{M\Omega}(\phi,\theta,\chi)$ are Wigner rotation matrices[39], corresponding to a well defined total angular momentum J, with projections M and Ω on the space-fixed and body-fixed z-axes, respectively. These functions are eigenfunctions of the total inversion of spatial coordinates, with eigenvalue ϵ.

The projection of the electronic orbital angular momentum is neglected in this adiabatic representation, and the parity of the electronic function under reflection through the $x-z$ body-fixed plane, $\hat{\sigma}_{xz}$, is given by

$$\hat{\sigma}_{xz}\xi_\alpha = \sigma\xi_\alpha \tag{13}$$

being in this case $\sigma = +1$ for the X, A and B $^2A'$ states, while it is -1 for the B' $^2A''$ state. Since the total Hamiltonian is symmetric, it does not couple the B' and X state. Therefore, the states belonging to B' do not predissociate. The description of nuclear and electronic motions should be improved, taking into account the correlation among electronic and nuclear angular momenta: in a coupled diabatic representation of the 3 excited electronic states, A,B and B', the bound states would present amplitude on the three electronic states and, therefore, the coupling amplitude with the ground electronic state will be shared. In the present treatment, the predissociation from the A and B states will be studied to get an idea of the dynamics and rates involved.

The radial functions in Eq.(11) are numerical solutions of monodimensional Schrödinger equations, in which the potential corresponds to the three-dimensional one in which all degrees of freedom are frozen at their equilibrium values except that radial coordinate under consideration[40, 31].

The $H_{\alpha,\alpha}$ Hamiltonian is represented in the basis set described, and the resulting matrix is diagonalized using standard diagonalization techniques, obtaining the $E^{\alpha,k}$ eigenvalues and the $C^{\alpha,k}_{\Omega,j,v,n}$ coefficients. The number of basis set functions is increased until a desired accuracy is reached.

The wavepackets, in Eq.(7), are analogously expanded as

$$\Phi^{\alpha,k}(\mathbf{r},\mathbf{R},t)\,\xi_\beta = \sum_\Omega \frac{\Phi^{\alpha,k}_\Omega(r,R,\gamma,t)}{rR}\, W^{JM\epsilon}_\Omega(\phi,\theta,\chi)\,\xi_\beta, \tag{14}$$

so that using Eq.(7.a), and considering that the electronic Hamiltonian is diagonal in this representation, the $\Phi^{\alpha,k}_\Omega(r,R,\gamma,t)$ coefficients at time zero becomes

$$\begin{aligned}
\Phi^{\alpha,k}_{\Omega'}(r,R,\gamma,t=0) &= \left\langle W^{JM*}_{\Omega'}\,\xi_\beta | T_N | \Psi^{\alpha,k}\,\xi_\alpha \right\rangle \qquad (15)\\
&= \sum_\Omega \sum_{j,v,n} C^{\alpha,k}_{\Omega,j,v,n} \left\{ -\frac{\hbar^2}{2\mu}\left(G^{\beta,\alpha}_R + 2F^{\beta,\alpha}_R \frac{\partial}{\partial R}\right)\delta_{\Omega,\Omega'} \right.\\
&\quad -\frac{\hbar^2}{2m}\left(G^{\beta,\alpha}_r + 2F^{\beta,\alpha}_r \frac{\partial}{\partial r}\right)\delta_{\Omega,\Omega'}\\
&\quad -\frac{\hbar^2}{2}\left(\frac{1}{\mu R^2}+\frac{1}{mr^2}\right)\left(G^{\beta,\alpha}_\gamma + F^{\beta,\alpha}_\gamma\left[\cot\gamma + 2\frac{\partial}{\partial\gamma}\right]\right)\delta_{\Omega,\Omega'}\\
&\quad \left. -\frac{\hbar^2}{2}\left(\frac{1}{\mu R^2}+\frac{1}{mr^2}\right)\frac{1}{\sin^2\gamma}\left(G^{\beta,\alpha}_\chi - 2\Omega F^{\beta,\alpha}_\chi\right)\right.
\end{aligned}$$

$$+\left\langle W_{\Omega'}^{JM*}\,\xi_\beta\left|\frac{\mathbf{J}\cdot\mathbf{j}}{\mu R^2}\right|W_{\Omega}^{JM*}\,\xi_\alpha\right\rangle\Big\}\,Y_{j\Omega}(\gamma,0)\;\varphi_v(r)\;H_n(R)$$

where the non-adiabatic couplings are, as usual:

$$\begin{aligned} F_X^{\beta,\alpha} &= \left\langle \xi_\beta\left|\frac{\partial}{\partial X}\right|\xi_\alpha\right\rangle \\ G_X^{\beta,\alpha} &= \left\langle \xi_\beta\left|\frac{\partial^2}{\partial X^2}\right|\xi_\alpha\right\rangle \end{aligned} \tag{16}$$

with $X = r, R, \gamma$ or χ. In this respect, the Coriolis coupling between different Ω values arises from the dependence of the electronic state on the χ angle, $i.e.$ it requires to consider the electronic Coriolis coupling. If such dependence is neglected the two last terms in the rhs of Eq.(15) disappear, and the sum over Ω restrict to a single value $\Omega = \Omega'$. In addition, the electronic functions depends relatively weakly on r, R and γ, and the terms involving second order derivatives are very small, $i.e.$, $G_X^{\beta,\alpha} \approx 0$. With all this approximations, the coefficients of the initial wavepacket become

$$\begin{aligned} \Phi_{\Omega'}^{\alpha,k}(r,R,\gamma,t=0) = \sum_{j,v,n} C_{\Omega',j,v,n}^{\alpha,k}\;\Big\{ &-\frac{\hbar^2}{\mu}F_R^{\beta,\alpha}\frac{\partial}{\partial R} - \frac{\hbar^2}{m}F_r^{\beta,\alpha}\frac{\partial}{\partial r} \\ &-\frac{\hbar^2}{2}\left(\frac{1}{\mu R^2}+\frac{1}{mr^2}\right)F_\gamma^{\beta,\alpha}\left[\cot\gamma + 2\frac{\partial}{\partial\gamma}\right]\Big\}\,Y_{j\Omega'}(\gamma,0)\;\varphi_v(r)\;H_n(R). \end{aligned} \tag{17}$$

The $F_X^{\beta,\alpha}$ non-adiabatic couplings have been calculated for $\alpha =$ A and B and $\beta =$X as a function of the Jacobi internal coordinates using a second order finite difference method[41], with the MOLPRO suite of programs[42]. Multi reference configuration interaction (MRCI) electronic wavefunctions were calculated using this program, with the electronic basis set and procedures described previously[31]. About 60 points have been calculated in the region of the wells of the excited electronic states. This is so because within the Golden Rule approach, the whole non-adiabatic dynamics is determined by the initial wavepacket and it will be zero for the nuclear configurations where the initial $\Psi^{\alpha,k}$ is zero, irrespective of the value of the non-adiabatic coupling. Finally, the matrix elements are well approximated in this region by monodimensional fits to an analytical function of the type:

$$F_X^{\beta,\alpha}(x) = a_0 + \sum_{i=1}^{2} a_i \exp\left\{-b_i(x-x_i)^2\right\}$$

where $X = r, R$ or γ. For the γ angle it is sometimes convenient to fit the NACME calculated with respect to $X = \cos\gamma$, in order to take into account the correct behavior at $\gamma = \pi$, and transform to γ with the relation $F_{\gamma}^{\beta,\alpha}(\gamma) = -\sin\gamma F_{\cos\gamma}^{\beta,\alpha}(\gamma)$.

The action of the derivatives appearing in Eq.(17) is performed independently on each monodimensional basis function used to build the rovibrational states in the excited state, $\Psi^{\alpha,k}$. Radial derivatives are performed on numerical functions using Fourier Transforms[43]. The angular derivatives have been done analytically using

$$F_{\gamma}^{\beta,\alpha}\left[\cot\gamma + 2\frac{\partial}{\partial\gamma}\right] Y_{j\Omega}(\gamma,0) \equiv -F_{\cos\gamma}^{\beta,\alpha}\left[\cos\gamma + 2\sin\gamma\frac{\partial}{\partial\gamma}\right] Y_{j\Omega}(\gamma,0) \qquad (18)$$

$$= -F_{\cos\gamma}^{\beta,\alpha}\sqrt{\frac{2j+1}{2j+3}}\left[\sqrt{(j+1)^2-\Omega^2}Y_{j+1,\Omega}(\gamma,0) - \sqrt{j^2-\Omega^2}Y_{j-1,\Omega}(\gamma,0)\right]$$

Once the initial wavepacket is constructed, it is propagated in time. The details of the calculations have been described elsewhere[44, 45, 40] and only few details are discussed here. The integration of the time-dependent Schrödinger equation was performed in the $\beta = X$ ground electronic state using a Tchebychev propagator[46, 47], modified by including absorbing boundary conditions in the polynomial expansion[48]. The time step used is 0.25fs, necessary to follow the rapid decay of the wavepacket in the lower electronic state. It must be noted that this propagation time is not directly related to the EP lifetime. This last quantity is obtained from the Fourier transform of the autocorrelation function, as expressed in Eq.(6). The integration was performed until the autocorrelation function is negligible, typically of the order of 500 fs.

The $\Phi_{\Omega'}^{\alpha,k}(r,R,\gamma,t)$ coefficients are represented in grids for the three internal coordinates: r and R are described by 384×384 equidistant points, in the intervals $0.25 \leq r \leq 11.5$Å and $0.5 \leq R \leq 12$Å, respectively, while the angle γ is described by 30 Gauss-Legendre quadrature points. It is necessary to use damping functions, as mention above, which in this case are $e^{-\alpha(x-x_{abs})^2}$ gaussian functions, with α= 0.03 and 0.08 Å^{-2} and x_{abs}= 4 and 8Å, for r and R, respectively.

The flux towards LiF products is calculated far from the absorbing region, at r_f=3Å, as explained elsewhere [49, 50, 51, 52, 53, 40]. Also, the energy distribution of the HF($v.j$) vibrotational states is obtained using the method of Balint-Kurti *et al*[54, 55, 40].

3. Results and Discussion

The electronic predissociation from different rovibrational levels of the A and B electronic states has been evaluated, to study the effect of the initial excitation on the process. The bounds states chosen are k=1,2,3 and 6 for A, and k=1,2,3,6 and 12 for B, which correspond to the bending progression of states appearing in the

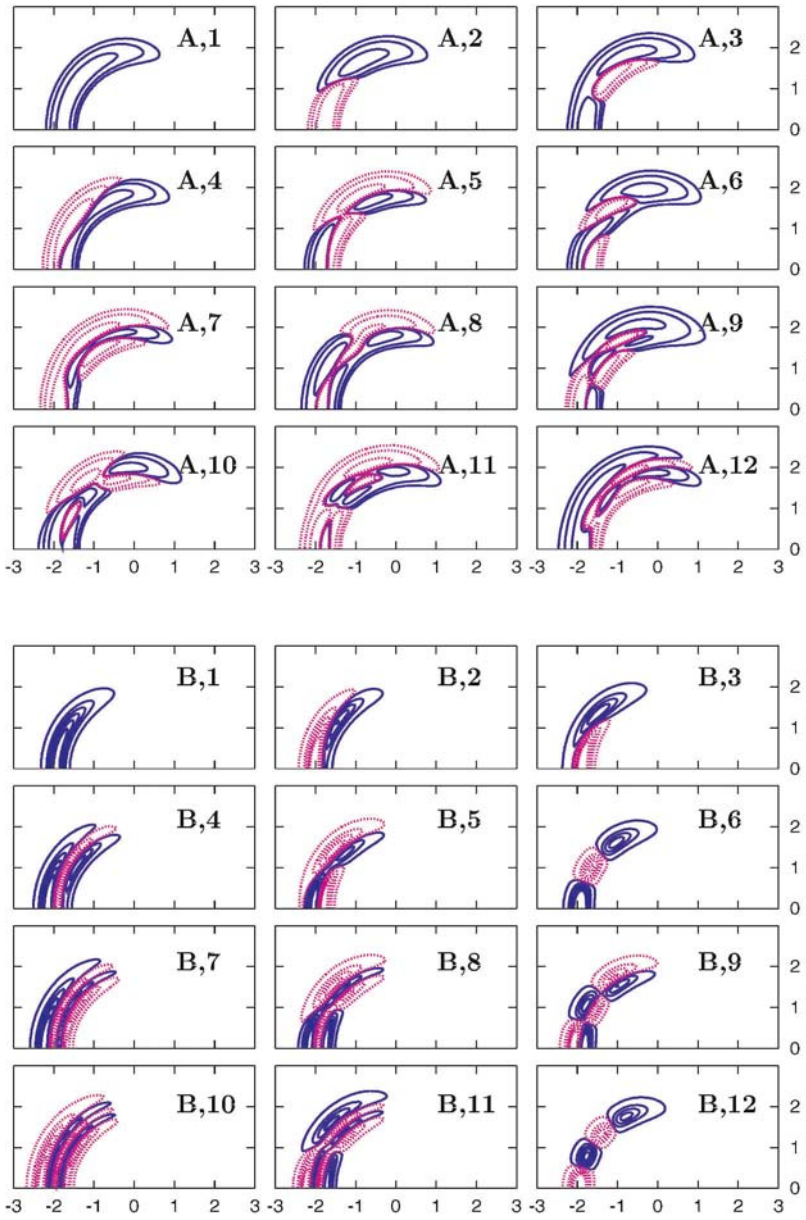

Figure 2. Contour plots of the bound state amplitude for the a) A and b) B electronic states as a function of x=R$\cos\gamma$ and y= R$\sin\gamma$, in Å, for the HF distance frozen at its equilibrium value.

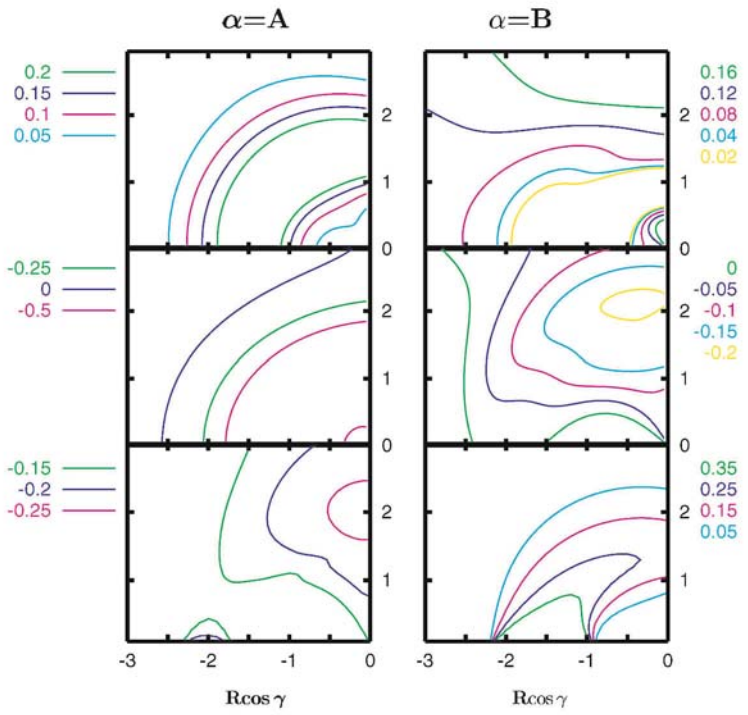

Figure 3. Contour plots of the NACMES's (with keys in a.u.) for A-X couplings (left panels) and B-X couplings (right panels) as a function of x=R$\cos\gamma$ and y= R$\sin\gamma$, in Å, for the HF distance frozen at its equilibrium value. Top panels corresponds to $F_R^{\alpha,\beta}$, middle panels to $F_r^{\alpha,\beta}$, and lower panels to $F_{\cos\gamma}^{\alpha,\beta}$.

spectrum for A and B electronic states, as discussed in Ref.[31]. The contour plots of the amplitude density associated to these states are shown in Fig.2.

The calculated NACMES's between the excited and the ground electronic states are shown in Figs.3. All of them are of the same order in the region of the wells, but in order to determine their effect it should be taken into account the reduced mass associated to each of them. Thus, since $\mu/m > 5$, the effect of $F_r^{\alpha,\beta}$ is more important than that of $F_R^{\alpha,\beta}$. The $F_{\cos\gamma}^{\alpha,\beta}$ angular NACME's contain both dividing mass factors, but multiplied by r^2 and R^2, respectively. The bound states are placed at relatively long R values, of $\approx$ 2Å, so that again the term depending on mr^2, is going to be the dominant because the $r \approx 1$Å.

The NACME's are multiplied by the corresponding derivatives acting on the initial bound rovibrational states. These derivatives are larger as the excitation of the vibration associated to each coordinate increases. In the excited electronic states, the HF frequency is much larger that those associated to the other two

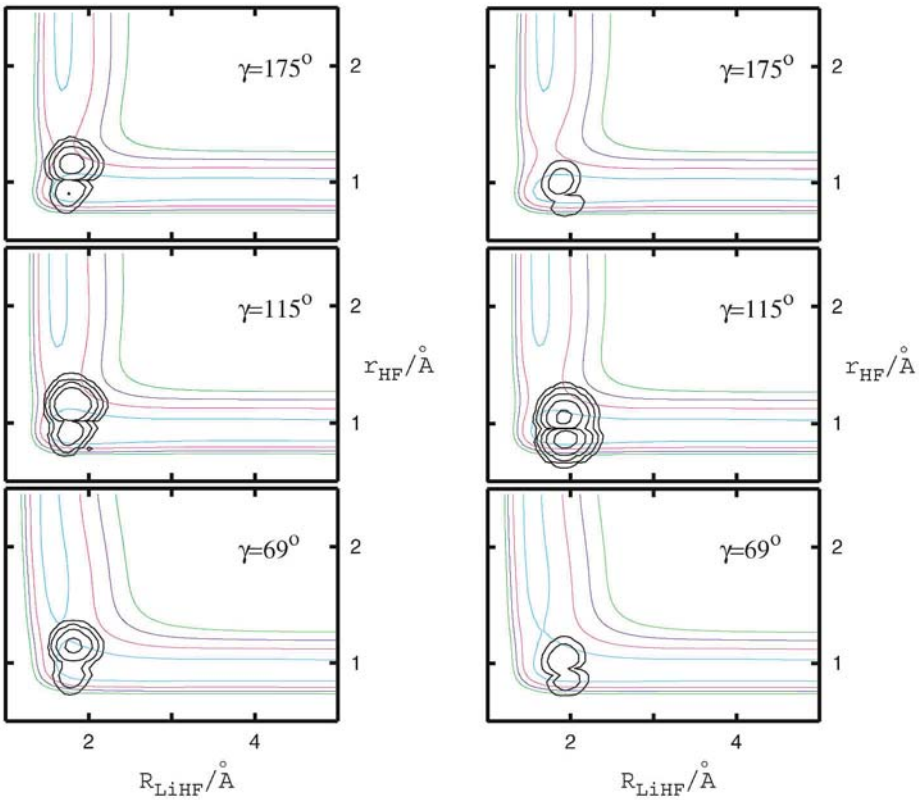

Figure 4. Contour plots of the wavepackets at t=0, built according to Eq.(17), for the ground vibrational states, k=0, of the A (left panels) and B (right panels) electronic states. Several angles are shown, the equilibrium value for the B state (top panels), the equilibrium value for the A state (middle panels) and that of the saddle point appearing in the ground X electronic state (bottom panel). The contour plots associated to the LiHF(X) PES are shown for E= eV.

vibrations. As a consequence most of the bound states reached in the electronic spectrum correspond to the ground HF vibration. The bending frequency, however, is much lower and it is the most relevant internal excitation in the spectrum since most of the structures appearing in the spectrum[22] were attributed to bending progressions in the A, B and B' electronic states. The EP dynamic of different bending excitations is then important not only to simulate the spectrum but also to understand the effect of angular versus radial non-adiabatic couplings.

The initial wavepackets are built combining the rovibrational bound states with these NACMES's and derivative terms, as expressed in Eq.(17). In Fig.4 the contour plots associated to the initial wavepackets for the EP of the ground vibrational levels of A and B electronic states are shown. The most relevant features is the node appearing along r, the HF vibration. This is the reaction coordinate at

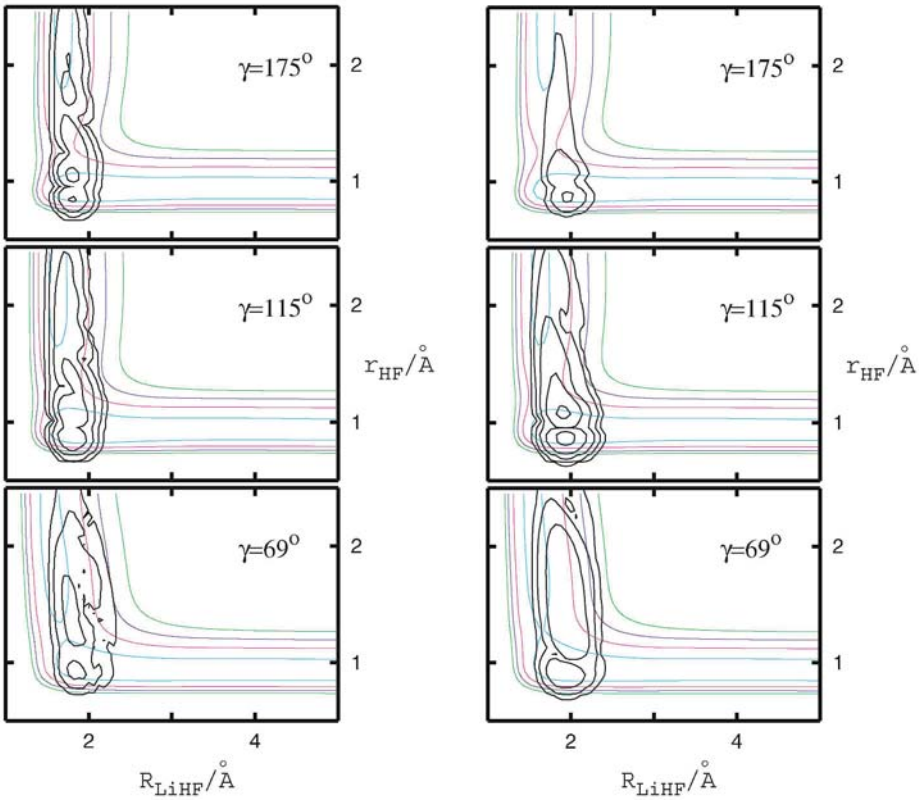

Figure 5. Same as Fig.4 but for t=7.75 fs.

the saddle point of the ground electronic state, as shown in Fig.4, and has very important relevance on the reaction dynamics. As an example, it has been found[45] that the reaction cross section for Li+HF(v=1) collisions is 10-50 times larger than for Li+HF(v=0): this was explained by the presence of the late barrier in PES of LiHF(X) along the HF distance. Also, the infrared spectrum from the van der Waals well in LiHF(X) has been simulated[56, 40], reaching to a nearly 90% of reaction probabilities because the excitation mainly correspond to the HF mode, the one which the dipole moment depend on. This last finding was later corroborated by different kind of calculations on different PES's[57], thus showing the robustness of the model.

In order to show the main features of the reaction dynamics after EP, it is relevant to follow the wavepacket evolution in time, and in Figs.5 and 6 two different snapshots are shown for t= 7.75 and 15.25 fs. The dynamics leads rapidly to LiF products at short times because of the node present in the r coordinate. At longer times, however, there is a relative small proportion of the wavepacket that remains

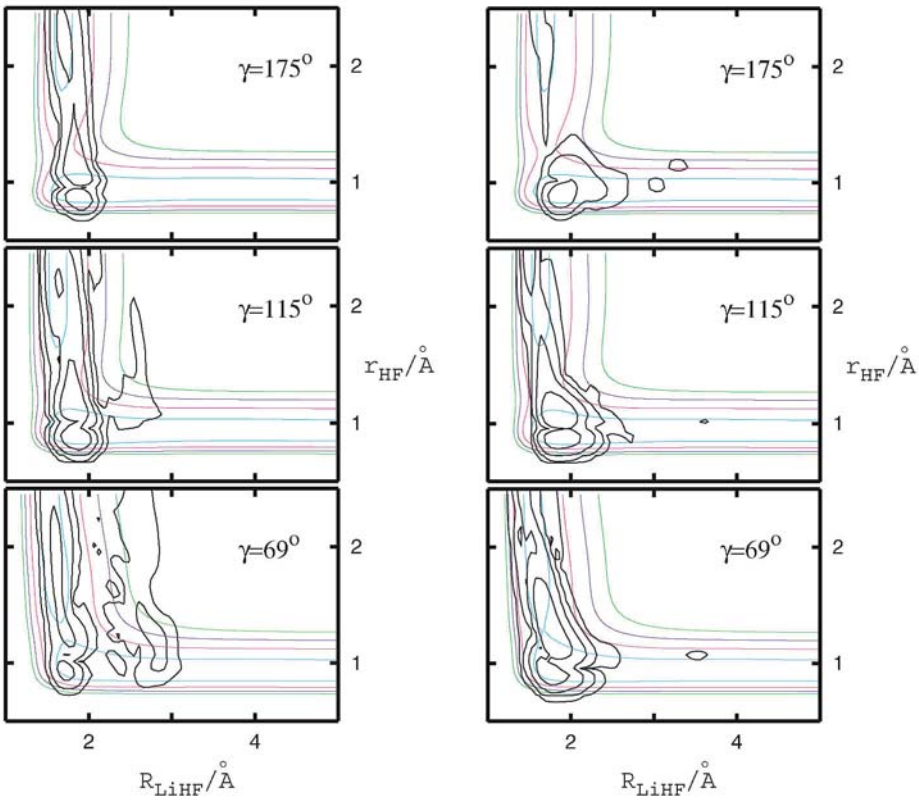

Figure 6. Same as Fig.4 but for t=15.25.

in the region of the well of the Li+HF(X) entrance channel, yielding to Li+HF reactants probably because at lower energies the barrier towards products can not be overpassed.

It is therefore relevant to resolve the reaction probability as a function of the energy, as shown in Fig.7 for different vibrational and electronic states, as a function of the kinetic energy with respect to the Li+HF(X,v=0,j=0) asymptote. The energy interval shown is the relevant for the process under study. In fact, in each calculation the only energy with physical interest is that of the initial energy, as written in Eq.(6), which are given in the corresponding figure caption. It is found that, as expected, the reaction probability is very large, being always about 90% or larger. There is always an oscillating structure, probably as a consequence of vibrations of the wavepacket in the transition state region.

Similar results have been found[58] in recent semiclassical simulations even when some variation was obtained depending on the particular method and on the electronic representation, either diabatic or adiabatic. The electronic representa-

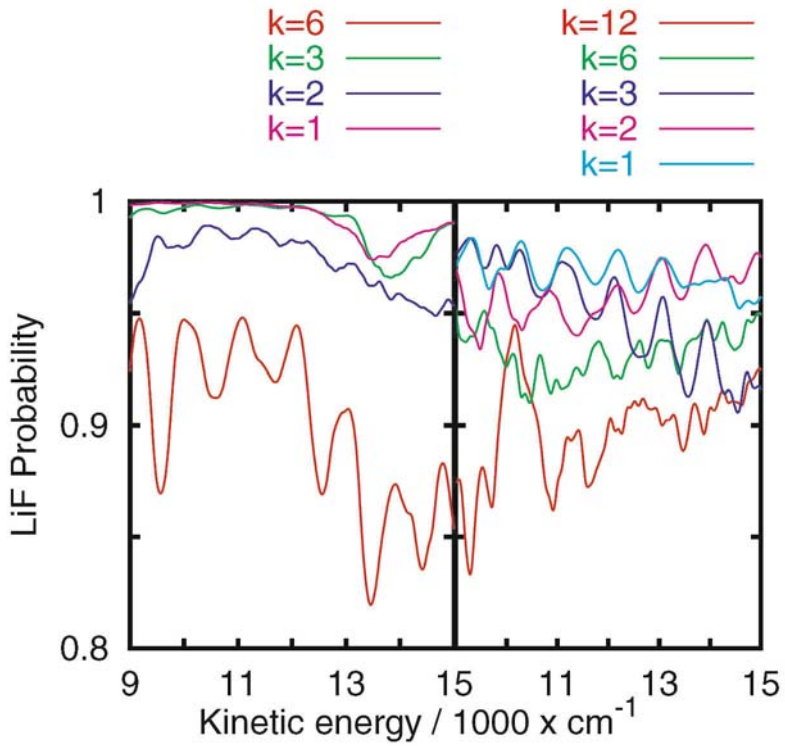

Figure 7. Reaction probabilities for forming LiF products as a function the kinetic energy, referred to the Li+HF(v=0,j=0) asymptote of the ground electronic states. The results are shown for different bending excitations in the A (left panel) and B (right panel) electronic states. The energies of the initial bound states in this energy scale are those given in Fig.2 plus ≈ 13000 cm^{-1}.

tion was built by fitting accurate *ab initio* points on the two lower adiabatic PES to a coupled quasidiabatic potential model, built by a 2×2 matrix[59]. In the adiabatic representation used by Jasper *et al*[58], the non-adiabatic couplings obtained are not directly calculated, while in the present treatment such non-adiabatic couplings are based on direct *ab initio* calculations. Another difference, is the nature of the dynamical method used to study dynamics: here an approximated quantum method is used, while that of Jasper *et al*[58] is semiclassical. Based on the important difference between the methods used, and the similarity of the results, we may conclude that the high reaction efficiency is a rather robust feature of the EP dynamics from the excited electronic states.

It is found that as bending excitation of the initial wavepacket increases the reaction probability decreases, but only slightly. To understand this fact, it should

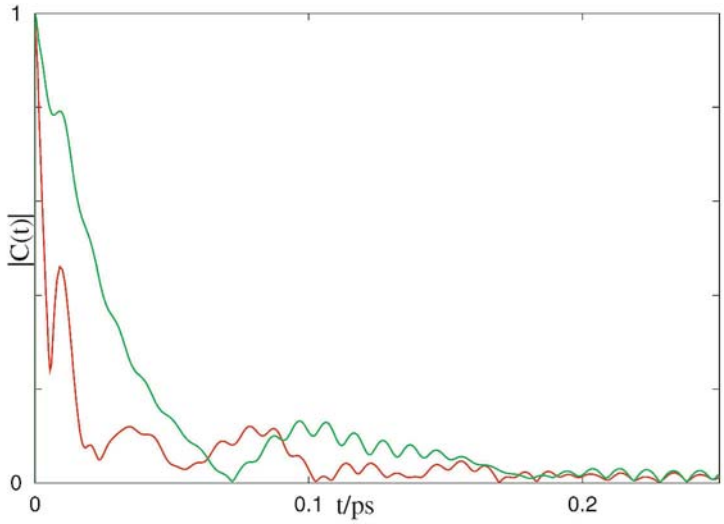

Figure 8. Autocorrelation functions $C(t) = \langle \Phi^{\alpha,k}(t=0) | \Phi^{\alpha,k}(t) \rangle / \langle \Phi^{\alpha,k}(t=0) | \Phi^{\alpha,k}(t=0) \rangle$, for k=1 and α = A and B.

be taken into account that as bending excitation increases, the initial wavepacket shifts towards larger angles γ. The saddle point for the reaction in the ground state is at $\gamma \approx 69^o$, and the barrier height increases rapidly when increasing γ. Also, the reaction probabilities are slightly larger in general for the A than for the B electronic state, as shown in Fig.7. Again, this can be understood by the structure of the initial wavepackets: the well in the A electronic states is at larger r and shorter R than for B, and are closer to the ground electronic state saddle point.

The first relevant quantity required to obtain the rates is the autocorrelation function which are shown in Fig.8 for the ground vibrational level of the two excited electronic states. The two cases present a very similar behavior. Simply, for the A case its decay seems much faster. What is notorious is the large difference between the EP halfwidths as a function of the energy for the two electronic states, of approximately 2-3 orders of magnitude, as shown in Fig.9. This is explain by the norm of the initial wavepackets, which is much smaller for the B state, because its well is at larger R and shorter r, where the non-adiabatic couplings are much smaller.

The widths and lifetimes obtained are summarized in Fig.10 for different initial states (k=1,2,3,6 and 12). The large difference between the lifetimes between A and B electronic states persists. Also, the lifetimes obtained for A state here are of $\approx$ 1-10 ps, while the semiclassical estimates obtained previously[58] are of 0.01-0.1 ps. This difference can be attributed to the difference on the dynamical method used and to the fact that the non-adiabatic couplings were not directly calculated in this last work[59].

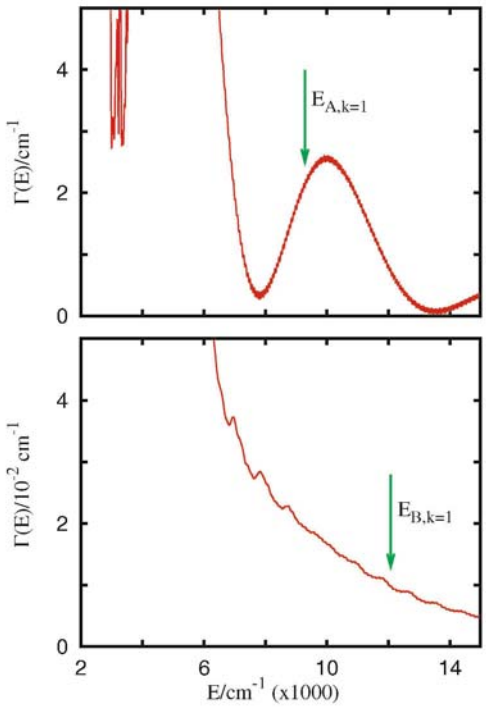

Figure 9. Halfwidths as a function of final energy relative kinetic energy for k=1 and α=A and B, calculated according to Eq.(6). The relevant value is $E = E_{\alpha,k}$ and is marked with an arrow.

In fact, in the simulation of the spectrum performed recently[31], the absorption lines were dressed with lorentzian functions which width were fitted to reproduced the experimental spectrum[22], finding that they could be of the order of 1-10cm^{-1}, more or less in agreement with the results obtained here for the A state, but differing significantly with the widths obtained for B state here.

These are not the only non-adiabatic effects in the spectrum. In the simulation[31] was found that the absorption intensity was too low for intermediate wavelengths, corresponding to energies between the A and B,B' bands. Such disagreement with the experimental spectrum was attributed to non adiabatic transitions among the excited A,B and B' states, the last two being degenerate at collinear geometry. Such conclusion, was based on a simple reduced dimensionality diabatic model, in which the two radial Jacobi coordinates were fixed at their equilibrium value, including all the rotational degrees of freedom while the diabatic electronic states were obtained with the method of the CI vector overlap when varying the angle between the two Jacobi vectors.

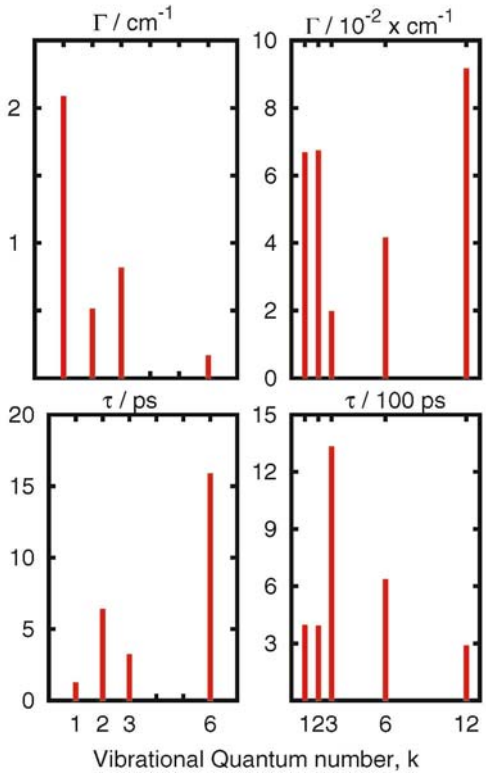

Figure 10. EP halfwidths (top panels) and lifetimes (top panel) of the different vibrational levels of the A (left panels) and B (right panels) electronic states.

One way to conciliate all these findings is to assume that the A adiabatic state is the only one responsible of the EP process, acting as the doorway state. However, because there are important $\Sigma - \Pi$ vibronic couplings among the A,B and B' states, the rovibrational states are mixed, thus sharing the absorption intensity and also the EP lifetimes.

4. Conclusions

In this work the electronic predissociation from the A,B and B' states has been studied using a time dependent Golden rule approach in an adiabatic representation. The PES's previously reported[31] to simulate the experimental spectrum[22] were used. Non-adiabatic couplings between A-X and B-X were computed using highly correlated electronic wavefunctions using a finite difference method, with the MOLPRO package[42].

It is found that the products obtained after electronic predissociation are mainly LiF products. The reason is that the non-adiabatic couplings excites the HF vibration, which is the reaction coordinate in the ground electronic state.

Also, it is found that the widths associated to A state are much wider than those of B, by 2-3 orders of magnitude, while those of B' are zero by symmetry. In the experimental spectrum, however, such situation was not present.

However, in a previous work[31] it was found that the simulated intensity between the bands associated to A and B,B' bands was too low, as compared with the experimental one[22]. Using a simple model in which the two radial coordinates were frozen, it was concluded that one reason for such disagreement would be the effect of non-adiabatic couplings among the A, B and B' electronic states, which would share the intensity among all bands.

One way to conciliate the two findings is to assume that in the predissociation, the B and B' states will predissociate by their couplings to the A state, which acts as a doorway state. Such finding support the hypothesis suggested previously by Topaler *et al*[60] in their studies of NaFH, justifying the use of a two-state diabatic model, X and A, to study the electronic predissociation of LiFH and NaFH[58, 59]. In addition, the couplings among the A,B and B' states would also be the responsible to the spreading of the absorption intensity in the region between the A and B,B' bands. For simulating such situation, a diabatic model should be built, considering either 3×3 diabatic states corresponding to the A,B and B' states, and then their coupling to the ground electronic states, or a 4×4 model, in which all states are coupled. Such models are now being built along all the reaction path, which presents a great difficulty.

4.1. ACKNOWLEDGEMENTS

This work was supported by MCYT (Spain) under grants BQU2001-0152 and BFM2001-2179. C.S. wants to acknowledge an I3P grant.

References

1. R. D. Levine and R. B. Bernstein " *Molecular Reaction Dynamics and Chemical Reactivity*" Oxford University Press (1987).
2. J.-M. Mestdagh, B. Soep, M.-A. Gaveu and J.-P. Visitcot, *Int. Rev. Phys. Chem.* **22**, 285 (2003).
3. U. Brinkmann and H. Telle, *J.Phys. B* **10**, 133 (1977).
4. M. Hoffmeister, L. Potthast and H.J. Loesch, *Chem. Phys.* **78**, 369 (1983).
5. H.H. Dispert, M. W. Geis and P.R. Brooks, *J. Chem.Phys.* **70**, 5317 (1979).
6. H. Telle and U. Brinkmann , *Mol. Phys.* **39**, 361 (1980).
7. M.G. Prisant, C.T. Rettner and R.N. Zare, *J. Chem. Phys* **75**, 2222 (1981).
8. C.T. Rettner and R.N. Zare, *J. Chem. Phys.* **77**, 2416 (1982).
9. P.S. Weiss, J.M. Mestdagh, M.H. Covinsky, B.A. Balko and Y.T. Lee, *Chem. Phys.* **126**, 93 (1988).
10. R. Düren, U. Lackschewitz and S. Milosevic, *Chem. Phys.* **126**, 81 (1988).
11. R. Düren, U. Lackschewitz, S. Milosevic and H.J. Waldapfel, *J. Chem. Soc., Faraday Trans. 2* **85**, 1017 (1989).
12. M. de Castro-Vítores, R. Candori, F. Pirani, V. Aquilanti, M. Menéndez, M. Garay and A. González-Ureña, *J. Phys. Chem.* **100**, 7997 (1996).

13. M. de Castro-Vítores, R. Candori, F. Pirani, V. Aquilanti, M. Garay and A. González-Ureña, *J. Phys. Chem.A* **102**, 9537 (1998).
14. C. Jouvet, M. Boivineau, M.C. Duval and B. Soep, *J. Phys.Chem.* **91**, 5416 (1987).
15. B. Soep, C.J. Whitham, A. Keller and J.P. Visticot, *Faraday Discuss. Chem. Soc.* **91**, 191 (1991).
16. B. Soep, S. Abbés, A. Keller and J.P. Visticot, *J. Chem. Phys.* **96**, 440 (1992).
17. A. Keller, R. Lawruszczuk, B. Soep and J.P. Visticot, *J. Chem.Phys.* **105**, 4556 (1996).
18. R. Lawruszczuk, M. Elhanine and B. Soep, *J. Chem. Phys.* **108**, 8374 (1998).
19. K. Liu, J.C. Polanyi and S. Yang, *J. Chem. Phys.* **98**, 5431 (1993).
20. J.C. Polanyi and J-X. Wang, *J. Phys. Chem.* **99**, 13691 (1995).
21. X.Y. Chang, R. Ehlich, A.J. Hudson, P. Piecuch and J.C. Polanyi, *Faraday Discuss.* **108**, 411 (1997).
22. A.J. Hudson, H.B. Oh, J.C. Polanyi and P. Piecuch, *J. Chem. Phys.* **113**, 9897 (2000).
23. A.J. Hudson, F. Y. Naumkin, H.B. Oh, J.C. Polanyi and S. Raspopov, *Faraday Discuss.* **118**, 191 (2001).
24. S. Skowronek, R. Pereira and A. González-Ureña, *J. Chem. Phys.* **107**, 1668 (1997).
25. S. Skowronek, R. Pereira and A. González-Ureña, *J. Phys. Chem. A* **101**, 7468 (1997).
26. S. Skowronek, J.B. Jiménez and A. González-Ureña, *Chem. Phys. Lett.* **303**, 275 (1999).
27. V. Stert, P. Farmanara, W. Radloff, F. Noack, S. Skowronek, J.B. Jiménez and A. González-Ureña , *Phys. Rev.* **A59**, 1727 (1999).
28. P. Farnamara, V. Stert, W. Radloff, S. Skowronek and A. González-Ureña, *Chem. Phys. Lett.* **304**, 127 (1999).
29. G.G. Balint-Kurti and R.N. Yardley, *Faraday Discuss. Chem. Soc.* **62**, 77 (1977).
30. M.M.L. Chen and H.F. Schaefer III, *J. Chem. Phys.* **72**, 4376 (1980).
31. A.Aguado, M. Paniagua, C. Sanz and O. Roncero, *J. Chem. Phys.* **119**, 10088 (2003).
32. P. Villarreal, S. Miret-Artés, O. Roncero, G. Delgado-Barrio, J.A. Beswick, N. Halberstadt and R.D. Coalson, *J. Chem. Phys.* **94**, 4230 (1991).
33. D.H. Zhang, J.Z.H. Zhang and Z. Bacić, *J. Chem. Phys.* **97**, 3149 (1992).
34. O. Roncero, N. Halberstadt and J.A. Beswick, *Chem. Phys. Lett.* **226**, 82 (1994).
35. O. Roncero, N. Halberstadt and J.A. Beswick, *J. Chem. Phys.* **104**, 7554 (1996).
36. U. Fano, *Phys. Rev.* **124**, 1866 (1961).
37. E.J. Heller, *J. Chem. Phys.* **68**, 2066 (1978).
38. E.J. Heller, *J. Chem. Phys.* **68**, 3891 (1978).
39. R.N. Zare " *Angular Momentum*" John Wiley and Sons, Inc. (1988).
40. M. Paniagua, A. Aguado, M. Lara and O. Roncero, *J. Chem. Phys.* **111**, 6712 (1999).
41. H-J. Werner, B. Follmeg and M. H. Alexander, *J. Chem. Phys.* **89**, 3139 (1988).
42. MOLPRO is a package of *ab initio* programs designed by H.-J. Werner and P.J. Knowles, with contributions from J. Almlöf, R. D. Amos, A. Berning, M. J. O. Deegan, F. Eckert, S. T. Elbert, C. Hampel, R. Lindh W. Meyer, A. Nicklass, K. Peterson, R. Pitzer, A. J. Stone, P. R. Taylor, M. E. Mura, P. Pulay, M. Schütz, H. Stoll, T. Thorsteinsson, and D. L. Cooper, (version 2002.7).
43. R. Kosloff, *J. Phys. Chem.* **92**, 2087 (1988).
44. A. Aguado, M. Paniagua, M. Lara and O. Roncero, *J. Chem. Phys.* **107**, 10085 (1997).
45. M. Lara, A. Aguado, O. Roncero and M. Paniagua, *J. Chem. Phys.* **109**, 9391 (1998).
46. H. Tal-Ezer and R. Kosloff, *J. Chem. Phys.* **81**, 3967 (1984).
47. C. Leforestier, R.H. Bisseling, C. Cerjan, M.D. Feit, R. Friesner, A. Guldberg, A. Hammerich, G. Jolicard, W. Karrlein, H.-D. Meyer, N. Lipkin, O. Roncero and R. Kosloff, *J. Comp. Phys.* **94**, 59 (1991).
48. V. A. Mandelshtam and H. S. Taylor, *J. Chem. Phys.* **103**, 2903 (1995).
49. W.H. Miller, *J. Chem. Phys.* **61**, 1823 (1974).
50. D.H. Zhang and J.Z.H. Zhang, *J. Chem. Phys.* **101**, 3672 (1994).
51. D. Neuhauser, *J. Chem. Phys.* **100**, 9272 (1994).
52. E.M. Goldfield, S.K. Gray and G.C. Schatz, *J. Chem. Phys.* **102**, 8807 (1995).
53. A. Aguado, M. Paniagua, M. Lara and O. Roncero, *J. Chem. Phys.* **106**, 1013 (1997).
54. G.G. Balint-Kurti, R.N. Dixon and C.C.Marston, *J. Chem. Soc. Faraday Trans.* **86**, 1741 (1990).

55. S. K. Gray and G.G. Balint-Kurti, *J. Chem. Phys.* **108**, 950 (1998).
56. M. Paniagua, A. Aguado, M. Lara and O. Roncero, *J. Chem. Phys.* **109**, 2971 (1998).
57. R. Burcl, P. Piecuch, V, Spirko and O. Bludský, *J. Mol. Strut.* **591**, 151 (2002).
58. A. W. Jasper, M. D. Hack, A. Chakraborty, D. G. Truhlar and P. Piecuch, *J. Chem. Phys.* **115**, 7945 (2001).
59. A. W. Jasper, M. D. Hack, D. G. Truhlar and P. Piecuch, *J. Chem. Phys.* **116**, 8353 (2002).
60. M.S. Topaler, D.G. Truhlar , X.Y. Chang, P. Piecuch and J.C. Polanyi, *J. Chem. Phys.* **108**, 5349, 5378 (1998).

DENSITY FUNCTIONAL STUDIES OF NOBLE METAL CLUSTERS. ADSORPTION OF O_2 AND CO ON GOLD AND SILVER CLUSTERS

EVA MARÍA FERNÁNDEZ
Departamento de Física Teórica, Atómica y Óptica, Facultad de Ciencias, Universidad de Valladolid, E-47011 Valladolid, Spain

MARÍA BEGOÑA TORRES
Departamento de Matemáticas y Computación, Escuela Politécnica Superior, Universidad de Burgos, E-09006 Burgos, Spain

AND

LUIS CARLOS BALBÁS
Departamento de Física Teórica, Atómica y Óptica, Facultad de Ciencias, Universidad de Valladolid, E-47011 Valladolid, Spain

Abstract. We study structural and chemisorption properties of pure and doped noble metal clusters by means of first-principles density functional calculations, based on norm-conserving pseudo-potentials and numerical atomic basis sets. First, we show that, together with relativistic effects, the level of theory, that is, the use of GGA or LDA exchange-correlation functionals, is of paramount importance to determine the onset of three dimensional structures in Au clusters, whereas for Ag or Cu clusters it is not so critical. Second, within the GGA framework, we find cage-like stable structures for neutral Au_{18}, Au_{20}, Au_{32}, Au_{50}, and Au_{162}. However, after addition or substraction of an electron only Au_{20}^{-} and Au_{32}^{+} remain cage-like. On the other hand, only Au_{20} results cage-like within LDA, whereas Ag_{20} and Cu_{20} clusters adopt compact amorphous-like C_s structures within both, LDA and GGA frameworks. Third, we investigate the element- and size-dependent electron stability of gold clusters cation doped with a transition metal impurity, Au_nTM^+ (TM = Sc, Ti, V, Cr, Mn, Fe; $n \leq 9$), and we obtain a clear explanation of the cluster abundance peaks observed recently in photo-fragmentation experiments. Fourth, we study the size

J.-P. Julien et al. (eds.),
Recent Advances in the Theory of Chemical and Physical Systems, 407–432.

dependent adsorption of m O_2 molecules on small Ag_n^- ($1 \leq n \leq 7$; m=1,2) and Au_n^- ($n \leq 7$; m=1) anion clusters, as well as the adsorption of O_2 and CO molecules on neutral Au_n ($5 \leq n \leq 10$) clusters. The adsorption energy of O_2 molecules show marked odd even effects in all the cases. For Ag_n^- anions with odd (even) n, the adsorption energy of a second O_2 molecule increases (decreases) with respect to the adsorption energy of the first O_2, in agreement with experiments and previous calculations for $n \leq 5$, which are extended here up to $n \leq 7$. Configurations of $Au_nO_2^-$ clusters with two dissociated oxygen atoms are more tightly bound than those with an adsorbed O_2 molecule, but the barrier for dissociative adsorption is not determined in this work. However, dissociative adsorption of O_2 on neutral gold clusters Au_n occurs without any barrier for n=5, 6, 7, 9, and it is the lowest energy state for n=6, 7. In the dissociative O_2 adsorption (with and without barrier), a linear O-Au-O unit is formed by rearranging the coordination of the involved Au in the cluster substrate. In molecular adsorption the cluster substrate is not modified substantially, and the O_2 binds preferably on top of Au atoms, except for Au_5, where a bridge site is favorable. Adsorption of CO molecules on Au clusters is non-dissociative, with the C atom bonded on top of a low coordinated Au atom, except for Au_5 and Au_7, where a bridge site is favorable. The structure of the free Au_n cluster is not modified substantially after CO adsorption, except for Au_7CO, where the gold substrate looks like the free Au_7^- anion instead of the neutral Au_7 cluster.

1. Introduction

The properties of small metal clusters have been studied experimentally and theoretically for more than two decades[1]. By studying the properties of clusters as a function of size, one hopes to learn how they evolve towards bulk properties, and to find unique properties for specific cluster sizes that differ largely from their bulk counterparts. Moreover, for these small clusters, every additional atom can drastically change the electronic and geometric structures. Interaction of oxygen with metals also changes significantly with the increasing number of atoms in a particle in this size regime. These facts mark the enormous potential of cluster studies for a wide range of applications. Specifically, for noble metal clusters, we can mention their application to construct new nanodevices for electronics[2] and novel nanocatalysis systems[3,4]. A comprehensive review of theoretical chemistry and physics of gold systems, both pure and mixed with other elements, has been recently published[5].

The coinage metals, Cu, Ag, Au, with atomic structures $nd^{10}(n+1)s^1$, can be viewed as a bridge between the simple *s*-only alkali metals and the more complicated transition metals. There exist a considerable number of

experimental and theoretical studies using a diversity of approaches and computational tools, for references see a recent work by two of us[6], and the reviews of Pyykkö.[5] For classical molecular dynamics simulations see the work of Bastung and coworkers[7]. Striking differences among Au_n^ν ($\nu = 0, \pm 1$) and Ag_n^ν or Cu_n^ν clusters are the following:

- Gold clusters adopt planar structures with larger numbers of atoms than silver and copper clusters, as demonstrated by combined experimental and theoretical studies[8–10].
- Photo-electron spectra experiments for clusters with 55 atoms[11] indicate that Ag_n and Cu_n adopt some symmetry, preferably icosahedral, whereas the pattern for Au_n clusters corresponds to amorphous structures.
- It has been shown experimentally[12] and theoretically[6,12,13] that Au_{20} adopts a tetrahedral T_d structure, but Ag_{20} and Cu_{20} have a compact C_s structure.
- A fullerene type structure has been found to be very stable for Au_{32}[14,15] but not for silver and copper[16].

A commonly invoked cause of these structural differences is that relativistic effects are more important for gold than for silver or copper clusters[17]. However, although Au_7 is planar, Pt_7 is three-dimensional (3D)[18], like Ag_7 or Cu_7, although Pt shows strong relativistic effects[5]. It has been shown that the competition between planar and 3D structures of Pt clusters is not affected by relativistic effects[19]. On the other hand, recent relativistic calculations of gold cluster structures,[20] but using the local density approximation (LDA) for exchange and correlation effects, lead to 3D gold clusters in the range of sizes where the generalized gradient approximation (GGA) predicts planar forms. Au_n clusters with planar form were optimized for $n \leq 20$ within a scalar relativistic LDA method by Zhao and coworkers[21]. Relativistic effects within both LDA and GGA approaches were studied[22] for given structures of Au_n clusters with $2 \leq n \leq 10$. The spin-orbit coupling does not alter the relative stability of Au_n clusters with $n \leq 20$ but increase the binding energy of the cluster by about 0.08 eV/atom[23].The spin-orbit coupling is smaller than the Jahn-Teller effect for Cu_3, but it is significant for Au_3 and quenches the Jahn-Teller distortion[24]. Comparison of DFT calculations at several levels of theory for Au_6 and Au_8 with second-order perturbation theory (MP2), and coupled cluster methods (CCSD(T)), indicate that DFT predict planar structures for both Au_6 and Au_8, but both MP2 and CCSD(T) predict the lowest Au_8 isomers to be non-planar[25]. In a recent paper, Grömbeck and Broqvist[26] study the different contributions to the bonding in Au_8 and Cu_8 clusters, concluding that the preference of planar configurations for Au_8 isomers is due to a sizeable *d*-*d* overlap and *d*-electron delocalization.

In subsection 3.1, we will present GGA and LDA calculations for Au_n clusters with $6 \leq n \leq 9$ using the first principles method outlined in section 2, which employs the same scalar-relativistic pseudo-potential for LDA and GGA (see Fig 1). These calculations show the crucial relevance of the level of density functional theory (DFT), namely the quality of the exchange-correlation functional, to predict the correct structures of Au clusters. Another, even more critical, example is presented in subsection 3.2, where we show that both approaches, LDA and GGA, predict the "cage-like" tetrahedral structure of Au_{20}[6,12,13] as having lower energy than "amorphous-like" isomers, whereas for other Au clusters, namely Au_{18},[16] Au_{32},[14–16] Au_{50},[16] and Au_{160},[16] the GGA leads to "cage-like" structures preferentially to "amorphous-like" ones, but the contrary happens by using LDA. Magic numbered Au_n clusters protected by glutathione monolayers were experimentally isolated and spectroscopically characterized for n=18 and n=32, among others[27]. The observation in solution of Au_{20} coordinated with eight PPh_3 (Ph = phenyl) ligands was reported also recently[28].

Another interesting topic that we address in this work is the adsorption of a transition metal (TM) atom on cationic Au_n^+ clusters, which is important, for example, in gold nanocontacts[29]. By means of photo - fragmentation experiments, Neukermans and coworkers[30] have investigated the stability of cationic gold clusters doped with a $3d$ TM atom, Au_nTM^+, resulting special stability (magic numbers) for Au_6Sc^+, Au_5Ti^+, and clusters with n=5,7, and TM = V, Cr, Mn, Fe, Co, among other TM elements and larger n values. A qualitative explanation of these magic numbers was given[30] in terms of a phenomenological shell-model approach, which leads to magic numbers for electronic shell closing with 2, 8,... electrons. Thus, in addition to 1 delocalized $6s$ electron for each Au atom, one needs to assume two $4s$ delocalized electrons for all the TM elements from Sc to Co, plus one (Sc), two (Ti), or zero (V to Co) $3d$ delocalized electrons. In a recent work[31] we have provided an *ab-initio* explanation of the experimental magic numbers from first principles calculations. An outline of these results is given in section 4.

Interaction of oxygen with metals changes significantly with increasing number of atoms in the small cluster size regime[32–38]. Consequently, unusual chemical activities can be observed for nanoclusters, which are not observed on their bulk counterparts[3,32–40]. For example, even-numbered Au clusters anions smaller than Au_{21}^- generally react with O_2, whereas the odd numbered clusters are inert[34–38]. This even-odd alternation of the O_2 chemisorption reactivity can also be found for Ag cluster anions. The difference between Ag and Au is that O_2 chemisorption on Ag_n anions can be detected up to Ag_{40}^-, whereas Au cluster anions larger than Au_{21}^- do not react with O_2[36,37]. Using vibrationally resolved ultraviolet photoelectron spectroscopy (UPS), has been found that O_2 adsorbed molecularly on the even-numbered Ag and Au cluster anions, and it has been suggested that the activated dioxygen species are important reactions intermediates in var-

ious catalytic reactions, such as low-temperature CO oxidation and partial oxidation of propylene[36,37]. These results are quite different from those for Ag and Au bulk crystals, on which oxygen dissociatively chemisorbs (Ag) or does not adsorb at all (Au)[41,42]. Recent experiments indicate, however, that mixed Au-Ag bimetallic nanoparticles as large as $\sim$ 30 nm, exhibit extraordinarily high activity with respect to CO oxidation[43], and here the size effect is no longer a critical factor. With respect to extended systems, the formation of O-Ag-O linear units in the adsorption of oxygen on metallic different vicinal Ag surfaces has been reported[44,45]. The linear O-Au-O unit, appears also recurrently in our calculations for the adsorption of atomic oxygen on anionic gold clusters.

In section 5 we report our results for oxygen adsorption on Ag_n^- (subsection 5.1) and on Au_n^- (subsection 5.2) cluster anions. In section 6 we present preliminary results for the molecular chemisorption of O_2 (subsection 6.1) and CO (subsection 6.2) on Au_n neutral clusters. In section 7 we present the conclusions.

2. Computational method

We use the first-principles code SIESTA[46] (Spanish Initiative for Electronic Simulations of Thousands of Atoms), to solve fully self-consistently the standard Kohn-Sham equations[47] of density-functional theory within two levels of spin-polarized exchange-correlation functionals: the generalized-gradients spin functionals (GGA) as parameterized by Perdew, Burke and Ernzerhof[48], and the local spin density approximation (LDA) as parameterized by Perdew and Zunger[49]. We use norm conserving scalar relativistic pseudopotentials[50] in their fully nonlocal form[51], generated from the atomic valence configurations $nd^{10}(n+1)s^1(n+1)p^0$, with n=3,4,5 for Cu, Ag and Au, respectively. For the "3d" TM elements Sc, Ti, V, Cr, Mn, and Fe, we use the valence configuration $4s^2 3p^6 3d^q$, with q=1, 2, 3, 4, 5, and 6, respectively. For C and O we use $2s^2 2p^2$ and $2s^2 2p^4$ respectively. The corresponding core radii have been tested and reported in previous publications[6,31,52]. We have included the valence among the semicore electrons $4d$ and $5d$ in Ag and Au, respectively, and $3p$ in TM elements. Specifically, for $4s$, $3p$, $3d$ orbitals of TM elements we use the core radii, in a. u., 2.57, 1.08, 1.38 (Sc, Ti, V), 2.36, 1.09, 1.09 (Cr), 2.47, 1.29, 1.29 (Mn), and 2.47, 1.00, 1.00 (Fe). For Cu, Ag and Au the core radii of (s,p,d) orbitals are (2.05, 2.30, 1.98), (2.49, 2.59, 2.20) and (2.47, 2.98, 2.00), respectively. For O and C, the core radii are (1.14, 1.14) and (1.25, 1.25) for (s,p) orbitals respectively. Non-linear partial-core corrections are not considered[31,52].

Flexible linear combinations of numerical (pseudo) atomic orbitals are used as the basis set, allowing for multiple-ζ and polarization orbitals. In order to limit the range of the basis pseudoatomic orbitals (PAO), they are slightly excited by a common "energy shift", E_{shift}, and truncated at the

resulting radial node. The basis functions and the electron density are projected onto a uniform real space grid in order to calculate the Hartree and exchange-correlation potentials and matrix elements. The grid fineness is controlled by the "energy cutoff" of the plane waves that can be represented in it without alliasing. For the Au_nTM^+ calculations we used, in the present work, E_{shift} = 0.0037 Ry, E_{cutoff}=100 Ry, and double-ζ $3p, 4s, 3d$-basis plus single $4p$ polarization orbital for TM elements and double-ζ $6s, 5d$-basis plus single $6p$ polarization orbital for Au, resulting maximum cutoff radii, in a.u, 9.07 (Sc), 8.66 (Ti), 8.49 (V), 8.35 (Cr), 8.01 (Mn), 7.90 (Fe), and 7.62 (Au). For the pure noble metal cluster calculations we use E_{shift} = 0.01 Ry, E_{cutoff}=120 Ry, and double-ζ s, d-basis plus single p polarization orbital, resulting maximum cutoff radius at 7.08, 7.39, and 6.72, for Cu, Ag, and Au, respectively. For the adsorption of O_m and CO on Ag and Au clusters, we used E_{shift} = 0.001 Ry, E_{cutoff}=120 Ry, and double-ζ s, d-basis plus single p polarization orbital for Ag and Au, and double-ζ $2s, 2p$-basis and a single d polarization orbital for C and O elements, resulting maximum cutoff radius (in a.u.) at 9.49, 8.63, 7.45, and 5.73 for Ag, Au, C, and O, respectively. Convergence tests with respect to size and cutoff radii of basis sets, and with respect to LDA or GGA xc-functionals, were presented in previous works[6,31,52]. For O_2, CO, and CO_2 we obtain, in this paper, bond distance (in Å) and binding energy per atom (in eV) (1.24, 6.55), (1.16, 11.16), and (1.19, 17.36), respectively, to be compared with experimental values[53] (1.21, 5.23), (1.13, 11.23), and (1.16, 17.08), respectively.

To obtain the equilibrium geometries, an uncostrained conjugate-gradient structural relaxation using the DFT forces[54] was performed for several initial cluster structures (typically more than ten), inspired in isomeric geometries for Au_n, Au_n^-, and Au_n^+ clusters obtained previously[6]. The calculation of density gradients is performed numerically[54] (with the five points Lagrange interpolation method) for the discrete set of grid points consistent with the discretized form used in SIESTA. Convergence in the geometry optimization is achieved for 0.04 eV/Å for pure noble metal and doped Au_nTM^+ clusters, and 0.01 eV/Å for the adsorption of O_2 and CO calculations.

3. Structure of neutral and charged noble metal clusters

3.1. ONSET OF THREE-DIMENSIONAL STRUCTURES

Recent GGA first principles pseudopotential calculations[6,17] conclude that Au_n clusters adopt planar structures up to larger sizes than silver and copper, particularly the anionic species, due to relativistic effects. Specifically, Fernández and coworkers[6] obtain planar structures for the ground state of anionic (ν=1), neutral (ν=0), and cationic (ν=+1) species of Au_n^ν clusters

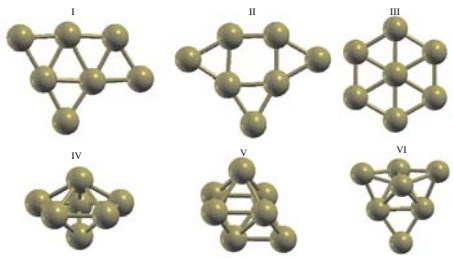

Figure 1. Equilibrium geometries of the two lowest energy isomers, X_7^ν and ${}^*X_7^\nu$, of anionic, neutral, and cationic noble metal clusters. The roman numerals identify each clusters in Table 1.

with up to 12,11, and 7 atoms respectively. In contrast, the maximum size of planar clusters with ν=-1,0,+1 are n=(5, 6, 5) for Ag, and (5, 6, 4) for Cu clusters. Nevertheless, a recent LDA calculation of gold cluster structures[20] using the same relativistic pseudo-potential and first principles code as in the GGA calculation of Fernández and coworkers[6], obtained the onset of three dimensional structures for Au_n clusters at n=7.

TABLE 1. Results of GGA calculations for the binding energy per atom (eV) of the two lowest energy isomers, X_7^ν and ${}^*X_7^\nu$, of noble metal clusters with ν=0,±1 (labels as in Fig. 1). Only geometries I, II, and III, are planar.

	Au		Ag		Cu	
X_7^-	II	2.72	V	2.45	V	3.18
${}^*X_7^-$	V	2.63	IV	2.44	IV	3.16
X_7	I	2.52	IV	2.28	IV	2.83
${}^*X_7$	IV	2.49	VI	2.26	V	2.78
X_7^+	III	2.92	IV	2.57	IV	3.10
${}^*X_7^+$	VI	2.92	V	2.53	VI	3.00

In Fig 1 are given the geometries of the first two isomers, X_7^ν and ${}^*X_7^\nu$, of anionic, neutral, and cationic noble metal clusters, and in Table 1 is tabulated the corresponding cohesive energy. We see that the energy for the transition from planar to 3D structures of Au heptamers increases when the number of electrons increases, showing the tendency of anionic Au aggregates to be planar. For Ag_7^ν and ${}^*Ag_7^\nu$ we obtain the same 3D geometries as for Cu heptamers, with the only exception being ${}^*Cu_7$, which adopts the structure V instead of the VI one. Solov'yov and coworkers[55] found for Na_7

and Na_7^+ the same pentagonal bypiramid IV that we obtain for Ag and Cu neutral and cationic heptamers.

By analyzing the density matrix composition of planar and 3D structures of seven atom clusters (II and IV of Fig 1), calculated using scalar relativistic pseudo-potential at the GGA theory level, Fernández and coworkers[6] conclude that the planarity of Au clusters is driven by the hybridization of the half-filled 6s orbital with the fully occupied $5d_{z^2}$ orbital, which is favored by relativistic effects. Thus, the three valence electrons in the orbitals 6s and $5d_{z^2}$, form a "sticky-waist cylinder", where the cylinder is due to the almost filled $s + d_{z^2}$ hybrid, and the "sticky-waist" is due to the nearly half-filled $s - d_{z^2}$ hybrid orbital.

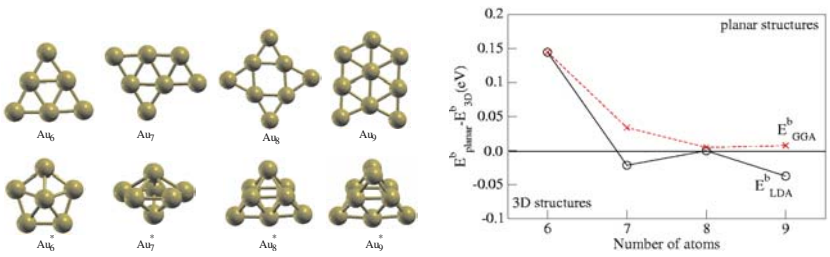

Figure 2. Left: equilibrium geometries of the two lowest energy isomeric states of Au_n clusters obtained using LDA or GGA scalar relativistic pseudo-potentials. The ground state is Au_n for GGA and Au_n^* for LDA (except for n=6, which LDA structure is also Au_6). Right: difference in the binding energy per atom of the planar and 3D structures given in the left panel for neutral gold clusters with $6 \leq n \leq 9$ atoms. Positive values indicate that planar structures are energetically favorable. Crosses corresponds to GGA (dotted line) and circles to LDA (continuous line) calculations.

TABLE 2. Average bond length, in Å, of structures in Fig 2 optimized within LDA and GGA xc-functionals.

	Au_6		Au_7		Au_8		Au_9	
	LDA	GGA	LDA	GGA	LDA	GGA	LDA	GGA
Au_n	2.64	2.70	2.65	2.71	2.62	2.69	2.66	2.72
Au_n^*	2.68	2.75	2.76	2.82	2.75	2.78	2.75	2.81

In this work we recalculate the structures of Au_n clusters with $6 \leq n \leq 9$ using both, LDA[49] and GGA[48] theory, with LDA and GGA scalar relativistic Troullier-Martins pseudo-potentials[50], respectively, and within the SIESTA code[46]. In Fig 2 we present our results for the structures and relative binding energies. We see that GGA leads to planar structures whereas LDA favors 3D structures for $n \geq 7$ clusters. Thus, in addition to relativistic effects, the observed planarity of Au clusters[8–10] is accounted for using only the GGA level of theory.

3.2. GOLDEN FULLERENES

Cage-like structures of gold clusters have been predicted recently within GGA for Au_{20}[6,12,13] and Au_{32}[14,15]. In fact, instead of a cage-like structure, Au_{20} can be considered as a small piece of bulk fcc gold, with four (111) surface faces forming a tetrahedron. Cage-like structures can be obtained from the Platonic solids (tetrahedron, octahedron, and icosahedron) with triangular faces. By decorating the triangles with fcc planes and adding a central atom to each new triangle, we obtain structures with a number of atoms $2+6(n+1)^2$ (T_d symmetry), $2+12(n+1)^2$ (O_h symmetry, and $2+30(n+1)^2$ (I_h symmetry), where n=0,1,2,.... In order to obtain a "magic" cage-like structure with a nearly spherical surface, we choose, among the selected sets of numbers above, those which complete electronic shells having well defined angular momentum L. On the other hand, as we look for an empty-cage "spherical surface", the radial nodes are excluded and the only allowed electronic shells are the 1L ones (1s,1p,1d,1f,...). This leads to a number of electrons $2(L+1)^2$, which is known as the spherical aromaticity rule[56]. Assuming that each atom in the Au clusters contributes with 1 valence electron to the bonding, the expected magic gold clusters contain n = 8, 18, 32, 50, 98, 162, 578,... electrons, and double anionic gold clusters should appear at n=6, 198,..., among others.

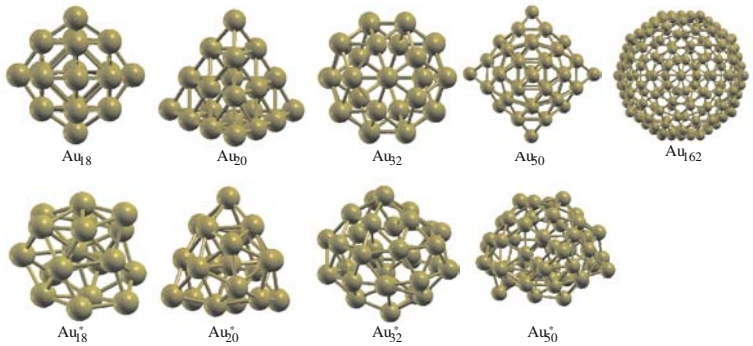

Figure 3. GGA and LDA equilibrium structures of cage-like (Au_n) and amorphous-like (Au_n^*) type for several Au clusters with magic numbers fulfilling the spherical aromaticity rule $n=2(L+1)^2$, where L is an integer number (see text).

In Fig 3 we represent the equilibrium geometries of several cage-like and compact Au clusters (including Au_{20}), optimized (with forces ≤ 0.01 eV/Å) at the GGA and LDA levels using the corresponding GGA and LDA scalar relativistic pseudo-potentials and the SIESTA code. The cage-like equilibrium structures were proven to be stable after performing an ab-initio molecular dynamics run starting with a temperature of 700 K. We performed calculations for several initial cage-like and compact geometries,

TABLE 3. Binding energy per particle, E_b, and average bond distance, d_{av}, for the optimized cage-like and compact structures of Fig 4 above, obtained at the GGA and LDA levels of theory. For Au_{162} we have only the results for optimized cage-like structures, given a binding energy 3.36 (4.44) eV/atom and average bond distance 2.78 (2.71) Å for GGA (LDA) calculation.

	Au_{18}		Au_{20}		Au_{32}		Au_{50}	
	GGA	LDA	GGA	LDA	GGA	LDA	GGA	LDA
$E_b(Au_n)$	3.05	3.8	3.17	3.95	3.31	4.09	3.37	4.20
$d_{av}(Au_n)$	2.81	2.74	2.86	2.78	2.80	2.75	2.80	2.72
$E_b(Au_n^*)$	3.04	3.87	3.14	3.94	3.30	4.15	3.36	4.34
$d_{av}(Au_n^*)$	2.86	2.77	2.87	2.80	2.86	2.81	2.82	2.80

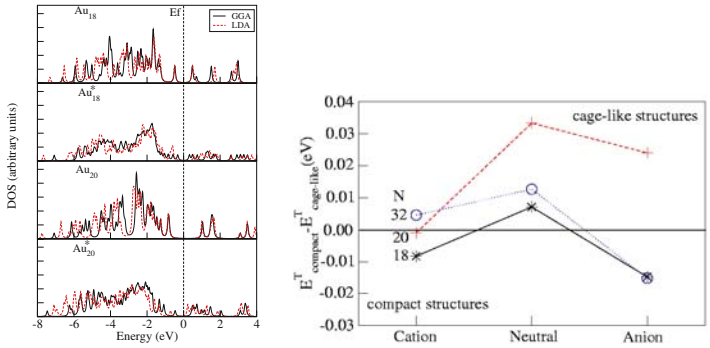

Figure 4. Left: Density of states (DOS) of cage-like and amorphous structures of Au clusters with 18 and 20 atoms, calculated at the LDA and GGA levels of theory. Right: Total energy difference between cage-like and compact equilibrium structures of cationic, neutral, and anionic clusters with 18 (starts), 20 (crosses), and 32 (circles) atoms.

but in Fig 3 we report only the lowest energy equilibrium isomer found for each case. The binding energies are tabulated in Table 3. We see that Au_{20} is the lowest energy state with both, LDA and GGA calculations. However, the compact Au_n^* clusters with n=18, 32, 50 are more (less) tightly bound than cage-like ones within LDA (GGA).

In the left panel of Fig 4 we compare the density of states (DOS) for the cage-like structures, Au_n (n=18,20), with the corresponding DOS for the amorphous Au_n^* structures. We see, as in previous works for Au_{55}[11] and Au_{32}[15,16], that the more ordered geometries show a more structured DOS, with well defined peaks, which is due to a higher geometrical symmetry. This fact is independent of the GGA or LDA. The LDA profile tends to be shifted to lower energies with respect to the GGA one, and the HOMO-LUMO gap is smaller for LDA than for GGA. On the other hand the

HOMO-LUMO gap is considerably larger for Au_{20} than for Au_{18}, indicating that the former is much more stable than the later.

As a further test of the relative stability of cage-like structures, we represent in the right panel of Fig 4 the total energy difference between cage-like and compact equilibrium structures of cationic, neutral, and anionic clusters of Au_n with n=18, 20, 32 atoms. We see that Au_{20} is the only one conserving a cage-like structure after accepting an extra electron. Interestingly, the lowest energy cationic and anionic Au_{18} species are not cage-like, contrary to the neutral cluster. The calculated adiabatic (vertical) ionization potential and electron affinity of neutral Au_{18} are 5.89 (6.08) eV and 1.75 (1.47) eV, respectively.

4. Doped Au clusters

In the left panel of Fig 5 we represent the calculated equilibrium geometries of the lowest energy isomer of cationic Au_nTM^+ clusters with $2 \leq n \leq 9$ and TM=Au,Sc,Ti, V,Cr,Mn,Fe. Up to n=6 all the geometries are planar, except Au_6Cr^+ with a 3D geometry (6-III, not shown) which is degenerate with the 6-II one. The right panel of Fig 5 shows the binding energy per atom, $E_b = (nE_{Au} + E_{TM^+} - E_n)/(n+1)$, for clusters with $3 \leq n \leq 8$. $E_b(n)$ for doped clusters is always smaller than for pure Au^+_{n+1} clusters, except for Au_nSc^+ and a few other exceptions. More detailed data will be published elsewhere[31].

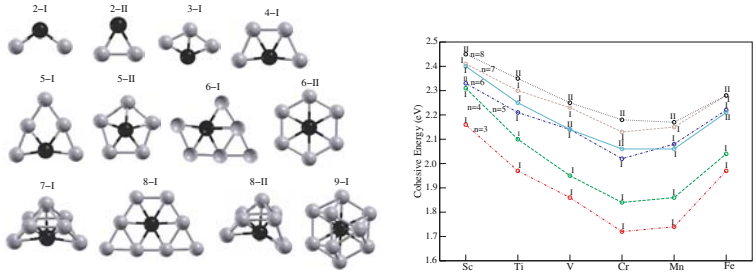

Figure 5. Left panel: lowest energy equilibrium structures of Au_nTM^+ clusters with $2 \leq n \leq 9$ and TM=Sc,Ti,V,Cr,Mn and Fe. The roman numerals identify each geometry in the Figure below. Structure 8-I corresponds to the pure Au_9 cluster. Right panel: binding energy per atom of Au_nTM^+ clusters with $3 \leq n \leq 8$. The labels identify the structure as given in the left panel.

In Fig 6 we represent the second difference of total energy, $\Delta_2 E_n = E_{n+1} + E_{n-1} - 2E_n = E_{ev}(n) - E_{ev}(n+1)$, where $E_{ev}(n) = E_{n-1} + E_{Au} - E_n$ is the monomer evaporation energy needed for the process in which Au_nTM^+ losses Au atoms, with energy E_{Au}, one by one. $\Delta_2 E_n$ is proportional to the logarithm of cluster abundance ratio, $ln(I_n/I_{n+1})$, obtained in photofragmentation experiments[30]. Positive values of $\Delta_2 E_n$ corresponds to abun-

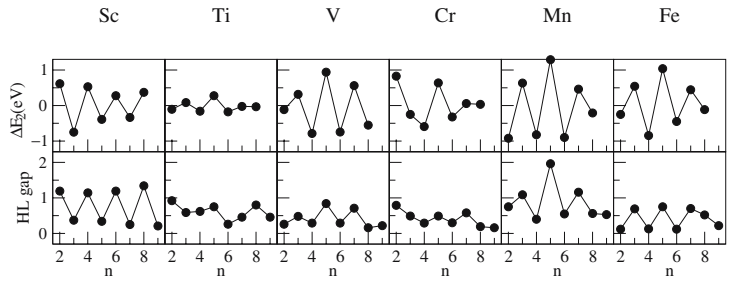

Figure 6. Second total energy difference (upper panel) and HOMO-LUMO gap (lower panel) for the lowest energy equilibrium structures of Au_nTM^+ clusters

dances $I_n > I_{n+1}$, and indicate that Au_nTM^+ is more stable to a monomer Au evaporation than the neighbor $Au_{n+1}TM^+$ cluster. The enhanced peaks in the $\Delta_2 E_n$ of Fig 5 correspond to the magic numbers observed at n=6 (Sc), n=5 (Ti), and n=5,7 for the other TM impurities considered in this work. Similar peaks are obtained in the calculated HOMO-LUMO gap, which is represented in the lower panel of Fig 6.

In the context of the spherical shell model for nearly-free electrons[1], assuming that Au, Sc, and Ti contribute with 1,3,5 delocalized valence electrons, respectively, it appears that Au_6Sc^+ and Au_5Ti^+ are magic clusters with 8 valence electrons. However, for the other TM impurities, delocalization of valence charge is restricted to the 4s electrons if this model is forced to explain the observed drops of intensity, I_n, at n=5 and 7. We obtain the experimental magic numbers[30] of Au_nTM^+ clusters without resorting to the empirical shell-model of delocalized electrons.

An analysis of the correlation between the magnetic and geometrical structures of Au_nTM^+ clusters, and a detailed study of the local magnetic moment of the TM impurity will be published elsewhere[31].

5. Adsorption of O_2 on Ag_n^- and Au_n^- anionic clusters

5.1. ADSORPTION OF O_M, M=2,4, ON ANIONIC SILVER CLUSTERS

Recent experimental and theoretical work[36,57–59] shows pronounced size and structure selective activity of anionic silver clusters towards molecular oxygen due to cooperative effects: odd n Ag_n^- anions, with even valence electron number, exhibit about an order of magnitude smaller reaction rates than even n Ag_n^- anions for the adsorption of a O_2 molecule, but they are able to activate the oxygen molecular bond to adsorb a second O_2 molecule. In this subsection we study the trends in the binding energies of O_2 on Ag_n^- anions with $1 \leq n \leq 7$, confirming and extending previous calculations for $1 \leq n \leq 5$[58]. The adsorption of the second O_2 on $Ag_nO_2^-$

changes substantially the substrate Ag_n^- geometry for n=3,6,7. The O-O distance in $Ag_nO_2^-$ with odd n becomes elongated $\sim$ 1.30 Å, and thus activated for further oxidation reactions such as CO combustion.

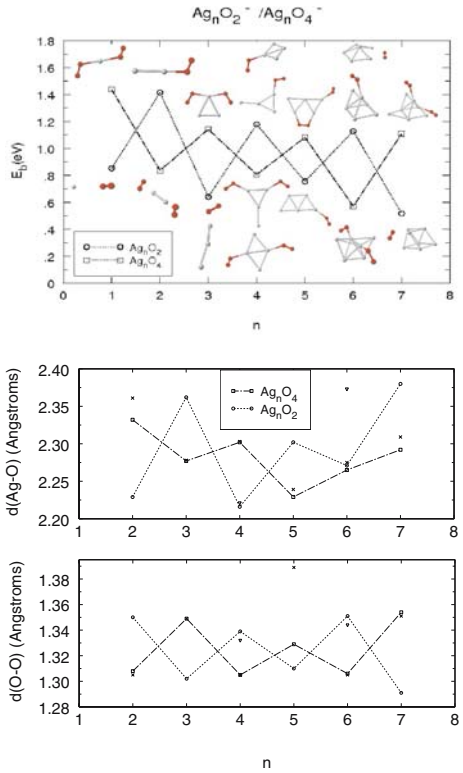

Figure 7. Upper panel: Lowest energy equilibrium geometries and calculated adsorption energies of O_2 and O_4 on Ag_n^- clusters. Isomeric structures for n=4 and 6 are also depicted. Minimum distance O-Ag (middle panel) and O-O (lower panel) in the equilibrium structures of $Ag_nO_2^-$ (circles) and $Ag_nO_4^-$ (squares) clusters. The crosses indicate the distance Ag-O and O-O for the next nearest O_2 adsorbed molecule in $Ag_nO_4^-$ anions. The triangles at n=4,6 correspond to the near degenerate structures depicted in the upper panel.

In the upper panel of Fig 7 we represent the calculated lowest energy equilibrium structure and the binding energy, $E_b^m = E(Ag_nO_m^-)$-$E(Ag_nO_{m-2}^-)$-$E(O_2)$, for the adsorption of O_2 (m=2) and O_4 (m=4) on Ag_n^- clusters with $1 \leq n \leq 7$. For $Ag_4O_m^-$ and $Ag_6O_m^-$ oxides, isomeric structures (within $\leq$ 0.03 eV difference in E_b^m) are also depicted. Similar odd-even alternations in E_b^m were calculated[58] in the size range $n \leq 5$. These trends are in agreement with experimental rate constants[58] for the adsorption of the first (m=2) and second (m=4) oxygen molecules on Ag_n^- clusters. Adsorption of two

oxygen atoms leading to (O-Ag_n-O)$^-$1 clusters is not studied in this work, except for the linear molecule (O-Ag-O)$^-$1. That molecule is more tightly bound by 0.11 eV than the equilibrium configuration AgO_2^- (with the angle O-O-Ag being 121.2°). In general, dissociated O_2 configurations can be energetically favorable but kinetically hindered, that is, require considerable activation energy not available under the experimental conditions[58,59]. Further details will be given in a forthcoming publication.

The angle O-O-Ag in the $Ag_nO_m^-$ clusters with m=2 is in the range ∼(119°-121°) for n odd, and ∼(112°-115°) for n even, whereas for m=4 we found no clear odd-even difference. The calculated O-O-Ag angle in the free AgO_2^- molecule is 121.2°, and for the neutral AgO_2 was determined[60] as ∼ 118.0°, by means of a mixed experimental-computational approach. The linear O-Ag-O molecule, which appears to be more tightly bound than AgO_2,[60] was found as a recurrent motif in the oxidation of silver vicinal surfaces[44,45]. As already commented, $Ag_nO_m^-$ clusters with dissociated O_2 seems to be kinetically hindered during molecular adsorption, and we have not investigated that process in this paper. On the other hand, the linear O-Au-O motif appearing in the oxidation of anionic gold clusters is discussed in a section below. In the middle and lower ponnels of Fig 7 are represented the minimum distance O-Ag (middle panel) and O-O (lower panel) in the equilibrium structures of $Ag_nO_2^-$ (circles) and $Ag_nO_4^-$ (squares) clusters with 2≤n≤7. The crosses correspond to $Ag_nO_4^-$ anions and indicate the distance Ag-O or O-O of the next nearest adsorbed O_2 molecule. For $Ag_5O_4^-$ that O-O distance in the next nearest O_2 molecule is very large. Notice that both O_2 molecules bind on different top Ag atoms except for $Ag_5O_4^-$, where an O_2 binds in a bridge position between two Ag atoms. The triangles correspond to the near degenerate structures of $Ag_nO_2^-$ for n=4,6 depicted in Fig 7. For n=4, the two isotopes have the same Ag-O distance (within a 0.005 Å interval), but for n=6 the Ag-O distance of the second isotope is exceedingly large. However, the O-O distance in the second isomer of $Ag_nO_2^-$ with n=4,6 is only slightly lower than in the first isomer. Notice that our calculation for the O-O distance in the free O_2 molecule is 1.24 Å.

The mechanism for the activation of molecular oxygen and the cooperative binding of two oxygen molecules on Ag_n^- anions in which the first adsorbed O_2 serves as an activator has been proposed by Hagen and coworkers[58]. That mechanism involves the electron transfer from the metal clusters anions with even number of electrons into the π^*-MO of O_2. The binding of the first O_2 molecule changes the electronic structure of the cluster and induces a stronger cooperative binding with the second O_2. In the case of Ag_5^- (and also Ag_3^- in the work of Hagen and coworkers[58]) this results in a new oxide species with double bond, superoxo-like O_2 subunit, that is, the O_2 molecule binds on a "bridge" site of the metal cluster instead of the "top" site. The cooperative effect is reflected in larger binding energies as shown

in Figure 7. The binding of the second O_2 molecule is stronger for clusters with an odd number of atoms and weaker for the ones with an even number of atoms. The later ones with one unpaired electron bind strongly only one oxigen molecule since the electron transfer leaves them with a closed shell electronic structure. The analysis of bond distances substantiates the arguments above.

5.2. ADSORPTION OF OXYGEN ON GOLD CLUSTER ANIONS

In early experiments[38,61], a definite pattern of oxygen adsorption to negatively charged small gold clusters was detected. Only anionic clusters with an even number of atoms showed a significant O_2 uptake, whereas odd-numbered clusters did not exhibit any propensity for reaction with oxygen[61] or showed very weak reactivity[38]. That finding has been confirmed by other groups[35,62]. Neutral clusters and positively charged ones were found to be inert toward oxygen uptake, with the only exception being Au_{10}^{+}.

Calculations of the electronic structure of AuO_2 and $Au_2O_2^{-}$ was reported by Okamura and coworkers[63] and Häkkinen and Landmann[64], respectively. They found that in the lowest configuration the O_2 molecule attaches to the gold atoms in an end-bonded, bent configuration. They reported a binding energy of 8.13 kcal/mol, for AuO_2[63], and 1.39 eV for $Au_2O_2^{-}$[64]. Mills et al[65] have investigated the adsorption of O_2 molecules on neutral and charged Au_n clusters with n=1-5, and found that the binding energy for the charged cluster is larger if the number of electrons in the cluster is odd.

More recently, Yoon and coworkers[66] have reported calculations, based on density functional theory, for the adsorption of O_2 on neutral and charged (negatively and positively) Au clusters containing up to eight Au atoms. That work predicts that: i) molecular O_2 adsorption is preferred to dissociative adsorption for anionic and neutral clusters with $n \geq 4$; ii) the binding energy of O_2 to anionic clusters, exhibit odd-even oscillations, being $\sim$ 0.5-1.0 eV higher for even-n than for odd-n clusters; iii) the binding energy of O_2 to neutral clusters is about 0.5 eV smaller than for the corresponding anions.

Franceschetti et al[67] have reported calculations about $Au_nO_2^{\nu}$ neutral ($\nu = 0$) and anionic ($\nu = -1$) clusters, with $3 \leq n \leq 6$. These authors found that: i) O_2 molecules chemiadsorb on Au_n^{ν} clusters with typical binding energies in the range 0.5-1.5 eV, being larger for anionic than for neutral clusters; ii) in the lowest energy configuration the oxygen molecule dissociates into two atoms, forming a nearly linear O-Au-O chain which bonds to the remanent (deformed) cluster with the oxygen atoms in bridge positions; the exceptions are the neutral Au_3O_2 and Au_5O_2 clusters, which prefer molecular adsorption; iii) the binding energy of O_2 to anionic Au clusters shows odd-even oscillations, being larger for even-n clusters.

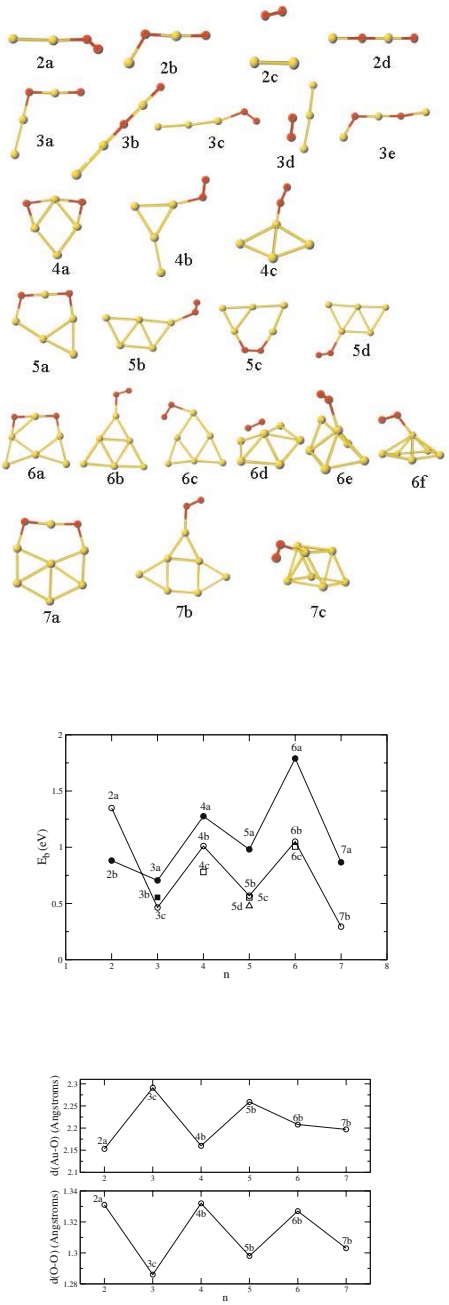

Figure 8. Structure (upper panel), binding energy (middle panel), and bond distances O-Au and O-O (lower panel), for a few lowest energy isomers of $Au_nO_2^-$ clusters. Except for n=2, the O_2 dissociation is energetically favorable but kinetically hindered.

In this subsection we investigate the lowest energy equilibrium structures of $Au_nO_2^-$ clusters starting with several initial positions for the O_2 molecules and for a considerable amount of configurations (relaxed or not) of Au_n^- anions. In subsection 6.1 we will investigate the adsorption of O_2 molecules on neutral relaxed Au_n clusters starting with several initial positions for the O_2 molecules relative to the cluster substrate. The structural and energetic details of the few lowest energy anionic complexes $Au_nO_2^-$ with $2 \leq n \leq 7$ are represented in Fig 8, and these results are compared to previous calculations[66,67] in Table 4.

For each cluster size, the few lowest energy equilibrium isomers with molecular adsorption (MA) and two atoms adsorption (TAA) complexes are represented in Fig 8. Most of these structures are planar or near planar. For 4c, 5b, and 5d, only an O atom is not in the plane. Two atom adsorption leads to major structural changes in the gold cluster, particularly for $n \geq 5$. For example, in the structures 5a, 6a, and 7a, a gold atom breaks the bonds to other Au atoms to form a highly stable linear O-Au-O unit which bind each O atom to one of the remaining Au atoms. On the other hand, molecular adsorption induces only a modest relaxation in the host cluster, and the O_2 molecule is attached on top of a Au atom preferably to the bridge position between two Au atoms.

The relative stability of the different MA and TAA $Au_nO_2^-$ complexes is compared by means of the energy to bind a O_2 molecule to the Au_n^- anion, defined as $E_b(O_2) = E(Au_n^-) + E(O_2) - E(Au_nO_2^-)$. This energy is given in Table 4, and presented in the middle panel of Fig 8 for several MA (open circles) and TAA (black circles) structures as a function of cluster size. We have not determined the energy barrier (transition state energy) to evolve from the MA to the TAA complexes. The difference between $E_b(O_2)$ and $E_b(2O) = E(Au_n^-) + 2E(O) - E(Au_nO_2^-)$ is just the binding energy of O_2. We see large odd-even alternations in the $E_b(O_2)$ of both MA and TAA structures. The MA species show a maximum value $E_b(O_2)$ for n=2, and for n=4,6 show relative maxima at $E_b \sim 1$ eV, whereas for n=3,5,7 MA show relative minima $E_b(O_2) \sim 0.3$-0.5 eV. The TAA structures are energetically favorable for $n \geq 3$, with the maximum E_b at n=6. In general, $E_b(O_2)$ increases (decreases) for TAA (MA) structures when the cluster size increases in the range studied here.

Yoon and coworkers[66] found that MA configurations are more tightly bound than TAA structures for n=2,3, whereas we find MA is favorable only for n=2. In this respect, our results coincide with those of Franceschetti and coworkers[67]. A difference with these autors is that we obtain the "top" MA isomer 5b in addition to (and practically degenerate with) the "bridge" 5c isomer found by Franceschetti and coworkers[67]. Our $E_b(O_2)$ values for MA are in very good agreement with those of Yoon and coworkers[66], including the isomeric structures (except 4c, for which we find a non planar structure, and 7b, which we comment below), but for TAA our $E_b(O_2)$ are

TABLE 4. Different properties of the $Au_nO_2^-$ clusters represented in Fig 8, identified by the label under the first column (Geo). In columns 2 and 3 are given details of the equilibrium geometry: α_1 is the angle O-O-Au for the MA complex with O_2 on a top site, and α_2 is the angle between planes O-O-Au and the Au_n^- planar substrate: 2D indicate a planar complex (α_2=0), and 3D a tridimensional substrate. The asterisk in geometries 2c and 3d indicate that the bond Au-O distance is exceedingly large in these isomers. In column 4 is given the integrated electronic charge difference of majority and minority spin densities, M_z, in atomic units ($\hbar$). In column 5 is given the computed binding energy, in eV, of the O_2 molecule to the Au_n^- anion: E_b=E(Au_n^-)+E(O_2)-E($Au_nO_2^-$). In columns 6 and 7 are given, for comparison, the binding energies computed in previous works: (a) Yoon *et al*[66], (b) Franceschetti *et al*[67]. In columns 8 and 9 are given in Å the distance between oxygen atoms computed in this work and by Yoon *et al*[66], respectively.

Geo	α_1	α_2	M_z	E_b	$E_b^{(a)}$	$E_b^{(b)}$	d_{O-O}	d^a_{O-O}
2a	118.6°	2D	1	1.35	1.39		1.33	1.34
2b	dissoc	2D	1	0.88			3.86	
2c	*105.7°	2D	3	0.46			1.28	
2d	dissoc	2D	3	0.42	0.79		3.82	
3a	dissoc	2D	2	0.70		0.99	3.86	
3b	dissoc	2D	2	0.55			3.82	
3c	121.3°	2D	2	0.46	0.46	0.36	1.29	1.30
3d	*111.1°	2D	2	0.18			1.26	
3e	dissoc	3D	0	-0.23	0.14		3.95	
4a	dissoc	2D	1	1.27	1.79	1.69	3.99	
4b	114.0°	2D	1	1.01	1.01	1.16	1.32	1.33
4c	116.8	67.3°	1	0.78	0.94		1.32	1.34
5a	dissoc	2D	2	0.98	1.33	1.14	3.97	
5b	119.0	49.2°	2	0.57	0.61		1.30	1.32
5c	bridge	near	0	0.55	0.48	0.54	1.41	1.49
5d	116.6°	59.8°	2	0.48			1.30	
6a	dissoc	2D	1	1.79	2.11	2.00	3.99	
6b	111.8°	2D	1	1.05	1.06	1.15	1.33	1.36
6c	105.0°	2D	1		1.02		1.34	1.36
6d	bridge	near	1	0.46			1.33	
6e	115.6°	3D	1	0.19			1.34	
6f	114.2°	3D	1	0.12			1.32	
7a	dissoc	2D	2	0.87	1.30		3.99	
7b	115.5°	2D	0	0.29	0.53		1.30	1.32
7c	119.5°	3D	2	-0.20			1.29	

systematically smaller. The agreement is only qualitative with the results of Franceschetti and coworkers[67]. For example, the MA structure 5b, with the O_2 molecule adsorbed on top of a Au atom, is not obtained[67], but instead,

these authors find the bridge O_2 adsorbed structure 5c. We find a difference of 0.23 eV in the $E_b(O_2)$ of 4a and 4b structures, which is very similar to the one found by Kim and coworkers[59] (0.28 eV), but much smaller than the difference found by Yoon and coworkers[66] (0.78 eV).

The linear O-Au-O chain that appears systematically in TAA complexes (see the progression of that linear unit in the structures 2b → 3a → 4a → 5a → 6a → 7a), was identified experimentally as a stable free neutral molecule[60], formed probably by adding atomic oxygen to the AuO diatomic molecule. We find that the free linear $(O\text{-}Au\text{-}O)^-$ anion is more stable than the MA AuO_2^- anion by ~ 0.23 eV/atom. The angle Au-O-O in the free MA anion is ~ 121.5, to be compared with the angle α_1 given in Table 4 for MA complexes.

The integrated difference of majority and minority spin electronic charges, denoted by M_z, is given in column 3 of Table 4. The spectroscopic multiplicity of the complex is M_z+1. We see that for MA complexes $Au_nO_2^-$ with even (odd) n, that is, with odd (even) number of electrons, the minimum energy isomer is a doublet (triplet). These M_z+1 values coincide with the ones found by Yoon and coworkers[66], except for 4c and 7b structures, where these authors obtained $M_z=3$ and $M_z=2$, respectively. Note that these two cases are the only MA complexes with significant different E_b values compared to our results.

There are significant correlations between the Au-O and O-O bond lengths, d_{Au-O} and d_{O-O}, respectively, with the binding energy $E_b(O_2)$, as shown in the middle and lower panels of Figure 8. Complexes with an even number of Au atoms, whose binding energies are higher than for odd n clusters, have smaller d_{Au-O} and larger d_{O-O} distances.

The reactivity of $Au_nO_2^-$ clusters to oxygen as a function of n was measured by Salisbury and coworkers[35] using time of flight mass spectroscopy. It was found that odd-n (even-n) clusters have negligible (significant) reactivity, which is explained by the fact that the O_2 molecule, acting as a one-electron aceptor, binds to anionic gold clusters, which have an unpaired electron.

6. Adsorption of O_2 and CO on neutral Au_n clusters

Gold is one of the least reactive metals in bulk form. However, in recent years a considerable amount of theoretical and experimental works have studied the reactivity of small neutral and charged Au clusters towards different molecules, like H_2, O_2, CO, and organic radicals[61,67–69,71–73]. The reactivity depends on the size and charge state of the cluster. In the previous section we have studied the reactivity towards oxygen adsorption of anionic silver and gold clusters. In this section we study the reactivity of neutral gold clusters towards molecular O_2 (subsection 6.1) and CO (subsection 6.2).

6.1. ADSORPTION OF O_2 ON NEUTRAL GOLD CLUSTERS

In this subsection we investigate the adsorption of O_2 molecules on neutral Au_n clusters with $5 \leq n \leq 10$ atoms. We optimize several initial positions of the O_2 molecule relative to the cluster substrate, which is chosen among the equilibrium structures of pure Au clusters obtained in a previous work[6]. We do not consider initial configurations with two separated O atoms. Thus, O_2 dissociative adsorption is obtained only when that process occurs without any barrier.

As commented in section 5.2, Yoon and coworkers[66] found by means of DFT calculations that molecular O_2 adsorption is dissociative for neutral and anionic Au clusters with more than 3 atoms, that the top position is preferable in molecular adsorption, and that anions are more reactive than neutral clusters. However, the structure of the Au_nO_2 neutral system was optimized starting from the structure of the anionic $Au_nO_2^-$ one, without a more general search of neutral structures. Instead, Franceschetti and coworkers[67] performed O_2 adsorption calculations starting with independently optimized structures for anionic and neutral pure gold clusters ($3 \leq n \leq 6$), reaching similar results to Yoon and coworkers[66] except for Au_5O_2, namely, that molecular adsorption is preferable to dissociative adsorption. We will follow the same strategy as Franceschetti and coworkers[67], but extending the calculations to larger sizes ($5 \leq n \leq 10$).

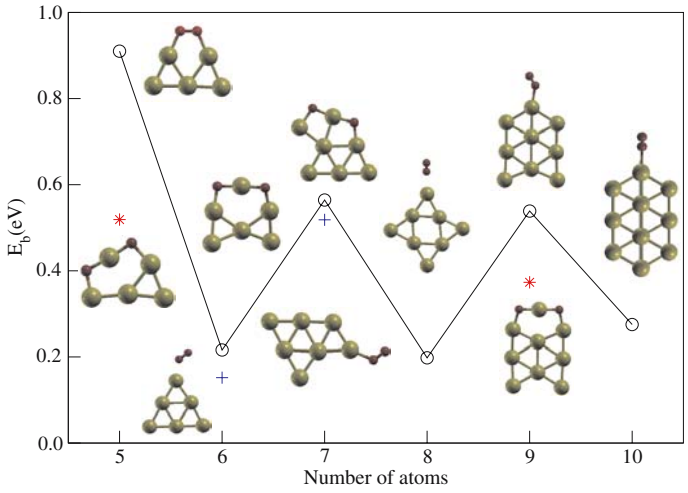

Figure 9. Lowest energy equilibrium geometries and calculated adsorption energies (denoted by the symbol ∘) of O_2 molecule on neutral Au_n clusters with $5 \leq n \leq 10$. Symbols * and + represent the adsorption energy for isomers with dissociated and molecularly adsorbed oxygen, respectively.

In Fig 9 we represent the lowest energy equilibrium geometry and the calculated adsorption energy of an O_2 molecule on neutral Au_n clusters with $5 \leq n \leq 10$. The adsorption energy is calculated as $E_{ads}(O_2) = E(Au_n) + E(O_2) - E(Au_nO_2)$. Dissociative adsorption without barrier is obtained for n=6,7. For non dissociative adsorption the O_2 molecule is adsorbed preferably on the top position of an Au atom with low coordination, except for n=5, where the bridge position between two Au atoms is favorable by 0.43 eV instead of the top position. The same effect was shown for Au_5^- anions in subsection 5.2 above. For all the sizes $5 \leq n \leq 10$ of the relaxed substrate, we considered several initial adsorption geometries with the O_2 on top, bridge, and hollow sites, and after energy optimization the initial hollow sites evolved toward top or bridge positions. For equilibrium top positions, the O_2 molecule binds out the plane formed by the Au cluster. The molecular adsorption does not modify substantially the substrate cluster geometry, whereas in the case of O_2 dissociation the cluster geometry changes radically, with the formation of a near lineal O-Au-O unit which binds to the remaining planar gold atoms, with the linear O-Au-O unit slightly out of the plane. The second isomer of Au_8O_2 binds O_2 to the same Au site than in our lowest energy state, and the second isomer of $Au_{10}O_2$ binds the O_2 molecule to an atom neighboring the one bonded in our lowest energy state.

In Table 5 we characterize the geometries of Fig 9, and list the spin multiplicity, the adsorption energy, and the O-O bond distance of Au_nO_2 clusters. The angle α_1 between O-O-Au atoms in $Au(O_2)$ free molecule is $\sim 119^\circ$, which is similar to the one found in adsorbed O_2Au_n and to the experimental one[60]. The near linear unit O-Au-O found in our ground state and isomeric structures of several Au_nO_2 clusters, was found experimentally and characterized theoretically as a free molecule[60]. The calculated adsorption energy $(E(Au^\nu + 2E(O) - E((O\text{-}Au\text{-}O)^\nu)$ for the neutral (ν=0) and anionic (ν=-1) linear $(O\text{-}Au\text{-}O)^\nu$ molecules, is 5.93 eV and 7.82 eV respectively, with bond Au-O distance 1.94 Å and 1.90 Å respectively. The bond distance O-O in adsorbed O_2 is larger than in the free O_2 molecule (1.22 Å). More details, including isomeric structures, Au-O distances, and vibrational frequencies of adsorbed O_2, will be published elsewhere[70] .

6.2. CO ADSORPTION ON NEUTRAL GOLD CLUSTERS

Wu and coworkers[71] studied CO adsorption on neutral and charged Au clusters. They found that the charge state influences the geometrical and electronic properties of the adsorption process. The top position is the preferable site for neutral clusters with less than 6 atoms. More recently, Phala and coworkers[72] found that the top site is favored up to a 13 Au atoms substrate, except for 5 atoms, competing with the bridge position. The geometries considered by these authors for more than 6 atoms are extracted from bulk fcc gold motifs.

TABLE 5. Geometry, spin multiplicity M=M_z+1, O-O and C-O bond distances (in Å), and adsorption energy: E^X_{ads} = E(Au_n) + E(X) - E(Au_nX), X =O_2, CO (in eV), for the lowest energy isomeric states of Au_nX clusters depicted in Figs 9-10. The geometry is specified by two angles: α_1 is the angle O-O-Au (O-C-Au), and α_2 is the angle between planes O-O-Au (O-C-Au) and the Au_n substrate. For the second isomer of Au_6CO and Au_8CO, the Au atom which binds to CO is out of the plane formed by the remaining Au atoms. This is indicate by the symbol * at the left of α_2.

	Au_nO_2					Au_nCO				
n	α_1	α_2	M	d_{O-O}	$E^{O_2}_{ads}$	α_1	α_2	M	d_{C-O}	E^{CO}_{ads}
5	bridge	2D	2	1.35	0.91	bridge	12.9°	2	1.20	1.26
5	dissoc	near	2		0.52	173.1°	58.0°	2	1.17	1.12
6	dissoc	near	3		0.21	164.2°	20.0°	1	1.17	0.96
6	115.3°	55.9°	3	1.26	0.15	175.6°	*86.0°	1	1.17	0.64
7	dissoc	2D	2		0.56	bridge	8.8°	2	1.21	1.28
7	115.8°	24.3°	2	1.28	0.52	169.7°	14.0°	2	1.21	1.23
8	121.7°	86.3°	3	1.26	0.20	175.2°	72.1°	1	1.17	1.16
8	116.8°	7.4°	3	1.26	0.08	172.9°	*39.1°	1	1.19	0.86
9	118.6°	54.2°	2	1.28	0.54	167.7°	3.6°	2	1.17	1.07
9	dissoc	near	2		0.37	169.2°	35.2°	2	1.17	1.03
10	119.3°	89.1°	1	1.27	0.28	172.2°	28.0°	1	1.17	1.06
10	116.5°	3.7°	3	1.27	0.25	168.0°	17.2°	1	1.17	1.05

In this subsection we present preliminary results about the adsorption of CO on neutral Au_n clusters with 5≤n≤10. More details will be given in a forthcoming publication. In Fig 10 we present the geometry and the calculated adsorption energy for the lowest energy equilibrium structure. In Table 5 we characterize these structures and isomeric states, and also give the corresponding spin multiplicity, C-O bond distance, and adsorption energy. The structures are obtained, for each size n, by relaxing several initial positions of the CO molecule attached to the ground state of a pure Au_n cluster obtained in a previous work[6]. In the relaxed equilibrium structures, CO binds to Au_n always through the C atom, and on top of a low coordinated Au atom, except for Au_5 and Au_7, which binds CO in a bridge position. The planar geometry of the Au clusters is preserved after adsorption with few modifications of Au-Au bond distances, except for Au_7. For Au_7CO we obtain an isomer with only 0.05 eV smaller binding energy, which have the CO in top position and without distortion of the Au_7 ground state structure. For Au_5CO the isomer with CO in top position has 0.14 eV lower adsorption energy. In all the cases, the C atom is in the same plane as the Au cluster. The CO bond distance increases after adsorption with respect to the free radical, and is larger in the bridge position. The largest adsorption energy E_{ads} is obtained for Au_5 and Au_7,

where CO binds in a bridge position, and with an odd number of valence electrons. The minimum E_{ads} occurs for Au_6, which is a magic cluster for planar configurations of delocalized electrons. No odd-even effects in E_{ads} are seen for $n \geq 7$. The second isomer reported in table 5 for n=6, 9, 10 clusters binds CO to the second less coordinated Au atom, although many isomeric equilibrium geometries exist by changing the angle α_2 reported for the lowest energy isomer.

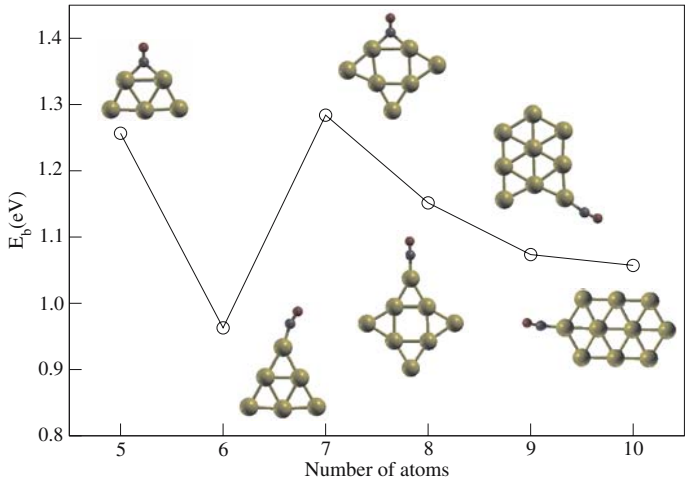

Figure 10. Lowest energy equilibrium geometries and calculated adsorption energies of CO molecules on neutral Au_n clusters with $5 \leq n \leq 10$. Dark small spheres bonded to Au (grey spheres) represent C atoms.

7. Conclusions

We have studied different properties of pure and doped noble metal clusters, and the adsorption of O_2 and CO on small anionic and neutral Ag and Au clusters. Pure Au clusters behave differently than Ag and Cu noble metal clusters and than alkali clusters due to relativistic effects leading to s-d hibridation. The contribution of exchange and correlation energy to the stabilization of planar structures is more critical in Au than in Cu clusters. Thus, GGA favors planar and cage-like structures whereas LDA leads to compact amorphous-like structures. Au_{20} is tetrahedral within GGA and LDA, but Au_{32} is cage-like only within GGA. We calculate within GGA novel cage-like equilibrium structures for Au_{18}, Au_{50}, and Au_{162}.

With respect to Au_nTM^+ cations, we have explained, from first principles calculations, the recently observed magic numbers[30], without resorting to the phenomenological shell model.

The adsorption of O_2 on Ag and Au clusters confirms and extends to larger cluster sizes the main results obtained in previous publications[58,66,67], although significative differences are also found.

With respect to the adsorption of an O_2 molecule on Ag_n^- clusters, odd-n anions exhibit about an order of magnitude smaller reaction rates than even-n anions, but they are able to activate the oxygen molecular bond to adsorb a second O_2 molecule. As proposed previously[58], the mechanism for the activation of molecular oxygen and the cooperative bonding of two oxygen molecules on Ag_n^- anions involves electron transfer from the Ag_n^- anions with even numbers of electrons into the π^*-MO of O_2. Thus, the binding of the first O_2 molecule changes the electronic structure of the cluster and induces a stronger cooperative binding with the second O_2.

With respect to gold, dissociative O_2 adsorption on Au_n^- is energetically favorable (but kinetically hindered) to molecular adsorption for anions with n≥3. Dissociative O_2 adsorption without any barrier is preferable for neutral Au_n clusters with n=6, 7. The binding energy of O_2 to anionic clusters, exhibit odd-even oscillations, and is a little bit larger than for the corresponding neutral clusters. We obtain qualitative and quantitative agreement with previous results[66,67], as well as some significant differences, mainly for the dissociative adsorption trend. We find that the linear unit O-Au-O appears as a structural motif in dissociative O_2 adsorption on neutral (spontaneous) and anionic (with barrier) Au clusters. That linear motif has been identified recently in the oxidation of vicinal surfaces of noble metal and transition metal systems[44,45].

With respect to CO adsorption on neutral Au_n clusters, our preliminary results show differences with previous calculations[72] using cluster geometries extracted from the fcc gold crystal. The adsorption energy of CO is minimum for the planar magic cluster Au_6 and shows maxima for the odd electron clusters Au_5 and Au_7, both with the CO absorbed on a bridge position, but the even-odd effect is not obtained for sizes larger than n=7.

In summary, the noble metal cluster studies presented in this work, provide a considerable amount of new electronic and structural data for pure and doped clusters, and for the behavior of O_2 and CO adsorption against the charge state and size of the cluster. We hope that this work will shed light on understanding the special physical and chemical properties of noble metal clusters, and particularly gold clusters.

Acknowledgements

This work was supported by the Junta de Castilla y León of Spain (grants VA073/02 and VA060/03) and by the Ministerio de Ciencia y Tecnología of Spain (grant MAT2002-04393-C02-01). EMF acknowledges a FPU grant from Ministerio de Educación y Ciencia of Spain.

References

1. W. Ekardt, *Metal Clusters* (Wiley, Chichester, 1999).
2. N. Agraït, A. L. Yeyati, and J. M. van Ruitenbeeck, Physics Reports **377**, 81 (2003).
3. M. Valden, X. Lai, and D. W. Goodman, Science **281**, 1647 (1998).
4. L. M. Molina and B. Hammer, Phys. Rev. Lett. **90**, 206102 (2003); Phys. Rev. B **69**, 155424 (2004).
5. P. Pyykkö, Angew. Chem. Int. Ed. **43**, 4412 (2004).
6. E. M. Fernández, J. M. Soler, I. L. Garzón, and L. C. Balbás, Phys. Rev. B **70**, 165403 (2004).
7. T. Bastug, M. Hirata, S. Varga, B. Fricke, S. Erkoc, and T. Mukoyama, Adv. Quantum Chem. **37**, 353 (2001).
8. F. Furche, R. Ahlrich, P. Weis, Ch. Jacob, S. Gilb, T. Bienweiler, and M. Kappes, J. Chem. Phys. **117**, 6982 (2002).
9. S. Gilb, P. Weis, F. Furche, R. Ahlrichs, and M. M. Kappes, J. Chem. Phys. **116**, 4094 (2002).
10. P. Weis, T. Bierweiler, S. Gilb, and M. M. Kappes, Chem. Phys. Lett. **355**, 355 (2002).
11. H. Häkkinen, M. Moseler, O. Kostko, N. Morgner, M. A. Hoffmann, and B. von Issendorff, Phys. Rev. Lett. **93**, 093401 (2004).
12. J. Li, X. Li, H.-J. Zhai, and L.-S. Wang, Science **299**, 864 (2003).
13. J. Wang, G. Wang, and J. Zhao, Chem. Phys. Lett. **380**, 716 (2003).
14. M. P. Johansson, D. Sundholm, and J. Vaara, Angew. Chem. Int. Ed. **43**, 2678 (2004).
15. X. Gu, M. Ji, S. H. Wei, and X. G. Gong, Phys. Rev. B **70**, 205401 (2004).
16. E. Fernández, L. C. Balbás, and J. M. Soler (Proceedings of Electronic Strcture: Principles and Applications, ESPA-2004; to be published).
17. H. Häkkinen, M. Moseler, and U. Landman, Phys. Rev. Lett. **89**, 033401 (2002). H. Häkkinen and U. Landman, Phys. Rev. B **62**, R2287 (2000).
18. W. Q. Tian, M. Ge, B. R. Sahu, D. Wang, T. Yamada, and S. Mashiko, J. Phys. Chem. A **108**, 3806 (2004).
19. L. Xiao and L. Wang, J. Phys. Chem. A **108**, 8605 (2004).
20. B. Soulé de Bas, M. J. Ford, and M. B. Cortie, Journal of Molecular Structure (Theochem) **686**, 193 (2004).
21. J. Zhao, J. Yang, and J. G. Hou, Phys. Rev. B **67**, 085404 (2003).
22. O. D. Häberlen, S. C. Chung, M. Stener and N. Rösch, J. Chem. Phys. **106**, 5189 (1997).
23. L. Xiao and L. Wang, Chem. Phys. Lett. **392**, 452 (2004).
24. Y. Shen and J. BelBruno, J. Phys. Chem. A **109**, 512 (2005).
25. R. M. Olson, et al, J. Am. Chem. Soc. **127**, 1049 (2005).
26. H. Grömbeck and P. Broqvist, Phys. Rev. B **71**, 73408 (2005).
27. Y. Negishi, et al, J. Am. Chem. Soc. **126**, 6518 (2004).
28. H.-F. Zhang, et al, J. Phys. Chem. B **108**, 12259 (2004).
29. K. Palotás and B. Lazorovits and L. Szunyogh and P. Weinberger, Phys. Rev. B **70**, 134421 (2004).
30. S. Neukermans and E. Janssens and H. Tanaka and R. E. Silverans and P. Lievens, Phys. Rev. Lett. **90**, 033401 (2003).
31. M. B. Torres, E. M. Fernández, and L. C. Balbás, Phys. Rev. B **71**, 155412 (2005).
32. A. Sanchez, S. Abbet, U. Heiz, W.-D. Scheineider, H. Häkkinen, R. N. Barnett, and U. Landman, J. Phys. Chem. A **103**, 9573 (1999).
33. L. D. Socaciu, J. Hagen, T. M. Bernhardt, L. Wöste, U. Heiz, H. Häkkinen, and U. Landman, J. Am. Chem. Soc. **125**, 10437 (2003).

34. W. T. Wallace and R. L. Wetten, J. Am. Chem. Soc. **124**, 7499 (2002).
35. B. E. Salisbury, W. T. Wallace, and R. L. Wetten, Chem. Phys. **262**, 131 (2000).
36. Y. D. Kim and G. Ganteför, Chem. Phys. Lett. **383**, 80 (2004).
37. D. Stolcic, M. Fischer, G. Ganteför, Y. D. Kim, Q. Sun, P. J. Jena, J. Am. Chem. Soc. **125**, 2848 (2003).
38. T. H. Lee and K. M. Ervin, J. Phys. Chem. **98**, 10023 (1994).
39. A. L. de Oliveira, A. Wolf, and F. Schüth, Catal. Lett. **73**, 157 (2001).
40. T. Hayashi, K. Tanaka, and M. Haruta, J. Catal. **178**, 566 (1998).
41. C. T. Campbell and M. Paff, Surf. Sci. **143**, 517 (1984).
42. N. Saliba, D. Holmes-Parker, and B. E. Koelb, Surf. Sci. **410**, 270 (1998).
43. J.-H. Liu, A.-QWang, Y.-S. Chi, H.-P. Lin, and C.-Y. Mou, J. Phys. Chem. B (Letters) **109**, 40 (2005).
44. N. Bonini, A. Kokalj, A. Dal Corso, S. de Gironcoli, and S. Baroni, arXiv:cond-mat/0403371.
45. M. Todorova, K. Reuter, and M. Scheffler, arXiv:cond-mat/0501018.
46. J. M. Soler, E. Artacho, J. D. Gale, A. García, J. Junquera, Pablo Ordejón, and Daniel Sánchez Portal, J. Phys.: Condens. Matter **14**, 2745 (2002).
47. W. Kohn and L. J. Sham, Phys. Rev. **145**, 561 (1965). See also, R. G. Parr and W. Yang, *Density Functional Theory of Atoms and Molecules*, Oxford UP, New York (1989).
48. J. P. Perdew, K. Burke, and M. Ernzerhof, Phys. Rev. Lett. **77**, 3865 (1996).
49. J. P. Perdew and A. Zunger, Phys. Rev. B **23**, 5075 (1991).
50. N. Troullier and J. L. Martíns, Phys. Rev. B **43**, 1993 (1991).
51. L. Kleinman and D. M. Bylander, Phys. Rev. Lett. **48**, 1425 (1982).
52. E. M. Fernández, M. B. Torres, and L. C. Balbás, International J. of Quantum Chem. **99**, 39 (2004).
53. M. D. Morse, Chem. Rev. (Washington D.C.) **86**, 1049 (1986).
54. L. C. Balbás, J. L. Martíns, and J. M. Soler, Phys. Rev. B **64**, 165110 (2001).
55. I. A. Solov'yov, A. V. Solov'yov, and W. Greiner, Phys. Rev. A, **65**, 053203 (2002).
56. A. Hirsch, Z. Chen, and H. Jiao, Angew. Chem. Int. Ed. **39**, 3915 (2000).
57. L. D. Socaciu, J. Hagen, J. Le Roux, D. Popolan, T. M. Bernhardt, and L. Wöste, J. Chem. Phys. **120**, 2078 (2004).
58. J. Hagen, L. D. Socaciu, J. Le Roux, D. Popolan, T. M. Bernhardt, L. Wöste, R. Mitrić, H. Noack, and V. Bonacic-Koutecky, J. Am. Chem. Soc. **126**, 3442 (2004).
59. Y. D. Kim, G. Ganteför, Q. Sun, and P. Jena, Chem. Phys. Lett. **396**, 69 (2004).
60. A. Citra and L. Andrews, Journal of Molecular Structure (Theochem) **489**, 95 (1999).
61. D. M. Cox, R. Brickman, K. Creegan, and A. Kaldor, Z. Phys. D **19**, 353 (1991).
62. J. Hagen, L. D. Socaciu, M. Elijazyfer, U. Heitz, T. M. Bernhardt, and L. Wöste, Phys. Chem. Chem. Phys. **4**, 1707 (2002).
63. M. Okamura, Y. Kitagawa, M. Haruta, K. Yamaguchi, Chem. Phys. Lett. **346**, 163 (2000).
64. H. Häkkinen and U. Landman, J. Am. Chem. Soc. **123**, 9704 (2001).
65. G. Mills, M. S. Gordon, and H. Metiu, Chem. Phys. Lett. **359**, 493 (2002).
66. B. Yoon, H. Häkkinen, and U. Landman, J. Phys. Chem. A **107**, 4066 (2003).
67. A. Franceschetti, S. J. Pennycook, and S. T. Pantelides, Chem. Phys. Lett. **374**, 471 (2003).
68. D. H. Wells, Jr., et al, J. Chem. Phys. **117**, 10597 (2002).
69. Z. P. Liu, P. Hu, and A. Alavi, J. Am. Chem. Soc. **124**, 14770 (2002).
70. E. Fernández, P. Ordejón, and L. C. Balbás, Chem. Phys. Lett. **408**, 252 (2003).
71. X. Wu, L. Senapati, S. K. Nayak, A. Selloni, and M. Hajaligol, J. Chem. Phys. **117**, 4010 (2002).
72. N. S. Phala, G. Klatt, and E. V. Steen, Chem. Phys. Lett. **395**, 33 (2004).
73. L. Jiang and Q. Xu, J. Phys. Chem. A **109**, 1026 (2005).

THREE-GOLD CLUSTER AS PROTON ACCEPTOR IN NONCONVENTIONAL HYDROGEN BONDS O-H···Au AND N-H···Au

E. S. KRYACHKO
Department of Chemistry, Bat. B6c, University of Liege, Sart-Tilman, B-4000 Liege 1, Belgium and Bogoliubov Institute for Theoretical Physics, Kiev, 03143 Ukraine
E-mail: eugene.kryachko@ulg.ac.be

AND

F. REMACLE
Maître de Recherche, FNRS (Belgium), Department of Chemistry, Bat. B6c, University of Liege, Sart-Tilman, B-4000 Liege 1, Belgium
E-mail: fremacle@ulg.ac.be

Abstract. The present work extends the family of nonconventional proton acceptors to the coinage metal Au. Based on high level computations, we demonstrate the ability of the triangle three-gold cluster to behave as nonconventional proton acceptor and hence to form hydrogen bonds with conventional hydrogen bond donors. Three molecules: formic acid, alanine, and adenine, involving O-H and N-H groups as typical conventional hydrogen bond donors, are chosen for this purpose.

1. Introduction: The Concept of Conventional Hydrogen Bond

At the beginning of the 20th century, Huggins [1], Latimer and Rodebush [2], and Pauling [3] introduced the concept of a classical or conventional hydrogen bond A-H···B[1] as that formed between a (conventional) hydrogen

[1]The hydrogen bond was likely quoted for the first time in 1923 by Lewis [4].

J.-P. Julien et al. (eds.),
Recent Advances in the Theory of Chemical and Physical Systems, 433–450.

bond donor A-H and a (conventional) proton acceptor B containing lone-pair electrons. Since then, it has been well accepted and widely used in many areas of physics, chemistry, and biology [5-20].

Usually, A is sufficiently electronegative to induce a rather polar bond. O-H and N-H groups (generally speaking, R′-X-H where X = O, N and R′ is the rest of molecule) are typical conventional hydrogen bond donors. Typical conventional hydrogen bond acceptors are the atoms F, N, O, C, P, S, Cl, Se, Br, and I whose electronegativities are larger than the electronegativity of hydrogen and which have an unshared electron pair. When a hydrogen atom H belonging to the A-H group of one molecule approaches closer enough the electronegative atom B of the other , it interacts with B and forms a bond, where the proton is shared between A and B. This sharing, graphically indicated as $\cdots$, rearranges the electron density of the A-H group and B, so that H partially loses its charge compared to the monomer A-H (it was already not neutral there). H is treated as a bridging hydron $H^{+\delta}(0 \leq \delta \neq 1)$ or, in the extreme case, as a bridging proton H^+.

When B is an atom or ion, a hydrogen (H-) bond A-H$\cdots$B is geometrically characterized by the two bond lengths, R(A-H) and r(H$\cdots$B), and by the bond angle $\phi_H \equiv \angle$AHB. When B has a more complex structure, the hydrogen bond is (are) graphically pictured as A-H$\cdots$B-R, and another bond angle(s), $\angle$RBH, is introduced. Sometimes, instead of ϕ_H, another angle $\psi_H \equiv \pi - \phi_H$ is used. Within the hydrogen bond A-H$\cdots$B, the A, H, and B do not severely deviate from a collinear arrangement. r(H$\cdots$B), defined as the distance between the bridging proton (hydron) and the proton acceptor B, is often called the hydrogen bond separation. One can also introduce the donor-acceptor distance R(A$\cdots$B). A formation of a hydrogen bond A-H$\cdots$B results in a new vibrational mode ν_σ that describes the H-bond A$\cdots$B stretch.

It is usually assumed that a conventional hydrogen bond A-H$\cdots$B is formed if the following structural and spectroscopic criteria are obeyed [5-20]:

(i) *There exists a firm evidence of the bond formation.*
This might be, e. g., the appearance of the H-bond stretching mode ν_σ. One can also rely on the energy criteria [8] requiring that the binding energy of a formed complex is larger than the dipolar or London dispersion energies;

(ii) *There exists a firm evidence that this bond specifically involves a hydrogen atom which is bonded to B predominantly along the bond direction A-H.*
This might be, e. g., indicated by changes (in comparison with the A-H group) in two bending modes, out-of-plane γ(A-H$\cdots$B) and in-plane δ(A-H$\cdots$B);

(iii) *The A-H bond elongates relative to that in the monomer*;

(iv) *A so called van der Waals cutoff*: the hydrogen bond separation r(H···B) defined as the distance between the bridging proton and the proton acceptor, B, is shorter than the sum of van der Waals radii of H and B, that is (see in particular Refs. [9, 10, 12] and Ref. [21] in [14]),

$$\mathrm{r(H\cdots B)} < w_{\mathrm{H}} + w_{\mathrm{B}} \tag{1}$$

where w_{X} is the van der Waals radius of X. Note that the distance r(A-B) between A and B is often referred to as the H-bond length. The necessary but insufficient condition imposed on r(A-B) that indicates that the H-bond is formed is the following:

$$\mathrm{r(A\cdots B)} < w_{\mathrm{A}} + w_{\mathrm{B}}. \tag{2}$$

In some cases, the van der Waals cutoff is a too strong constraint from the experimental point of view and can be extended to the condition r(H···B) $\leq$ 3.0 or even 3.2 Å [10, 11, 13, 16] (see also note [21] in Ref. [16]);

(v) *The proton-stretching vibrational mode ν(A-H) undergoes a red shift (a downshift to lower wavenumbers) with respect to that in the corresponding monomer and its IR absorption increases.*
This is the most unequivocal probe of the existence of a hydrogen bond;

(vi) *Proton nuclear magnetic resonance (^{1}H NMR) chemical shifts in the A-H···B hydrogen bond are shifted downfield compared to the monomer.*

Actually, **(i)** - **(vi)** are those geometric and spectroscopic aspects of the interaction upon which crystallographers, molecular spectroscopists, and quantum chemists primarily rely and most widely employ, considering them as evidence of an attractive interaction involving charge rearrangement. Note that **(iii)** - **(vi)** may be also treated as an indirect confirmation of **(i)** and **(ii)**. There exist other features related with the H-bond formation. They are, e. g., an increase of the polarity of the A-H bond; an increase of the total dipole moment of the complex, that is larger than a vector sum of the dipole moments of monomers. Steiner [16] has recently revised the definition of a hydrogen bond and proposed the following one:

An A-H···B interaction is called a "hydrogen bond" if **(a)** *it constitutes a local bond and if* **(b)** *A-H acts as proton donor to B.*

TABLE 1. Jeffrey's classification of hydrogen bonds [11] (see also Refs. [16, 21]).

	Strong (proton-shared)	Moderate	Weak (conventional)
Type of interaction	strongly covalent	dominant electrostatic	electrostatic dispersion
r(H$\cdots$B), Å	1.2 - 1.5	1.5 - 2.2	$\geq$ 2.2
ΔR(A-H), Å	0.08 - 0.25	0.02 - 0.08	$\leq$ 0.02
R(A-H)/r(H$\cdots$B)	≈ 1	< 1	$\ll 1$
R(A$\cdots$B), Å	2.2 - 2.5 (2.6)	2.5 (2.6) - 3.2	$\geq$ 3.2
directionality	strong	moderate	weak
$\angle$AHB, ^{o}	$170^o - 180^o$	$170^o - 130^o$	$130^o - 90^o$
$\mid E_{HB} \mid$, kcal/mol	15 - 40 (60 [21])	4 - 15	$\leq$ 4
$\Delta\nu$(A-H$\cdots$B)/ν(A-H), %	25	10 - 25	$\leq$ 10
$\mid \delta\sigma$(H)$\mid$, ppm	14 - 22	$\leq$ 14	

Hydrogen bonds are classified as strong or proton-shared (ion-pair), moderate, and normal or weak (conventional). See Table 1. Strong H-bonds are two-center bonds with short separations R(A$\cdots$B) $\in$ (2.2 Å, 2.60 Å) (for very strong H-bonds R(A$\cdots$B)$\leq$ 2.45 Å). Obviously, the symbolic notation $\cdots$ for H$\cdots$B is no longer valid for strong H-bonds where the proton is (almost) equally shared and thus roughly centered between A and B. They are therefore depicted as A-H-B. Strong hydrogen bonds are almost linear and characterized by the H-bond formation energies, $\mid E_{HB} \mid \geq$ 15 kcal/mol.

Weak or conventional H-bonds are characterized by longer R(A$\cdots$B) $>$ 3.20 Å distances, their A-H bonds are slightly elongated relative to the R(A-H) in the monomers; and their r(H$\cdots$B) bond lengths are much longer than a covalent H$\cdots$B distance. The strength of a conventional hydrogen bond A-H$\cdots$B is typically estimated by the electrostatic attraction of the bond dipole A-H with a negative charge on B [10]. Usually, this strength is an order of magnitude weaker than a covalent bond.

Nowadays, the concept of a hydrogen bond is much broader than it was expected nearly century ago [13, 15]. Many new bonds, similar to the hydrogen ones, i. e., sharing similar features **(i)** - **(vi)**, have been identified, both experimentally and theoretically. To distinguish them from the

conventional hydrogen bonds, they are referred to as 'nonconventional'. A family of nonconventional hydrogen bonds are the A-H$\cdots$M ones, formed between conventional hydrogen bond donors and electron-rich transition metals M, such as Co, Ru, Rh, Os, Ir, and Pt functioning as weak proton acceptors [22-24]. Rigorously speaking, those metals must be referred to nonconventional proton acceptors.

The aim of the present work consists in extending the existing family of nonconventional proton acceptors to the coinage metal Au. On the basis of high-level calculations, we show that the triangle Au_3 cluster can behave as a proton acceptor and hence take part in hydrogen bonds with conventional hydrogen bond donors. In the present study, the latter are restricted to formic acid, alanine, and adenine, which contains O-H and N-H groups, the typical conventional hydrogen bond donors.

The motivation of the present work has also more technologically oriented aspects. One is connected to the "bottom-up" strategy in molecular electronics and biosensor design which often use biological molecules, DNA in particular, as templates [25]. The other is related to the recent studies of DNA bases at gold electrodes [26]. Recent experiments have demonstrated that the four DNA bases (adenine A, thymine T, guanine G, and cytosine C) interact with Au surfaces in a complex and sequence-dependent manner which is different for each base [27]. Their relative affinities to adsorb on polycrystalline Au films obey the following order: A > C $\geq$ G > T [27c]. The energetics of the DNA base-gold interactions can be understood from the heats ΔH_{des} of desorption of the bases from Au thin films, ΔH_{des}(T) = 26.5 $\pm$ 0.5 kcal/mol, ΔH_{des}(C) = 30.6 $\pm$ 1.0 kcal/mol, ΔH_{des}(A) = 31.3 $\pm$ 0.7 kcal/mol, and ΔH_{des}(G) = 34.9 $\pm$ 0.5 kcal/mol [27a]. Structurally, it has been suggested that adenine anchors gold either at the N_6 exocyclic amino group [27d] or the N_7 atom [27e], although the precise geometry of the bonded complex A·Au has not yet been determined [27c]. The third reason stems out from quite recent experiments on the binding of amino acids to gold nanoparticles [28]. In particular, one of these studies shows [28e] that amino acids such as lysine and aspartic acid bind extremely strongly to gold particles when unprotonated.

2. Computational Methodology

All computations reported in the present work were conducted with the GAUSSIAN 03 package of quantum chemical programs [29]. The Kohn-Sham self-consistent field formalism with the hybrid density functional B3LYP potential was used together with relativistic effective core potential RECP (gold) and the basis sets 6-31++G(d,p) (formic acid and alanine) and 6-31+G(d) (adenine). Three different energy-consistent 19-($5s^2 5p^6 5d^{10} 6s$)

valence electron RECPs for gold atoms were used: the one developed by Ermler, Christiansen and co-workers (EC) with the primitive basis set $(5s5p4d)$ [30], by the Stuttgart group (S) with the basis set $(8s7p6d)/[6s5p3d]$ [31], and by Hay and Wadt (Los Alamos RECP or shortly HW-LA) [32][2]. The main features of the triangle Au_3 cluster are gathered in note [35]. One of the studied complexes, that of formic acid with Au_3, was also investigated at the MP2/HW-LA (gold) $\cup$ 6-31++G(d,p) (formic acid) computational level (see also Ref. [36]).

All geometrical optimizations were performed with the keywords "tight" and "Int=UltraFine". The unscaled harmonic vibrational frequencies, zero-point vibrational energies (ZPVE), and enthalpies were also calculated. The ZPVE-corrected binding energies E_b are reported throughout the work.

3. Nonconventional Hydrogen Bond in Formic Acid·Au_3 Complex

The most stable planar cyclic complex between a three-gold cluster and formic acid (FA) is shown in Figure 1. Au_3 builds with formic acid an anchor Au-O bond whose length varies within 2.240 - 2.280 Å (depending on the RECP used). The anchoring of the Au_3 cluster to the carbonyl oxygen is accompanied by the formation of the O-H$\cdots$Au bond. We intend to prove that this intramolecular bond satisfies all necessary and sufficient conditions **(i)** - **(vi)** defining conventional H-bonds. The existence of the bond (condition **(i)**) is confirmed by the appearance of the H-bond stretching mode $\nu_\sigma(O_2\cdots Au_5)$ in the complex FA·Au_3, whose frequency falls within the range of 133 - 142 cm^{-1} depending on the RECP used. This mode is coupled to the stretching mode of the O_3-Au_4 anchor bond. We provide below the energetic, structural and spectroscopic information that shows that the conditions **(iii)** - **(vi)** are satisfied for the O_2-$H_2\cdots Au_5$ bond[3]:

Note: the binding energy E_b(FA·Au_3) = 14.4 (EC), 13.2 (S), 12.0 (HW-LA) kcal/mol and the enthalpy of formation -ΔH_f = 14.3 (EC), 13.0 (S), 11.8 (HW-LA) kcal/mol. The total dipole moment d_{tot}(FA·Au_3) = 2.57 (EC), 2.57 (S), 2.49 (HW-LA) D. The bond angle in O_2-$H_2\cdots Au_5$ is close to π ($\angle O_2H_2Au_5 = 173.4^o - 173.8^o$, see Figure 1) so this bond is practically linear.

(iii) $\Delta R(O_2\text{-}H_2)$ = 0.026 (EC), 0.022 (S), 0.023 (HW-LA) Å;

(iv) $r(H_2\cdots Au_5)$ = 2.493 (EC), 2.450 (S), 2.506 (HW-LA) Å $< w_H + w_{Au}$ = 2.86 Å;

[2]For a recent review on small gold clusters see Ref. [33] and Ref. [34] for the 2D-3D coexistence in small neutral and charged gold clusters.

[3]The related properties of formic acid are collected in note [37].

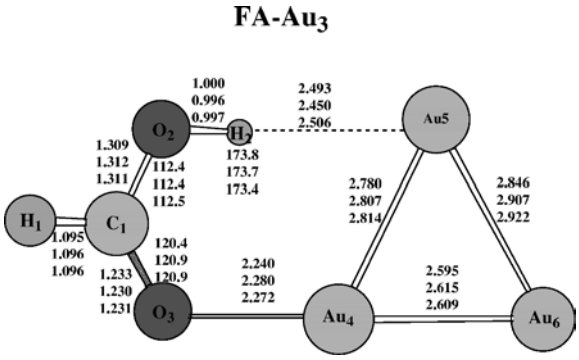

Figure 1. The most stable plannar complex between formic acid and Au_3. The bond lengths are given in and bond angles in ˚ (reading from top to bottom: B3LYP/RECP = EC, S, HW-LA (gold) ∪ 6-31++G(d, p) (formic acid)).

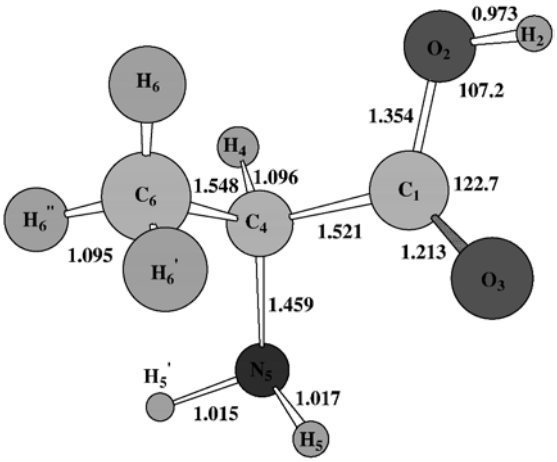

Figure 2. One of the lowest-energy conformers of alanine. The bond lengths are given in and bond angles in˚.

(v) -$\Delta\nu$(O_2-H_2) = 520 (EC), 453 (S), 463 (HW-LA), 422 (MP2/HW-LA (gold) $\cup$ 6-31++G(d,p) (formic acid)) cm^{-1}
A_{IR}[4](O_2-$H_2\cdots Au_5$)/A_{IR}(O_2-H_2) = 14.7 (EC), 13.8 (S), 14.2 (HW-LA), 12.3 (MP2/HW-LA (gold) $\cup$ 6-31++G(d,p) (formic acid))
-$\Delta\nu$(O_2-D_2) = 374 (EC), 325 (S), 337 (HW-LA) cm^{-1}
A_{IR}(O_2-$D_2\cdots Au_5$)/A_{IR}(O_2-D_2) = 13.6 (EC), 12.1 (S), 12.4 (HW-LA);

(vi) $\delta\sigma_{iso}(H_2)$ = -4.1 (EC), -3.5 (S), -4.0 (HW-LA) ppm
$\delta\sigma_{iso}(O_2)$ = -41.3 (EC), -35.6 (S), -37.3 (HW-LA) ppm
$\delta\sigma_{an}(H_2)$ = 14.3 (EC), 13.3 (S), 14.4 (HW-LA) ppm
$\delta\sigma_{an}(O_2)$ = -82.2 (EC), -75.0 (S), -76.7 (HW-LA) ppm.
Note: the changes in the NMR chemical shift of the bridging proton H_2 resulting from the formation of a hydrogen bonding-type interaction is a well-known indicator of a hydrogen bond formation **(vi)** (see also Ref. [38]). For the studied complex, $\delta\sigma_{iso}(H_2)$ is negative, as it should be if a hydrogen bond is formed since its formation in FA·Au_3 induces a deshielding of the bridging proton. Note that it is also lower than the $\delta\sigma_{iso}$(H) = -2.8 ppm of the bridging proton in water dimer [38c]. The range of the anisotropic shifts $\delta\sigma_{an}(H_2)$ is much wider and larger than that of water dimer (= 11.2 ppm) but equal to those of water chains $(H_2O)_{4-5}$ [38c].

We conclude that the bond O_2-$H_2\cdots Au_5$ formed in the complex FA·Au_3 is an example of a nonconventional hydrogen bond. The 5*d* orbital of the gold atom Au_5 in three-gold cluster exhibits a lone-pair character which induces its proton acceptor ability.

4. Au_3 as Nonconventional Proton Acceptor with Alanine

Alanine (Ala) is one of the simplest natural α-amino acids. As all amino acids, alanine is a very floppy molecule and its potential energy surface landscape exhibits a large number of low-energy conformers (see Ref. [39] and references therein). Only one of them, shown in Figure 2, is used in the present work to study the interaction of alanine with Au_3. The most stable planar, cyclic complex Ala·Au_3 resulting from this interaction is shown in Figure 3. As in the formic acid case discussed above, it is stablized by two Ala - Au_3 bonds. One of them is the anchor Au_7-O_3 bond whose length falls within the interval of 2.225 - 2.263 Å and thus is shorter by $\approx$ 0.01 - 0.02 Å than the similar bond in FA·Au_3. The other bond is O_2-$H_2\cdots Au_8$. This intramolecular bond shares common features with the conventional hydrogen bonds and obeys the necessary and sufficient conditions **(i)** - **(vi)**. A spectroscopic evidence of the existence of this bond is the appearance of

[4]A_{IR} stands for IR activity.

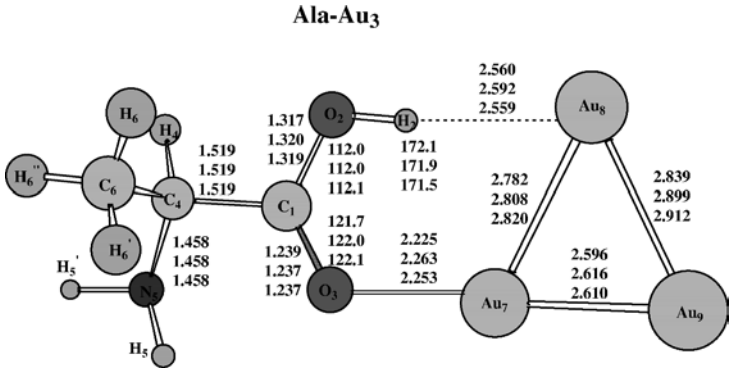

Figure 3. The most stable complex Ala.Au_3. The bond lengths are given in and bond angles in ° (reading from top to bottom: B3LYP/RECP = EC, S, HW-LA (gold) ∪ 6-31++G(d, p) (alanine)).

the H-bond stretching mode $\nu_\sigma(O_2 \cdots Au_8)$ in the complex Ala·Au_3 ranging within 118 - 125 cm^{-1} and coupled to the stretching mode of the anchor bond O_3-Au_7. This bond is almost linear ($\angle O_2H_2Au_8 = 171.5^o - 172.1^o$, see Figure 3). The energetic, structural and spectroscopic details showing that the conditions **(iii)** - **(vi)** are satisfied for the O_2-$H_2 \cdots Au_8$ bond are given below:

Note: the binding energy E_b(Ala·Au_3) = 14.1 (EC), 13.2 (S), 12.7 (HW-LA) kcal/mol and the enthalpy of formation -ΔH_f = 13.7 (EC), 12.8 (S), 11.7 (HW-LA) kcal/mol. The total dipole moment d_{tot}(Ala·Au_3) = 4.67 (EC), 4.61 (S), 4.59 (HW-LA) D;

(iii) $\Delta R(O_2\text{-}H_2)$ = 0.022 (EC), 0.020 (S), 0.020 (HW-LA) Å;

(iv) $r(H_2 \cdots Au_8)$ = 2.560 (EC), 2.592 (S), 2.559 (HW-LA) Å $< w_H + w_{Au}$ = 2.86 Å.

Note: The H-bond in Ala·Au_3 undergoes a larger lengthening (by ≈ 0.05 - 0.14 Å) than in FA·Au_3;

(v) -$\Delta\nu(O_2\text{-}H_2)$ = 461 (EC), 410 (S), 423 (HW-LA) cm^{-1}
$A_{IR}(O_2\text{-}H_2 \cdots Au_8)/A_{IR}(O_2\text{-}H_2)$ = 15.1 (EC), 13.6 (S), 13.9 (HW-LA)
-$\Delta\nu(O_2\text{-}D_2)$ = 331 (EC), 294 (S), 304 (HW-LA) cm^{-1}
$A_{IR}(O_2\text{-}H_2 \cdots Au_8)/A_{IR}(O_2\text{-}H_2)$ = 13.1 (EC), 11.8 (S), 12.1 (HW-LA);

(vi) $\delta\sigma_{iso}(H_2)$ = -3.9 (EC), -3.4 (S), -3.6 (HW-LA) ppm
$\delta\sigma_{iso}(O_2)$ = -36.9 (EC), -32.9 (S), -34.4 (HW-LA) ppm
$\delta\sigma_{an}(H_2)$ = 13.3 (EC), 12.6 (S), 13.4 (HW-LA) ppm
$\delta\sigma_{an}(O_2)$ = -71.5 (EC), -66.4 (S), -68.6 (HW-LA) ppm.

5. Nonconventional Intramolecular Hydrogen Bond in Adenine·Au_3 Complexes

A single atom of gold binds adenine very weakly, at its nitrogen atoms N_1, N_3, and N_7 [40]. The Au-N_i anchor bond length varies therein from 2.343 Å (A·$Au_1(N_1)$) to 2.320 Å (A·$Au_1(N_3)$), and 2.305 Å (A·$Au_1(N_7)$). The binding energies E_b of the resulting complexes are equal to 2.5, 2.5 and 2.2 kcal/mol, respectively. These nitrogen atoms of adenine remain the favorable sites to anchor the triangle three-gold cluster. In Figure 4, we show the three most stable and planar conformers of A·Au_3 resulting from these N anchoring sites. They are characterized by the following binding energies: E_b = 22.6 kcal/mol (N_1), 24.4 (N_3), and 22.3 kcal/mol (N_7)[5]. The binding energy of adenine to Au_3 raises by a factor of ca. 10 compared to that of adenine to a single gold atom.

Two main reasons can be invoked to explain the significant strengthening of the bonding between Au_3 and adenine compared to that in A·Au_1. The first and likely the dominant one is a strengthening of the anchor bonds Au-N_i in the complexes A·$Au_3(N_i)$, as indicated by their considerable contraction by $\approx$ 0.19 Å compared to those in A·$Au_1(N_i)(i = 1, 3, 7)$. As reported in Figure 4, r(Au_{10}-N_1) = 2.153 Å in A·$Au_3(N_1)$), r(Au_{10}-N_3) = 2.138 Å in A·$Au_3(N_3)$, and r(Au_{10}-N_7) = 2.130 Å in A·$Au_3(N_7)$. However the binding energies of the complexes A·$Au_3(N_i)(i = 1, 3, 7)$ do not fully correlate with their anchor bond lengths. For example, the most stable complex is formed with Au_3 bonded at N_3. Its anchor bond Au-N is not the shortest one. The reason is that the binding of Au_3 to adenine is accompanied by the formation of a N-H$\cdots$Au bond. As in Sections 3 and 4, we gather below the energetic, structural and spectroscopic characteristics

[5]A nonplanar and less stable (by 14.5 kcal/mol, compared to that formed at the N_3 atom) complex is formed by anchoring at the N_6 atom.

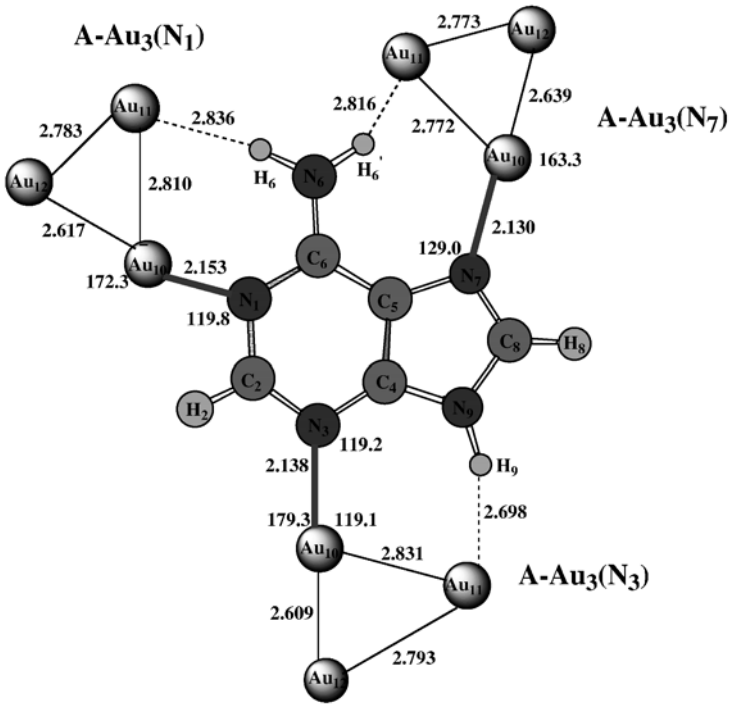

Figure 4. Three different anchoring positions for a Au_3 cluster on adenine. The most stable A. Au_3 complexes are planner and cyclic. The bond lengths are given in and bond angles in°.

showing that the bond N-H$\cdots$Au in the complexes A·$Au_3(N_i)(i = 1, 3, 7)$ is a nonconventional hydrogen bond[6].

5.1. COMPLEX A·$AU_3(N_1)$

Note: The N_6-$H_6 \cdots Au_{11}$ bond is almost linear (the H-bond angle $\angle N_6H_6Au_{11}$= 175.2^o). The very large polarity of this complex ($d_{tot} = 8.28$ D) results from the fact that the Au_{12}-Au_{10}-N_1 bond dipole is almost collinear to the dipole moment of adenine;

(iii) $\Delta R(N_6\text{-}H_6) = 0.009$ Å;

[6]The total dipole moment of adenine $d_{tot} = 2.50$ D.

(iv) $r(H_6 \cdots Au_{11}) = 2.836$ Å $< w_H + w_{Au} = 2.86$ Å;
(v) $-\Delta\nu(N_6\text{-}H_6) = 153$ cm^{-1}
$A_{IR}(N_6\text{-}H_6 \cdots Au_{11})/A_{IR}(N_6\text{-}H_6) = 5.6$.
Note: Another N-H stretching mode $\nu(N_6\text{-}H_6')$ weakly coupled to $\nu(N_6\text{-}H_6)$ becomes red-shifted by only 55 cm^{-1};
(vi) $\delta\sigma_{iso}(H_6) = -2.4$ ppm
$\delta\sigma_{iso}(N_6) = -18.9$ ppm
$\delta\sigma_{an}(H_6) = 10.3$ ppm
$\delta\sigma_{an}(N_6) = -21.3$ ppm.

5.2. COMPLEX A·AU$_3$(N$_3$)

Note: Its total dipole moment is equal to 5.66 D. For the present calculations, A·Au$_3$(N$_3$) is the most stable complexes among these three. The H-bond angle $\angle N_9H_9Au_{11} = 160.8^o$;
(iii) $\Delta R(N_9\text{-}H_9) = 0.014$ Å;
(iv) $r(H_9 \cdots Au_{11}) = 2.698$ Å $< w_H + w_{Au} = 2.86$ Å;
(v) $-\Delta\nu(N_9\text{-}H_9) = 252$ cm^{-1}
$A_{IR}(N_9\text{-}H_9 \cdots Au_{11})/A_{IR}(N_9\text{-}H_9) = 8.7$.
Note: This is the largest red shift among all studied complexes between A and a cluster of three gold atoms;
(vi) $\delta\sigma_{iso}(H_9) = -2.4$ ppm
$\delta\sigma_{iso}(N_9) = -18.1$ ppm
$\delta\sigma_{an}(H_9) = 13.0$ ppm
$\delta\sigma_{an}(N_9) = 2.5$ ppm.

5.3. COMPLEX A·AU$_3$(N$_7$)

Note: The total dipole moment $d_{tot} = 5.58$ D. $\angle N_6H_6'Au_{11} = 165.1^o$;
(iii) $\Delta R(N_6\text{-}H_6') = 0.007$ Å.
Note: This change in the $N_6\text{-}H_6'$ bond is smaller than that of the elongation of the $N_9\text{-}H_9$ bond in the complex A·Au$_3$(N$_3$) discussed in Subsection 5.3. Therefore by the absolute value, the red shift of $\nu(N_9\text{-}H_9)$ is also larger than that of $\nu(N_6\text{-}H_6')$. To explain this difference, let us recall that the deprotonation energy (enthaply) $DPE(N_9\text{-}H_9) = 336.8$ kcal/mol $< DPE(N_6\text{-}H_6') = 355.2$ kcal/mol (see, e. g., Ref. [41] and references therein), and therefore, the $N_9\text{-}H_9$ bond is stronger perturbed by Au$_3$ than $N_6\text{-}H_6'$;
(iv) $r(H_6' \cdots Au_{11}) = 2.816$ Å $< w_H + w_{Au} = 2.86$ Å;
(v) $-\Delta\nu(N_6\text{-}H_6') = 116$ cm^{-1}
$A_{IR}(N_6\text{-}H_6' \cdots Au_{11})/A_{IR}(N_6\text{-}H_6') = 9.0$.

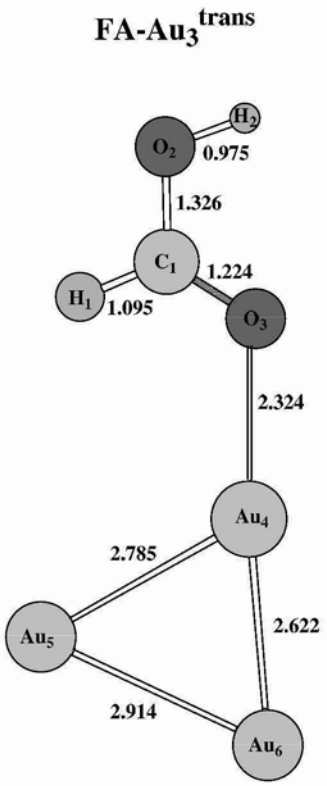

Figure 5. Complex FA·Au_3^{trans} optimized at the B3LYP/HW-LA (gold) ∪ 6-31++G(d,p) (formic acid) computational level. The bond lengths are given in and bond angles in °.

Note: The other amino-group stretching mode $\nu(N_6\text{-}H_6)$ is almost decoupled from $\nu(N_6H_6')$ and undergoes a smaller red shift by 54 cm^{-1};
(vi) $\delta\sigma_{iso}(H_6')$ = -2.2 ppm
$\delta\sigma_{iso}(N_6)$ = -18.4 ppm
$\delta\sigma_{an}(H_6')$ = 14.0 ppm
$\delta\sigma_{an}(N_6)$ = -17.1 ppm.

The details given above gather the features that the nonconventional N-H···Au bond formed between adenine and the triangle three-gold cluster shares with the conventional ones. In these bonds, the nitrogen atom of adenine is a H-bond donor and Au plays a role of a nonconventional H-bond acceptor.

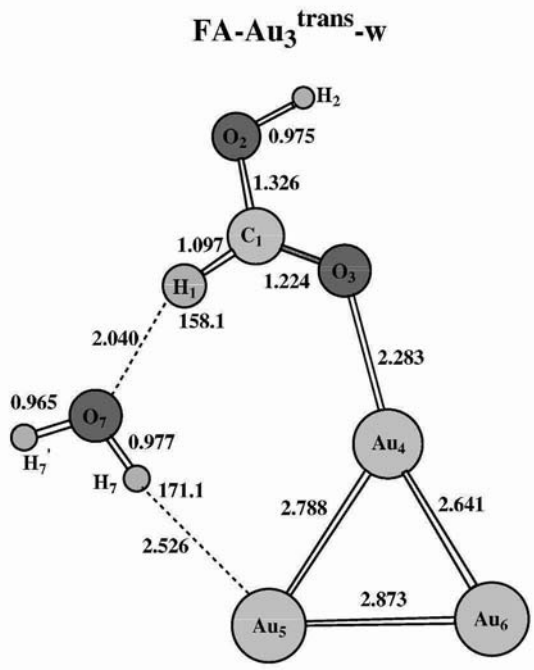

Figure 6. Complex FA·Au_3^{trans} with a water molecule computed at the B3LYP/HW-LA (gold) ∪ 6-31++G(d,p) (formic acid and water) computational level. The bond lengths are given in and bond angles in °.

6. Summary: Three-Gold Cluster as Nonconventional Proton Acceptor

In summary, we have characterized computationally the ability of a three-gold cluster to act as a proton acceptor and to form nonconventional hydrogen bonds with the O-H and N-H groups of formic acid, alanine, and adenine. It is important to emphasize that the formation of the donor-acceptor coordinative (anchor) bond Au-O in these planar cyclic complexes between the Au atom and an n-donor group is a prerequisite to the formation of the hydrogen bonds, O-H···Au or N-H···Au. This is actually the anchor bond that induces a charge through-bond transfer over the gold cluster and thus, cooperatively, leads to a consistent flow of electron density from the proton acceptor atom to the donor.

A common point of view on the hydrogen bond conditions **(iii)** - **(vi)** is that they provide an estimation of the strength of the hydrogen bond. The latter is typically expressed in terms of the energy E_{HB} of the H-bond

formation. This is not possible in the present case because of the anchor bond. The bonding between the gold cluster Au_3, and formic acid, alanine, or adenine is governed by the balance between the anchor and the nonconventional hydrogen bonds where the former, which is stronger and partially covalent, plays a leading role. Nevertheless, the strength of the hydrogen bond in one of the studied complex, FA·Au_3, can be estimated because formic acid forms with Au_3 another, less stable complex, FA·Au_3^{trans}, where Au_3 anchors at the same oxygen atom O_3 as in FA·Au_3, but is placed on the C_1-H_1 side, so that it is not possible to form a hydrogen bond with the O_2-H_2. The geometry of this complex is shown in Figure 5. The energy difference between FA·Au_3 and FA·Au_3^{trans} is equal to 5.1 (EC), 4.4 (S), and 4.5 (HW-LA) kcal/mol, that is about 35 % of the total binding energy. This energy difference is a reasonable estimation of the strength of the hydrogen bond O-H$\cdots$Au in FA·Au_3, provided that one neglects other structural differences between FA˙Au_3 and FA˙Au_3^{trans}.

So far, we have discussed the fact that the formation of the anchor bonds, either of the Au-O or Au-N types, in the planar complexes FA·Au_3, Ala·Au_3, and A·Au_3, induces a through-bond charge transfer within the three-gold cluster that allows one of its unanchored gold atom to act as a proton acceptor. The lone-pair-like 5*d* orbital of this gold atom provides electron density to the proton donor and the bridging proton. Another example that support this mechanism is shown in Figure 6 where the complex FA·Au_3^{trans}·w, obtained at the B3LYP/HW-LA (gold) $\cup$ 6-31++G(d,p) (formic acid, water) computational level is plotted. In this complex, the water molecule, w, accepts one hydrogen bond C_1-$H_1\cdots O_7$ from formic acid and donates another, O_7-$H_7\cdots Au_5$, to gold cluster. The former is known to be very weak (see, e. g., Ref. [42]) and this is indicated by a small lengthening of the C_1-H_1 bond by 0.002 Å and a small red-shift of the C_1-H_1 stretch equal to 30 cm^{-1}. The other H-bond is a weak nonconventional hydrogen bond since, first, its O_7-H_7 bond elongates by 0.012 Å; second, the $\nu(O_7\text{-}H_7)$ downshifts by 208 cm^{-1}; and third, its IR activity increases by a factor of almost 11. The binding energy of FA·Au_3^{trans}·w taken with respect to the infinitely separated FA·Au_3^{trans} and water molecule amounts to 7.0 kcal/mol. This value also gives a reasonable estimate of the strength of the nonconventional hydrogen bond O-H$\cdots$Au that FA·Au_3^{trans} complex forms with a water molecule, even though some corrections due to the geometrical relaxation of the monomer FA·Au_3^{trans}, mainly within a vicinity of the anchor bond Au-O which itself is contracted by 0.041 Å should be taken into account.

In conclusion, this work discusses the ability of the triangle three-gold cluster to behave as a nonconventional proton acceptor and form noncon-

ventional hydrogen bonds with conventional proton donors. Such functioning of the triangle three-gold cluster might be interesting from the point of view of recognition of molecular interactions on metal surfaces and thus catalytic processes.

Acknowledgements

This work was supported by the Region Wallonne (RW. 115012). The computational facilities were provided by NIC (University of Liege) and by F.R.F.C. 9.4545.03F (Belgium). One of the authors, E. S. K., gratefully thanks Professors Lina M. Epstein, Camille Sandorfy, and George V. Yukhnevich for interesting discussions on the nonconventional hydrogen bonds N-H···Au and O-H···Au and valuable suggestions, and also the F.R.F.C. 2.4562.03F (Belgium) for fellowship. We also thank the reviewer for comments and suggestions.

References

1. M. Huggins, *Thesis* (University of California, 1919).
2. W. M. Latimer and W. H. Rodebush, J. Am. Chem. Soc. **42**, 1419 (1920).
3. L. Pauling, *The Nature of the Chemical Bond* (Cornell University Press, Ithaca, 1939). See also L. Pauling, Proc. Natl. Acad. Sci. USA **14**, 359 (1928).
4. G. N. Lewis, *Valence and Structure of Atoms and Molecules* (Chemical Catalog, New York, 1923).
5. D. Hadži and H. W. Thompson (Eds.), *Hydrogen Bonding* (Pergamon Press, London, 1959).
6. C. G. Pimentel and A. L. McClellan, *The Hydrogen Bond* (Freeman, San Francisco, 1960).
7. W. C. Hamilton and J. A. Ibers, *Hydrogen Bonding in Solids* (Benjamin, New York, 1968).
8. P. A. Kollman and L. C. Allen, Chem. Rev. **72**, 283 (1972).
9. P. Schuster, G. Zundel, and C. Sandorfy (Eds.), *The Hydrogen Bond. Recent Developments in Theory and Experiments* (North-Holland, Amsterdam, 1976).
10. G. A. Jeffrey and W. Saenger, *Hydrogen Bonding in Biological Structures, 2nd edition* (Springer, Berlin, 1994).
11. G. A. Jeffrey, *An Introduction to Hydrogen Bonding* (Oxford University Press, Oxford, 1997).
12. S. Scheiner, *Hydrogen Bonding. A Theoretical Perspective* (Oxford University Press, Oxford, 1997).
13. G. R. Desiraju and T. Steiner, *The Weak Hydrogen Bond in Structural Chemistry and Biology* (Oxford University Press, Oxford, 1999).
14. P. Schuster, in *Intermolecular Interactions: From Diatomics to Biopolymers, edited by B. Pullman* (Wiley, Chichester, 1978). p. 363.
15. T. Steiner, Angew. Chem. Int. Ed. **41**, 48 (2002).
16. T. Steiner and G. R. Desiraju, Chem. Commun. 891 (1998).
17. M. S. Gordon and J. H. Jensen, Acc. Chem. Res. **29**, 536 (1996).
18. C. Sandorfy, Top. Curr. Chem. **120**, 41 (1984).
19. S. Scheiner, in *Pauling's Legacy - Modern Modelling of the Chemical Bond, Vol. 6, edited by Z. B. Maksic and W. J. Orville-Thomas* (Elsevier, Amsterdam, 1977). p. 571.

20. (a) J. E. Del Bene, in *The Encyclopedia of Computational Chemistry, edited by P. v. R. Schleyer, N. L. Allinger, T. Clark, J. Gasteiger, P. A. Kollman, H. F. Schaefer III, and P. R. Schreiner* (Wiley, Chichester, 1998). Vol. 2, p. 1263; (b) J. E. Del Bene and M. J. T. Jordan, Int. Rev. Phys. Chem. **18**, 119 (1999); (c) J. E. Del Bene, in *Recent Theoretical and Experimental Advances in Hydrogen Bonded Clusters, NATO ASI Series C, Vol. 561, edited by S. S. Xantheas* (Kluwer, Dordrecht, 2000). p. 309.
21. I. G. Kaplan, *Theory of Molecular Interactions. Studies in Physical and Theoretical Chemistry, Vol. 42* (Elsevier, Amsterdam, 1986).
22. (a) L. Brammer, M. C. McCann, R. M. Bullock, R. K. McMullan, and P. Sherwood, Organometallics **11**, 2339 (1992); (b) S. G. Kazarian, P. A. Hanley, and M. Poliakoff, J. Am. Chem. Soc. **115**, 9069 (1993); (c) A. Albinati, F. Lianza, P. S. Pregosin, and B. Müller, Inorg. Chem. **33**, 2522 (1994); (d) Y. Gao, O. Eisenstein, R. H. Crabtree, Inorg. Chim. Acta **254**, 105 (1997); (e) L. Brammer, D. Zhao, F. T. Lapido, and J. Braddock-Wilking, Acta Crystallogr. Sect. B **53**, 680 (1995); (f) D. Braga, F. Grepioni, and G. R. Desiraju, Chem. Rev. **98**, 1375 (1998).
23. (a) E. S. Shubina, N. V. Belkova, and L. M. Epstein, J. Organomet. Chem. **17**, 536 (1997); (b) G. Orlova and S. Scheiner, Organometallics **17**, 4362 (1998); (c) L. M. Epstein and E. S. Shubina, Ber. Bunsenges. Phys. Chem. **102**, 359 (1998).
24. (a) L. M. Epstein and E. S. Shubina, Coord. Chem. Rev. **231**, 165 (2002); (b) L. Brammer, Dalton Trans. 3145 (2003); and references therein.
25. (a) C. A. Mirkin, R. L. Letsinger, R. C. Mucic, and J. J. Storhoff, J. J. Nature **382**, 607 (1996); (b) R. Elghanian, J. J. Storhoff, R. C. Mucic, R. L. Letsinger, and C. A. Mirkin, Science **277**, 1078 (1997); (c) J. J. Storhoff and C. A. Mirkin, Chem. Rev. **99**, 1849 (1999); (d) Y. W. C. Cao, R. Jin, and C. A. Mirkin, Science **297**, 1536 (2002); (e) S.-J. Park, T. A. Taton, C. A. Mirkin, Science **295**, 1503 (2002); (f) J.-M. Nam, C. S. Thaxton, and C. A. Mirkin, Science **301**, 1884 (2003); (g) C. M. Niemeyer, Angew. Chem., Int. Ed. **40**, 4129 (2001); (h) C. M. Niemeyer, W. Burger, and J. Peplies, Angew. Chem., Int. Ed. **37**, 2265 (1998); (i) A. P. Alivisatos, K. P. Johnsson, X. Peng, T. E. Wislon, C. J. Loweth, M. P. Bruchez, Jr., G. C. Schultz, Nature **382**, 609 (1996); (j) M. C. Pirrung, Angew. Chem. Int. Ed. **41**, 1277 (2002); (j) M.-C. Daniel, and D. Astruc, Chem. Rev. **104**, 293 (2004); (k) N. C. Seeman, Nature **421**, 427 (2003); (l) H. Yan, S. H. Park, G. Finkelstein, J. H. Reif, and T. H. LaBean, Science **301**, 1882 (2003); and references therein.
26. (a) W. Li, W. Haiss, S. Floate, and R. Nichols, Langmuir **15**, 4875 (1999); (b) Y. J. Xiao and Y. F. Chen, Spectrochim. Acta A **55**, 1209 (1999); (c) A. P. M. Camargo, H. Baumgärtel, and C. Donner, PHYSCHEMCOMM 151 (2002); and references therein.
27. (a) L. M. Demers, M. Östblom, H. Zhang, N.-H. Jang, B. Liedberg, and C. A. Mirkin, J. Am. Chem. Soc. **124**, 11248 (2002); (b) J. J. Storhoff, R. Elghanian, C. A. Mirkin, and R. L. Letsinger, Langmuir **18**, 6666 (2002); (c) H. Kimura-Suda, D. Y. Petrovykh, M. J. Tarlov, and L. J. Whitman, J. Am. Chem. Soc. **125**, 9014 (2003); (d) Q. Chen, D. J. Frankel, and N. V. Richardson, Langmuir **18**, 3219 (2002); (e) B. Giese and D. McNaughton, J. Phys. Chem. B **125**, 1112 (2002).
28. (a) D. V. Leff, L. Brandt, and J. R. Heath, Langmuir, **12**, 4723 (1996); (b) L. O. Brown and J. E. Hutchison, J. Phys. Chem. B **105**, 8911 (2001); (c) M. Sastry, A. Kumar, and P. Mukherjee, Colloids Surf. A: Physicochem. Eng. Aspects **181**, 255 (2001); (d) P. R. Selvakannan, S. Mandal, S. Phadtare, S. Pasricha, and M. Sastry, Langmuir **19**, 3545 (2003); (e) H. Joshi, P. S. Shirude, V. Bansal, K. N. Ganesh, and M. Sastry, J. Phys. Chem. B **108**, 11535 (2004).
29. M. J. Frisch, G. W. Trucks, H. B. Schlegel, G. E. Scuseria, M. A. Robb, J. R. Cheeseman, J. A. Montgomery, Jr., T. Vreven, K. N. Kudin, J. C. Burant, J. M. Millam, S. S. Iyengar, J. Tomasi, V. Barone, B. Mennucci, M. Cossi, G. Scalmani, N. Rega, G. A. Petersson, H. Nakatsuji, M. Hada, M. Ehara, K. Toyota, R. Fukuda, J.

Hasegawa, M. Ishida, T. Nakajima, Y. Honda, O. Kitao, H. Nakai, M. Klene, X. Li, J. E. Knox, H. P. Hratchian, J. B. Cross, C. Adamo, J. Jaramillo, R. Gomperts, R. E. Stratmann, O. Yazyev, A. J. Austin, R. Cammi, C. Pomelli, J. W. Ochterski, P. Y. Ayala, K. Morokuma, G. A. Voth, P. Salvador, J. J. Dannenberg, V. G. Zakrzewski, S. Dapprich, A. D. Daniels, M. C. Strain, O. Farkas, D. K. Malick, A. D. Rabuck, K. Raghavachari, J. B. Foresman, J. V. Ortiz, Q. Cui, A. G. Baboul, S. Clifford, J. Cioslowski, B. B. Stefanov, G. Liu, A. Liashenko, P. Piskorz, I. Komaromi, R. L. Martin, D. J. Fox, T. Keith, M. A. Al-Laham, C. Y. Peng, A. Nanayakkara, M. Challacombe, P. M. W. Gill, B. Johnson, W. Chen, M. W. Wong, C. Gonzalez, and J. A. Pople, *GAUSSIAN 03* (Revision A.1), Gaussian, Inc., Pittsburgh, PA, 2003.

30. R. B. Ross, J. M. Powers, T. Atashroo, W. C. Ermler, L. A. LaJohn, and P. A. Christiansen, J. Chem. Phys. **93**, 6654 (1990).
31. D. Andrae, U. Haeussermann, M. Dolg, H. Stoll, and H. Preuss, Theor. Chim. Acta **77**, 123 (1990).
32. P. J. Hay and W. R. Wadt, J. Chem. Phys. **82**, 270, 299 (1985).
33. F. Remacle and E. S. Kryachko, Adv. Quantum Chem. **47**, 423 (2004).
34. F. Remacle and E. S. Kryachko, J. Chem. Phys. **122**, 044304 (2005).
35. The triangle Au_3 cluster is characterized by the electronic energy of -407.907290 (EC), -407.787835 (S), -406.420509 (HW-LA) hartree; ZPVE = 0.418 (EC), 0.391 (S), 0.398 (HW-LA) kcal/mol; enthalpy equal to -407.900617 (EC), -407.781168 (S), -406.413836 (HW-LA) hartree; entropy of 89.66 (EC), 90.51 (S), 90.97 (HW-LA) cal/mol·T; the bond lengths $r(Au_1\text{-}Au_2) = r(Au_2\text{-}Au_3) = 2.654$ (EC), 2.675 (S), 2.640 (HW-LA) Å, $r(Au_1\text{-}Au_3) = 2.992$ (EC), 3.110 (S), 4.975 (HW-LA) Å; and the total dipole moment $d_{tot} = 0.97$ (EC), 0.84 (S), 0.37 (HW-LA) D.
36. E. S. Kryachko and F. Remacle, Chem. Phys. Lett. **000**, 000 (2005).
37. Some B3LYP/6-31++G(d,p) properties of formic acid (see Figure 1 for atomic numbering): $r(C_1\text{-}O_2) = 1.347$ Å, $r(C_1{=}O_3) = 1.207$ Å, $r(O_2\text{-}H_2) = 0.974$ Å, $r(C_1\text{-}H_1) = 1.098$ Å; $\angle C_1N_2H_2 = 107.9^o$; $\nu(O_2\text{-}H_2) = 3732$ cm^{-1} ($A_{IR} = 60$ km/mol), $\nu(O_2\text{-}D_2) = 2714$ cm^{-1} ($A_{IR} = 40$ km/mol); $\delta\sigma_{iso}(O_2) = 134.8$ ppm, $\delta\sigma_{iso}(H_2) = 25.4$ ppm, $\delta\sigma_{an}(O_2) = 190.2$ ppm, $\delta\sigma_{an}(O_2) = 9.5$ ppm; the total dipole moment $d_{tot} = 1.53$ D. The B3LYP/6-31++G(d,p) computational approach invoked in the present work rather accurately describes the properties of formic acid: cf. J. H. Lim, E. K. Lee, and Y. Kim, J. Phys. Chem. **101**, 2233 (1997) and D. Wei, J.-F. Truchon, S. Sirois, and D. Salahub, J. Chem. Phys. **116**, 6028 (2002) and references therein.
38. (a) J. F. Hinton and K. Wolinski in *Theoretical Treatments of Hydrogen Bonding, edited by D. Hadzi* (Wiley, Chichester, 1997). p. 75; (b) E. D. Becker in *Encyclopedia of Nuclear Magnetic Resonance, edited by D. M. Grant and R. K. Harris* (Wiley, New York, 1996). p. 2409; (c) T. Kar and S. Scheiner, J. Phys. Chem. A **108**, 9161 (2004); and references therein.
39. S. Blanco, A. Lesarri, J. C. López, and J. L. Alonso, J. Am. Chem. Soc. 126, 11675 (2004).
40. F. Remacle and E. S. Kryachko, J. Phys. Chem. B (submitted).
41. (a) A. K. Chandra, M. T. Nguyen, T. Uchimaru, and T. Zeegers-Huyskens, J. Phys. Chem. A **103**, 8853 (1999); (b) E. S. Kryachko, M. T. Nguyen, and T. Zeegers-Huyskens, Ibid. **105**, 1288, 1934 (2001); and references therein.
42. (a) Y. Gu, T. Kar, and S. Scheiner, J. Am. Chem. Soc. **121**, 9411 (1999); (b) E. S. Kryachko and T. Zeegers-Huyskens, J. Phys. Chem. A **105**, 7118 (2001); (c) E. S. Kryachko and T. Zeegers-Huyskens, Ibid. **105**, 7118 (2001); (d) E. S. Kryachko and T. Zeegers-Huyskens, Ibid. **106**, 6832 (2002); and references therein.

MOLECULAR MODELLING OF METAL COMPLEXES WITH OPEN d-SHELL

A. L. TCHOUGRÉEFF AND M. B. DARKHOVSKII
Karpov Institute of Physical Chemistry,
Vorontsovo Pole 10, 105064 Moscow, Russia

Abstract. With use of cumulants of two-electron density matrices semiempirical and DFT methods are analyzed from a point of view of their suitability to describe qualitative features of electronic correlation important for molecular modelling of electronic structure of the transition metal complexes (TMC). It is shown that traditional semiempirical methods relying upon the Hartree-Fock-Roothaan form of the trial wave function suffer from a structural deficiency not allowing them to distinguish the energies of the atomic multiplets of the TMCs' d-shells. The same applies to the DFT methodology. On the other hand, the effective Hamiltonian of the crystal field (EHCF) previously proposed by the authors is shown to be suitable for further parameterization. It has been applied for calculations of geometries in a series of polyatomic spin-active TMCs and has shown remarkable precision and an overall consistency. This allowed to solve in a sequential manner two long standing problems: extending molecular mechanics to transition metals and developing semiempirical quantum mechanical (QM) methods for transition metals.

Sicut omnes homines naturaliter scire desiderant veritatem, ita naturale desiderium inest hominibus fugiendi errores, et eos cum facultas adfuerit confutandi [1].

1. Introduction

Molecular modelling of transition metal complexes (TMC), reproducing characteristic features of their stereochemistry and electronic structure, is in high demand in relation with studies and development of various processes of complex formation with an accent on ion extraction, ion exchange, isotope separation, neutralization of nuclear waste, and also when studying structure and reactivity of metal-containing enzymes. Solving these techno-

J.-P. Julien et al. (eds.),
Recent Advances in the Theory of Chemical and Physical Systems, 451–505.

logical problems requires modelling methods allowing massive simulations of potential energy surfaces (PES) of TMCs in a wide range of molecular geometries including (in the case of, say, complexation processes) internuclear separations corresponding to dissociation of coordination bonds between metal ions and ligands' donor atoms. The tools generally available for performing a required modelling range from fully empirical molecular mechanics (MM) to quantum mechanical (QM) or quantum chemical (QC) methods of different degree of refinement and sophistication.

From a bird view perspective all mentioned approaches seem to be rather successful in a technical sense since normally it is possible to find a suitable and inexpensive method for modelling at least certain classes of molecules. However, when it goes about TMCs the methods of each family may turn to be inconsistent with the problem at hand. The sources of these seemingly unpredictable and nonsystematic failures of all mentioned modelling methods will be one of the main topics of the present paper. In the next Section we briefly review the existing methodologies as applied to TMCs and provide explanations of their limitations in this context. Further Sections present a formal point of view on constructing a QM (likely *ab initio*, semiempirical, and DFT) description of TMCs and apply it to analysis of the corresponding difficulties. The rest of the paper is devoted to description of the effective Hamiltonian of crystal field (EHCF) method and of its semiempirical implementation satisfying which can be used for TMCs' modelling and to its application to analysis of spin-active complexes of iron (II). Finally discussion and conclusions are given.

2. Methods for evaluating TMCs' PES and electronic structure

2.1. METHODS OF MOLECULAR MECHANICS

The elementary empirical tool for the molecular modelling of polyatomic systems is the method of molecular mechanics (MM) [2, 3]. It explicitly employs intuitively transparent features of molecular electronic structure like localization of chemical bonds and groups. The basic assumption of the MM is the possibility to directly parameterize molecular PES in the form of a sum of contributions (force fields) relevant to bonds, their interactions, and to interactions of non-bonded atoms:

$$E = E_{bond} + E_{bend} + E_{tors} + E_{imp} + E_{nb} + E_{rep} \tag{1}$$

The contributions related to bonding are the sum of bond stretching energies E_{bond}, that of energies of valence angles bending E_{bend}, and that of torsion interactions E_{tors}. In case of stretching and bending energies the additional guess of the Hook-like law is accepted for the dependence of these contributions on variations of the corresponding geometry parameters: the deviations of the bond lengths and valence angles from their ideal

values. Respective elasticity constants, the ideal bond lengths and valence angles pertain to the MM parameter set. The sum of the Lennard-Jones pair potentials E_{nb}, the energy of improper plane deformations E_{imp} and energy of electrostatic interaction of effective charges residing on atoms E_{rep} are listed among interactions of non-bonded atoms. The correct description of the dissociation limit under the infinite separation of metal and ligands in term E_{bond} is achieved by employing the Morse potential for the bond-stretch energies instead of the Hook law.

In the literature [4–10] various MM constructions are considered as effective methods for modelling PES of TMCs. It is noteworthy that in the case of metal complexes in general and of TMCs in particular the very basic characteristics of electronic structure comprising the basis of MM may be questioned. In fact when it goes about the metal ion in a complex it is not possible to single out transferable two-center bonds involving the metal. Also the number of bonds formed by a metal atom (the coordination number) may be variable and namely these variabilities may be the main topic requiring the modelling as indicated in the Introduction. Also the great variety of accessible coordination polyhedra makes it difficult to set the preferential valence angles. In review [6] the extensive summary of results of calculations on coordination compounds of a wide variety of metals by the MM methods (as of 1993) is given. During the following decade, numerous subsequent works quoted in reviews [8, 11, 12] were performed, in which PES of special classes of metal complexes in that or another manner is parameterized by some MM-like force fields. As it can be seen from the recent review [9] the situation did not change too much since then. The conceptual problems mentioned above manifest themselves in extremely cumbersome and awkward appearance of the set of force fields in case of metal atoms as compared to traditional 'organic' force field systems. For example, it becomes necessary to introduce a double set of optimal valence angles for octahedral (or plane squared) complexes to assure these important molecular shapes are reproduced in the calculation as are the relative energies of the *cis*- and *trans*-isomers [6, 8]. The number of other bonding parameters also rapidly grows, and it is difficult either to assign any clear physical sense to all these, or to restrict reasonable interval of parameter values and thus to separate probable ones from improbable.

An alternative to the valence force field approach based on the concept of preferable valence angles is to reload the responsibility for the description of the shapes of coordination polyhedra in TMCs to the non-bonding interactions. Such approach exists in the literature in two versions. The first is represented by the Kepert model, termed also as one of the 'points on a sphere' (POS) [13, 14] in which the terms responsible for the metal-ligand bond stretching energy are taken into account by harmonic terms as previously. Everything that concerns the dependence of the bending energy of the valence angles at the metal atom, is replaced by the terms rep-

resenting an effective interaction (van-der-Waals-like) either between the donor atoms, or between effective repulsion centers placed somewhere on the metal-donor atom bond [15,16]. The second version is called the electrostatic model [17,18]. It completely neglects any specific bonding interactions in the nearest coordination sphere and substitutes the Coulomb interaction between effective charges residing on atoms of the complex for the overall interaction energy. The repulsive part of the metal-ligand van-der-Waals potential acts to prevent collapse of the system. The basic weakness of this approach is, certainly, lack of the reasonable method allowing independent estimates for effective charges.

Despite the considerable progress achieved in MM modelling of TMCs (for example, MM models of the complexes of cyclic polyamines with metals like Cu(II), Co(III), Ni(II) are reported [11, 12, 19, 20]), many questions including those of practical importance, remain unanswered. The first one is the problem of consistent modelling of metal complexes with variable number of the ligands. The need for such description arises in the context of molecular-dynamic studies (see, for example, [21]) of metal ions soluted in complexation solvents containing chelating ligands (crown-ethers, cyclic polyamines etc.). In such systems one may expect formation of numerous complexes with different number of ligands or degree of coordination (the chelate number), which should be considered at one level of accuracy to keep uniform energy scale. Obviously, the harmonic approximation for stretching energy of metal-donor atom bond usually employed in MM, as, for example, in [7], cannot describe such effects. A direct replacement of the harmonic potential by another one, with more suitable asymptotic behavior (for example, by the Morse potential), does not solve the problem, since it neglects many other factors, that apparently matter (different mutual influence effects just to give an example).

Another important point specific namely for TMCs is the presence of the partially filled *d*-shell on the metal ion which produces a whole set of electronic states of the complex of different total spin and spatial symmetry in a narrow energy range close to the ground state energy. Geometry dependence of these energies may be rather confusing which results in existence of the areas in the nuclear coordinate space where the PESs belonging to different electronic terms, closely approach each other and even intersect, leading to experimentally observed spin transitions [22–25] or Jahn-Teller distortions [26]. Thus, the very problem of including the transition metals in the MM context implies certain contradiction: in the presence of several close in energy (or even crossing) electronic terms there is no object for the MM modelling in a strict sense, since there is no uniform (and single) PES of the complex. This specificity of the electronic structure of TMCs can be clearly observed in the results on blue copper proteins with approximately trigonal-bipyramidal coordination of the copper ion as reviewed in [9]. The Cu^{2+} cation is known to be a Jahn-Teller ion due to the spatial degen-

eracy of its respective ^2E_g and $^2T_{2g}$ ground state terms in the octahedral and tetrahedral environments. The latter Jahn-Teller instability is inherited also by the trigonal bipyramidal environment where the ground state is ^2E due to the electron count in the d-shell of the Cu^{2+} cation. Clearly the spatial degeneracy of the ground state is the limiting case of the closeness of electronic terms on the energy scale. This degeneracy is lifted when the molecular geometry deviates from the symmetrical arrangement and this is the content of the Jahn-Teller theorem (see for details [26]; an original and – what is important – concise proof is given in [27]). Technically the Jahn-Teller instability manifests itself in the presence of multiple minima on the PES, having a close total energy. It must be understood, however, that these minima are a result of the sufficiently quantum behavior of the d-shell of the Cu^{2+} cation which as it has been noticed previously in a certain sense prevent the usage of the classical MM picture. Indeed, as it is mentioned in [28, 29], the physical pre-condition of successful use of MM theories for common organic molecules is that their electronic excited states are well separated from the respective ground states on the energy scale. Only one quantum state of their electronic system is experimentally observed in 'organics' at ambient conditions and the MM (a sort of classical) description becomes valid. By contrast, the behavior of the metal valence d-shell is sufficiently quantum: several electronic states may appear in a narrow energy range close to its ground state and this quantum feature requires a special care, not reducible to a simplistic adjustment of the form and parameters of no matter how sophisticated force fields.

A plausible way out of this situation has been proposed by R. Deeth (see [30] and references therein). In order to handle quantum behavior of the d-shell the ligand filed stabilization energy (LFSE) term is added to the MM energy expression Eq. (1). The LFSE is written as a sum of the orbital energies of the d-orbitals in its turn calculated in the angular overlap approximation (see below) whose parameters are taken to be linearly dependent on the internuclear separation between the metal and donor atoms. Applying such a model solves many complications inherent to the MM of TMCs, since the LFSE is a pure quantum contribution to the energy. For example the Jahn-Teller in Cu^{2+} compounds must be perfectly covered within such a setting. On the other hand the LFSE is by construction a sum of one-electron energy contributions whereas the energy of the d-shell is very much dependent of the two-electron contributions to the energy particularly when it goes about relative energies of the states of different total spins and spatial symmetries. Bringing the latter into the MM context requires much more evolved and refined theory which will be explained below.

Turning in this context to a main topic of our interest, namely to modelling of the spin active TMCs we notice that the above considerations apply to them in a large extent. The change of the spin state of a complex

is possible if at least two different electronic states (differing by the value of the total spin) have their respective minima at quite similar geometries of the complex at hand so that their respective total energies become equal at some intermediate geometry. As in the case of the Jahn-Teller Cu^{2+} cation in that of the spin-active ions (*e.g.* d^6 Fe^{2+}) the unique PES of the complex does not exist and at least two of them (the low-spin – LS – for $S = 0$ and the high-spin – HS – for $S = 2$) must be considered. Previously the MM force fields using different parameter sets for different spin states of the central atom were in use [31], but due to no predictive force they are considered to be obsolete by now. However, the basic principles of their construction do not differ from those which explicitly use different parameter sets for say axial and equatorial ligands in the Cu^{2+} complexes [8] since the latter are as well designed to imitate by means of a classical potential sufficiently quantum characteristics of the TMC's electronic structure. On this way one can expect pretty different sets of parameters say for four-coordinate complexes of the Ni^{2+} ion which must be tetrahedral in their triplet states and square planar in the singlet states. In this respect the recent paper [32] is very remarkable. The authors try to construct the MM potential capable to describe transformation between the square pyramidal and two trigonal bipyramidal forms of the pentacoordinate $[Ni(acac)_2py]$ complex (acac stands for acetylacetone, py – for pyridine ligands). To do so these authors propose to employ a specially designed force field dependent on L–Ni–L′ angle possessing two minima at 90° and 120° separated by a barrier of the height larger than 5 eV (500 kJ/mole). This clearly indicates some problems which can be clearly revealed by a simple analysis: The trigonal bipyramidal forms of the complex are obviously [33] triplet (two *d*-levels degenerate in the trigonal field filled by two electrons) whereas the square pyramidal from may well be singlet. This spin switch has to take place somewhere along the rearrangement reaction coordinate but is by no means reflected in the MM picture. There remains a question whether the approach employing the LFSE is capable to describe such a low-symmetric and potentially correlation dependent situation.

2.2. METHODS OF QUANTUM CHEMISTRY

We see that in the case of TMC any description of PES by the MM methods may be as well rather successful and rather poor. The borderline between potentially successful and unsuccessful cases looks out rather peculiar from the point of view of standard chemical nomenclature. Why Ni(II) is sometimes successful, and sometimes not, Cu(II), Fe(II), and Co(II) are very difficult, whereas Co(III) brings no special problem? A general conclusion is that a more detailed description of the electronic structure of TMCs than one implicitly put in the base of the entire MM picture is necessary. It must take into account all the important features of the former. Physically it is

rather clearly formulated in terms of experimental accessibility of low-lying excited states, whose spectrum is responsible for the observed *i.e.* quantum, behavior of the TMCs.

Quite naturally a quantum description is given by methods of quantum chemistry (QC). The latter further subdivides into *ab initio,* DFT, and semiempirical domains. Although the semiempirical methods are nowadays frequently treated as obsolete, taking into account the number of atoms in TMCs and thus incurred computational costs (see [10] and below) which may become prohibitive despite considerable progress of the computational hardware they still deserve attention as a pragmatic tool for the massive PES simulations. On the other hand the DFT based methods which are almost unanimously considered to be the method of choice for TMCs [34] will be shown to suffer of basically the same structural deficiency as do the semiempirical ones. We shall analyze briefly these extended classes of QC methods used for evaluation of PESs and of other properties of TMCs from a common point of view allowing to further consider specific difficulties pertinent to each of these classes of methods when applied to numerical modelling of TMCs. The main problem referenced in the literature in relation to QC description of TMCs is that of electron correlation [35]. It is a general belief that the correlations are possibly reproduced only by high-quality *ab initio* methods, but also can be adequately modelled by the DFT based methods. On the other hand the common opinion is that the semi-empirical methods are not suitable for modelling correlation effects at all. We shall show that two latter opinions are largely an exaggeration and that the potential of the DFT when applied to TMCs is considerably oversold whereas broadly understood semi-empirical methods by contrast still may be useful.

2.3. ELECTRONIC STRUCTURE IN TERMS OF DENSITY MATRICES AND THEIR CUMULANTS

The relevant formal treatment starts from the notion that all the quantities related to electronic structure of molecules can be calculated with use of only one- and two-electron density matrices for the relevant electronic state of the system under study [36]. Taking the energy for the sake of definiteness we get:

$$\begin{aligned} E(C\mathbf{Q}\Gamma S|\omega) &= \min_{\xi}\left[\mathrm{Sp}\rho^{(1)}h^{(1)} + \mathrm{Sp}\rho^{(2)}h^{(2)}\right] = \\ &= \langle\hat{T}_e\rangle + \langle\hat{V}_{ne}(\mathbf{Q})\rangle + \langle\hat{V}_{ee}\rangle + V_{nn}(\mathbf{Q}) \\ \mathrm{Sp}\rho^{(1)}h^{(1)} &= \int \rho^{(1)}_{C\mathbf{Q}\Gamma S}(\xi\omega \mid x,x')h^{(1)}(C\mathbf{Q}\omega \mid x',x)dxdx' \\ \mathrm{Sp}\rho^{(2)}h^{(2)} &= \int \rho^{(2)}_{C\mathbf{Q}\Gamma S}(\xi\omega \mid x_1x_2,x_1'x_2')\times \\ &\times\ h^{(2)}(C\mathbf{Q}\omega \mid x_1'x_2',x_1x_2)dx_1dx_2dx_1'dx_2' \end{aligned} \tag{2}$$

The meaning of the notations introduced is the following. We assume that the electronic energy of a chemical species of composition C is calculated at the nuclear configuration $\mathbf{Q}$ for its ground electronic state having the spatial symmetry Γ and the total spin S. Considering the ground states of different total spin or symmetry allows for description of the electronic spectra (the low-energy excited states) of the species to some extent. Symbols ω refer to the set of *parameters* of the QC method: Slater or gaussian exponents, constant contraction coefficients, semiempirical parameters of the Hamiltonians (Fockians). Symbols ξ refer to *variables* of the (electronic) problem: MO LCAO expansion coefficients, CI configurations' or coupled clusters' amplitudes, *etc.* The matrix elements of the one- and two-electron parts of the Hamiltonian: $h^{(1)}(C\mathbf{Q}\omega \mid x', x)$ and $h^{(2)}(C\mathbf{Q}\omega \mid x'_1 x'_2, x_1 x_2)$, respectively, depend on the system composition, nuclear configuration (defining the "external" Coulomb field acting upon electrons) and also on the parameters ω adopted in the method. The one-electron state indices $x = (\mathbf{r}, s), x', x_1, x_2, x'_1, x'_2$ can be understood either as continuous spatial coordinates of electrons or as discrete set of quantum numbers characterizing the states in the adopted restricted basis set. In the latter case the integration must be understood as summation over discrete values of x's giving the necessary traces of the matrix products.

In the coordinate representation the above averages acquire familiar forms:

$$
\begin{aligned}
&\left\langle \hat{T}_e \right\rangle = -(1/2) \sum_{\sigma} \int\limits_{\mathbf{r}=\mathbf{r}'} \Delta' \rho^{(1)}(\mathbf{r}\sigma, \mathbf{r}'\sigma) d\mathbf{r} \\
&\left\langle \hat{V}_{ne}(\mathbf{Q}) \right\rangle = e^2 \sum_i Z_i \sum_{\sigma} \int \frac{\rho^{(1)}(\mathbf{r}\sigma, \mathbf{r}\sigma) d\mathbf{r}}{|R_i - \mathbf{r}|} \\
&\left\langle \hat{V}_{ee} \right\rangle = \frac{e^2}{2} \sum_{\sigma\sigma'} \int \frac{\rho^{(2)}(\mathbf{r}\sigma, \mathbf{r}\sigma; \mathbf{r}'\sigma', \mathbf{r}'\sigma')}{|\mathbf{r} - \mathbf{r}'|} d\mathbf{r} d\mathbf{r}' \\
&V_{nn}(\mathbf{Q}) = \frac{e^2}{2} \sum_{i \neq j} \frac{Z_i Z_j}{|R_i - R_j|}; \text{where} \\
&\Delta' = \tfrac{\partial^2}{\partial x'^2} + \tfrac{\partial^2}{\partial y'^2} + \tfrac{\partial^2}{\partial z'^2}
\end{aligned}
\tag{3}
$$

where the density matrices and the left parts of the above equations are assumed to be specific for a given composition, geometry and electronic state; and the first row is the kinetic energy of electrons, second row is the energy of Coulomb attraction of electrons to nuclei, the third row is the energy of interelectronic repulsion; the last one is the energy of Coulomb repulsion nuclei. The sum of the first two rows yields the average of the one-electron part of the Hamiltonian $h^{(1)}(C\mathbf{Q})$ and the energy of the electron-electron repulsion is the average of the two-electron part $h^{(2)}(C\mathbf{Q})$. In the above expressions the nuclear radius-vectors R_i have to be understood as functions of configuration variables $\mathbf{Q}$: $R_i = R_i(\mathbf{Q})$, whereas the composition

C is a designation for the set of nuclear charges present in the system: $C = \{Z_i | i = 1, ...\}$.

The density matrices are by definition partial integrals of the corresponding trial wave functions $\Psi_{C\mathbf{Q}\Gamma S}(\xi\omega \mid x_1, x_2, \ldots, x_N)$ obtained for the given composition C and nuclear configuration $\mathbf{Q}$ so that they have the specified total spin S and spatial symmetry Γ:

$$\begin{array}{lcl} \rho^{(1)}_{C\mathbf{Q}\Gamma S}(\xi\omega \mid x, x') & = & N \int \Psi^*_{C\mathbf{Q}\Gamma S}(\xi\omega \mid x, x_2, \ldots x_N) \times \\ & \times & \Psi_{C\mathbf{Q}\Gamma S}(\xi\omega \mid x', x_2, \ldots, x_N) dx_2 \ldots dx_N \\ \rho^{(2)}_{C\mathbf{Q}\Gamma S}(\xi\omega \mid x_1 x_2, x'_1 x'_2) & = & \frac{N(N-1)}{2} \int \Psi^*_{C\mathbf{Q}\Gamma S}(\xi\omega \mid x_1, x_2, x_3, \ldots x_N) \times \\ & \times & \Psi_{C\mathbf{Q}\Gamma S}(\xi\omega \mid x'_1, x'_2, x_3, \ldots, x_N) dx_3 \ldots dx_N \end{array} \tag{4}$$

The expressions Eqs. (2) ,(4) are completely general. To address the aspects important for the TMCs' modelling, *i.e.* the energies of the corresponding electronic states, we notice that the statement that the motion of electrons is correlated can be given an exact sense only with use of the two-electron density matrix Eq. (4). Generally, it looks like [35] (with subscripts and variables' notations $\xi\omega$ omitted for brevity):

$$\rho^{(2)}(x_1, x_2; x'_1, x'_2) = \begin{vmatrix} \rho^{(1)}(x_1, x'_1) & \rho^{(1)}(x_2, x'_1) \\ \rho^{(1)}(x_1, x'_2) & \rho^{(1)}(x_2, x'_2) \end{vmatrix} - \chi(x_1, x_2; x'_1, x'_2), \tag{5}$$

where the first term corresponds to the model where electrons are independent *i.e.* noncorrelated. The second term in Eq. (5) – the cumulant of the two-particle density matrix [37] – is responsible for deviation of electrons behavior from the model of independent fermions, *i.e.* for their correlations. The correspondence of the above picture with the standard language of quantum chemistry based on the many-electron wave functions rather than on the density matrices can be reestablished by noticing that the trial wave function Ψ taken in the form of a single Slater determinant formed by molecular orbitals (MO), where the variation parameters ξ are the expansion coefficients of MOs taken as linear combinations of atomic orbitals (LCAO) (Hartree-Fock-Roothaan – HFR – approach) automatically results in the two-electron density matrix of the determinantal form [38]. So, in the HFR framework the two-electron density matrix is not an independent quantity any more and the properties of the system are ultimately expressed through its one-electron density matrix.

In the following Sections we analyse the previously listed classes of QC methods of electronic structure modelling in terms of the density matrices.

2.3.1. *Ab initio methods*

The modelling by *ab initio* QC methods bases on complete description of electronic structure for which it is necessary to consider a set of one-electron states (basis functions), number of electrons in the system and nuclear

charges. All consequent modelling is the computer work which involves calculating the matrix components $h^{(1)}$, $h^{(2)}$ of the electronic Hamiltonian, for the set of selected basis functions (whose parameters are above denoted as ω).

In *ab initio* methods the HFR approximation is used for build-up of initial estimate for $\rho^{(1)}$ and $\rho^{(2)}$ which have to be further improved by methods of configurational interaction in the complete active space (CAS) [39], or by Møller-Plesset perturbation theory (MPn) of order n, or by the coupled clusters' [40,41] methods. In fact, any reasonable result within the *ab initio* QC *requires* at least minimal involvement of electron correlation. All the technical tricks invented to go beyond the HFR calculation scheme in terms of different forms of the trial wave function or various perturbative procedures represent in fact attempts to estimate somehow the second term of Eq. (5) – the cumulant χ of the two-particle density matrix.

In application of non-empirical methods to TMCs there exist specific difficulties caused by the correlation strength. This can be formulated as essential deviation of $\rho^{(2)}$ from the HFR approximate form which makes it necessary to take it into account at the initial stage of calculation. Meanwhile, the listed (systematic) methods of taking the correlation into account are based on the assumption that the correlations appear as a smaller corrections to the mainly HFR approximate wave function at least when it goes about the ground state. This is an assumption leading to the whole variety of the single-reference (SR) perturbative and coupled cluster methods, where by the SR state to be improved is assumed to be a single Slater determinant. The actual physics of TMC's is sometimes much more complex. Even obtaining of the approximate solutions of the electronic problem within the HFR approximation although they are required only as starting points (reference states) for further improvements in case of TMCs may represent a serious problem. It is known that for TMCs the HFR methods in many cases yield the electronic structure breaking the *Aufbauprinzip*, according to which MOs are filled by electrons beginning from the lowest energy levels. However, any variational function of the HFR approximation giving the minimum of energy with respect to relevant variational parameters must satisfy this requirement.

Another problem, well known to practical workers in the field, is the slow convergency of the HFR iterations or non-rare cases of being trapped into oscillatory regime. These problems are numerical manifestations of electron correlation. In this situation the HFR solution even if it is obtained may lay too far from the correct ground state of the TMC. The latter cannot be derived from this approximation by those homeopathic medication which is provided by the perturbation or coupled cluster theories. The problem is that for example the formally 'excited' configuration may have the same energy as the 'ground state' one thus preventing proper treatment by either MP or CC methods. From the general point of view the situation is

completely clear – one has to use configuration interaction (CI – multireference – MR) or CAS methods. Pragmatically, however, there remains the question: what amount and which configurations have to be included. In any case the poor initial approximation requires for curing a large number of configurations.

The *ab initio* calculations on TMCs date back to late sixties when the first examples of such calculations in the HFR approximation as applied to simple NiF_6^{4-} ion had been published [42–44]. In those early times the optimistic belief [45] was that 'It is mostly computational limitations which have in the past more or less prevented a wide application of the *ab initio* techniques to the chemistry of transition metal compounds ... with technical developments which may be forecast for the next few years, this type of calculations will probably become much more common'. It, however, happened that within ten years a collection of papers edited by one of the previous authors came out where the description of TMCs has been recognized as a 'challenge' [46]. The above analysis shows the reason. Nevertheless, within two subsequent decades the hardware improved significantly so that the TMCs of modest size became available for direct more or less complete numerical *ab inito* study. Examples of such approach are numerous in the literature. Their range is extremely wide: from studies of structure and properties of 'helide' molecules HeM^{2+}, where M is the doubly charged cation of the first transition row metal [47] by various *ab initio* methods (including those with relativistic corrections). Of course, this is not the topic of our main interest.

On the other hand, the wide use of the *ab initio* methods as a molecular modelling tool for TMCs is still prevented by enormous computational costs. In *ab initio* HFR MO LCAO methods used as zero-approximation calculations of correlation corrections required to make the result somehow acceptable are so complex that the dependence of time and other necessary computing resources on the size of the molecular system (N as number of AOs) scales up as $N^5 \div N^7$. Therefore, at larger sizes of systems under study calculations of TMCs electronic structure become very expensive. This prompted an approach which hardly can be called methodologically sound, but which is widely represented in the literature: considering at a (currently acquired) *ab initio* level only a smaller part of the molecule of interest ignoring the rest of the system as it is demonstrated in the representative collection of reviews [48]. It is clear that the *ab initio* methods do not provide any tool for adjusting the presumably "exact" result obtained for a nonexisting model to the needs of analysis of an experimental situation. Nevertheless, when cautiously applied this model approach can be useful. In most studies on TMCs of say biological or industrial interest only a model small compound of it is actually considered. The following provides representative examples.

In paper [49] various models of the active site of metal-containing enzyme glutathion-transferase having structures with five and six coordinated ions Mn^{2+} and Fe^{2+} are explored. In both cases it is assumed, that the respective metal ion is in its HS state. It essentially facilitates calculation since such a ground state can be reasonably modelled by a single-configuration (HFR) wave function. Structural studies of the Jahn-Teller effect in TMCs by the *ab initio* CC methods are performed in [50, 51].

An attractive test-bed for testing various QC methods as applied to TMCs is provided by metal-porphyrins being rather interesting from various practical points of view but simultaneously polyatomic enough to raise the efficiency issues and also well studied experimentally. The early attempts to apply *ab initio* QC methods are reviewed in Ref. [52]. With use of models of various extent of realism (including those with exact number of atoms and electrons) it was shown that HFR MO LCAO turns out to be good in the extremal cases of Co(II) and Mn(II) whose ground state spin were reproduced correctly to be 1/2 and 5/2, respectively, and fails in the practically most important case of Fe(II) porphyrin which was known to be of intermediate total spin $S = 1$ in its ground state. Despite 20 years of development this result quite well established experimentally many times escaped from *ab initio* workers. Even the most recent results [53, 54] do not allow to make a definitive conclusion on the capacity of the *ab initio* methods.

Unfortunately the *ab initio* workers are not always cautious enough as is exemplified by Ref. [55]. In it a wide set of experimental data on catalytic reactions taking place in the presence of Pd complexes with substituted phosphine ligands PR_3 is modelled by *ab initio* methods applied to models where the whole variety of the ligands is represented by the unsubstituted phosphine PH_3 molecule. The main problem with such an approach is that the sensitivity of the processes under study to the number and nature of organic substituents at the phosphorous atom is well known in the literature.

The above mentioned computational costs lead to a necessity to find a fragile compromise between the requirements of precision and feasibility of a calculation. That of course raises interest to applying the hybrid QM/MM methods to TMCs. The more traditional version of this approach consists in taking rather large portion of the TMC (including the metal atom) to the QM subsystem and in treating the distant groups on a lower level of the theory. Approaches of that type are quite frequently applied to the TMCs and the recent review of it is given in [56]. The general problem of this approach is the nonsystematic character of the treatment of the inter-subsystem border (junction) accepted in most standard packages. The detailed discussion of these problems is given in our recent review [57]. More specific argument can be borrowed from the metal porphyrin problem as well. In the literature there are reliable experimental data concerning the influence of the peripheral substituents on the electronic structure of the

central ion in the case of tetraphenyl porphyrinates of iron (III) additionally substituted in the phenyl rings (see [58] and references therein). This type of effect cannot be attributed to any steric hindrance or whatever of that sort and must be ascribed to the influence of the substituent upon the electronic structure of the transition metal atom. In the standard setting employing the QM/MM technique is precluded for such a problem and a total QC calculation is required. The latter is, however, very difficult since although chemically tetraphenyl porphyrins do not seem to be very different from the unsubstituted ones the total number of basis functions is approximately as twice as large for the substituted species thus increasing the required computational resources by factors 2^5 to 2^7.

2.3.2. *HFR-based semiempirical treatments of TMCs*
In the previous Section we briefly described the problems arising when the *ab initio* QC methods are applied to the modelling of TMCs. These problems may be considered largely as technical ones: if the computer power is sufficient the required solution of the many electron problem can be obtained by brute force even if the initial guess for the wave function is poor. Pragmatically, however, the resource requirements may become prohibitively high for using the *ab initio* QC techniques as a tool for massive PES modelling. In this situation the semi-empirical methods can again come into play as 40 years after the pioneer works [59–61] where the CNDO and INDO parameterizations by Pople and Beveridge [62] were extended to transition metal compounds. Now there is an extensive sector of semi-empirical methods differing by expedients of parameterizations of the HFR approximation in the valence basis. In many of them the parameterization at least is formally extended to the transition metal atoms, for example, in methods ZINDO/1, SAM1, PM3(tm), PM3* *etc.* [63–69], although, principles of parameterization may differ as stipulated by the need to reproduce different experimental characteristics.

The attempts to construct an acceptable parameterization for TMCs are almost exclusively undertaken within the framework of the HFR MO LCAO paradigm. It is easy to understand that the nature of failures which accompany this direction of research as long as it exists lays precisely in the inadequate treatment of the cumulant of the two-electron density matrix by the HFR MO LCAO.

The procedure of developing a semi-empirical parameterization can be generally formalized in terms of Eq. (2) as follows. A set of experimental energies $\mathcal{E}(C\mathbf{Q}\Gamma S)$ corresponding to different chemical compositions C, molecular geometries $\mathbf{Q}$, and electronic states with specific values of S and Γ is given. In the case when a response to an external field is to be reproduced the latter can be included into the coordinate set $\mathbf{Q}$. Developing a parameterization means to find certain (sub)set of parameters ω which minimizes the norm of the deviation vector $\delta\mathbf{E}_\omega$ with the components

$\mathcal{E}(C\mathbf{Q}\Gamma S) - E(C\mathbf{Q}\Gamma S|\omega)$ numbered by the tuples $C\mathbf{Q}\Gamma S$:

$$\min_{\omega} \left(\delta\mathbf{E}_{\omega} \left|M\right| \delta\mathbf{E}_{\omega}\right) \tag{6}$$

which is calculated with some positively (semi)definite metric matrix M. Quite a number of endeavors of this sort were very successful leading to the whole family of semi-empirical procedures useful largely for describing the ground state of "organic" molecules [70]. In the case of TMCs the success is known to be much more modest and even the ground state multiplicities and spatial symmetries escape from being correctly reproduced. We shall show that the reason is the HFR approximation built in the computation scheme of semiempirical methods.

Indeed, the calculated energies $E(C\mathbf{Q}\Gamma S|\omega)$ are the *linear* functionals of the density matrices Eq.(4). When the cumulants of the two-electron density come into play the energies $E(C\mathbf{Q}\Gamma S|\omega)$ and the deviations $\delta\mathrm{E}_{\omega}$ become quadratic functionals of the one-electron density matrices and remain the linear functionals of the cumulant (just the same as the previous linear functional of the two-electron density matrix). The HFR approximation is nothing but restricting the corresponding functionals to their quadratic parts in the one-electron density matrix and dropping the cumulant dependent contribution completely. By this two states having the wave functions yielding the same one-electron density matrices but different two-electron density matrices are deemed to have the same energy. This is precisely the situation one can face while treating the electronic structure of the TMC's the most important characteristic of which is the sophisticated structure of the low energy spectrum of their partially filled d-shell. It can be easily understood that namely the cumulant of the two-particle density matrix serves to distinguish the different many-electron states in the d-shell.

Let us consider *e.g.* a two-orbital two-electron model system with the orbitals a and b which can be understood as notation for one-dimensional irreducible representations of the point group of a TMC. In this case it is easy to see that the corresponding singlet and triplet states ${}^1B$ and ${}^3B$ ($\Gamma = B, S = 0, 1$) are given correspondingly by:

$$\begin{array}{l} \Psi_{B0}(x_1, x_2) = \frac{1}{2}\left(\alpha(s_1)\beta(s_2) - \beta(s_1)\alpha(s_2)\right)\left(a(\mathbf{r}_1)b(\mathbf{r}_2) + b(\mathbf{r}_1)a(\mathbf{r}_2)\right) \\ \Psi_{B1}(x_1, x_2) = \frac{1}{2}\left(\alpha(s_1)\beta(s_2) + \beta(s_1)\alpha(s_2)\right)\left(a(\mathbf{r}_1)b(\mathbf{r}_2) - b(\mathbf{r}_1)a(\mathbf{r}_2)\right) \end{array} \tag{7}$$

irrespective to the values of subscripts $C\mathbf{Q}$ introduced after Eq. (2) and the actual values of either parameters ξ and ω. Performing the integration according to Eq. (4) we immediately get that irrespective to the total spin of these states the *exact* one-electron density matrices become:

$$\rho^{(1)}_{BS}(x, x') = \frac{1}{2}\left(\alpha^*(s)\alpha(s') + \beta^*(s)\beta(s')\right)\left(a^*(\mathbf{r})a(\mathbf{r}') + b^*(\mathbf{r})b(\mathbf{r}')\right) \tag{8}$$

and do not depend on the total spin. This result is well known for decades and appears even in textbooks [71]. Obviously, the HFR approximate two-electron density matrices coming from the one-electron densities Eq. (8) give a wrong result since the *exact* two electron density matrices calculated according to their definition Eq. (4) from the wave functions Eq. (7) *are* different:

$$\rho^{(2)}_{B\binom{0}{1}}(x_1x_2, x_1'x_2') = \\ \tfrac{1}{4}\left(\alpha^*(s_1)\beta^*(s_2) \mp \beta^*(s_1)\alpha^*(s_2)\right)\left(\alpha(s_1')\beta(s_2') \mp \beta(s_1')\alpha(s_2')\right) \times \\ \left(a^*(\mathbf{r}_1)b^*(\mathbf{r}_2) \pm b^*(\mathbf{r}_1)a^*(\mathbf{r}_2)\right)\left(a(\mathbf{r}_1')b(\mathbf{r}_2') \pm b(\mathbf{r}_1')a(\mathbf{r}_2')\right)$$

with the upper sign corresponding to $S = 0$ and the lower one to $S = 1$, irrespective to the values of the subscripts $C\mathbf{Q}$ and parameters $\xi\omega$. The physical consequences of this difference are well known: namely it is responsible for the validity of the first Hund's rule stating that in an atom the term of a higher spin has a lower energy (under other equal conditions).

A capacity of a theoretical method to reproduce such characteristics is intimately related to the (*grammatically*) correct treatment of the cumulant of the two-electron density matrix. Let us assume that we want to fit some experimental data to the model

$$\begin{array}{lcl} f(x,y) & = & ax + by \\ y & = & x^2 + z \\ f(x,z) & = & ax + bx^2 + bz \end{array} \tag{9}$$

Quantitatively a simplified model

$$f_0(x) = ax + bx^2 \tag{10}$$

may be even not that bad: if z is small. But *qualitatively* the approximate model Eq. (10) cannot distinguish experimental points which have the same value of x and differ by the value of z only. This situation clearly is one we face in TMCs when the data related to a set of states of the different spin with the same number of d-electrons are to be reproduced in different ligand environments. The HFR theory in its simplest form (see below) does not provide any quantity to which this difference can be anyhow ascribed. The problem is not in that or another type of the Coulomb exchange integrals whether appearing or not in the parameterization scheme, but in their density matrix cumulant counterpart. Even in the case when the HFR part of the two-electron density matrix provides a multiplier to be combined with that or another exchange integral ultimately responsible for the energy difference between the states of the different total spin, in the absence of the component of the two-electron cumulant dual to this exchange integral this difference remains zero any way.

In a more complex situation than that of two electrons occupying each its orbital one can expect much more sophisticated interconnections between the total spin and two-electron densities than those demonstrated above. The general statement follows from the theorem given in [72] which states that no one-electron density can depend on the permutation symmetry properties and thus on the total spin of the wave function. For that reason the difference between states of different total spin is concentrated in the cumulant. If there is no cumulant there is no chance to describe this difference. This explains to some extent the failure of almost 40 years of attempts to squeeze the TMCs into the semiempirical HFR theory by extending the variety of the two-electron integrals included in the parameterization.

We do not intend to further elaborate on characteristics of the semiempirical methods. It it enough to say, that all of them which are restricted to the HFR approximation suffer from the shortcoming described above and, hence, one has not to have too much hope to reach a consistent description of TMCs within the HFR framework. The recent semiempirical attempt to parameterize the TMCs in the PM3(tm) method [73] is very instructive in this respect. The calculations carried out in Ref. [74] show that the method is not capable to reproduce even very simple characteristics in a series of TMCs having similar structure, though other authors [68,75] state that in some cases reasonable estimates of geometrical characteristics may be received, nevertheless. This situation can be understood by thorough consideration of the sets of objects chosen for analysis in different works. In [74] authors study a uniform set of about 30 Ni^{2+} complexes with the ligands bound by nitrogen donor atoms. The analysis of this series performed there clearly shows that the PM3(tm) method fails for these Ni^{2+} complexes for the now understandable reason. However, in [68,75] the authors try to explore a comparable number of complexes but much more dispersed over the range of classes, which includes compounds of the first and second transition row atom, HS and LS ones, those having "ionic" and "covalent" bonds *etc.* For that reason in the test sets [68,75] the problematic *classes* are represented by a couple of examples each, which look out as completely isolated exceptions. This can serve as an example of how trying to test the method on a wide and apparently "random" selection of objects may lead to a smeared picture due to absence of clear criteria of any adequate classification of the chosen set.

That said above does not mean that a semiempirical parameterization based on the HFR MO LCAO scheme and valid for a certain narrow class of compounds or even for a specific purpose cannot be built. It is done for example in [69] for iron(II) porphyrins. But in a more general case there is no way to arrive to any definite conclusion [76] about the validity of a semiempirical parameterization in the HFR context. On the other hand we have to mention that the semiempirical method ZINDO/1 [77] which allows for

some true correlation by taking into account the configuration interaction may be considered as a prospective setting for further parameterization, provided the HFR solution required by this method as a zero approximation can be obtained. This will be discussed in a more detail below.

2.3.3. *Density functional theory methods. Why not DFT?*
Methods of density functional theory (DFT) originate from the X_α method originally proposed by Slater [78] on the base of statistical description of atomic electron structure within the Thomas-Fermi theory [79]. From the point of view of Eq. (3), fundamental idea of the DFT based methods consist first of all in approximate treatment of the electron-electron interaction energy which is represented as:

$$\begin{aligned} \langle V_{ee} \rangle &= E_H + E_{xc}; \\ E_{xc} &= E_x + E_c. \end{aligned}$$

The "classical" part of the interaction energy – the Hartree energy:

$$E_H = \frac{e^2}{2} \sum_{\sigma\sigma'} \int \frac{\rho^{(1)}(\mathbf{r}\sigma, \mathbf{r}\sigma)\rho^{(1)}(\mathbf{r}'\sigma', \mathbf{r}'\sigma')}{|\mathbf{r} - \mathbf{r}'|} d\mathbf{r} d\mathbf{r}' \tag{11}$$

is taken exactly, whereas the exchange and correlation parts:

$$E_x = -\frac{e^2}{2} \sum_{\sigma} \int \frac{\rho^{(1)}(\mathbf{r}\sigma, \mathbf{r}'\sigma)\rho^{(1)}(\mathbf{r}'\sigma, \mathbf{r}\sigma)}{|\mathbf{r} - \mathbf{r}'|} d\mathbf{r} d\mathbf{r}' \tag{12}$$

$$E_c = -\frac{e^2}{2} \sum_{\sigma\sigma'} \int \frac{\chi(\mathbf{r}\sigma, \mathbf{r}\sigma; \mathbf{r}'\sigma', \mathbf{r}'\sigma')}{|\mathbf{r} - \mathbf{r}'|} d\mathbf{r} d\mathbf{r}' \tag{13}$$

whose precise definitions Eqs. (12), (13) consistent with the theoretical setting given by Eqs. (2),(5), are assumed to be functionals of the one-electron density only (diagonal of the one-electron density matrix in the coordinate representation).

The main goal of the DFT paradigm is to reduce the whole electronic structure theory to a single quantity: one-electron density — the diagonal part of the one-electron density matrix. If it had been possible it would considerably simplify the theory. Pragmatic methods pertaining to the DFT realm are based on use of the Hohenberg-Kohn "existence theorems" [80,81] which state, first, an existence of a universal one-to-one correspondence between one-electron external potential and the one-electron density in that sense that not only the one-electron potential acting upon a given number of electrons uniquely defines the ground state of such a system *i.e.* its wave function and thus the one-electron density – which is trivial, – but also that for each given density integrating to a given number of electrons a one-electron potential yielding that given density is uniquely defined (v-representability).

Further pragmatic moves are described in details in numerous books and reviews of which we cite the most concise and recent Ref. [82]. Two further *hypotheses* are an important complement to the above cited *theorems*. One is the locality hypothesis, another is the Kohn-Sham representation of the single determinant reference state in terms of orbitals. The locality has been seriously questioned by Nesbet in recent papers [83, 84], however, it remains the only practically implemented solution for the DFT. The single determinant form of the reference state in its turn guarantees that all the averages of the electron-electron interaction appearing in this context are in fact calculated with the two-electron density given by the determinant term in Eq. (5) with no cumulant.

During last decades the DFT based methods have received a wide circulation in calculations on TMCs' electronic structure [34, 85–88]. It is, first of all, due to widespread use of extended basis sets, allowing to improve the quality of the calculated electronic density, and, second, due to development of successful (so called – hybrid) parameterizations for the exchange-correlation functionals (*vide infra* for discussion). It is generally believed, that the DFT-based methods give in case of TMCs more reliable results, than the HFR non-empirical methods and that their accuracy is comparable to that which can be achieved after taking into account perturbation theory corrections to the HFR at the MP2 or some limited CI level [88–90].

As in all axiomatic theories relying upon existence theorems particular attention has to be paid to the consequences of these theorems which sometimes can be rather peculiar. Although the general validity of the Hohenberg-Kohn theorems cannot be questioned the example Eq. (7) obviously presents two *different* wave functions with *different* energies yielding *the same* one-electron density matrix and thus of course the density itself. For that reason the qualitative effects of electron correlation which are crucially important for correct TMC modelling and for which the term χ in Eq. (5) takes care, cannot be reproduced by the DFT based methods at all since these do not contain the necessary elements of the theory for it (although MP2 and even limited CI do). Whatever attempt to do that will have a restricted character due to absence of the cumulant. In that respect the situation is analogous to that in the HFR-based semi-empirical methods. In terms of the "data-fit" model Eq. (6) the DFT methods can be understood as ones with the fitting model of the form:

$$\tilde{f}_0(x) = ax + g(x)$$

using may be a very sophisticated function $g(x)$ instead of bx^2 in order to mimic the independent variable y. Whatever refined is $g(x)$ the resulting model will not be able to distinguish the data which differ only by the value of the independent variable z (see above) and have the same values

of x. However, namely the relative energies of the states differing by the cumulant of the two-electron density matrix must be correctly reproduced in order to obtain a satisfactory description of the spectra (relative energies of the states) of the TMCs' d-shells. In this context it is possible to say, that the DFT-based methods take into account electron correlations in the same sense, as all (even the elementary) semiempirical QC methods do. If these latter are parameterized to reproduce some experimental characteristics of molecules the parameters of these methods implicitly take into account correlation. By this it may be possible to achieve quantitative agreement with a narrow segment of experimental data, but not with those which require reproducing qualitative effects of correlations. The latter can be simulated neither by semiempirical methods nor by the DFT-based methods. Therefore advantages of the DFT-based methods are primarily observed for trivial TMCs where the correlations in the open d-shell representing a problem for single determinant methods actually absent (as in d^0- or d^{10}-complexes or in the complexes of the second and third transition row or in carbonyls or other organometallic compounds cited in abundance in [34]).

Remarkably enough that the counter-example Eq. (7) is well known in the DFT context, and it brought the author [34, 91] to the conclusion that the theory employing the local spin density approximation for the exchange energy is valid only for the single determinant wave function. That is precisely what other people meant saying that the DFT (at least in its original form) does not apply to TMCs at all which also may be an exaggeration.

The recipe proposed in Ref. [91] to cure this problem is to apply the Slater sum rules. These represent a special case of the Roothaan prescriptions for the open shells [92]. They are valid only in those cases when the energy of a multiplet state can be represented as a weighted *sum* of determinant energies *i.e.* of the diagonal matrix elements of the Hamiltonian in the one-determinant basis. This can be only possible if the multiplet states are uniquely obtained by applying operators projecting to the specific rows of the irreducible representations to the basis Slater determinants. Obviously it is not possible when the symmetry is not high enough: in this case the number of different symmetry labels simply does not suffice to distinguish all the Slater determinants. In the case of the p-shell the recipe [92] worked well.

It turned out, however, that for the d-shells the recipe [92] of constructing the two-electron density matrix does not work for a major part of the atomic electronic terms of the transition metal ions [93]. Further studies revealed that constructs similar to [92] are, nevertheless, possible also for some other terms for which the name of the non-Roothaan terms [94, 95] was coined not very conveniently (the point is that the Roothaan and non-Roothaan terms together do not exhaust the entire set of terms). The Roothaan and non-Roothaan terms together are those where it is possible

to get the precise CI amplitudes from the one-electron occupation numbers for the *d*-orbitals on purely symmetry grounds. However, even in free ions the extra terms (as compared to the Roothaan and non-Roothaan together) namely the multiple terms of the same spin and orbital momentum – which are correlated by nature do exist. Their energies cannot be expressed linearly through the say Racah or Slater-Condon parameters. In the free ions these energies require maximum 2×2-diagonalization [96] and thus their analytical expressions contain square roots (for a handy reference see [97]). This moment is crucial – it is not possible to get rid out of the irrationality (square root) in the expression for the energy by linearly combining the parameters of the Hamiltonian. The example of such possibility given in [87] applies only to the case explicitly considered in that paper: that of the d^2 configuration, for which as one can see from [96,97] the energies of all terms can be linearly expressed through the Racah parameters.

The situation clearly becomes less favorable in lower symmetries where the terms of the same spin and symmetry span the subspaces of dimensionalities higher than two. For example, in the octahedral environment the LS states of d^4- (d^6-) configuration span up to seven-dimensional spaces of many-electronic states [98]. Clearly that at an arbitrarily low symmetry the problem of linearly expressing the exact energy of many-electronic terms through the Racah parameters cannot be solved and obviously the energy of any of such multiple terms cannot be expressed as a linear combination of only *diagonal* matrix elements of the Hamiltonian.

In a more general setting the recipe [91] can be considered as an implementation of another suggestion by Gunnarsson and Lundqvist [99] and von Barth [100] known also at a pretty early stage of the development of the DFT technique of employing different functionals to describe different spin or symmetry states. In other words the simplified model for the data fit Eq.(10) changes to:

$$\tilde{f}_0^{\Gamma S}(x) = ax + g_{\Gamma S}(x)$$

where $g_{\Gamma S}(x)$ represent exchange-correlation functionals specific for each ΓS. As the model $f_0(x)$ the model $\tilde{f}_0^{\Gamma S}(x)$ cannot distinguish experimental points with equal values of x differing by the values of z if they belong to the same spin and symmetry, but the difference in z which distinguishes one set ΓS from another one is implicitly built into the functional.

This all explains the nature of failures of the DFT based methods in those cases, when correlations substantially come into play as in *e.g.* d^6-iron (II) ferrocene molecule. Here the errors even of advanced DFT methods become catastrophic. For example, in Ref. [86] the calculated enthalpies of dissociation of ferrocene to the free Fe^{2+} ion and two Cp^- anions (Cp = C_5H_5 – cyclopentadienyl) depending on the functional used appear to be by 3-4 eV smaller than the experimental value. The reason is transparent

enough in the context of the above consideration. It is the insufficiency of whatever DFT for the description of the switching between the electronic terms: from the LS d^6 Fe^{2+} in ferrocene to the HS one in the free ion, along the dissociation pathway.

Authors of work [101] have faced the same problem, when addressed the spin isomers of the iron(II) complex with the hexadentate ligand tetrakis(2-pyridylmethyl)-ethylenediamine. The DFT (B3LYP/3-21G/6-311G(d)) method they used could properly reproduce neither the ground state spin nor the structural parameters of the isomers. This result is not an isolated failure. An analogous picture appears in [102–104] despite the use of the B3LYP/6-311G* functional/basis the results are somewhat mixed: The relative energies of the HS and the LS states of the nitrogen bound $[Fe(tpa)(NCS)_2]$ complex appear to be in a correct order on the energy scale, whereas the Fe–N bond lengths come out with a considerable and nonsystematic error between -0.06 and $+0.05$ Å which is pretty much as compared to the magnitude of the effect itself: the spin transitions in iron(II) complexes are accompanied by the average displacement of nitrogen atoms by 0.15 Å [23,105]. On the other hand the calculations performed on the charged complex ions with tris(pyrazolyl) ligands in [104] manifest significant dependence of the result obtained on the functional/basis set used for calculation. Their B3LYP/6-311G* combination while being successful in the previous case turned out to yield the qualitatively wrong order on the energy scale of the LS and HS forms of the tris(pyrazolyl) complexes. Other combinations possible for the BLYP and PW91 functionals and LANL2DZ basis set performed not too much better. The most recent review of this activity [106] does not indicate serious improvement either in terms of the geometry reproduction or that of the energy gaps between the HS and LS states.

In the remarkable series of papers [107–109] the authors attempted to reproduce the relative energies of the LS and HS terms in a series of pseudo-octahedral Fe(II) complexes with ligands bound to the metal atom through sulfur and nitrogen donor atoms. It was achieved only by the cost of adjustment of the weight of the Hartree-Fock exchange energy in the hybrid B3LYP functional leading to development of the B3LYP* functional (see below). These authors conclude, that the hybrid functionals (B3LYP) in the DFT based methods favor mainly the HS states. As one can see namely the Fock exact exchange is responsible for the Hund's rule conformity. Indeed the HFR estimates of the LS-HS splitting given in all the cited papers amount several eV with the wrong sign (HS state below the LS state). The reason is transparent: unbalanced account of correlations and exchange in the DFT schemes. The Hartree-Fock exchange strongly stabilizes the HS state of the open *d*-shell even if the single-determinant wave function is used, whereas the correlations which can potentially stabilize (in fact multi-determinant) LS states are absent. The LSDA estimate

of exchange gap taken together with some contribution of correlation by contrast strongly underestimates the latter and by this favors the LS states to become lower on the energy scale. This discrepancy has been tried to remove by developing hybrid functionals which reduce the unbalance between different contributions to the exchange and correlation terms by taking different estimates of the latter and ascribing them different weights fit to reproduce some data (in our days taken largely from a numerical experiment performed on an *ab initio* level, but for sure whatever experimental data could be used). For the specific example of the B3LYP functional – the most popular one:

$$E_{xc}^{\mathrm{B3LYP}} = E_x^{\mathrm{LSDA}} + c_1 E_x^{\mathrm{B88}} + c_2 E_c^{\mathrm{LYP}} + (1-c_2) E_c^{\mathrm{VWN}} + c_3 [E_{ex.ex.} - E_x^{\mathrm{LSDA}}],$$

where E_x^{LSDA} is the Slater exchange, $E_{ex.ex.}$ is the exact (Hartree-Fock) exchange energy computed by Eq. (12) from the one-electron density matrix obtained from the Kohn-Sham orbitals; E_c^{LYP} and E_c^{VWN} are the Lee-Yang-Parr (LYP) Ref. [110], and the Vosko-Wilk-Nusair (VWN) Ref. [111] correlation functionals which have too complex analytical expressions to be given here. The parameters in common use are $c_1 = 0.72, c_2 = 0.81, c_3 = 0.20$. From the point of view of our general consideration the B3LYP procedure is one of semi-empirical parameterization schemes whose parameters $(c_i; i = 1 \div 3)$ take certain amount of correlation upon themselves. The actual amount taken is determined ultimately by the set of the objects used for parameterization. When the B3LYP parametric functional is applied to the spin-active compounds of iron(II) it turns out that it still underestimates the relative role of correlation *vs.* exchange in the *d*-shell of the metal atom. The B3LYP* functional cures this overestimate of the exchange energy by taking a smaller fraction of the Hartree-Fock one in the overall energy estimate. Purely empirically the value of its relative weight $c_3(= 0.15)$ has been found to be acceptable to reproduce the energy difference between the minima of the HS and LS forms of the Fe(II) complexes with the ligands with the sulphur donor atoms.

In order to reach an agreement with similar data on iron(II) complexes with ligands containing nitrogen donor atoms [107] the value of $c_3 = 0.12$ had had to be introduced. Similar measures are necessary even for very simple cations like Cu^{2+}. In [112] it was found that the most commonly used DFT functionals give a too covalent ground state of D_{4h} $[CuCl_4]^{2-}$. A novel hybrid functional with 38% HF exchange ($c_3 = 0.38$) can give the good agreement between the calculated and experimental ligand field and ligand-to-metal charge transfer excited state energies. Of course, there is neither explanation for these values nor any hope that they are anyhow stable. Incidentally, the EHCF theory (see below) gives as much as accurate results on the *d-d* transitions as all the standard DFT procedures whereas the much better agreement in [112] is achieved by the cost of unusually high

weight of the HF exchange, which basically has no other substantiation. The entire situation thus looks out to be rather comic: after 40 years of claims of existence of the *unique* density functional and after 30 years of similar claims of an extraordinary power of the DFT-based theories in the realm of TMCs it turns out that namely for TMCs no single functional could be found so far. Whatever implementation reasonable from a practical point of view requires specific non-universal functionals dependent on spin, symmetry and chemical nature not only of the metal, but also of the donor atoms in the ligands.

We see from the above discussion that staying within the DFT it is not possible to describe the multiplet structure of the *d*-shell (incidentally all the success stories reported so far are limited to the *p*-shells [82,113] whereas in the *d*-shells only *average* energies of several multiplet states would be reproduced [114]). In this context it seems to be necessary to analyze the attempts to achieve it which are available in the literature (see [87, 115]). These attempts, however, have a nature absolutely different from the DFT itself so they will be described in an appropriate place below.

2.3.4. *TDDFT: the same but not the same*

Currently the time dependent DFT methods are becoming popular among the workers in the area of molecular modelling of TMCs. A comprehensive review of this area is recently given by renown workers in this field [116]. From this review one can clearly see [117] that the equations used for the density evolution in time are formally equivalent to those known in the time dependent Hartree-Fock (TDHF) theory [118–120] or in its equivalent – the random phase approximation (RPA) both well known for more than three quarters of a century (more recent references can be found in [36,121,122]). This allows to use the analysis performed for one of these equivalent theories to understand the features of others.

According to analysis of Ref. [117] the excitation energies evaluated by TDDFT correspond to taking into account interactions between configurations obtained from the original single-determinant ground state by single electron excitations (CIS). This is obviously equivalent to the so called Tamm-Dankoff approximation in the energy domain [121]. For the latter it is known that in certain situations when the HOMO-LUMO gap becomes small as compared to the Coulomb interaction matrix elements or in other words in a vicinity of the stability loss by the corresponding HFR solution the excitation energies thus obtained may become negative thus indicating some serious problems. The reason is quite transparent: the electron correlation (interaction of the configurations) is taken into account in an unbalanced manner; it is accounted in the singly excited manyfold but is completely neglected for the ground state. If the bare gap (orbital energy difference) is not too small (otherwise the problem becomes evident) the unbalanced correlation account manifests itself in that the excitation en-

ergies estimated in the Tamm-Dankoff approximation are somewhat lower than necessary.

That is precisely which is reported say in [123] on example of Pd complexes (and for other systems in Ref. [124]): the TDDFT excitation energies are systematically lower than the experimental ones. In this context it becomes clear that the TDDFT may be quite useful for obtaining the excitation energies in those cases when the ground state is well separated from the lower excited states and can be reasonably represented by a single determinant wave function may be for somehow renormalized quasiparticles interacting according to some effective law, but shall definitely fail when such a (basically the Fermi-liquid) picture is not valid.

In a way this is what the other prominent authors in the field of the TDDFT recognize as inherent drawbacks of this approach [124, 125]. According to these authors nothing can be done if the one-electron states used have wrong one-electron energies or if the ground state is not a single determinant built of the Kohn-Sham orbitals. But these are the situations we must be ready for when addressing the TMCs.

This brief analysis allows to conclude that the fact that "the superiority of the TDDFT method ... has not been unequivocally established ... in particular for $d \rightarrow d$ transitions" [116] is not an unfortunate accident but a logical consequence of deeply rooted deficiencies inherent to the underlying single-determinant nature of the TDDFT method and the announced proof of superiority will hardly whenever take place.

3. Basic principles of the description of TMC electronic structure

3.1. PHYSICAL PICTURE OF TMC ELECTRONIC STRUCTURE

The above review of the methods of molecular modelling (both QC – including DFT – and MM), given above, has shown that none of them is completely suitable for molecular modelling of TMCs. The MM methods do not allow to consider multiple PES corresponding to several energetically close electronic states of TMCs. *Ab initio* QC methods appear to be too demanding to computational resources when employed to model chemically interesting TMCs with bulky organic ligands; HFR-based semiempirical methods and even the DFT-based methods suffer from the same deficiencies as MM methods, since within their respective frameworks it is not possible to reproduce relative energies of electronic states of different spin multiplicity without serious *ad hoc* assumptions.

We shall note, that the difficulties arise precisely when modelling is to be applied to molecules involving transition metal atoms mainly of the second half of the first transition row. Moreover, even among the TMCs formed by these atoms the problems are not uniformly distributed: the normal chemical nomenclature does not provide here an adequate classification.

When it goes about metal carbonyls or about metals of the second or even third transition row, the DFT methods seem to be able to do the job quite decently. However, turning to compounds of the first transition row metals with open *d*-shells raises many problems. Intuitively distinction in behavior of two types of the metal compounds is clear to any chemist. In a row of isoelectronic species $Ni(CO)_4$, $Co(CO)_4^-$, $Ni(CN)_4^{2-}$, $Fe(CO)_4^{2-}$ they readily recognize the "not a family member", but probably fail to give a reason.

In the traditional theory of chemical bonding the classification is rather vaguely formulated in terms of covalent, polar covalent, ionic, metallic, coordination, donor-acceptor and other types of chemical bonds. Clearly enough such a classification is not relevant in the case of interest. Remarkable alternative systematic of types of chemical bonds is given in [97]. We reproduce it in Table 1 partially abridging. Although this classification also is not particularly satisfying it can be used as a starting point for further discussion. The classification of Table 1 relies upon the MO LCAO, *i.e.* ultimately the HFR, picture of molecular electronic structure. As it is discussed above, the HFR is not very much reliable when it goes about TMCs. Nevertheless we can observe that the lack of regularity both in bond lengths, and in oscillatory frequencies of bonds in complexes is associated, according to [97], with a three-dimensional delocalization of one-electronic states involved. As an example though, the metal-ligand bonds in TMCs are given and the optical spectra and magnetic moment distinguishing them from all other compounds are given as specific characteristics. However, the "non-characteristicity" of the bond lengths and valence angles leading to flexibility of shapes of coordination polyhedra and the coordination numbers themselves are equally common for the complexes of non-transition metals (for example, alkaline or alkali earths). This shows a necessity to turn to somewhat more formal description of molecular electronic structure than it can be provided by the traditional theory of chemical bonding, but still more qualitative than it appears from the numerical experiments arranged in the framework of no-matter-how-precise QC methods.

The qualitative description of the electronic structure can be given in terms of even older concept of "chromophores". According to the IUPAC definition the chromophore is an atom or group of atoms in the molecule that gives color to the molecule. This definition unites two aspects — one related to the system's response to an external perturbation: the spectrum. By this the concept of chromophore is related to experimental behavior of molecular systems. Another aspect relates to the structure understood as a localization of the excited states controlling the tentative response to that perturbation. The examples of chromophores are well known from the textbooks. On the part of the modern theory of electronic structure the concept of chromophore formalizes in the McWeeny's theory of electron groups. (The analogy between chromophore concept and McWeeny's theory

TABLE 1. Chemical bond classification [97]

Bond type	Electronic structure	Compounds example	Typical properties
Valence	MOs are localized between pairs of atoms and occupied by two paired electrons	CH_4 NH_4^+ Diamond C_2H_4	Distinct character of bond energy, dipole moments, frequencies, polarizabilities, etc.
Orbital	MOs are delocalized in one or two dimensions	Benzene Graphite	There are no distinct characteristics; conductivity, cycles aromaticity
Coordination	MOs are delocalized in space — three-dimensional	$CuCl_4^{2-}$ $CoCl_2$ (crystal)	There are no distinct characteristics; variable coordination number and magnetic moment, strong mutual influence of ligands

for the special case of TMCs has been early noticed also in a remarkable work [126]). Within this theory the zero approximation to the system's electronic wave function is taken as an antisymmetrized product of rather local group multipliers referring to relatively isolated elements of molecular electronic structure. These elements – electron groups – are physically identified as two-electron two-center bonds, conjugated π-systems *etc.* Of course, these groups are not totally isolated and ascribing excitations to only one of them is an idealization. Nevertheless, the effective Hamiltonian technique is available to reduce manifestations of the intergroup interactions to renormalizations of the effective group Hamiltonians which allows to interpret the response of the system to any external perturbation in terms of excitations localized in the groups.

Further analysis is based on the idea that the characteristic experimental behavior of different classes of compounds and the suitability of those or other models used to describe this behavior is ultimately related to the extent to which the chromophores or electron groups physically present in the molecular system are reflected in these models. It is easy to notice, that the MM methods work well in case of molecules with local bonds designated in Table 1 as valence bonds; the QC methods apply both to the valence bonded systems, and for the systems with delocalized bonds (referred as "orbital bonds" in Table 1). The TMCs of interest, however, not covered either by MM or by standard QC techniques can be physically characterized as those bearing the *d*-shell chromophore. The magnetic and optical properties characteristic for TMCs are related to *d*- or *f*-states of metal ions. The basic features in the electronic structure of TMCs of interest, distinguishing these compounds from others are the following:

1. Molecule contains strongly correlated electrons in the partially filled valence *d*-shell of the transition metal central atom;
2. The overall charge transfer (electron density) between the *d*-shell of transition metal atom and its ligand environment is small;
3. The low-energy spectrum is spanned by excited states of the partially filled *d*-shell (*d*-*d*-spectrum) and it is rather dense.

These properties of the *d*-shell chromophore (group) prove the necessity of the localized description of *d*-electrons of transition metal atom in TMCs with explicit account for effects of electron correlations in it. Incidentally, during the time of QC development (more than three quarters of century) there was a period when two directions based on two different approximate descriptions of electronic structure of molecular systems coexisted. This reproduced division of chemistry itself to organic and inorganic and took into account specificity of the molecules related to these classical fields. The organic QC was then limited by the Hückel method, the elementary version of the HFR MO LCAO method. The description of inorganic compounds — mainly TMCs,— within the QC of that time was based on the crystal field

theory (CFT) [127,128]. The latter allowed qualitatively correct description of electronic structure, magnetism and optical absorption spectra of TMCs by explicitly addressing the d-shell chromophore. Let us consider the CFT in more detail.

3.2. CRYSTAL FIELD THEORY

Basics of the CFT were introduced in the classical work by Bethe [127] devoted to the description of splitting of atomic terms in crystal environments of various symmetry. The splitting pattern itself is established by considering the change of symmetry properties of atomic wave functions while spatial symmetry goes down from the spherical (in the case of a free atom) to that of a point group of the crystal environment. The energies of the d-d-excitations in this model are obtained by diagonalizing the matrix of the Hamiltonian constructed in the basis of n_d-electronic wave functions (n_d is the number of d-electrons). Matrix elements of the Hamiltonian are expressed through the parameters describing the crystal field and those of the Coulomb repulsion of d-electrons, that is Slater-Condon parameters F^k, $k = 0, 2, 4$, or the Racah parameters A, B, and C. In the simplest version of the CFT these quantities are considered as empirical parameters and determined by fitting the calculated excitation energies to the experimental ones. This approach is devoid of any predictive force (except for the splitting pattern itself) due to presence of empirical parameters in the theory, which are specific for each compound.

The CFT gives a description to the characteristic properties of TMCs at the phenomenological level. The important features of their electronic structure are fixed by this theory and the perpetual problem remains obtaining consistent estimates of its parameters (strength of the crystal field). All further development of the CFT was concentrated on this [129]. Within the standard CFT this problem, however, has no solution due to oversimplified picture of the transition metal ion environment (ligands). Indeed the CFT theory uses the ionic model of the environment and calculates the splitting of the initial term of the free metal ion as if it were a pure electrostatic effect. The symmetry dependent features of the splitting are correctly reproduced even in this simplistic model, whereas all the chemical specifics of this environment gets lost. For this reason it is not surprising that the heaviest strike upon the CFT from the (semi)quantitative side was given by TMC spectroscopy yet in 30-ties. Spectroscopic experiments allowed to range the strengths of the crystal fields exerted by different ligands to the so called spectrochemical series [97, 128, 130]:

$$\begin{aligned} \mathrm{F^-} \;&<\; \mathrm{OH^-} < \mathrm{Cl^-} < \mathrm{Br^-} < \frac{1}{2}\mathrm{Ox^{2-}} < \mathrm{H_2O} < \mathrm{SCN^-} < \mathrm{NH_3, py} < \\ &<\; \frac{1}{2}\mathrm{En} < \mathrm{CN^-} < \mathrm{CO} \end{aligned}$$

It turned out that the fields are systematically weaker for charged species than for the uncharged ones with the utter example of the CO molecule exerting the strongest crystal field, but bearing neither charge nor noticeable dipole moment. Other relative strengths observed in the experiment also cannot be explained within the CFT by means of the ionic model of the environment. These observations clearly indicate that purely electrostatic effects may be only of minor significance in determining the strength of the crystal field.

Early attempts to get the required estimates led to the ligand field theory (LFT) [128, 131]. In it the environment is considered more realistically: the one electron states of the surrounding atoms are explicitly considered. However, within such a setting also only qualitative explanations could be obtained. They had been formalized within the angular overlap model (AOM) [129, 132] with an additional observation that different ligands (or more precisely – donor atoms) contribute to the effective crystal ligand field almost independently and that each ligand when coming in interaction with a given transition metal ion can be characterized by a small number of parameters (AOM parameters) describing its contribution to the total effective field felt by the d-shell. The AOM parameters remained as much empirical quantities, both ligand and metal dependent, as were the $10Dq$'s in the original CFT.

The problem of estimating crystal field parameters can be solved by considering the CFT/LFT as a special case of the effective Hamiltonian theory for one group of electrons of the whole N-electronic system in the presence of other groups of electrons. The standard CFT ignores all electrons outside the d-shell and takes into account only the symmetry of the external field and the electron-electron interaction inside the d-shell. The sequential deduction of the effective Hamiltonian for the d-shell, carried out in the work [133] is based on representation of the wave function of TMC as an antisymmetrized product of group functions of d-electrons and other (valence) electrons of a complex. This allows to express the CFT's (LFT's or AOM's) parameters through characteristics of electronic structure of the environment of the metal ion. Further we shall characterize the effective Hamiltonian of crystal field (EHCF) method and its numerical results.

3.3. EFFECTIVE HAMILTONIAN FOR THE CRYSTAL FIELD (EHCF)

The TMCs' electronic wave function formalizing the CFT ionic model is one with a fixed number of electrons in the d-shell. In the EHCF method it is used as a zero approximation. The interactions responsible for electron transfers between the d-shell and the ligands are treated as perturbations. Following the standards semiempirical setting we restrict the AO basis for all atoms of the TMC by the valence orbitals. All the AOs of the TMC are

then separated into two subsets from which one (the d-system) contains $3d$-orbitals of the transition metal atom, and another (the "ligand subsystem", or the l-system) contains the $4s$- and $4p$-orbitals of the transition metal atom and the valence AOs of all ligand atoms. Within the present theory we shall try to cover only the complexes, where excitation energies in the l-system are by far larger than the excitation energies in the d-shell of the metal atom. This singles out a subset: the Werner-type TMCs which from the point of view of chemical nomenclature can be characterized as ones with the closed electronic shell ligands, such as F^-, Cl^-, Br^-, I^-, saturated organic molecules with donor atoms *etc.*

Formally the theory evolves in a following way. The low-energy d-d-spectrum of the TMC can be obtained if the Hamiltonian is rewritten in the form:

$$H = H_d + H_l + H_c + H_r \tag{14}$$

where H_d is the Hamiltonian for the d-shell, H_l is the Hamiltonian for the ligand system, H_c is the Coulomb interaction, H_r is the resonance one. The electronic wave function for the n-th state of the complex is written as antisymmetrized product of the wave functions of the electron groups introduced above:

$$\Psi_n = \Phi_d^{(n)} \wedge \Phi_l, \tag{15}$$

where $\Phi_d^{(n)}$ is assumed to be a full CI function for n_d electrons in the d-shell, Φ_l is a HFR single determinant ground state for the l-system, and $\wedge$ stands for the antisymmetrized product. This reflects the main feature of electronic structure of the TMC, that is the presence of the strongly correlated d-shell with low energy excitations localized in it and of relatively inert ligands. Under these assumptions the spectrum of the low-energy excitations is that of the effective Hamiltonian for the d-shell only:

$$H_d^{eff} = \sum_{\mu\nu\sigma} U_{\mu\nu}^{eff} d_{\mu\sigma}^+ d_{\nu\sigma} + \frac{1}{2} \sum_{\mu\nu\rho\eta} \sum_{\sigma\tau} (\mu\nu \mid \rho\eta) d_{\mu\sigma}^+ d_{\rho\tau}^+ d_{\eta\tau} d_{\nu\sigma} \tag{16}$$

where the d-electron Coulomb interaction term is inherited from the free ion and the effective core parameters $U_{\mu\nu}^{eff}$ contain contributions from the Coulomb and the resonance interaction between the d- and l-systems:

$$U_{\mu\nu}^{eff} = \delta_{\mu\nu} U_{dd} + W_{\mu\nu}^{atom} + W_{\mu\nu}^{field} + W_{\mu\nu}^{cov}, \tag{17}$$

where

$$W_{\mu\nu}^{atom} = \delta_{\mu\nu} \Big(\sum_{\alpha \in s,p} g_{\mu\alpha} P_{\alpha\alpha} \Big) \tag{18}$$

is the repulsion of electrons in the d-shell from those in the $4s$- and $4p$-AO's of the metal;

$$W_{\mu\nu}^{field} = \sum_L Q_L V_{\mu\nu}^L \tag{19}$$

is the Coulomb interaction of d-electrons with the net charges on the ligand atoms, having the standard CFT form [130]; and the covalence part:

$$W_{\mu\nu}^{cov} = -\sum_i \beta_{\mu i}\beta_{\nu i}\left(\frac{1-n_i}{\Delta E_{di}} - \frac{n_i}{\Delta E_{id}}\right) \tag{20}$$

ultimately comes from the resonance interaction between the d- and l-systems.

Within the EHCF method [133] the single Slater determinant Φ_l has to be obtained from semiempirical HFR procedure. Solving the HFR problem for the l-system yields the one-electron density matrix $P_{\alpha\beta}$, orbital energies ε_i, and the MO-LCAO coefficients $c_{i\alpha}$. These quantities completely define the electronic structure of the l-system and are used to calculate the effective Hamiltonian Eq. (16) by Eqs. (18)-(20), where $Q_L = \sum_{\alpha\in L} P_{\alpha\alpha} - Z_L$ is the effective charge of the ligand atom L; Z_L is the core charge of the ligand atom L; $V_{\mu\nu}^L$ is the matrix element of the potential energy operator describing the interaction between a d-electron and a unit charge placed on the ligand atom L; n_i is the occupation number of the i-th l-MO ($n_i = 0$ or 1); ΔE_{di} (ΔE_{id}) is the energy necessary to transfer an electron from the d-shell (from the i-th l-MO) to the i-th l-MO (to the d-shell):

$$\begin{aligned} \Delta E_{di} &= -A_i + I_d \\ \Delta E_{id} &= I_i - A_d, \end{aligned} \tag{21}$$

where I_i and A_i are the ionization potential and the electron affinity of the i-th l-MO within the HFR scheme equal to $-\varepsilon_i$ — the corresponding orbital energy with the opposite sign, I_d and A_d are respectively, the effective ionization potential and the electron affinity of the d-shell. The resonance integrals $\beta_{\mu i}$ in Eq. (20) are given by:

$$\beta_{\mu i} = \sum_\alpha \beta_{\mu\alpha} c_{i\alpha}$$

where $c_{i\alpha}$ is the MO-LCAO coefficient, and $\beta_{\mu\alpha}$ is the resonance integral between the α-th l-AO and the μ-th d-AO.

3.4. SEMIEMPIRICAL IMPLEMENTATIONS OF THE EHCF CONSTRUCT

In the context of the EHCF construct described in the previous Section, the problem of semiempirical modelling of TMCs' electronic structure is seen in a perspective somewhat different from that of the standard HFR MO LCAO-based setting. The EHCF provides a framework which implicitly contains the crucial element of the theory: the block of the two-electron density matrix cumulant related to the d-shell. Instead of hardly systematic attempts to extend a parameterization to the transition metals it is now

possible to check in a systematic way the value of different parameterization schemes already developed in the "organic" context for the purpose of estimating the quantities necessary to calculate the crystal field according to prescriptions Eqs. (18) - (20) of the EHCF theory. Solving the eigenvalue problem with the effective Hamiltonian for the d-subsystem (H_d^{eff}) with the matrix elements which are estimated with use of any "organic" semiempirical scheme with the CI wave function constructed in the basis of the d-system, one obtains the complete description of the many-electron states of the d-shell of the metal ion in the complex. In such a formulation the EHCF method was parameterized for calculations of various complexes of metals of the first transition row, with mono- and polyatomic ligands. In papers [133–136] the parameters for the compounds with donor atoms C, N, O, F, Cl and for doubly and triply charged ions of V, Cr, Mn, Fe, Co, Ni and Cu are fitted. These parameters do not depend on details of chemical structure of the ligands, rather they are characteristic for each pair metal-donor atom. The dependence of the exerted effective field on the details of geometry and chemical composition of the ligands is to be reproduced in a frame of a standard HFR-based semiempirical procedure applied to the latter. The further evaluations [137, 138] have shown applicability of the fitted system of parameters for calculations of electronic structure and spectra of numerous complexes of divalent cations with use of merely the CNDO parameterization for the l-system. In [139, 140] the EHCF method is also extended for calculations of the ligands by the INDO and MINDO/3 parameterizations. In all calculations the experimental multiplicity (spin) and spatial symmetry of the corresponding ground states was reproduced correctly. The summit of this approach had been reached in Ref. [141] by calculations on the *cis*-$[Fe(NCS)_2(bipy)_2]^{2+}$ complex. Its molecular geometry is known both for the HS and LS isomers of the said compound. The calculation for the both reproduces the respective ground state spins and the spectra of low lying d-d-excitations in a remarkable agreement with experimental data.

Another good example is the treatment of metal porphyrins with use of the EHCF method. As it is already said above, for the decades the *ab initio* methods fail to reproduce the experimental ground state of Fe(II) porphyrin. It is really a complex case since it is an intermediate spin ($S = 1$— *i.e.* neither HS nor LS) and spatially degenerate state (^3E). Applying even very sophisticated methods (including CASPT2 which is considered to be a method of choice for TMCs in the *ab initio* area) has not yet led to the desired success. According to [54] the HS forms are ground states and the hope to get a correct result is rather meagre since the gap amounts up to 1 eV in favor of the HS state (although the interpretation given in Ref. [54] is quite different). Meanwhile the EHCF method in its simplest setting (CNDO type of parameterization employed for the l-system) yields the experimental ground state ^3E without any further adjustment of parameters.

3.5. EHCF *VS.* LFT AND AOM

The success of the EHCF method in reproducing the crystal field from geometry data and ligand electronic structure as described by semiempirical QC procedure poses a question on possible relation between the EHCF method and the successful parameterization scheme for the LFT, the already mentioned AOM. As it is shown below, a local version of the EHCF method EHCF(L) derived and tested in our papers [28, 29] represents an effective tool allowing to estimate the AOM parameters with a good precision. The derivation consists of two unitary transformations. The first one is from the basis of canonical MOs (CMOs) of the l-system used in Eq. (20) to the basis of localized one-electron states representing characteristic features of the ligand electronic structure — like presence of lone pairs on the donor atoms. These are obtained by the max Ψ^4 localization procedure [142]. This leads to the approximate formula for the covalent contribution Eq. (20) to the effective crystal field:

$$W_{\mu\nu}^{cov} = \sum_{\Lambda} \sum_{L\in\Lambda} \beta_{\mu L}\beta_{\nu L} G_{LL}^{adv}(A_d) \tag{22}$$

where Λ enumerates the ligands, the subscripts L enumerate the one-electron local states (*e.g.* lone pairs – LP's) residing on the donor atoms, and $\beta_{\mu L}$ is the resonance integral between the μ-th AO of the d-shell and the L-th local state. The advanced Green's function $G_{LL}^{adv}(\epsilon)$ for the local state L in Eq. (22) is given by

$$G_{LL}^{adv}(\epsilon) \;=\; -\sum_i \frac{n_i c_{iL}^2}{\epsilon - (g_{di} - \epsilon_i)} \tag{23}$$

where c_{iL} is the coefficient of the LP's expansion over CMO's, g_{di} is the interaction energy between d-electron and electron on the i-th MO, and ϵ_i is the energy of the i-th CMO of the l-system in the TMC.

The second transformation is that of the d-orbitals from the global (laboratory) coordinate frame (GCF) to the diatomic coordinate frame (DCF) related to the ligand Λ, defined so that its z-axis is the straight line connecting the metal atom with the ligand donor atom, so that the resonance integrals $\beta_{\mu L}$ in Eq. (22) can be expressed through the $\mathbf{t}^L$ vector of the resonance integrals between the metal d-AO's and the L-th LMO in the DCF:

$$\beta_{\mu L} = \sum_{\lambda} R_{\lambda\mu}^{\Lambda} t_{\lambda}^{L}. \tag{24}$$

The coefficients $R^{\Lambda}_{\lambda\mu}$ form a unitary matrix $\mathbf{R}^{\Lambda}$ transforming d-orbitals from the GCF to the DCF. Then, introducing the quantities:

$$e^{\Lambda}_{\lambda\lambda'} = \sum_{L\in\Lambda} t^{L}_{\lambda} G^{adv}_{LL}(A_d) t^{L+}_{\lambda'}, \tag{25}$$

we obtain

$$W^{cov}_{\mu\nu} = \sum_{\Lambda\lambda\lambda'} R^{\Lambda}_{\mu\lambda} e^{\Lambda}_{\lambda\lambda'} R^{\Lambda}_{\nu\lambda'} \tag{26}$$

where the matrix elements $e^{\Lambda}_{\lambda\lambda'}$ of the $\mathbf{e}^{\Lambda}$ matrix in the DCF are labelloed by the indices $\lambda\lambda'$ taking values $\sigma, \pi_x, \pi_y, \delta_{xy}, \delta_{x^2-y^2}$ according to the symmetry of the metal d-orbitals with respect to the z-axis of the DCF. Eq. (26) precisely coincides with the definition of the synonymic AOM parameters. On the other hand the expression Eq. (25) defines the $e^{\Lambda}_{\lambda\lambda'}$ parameters in terms of the quantities which can be calculated within the EHCF(L) method. Thus Eq. (25) can be accepted as their definition in the EHCF context. Their relation with the standard AOM [129, 132, 143] is described in details in Ref. [28]. These equations have been used to calculate the values of the e_σ and e_π parameters for a series of octahedral complexes with nitrogen containing ligands. The results were in a good agreement with experimental $10Dq$ values (within 10% accuracy). By this it was shown that the splitting parameter $10Dq$ can be estimated with the error not exceeding 0.1 eV which compares to that of the EHCF method itself.

3.6. HYBRID EHCF/MM METHOD

The EHCF methodology allowed to perform systematic calculations of the crystal field for various ligand environments. The results of these calculations are in fair agreement with the experimental data, particularly with respect to the spin multiplicity of the ground states of the complexes. In the respective simple versions the EHCF/X methods treat the electronic structure of the ligands within a semiempirical approximation X. These methods are not, however, well suitable to conduct the systematic studies on PESs of TMCs. Further application of the EHCF methodology would be to develop a method for the calculation of PESs of TMCs. To do so we notice that the CNDO or INDO parameterizations for the ligands are probably enough accurate when it goes about the charge distribution in the ligands and the orbital energies at fixed experimental geometries, although, they do not suit for geometry optimizations (or more generally for searching PESs) of TMCs. Nevertheless, the EHCF method can be adapted for the PES search in a more general framework of the hybrid QM/MM methodology (standard reference here is [144]; for recent review see [57]). This finally allows to "incorporate" quantum and correlated behavior of TMC into the "classical" methodology of MM and to provide necessary flexibility for quantum/classical interface (see below).

This is done as follows. According to [36] the total electronic energy of the n-th state of a system with the wave function Eq. (15) is

$$E_n = E_d^{eff}(n) + E_l \tag{27}$$

where $E_d^{eff}(n)$ is the energy of n-th state of the effective Hamiltonian for the d-shell in the crystal field. For estimating the total energy E_n for the complex in n-th state, in work [28] we proposed to replace the energy of ligands E_L by its E_{MM} estimate calculated in certain MM approximation. Then the expression for the PES of the state n becomes:

$$E_n = E_d^{eff}(n) + E_{MM} \tag{28}$$

This represents a natural way of combining MM and EHCF [28], allowing to calculate energies of low-level electronic states of the d-shell $E_d^{eff}(n)$ and the ligand energy E_{MM} for different nuclear configurations of TMC. In variance with the LFSE-based method proposed by Deeth [30] the energy of the d-shell is calculated by a procedure taking into account qualitative manifestations of electronic correlation rather than using a one-electron estimates of the energy. By this it becomes possible to obtain approximate PES for various spin states of the d-shell of TMC.

Appropriate test objects for this approach are provided by the spin isomers of TMCs already addressed in the context of the attempts to apply the DFT-based methods to them. As during spin transition (ST) variation of the Fe–N bond lengths makes up more than 10% of the bond length itself in the LS complex, the harmonic approximation does not suffice for the MM part of the energy. Thus, for Fe–N bond stretching potentials the Morse potential was used. By Eq. (28) terms of the singlet, triplet and quintet lowest states of the considered complex were constructed. Parameters of MM-potentials at metal atom (angle bending and bond stretching) are fitted so that positions of minima on terms of singlet and quintet as much as possible coincide with experimental distances Fe–N in HS- and LS-structures. The calculation has been carried out in our work [28].

The general scheme Eq. (28) of energy evaluation using the EHCF method for $E_d^{eff}(n)$ requires an HFR semiempirical calculation of the l-system for each geometry of a complex. To clear this, the local version of the EHCF method which allows to calculate the crystal field at each geometry without repeating HFR calculations can be employed. The problem is how to calculate the covalent contribution to the splitting without recalculating the one-electron states of the l-system at each geometry. In Section 3.5 we reviewed the EHCF(L) theory which allows to estimate the crystal field in terms of local electronic structure parameters (ESP) of the ligands. By this method it can be done for arbitrary geometry of the complex, which is necessary for developing a hybrid QM/MM method.

The proposed approach in certain respects is resemblant to the general QM/MM techniques which are invented with the general purpose to treat different parts of polyatomic systems at different levels of theory. The general setting of this theory is discussed in detail in [57]. The main difference between the setting of the standard QM/MM technique and the present one is that the majority of authors working in the area of QM/MM see as a desirable feature a possibility to extend the subsystem to be treated on a quantum level as much as possible. This is seen as a medicine against the uncontrollable errors introduced by non-cautious cutting the entire electronic system in parts treated by the QM and MM techniques respectively. The hybrid EHCF/MM technique uses somewhat opposite approach: it tries not to extend but to reduce the QM subsystem as much as possible and to treat the inter-subsystem frontier in such a way that the interactions between the quantically and classically treated parts are sequentially taken into account. Since physically the true quantum effects — the low-energy excited states in TMCs, — are located in the *d*-shell we restrict the true quantum description to these latter. This is related to the very understanding of the notion "quantum" relevant to the present problem which we have already mentioned at the beginning: in organic chemistry one normally deals with the ground state only which on the energy scale is well separated from the lowest excited state. This is the physical reason why the classical (MM) description is possible for organics. The TMCs differ from that picture obviously due to low-energy excitations in the *d*-shell accessible in experiment, thus it must be treated on a quantum level.

The technical problem was to develop an adequate form of the inter-subsystem junction for the case when the quantum subsystem reduces to the *d*-shell. The problem here is to keep clear advantage of the LFT taking into account the ligands' electronic structure over the CFT reproducing it economically in the otherwise MM calculation.

Since in the EHCF(L) the effective crystal field is given in terms of the l-system Green's function, the natural way to go further with this technique is to apply the perturbation theory to obtain estimates of the l-system Green's function entering Eqs. (22) and/or (25). It was assumed and reasoned in [29] that the bare Green's function for the l-system has a block-diagonal form:

$$\mathbf{G}^{l}_{00} = \bigoplus_{\Lambda} \mathbf{G}^{\Lambda}_{0}, \tag{29}$$

where $\oplus$ stands for the direct summation over ligands. The non-vanishing block $\mathbf{G}^{\Lambda}_{0}$ corresponds to a separate ligand Λ containing the unperturbed diagonal Green's function matrix elements $(G^{\Lambda}_{0}(\epsilon))^{adv}_{LL}$ corresponding to the LP L located on the ligand Λ:

$$(G^{\Lambda}_{0}(\epsilon))^{adv}_{LL} = \lim_{\delta\to 0^{+}} \sum_{i\in\Lambda} \frac{(c^{\Lambda}_{iL})^{2} n_i}{\epsilon - \epsilon^{(0)}_{\Lambda i} + i\delta} \tag{30}$$

where c^{Λ}_{iL} is the same expansion coefficient as in eq.(23) but for the LP of the separate ligand Λ, and $\epsilon^{(0)}_{\Lambda i}$ is the i-th MO energy of that same free ligand. Then Eq. (22) contains the Green's function $(G^{\Lambda}_0(\epsilon))^{adv}_{LL}$ of the free ligand and the summations in Eq. (22) is performed over the separate ligands Λ and their LPs indexed by L.

The Coulomb interaction between the ligands themselves and between each of them and the metal ion when turned on does not break the block diagonal structure of the bare Green's function $\mathbf{G}^{l}_{00}$. Then the approximate Green's function for the l-system conserves the form Eq. (29) but with the poles corresponding to the orbital energies of the ligand molecules in the Coulomb field induced by the central ion and by other ligands ($\Lambda' \neq \Lambda$) rather than to those of the free ligands.

The simplest picture of the effect of the central ion on the surrounding ligands reduces to that of the Coulomb field affecting the positions of the poles of the Green's function (orbital energies) of the free ligand. The form of the CMO's of each ligand is left unchanged which corresponds to the rigid ligands' MO's (RLMO) picture Ref. [29]. According to [145], the effect of the Coulomb field upon the orbital energies is represented by:

$$(G^{\Lambda})^{-1} = (G^{\Lambda}_0)^{-1} - \Sigma^{(f)} \tag{31}$$

where G^{Λ}_0 is the Green's function for the free ligand and the self-energy term $\Sigma^{(f)}$ is due to the external Coulomb field. The perturbed Green's function G^{Λ} within the first order has the same form as G^{Λ}_0 but its poles are shifted by the self-energy parts $\Sigma^{(f)}_{ii}$:

$$\begin{aligned} \epsilon_i &= \epsilon^{(0)}_i + \Sigma^{(f)}_{ii}, \\ \Sigma^{(f)}_{ii} &\approx \sum_{N\in\Lambda} \rho_{iN}\delta h_N, \end{aligned} \tag{32}$$

where ρ_{iN} is the partial electron density of the i-th CMO of the ligand Λ on the N-th atom of the ligand:

$$\rho_{iN} = \sum_{\alpha\in N} c^2_{i\alpha}, \tag{33}$$

where $c_{i\alpha}$ are the i-th MO LCAO coefficients of the free ligand, and the core Hamiltonian perturbation δh_N is:

$$\delta h_N = -e^2 \left(\frac{(Z_M - n_d)}{R_N} + \sum_{\substack{\Lambda'\neq\Lambda \\ N'\in\Lambda'}} \frac{Q_{N'}}{R_{NN'}} \right) \tag{34}$$

The atomic quantities δh_N are equal to the perturbations $\delta h_{\alpha\alpha}$ of the corresponding core Hamiltonian matrix elements in the ligand AO basis. This

is like that since within the CNDO approximation [62] accepted in [29],the quantities $\delta h_{\alpha\alpha}$ are the same for all $\alpha \in N$.

This model can be improved by taking into account polarization effects in the ligand sphere. For this end the metal ion is considered as a point charge equal to its oxidation degree or formal charge, which is the "sparkle" model [146].

Within models of the sparkle family the effect of the external Coulomb field does not reduce to the renormalization of the orbital energies as it is within the RLMO model (see above). By contrast, the electron distribution also changes when the ligand molecules are put into the field. We model this by classical polarizability. Accordingly the difference between effective charge on atom A in the complex (polarized) and that in the free ligand (non-polarized) is:

$$\begin{aligned} \delta Q_A{=}Q_A - Q_A^0 &= \sum_B \Pi_{AB}\delta h_B{=} \\ &= \sum_B \Pi_{AB}(\delta h_B^0 + \sum_{C\neq B} \Gamma_{AC}\delta Q_C) \end{aligned} \tag{35}$$

where Π_{AB} is the atomic mutual polarizability and δh_A^0 taken from Eq. (34). Going to the vector notation this can be rewritten as:

$$\begin{aligned} \delta\mathbf{Q} &= \mathbf{Q} - \mathbf{Q}^0 = \mathbf{\Pi}(\delta\mathbf{h}^0 + \mathbf{\Gamma}\delta\mathbf{Q}) \\ \delta\mathbf{Q} &= (1 - \mathbf{\Pi\Gamma})^{-1}\mathbf{\Pi\delta h}^0 \\ \delta\mathbf{Q} &= \mathbf{\Pi\delta h}^0 + \sum_{n=1}^{\infty}(\mathbf{\Pi\Gamma})^n\mathbf{\Pi\delta h}^0 = \sum_{n=1}^{\infty}\delta\mathbf{Q}^{(n)}. \end{aligned} \tag{36}$$

Though procedures of that sort are admitted in modern MM schemes directed to the systems with significant charge redistribution [147] we consider such a procedure to be too resource consuming and restrict ourselves by several lower orders with respect to $\mathbf{\Pi}$ in the expansion Eq. (36). The details on calculating mutual polarizabilities relevant to the EHCF/MM context can be found in Ref. [148]. The charges thus obtained are used for calculation of the $\Sigma_{ii}^{(f)}$ term according to Eq. (32). This model can be termed as PS model (PS stands for Perturbative Sparkle). Specifically, PSn approximation level of the PS model stands for the charge corrections employing the series Eq. (36) up to the n-th order, while PS itself stands for the exact expression with the inverse matrix in the second row of the same equation.

The local version of EHCF method was implemented and used for the analysis of the molecular geometries of complexes of iron (II) in works [29, 148,149]. The satisfactory agreement in the description of complexes geometry with different total spins is achieved when the effect of electrostatic field of the metal ion on the ligands is taken into account through the electrostatic polarization of the ligands. Satisfactory estimates of parameters

of the crystal field for series of complexes of iron (II) and cobalt (II) (both LS and HS ground states) are achieved. Totally 35 six-coordinated iron complexes with mono– and polydentate ligands, containing both aliphatic, and aromatic donor nitrogen atoms (mixed complexes with different types of donor nitrogen atoms and different spin isomers of one complex are included to this number) and ten cobalt complexes also with different types of donor nitrogen atoms and coordination numbers ranging from four to six have been considered. Deviations of calculated bond lengths Fe–N and Co–N from the experimental values are well enough described by the normal distribution. Parameters of that distributions were the following: the mean value (average deviation over the data set, $\mu = -0.037$ Å and σ=0.054 Å in the case of Fe(II) complexes, and μ=0.017 Å and σ=0.044 Å in the case of Co(II) complexes. The above values are quite acceptable for the entire set of data but it turned out that they mask an inherent bias of the proposed approach. In the iron(II) complexes the Fe–N bond lengths of the HS complexes are systematically underestimated whereas those in the LS come out slightly overestimated. In fact the parameters of the fit of the empirical distribution function of deviations restricted to the LS complexes are μ=0.011Å and σ=0.034Å and those restricted to the HS complexes are $\mu = -0.023$Å and σ=0.054Å. The reason seemed to be in the "stiffness" of the Morse potential. In order to avoid this, we tested another MM bond stretching potential for the metal-ligand bonds in Fe(II) complexes:

$$E_{NR}(r) = \frac{A}{r} + \frac{B}{r^5} + \frac{C}{r^9} \tag{37}$$

originally proposed by Níketič and Rasmussen (NR) [150] in their version of the CFF force field. The NR potential can be characterized as a softer potential than the Morse one in the following sense. The two potentials are both three-parametric so that a one-to-one correspondence can be established between the both by defining the potentials of two forms to be equivalent if the well depth, minimum position, and elasticity constants K_{NR} and K_M (the second derivative in the minimum) expressed through the A, B, C parameters of the NR potential Eq. (37) or the r_0, D_0, and α parameters of the Morse potential, respectively, coincide. The necessary estimates can be easily obtained:

$$\begin{aligned} r_0^4 &= \frac{-5B - \sqrt{25B^2 - 36AC}}{2A} \\ D_0 &= \frac{A}{r_0} + \frac{B}{r_0^5} + \frac{C}{r_0^9} \\ K_{NR} &= \frac{A}{r_0^3} + \frac{15B}{r_0^7} + \frac{45C}{r_0^{11}} \\ K_M &= D_0\alpha^2. \end{aligned} \tag{38}$$

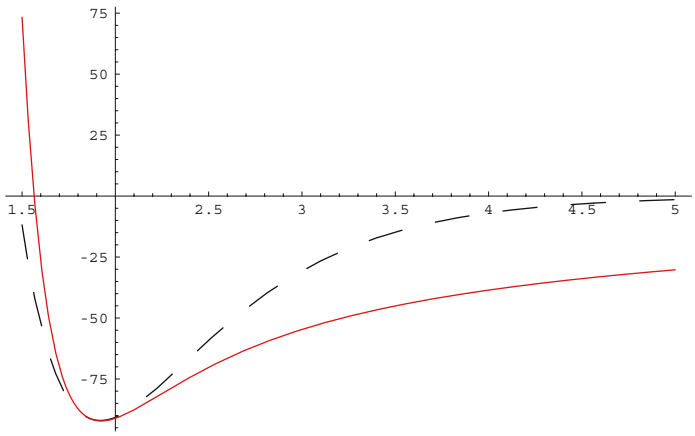

Figure 1. Comparison of the Morse (dashed line) and Níketič–Rasmussen (solid line) potentials. The abscissa axis is the bond length in Å and the ordinate is the energy in kcal/mol.

TABLE 2. Fitted parameters of the NR potential for Fe–N bonds in the EHCF/MM method. Corresponding parameters of the Morse potential calculated by Eq. (38) are also given.

Parameter	Bond	
	Fe–NA	Fe–N3
A, kcal/mol·Å	-189.3	-161.3
B, kcal/mol·Å^5	-1084.4	-1940.9
C, kcal/mol·Å^9	10817.4	19803.2
D_0	110.0	102.9
α	1.49	1.59
r_0	1.88	1.96

Fig. 1 presents the curves of the equivalent Morse and NR potentials. One can see that the NR potential increases much slower in the asymptotic region than the Morse one. The parameters of the NR potential equivalent to the Morse potential fitted in our paper [148] are given in Table 2. The value of the A parameter can be identified with the interaction of some Coulomb charges. Extracting these effective values in Fe(II) complexes with nitrogen-containing complexes we get Q_{Fe}=1.757 e and $Q_N = -0.293$ e; the latter is close to the CNDO charges on the donor nitrogen atoms obtained in the EHCF calculations for hexamine Fe(II) complex [137].

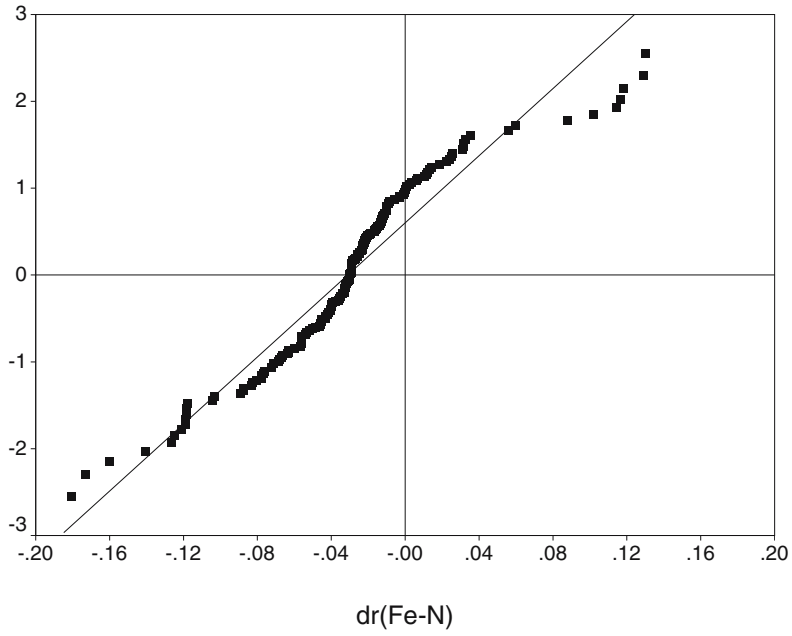

Figure 2. EDF for the difference between the experimental and the EHCF/MM calculated bond lengths (Å) over the entire test set of Fe(II) complexes. The NR potential is used for the Fe–N bond.

Then the NR potential with the parameters of Table 2 is tested on the set of Fe(II) HS and LS molecules described in the paper [148]. The corresponding empirical distribution functions (EDFs) for the Fe–N distances' deviations for the overall data set and for the HS and LS subsets separately, are given in Figs. 2–4 We get the following characteristics of the normal distribution of the deviations for the EHCF/MM calculations with NR potential on the overall data set: $\mu = -0.031$ Å, σ=0.052Å. The both parameters are smaller than those obtained for the Morse potential thus indicating some improvement both in terms of systematic errors and the scattering of data. It is clearly seen from the EDF plots however that the systematic error remains; on the other hand, it is also seen that the mentioned difference in descriptions of the LS and HS complexes is now removed so the structures of both types of complexes are now reproduced accordingly with almost the same systematic error.

As it is known, the minima of the HS and LS terms lie on the right and on the left positions relative to the cross-section point of the pure electronic quintet and singlet terms of the *d*-shell in Fe(II) complexes. Systematic error may be due to some shift of that point from its true position. We obtained a negative value of the mean error which is an indication that the cross-section point is shifted towards shorter bond lengths. Thus, moving

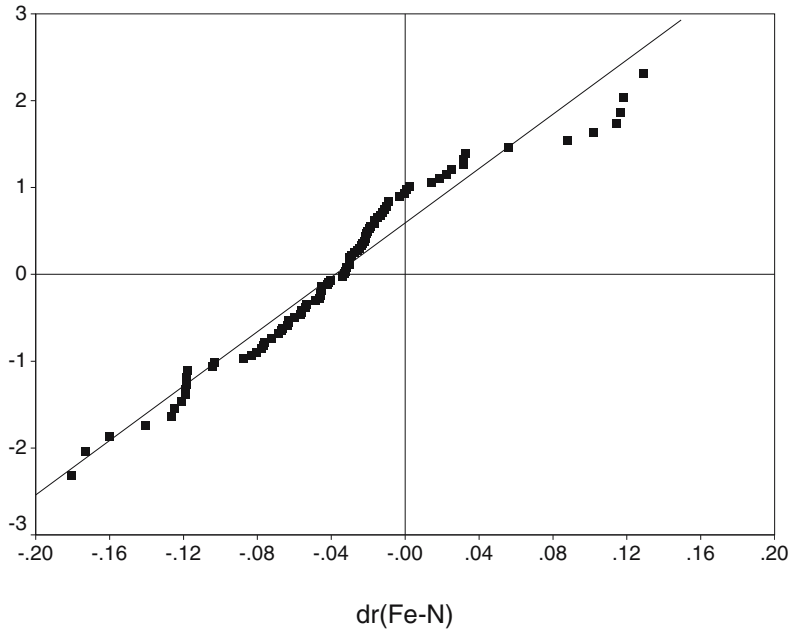

Figure 3. EDF for the difference between the experimental and the EHCF/MM calculated bond lengths (Å) over the HS Fe(II) complexes. The NR potential is used for the Fe–N bond.

the cross-section point to larger Fe–N distances, it is possible to remove the systematic error. To get rid of the systematic error its possible source has to be identified. As discussed in our paper [29], the position of the cross-section point in the EHCF/MM method depends on the the Racah parameters B and C, which we have previously accepted as those for the free ion. The intersection point shift can be achieved by slightly reducing of the Racah parameters as compared to the free ion values, to the values B=850 cm^{-1} and C=3400 cm^{-1}. The set of MM parameters should be also changed in this case. We have done it first for the NR potential. The parameters for the Morse potential are also calibrated independently for the scaled Racah parameters. For the new values see Table 3.

The corresponding EDFs for both potentials calculated for the same test set of the Fe(II) complexes are plotted in Figs. 5, 8. The systematic errors in all cases are close to zero, as can be seen from the parameters of the EDFs: for the EHCF/MM with the Morse potential — $\mu = -0.005$, σ=0.056; with the NR potential — μ =0.002, σ=0.052. However, although somewhat improved the stiffness of the Morse potential again manifests itself: the systematic errors for the separate LS and HS sets do exist and only approximately cancel each other in the total set, whereas for the NR

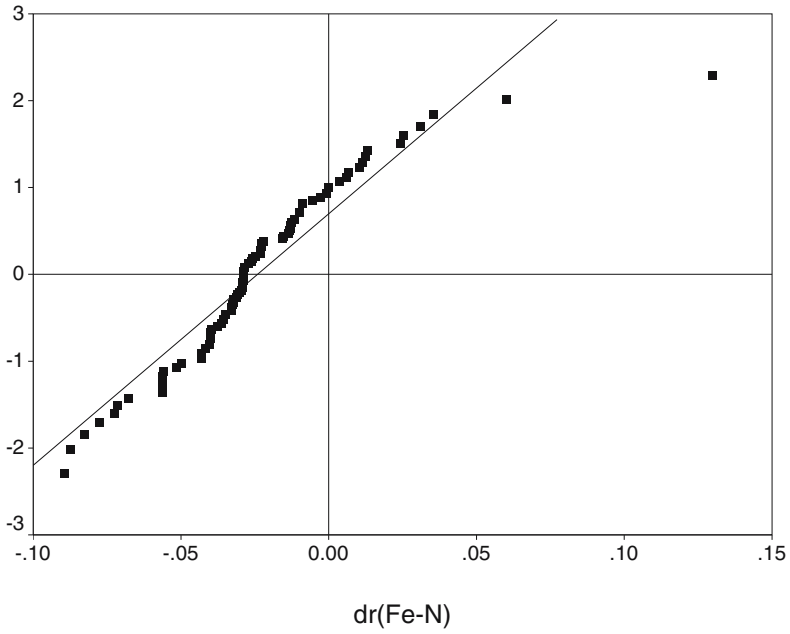

Figure 4. EDF for the difference between the experimental and the EHCF/MM calculated bond lengths (Å) over the LS Fe(II) complexes. The NR potential is used for the Fe–N bond.

TABLE 3. Fitted parameters of the NR and Morse potentials for Fe–N bonds in the EHCF/MM method. The Racah parameters are B=850 cm^{-1}, C=3400 cm^{-1}.

Parameter	Bond	
	Fe–NA	Fe–N3
A, kcal/mol·Å	-149.0	-136.0
B, kcal/mol·Å^5	-1385.0	-1660.0
C, kcal/mol·Å^9	13650.0	18000.0
D_0	73.0	65.0
α	1.69	1.73
r_0	1.94	1.97

potential errors distributions for HS and LS complexes are consistent both having small and close systematic errors due to its "softness", as opposed to the Morse potential.

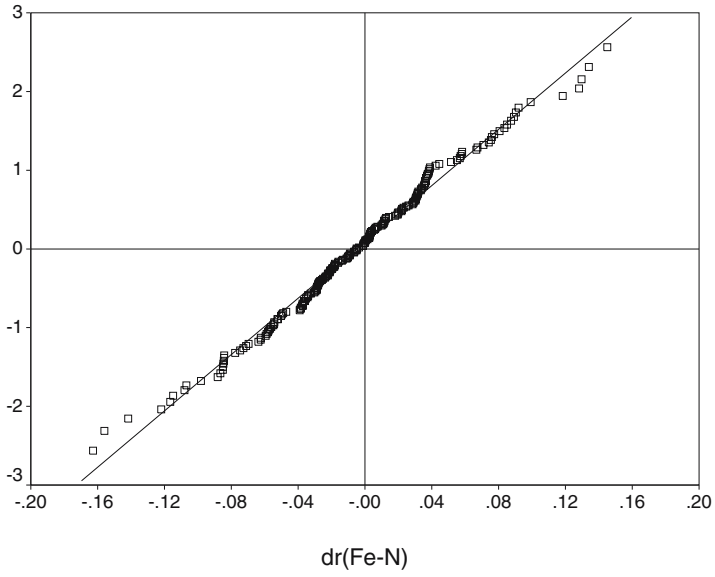

Figure 5. EDF for the difference between the experimental and the EHCF/MM calculated bond lengths (Å) over the entire test set of Fe(II) complexes. The Morse potential is used for the Fe–N bond. The scaled Racah parameters are used for the EHCF calculations (see text).

Among the applications of the EHCF methodology one can also mention a recent one to analysis of the Mössbauer spectra of spin-active compounds. This experimental method received a great attention as one capable to monitor the spin transition due to strong difference between the parameters of the Mössbauer spectra of the LS and HS forms of the iron(II) complexes. In our paper [151] we addressed this topic and it has been shown that, first the EHCF method yields more than acceptable description of the quadrupole splitting in the spin active complexes of iron(II) where the complex geometry was known. In those cases, however, when the geometry was not known from the experiment the EHCF/MM derived geometry has been used to estimate the Mössbauer parameters. It turned out that the agreement with experiment even in the case of the calculation based on the EHCF/MM optimized geometry is very good. Particularly in the more difficult case of LS complexes the results in all cases practically coincided with experimental ones although the magnitude of the quadrupole splitting itself is rather small (in the range $0.1 \div 0.2$ mm s^{-1}). By contrast applying the DFT (hybrid) procedure to estimating the Mössbauer parameters in [104] in the case of the LS complexes gave rather poor results: the experimental splittings for the series of complexes in that paper were in the range 0.30

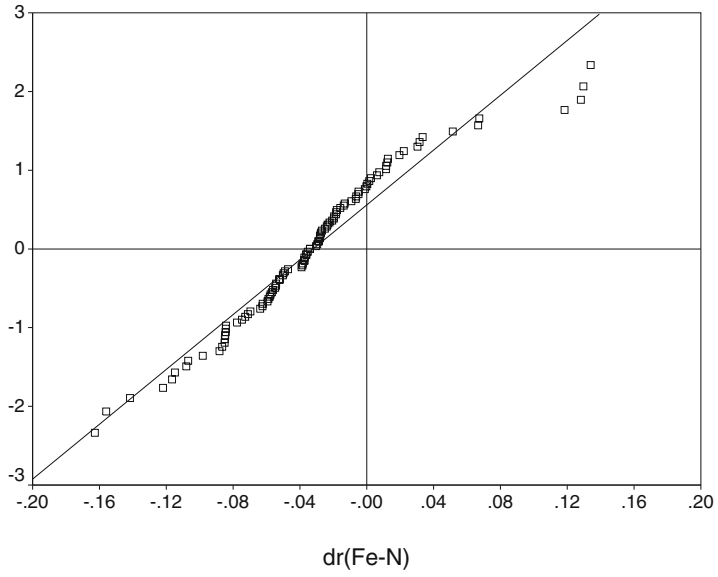

Figure 6. EDF for the difference between the experimental and the EHCF/MM calculated bond lengths (Å) over the HS Fe(II) complexes. T he Morse potential is used for the Fe–N bond. The scaled Racah parameters are used for the EHCF calculations (see text).

$\div$ 0.43 mm s^{-1}, whereas the DFT estimates were in the range 0.01$\div$ 0.12 mm s^{-1} which is obviously too low. Meanwhile for the HS complexes even the temperature dependence of the quadrupole splitting is quite decently reproduced [151] within the EHCF method.

Thus, a set of semiempirical methods based on EHCF approach allows with good precision to calculate geometrical (structure) and spectral (splitting, electronic and Mössbauer spectra) characteristics of Fe(II) and Co(II) complexes, which is hardly accessible by existent QC methods or can be done only by enormous computational cost.

4. Discussion

In the present paper we tried to demonstrate that the problems faced by most empirical and by (actual and so called) *ab initio* techniques when applied to modelling TMCs have deep roots in the specific features of the electronic structure of the latter and in approximations which tacitly drop the necessary elements of the theory required to reproduce these features. Of course, the EHCF approach whose success story is described here in details is not completely isolated from other methods. In general picture, the various CAS techniques must be mentioned in relation to it. The char-

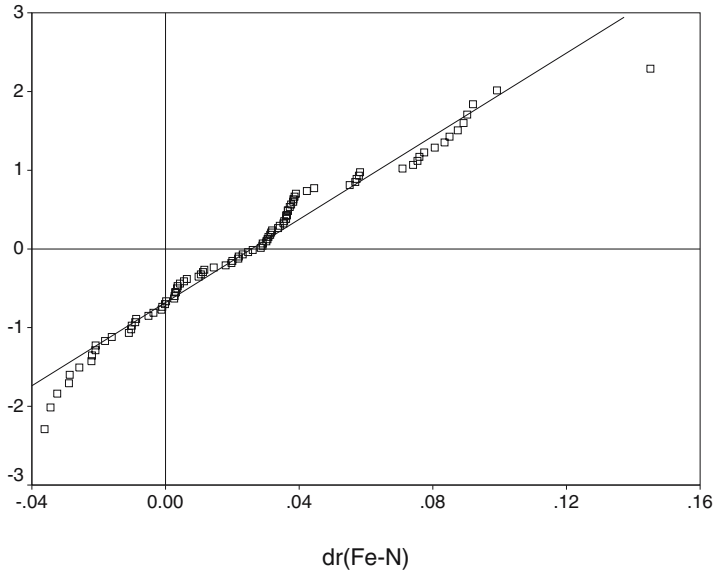

Figure 7. EDF for the difference between the experimental and the EHCF/MM calculated bond lengths (Å) over the LS Fe(II) complexes. The Morse potential is used for the Fe–N bond. The scaled Racah parameters are used for the EHCF calculations (see text).

acteristic feature uniting these two otherwise very different approaches is the selection of a small subset of one electron states followed by performing adequately complete correlation calculation restricted to this smaller subset. The general problem with such approaches is that usually it is taken for granted that the HRF MO LCAO is a good source for obtaining the states to be used in the correlated calculation. Two pitfalls can be expected and actually occur on this route. The first is that in the TMCs the HFR MO LCAOs can be difficult to obtain or those obtained are of a poor quality. The second is that even if the MO LCAOs are obtained correctly, they provide too much delocalized picture of electron distribution. In terms first proposed by J.-P. Malrieu and then extensively used by P. Fulde it is equivalent to saying that in the HFR solution for the TMC the number of electrons in the *d*-shell too much fluctuates around may be correct average (integer) value. In both cases the limited CI (CAS) techniques are applied to improve a very poor zero approximation. Taking only five MOs of appropriate symmetry to model the *d*-shell may be too naïve since the number of states to be included in the CI formation to reduce the excessive fluctuations must be much larger. Going to the one-electron states obtained from the canonical MO LCAOs by some localization technique, may be useful, but numerically expensive. The EHCF here advantageously uses the fact that the exact wave function of the TMCs most probably corresponds to very

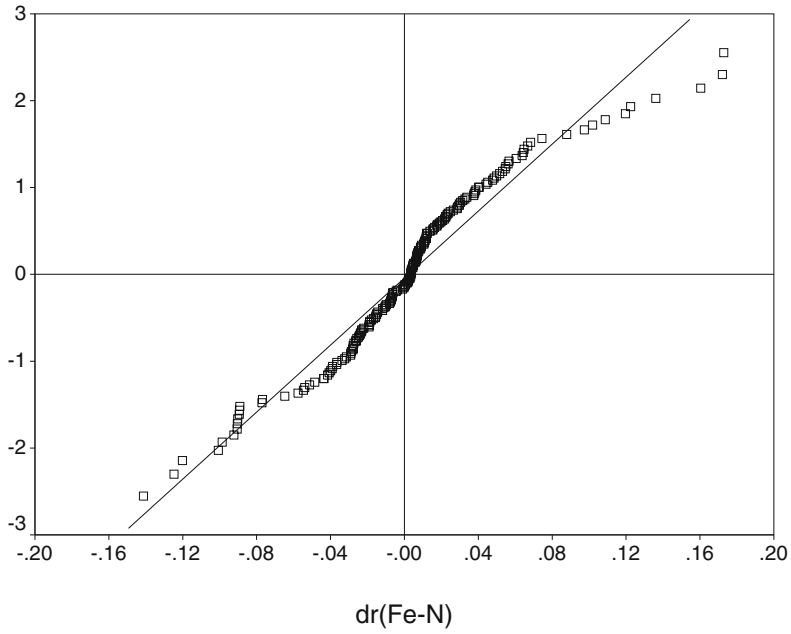

Figure 8. EDF for the difference between the experimental and the EHCF/MM calculated bond lengths (Å) over the entire test set of Fe(II) complexes. The NR potential is used for the Fe–N bond. The scaled Racah parameters are used for the EHCF calculations (see text).

high localization of electrons in the *d*-shell which enables taking their delocalization into account as a perturbation. Among other approaches based on a similar vision of the situation in TMCs ones of Refs. [152, 153] must be mentioned.

When it comes to the analysis of similar approaches stemming from the DFT the numerous attempts to cope with the multiplet states must be mentioned [113, 154]. In these papers attempts are made to construct symmetry dependent functionals capable to distinguish different multiplet states in a general direction proposed by [99, 100]. It turns out, however, that the result [113] is demonstrated for the lower multiplets of the C atom which are all Roothaan terms. It is not clear whether this methodology is going to work when applied to the *d*-shell multiplets which may be either non-Roothaan ones or even nontrivially correlated multiple terms.

Another group of approaches can be qualified as an attempt of using DFT based methods in order to evaluate the parameters of the CFT/LFT theory. In this respect the papers [87,115] must be mentioned. The latter, in a sense, follows the same line as the old semiempirical implementation [77] where the MOs for the TMC molecule are first obtained by an approximate

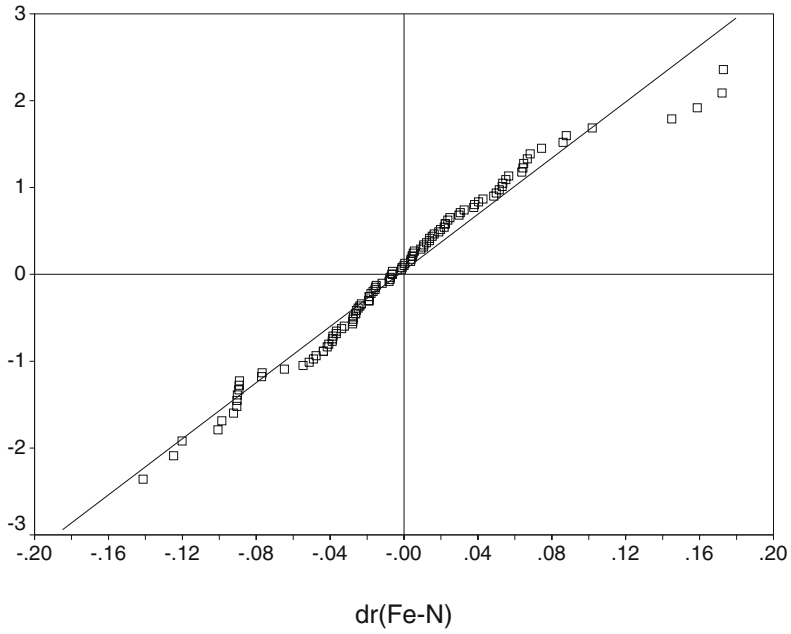

Figure 9. EDF for the difference between the experimental and the EHCF/MM calculated bond lengths (Å) over the HS Fe(II) complexes. The NR potential is used for the Fe–N bond. The scaled Racah parameters are used for the EHCF calculations (see text).

SCF-like procedure and then a CI is done in some restricted subspace of the latter. In some sense, this approach is similar to the EHCF model too with the general difference that the one-electron states used to construct the complete CFT/LFT manifold are taken "as is" from the KS calculation. In this case one can expect some difficulties while selecting the MOs into the set of those to be used in constructing the CI (it is not obvious whether simple energy/symmetry criteria allow to select the necessary manifold of the KS orbitals to reproduce the states in the *d*and what shall be done when the symmetry is low?). Also the degree of delocalization of the KS orbitals may interfere in evaluation of the CFT/LFT parameters from the results of the DFT calculation. It looks like that it happened in [115] where the values of the Racah parameters turned out to be strongly underestimated as compared to the values known to fit the experiment within the CFT/LFT model by this indicating the excess of delocalization of the KS orbitals as compared to that necessary to reproduce the experimental data.

Generally one can notice that almost whatever review on computational chemistry of TMCs starts from a sort of "triple denial" of the old CFT/LFT approaches as being pertinent to something which was happening "once upon a time". Our point of view on the CFT/LFT picture is absolutely

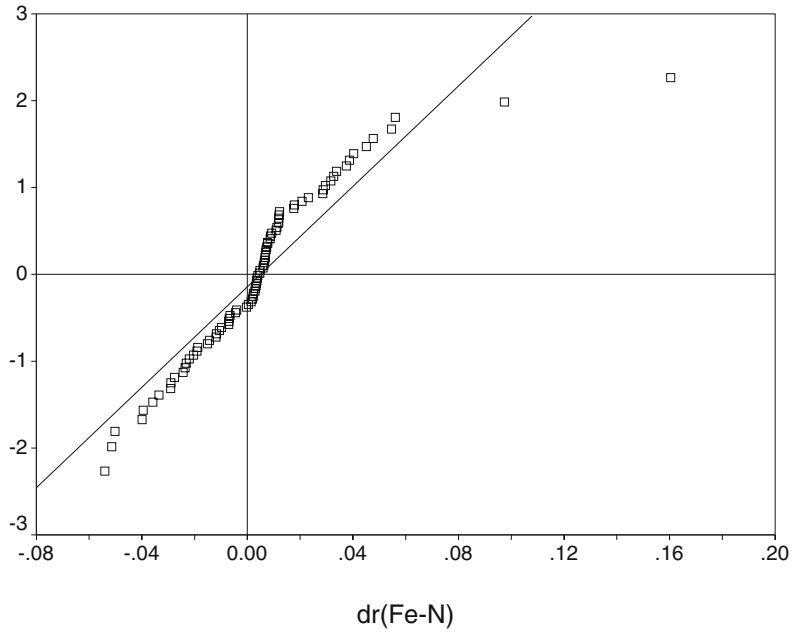

Figure 10. EDF for the difference between the experimental and the EHCF/MM calculated bond lengths (Å) over the LS Fe(II) complexes. The NR potential is used for the Fe–N bond. The scaled Racah parameters are used for the EHCF calculations (see text).

different. It more or less corresponds to that given in the brilliant introduction to the paper [87]. The clear-cut conclusion to be derived from there is that the CFT/LFT picture keeps track of very physical picture of the low-energy spectrum of the TMCs. Whatever discrepancy between the results obtained by no matter how refined QC methods and those appearing from the CFT/LFT must be considered as failures of the QC rather than "age effects" of the CFT/LFT. It is the purpose for a QC study to reproduce results obtained within the CFT/LFT paradigm and it is not easily reachable and in many cases has not been reached yet. This idea was the leading one in our studies on TMCs from very beginning and its adequate formal representation in terms of the group functions and the Löwdin partition technique provided a crucial step forward which allowed the numerical implementation of the EHCF method [133]. It immediately solved the problem of constructing semi-empirical description of the TMCs which otherwise remained unaccessible for 30 years. The cost of this was rejecting the HFR from of the wave function of the TMC which in the present context cannot be considered as a big loss. Further development of this approach and realizing its deeper relation to the general QM/MM setting helped in evolving the corresponding EHCF/MM hybrid scheme.

The latter is in relation with those proposed by Deeth [30] and Berne [155]. Both involve the *d*-shell energy as an additional contribution to that of the MM scheme and use the AOM model with interpolated parameters to estimate the latter. In the case of the approach [30] there are two main problems. First is that the AOM parameters involved are assumed to depend only on the separation between the metal and donor atoms. This is obviously an oversimplification since from the formulae Eq. (25) it is clear that the lone pair orientation is of crucial importance. This is taken into account in the EHCF/MM method. Second important flaw is the absence of any correlation in describing the *d*-shell in the model [30]. This precludes correct description of the switch between different spin states of the open *d*-shell, although in some situations different spin states can be described uniformly.

5. Conclusion

In the present paper we demonstrated the feasibility of a semiempirical description of electronic structure and properties of the Werner TMCs on a series of examples. The main feature of the proposed approach was the careful following to the structural aspects of the theory in order to preclude the loss of its elements responsible for description of qualitative physical behavior of the objects under study, in our case of TMCs. If it is done the subsequent parameterization becomes sensible and successful solutions of two long lasting problems: semi-empirical parameterization of transition metals complexes and of extending the MM description to these objects can be suggested.

Acknowledgements

This work is supported by RFBR grants Nos 04-03-32146 and 04-03-32206. The authors are thankful to Profs. Paul Ziesche, Lothar Fritsche, Francesc Illas, and Marc Casida for sending (p)reprints of their work, to Profs. I.G. Kaplan, E. Ludeña, J.-P. Julien and Dr. V.I. Pupyshev for valuable discussions. The organizers of the 9-th European Workshop on Quantum Systems in Chemistry and Physics (QSCP-9) at Les Houches (France) are acknowledged for a kind support extended to A.L.T.

References

1. Thomas Aquinas. *De Unitate Intellectus Contra Averroistas*. Sancti Thomae Aquinatis Opera Omnia. 1980.
2. U. Burkert, N. L. Allinger. *Molecular mechanics*. Washington: ACS, 1982.
3. V. G. Dashevskii. *Conformational Analysis of Organic Molecules*. Khimiya, Moscow, 1982. [in Russian].
4. A. K. Rappé, C. J. Casewit, K. S. Colwell, III W. A. Goddard, W. M. Skiff. *J. Am. Chem. Soc.*, 1992, 114:10024–10053.

5. A. K. Rappé, K. S. Colwell, C. J. Casewit. *Inorg.Chem.*, 1993, 32:3438–3450.
6. B.P. Hay. *Coord. Chem. Rev.*, 1993, 126:177–236.
7. B. P. Hay, L. Yang, J.-H. Lii, N. L. Allinger. *J. Mol. Struct. (THEOCHEM)*, 1998, 428:203–219.
8. P. Comba, T. Hambley. *Molecular modeling of inorganic compounds*. VCH, 1995.
9. P. Comba, R. Remenyi. *Coord. Chem. Rev.*, 2003, 238-239:9–20.
10. H. Erras-Hanauer, T. Clark, R. Van Eldik. *Coord. Chem. Rev.*, 2003, 238-239:233–253.
11. P. Comba. *Coord. Chem. Rev.*, 1999, 182:343–371.
12. M. Zimmer. *Coord. Chem. Rev.*, 2003, 212:133–163.
13. R. D. Hancock. *Prog. Inorg. Chem*, 1989, 37:187.
14. D. L. Kepert. *Inorganic Stereochemistry*. Springer, Berlin, 1982.
15. I. V. Pletnev, V. L. Melnikov. *Koord. Khim.*, 1997, 23:205. [in Russian].
16. M. G. Razumov, V. L. Melnikov, I. V. Pletnev. *J. Comp. Chem.*, 2001, 22:38.
17. J. Sabolović. *Polyhedron*, 1993, 12:1107–1113.
18. J. Sabolović, Kj. Rasmussen. *Inorg. Chem.*, 1995, 34:1221–1232.
19. I. M. Atkinson, L. F. Lindoy. *Coord. Chem. Rev.*, 2000, 200-202:207–215.
20. M. Gruden, S. Grubišić, A. G. Coutsolelos, S. R. Niketić. *J. Mol. Struct.*, 2001, 595:209–224.
21. C. Millot, R. Dehez. *J. Comp. Meth. Sci. Eng.*, 2002, 2(3s-4s):451–456.
22. P. Gütlich. *Struct. Bond.*, 1981, 44:83.
23. E. König, G. Ritter, S. K. Kulshreshtha. *Chem. Rev.*, 1985, 85:219–234.
24. E. König. Nature and dynamics of spin-state interconversion in metal complexes. volume 76 of *Struct. Bond.*, pages 53 – 151. Springer-Verlag, 1991.
25. P. Gütlich, H. A. Goodwin, editors. *Spin Crossover in Transition Metal Compounds*, volume 233-235 of *Topics Curr. Chem.* Springer-Verlag, 2004.
26. I. B. Bersuker. *Jahn-Teller Effect and Vibronic Interactions in Chemistry*. Nauka, Moscow, 1990. [in Russian].
27. V.I. Pupyshev. *Int. J. Quant. Chem.*, 2005. [Submitted].
28. M. B. Darkhovskii, A. L. Tchougréeff. *Khim. Fiz.*, 1999, 18(1):73–79. [in Russian].
29. M. B. Darkhovskii, M. G. Razumov, I. V. Pletnev, A. L. Tchougréeff. *Int. J. Quant. Chem.*, 2002, 88:588–605.
30. R. J. Deeth. *Coord. Chem. Rev.*, 2001, 212:11–34.
31. H. M. Marques, O. Q. Munro, N. E. Grimmer, D. C. Levendis, F. Marsicano, G. Pattrick, T. Markoulides. *J. Chem. Soc. Faraday Trans.*, 1995, 91(2):1741.
32. C. Daul, S. Niketić, C. Rauzy, C.-W. Schlöpfer. *Chemistry - A European Journal*, 2004, 10:721–727.
33. M.B. Darkhovskii, A.L. Tchougréeff. *Unpublished*.
34. T. Ziegler. *Chem. Rev.*, 1991, 91:651–667.
35. P.-O. Löwdin. *Adv. Chem. Phys.*, 1959, 2:207 – 322.
36. R. McWeeny. *Methods of Molecular Quantum Mechanics*. Academic Press, London, second edition, 1992.
37. P. Ziesche. *Physics Lett. A*, 1994, 195:213–220.
38. M.M. Mestechkin. *Density Matrix Method in Theory of Molecules*. Naukova Dumka, Kiev, 1977. [in Russian].
39. B. O. Roos. The complete active space self-consistent field method and its application in electronic structure calculations. In K. P. Lawley, editor, *Ab Initio Methods in Quantum Chemistry. Part II*, volume 69 of *Adv. Chem. Phys.*, pages 399–446. John Wiley, Chichester, 1987.
40. G. D. Purvis, R. J. Bartlett. *J. Chem. Phys.*, 1982, 76:1910.
41. R. A. Chiles, C. E. Dykstra. *Chem. Phys. Lett.*, 1981, 80:69.
42. H.M. Gladney, A. Veillard. *Phys. Rev.*, 1969, 180:385–395.
43. J. W. Richardson, D. M. Vaught, T. F. Soules, R. R. Powell. *J. Chem. Phys.*, 1969, 50(8):3633–3634.
44. J. W. Moskowitz, C. Hollister, C. J. Hornback, H. Basch. *J. Chem. Phys.*, 1970, 53(7):2570–2580.

45. J. Demuynck, A. Veillard. Transition metal compounds. In III H. F. Schaefer, editor, *Applications of Electronic Structure Theory*, pages 187–222. Plenum Press, New York, London:, 1977.
46. A. Veillard. *Quantum Chemistry: The Challenge of Transition Metals and Coordination Chemistry*. Kluwer Academic, 1986.
47. D. J. D. Wilson, C. J. Marsden, E. I. von Nagy-Felsobuki. *J. Phys. Chem. A*, 2002, 106:7348–7354.
48. *Chem. Rev.*, 2000, 100.
49. M. Krauss. *Int. J. Quant. Chem.*, 2002, 76:331–340.
50. V. G. Solomonik, J. E. Boggs, J. F. Stanton. *J. Phys. Chem. A*, 1999, 103:838–840.
51. L. Rulíšek, Z. Havlas. *J. Chem. Phys.*, 2002, 112(1):149–157.
52. A. Dedieu, M.-M. Rohmer, A. Veillard. *Adv. in Quant. Chem.*, 1982, 16:43–97.
53. K. Pierloot. The electronic ground state of iron (II) porphine: A continuing story. In *WATOC'02 Book of Abstracts*, page PC393, Palazzo dei Congressi, Lugano, Switzerland, 2002. WATOC'02.
54. K. Pierloot. *Molecular Physics*, 2003, 101:2083 – 2095.
55. K. Nobuaki, K. Morokuma. *Chemical Reviews*, 1991, 91:823 – 842.
56. D. Balcells, G. Drudis-Solé, M. Besora, N. Dölker, G. Ujaque, F. Maseras, A. Lledós. *Faraday Discuss.*, 2003, 124:429–441.
57. A. L. Tchougréeff, A. M. Tokmachev. Physical principles of constructing hybrid QM/MM procedures. In J. Maruani, R. Lefebvre, E. Brändas, editors, *Advanced Topics in Theoretical Chemical Physics*, volume 12 of *Progress in Theoretical Chemistry and Physics*, pages 207–246. Kluwer, Dordrecht, 2003.
58. G. E. Toney, A. Gold, J. Savrin, L. W. TerHaar, R. Sangaiah, W. E. Hatfield. *Inorg. Chem.*, 1984, 23:4350–4352.
59. D.W. Clack, N.S. Hush, S.R. Yandle. *J. Chem. Phys.*, 1972, 57:3503–3510.
60. D. W. Clack. *Mol.Phys.*, 1974, 27:1513–1519.
61. D. W. Clack, W. Smith. *J. Chem. Soc. Dalton Trans.*, 1974, page 2015.
62. J. A. Pople, D. L. Beveridge. *Approximate Molecular Orbital Theory*. McGraw-Hill Book, New York, 1970.
63. A. D. Bacon, M. C. Zerner. *Theor. Chim. Acta*, 1979, 53:21–54.
64. M. C. Böhm, R. Gleiter. *Theor. Chem. Acta*, 1981, 59:127–152.
65. M. C. Böhm, R. Gleiter. *Theor. Chem. Acta*, 1981, 59:153 – 179.
66. M. J. S. Dewar, C. Jie, J. Yu. *Tetrahedron*, 1993, 49:5003–5038.
67. T. R. Cundari. *J. Chem. Soc., Dalton Trans.*, 1998, pages 2771–2776.
68. T. R. Cundari, J. Deng. *J. Chem. Inf. Comp. Sci.*, 1999, 39:376–381.
69. M. Mohr, J. P. McNamara, H. Wang, S. A. Rajeev, J. Ge, C. A. Morgado, I. H. Hillier. *Faraday Discuss.*, 2003, 124:413–428.
70. T. Clark. *Computational Chemistry*. VCH Verlag, Berlin, 1991.
71. L. Zülicke. *Quantenchemie. Band 1.* Deutscher Verlag der Wissenschaften, Berlin, 1973.
72. I. G. Kaplan. *Int. J. Quant. Chem.*, 2002, 89(4):268–276.
73. T. R. Cundari, J. Deng, W. Fu. *Int. J. Quant. Chem.*, 2000, 77:421.
74. K. R. Adam, I. M. Atkinson, L.F. Lindoy. *J. Mol. Struct.*, 1996, 384:183.
75. V. A. Basiuk, E. V. Basiuk, J. Gómez-Lara. *J. Mol. Struct. (THEOCHEM)*, 2001, 536:17–24.
76. R. Bosque, F. Maseras. *J. Comp. Chem.*, 2000, 21(7):562–571.
77. M. C. Zerner. Intermediate neglect of differential overlap calculations on the electronic spectra of transition metal complexes. In N. Russo D. R. Salahub, editors, *Metal-ligand interactions: structure and reactivity*, pages 493–531, Dordrecht, 1996. NATO ASI Workshop, Kluwer.
78. J. C. Slater. *Adv. Quant. Chem.*, 1972, 6:1–92.
79. A. Messiah. *Quantum Mechanics*, volume 2. 1958.
80. P. Hohenberg, W. Kohn. *Phys. Rev.*, 1964, 136:B864–B871.
81. W. Kohn, L. J. Sham. *Phys. Rev*, 1965, 140(4A):A1133–A1138.
82. Á. Nagy. *Physics Reports*, 1998, 298:1–79.

83. R.K. Nesbet. *Int. J. Quant. Chem.*, 2001, 85:405–410.
84. R. K. Nesbet. *Int. J. Quant. Chem.*, 2004, 100:937–942.
85. J. Li, P. Beroza, L. Noodleman, D. A. Case. In L. Banci P. Comba, editors, *Molecular modeling and dynamics of bioinorganic systems*, page 279, Dordrecht, 1997. Proceedings of NATO ASI workshop, Kluwer.
86. H. Chermette. *Coord. Chem. Rev.*, 1998, 178-180:699.
87. C. Anthon, C. E. Schäffer. *Coord. Chem. Rev.*, 2002, 226:17–38.
88. P. E. M. Siegbahn. *Faraday Discuss.*, 2003, 124:289–296.
89. M. Freindorf, P. M. Kozlowski. *J. Phys. Chem. A*, 2001, 105:7267–7272.
90. L. Rulíšek, Z. Havlas. *Int. J. Quant. Chem.*, 2003, 91:504–510.
91. T. Ziegler, A. Rauk, E.J. Baerends. *Theor. Chem. Acta*, 1977, 43:261.
92. C. C. J. Roothaan. *Rev. Mod. Phys.*, 1960, 32:179–185.
93. B. N. Plakhutin, G. M. Zhidomirov. *Zh. Strukt. Khim.*, 1986, 27(2):3–8. [in Russian].
94. B. N. Plakhutin, G. M. Zhidomirov, A. V. Arbuznikov. *Int. J. Quant. Chem.*, 1992, 41:311–325.
95. A. V. Arbuznikov, B. N. Plakhutin. *Zhurn. Fiz. Khim.*, 1993, 67:1173–1176. [in Russian].
96. E. U. Condon, G. H. Shortley. *The theory of atomic spectra.* Cambridge University Press, Cambridge, second edition, 1951.
97. I. B. Bersuker. *Electronic Structure of Coordination Compounds.* Khimiya, Moscow, 1986. [in Russian].
98. D. T. Sviridov, Yu. F. Smirnov. *Theory of Optical Spectra of Transition-Metal Ions.* Nauka, Moscow, 1977. [in Russian].
99. O. Gunnarsson, B. I. Lundqvist. *Phys. Rev. B*, 1976, 13:4274–4298.
100. U. von Barth. *Phys. Rev. A*, 1979, 20:1693–1703.
101. G. Chen, R. Liu, I. Silaghi-Dumitrescu, G. Espinosa-Perez, A. Zentella-Dehesa, F. Lara-Ochoa. *Int. J. Quant. Chem.*, 2002, 83(2):60–69.
102. H. Paulsen, L. Duelund, H. Winkler, H. Toftlund, A. X. Trautwein. *Inorg. Chem.*, 2001, 40:2201–2203.
103. H. Paulsen, H. Grunsteudel, W. Meyer-Klaucke, M. Gerdan, H.F. Grunsteudel, A.I. Chumakov, R. Ruffer, H. Winkler, H. Toftlund, A.X. Trautwein. *The European Phys. J. B*, 2001, 23:463–472.
104. H. Paulsen, L. Duelund, A. Zimmermann, F. Averseng, M. Gerdan, H. Winkler, H. Toftlund, Alfred X. Trautwein. *Monatshefte für Chemie*, 2003, 134:295–306.
105. P. Gütlich, J. Jung, H. Goodwin. Spin crossover in iron(II)-complexes. In E. Coronado, P. Delhaés, D. Gatteshi, J. Miller, editors, *Molecular Magnetism: From Molecular Assemblies to the Devices*, page 327. Kluwer, 1996.
106. H. Paulsen, A. X. Trautwein. Density functional theory calculations for spin crossover complexes. In P. Gütlich H.A. Goodwin, editors, *Spin Crossover in Transition Metal Compounds III*, volume 235 of *Top Curr Chem*, pages 197–219. Springer-Verlag, 2004.
107. M. Reiher, O. Salomon, B. A. Hess. *Theor. Chem. Acc.*, 2001, 107:48–55.
108. M. Reiher. *Inorg. Chem.*, 2002, 41:6928–6935.
109. O. Salomon, M. Reiher, B. A. Hess. *J. Chem. Phys.*, 2002, 117:4729–4737.
110. C. Lee, W. Yang, R. G. Parr. *Phys. Rev. B*, 1988, 37:785–789.
111. S. H. Vosko, L. Wilk, M. Nusair. *Can. J. Phys.*, 1980, 58:1200.
112. R. K. Szilagyi, M. Metz, E. I. Solomon. *J. Phys. Chem. A*, 2002, 106:2994–3007.
113. Á. Nagy. *Phys. Rev. A*, 1998, 57:1672–1677.
114. N. Hamamoto, C. Satoko. *J. Phys. B*, 2004, 37:4309–4328.
115. M. Atanasov, C. A. Daul, C. Rauzy. *Chem. Phys. Lett.*, 2003, 367:737–746.
116. A. Rosa, G. Ricciardi, O. Gritsenko, E. J. Baerends. Excitation energies of metal complexes with time-dependent density functional theory. In N. Kaltsoyannis J.E. McGrady, editors, *Principles and Applications of Density Functional Theory in Inorganic Chemistry I*, volume 112 of *Structure and Bonding*, pages 49–116. Springer-Verlag, 2004.

117. S. Grimme, M. Waletzke. *J. Chem. Phys.*, 1999, 111:5645.
118. P. A. M. Dirac. *Proc. Camb. Phil. Soc.*, 1929, 25:62.
119. J. Frenkel. *Wave Mechanics: Advanced General Theory.* Clarendon Press, Oxford, 1934.
120. D. J. Thouless. *The Quantum Mechanics of Many-Body Systems.* Academic Press, New York, 1961.
121. D. J. Rowe. *Rev. Mod. Phys.*, 1968, 40:153 – 166.
122. J.-P. Blaizot, G. Ripka. *Quantum Theory of Finite Systems.* The MIT Press, Cambridge, Mass., 1986.
123. R. J. Deeth. *Faraday Discuss .*, 2003, 124:379–391.
124. F. Furche, K. Burke. Time-dependent density functional theory in quantum chemistry. Ann. Rev. Comp. Chem., chapter XX. 2004.
125. K. Burke, J. Werschnik, E. K. U. Gross. *J. Chem. Phys.*, 2005, 123(6):062206. 2005.
126. P. E. Schipper. *J. Phys. Chem.*, 1986, 90(18):4259–4265.
127. H. A. Bethe. *Ann. Physik*, 1929, 3:133–206.
128. C. K. Jorgensen. *Absorption Spectra and Chemical Bonding in Complexes.* Pergamon Press, Oxford, 1962.
129. C. E. Schäffer. *Pure Appl. Chem.*, 1971, pages 361–392.
130. A. V. P. Lever. *Inorganic electronic spectroscopy.* John Wiley, 1985.
131. C. J. Ballhausen. *Indroduction to Ligand Field Theory.* McGraw Hill, New York, 1962.
132. C. E. Schäffer, C. K. Jorgensen. *Mol. Phys.*, 1965, 9:401.
133. A. V. Soudackov, A. L. Tchougréeff, I. A. Misurkin. *Theor. Chim. Acta*, 1992, 83:389.
134. A. V. Soudackov, A. L. Tchougréeff, I. A. Misurkin. *Int. J. Quant. Chem.*, 1996, 57:663.
135. A. V. Soudackov, A. L. Tchougréeff, I. A. Misurkin. *Int. J. Quant. Chem.*, 1996, 58:161.
136. A. V. Sinitsky, M. B. Darkhovskii, A. L. Tchougréeff, I. A. Misurkin. *Int. J. Quant. Chem*, 2002, 88:370–379.
137. A. V. Soudackov, A. L. Tchougréeff, I. A. Misurkin. *Zh. Fiz. Khim.*, 1994, 68(7):1256–1263. [in Russian].
138. A. V. Soudackov, A. L. Tchougréeff, I. A. Misurkin. *Zh. Fiz. Khim.*, 1994, 68(7):1264–1270. [in Russian].
139. A.M. Tokmachev, A.L. Tchougréeff. *Khim. Fiz.*, 1999, 18(1):80–87. [in Russian].
140. A. M. Tokmachev. PhD thesis, Moscow, 2003. [in Russian].
141. A. L. Tchougréeff, A. V. Soudackov, I. A. Misurkin, H. Bolvin, O. Kahn. *Chem. Phys.*, 1995, 193:19.
142. P. G. Perkins, J. J. P. Stewart. *J. Chem. Soc. Faraday Trans.(II)*, 1982, 78:285.
143. M. Gerloch, R. G. Wooley. *Struct. Bond.*, 1983, page 371.
144. A. Warshel, M. Levitt. *J. Mol. Biol.*, 1976, 103(2):227–249.
145. A. A. Abrikosov, L. P. Gor'kov, I. Ye. Dzyaloshinskii. *Quantum Field Theoretical Methods in Statistical Physics.* Pergamon Press, Oxford, 1965.
146. A. V. M. de Andrade, N. B. da Costa Jr., A. M. Simas, G. F. de Sá. *Chem. Phys. Lett.*, 1994, 227:349–353.
147. P. Ren, J. W. Ponder. *J. Comput. Chem.*, 2002, 23:1497–1506.
148. M. B. Darkhovskii, A. L. Tchougréeff. *J. Phys. Chem. A*, 2004, 108:6351–6364.
149. M. B. Darkhovskii, I. V. Pletnev, A. L. Tchougréeff. *J. Comp. Chem.*, 2003, 24:1703–1719.
150. S. R. Níketiĉ, Kj. Rasmussen. *The Consistent Force Field: A Documentation*, volume 3 of *Lecture Notes in Chemistry.* Springer-Verlag, 1977.
151. M.B. Darkhovskii, A.V. Soudackov, A.L. Tchougréeff. *Theor. Chem. Acc.*, Accepted.
152. G. J. M. Janssen, W. C. Nieuwpoort. *Int. J. Quant. Chem.*, 1988, 22:679–696.
153. L. Seijo, Z. Barandiaran. The Ab Initio model potential method: a common strat-

egy for effective core potential and embedded cluster calculations. In J. Leszczynski, editor, *Computational chemistry: Reviews of current trends*, volume 4. World Scientific, Singapur, 1999.
154. A. Görling. *Phys. Rev. A*, 1993, 47:2783–2799.
155. C. J. Margulis, V. Guallar, E. Sim, R. A. Friesner, B. J. Berne. *J. Phys. Chem. B*, 2002, 106:8038–8046.

PART IV
COMPLEX SYSTEMS

AB-INITIO GUTZWILLER METHOD: FIRST APPLICATION TO PLUTONIUM

J.-P. JULIEN
Laboratoire d'Etudes des Propriétés Electroniques des Solides, CNRS, B.P. 166, 38042 Grenoble Cedex 9, France

AND

J. BOUCHET
DPTA, CEA-DAM, 91680 Bruyères-le-Châtel, France

Abstract. Using a density matrix approach to Gutzwiller method, we present a formalism to treat *ab-initio* multiband Tight-Binding Hamiltonians including local Coulomb interaction in a solid, like, for e.g., the degenerate Hubbard model. We first derive the main results of our method: starting from the density matrix of the non-interacting state, we build a multi-configurational variational wave function. The probabilities of atomic configurations are the variational parameters of the method. The kinetic energy contributions are renormalized whereas the interaction contributions are exactly calculated. A renormalization of effective on-site levels, in contrast to the usual one-band Gutzwiller approach, is derived. After minimization with respect to the variational parameters, the approximate ground state is obtained, providing the equilibrium properties of a material. Academic models will illustrate the key points of our approach. Finally, as this method is not restricted to parametrized Tight-Binding Hamiltonians, it can be performed from first principles level by the use of the so-called "Linearized Muffin Tin Orbitals" technique. To avoid double counting of the repulsion, one subtracts the average interaction, already taken into account in this density functional theory within local density approximation (DFT-LDA) based band structures method and one adds an interaction part "a la Hubbard". Our method can be seen as an improvement of the more popular LDA+U method as the density-density correlations are treated beyond a standard mean field approach. First application to Plutonium will be presented with peculiar attention to the equilibrium volume, and investigations for other densities will be discussed.

J.-P. Julien et al. (eds.),
Recent Advances in the Theory of Chemical and Physical Systems, 509–534.

1. Introduction

Except for small molecules, it is impossible to solve many electrons systems without imposing severe approximations. If the configuration interaction approaches (CI) or Coupled Clusters techniques [1] are applicable for molecules, their generalization for solids is difficult. For materials with a kinetic energy greater than the Coulomb interaction, calculations based on the density functional theory (DFT), associated with the local density approximation (LDA) [2, 3] give satisfying qualitative and quantitative results to describe ground state properties. These solids have weakly correlated electrons presenting extended states, like *sp* materials or covalent solids. The application of this approximation to systems where the wave functions are more localized (*d* or *f*-states) as transition metals oxides, heavy fermions, rare earths or actinides is more questionable and can even lead to unphysical results : for example, insulating FeO and CoO are predicted to be metalic by the DFT-LDA. On another hand, theoretical "many body" approaches like diagrammatic developments [4], slave bosons [5], decoupling of the equations of motion of Green functions by projection techniques [6], and more recently dynamical mean field theory (DMFT) in infinite dimension [7], treat in a much better way correlation effects than the DFT-LDA does. However the price to be paid is an oversimplification of the system, generally reducing the number of involved orbitals and using parameterized Hamiltonians (like Hubbard model) where the *ab-initio* aspect of the DFT-LDA is lost. Finally, these methods, contrary to the DFT-LDA, are scarcely variational. Recently several attemps have been proposed to couple these two points of view as in the LDA+U [8], or LDA+DMFT [9,10] approaches. In the same spirit, the approach we describe below, tries to keep advantages on both sides: it is a variational method which is multi-configurational, contrary to the DFT-LDA, but without loosing the "adjustable parameters free" advantages of the *ab-initio* side. The next section is devoted to the derivation of our formalism. It is then applied to known academic cases to prove the reliability of our approach. The insertion of this approach at the *ab-initio* level is presented in section 2.5. The nature of the electronic structure of Plutonium being still under discussion, the application of our method, in the last section, is in accordance with previous works and also gives some new insights for this material.

2. Method

2.1. GUTZWILLER APPROACH FOR THE ONE-BAND HUBBARD MODEL

Among numerous theoretical approaches, the Gutzwiller method [11, 12] provides a transparent physical interpretation in term of atomic configurations of a given site. Originally it was applied to the one-band Hubbard model Hamiltonian [13]:

$$H = H_{kin} + H_{int} \tag{1}$$

with

$$H_{kin} = \sum_{i \neq j, \sigma} t_{ij} c^{\dagger}_{i\sigma} c_{j\sigma} \tag{2}$$

and

$$H_{int} = U \sum_{i} n_{i\uparrow} n_{i\downarrow} \tag{3}$$

which contains a kinetic part H_{kin} with a hopping integral t_{ij} from site j to site i, and an interaction part with a local Coulomb repulsion U for electrons on the same site. $c^{\dagger}_{i\sigma}$ (respectively $c_{i\sigma}$) is the creation (respectively destruction) operator of an electron at site i with up or down spin σ. $n_{i\sigma} = c^{\dagger}_{i\sigma} c_{i\sigma}$ measures the number (0 or 1) of electron at site i with spin σ. This Hamiltonian contains the key ingredients for correlated up and down spin electrons on a lattice: the competition between delocalization of electrons by hoppings and their localization by the interaction. It is one of the most used models to study electronic correlations in solids (for a review see Ref. [14]).

In the absence of the interaction U, the ground state is that of uncorrelated electrons $|\Psi_0\rangle$ and has the form of a Slater determinant. As U is turned on, the weight of doubly occupied sites must be reduced because they cost an additional energy U per site. Accordingly, the trial Gutzwiller wave function (GWF) $|\Psi_G\rangle$ is built from the Hartree-like uncorraleted wave function (HWF) $|\Psi_0\rangle$,

$$|\Psi_G\rangle = g^D |\Psi_0\rangle \tag{4}$$

The role of g^D is to reduce the weight of configurations (i.e. a way of spreading N electrons over the lattice) with doubly occupied sites, where $D = \sum_i n_{i\uparrow} n_{i\downarrow}$ measures the number of double occupations and g (< 1) is a variational parameter. In fact, this method corrects the mean field (Hartree) approach for which up and down spin electrons are independent, and, some how, overestimates configurations with double occupied sites. Using the Rayleigh-Ritz principle, this parameter is determined by minimization of the energy in the Gutzwiller state $|\Psi_G\rangle$, giving an upper bound to the true unknown ground state energy of H. Note that to enable this calculation to be tractable, it is necessary to use the Gutzwiller's approximation which assumes that all configurations in the HWF have the same weight. Details of the derivation can be found in the article of Vollhardt [15].

Nozières [16] proposed an alternative way, showing that the Gutzwiller approach is equivalent to renormalize the density matrix in the GWF which can be reformulated as:

$$\rho_G = T^\dagger \rho_0 T \tag{5}$$

The density matrices $\rho_G = |\psi_G\rangle\langle\psi_G|$ and $\rho_0 = |\psi_0\rangle\langle\psi_0|$ are projectors on the GWF and HWF respectively. T is an operator, diagonal in the configuration basis, $T = \prod_i T_i$ and T_i is a diagonal operator acting on site i

$$T_i|L_i, L'\rangle = \sqrt{\frac{p(L_i)}{p_0(L_i)}}|L_i, L'\rangle \tag{6}$$

L_i is an atomic configuration of the site i, with probability $p(L_i)$ in the GWF and $p_0(L_i)$ in the HWF respectively, whereas L' is a configuration of the remaining sites of the lattice. Note that this prescription does not change the phase of the wave function as the eigenvalues of the operators T_i are real. The correlations are local, and the configuration probabilities for different sites are independent.
The expectation value of Hamiltonian (1) is given by

$$\langle H\rangle_G = Tr(\rho_G H) \tag{7}$$

The mean value of one-site operators (interaction U) is exactly calculated with the double occupancy probability $d_i = \langle n_{i\uparrow} n_{i\downarrow}\rangle_G$. d_i is the new variational parameter replacing g. From expressions (5) and (6), the two-sites operators contributions of the kinetic energy can be written as

$$\langle c^\dagger_{i\sigma} c_{j\sigma}\rangle_G = Tr(\rho_G c^\dagger_{i\sigma} c_{j\sigma}) = \langle c^\dagger_{i\sigma} c_{j\sigma}\rangle_0 \sum_{L_{-\sigma}} \sqrt{\frac{p(L'_\sigma, L_{-\sigma})}{p_0(L'_\sigma)}} \sqrt{\frac{p(L_\sigma, L_{-\sigma})}{p_0(L_\sigma)}} \tag{8}$$

where L'_σ and L_σ are the only two configurations of spin σ at sites i and j that give non-zero matrix element to the operator in the brackets as illustrated on Fig.1. The summation is performed over the configurations of opposite spin $L_{-\sigma}$. Their corresponding probabilities are pictured on Table 1 for an homogeneous state (for any site i, $\langle n_{i\sigma}\rangle = n$ and $\langle n_{i\uparrow} n_{i\downarrow}\rangle = d$). The probabilities p_0 in the HWF depend only on the number of electrons, whereas the p in the GWF also depend on d_i.

After some elementary algebra, one can show that the Gutzwiller mean value can be factorised:

$$\langle c^\dagger_{i\sigma} c_{j\sigma}\rangle_G = \sqrt{q_{i\sigma}}\langle c^\dagger_{i\sigma} c_{j\sigma}\rangle_0 \sqrt{q_{j\sigma}} \tag{9}$$

where these renormalization factors $q_{i\sigma}$ are local and can be expressed as:

$$\sqrt{q_{i\sigma}} = \frac{\left(\sqrt{1 - n_{i\sigma} - n_{i-\sigma} + d_i} + \sqrt{d_i}\right)\sqrt{n_{i-\sigma} - d_i}}{\sqrt{n_{i\sigma}(1 - n_{i\sigma})}} \tag{10}$$

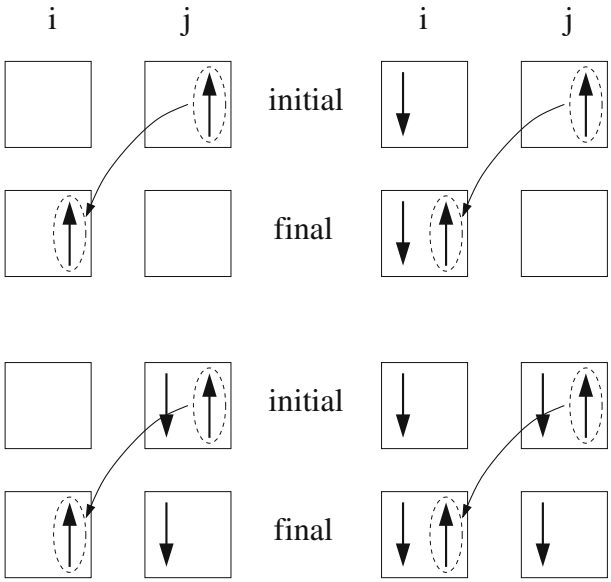

Figure 1. Initial and final configurations contributing to the mean value $\langle c^{\dagger}_{i\sigma} c_{j\sigma} \rangle_G$.

L_i	$p_0(L_i)$	$p(L_i)$
$\emptyset$	$(1-n)^2$	$1-2n+d$
$\uparrow$	$n(1-n)$	$n-d$
$\downarrow$	$n(1-n)$	$n-d$
$\uparrow\downarrow$	n^2	d

TABLE 1. Different possible configurations of one site and the corresponding probabilities in the HWF (p_0) and GWF (p).

where $n_{i\sigma}$ is a shorthand for $\langle n_{i\sigma} \rangle$, the average number of electron on the considered "orbital-spin" in the HWF, which could be site and/or spin independent if the state is homogeneous and/or paramagnetic (it is the case we consider here for pedagogy, dropping indices $i\sigma$). The kinetic energy ϵ^0_{kin} of the non-interacting electrons state is renormalized by a factor q which is smaller than one in the correlated state, and equal to one in the HWF. Then, we minimize the variational energy

$$E(d) = \langle H \rangle_G = q\epsilon^0_{kin} + Ud \tag{11}$$

with respect to d. In the case of half filling ($n = 1/2$), if the repulsion U exceeds a critical value $U_c = 8\epsilon^0_{kin}$, q is equal to zero, leading to an infinite quasiparticle mass with a Mott-Hubbard Metal-Insulator transition which is, in this context, often referred to as "the Brinkmann-Rice transition" [17], as these authors first applied the Gutzwiller approximation to the Metal-Insulator transition. Application of this "one orbital per site" formalism for inhomogeneous states is possible because all involved quantities are local. An example can be found in [18] for model CuO_2 planes, in connection with the electronic structure of High T_C superconductors.

2.2. INEQUIVALENT SITES: RENORMALIZATION OF LEVELS

When sites are inequivalent, or if orbitals belong to different symmetries as in a multiorbital *spdf* basis case of further sections, it is necessary to add to the Hamiltonian an on-site energy term

$$H_{on-site} = \sum_{i\sigma} \epsilon^0_{i\sigma} n_{i\sigma} \tag{12}$$

Hence this enlarged Hubbard Hamiltonian can be written as

$$H = \sum_{i\neq j,\sigma} t_{ij} c^\dagger_{i\sigma} c_{j\sigma} + \sum_{i\sigma} \epsilon^0_{i\sigma} n_{i\sigma} + U \sum_i n_{i\uparrow} n_{i\downarrow} \tag{13}$$

In that case, the starting HWF, directly obtained from the non-interacting part of the Hamiltonian, is not automatically the best choice, giving the optimal GWF, i.e. having the lowest energy. For example, if we look for the ground state of Hamiltonian (13) in the Hartree-Fock (HF) self-consistent field formalism, it is necessary to vary the orbital occupations. Practically, it can be achieved by replacing this Hamiltonian, by an effective Hamiltonian H_{eff} of independent particles with renormalized on-site energies $\epsilon_{i\sigma}$:

$$H_{eff} = \sum_{i\neq j,\sigma} t_{ij} c^\dagger_{i\sigma} c_{j\sigma} + \sum_{i\sigma} \epsilon_{i\sigma} n_{i\sigma} (+C) \tag{14}$$

The HWF we are looking for, is an *approximate* ground state of the *true* many-body Hamiltonian (13) and is the *exact* ground state of *effective* Hamiltonian (14). The additive constant C accounts for double counting energy reference, so that the ground state energies are the same for both Hamiltonians:

$$\langle H_{eff} \rangle = \langle H \rangle \tag{15}$$

The effective Hamiltonian depends on pararemeters $\epsilon_{i\sigma}$. The optimal choice can be obtained by minimizing the ground state energy of H_{eff} with respect

to these parameters. With the help of Hellmann-Feyman theorem, one can easily see that the derivative of the kinetic energy is

$$\frac{\partial\langle H_{kin}\rangle}{\partial\epsilon_{i\sigma}} = -\sum_{j\neq i,\sigma}\epsilon_{j\sigma}\frac{\partial\langle n_{j\sigma}\rangle}{\partial\epsilon_{i\sigma}} \tag{16}$$

On another hand, differentiation of equality (15) associated with expression (16) and the mean field approximation $\langle n_{i\uparrow}n_{i\downarrow}\rangle \approx \langle n_{i\uparrow}\rangle\langle n_{i\downarrow}\rangle$ enables to retrieve the well-known formula for the on-site energies

$$\epsilon_{i\sigma} = \epsilon^0_{i\sigma} + U\langle n_{i-\sigma}\rangle \tag{17}$$

and the constant C is simply $-U\sum_i\langle n_{i\uparrow}\rangle\langle n_{i\downarrow}\rangle$.

In the Gutwiller approach, the same argument about the variation of orbital occupation, i.e. flexibility on the HWF $|\Psi_0\rangle$, is true. It is necessary to find a way to vary this Slater determinant from which the GWF $|\Psi_G\rangle$ is generated, so that the Gutzwiller ground-state energy is minimum. Clearly one has to find an equivalent of formula (17) in the Gutzwiller context, which has never been established, to our knowledge. The average value of Hamiltonian (13) on a GWF is given by:

$$\langle\Psi_G|H|\Psi_G\rangle = \sum_{ij\sigma} t_{ij}\sqrt{q_{i\sigma}}\langle c^\dagger_{i\sigma}c_{j\sigma}\rangle_0\sqrt{q_{j\sigma}} + U\sum_i d_i + \sum_{i\alpha\sigma}\epsilon^0_{i\sigma}\langle n_{i\sigma}\rangle_0 \tag{18}$$

Following the same footing of previous HF self-consistent field approach, one has to find an effective Hamiltonian H_{eff} of independent particles having $|\Psi_0\rangle$ as *exact* ground state. This state $|\Psi_0\rangle$ generates the GWF $|\Psi_G\rangle$ which is an *approximate* ground state of the true interacting Hamiltonian (13). In analogy with (15), the condition

$$\langle\Psi_0|H_{eff}|\Psi_0\rangle = \langle\Psi_G|H|\Psi_G\rangle \tag{19}$$

leads to the expression for the searched H_{eff}:

$$H_{eff} = \sum_{i\neq j,\sigma}\tilde{t_{ij}}c^\dagger_{i\sigma}c_{j\sigma} + \sum_{i\sigma}\epsilon_{i\sigma}n_{i\sigma} + C' \tag{20}$$

with effective but *fixed* renormalized hoppings $\tilde{t_{ij}} = \sqrt{q_{i\sigma}}t_{ij}\sqrt{q_{j\sigma}}$ and having effective on-site energies $\epsilon_{i\sigma}$ which have still to be determined. Hellmann-Feynman theorem applied to H_{eff} provides again an expression similar to (16), but with effective hoppings. Taking into account the dependence of the $q_{i\sigma}$'s through $n_{i\sigma}$ in differentiating (18) and (19) with respect to the parameters $\epsilon_{i\sigma}$, after some calculations, one obtains the equivalent expression of (17) in the Gutzwiller context:

$$\epsilon_{i\sigma} = \epsilon^0_{i\sigma} + 2e_{i\sigma}\frac{\partial ln(\sqrt{q_{i\sigma}})}{\partial n_{i\sigma}} \tag{21}$$

Here $e_{i\sigma}$ is the partial kinetic energy of orbital-spin $i\sigma$, it is given by

$$e_{i\sigma} = \sum_{j\sigma} \tilde{t_{ij}} \langle c^\dagger_{i\sigma} c_{j\sigma} \rangle_0 = \int_{-\infty}^{\mathrm{E_F}} E\tilde{N_{i\sigma}}(E)dE - \epsilon_{i\sigma}\langle n_{i\sigma}\rangle_0 \tag{22}$$

with $\tilde{N_{i\sigma}}$ the $i\sigma$-projected density of states (DOS) for Hamiltonian H_{eff}. The remaining constant C' that ensures (19) explicitly reads

$$C' = U\sum_i d_i - \sum_{i\sigma} 2e_{i\sigma}\frac{\partial ln(\sqrt{q_{i\sigma}})}{\partial n_{i\sigma}} \tag{23}$$

To solve the full problem of finding an approximate ground state to Hamiltonian (13), one is faced to a self-consistent loop which can be proceeded in two steps. First one can get the occupations $\langle n_{i\sigma}\rangle_0$ from a HWF, and a set of 'bare' $\epsilon^0_{i\sigma}$ levels. Then one obtains a set of configuration parameters, the probabilities of double occupation, d_i by minimizing (18) with respect to these probabilities. Afterwards the on-site levels are renormalized according to (21) and the next loop starts again for the new effective Hamiltonian H_{eff} till convergence is achieved.

As illustration of the importance of the renormalization of levels, we studied the case of an alternate Hubbard chain (often called Ionic Hubbard model). This model contains two kinds of alternating atoms A and B on an infinite chain, having on-site energies ϵ^0_A and ϵ^0_B respectively, coupled by a hopping integral t. The same local Coulomb repulsion U acts on each site. For a given total number of electrons, one can fix a repartition of electrons among sites A and B, and compute the energy of the ground state: first within the HF mean field approximation, and secondly, within the Gutzwiller approach. Browsing the electronic occupation of A-site, by adjunction of Lagrange multiplier to fix it to a given value, one looks for the lowest energy state. The corresponding ground state energies as function of the A-filling are presented on Fig. 2. First of all, the lowest Hartree state could be more efficiently directly found, after some self-consistent loops, via the on-site renormalization of levels of equation (17) in the HF context, as explained in the paragraph above. By inspection of the curve, it is also obvious that this Hartree state does not generate the lowest Gutzwiller state. It is necessary to browse among different A-fillings to find the best Gutzwiller ground state. If this browsing procedure is still tractable for simple models, as we did in Ref. [18], its generalization to multiorbitals cases would be practically impossible. It is the main advantage of formula (21) to avoid this cumbersome search for optimized levels and to provide a systematic way of finding them, similar to (17), leading to the best (i.e. lowest) Gutzwiller ground state.

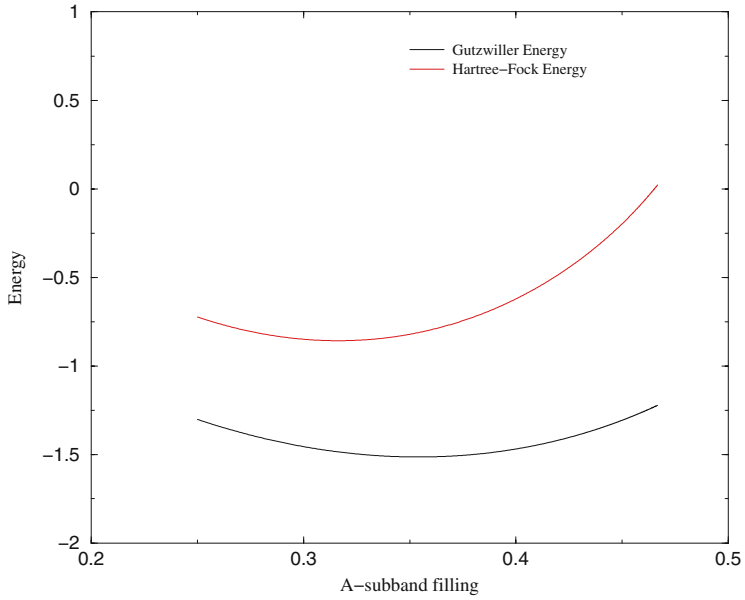

Figure 2. Total energy of the alternate chain versus A-subband filling. Upper curve: Hartree-Fock result, Lower curve: Gutzwiller result. The 2 minima are clearly different.

2.3. GENERALIZATION TO THE DEGENERATE HUBBARD HAMILTONIAN

Now we generalize this density matrix formalism [19,20] for the degenerate Hubbard Hamiltonian which, with usual notations, reads:

$$H = \sum_{i \neq j \alpha \beta \sigma} t_{i\alpha,j\beta} c^{\dagger}_{i\alpha\sigma} c_{j\beta\sigma} + H_{\text{int}} \tag{24}$$

with the model interaction

$$H_{\text{int}} = \frac{1}{2} \sum_{i,\alpha\sigma \neq \beta\sigma'} U_{\alpha\sigma\beta\sigma'} n_{i\alpha\sigma} n_{i\beta\sigma'} \tag{25}$$

where α, β and σ, σ' are orbitals and spins index respectively, necessary to account for orbital degeneracy. The case $\alpha\sigma = \beta\sigma'$ is excluded from the interaction because of Pauli principle. We neglect any spin flip term in the interaction for simplicity. They could be in principle taken into account in our approach, as it is done in a different work by Bünemann et al [21]. However this procedure would involve a diagonalization of atomic part of Hamiltonian, that complicates the presentation of our approach without bringing any new physical ingredients.

As in the one-band case, we define a Gutzwiller renormalized density matrix with the operator T given by eqs (5) and (6). The main difference being the greater number of atomic configurations, equal to 2^{2N}, with N the orbital degeneracy. For a given site we have now probabilities for double, triple, etc... multiple occupancy, which are the new variational parameters generalizing the role of d. Of course, the number of independent variational probabilities is smaller than the number of configurations, as different configurations could have the same probabilities for symmetries reasons. For example, in a paramagnetic case, a configuration and its spin reverse are equivalent leading to the same probability. Moreover, the probabilities are not independent of each other as the sum over all probabilities have to be equal to 1, and we have also to conserve the average electronic occupation of given orbital-spin $\langle n_{i\alpha\sigma}\rangle$. These constraints could be either directly included in the expressions of empty and single occupied configurations probabilities, or treated by adjunction of Lagrange multipliers as in the slaves bosons approach [5]. This last formulation has the advantage of giving more symmetric expressions. Using the expression (6) of T_i operators, we can directly obtained the factorized form of the kinetic energy terms:

$$\langle c^{\dagger}_{i\alpha\sigma} c_{j\beta\sigma}\rangle_G = \sqrt{q_{i\alpha\sigma}}\langle c^{\dagger}_{i\alpha\sigma} c_{j\beta\sigma}\rangle_0 \sqrt{q_{j\beta\sigma}} \tag{26}$$

where the q-factors reduce the kinetic energy and are expressed as functions of the variational parameters and the number of electrons according to:

$$\sqrt{q_{i\alpha\sigma}} = \frac{1}{\sqrt{n_{i\alpha\sigma}(1-n_{i\alpha\sigma})}} \sum_{L'_i} \sqrt{p(i\alpha\sigma : unocc, L'_i)p(i\alpha\sigma : occ, L'_i)} \tag{27}$$

Here $p(i\alpha\sigma : occ, L'_i)$ (respectively $p(i\alpha\sigma : unocc, L'_i)$) represents the probability of the atomic configuration of site i, where the orbital α with spin σ is occupied (resp. unoccupied) and where L'_i is a configuration of the remaining orbitals of this site. This result is similar to the expression obtained by Bünemann *et al.* [22], but it is obtained more directly by the density matrix renormalization (5). To obtain the expression of the $q_{i\alpha\sigma}$ factors, an additional approximation to the density matrix of the uncorrelated state was necessary. This approximation can be viewed as the multiband generalization of the Gutzwiller approximation, exact in infinite dimension [23]

$$\langle LL''|\rho_0|L'L''\rangle \approx p_0(L'') \sum_{L''} \langle LL''|\rho_0|L'L''\rangle \tag{28}$$

Where we have replaced an off-diagonal element of the density by its average value over the configurations L''. L and L' are configurations of one or two sites, involved in the calculation of interaction or kinetic term and L'' is the configuration of remaining sites. This approximation allows to perform calculations, and however preserves sum rules of the density matrix.

Similarly, the interaction between an electron at site i on orbital α with spin σ and an electron on orbital β with spin σ' involves a term

$$\langle n_{i\alpha\sigma} n_{i\beta\sigma'} \rangle = \sum_{L_i'} p(i\alpha\sigma : occ, i\beta\sigma' : occ, L_i') \tag{29}$$

where L_i' is a configuration of the remaining spin-orbitals of this site, other than $\alpha\sigma$ and $\beta\sigma'$.

As illustration, we studied the academic case of paramagnetic state for doubly degenerate bands like, for instance, e_g-symmetry d-orbitals in cubic or octahedral environment. Hybridization among these degenerate orbitals is supposed to produce a kinetic energy ϵ_{kin}^0 in the uncorrelated state. We take a model interaction where the general expression (25) reduces to:

$$\begin{aligned} H_{\text{int}} = U \textstyle\sum_{i\alpha\sigma} n_{i\alpha\sigma} n_{i\alpha-\sigma} + U' \sum_{i\alpha\neq\beta\sigma} n_{i\alpha\sigma} n_{i\beta-\sigma} \\ +(U'-J) \textstyle\sum_{i\alpha\neq\beta\sigma} n_{i\alpha\sigma} n_{i\beta\sigma} \end{aligned} \tag{30}$$

with two independent parameters U and U' as the relation $U - U' = 2J$ stands [24]. The interaction between electrons of same spin is reduced by the exchange integral J, which is essential to reproduce first Hund's law of maximum spin. The application of the above prescription directly leads to the variational energy:

$$E_G = 2q\epsilon_{kin}^0 + 2Ud_0 + 2U'd_1 + 2(U'-J)d_2 + 2(U+2U'-J)(2t+f) \tag{31}$$

f and t are the quadruple and triple occupancy respectively, whereas there are three possibilities of double occupancies : d_0 (same orbital, different spin), d_1 (different orbital, different spin)and d_2 (different orbital, same spin). Some of the corresponding configurations with multiple occupancy are pictured on Table 2, followed by their probability and their interaction energy. This expression is identical to the result obtained by different authors using Gutzwiller-type wave function [25, 26], or multiband slave-boson approach [27] which is a multiorbital generalization of Ref. [5]. It is to be stressed the very physical "transparent" approach with the density matrix formalism, leading to simple expressions. Also, there is no approximation about less favorable configurations, discarded from the beginning as in Ref. [28]. For a given electronic filling, we use a Newton-Raphson procedure to minimize E_G with respect to d_0, d_1, d_2, t and f. We again choose a half filled case, and we scale all contributions in term of the kinetic energy.

On Fig. 3 we plot the probabilities of different configurations versus the direct Coulomb interaction U. It can be seen that the system undergoes a metal-insulator transition for a sufficiently high value of U, close to 9. It is easy to perform the same kind of calculation in the case of triply degenerate

$\vert\uparrow\downarrow\vert\quad\vert\vert$	d_0	U
$\vert\uparrow\vert\downarrow\vert$	d_1	U'
$\vert\uparrow\vert\uparrow\vert$	d_2	$U'-J$
$\vert\uparrow\downarrow\vert\downarrow\vert$	t	$U+2U'-J$
$\vert\uparrow\downarrow\vert\uparrow\downarrow\vert$	f	$2U+2(2U'-J)$

TABLE 2.

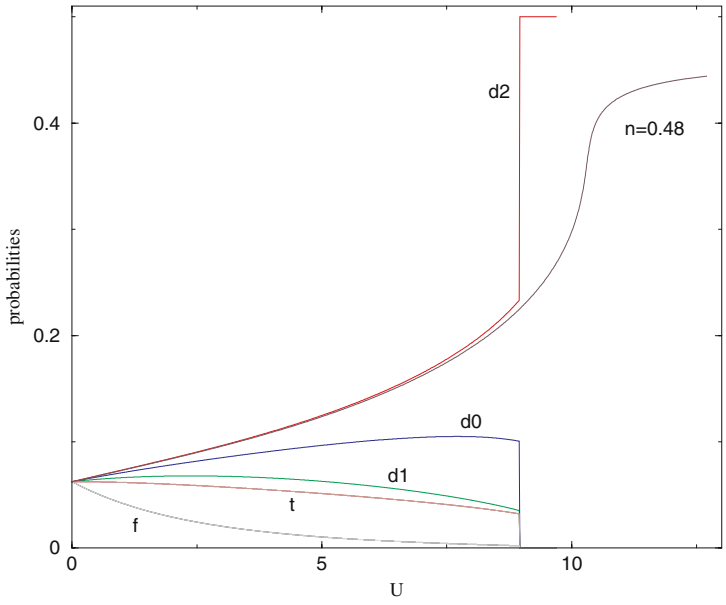

Figure 3. For the half filling case all the probabilities are equal for $U = 0$. For $U_c \sim 9$ we have a transition from the metallic to the insulator state which is of first order at half filling and second order for other concentration as seen for $n = 0.48$.

orbitals relevant for d-orbitals with the symmetry t_{2g}, (for instance Ti t_{2g} in $LaTiO_3$), f-orbitals with the symmetry T_1 or T_2 in cubic or octahedral environment (rare-earth element or actinides) or p-orbitals like in fullerene C_{60}.

2.4. DIFFERENT ORBITAL SYMMETRIES: FULLY HYBRIDIZED HAMILTONIAN

As our aim is to describe realistic materials from the *ab-initio* level, it is necessary to have a full set of *spd* and possibly f (for actinides or rare earths) basis. The system can be described by the following Hamiltonian which is the sum of a kinetic term, local Coulomb repulsions and an on-site contribution accounting of difference of site (and/or symmetries)

$$\begin{aligned} H = & \sum_{i\neq j\alpha\beta\sigma} t_{i\alpha,j\beta} c^{\dagger}_{i\alpha\sigma} c_{j\beta\sigma} \\ & + \tfrac{1}{2} \sum_{i,\alpha\sigma\neq\beta\sigma'} U_{\alpha\sigma\beta\sigma'} n_{i\alpha\sigma} n_{i\beta\sigma'} \\ & + \sum_{i\alpha\sigma} \epsilon^{0}_{i\alpha\sigma} n_{i\alpha\sigma} \end{aligned} \tag{32}$$

The kinetic term is responsible of the hybridization of orbitals with different ℓ-symmetries on neignboring sites among each others. Moreover,we assume that the interaction part of the Hamiltonian H_{int} only concerns one subset of correlated orbitals (say f). All atomic configurations Γ of this subset on each site i will be considered. Note that H can be seen as a multiband hybrid between the Hubbard Hamiltonian and the periodic Anderson Hamiltonian. It contains hybridization of localized interacting f orbitals among each others (Hubbard) but also with extended *spd* states (Anderson). Using the results of previous sections, the variational energy in the Gutzwiller state reads

$$\begin{aligned} E_G = & \sum_{i\neq j\alpha\beta\sigma} \sqrt{q_{i\alpha\sigma}} t_{i\alpha,j\beta} \langle c^{\dagger}_{i\alpha\sigma} c_{j\beta\sigma} \rangle_0 \sqrt{q_{j\beta\sigma}} \\ & + \sum_{i,\Gamma} U_{\Gamma} p_i(\Gamma) + \sum_{i\alpha\sigma} \epsilon^{0}_{i\alpha\sigma} \langle n_{i\alpha\sigma} \rangle_0 \end{aligned} \tag{33}$$

In this expression the q-factors of site i are functions, through (27), of the probabilities $p_i(\Gamma)$ of the atomic configurations Γ of f-orbitals at the same site. They are equal to 1 if orbital α or β does not belong to this subset, i.e. for extended states. U_{Γ} is a proper combination of Coulomb direct and exchange contributions $U_{\alpha\sigma\beta\sigma'}$, accounting for the interaction energy which arises as prefactors of expressions (29), and which can be seen for e.g. on simplified case of (31). As in our previous simpler models, the probabilities $p_i(\Gamma)$ are the variational parameters and one has to minimize E_G with respect to each of them (and at each inequivalent site) according to

$$\begin{aligned} 0 = \frac{\partial E_G}{\partial p_i(\Gamma)} = & \sum_{\alpha j\beta\sigma} \frac{\partial \sqrt{q_{i\alpha\sigma}}}{\partial p_i(\Gamma)} t_{i\alpha,j\beta} \langle c^{\dagger}_{i\alpha\sigma} c_{j\beta\sigma} \rangle_0 \sqrt{q_{j\beta\sigma}} \\ & + \sum_{j\beta\sigma} \sqrt{q_{j\beta\sigma}} t_{j\beta,i\alpha} \langle c^{\dagger}_{j\beta\sigma} c_{i\alpha\sigma} \rangle_0 \frac{\partial \sqrt{q_{i\alpha\sigma}}}{\partial p_i(\Gamma)} + U_{\Gamma} \end{aligned} \tag{34}$$

To avoid the cumbersome calculations of all $\langle c^{\dagger}_{i\alpha\sigma} c_{j\beta\sigma} \rangle_0$ cross-terms which are present in a fully hybridized case, we propose a recursive procedure for the minimization of E_G, i.e. the search for the optimal set of probabilities. In spirit close to the impurity model of the DMFT approach, we first consider that there is only one correlated site, say $i = 0$. This site is supposed to be embedded in a reference fixed medium where all q's other than the considered site '0', are equal to 1 at beginning or to their previous values in the self-consistent process that has to be performed afterwards. Then the set of equations (34) for all configurations Γ of site 0 can be rewritten as

$$\frac{\partial E_G}{\partial p_0(\Gamma)} = \sum_{\alpha\sigma} 2e_{i=0\alpha\sigma} \frac{\partial ln(\sqrt{q_{0\alpha\sigma}})}{\partial p_0(\Gamma)} + U_{\Gamma} \tag{35}$$

The partial kinetic energies $e_{i=0\alpha\sigma}$ of orbital $\alpha\sigma$ at site $i = 0$, generalizing (22), are obtained from partial projected DOS, available from any electronic structure code, and computed with site $i = 0$ embedded in the reference medium. To ensure numerical stability when solving system of eqs. (35) and according to the spirit of Landau theory of Fermi liquids, the interactions are progressively switched on from zero to their final values starting from the probabilities of uncorrelated case. After solution, the probabilities $p_0(\Gamma)$ are used to compute the local q-factors of site 0. If all sites are equivalent, one would get the same results on other sites. Accordingly, the q-factors of other sites are all set equal to the '0'-th ones (one would have to repeat this impurity-like calculation if there are inequivalent sites, i.e. crystal structures with more than one atom per cell or disordered systems). Changing the q-factors affects the partial kinetic energies $e_{i=0\alpha\sigma}$ and also the occupation of orbitals, as the reference medium now has new effective hoppings. Process must be iterated till convergence. The advantage of this way of solving iteratively eqs. (34) is that the only required ingredients to get the solutions are partial (local) kinetic energies and occupations of orbitals at site 0 directly obtained from partial DOS's. The price to be paid is a greater number of electronic structure paths. It can be easily implemented in existing codes, without searching to get cross-terms, reducing the numerical effort to adapt our method in these codes.

Finally, as in the one-band case, it is necessary to find the best Slater determinant leading to optimized effective levels. One can easily show that expression (21) can be generalized for orbital degeneracy:

$$\epsilon_{i\alpha\sigma} = \epsilon^0_{i\alpha\sigma} + 2e_{i\alpha\sigma} \frac{\partial ln(\sqrt{q_{i\alpha\sigma}})}{\partial n_{i\alpha\sigma}} \tag{36}$$

Again, as in the one-band case, it is necessary to perform self-consistent calculations (for a given previously converged $\{p_0(\Gamma)\}$ set) till the overall convergence is reached i.e. the on-site effective levels as well as the hoppings are converged. Once achieved, the effective Hamiltonian H_{eff} can be used

to a quasiparticles description of the system as proposed by Vollhardt [15]. In fact, he has shown that the Gutzwiller method is a natural frame to obtain the parameters of the phenomenological Landau theory of Fermi liquids. One can also expect finite temperature extension of our method in analogy with [47] and references therein.

2.5. AB-INITIO APPROACH: ALTERNATIVE TO THE LDA+U METHOD

We present now how to implement such an approach in an *ab-initio* calculation of solids. The linearized muffin-tin orbital in the atomic sphere approximation (LMTO-ASA) is widely used and peculiarly suited for our purpose as the basis set has a local representation. Other *ab-initio* approaches could be used, and if they have not this local property, one could transform the basis into a Wannier representation. The LMTO method is well described elsewhere [29, 30] and we would like to remind here only the main results which are usefull for this paper. In the frame of DFT-LDA band structure calculations, the LMTO method is based on some approximations. The space is divided in atomic spheres where the potential is spherically symmetric and interstitial region where it is flat ("Muffin Tin" potential). In the Atomic Sphere Approximation (A.S.A.), the spheres radii are chosen so that the total volume of the spheres equals that of the solid. One makes a further approximation by supposing that the kinetic energy in the interstitial region is zero (without this non-essential assumption, Laplace equation, as used below, should be replaced by Helmoltz equation). In this region, the Schrödinger equation reduces to Laplace equation having regular and irregular solutions: $Y_L(\hat{r})r^{\ell}$and $Y_L(\hat{r})r^{-\ell-1}$ respectively. Here $L = (\ell, m)$ represents the angular momentum index and $Y_L(\hat{r})$ the spherical harmonics in direction $\hat{r} = (\theta, \phi)$. For the sphere centered at site R and in the momentum index ℓ ($\ell = 0, 1, 2, 3$), one finds the solution $\varphi_{R\ell\nu}$ of the radial Schroedinger equation for a given energy E_ν, usually taken at the center of gravity of the occupied part of the ℓ-band and the energy derivative of $\varphi_{R\ell\nu}$ noted $\dot{\varphi}_{R\ell\nu}$. It can be shown that the corresponding orbitals $\varphi_{R\ell\nu}$ and $\dot{\varphi}_{R\ell\nu}$ are orthogonal to each other and nearly orthogonal to the core levels. It is thus possible to build a basis set of orbitals χ_{RL} centered at sphere of site R in the following way. Outside the sphere, in the interstitial region χ_{RL} is proportional to the irregular solution $Y_L(\hat{r})r^{-\ell-1}$ of Laplace equation and it is augmented (i.e. substituted according to Slater terminology) in its own sphere by a linear combination of $\varphi_{R\ell\nu}$ and $\dot{\varphi}_{R\ell\nu}$ having logarithmic derivative $-\ell - 1$ at the radius s_R of the sphere so that the orbital is continuous and derivable at the sphere boundary. In any other sphere R', the irregular solution of Laplace equation can be expanded in term of regular solutions in that sphere:

$$Y_L(\hat{r}_R)(\frac{r_R}{a})^{-\ell-1} = -\sum_{L'} \frac{1}{2(2\ell'+1)} S^0_{R'L',RL} Y_{L'}(\hat{r}_{R'})(\frac{r_{R'}}{a})^{\ell'} \qquad (37)$$

and the orbital χ_{RL} should be augmented in sphere R' with the same expansion of linear combination of $\varphi_{R'\ell'\nu}$ and $\dot{\varphi}_{R'\ell'\nu}$ having the logarithmic derivative ℓ' at the radius $s_{R'}$ of sphere R'. In (37), a is a scale factor and $S^0_{R'L',RL}$ are the so-called "structure constants" which depend only on the crystallographic structure of the material. In this basis set of the orbitals χ_{RL} both Hamiltonian and Overlap matrices can be expressed in terms of $S^0_{R'L',RL}$, and the potential parameters $\varphi_{R\ell\nu}(s_R)$, $\dot{\varphi}_{R\ell\nu}(s_R)$ and their logarithmic derivatives $D_{R\ell\nu}$ and $\dot{D}_{R\ell\nu}$ at sphere boundary. Since the structure constants $S^0_{R'L',RL}$, decreasing as $r^{-\ell-\ell'-1}$ with distance, are very long ranged for s and p orbitals, it can be more convenient to change the basis set so that the Hamiltonian can have the Tight-Binding (TB) form or any desired properties (like the orthogonality of overlap). It can be achieved by adding to the regular solution of Laplace equation an amount of the irregular solution for a given angular momentum. It is possible to choose this amount $\bar{Q}_\ell$ so that the transformed structure constants S can be screened with a short-range dependence with the distance or so that the orbitals of the transformed basis set are orthogonal (the so-called TB or most localized and orthogonal representations, respectively). With appropriate choice for $\bar{Q}_\ell$, the transformed structure constant matrix obeys to the following equation:

$$S = S^0(1 - \bar{Q}_\ell S^0)^{-1} \qquad (38)$$

Matrix elements fo the Hamiltonian can be written as:

$$H_{RL,R'L'} = C_{RL}\delta_{RL,R'L'} + \Delta^{1/2}_{RL} S_{RL,R'L'} \Delta^{1/2}_{R'L'} \qquad (39)$$

which is limited to first order in $(E - E_\nu)$ in the TB representation, whereas it is valid up to second order in the orthogonal representation (and it is even possible to add third order correction). C_{RL} determines the middle of the band "RL" and Δ_{RL} its width and the strength of hybridization. These parameters are expressed in terms of the 4 potential parameters: $\varphi_{R\ell\nu}(s_R)$, $\dot{\varphi}_{R\ell\nu}(s_R)$, $D_{R\ell\nu}$ and $\dot{D}_{R\ell\nu}$. It should be stressed that hybridization between bands of different angular moments is due to the matrix elements $S_{RL,R'L'}$ which couples RL-states to $R'L'$ ones. When these matrix elements are set equal to zero for $\ell \neq \ell'$, one obtains bands having pure ℓ character. This approximation was suggested in the standard (unscreened) representation and the resulting bands were called "canonical" bands. In that case it would be quite easy to apply single band Gutzwiller method (one equation per ℓ symmetry) without the need of the previous fully hybridized generalization. However, as we want to treat realistic bands, we do not use the canonical

bands in this paper. We use a scalar relativistic LMTO-ASA code neglecting spin-orbit coupling, with the so-called "combined corrections" which correct the ASA. The density functional formalism, before the Gutzwiller correction explained below, was treated within the LDA with the exchange and correlation potential of von Barth and Hedin [31].

The Hamiltonian of valence electrons (39), in the so-called orthogonal representation (or in the most localized representation, neglecting orbital overlap) can be mapped on a tight-binding form Hamiltonian

$$H_{LMTO} = \sum_{i \neq j \alpha \beta \sigma} t_{i\alpha,j\beta} c^{\dagger}_{i\alpha\sigma} c_{j\beta\sigma} + \sum_{i\alpha\sigma} \epsilon_{i\alpha\sigma} n_{i\alpha\sigma} \tag{40}$$

The hoppings and on-site energies are directly outputs of the *ab-initio* calculation, as explained in Ref. [30] and by identification of expression (40) with (39), making the correspondance: $R \rightarrow i$, $L \rightarrow \alpha$. This opens the possibility of treating our approach from first principle level, without any adjustable parameters, except the interactions U. They could be however also computed from constrained LDA calculations but in the following we rather treat them as free parameters. As in (32), (40) describes a full *spd* (and possibly f as in application of this method to Plutonium, see next section) basis. The terms $\epsilon_{i\alpha\sigma}$ account for different on-site energies for orbitals with different angular momentum or lying on inequivalent sites with possible crystal field splitting between orbitals of same angular momentum, but belonging to different irreducible group representations: it is due to the on-site contribution of $S_{RL,RL}$ that arises in the TB or in the nearly orthogonal representation.

In the spirit of the Anderson model, we separate electrons into two subsystems: delocalized electrons for which the LDA is assumed to give reasonable results and localized electrons for which it is well known that the LDA can lead to unphysical results. To treat these states in a better way, and to avoid double counting, we exclude the interaction between localized electrons (f or d) already taken into account in an average way in the LDA-on-site energy

$$\epsilon^{0}_{i\alpha\sigma} = \epsilon^{\mathrm{LDA}}_{i\alpha\sigma} - U(n_f - \frac{1}{2}) \tag{41}$$

where U is a proper combination of direct and exchange Coulomb integral giving a true one-electron Hamiltonian H_0. n_f is the average number of f (or d) electrons given by the LDA calculation. We then re-add an interaction part H_{int} " a la Hubbard" for the localized electrons and the full Hamiltonian $H' = H_0 + H_{\mathrm{int}}$ is treated within the previously described multiband Gutzwiller approach. In fact this starting Hamiltonian H' is the same one used in the so-called "LDA+U" method [8], the difference being in the way the interaction part is treated. In the LDA+U method, it is treated

in a mean field Hartree-Fock like approach, which can be questionable in case of strong correlations. It is however a suitable way of introducing an orbital-dependent potential which is absent in DFT formalism. In our approach the correlation is treated exactly, within the approximation of the Gutzwiller ansatz. Note that our method also contains orbital-dependent potential through the renormalization of levels (36). A detailed study of the involved derivative indeed reveals an orbital filling dependence when rewriting this formula:

$$\epsilon_{i\alpha\sigma} = \epsilon^0_{i\alpha\sigma} - \frac{2e_{i\alpha\sigma}}{n_{i\alpha\sigma}(1-n_{i\alpha\sigma})}(\frac{1}{2} - n_{i\alpha\sigma}) + \frac{\partial}{\partial n_{i\alpha\sigma}} \quad ln \sum_{L'_i} \sqrt{p(i\alpha\sigma : unocc, L'_i)p(i\alpha\sigma : occ, L'_i)} \tag{42}$$

Similarly to what happens in the LDA+U method, one sees the tendency of lowering for levels with occupation greater than one half, and a rising upwards for the less than half filled ones (the partial kinetic energy $e_{i\alpha\sigma}$ is always negative, it would be zero for a filled band). The difference with LDA+U method is the partial kinetic energy prefactor (instead of U) and other terms that come from the derivative of the empty and single occupied configurations.

The starting Hamiltonian H' has been also used to make a link between *ab-initio* LMTO band structure calculation and a DMFT treatment of correlations for the studies of $LaTiO_3$ [9] and Plutonium [10]. This last approach, assuming infinite dimension, goes beyond our approach. We only expect to be able to describe the coherent part of the spectrum, whereas the incoherent part leading to lower and upper Hubbard subbands are not accessible in our model, however as already stressed, variationally based.

The practical scheme we proposed to perform our *ab-initio* Gutzwiller approach is the following one. First, we perform a LDA *ab-initio* LMTO-ASA calculation of the solid in a given crystal structure. This calculation provides the core and the valence (band) electrons contribution total energy, as well as occupations and partial kinetic energies for valence orbitals. From these ingredients, and for a given model interaction Hamiltonian, it is possible to evaluate the variational Gutzwiller energy, which will be minimized, providing an optimized set of variational configurational probabilities. Then the on-site levels are varied according to the prescription renormalization of levels (36) as well as the adjunction of q-factors (27) which modified hoppings. New partial kinetic energies and occupations are recalculated from the modified Hamiltonian H', until self-consistency is achieved. At the end of procedure, the total energy, sum of the core and band energies, is calculated, leading to the properties of the ground state. One can then change, for example, the volume and redo the whole loop to obtained the

equilibrium properties and the most favorable atomic configurations in the solid. Close to the Fermi level we can also obtain an approximate *ab-initio* description of quasiparticles spectrum which enables comparison with spectroscopy experiments for moderately correlated electron systems. That way, one has an *ab-initio* method which is multi-configurational and variational.

In this first application, we made a slight simplification, with respect to the general process described in last paragraph, for the band calculation part: starting from converged LMTO potential parameters, we build up a first order Hamiltonian in TB representation with neglect of overlap matrix (i.e. equal to unity) as explained in [32] and references therein. As our scheme only reorganizes valence (band) electrons, we make a frequently used frozen core approximation assuming that the core energy remains unaffected by this reorganization and we will now concentrate on the band energies. It is well-known that this first order Hamiltonian is accurate close to E_ν, i.e. close to the center of gravity of the occupied part of the bands. Far from it, it has the effect of a slight reduction of the bandwidth, but we have verified that it has a negligible effect on integrated quantities: for example, before the Gutzwiller process is switched on, we have checked that the band energies calculated from the third order Hamiltonian and from the first order one with the recursion process described below, are in excellent agreement. We used a full *spdf* basis set with hoppings up to second nearest neighbors. For all 7 inequivalent orbitals, in cubic environment from the overall 16 orbitals, we performed a real space recursion procedure [33] to get the partial projected densities of states (DOS) from which all needed quantities, like occupancies or band energies, can be calculated. These partial DOS are obtained from the imaginary part of diagonal elements of a Green function, which are developed in a continued fraction expansion up to a given level. This level is chosen so that a convergence criterium is reached, i.e. adding one more level does not affect the result. Practically we took 40 steps of recursion. Various terminators (the well-known square root terminator, or more elaborated ones in presence of gaps [34]) are then used to close the continued fraction expansion. A full self-consistent approach within the Gutzwiller loop, using third order Hamiltonians and including spin-orbit coupling, is still in preparation, and some intermediary results will be given in next section.

3. Application to Plutonium

We now give a simple application of the present method to Plutonium which is a good test case. Pu lies between light actinides with itinerant $5f$ electrons and heavy actinides with localized $5f$ electrons. The competition between these two electronic regimes in Pu is responsible for a lot of unusual properties as large values of the linear term in the specific heat coefficient and of the electrical resistivity or a very complex phase diagram.

The ground state α phase (monoclinic with 16 atoms by cell) is known to be well described by *ab-initio* DFT-LDA calculations, whereas for the high temperature δ phase (fcc), the calculated equilibrium volume is of the order of 30 percent smaller than the experimental one. It is very important to reproduce the properties of Pu to take into account the delicate balance between the itinerancy of the f electrons and the large intra atomic Coulomb interaction. This requires a much more complicated theory for the electrons than the LDA which is like a mean-field treatment of the correlations [35]. Recently several attempts to go beyond LDA have given a new understanding of the α-δ transition. In the LDA+U method [36] an orbital-dependent correction, treated in the mean-field approximation is added to the LDA functional. These calculations have showed how the equilibrium volume is improved in comparison to previous results using LDA, and how an augmentation of the orbital moment is observed following Hund's rules, reducing the total magnetic moment in agreement with experiments. Going a step beyond the LDA+U, Savrasov *et al* [37] have used an implementation of DMFT. The LDA+U can be viewed as the static approximation of the DMFT. With this dynamical treatment of the f-electrons they have recovered the experimental equilibrium volume of δ-Pu, the photoemission peak at the Fermi level and given an understanding picture of the transition between α and δ phases. Different approaches, using the spin-polarized generalized gradient approximation (GGA) and antiferromagnetic configurations [38–40] have well reproduced the ground state properties of δ-Pu. All these works show how a spin/orbital polarization is crucial to describe the δ-phase. In the Gutzwiller method, the correlations, via the q-factors, are supposed to reduce the hoppings, and so to weaken the covalency character of the bonding, and consequently the attraction between atoms. Thus we expect to increase the interatomic distance, leading to a greater equilibrium volume. Of course, the same approach has to be performed for α and δ phase.

An extra difficulty arises from the Atomic Sphere Approximation (ASA) of the LMTO method: the atomic potential, inside an atomic "muffin-tin" sphere, is spherized, or equivalently, the true "full" potential is approximated by its first $\ell = 0$ component. This approximation greatly simplifies the calculation, as the wave function basis in a sphere, used to build the LMTO set, can be factorized in a product of a radial wave function and a spherical harmonics as explained above. It presents however the shortcomings that, it is not a "full potential" approach and forbids to change the symmetry when making comparison between structures. We overcome this difficulty here by performing the calculation in a fcc structure browsing different volume: it is correct for the δ phase, but the α phase will be replaced by a "pseudo"-α phase, in a fcc structure, having however the same density than the experimental one.

The valence states taken into account in the LMTO part were the $7s$, $6p$, $6d$, $5f$ of Pu with 16 fully hybridized orbitals per site, the remaining orbitals being treated as core states. In this first approach, as we concentrate more on the correlation effects, we neglect, however important for this heavy element, the spin-orbit coupling. The crystal field splitting on f orbitals (and other ones), is directly accounted by the LMTO method, lifting the f degeneracy in the 6-fold (including spin) T_1, the 6-fold T_2 and 2-fold A_2 symmetries. Finally, the interaction H_{int}, added to H_0, is simply given by the same local term between electrons on different f-orbitals

$$H_{\rm int} = \frac{U}{2} \sum_{i,\alpha\sigma\neq\beta\sigma'} n_{i\alpha\sigma} n_{i\beta\sigma'} \tag{43}$$

neglecting any exchange term as done in [36,37]. In this simplified paramagnetic version, the number of inequivalent atomic configurations, necessary to perform the Gutzwiller part, reduces to 14 because all atomic configurations having the same electronic occupancy are equivalent in this model. Similarly, we took an average occupation per f orbital in the expression of q-factors, leading to a single q for all f orbitals, regardless to crystal field splitting. It was, however, included for the on-site levels renormalization, since the partial kinetic energy and occupations are not exactly equal for different symmetries. We have nevertheless checked this assumption by performing a much heavy calculation, including 3 different q's, one per crystal symmetry with 7x7x3 = 147 variational parameters: the final result was not sensitive to this detail. It reflects the small f-crystal field splitting in Plutonium, producing very similar occupations and partial kinetic energies.

The Coulomb interaction U could be also provided by constrained LDA calculations. In that sense, it would not be an adjustable parameter. However, we did not recalculate its value and took it from literature, close to 0.3Ry, as in the LDA+DMFT calculation of Savrasov et al. [10], or as in the LDA+U calculation of Bouchet et al. [36]. An improved version of calculation, including exchange interaction, as in the degenerate Hubbard model, with one q-factor per symmetry, will be used in a forthcoming paper, in which we will investigate also ferromagnetic and antiferromagnetic ground states. In this work we just want to appreciate the effect of our method and of the Gutzwiller approximation on a simple case,where there exists known results with other methods.

The total energy versus volume for fcc-Pu and different values of the interaction U is presented in Fig. 4. The curve $U = 0$ corresponds to a LDA calculation. As previously found in several works the minimum of this curve is very low ($\sim$ 7.70 ua) compared to the experimental value of the δ phase (8.60 ua) and closer to the α phase value (8.0 ua). In fact there is no sign of the correlated δ phase in the $U = 0$ calculation. As we turn on the correlations, a new feature appears in the curves, almost instantly. We observe a new energy minimum close to the experimental volume of the δ

phase. Moreover the first minimum increases to approach the value of the experimental α volume, showing that correlations are already important to reproduce the properties of this phase. For a value of U close to 0.3 Ry, the two minimums correspond to the experimental values of α and δ-Pu. This double-well feature of the total energy curve of Pu was previously discovered by Savrasov *et al* [10], using a DMFT approach. In our calculations the first minimum is the lower one, since the α phase is the ground state for Pu, and we haven't added any temperature effect in our calculations. As U increases we see a tendency of the two minimums to be closer. In fact the energies of the two phases are very similar and a small perturbation, for example the temperature, can be sufficient for the phase transition. Of course the model studied in this work is still very simple and we don't want to conclude too far but we think that it already contains the key ingredients (competition between localization and delocalization, atom-like or bands-like descriptions) to reproduce the main characteristics of Plutonium phase diagram. Due to the roughness of our first approach, the (rather) good agreement for the equilibrium properties, may be incidental or due to some compensation effect, and the disagreement with other aspects (like bulk modulus, see below) is not surprising. Indeed, it is well known the the spin-orbit coupling is a key ingredient for this element: the splitting between 5/2 and 7/2 states could give significant differences in occupation and kinetic energies. One may expect then a difference between $q_{5/2}$ and $q_{7/2}$, and obtain localized and less localized behaviors as suggested by Pénicaud [41] who proposed to split f states between localized and more delocalized ones to explain the properties of Plutonium. The freezing of f-states to similar occupation in our present calculation could be responsible for the high value of the bulk modulus (637 GPa) we get, in contrast with the experimental value of 30 GPa [42]. Primary result with an improved version involving third order LMTO Hamiltonian full self-consistent computation, neglecting yet spin-orbit coupling, reduces this value to 196 GPa, which is slightly better than the LDA result of 214 GPa [43].

This *ab-initio* Gutzwiller approach is able to handle correctly the correlation aspects without loosing the *ab-initio* adjustable parameters free aspect of the more familiar DFT-LDA, and that way, corrects the deficiency of this method. It gives similar results to the methods that account for many-body effects like the LDA+DMFT of Ref. [10] from the *ab-initio* levels or that can have an orbital dependent potential like in the LDA+U calculation of Ref. [36], which is impossible to DFT-LDA approach. On another hand, we stress again that our approach is clearly variational, and is able to provide an approximate ground state in contrast with those of Refs. [10] and [36].

The effective optimized Hamiltonian H', was used to compute quasiparticles density of states, in the vicinity of Fermi energy. The result, shown on Fig. 5, is restricted to an energy window of 2eV on both sides of Fermi

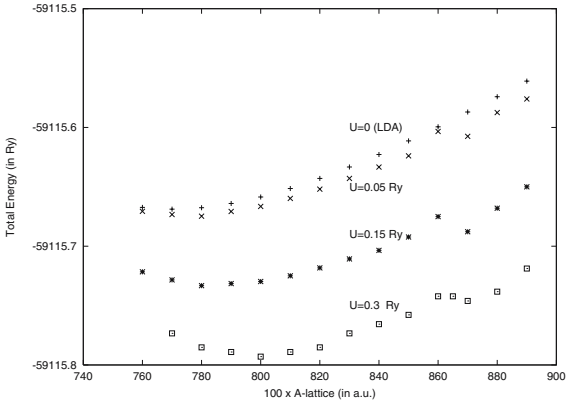

Figure 4. Total energy of fcc-Pu versus volume for different values of the interaction U. $U = 0$ corresponds to a LDA calculation.

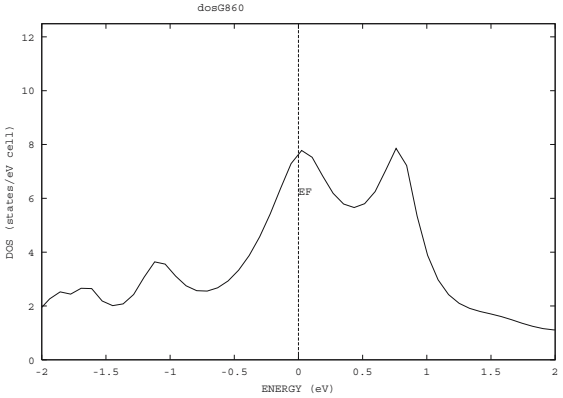

Figure 5. Quasiparticles density of states obtained from Gutzwiller method for Plutonium in δ phase.

level: further, the spectrum would be in the region of the Hubbard subbands, which are beyond the scope of our approach (it should be necessary to include fluctuations to get the incoherent part of the spectrum). It is to be stressed that our result compares well, in the presented region, with the more elaborated LDA+DMFT result of Ref. [10]. Both results are also in good agreement with the photoemission experiments of Arko et al. [44]. The peak at the Fermi level, which results mainly from the reduction of hoppings due to q-factors, associated with a small shift of Fermi level due to the renormalization of levels (36), has the consequence of a significant improvement of the electronic specific heat contribution, multiplied by a factor of 2 with respect to the LDA value. Our result, of the order of 13 mJ K^{-2} $mol^{-1}$is however yet far from the experimental value of 64 mJ K^{-2}

mol^{-1} found by Lashley *et al* [45]. The q-factor, responsible for this increase of the DOS at the Fermi level, is of the order of 0.8 in the equilibrium δ phase. This moderate renormalization is due to hybridization of the f states with the low lying p-states which lead to a significant partial f kinetic energy, greater than what it would be considering only the narrow group of predominant f-character states. With a naive single f-band argument, if we had used for example canonical (i.e. unhybridized) bands, one obtains a much reduced q-factor close to .3 [46]. It can be shown that the q-factor is the spectral weight of the quasiparticles. A moderate value, as obtained by our realistic calculation (i.e. fully hybridized bands), means a rather high weight: for independent particles it would be equal to one. It validates a quasiparticles picture description, allowing *a posteriori* comparison we did with spectroscopy experiments. At the volume of the "pseudo" α phase, this q factor reduces to .9, indicating that the electrons are less correlated in this phase, which can explain the relative success of its description by LDA calculation.

4. Conclusion

To conclude, we have generalized the density matrix approach to Gutzwiller method for the degenerate Hubbard Hamiltonian. We have shown that we can express the total energy in the Gutzwiller state in terms of the different probabilities of configurations. Moreover to apply the method to cases of physical interest we have developed this method for inequivalent sites and for different orbital symmetries. In this way we have given the expression of the different q factors which renormalize the hopping terms and an expression to renormalize the on-site energies in the Gutzwiller context. This method is limited to ground state properties but can extend to finite temperature and low-frequency excitations in analogy with the work of Gebhard [47]. Of course, as a quasiparticle approach, this method is limited to cases where the Fermi-liquid theory is valid, i.e. close to Fermi energy. Thereafter we have have described a simple implementation of our method in a *ab-initio* calculation as the LMTO method. To give an example, we have applied this technique to the particular case of Pu in fcc structure. In despite of the simplicity of our model, we were able to extract interesting results such as the double-well feature in the energy-volume curve and more generally improve the LDA results. Our results compare well with previous works.

5. Acknowledgements

This work was performed under the auspices of the Commissariat à l'Energie Atomique under Contract No 9M 1898. The authors wish to thank R.C Albers of Los alamos National Laboratory for supporting of the present work.

We are also grateful to F. Jollet, A. Pasturel and A. Georges for stimulating discussions.

References

1. P. Fulde, *Electron Correlations in Molecules and Solids*, vol. 100 (Solid-State Sciences, Springer, 1995).
2. P. Hohenberg and W. Kohn, Phys. Rev., **136**, 864 (1964).
3. W. Kohn and L. J. Sham, Phys. Rev., **140**, 1133(1965).
4. R.D. Mattuck, *A Guide to Feynman Diagrams in the Many-Body Problem*, second edition (Dover, 1974).
5. G. Kotliar and A.R. Ruckenstein, Phys. Rev. Lett., **57**, 1362 (1986).
6. H. Mori, Prog. Theor. Phys., **33**, 423 (1965).
   R. Zwanzig, *Lectures in Theoretical Physics*, Vol. 3 (Interscience, New York, 1961).
7. A. Georges, G. Kotliar, W. Krauth and J. Rozenberg, Rev. Mod. Phys., **68**, 13 (1996).
8. V.I. Anisimov, F. Aryasetiawan and A.I. Lichtenstein, J. Phys.: Condens. Matter, **9**, 767 (1997).
9. V. I. Anisimov, A. I. Poteryaev, M. A. Korotin, A. O. Anokhin and G. Kotliar, J. Phys.: Condens. Matter, **9**, 7359 (1997).
10. S.Y. Savrasov, G. Kotliar and E. Abrahams, Nature (London), **410**,793 (2001).
11. M.C. Gutzwiller, Phys. Rev. Lett., **10**, 159 (1963).
12. M.C. Gutzwiller, Phys. Rev., **137**, A1726 (1965).
13. J. Hubbard, Proc. Roy. Soc. London, **A 276**, 238 (1963).
14. F. Gebhard, *The Mott Metal-Insulator Transition- Models and Methods*, Tracts in Modern Physics, **137**, Springer (1997).
15. D. Vollhardt, Rev. Mod. Phys., **56**, 99 (1984).
16. P. Nozières, *Magnétisme et localisation dans les liquides de Fermi*, Cours du Collège de France, Paris (1986).
17. W.F. Brinkmann and T.M. Rice, Phys. Rev. B, **2**, 1324 (1970).
18. D. Mayou, D.N. Manh and J.-P. Julien, Solid State Comm., **68**, 665 (1988).
19. J.-P. Julien, Physica B, **259**, 757 (1999).
20. J.-P. Julien and J. Bouchet, Physica B, **359-361**, 783 (2005).
21. J. Bünemann, W. Weber and F. Gebhard, Phys. Rev. B, **57**, 6806 (1998).
22. J. Bünemann, F. Gebhard and W. Weber, J. Phys.: Condens. Matter, **9**, 7343 (1997).
23. W. Metzner and D. Vollhardt, Phys. Rev. Lett., **59**, 121 (1987).
24. S. Sugano, Y. Tanabe and H. Kamimura, Pure Appl. Phys., **33**, 38 (1970).
25. J. Bünemann and W. Weber, Phys. Rev. B, **55**, 4011 (1997).
26. T. Okabe, J. Phys. Soc. Jpn., **66**, 2129 (1997).
27. H. Hasegawa, J. Phys. Soc. Jpn., **66**, 1391 (1997).
28. J.P. Lu, Internat. Journal of Modern Phys., **B10**, 3717 (1996).
29. O.K. Andersen, Phys. Rev. B, **12**, 3060 (1975).
30. O.K. Andersen, O. Jepsen and D. Gloetzel, *Highlights of Condensed Matter Theory - Varenna notes - Proceedings of The International School of Physics Enrico Fermi*, North Holland, New York(1985).
31. U. von Barth and L. Hedin, J. Phys. C, **5**, 1629 (1972).
32. P. Vargas, *Methods of Electronic Structure Calculations*, 147 (Proceedings of the Miniworkshop on Methods on Electronic Structure Calculations, Trieste, 1992).
33. R. Haydock, in *Solid State Physics*, **35**, 215 (Academic Press, New York,1980).
34. P. Turchi, F. Ducastelle and G. Tréglia, J. Phys. C, **15**, 2891 (1982).
    32
35. S. Lundqvist and N.H. March, *Theory of the inhomogeneous electron gas* (Plenum Press, New York, 1983).
36. J. Bouchet, S. Siberchicot, A. Pasturel and F. Jollet, J. Phys.: Condens. Matter, **12**, 1723 (2000).
37. S.Y. Savrasov and G. Kotliar, Phys. Rev. Lett., **84**, 3670 (2000).

38. Y. Wang and Y. Sun, J. Phys.: Condens. Matter, **12**, L311 (2000).
39. A.L. Kupetov and S.G. Kupetova, J. Phys.: Condens. Matter, **15**, 2607 (2003).
40. P. Söderlind, Europhys. Lett., **55**, 525 (2001).
41. M. Pénicaud, J. Phys.: Condens. Matter, **9**, 6341 (1997).
42. H.M. Ledbetter and R.L. Moment, Acta Metallurgica, **24**, 891 (1976).
43. P. Söderlind, *Theoretical Studies of Elastic, Thermal and Structural Properties of Metals* (PhD Thesis, 1994).
44. A.J. Arko, J.J. Joyce, L. Morales, J. Wills, J.C. Lashley, F. Wastin and J. Rebizant, Phys. Rev. B, **62**, 1773 (2000).
45. J.C. Lashley, J. Singleton, A. Migliori, J.B. Betts, R.A. Fisher, J.L. Smith and R.J. McQueeney, Phys. Rev. Lett., **91**, 205901 (2003).
46. J. Bouchet, *Etude du Plutonium en Phase δ et de ses Alliages avec les Eléments de la Colonne IIIB* (PhD Thesis, unpublished, Université Paris VI, 2000).
47. F. Gebhard, Phys. Rev. B, **44**, 992 (1991).

AB-INITIO QUANTUM DIFFUSION IN QUASICRYSTALS

J.-P. JULIEN
Laboratoire d'Etudes des Propriétés Electroniques des Solides, CNRS, B.P. 166, 38042 Grenoble Cedex 9, France

G. TRAMBLY DE LAISSARDIERE
Laboratoire de Physique Théorique et Modélisation, Université de Cergy-Pontoise and CNRS, 95302 Cergy-Pontoise, France

AND

D. MAYOU
Laboratoire d'Etudes des Propriétés Electroniques des Solides, CNRS, B.P. 166, 38042 Grenoble Cedex 9, France

Abstract. We compute the velocity correlation function of electronic states close to the Fermi energy, in approximants of quasicrystals. As we show the long time value of this correlation function is small. This means a small Fermi velocity, in agreement with previous band structure studies. Furthermore the correlation function is negative on a large time interval which means a phenomenon of backscattering. As shown in previous studies the backscattering can explain unusual conduction properties, observed in these alloys, such as for example the increase of conductivity with disorder.

1. Introduction

In 1984, Schechtman, Blech, Gratias, and Cahn [1] presented a new metastable phase of an Al–Mn binary alloy. The diffraction pattern was formed by intense Bragg peaks organized according to the icosahedral symmetry strictly forbidden from conventional crystallography. The underlying order was claimed to be described by the mathematical concept of quasiperiodicity [2, 3]. The confirmation of a new state of matter has been an intense subject of controversy. In particular, Pauling proposed an alternative description of five-fold diffraction patterns based on icosahedral glasses formed

J.-P. Julien et al. (eds.),
Recent Advances in the Theory of Chemical and Physical Systems, 535–546.

by twins [4]. However, the situation changed after the discovery of stable phases (icosahedral AlCuFe, AlPdMn, AlCuCo...) by Tsai et al. [5], and the existence of quasiperiodic crystals (quasicrystals) is now well accepted. Furthermore, these materials have revealed a lot of unexpected physical properties [6].

Among many fascinating properties, quasicrystals with high structural quality, such as the icosahedral AlCuFe and AlPdMn alloys, have unconventional conduction properties when compared with standard intermetallic alloys. Their conductivities can be as low as 150–200 $(\Omega\,\mathrm{cm})^{-1}$ [7]. Furthermore the conductivity increases with disorder and with temperature, a behaviour just at the opposite of that of standard metal. In a sense the most striking property is the so-called *"inverse Mathiessen rule"* [8] according to which the *increases of conductivity* due to different sources of disorder seems to be *additive*. This is just the opposite that happens with normal metals where the increases of resistivity due to several sources of scattering are *additive*. Finally the Drude peak which is a signature of a normal metal is also absent in the optical conductivity of these quasicrystals.

An important result is also that many approximants of these quasicrystalline phases have similar conduction properties. For example the crystalline α-AlMnSi phase with a unit cell size of about 12 Å and 138 atoms in the unit cell has a conductivity of about 300 $(\Omega\,\mathrm{cm})^{-1}$ at low temperature [7, 9]. The conductivity has the same defect and temperature dependence as that of the AlCuFe and AlPdMn icosahedral phase. There is, to our knowledge, no experimental result on the optical conductivity of this α-AlMnSi phase, but it is very likely that it is similar to that of AlCuFe and AlPdMn icosahedral phase.

The interpretation of these unconventional conduction properties is still a challenge for condensed matter physicists. Several models have been proposed including thermally activated hopping [10] band structure effects due to small density of states and narrow pseudo-gap [11, 12] or anomalous quantum diffusion [13, 14]. Yet all these models are difficult to compare in a quantitative way with experiments.

In this paper we present preliminary results of an *ab-initio* study of quantum diffusion in the crystalline α-AlMnSi phase. The number of atoms in the unit cell (138) is sufficiently small to permit computation with the *ab-initio* Linearized Muffin Tin Orbitals (LMTO) method and provides us a good starting model. Within the Density Functional Theory (DFT) [15, 16], this approach has still limitations due to the Local Density Approximation (LDA) for the exchange-correlation potential treatment of electron correlations and due to the approximation in the solution of the Schrödinger equation as explained in next section. However, we believe that this starting point is much better than simplified parametrized tight-binding like s-band models.

The central quantities are the velocity correlation function of states of energy E at time t: $C(E,t)$, and the average square spreading of states of energy E at time t along the x direction: $\Delta X^2(E,t)$. The velocity correlation function is defined by:

$$C(E,t) = \Big\langle V_x(t)V_x(0) + V_x(0)V_x(t)\Big\rangle_E = 2\,\mathrm{Re}\,\Big\langle V_x(t)V_x(0)\Big\rangle_E, \tag{1}$$

and the average square spreading:

$$\Delta X^2(E,t) = \Big\langle [X(t) - X(0)]^2\Big\rangle_E \tag{2}$$

where $\langle \mathrm{A}\rangle_E$ is the average of the operator A on states of energy E of Hamiltonian H, explicitly given by the traces fraction:

$$\langle A\rangle_E = \frac{Tr[\delta(E-H)A]}{Tr[\delta(E-H)]} \tag{3}$$

In (1), $\mathrm{Re}\,B$ is the real part of B and $V_x(t)$ is the Heisenberg representation of the velocity operator along x direction at time t. $C(E,t)$ is related to quantum diffusion by:

$$\frac{\mathrm{d}}{\mathrm{dt}}\Big(\Delta X^2(E,t)\Big) = \int_0^t C(E,t')\mathrm{dt}'. \tag{4}$$

Once the bandstructure is computed in a self-consistent way the velocity correlation function can be computed exactly in the basis of Bloch states. Relation (4) shows that an anomalous behaviour of $C(E,t)$ also implies an anomalous behavior of the quantum diffusion which is the basis for the model [13,14] of optical conductivity of quasicrystals. In the long time limit one knows that the propagation is ballistic, this means that $\Delta X^2(E,t)$ is given by $v_{\mathrm{F}}^2 t^2$ at large time. From (4) one deduces that $C(E,t)$ is of the order of $2v_{\mathrm{F}}^2$ at large time. But at intermediate times (see below) the behaviour of $C(E,t)$ is more specific of the crystal and we show that the α-AlMnSi phase is different compared to other good metals such as Al (f.c.c.), cubic $\mathrm{Al_{12}Mn}$ ...

In particular we find that there is on the average a phenomenon of *backscattering* in α-AlMnSi phase. This means that the velocity correlation function is often negative. This negative value has been shown previously [14] a sufficient condition to explain the unusual conduction properties of these alloys.

2. *Ab-initio* electronic structure

2.1. LMTO METHOD

Electronic structure determinations have been performed using the self-consistent LMTO method in the Atomic Sphere Approximation (ASA).

The LMTO method is well described elsewhere [17, 18] and we would like to remind here only the principal results which are usefull for this paper. In the frame of DFT-LDA band structure calculations, the LMTO method is based on some approximations. The space is divided in atomic spheres where the potential is spherically symmetric and interstitial region where it is flat ("Muffin Tin" potential). In the Atomic Sphere Approximation (ASA), the spheres radii are chosen so that the total volume of the spheres equals that of the solid. One makes a further approximation by supposing that the kinetic energy in the interstitial region is zero (without this non-essential assumption, Laplace equation, as used below, should be replaced by Helmoltz equation). In this intersticial region, the Schrödinger equation reduces to Laplace equation having regular and irregular solutions: $Y_L(\hat{r})r^{\ell}$ and $Y_L(\hat{r})r^{-\ell-1}$ respectively. Here $L = (\ell, m)$ represents the angular momentum index and $Y_L(\hat{r})$ the spherical harmonics in direction $\hat{r} = (\theta, \phi)$. For the sphere centered at site R and in the momentum index ℓ ($\ell = 0, 1, 2 \ldots$), one finds the solution $\varphi_{R\ell\nu}$ of the radial Schrödinger equation for a given so-called linearization energy E_ν, usually taken at the center of gravity of the occupied part of the ℓ-band and the energy derivative of $\varphi_{R\ell\nu}$ noted $\dot{\varphi}_{R\ell\nu}$ (Note that for the velocity correlation function, we need a great accuracy close to the Fermi level. Consequently, after self-consistency, we perform one iteration choosing $E_\nu = E_{\mathrm{F}}$). It can be shown that the corresponding orbitals $\varphi_{R\ell\nu}$ and $\dot{\varphi}_{R\ell\nu}$ are orthogonal to each other and nearly orthogonal to the core levels. It is thus possible to build a basis set of orbitals χ_{RL} centered at sphere of site R in the following way. Outside the sphere, in the interstitial region χ_{RL} is proportional to the irregular solution $Y_L(\hat{r})r^{-\ell-1}$ of Laplace equation and it is augmented (i.e. substituted according to Slater terminology) in its own sphere by a linear combination of $\varphi_{R\ell\nu}$ and $\dot{\varphi}_{R\ell\nu}$ having logarithmic derivative $-\ell - 1$ at the radius s_R of the sphere so that the orbital is continuous and derivable at the sphere boundary. In any other sphere R', the irregular solution of Laplace equation can be expanded in term of regular solutions in that sphere:

$$Y_L(\hat{r}_R)\left(\frac{r_R}{a}\right)^{-\ell-1} = -\sum_{L'} \frac{1}{2(2\ell'+1)} S^0_{R'L',RL} Y_{L'}(\hat{r}_{R'})\left(\frac{r_{R'}}{a}\right)^{\ell'} \qquad (5)$$

and the orbital χ_{RL} should be augmented in sphere R' with the same expansion of linear combination of $\varphi_{R'\ell'\nu}$ and $\dot{\varphi}_{R'\ell'\nu}$ having the logarithmic derivative ℓ' at the radius $s_{R'}$ of sphere R'. In (5), a is a scale factor and $S^0_{R'L',RL}$ are the so-called "structure constants" which depend only on the crystallographic structure of the material. In this basis set of the orbitals χ_{RL} both Hamiltonian and Overlap matrices can be expressed in terms of $S^0_{R'L',RL}$, and the potential parameters $\varphi_{R\ell\nu}(s_R)$, $\dot{\varphi}_{R\ell\nu}(s_R)$ and the logarithmic derivative $D_{R\ell\nu}$ and $\dot{D}_{R\ell\nu}$ of these functions at sphere boundary. Since the structure constants $S^0_{R'L',RL}$, decreasing as $r^{-\ell-\ell'-1}$ with distance, are

very long ranged for s and p orbitals, it can be more convenient to change the basis set so that the Hamiltonian can have the Tight-Binding (TB) form or any desired properties (like the orthogonality i.e. overlap matrix equals unit matrix). It can be achieved by adding to the regular solution of the Laplace equation an amount of the irregular solution for a given angular momentum. It is possible to choose this amount $\bar{Q}_\ell$ so that the transformed structure constants S can be screened with a short-range dependence with the distance or so that the orbitals of the transformed basis set are orthogonal (the so-called TB or most localized and orthogonal representations, respectively). With appropriate choice for $\bar{Q}_\ell$, the transformed structure constant matrix obeys to the following equation:

$$S = S^0(1 - \bar{Q}_\ell S^0)^{-1} \tag{6}$$

The Hamiltonian can be written as:

$$H_{RL,R'L'} = C_{RL}\delta_{RL,R'L'} + \Delta_{RL}^{1/2} S_{RL,R'L'} \Delta_{R'L'}^{1/2} \tag{7}$$

which is limited to first order in $(E - E_\nu)$ in the TB representation, whereas it is valid up to second order in the orthogonal representation. C_{RL} determines the middle of the band "RL" and Δ_{RL} its width and the strength of hybridization. These parameters are expressed in terms of the 4 potential parameters:$\varphi_{R\ell\nu}(s_R)$, $\dot{\varphi}_{R\ell\nu}(s_R)$, $D_{R\ell\nu}$ and $\dot{D}_{R\ell\nu}$. It should be stressed that hybridization between bands of different angular moments is due to the matrix elements $S_{RL,R'L'}$ which couples RL-states to $R'L'$ ones. Due to the periodicity of the approximant phases, one can apply Bloch theorem. Thus, once the potential parameters are known for each site and each ℓ-component, with an appropriate choice of screening constants, structure constants (6) and Hamiltonian (7) are transformed to k-space. Diagonalization provides energies with their respective eigenstates for each k-point $\vec{k}$ of the first Brillouin zone. These eigenstates are expressed on the basis of the

$$\chi_{\vec{t}L}(\vec{k}) = \frac{1}{\sqrt{N}} \sum_{\vec{T}} e^{i\vec{k}\cdot\vec{T}} \chi_{(\vec{T}+\vec{t})L} \tag{8}$$

which are the Bloch states obtained from the real space orbital $\chi_{(\vec{T}+\vec{t})L}$, located at site $\vec{t}$ of the unit cell $\vec{T}$: any general atomic site $\vec{R}$ can be decomposed as $\vec{R} = \vec{T} + \vec{t}$. ($N$ is the total number of cells, introduced here for normalization).

2.2. RESULTS: DENSITY OF STATES

For our practical applications, the LMTO basis includes all angular moments up to $\ell = 2$ and the valence states are Al (3s, 3p, 3d), Mn (4s, 4p, 3d).

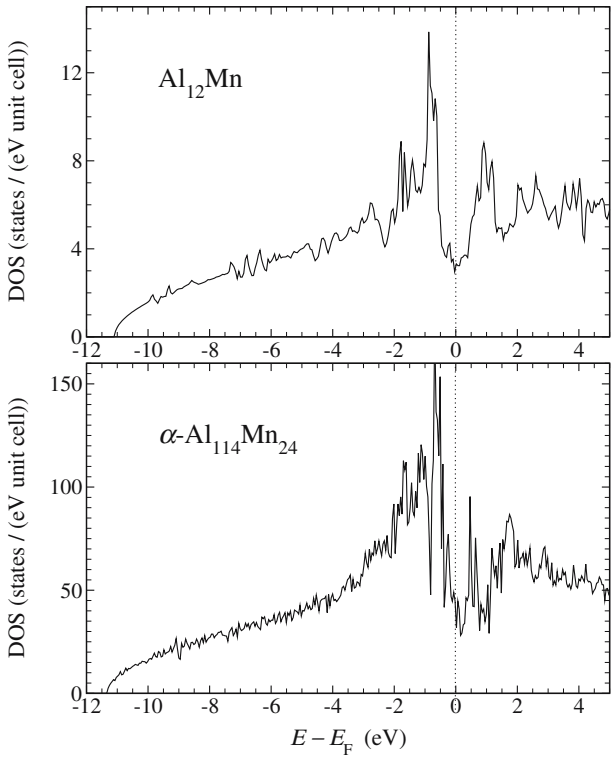

Figure 1. LMTO DOS of cubic $Al_{12}Mn$ (13 atoms / unit cell) and cubic α-$Al_{114}Mn_{24}$ approximant (experimental atomic structure of α-AlMnSi [26] with Si = Al, 138 atoms/ unit cell) [22].

The LMTO density of states (DOS) of an α-AlMn idealized approximant (structural model of Elser-Henley [19]) has been first calculated by T. Fujiwara [12, 20]. This original work shows the presence of a Hume-Rothery pseudo-gap near the Fermi energy, E_F, in agreement with experimental results [7, 11]. E.S. Zijlstra and S.K. Bose [24] gave a detailed *ab initio* electronic structure study of the α-phase. They show the difference between the DOS of the idealized 1/1 approximant and the experimental atomic structure [26]. The pseudogap is present in both cases. But one of the main difference is the spikiness of the DOS which is reduced for the experimental structure with respect to the idealized structure. DOSs of α-$Al_{114}Mn_{24}$ with experimental atomic positions [26] (Si atoms are replaced by Al atoms) is presented Fig. 1. The role of the transition metal (TM) element in the pseudo-gap formation has also been shown from *ab-initio* calculations [21, 22] and experiments. Indeed the formation of the pseudo-gap results from a strong sp–d coupling associated to an ordered sub-lattice of TM atoms. Just as for Hume-Rothery phases a description of

the band energy can be made in terms of pair interactions. We have shown that a medium-range Mn–Mn interaction mediated by the sp(Al)–d(Mn) hybridization plays a determinant role in the occurrence of the pseudo-gap [22, 23]. It is thus essential to take into account the chemical nature of the elements to analyze the electronic properties of approximants. It has been shown [24] that Si atoms are in substitution with some Al atoms. The main effect of Si is to shift E_{F} in the pseudo-gap in agreement with Hume-Rothery mechanism to minimize band energy.

The electronic structures of simpler crystals such as orthorhombic Al_6Mn, cubic $Al_{12}Mn$, present also a pseudo-gap near E_{F} but it is less pronounced than for complex approximants phases [22].

3. Velocity correlation function

3.1. COMPUTATIONAL DETAILS

Starting from the self-consistent LMTO eigenstate Ψ_n with energy E_n, the velocity correlation function is [13]:

$$C(E,t) = 2 \left\langle \mathrm{Re}\left\{ \mathrm{e}^{\mathrm{i}\frac{\mathrm{E_n t}}{\hbar}} \langle \Psi_{\mathrm{n}} | \mathrm{V_x}\, \mathrm{e}^{-\mathrm{i}\frac{\mathrm{Ht}}{\hbar}} \mathrm{V_x} | \Psi_{\mathrm{n}} \rangle \right\} \right\rangle_{\mathrm{E_n=E}} \tag{9}$$

By using the closure properties of the eigenstates one obtains easily:

$$C(E,t) = 2 \left\langle \sum_p \cos\left((E_n - E_p)\frac{t}{\hbar} \right) \left| \langle \Psi_n | V_x | \Psi_p \rangle \right|^2 \right\rangle_{E_n=E}. \tag{10}$$

where the sum is over all the eigenstates Ψ_p with the same vector $\vec{k}$ than Ψ_n. In (10) the terms $n = p$ are the Boltzmann contribution to the velocity correlation function:

$$C_{\mathrm{B}}(E,t) = 2 \left\langle \sum_n \left| \langle \Psi_n | V_x | \Psi_n \rangle \right|^2 \right\rangle_{E_n=E} = 2v_{\mathrm{B}}^2 \tag{11}$$

which does not depend on the time t.

The products $\langle \Psi_n | V_x | \Psi_p \rangle$ are calculated from LMTO eigenstates by using a numerical derivation of the hamiltonian in the reciprocal space: as explained in last section, diagonalization provides the components of eigentstates on the basis set $\chi_{tL}(\overrightarrow{k})$. In this basis the velocity operator, $V_x = \frac{1}{i\hbar}[X, H]$, has the following matrix elements:

$$\langle \chi_{tL}(\overrightarrow{k}) | V_x | \chi_{t'L'}(\overrightarrow{k}) \rangle = \frac{1}{\hbar} \frac{\partial}{\partial k_x} \langle \chi_{tL}(\overrightarrow{k}) | H | \chi_{t'L'}(\overrightarrow{k}) \rangle \tag{12}$$

k_x is the component of k-point $\vec{k}$ in the x direction. Because of Bloch theorem, different k-points are not coupled in the Hamiltonian nor in the

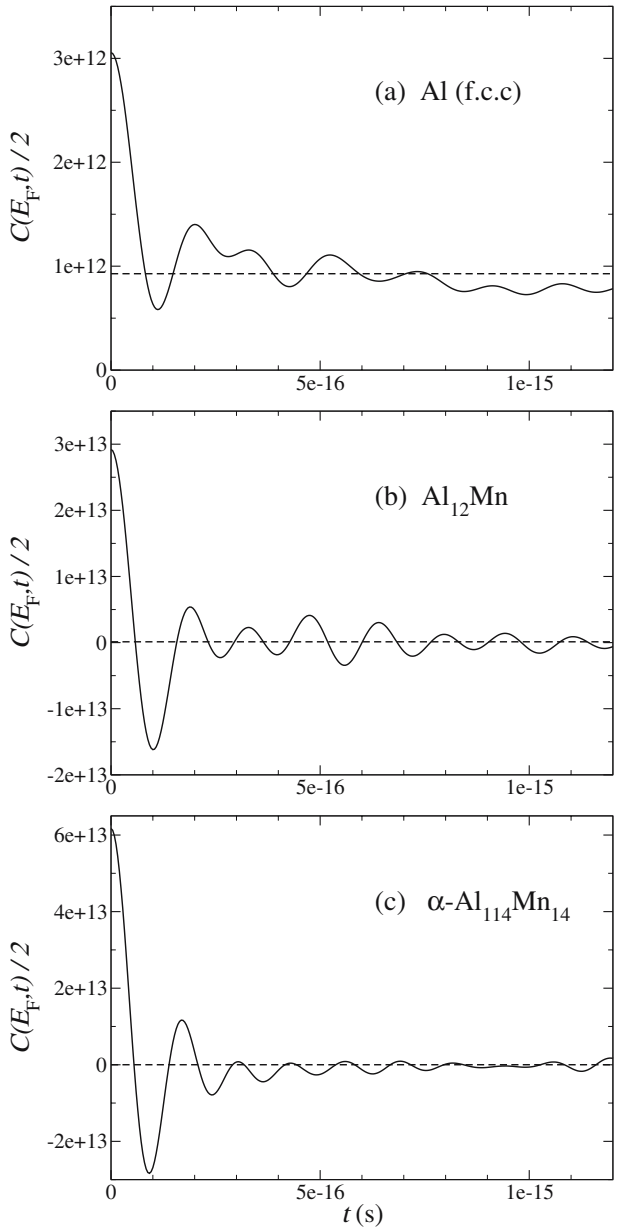

Figure 2. Velocity correlation function $C(E_{\rm F}, t)$ $({\rm m}^2\,{\rm s}^{-2})$ versus time t (s), for (a) Al (f.c.c), (b) cubic $Al_{12}Mn$, and (c) cubic approximant α-$Al_{114}Mn_{24}$. The dashed lines are the Boltzmann velocity correlation function $C_{\rm B}(E_{\rm F}, t) = 2v_{\rm F}^2$ [27].

velocity operator. Having performed the numerical derivation of (12), it is just a matrix multiplication to get expression (10). Formula (12) is an

approximation as one can show that there are additional terms on its right hand side. However these terms are of the order of $(E_n - E_\nu)^2$ and thus vanish for the energies of interest close to E_ν chosen at E_F. Finally equation (10) is integrated according to equation (4), to obtain the average square spreading $\Delta X^2(E,t)$.

3.2. RESULTS: EVIDENCE OF BACKSCATTERING IN AN APPROXIMANT OF QUASICRYSTALS

We compute $C(E,t)$ for crystals (complex approximants and simple crystals). In equations (10)–(11), the average on states of energy E is obtained by taking the eigenstates of each $\vec{k}$ vector with an energy E_n such as:

$$E - \frac{1}{2}\Delta E < E_n < E + \frac{1}{2}\Delta E. \tag{13}$$

ΔE is a kind of energy resolution of the calculation. The calculated $C(E,t)$ is rather sensible to the small number N_k of $\vec{k}$ vectors in the first Brillouin zone. Therefore N_k is increases until $C(E,t)$ does not depend significantly on N_k.

$C(E_\mathrm{F},t)$ for Al (f.c.c), cubic $Al_{12}Mn$ [25], and the cubic approximant α-$Al_{114}Mn_{24}$ (with the experimental atomic structure [26]) are shown in figure 2. E_F is the Fermi energy calculated by the self-consistent L.M.T.O. procedure. The energy resolution is $\Delta E = 1.36\,\mathrm{eV}$. The number of $\vec{k}$ points in the first Brillouin zone is $N_k = 80^3$, 40^3 and 10^3 for Al, $Al_{12}Mn$, and α-$Al_{114}Mn_{24}$, respectively.

For large t,

$$\lim_{t\to+\infty} C(E_\mathrm{F},t) \simeq C_\mathrm{B}(E_\mathrm{F},t) = 2v_\mathrm{F}^2\,, \tag{14}$$

where v_F is the Boltzmann velocity (intra-band velocity) at the Fermi energy: $v_\mathrm{F} = 9.6\,10^7$, $3.4\,10^7$, and $6.2\,10^6\,\mathrm{cm\,s^{-1}}$, for Al, $Al_{12}Mn$ and α-$Al_{114}Mn_{24}$, respectively. This last result is very similar to the original work of T. Fujiwara et al. [12] for the α-$Al_{114}Mn_{24}$ (with the atomic structure model of Elser-Henley). The strong reduction of v_F in the approximant phase with respect to simple crystal phases shows the importance of a quasiperiodic medium-range order (up to distances equal to 12–20 Å). This leads to a very small Boltzmann conductivity for the approximant [12].

When t is finite (figure 2), $C(E_\mathrm{F},t)$ and $C_\mathrm{B}(E_\mathrm{F},t)$ differ, and there is a new difference between approximant and simple crystal. In the case of Al (f.c.c.) phase, $C(E_\mathrm{F},t)$ is always positive, and the Boltzmann value is reached rapidly when t increases. But for some t values the velocity correlation function $C(E_\mathrm{F},t)$ is negative for $Al_{12}Mn$ and α-$Al_{114}Mn_{24}$. That means that at these times the phenomenon of *backscattering* occurs.

Roughly speaking, the transports properties depends on the values of $C(E_\mathrm{F},t)$ over all times t from 0 to the scattering time τ [13, 14] (see for

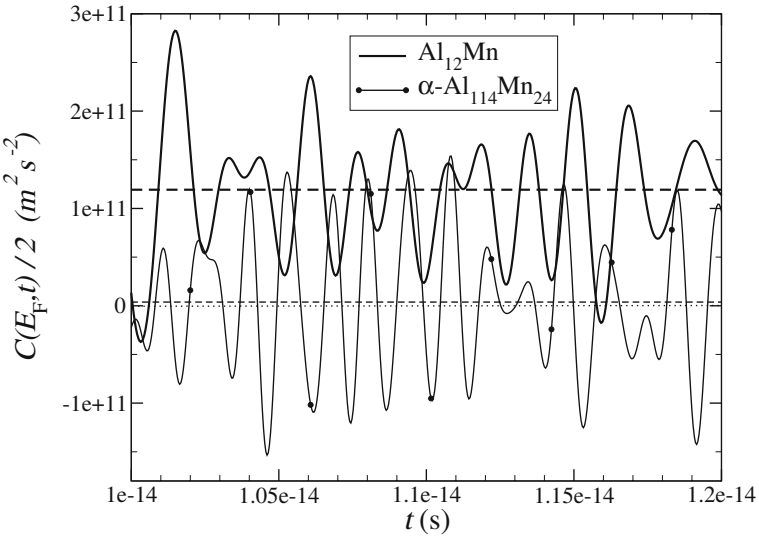

Figure 3. Velocity correlation function $C(E_{\mathrm{F}}, t)$ ($\mathrm{m}^2\,\mathrm{s}^{-2}$) versus large time t (see figure 2). The dashed lines are the corresponding Boltzmann velocity correlation function $C_{\mathrm{B}}(E_{\mathrm{F}}, t) = 2v_{\mathrm{F}}^2$.

instance equation (4)). A realistic value of τ has been estimated to about 10^{-14} s [8]. For the simple crystals $Al_{12}Mn$, $C(E_{\mathrm{F}}, t)$ is meanly positive when $t > 2\,10^{-15}$ s. But for the complex approximant α-$Al_{114}Mn_{24}$, a lot of t values correspond to $C(E_{\mathrm{F}}, t) < 0$, even when t is close to τ or larger (figure 3). Therefore, in the case of $Al_{12}Mn$, the backscattering (negative range of $C(E_{\mathrm{F}}, t)$) should have a negligible effect on the transport properties, whereas this effect must be determinant for the approximant.

The phenomenon of backscattering leads to unusual quantum diffusion. It is illustrated on the plot of the average spreading of states ΔX^2 (equation (2)) versus time t (figure 4). It shows that ΔX^2 results in two term: a Boltzmann term and a non-Boltzmann term. The Boltzmann term has the usual t^2 behavior: $\Delta X_{\mathrm{B}}^2 = v_{\mathrm{B}}^2 t^2$. The new non-Boltzmann contribution, which comes from the non-diagonal matrix element in (10), has an atypical constant asymptotic behavior. In a normal crystal this last term is negligible with respect to the Boltzmann term. On the contrary, in approximant both terms have the same order of magnitude for realistic times, typically t less than fews 10^{-14} s.

4. Conclusion

We present *ab-initio* calculations of the velocity correlation function of the electronic states close to the Fermi energy, in a complex approximant and simple crystals. These calculations are the first numerical proof of the exis-

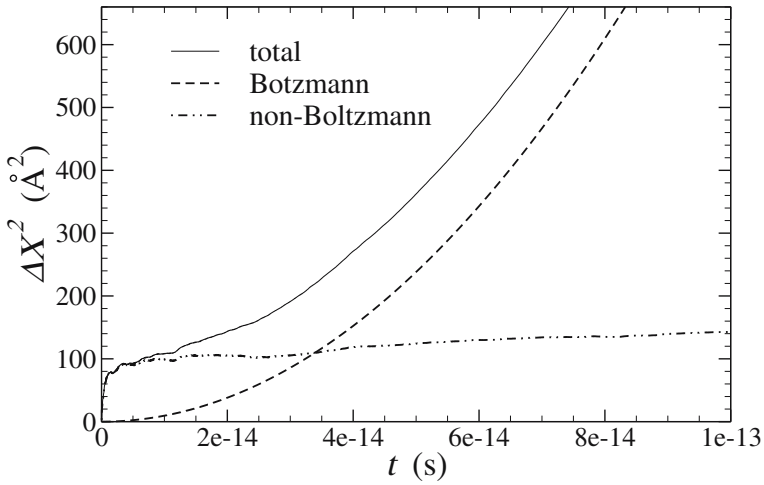

Figure 4. Average spreading of states $\Delta X^2(E,t)$ for energy $E = E_{\mathrm{F}}(\mathrm{LMTO})$, in α-Al–Mn. $\Delta X^2(E,t)$ can be decomposed in a Boltzmann term and a non-Boltzmann term.

tence of the phenomenon of backscattering in an approximant of quasicrystals. This shows that a Boltzmann approach is not enough to understand the unusual transport properties of quasicrystals. It will be shown elsewhere [28] that these results on the quantum diffusion explain fairly well the experimental conduction properties of the α-AlMnSi phase and of the related QC phases.

References

1. D. Shechtman, I. Blech, D. Gratias and J. W. Cahn, Phys. Rev. Lett. **51**, 1951 (1984).
2. H. Bohr and H. Cohn, Almost Periodic Functions (Chelsea, New York, 1947).
3. *Quasicrystals, The State of the Art*, edited by D. P. DiVicenzo and P. J. Steinhardt (World Scientific, Singapore, 1991), Vol. 11.
4. L. Pauling, Phys. Rev. Lett. **58**, 365 (1987).
5. A. P. Tsai, A. Inoue and T. Masumoto, Jpn. J. Appl. Phys. **26**, L1505 (1987); A. P. Tsai, A. Inoue and T. Masumoto, Mat. Trans. JIM **31**, 98 (1990).
6. *Proceedings of the 5th International Conference on Quasicrystals*, edited by C. Janot and R. Mosseri (World Scientific, Singapore, 1995).
7. C. Berger, *Lectures on Quasicrystals*, edited by F. Hippert and D. Gratias (Les Ulis: Les Editions de Physique, 1994), p. 463-504.
8. D. Mayou, C. Berger, F. Cyrot–Lackmann, T. Klein and P. Lanco, Phys. Rev. Lett. **70**, 3915 (1993).
9. C. Berger, C. Gignoux, O Tjernberg, P. Lindqvist, F. Cyrot-Lackmann and Y. Calvayrac, Physica B **204**, 44 (1995).
10. C. Janot, J. Phys. Condens. Mat., **9**, 1493 (1997).
11. S.J. Poon, Adv. Phys., **41**, 303 (1992); S.E. Burkov, T. Timusk and N.W. Ashcroft, J. Phys.: Condens. Matter **4**, 9447 (1992).

12. T. Fujiwara, S. Yamamoto and G. Trambly de Laissardière, Phys. Rev. Lett. **71**, 4166 (1993).
13. D. Mayou, Phys. Rev. Lett. **85**, 1290 (2000).
14. F. Triozon and D. Mayou, J. Non. Cryst. Solids **334-335**, 376 (2004).
15. P. Hohenberg and W. Kohn, Phys. Rev. **136**, 864, (1964).
16. W. Kohn and L. J. Sham, Phys. Rev. **140**, 1133 (1965).
17. O.K. Andersen, Phys. Rev. B **12**, 3060 (1975); L.H. Skriver, *The LMTO Method* (Springer, New-York, 1984).
18. O. K. Andersen, O. Jepsen and D. Gloetzel, *Highlights of Condensed Matter Theory - Varenna notes - Proceedings of The International School of Physics Enrico Fermi*, (North Holland, New York, 1985).
19. V. Elser, C. Henley, Phys. Rev. Lett. **55**,2883 (1985).
20. T. Fujiwara, Phys. Rev. B **40**, 942 (1989).
21. G. Trambly de Laissardière, D. Mayou and D. Nguyen Manh, Europhys. Lett. **21**, 25-30 (1993); G. Trambly de Laissardière, D. Nguyen Manh, L. Magaud, J.-P. Julien, F. Cyrot–Lackmann and D. Mayou Phys. Rev. B, **52**, 7920-7933 (1995).
22. G. Trambly de Laissardière, D. Nguyen Manh and D. Mayou, Prog. Mater. Sci. **50**, 679 (2005).
23. G. Trambly de Laissardière, D. Nguyen Manh and D. Mayou, J. Non-Cryst. Solids **334-335**, 347 (2004).
24. E.S. Zijlstra and S.K. Bose, Phys. Rev. B **67**,224204 (2003).
25. W.P. Pearson, *Handbook of Lattice Spacing and Structure of Metals* (Pergamon, New York, 1967), Vol. 2.
26. K. Sugiyama, N. Kaji and K. Hiraga, Acta Cryst. **C 54**, 445 (1998).
27. G. Trambly de Laissardière, J.-P. Julien and D. Mayou, *Proceedings of the 9th International Conference on Quasicrystals* (Ames, May, 2005), to be published in Phil. Mag.
28. G. Trambly de Laissardière, J.-P. Julien and D. Mayou, submitted to Phys. Rev. Lett. (2005).

TOWARDS NANOSTRUCTURED MATERIALS: AN EXAMPLE OF BORON NANOTUBES

I. BOUSTANI

Bergische Universität Wuppertal, FB C - Theoretische Chemie, Gaußstr. 20, D-42097 Wuppertal, Germany[†]

A. QUANDT

Universität Greifswald, Institut für Physik, Domstraße 10a, D-17489 Greifswald, Germany

J. A. ALONSO

Universidad de Valladolid, Departamento de Fisica Teorica, E-47011 Valladolid, Spain & Donostia International Physics Center, P. Manuel de Lardizabal 4, E-20018 San Sebastian, Spain

AND

A. RUBIO

Donostia International Physics Center, P. Manuel de Lardizabal 4, E-20018 San Sebastian, Spain

Abstract. Boron nanostructures B_{96} in form of α-rhombohedral nanocrystals and of nanotubes with different diameters were first calculated at the Hartree-Fock Self-Consistent-Field level of theory to generate the electron density. The obtained HF-SCF density-matrix was used as initial input to solve the Kohn-Sham equations of the density functional theory with the Becke-Lee-Yang-Parr Exchange-Correlation Potentials (B3LYP). The total B3LYP energy of each supercluster was determined. The stability of B_{96} nanotubes at the B3LYP level seems to be similar to or higher than the stability of naturally existing α-boron.

[†]email:boustani@uni-wuppertal.de

J.-P. Julien et al. (eds.),
Recent Advances in the Theory of Chemical and Physical Systems, 547–556.

1. Introduction

The ultimate goal of this research field is to develop, simulate and predict new arrays of nanoclusters and nanotubes with desired, pre-selected, uniform and specific properties. The development of nanoclusters, nano-tubes and nanocrystals into nanostructured materials can be expressed in form of miniaturization of these new materials towards nanoscaled electronic devices. Possible application fields for instance are in medicine and materials science. During the last decade many researchers focused their intention on a systematical search for new materials mainly consisting of pure or mixed boron, carbon, nitrogen, boron-hydrogen and metal-boron types of chemical systems. Those systems show a large variety of possible structures supposing that yet there are a lot of additional structures waiting to be discovered, like nano- structured crystals, quasi-crystals, nanotubes, nanowires, and their related compounds. In order to achieve this, there are several numerical structural optimisation methods based on a variety of concepts, ranging from the most accurate ab initio type of methods suited for small or medium sized systems to semi-empirical methods for very large systems.

Therefore, it became clear that those methods are reliable tools to detect, to analyze and to optimize all sorts of materials, and in many cases they already turn out to be some sort of cheap, fast and reliable alternative to standard experimental methods in materials science. But still, a lot of work is needed to be done in gaining a more profound experience in what could be called 'materials engineering', which means systematical understanding and development of new nanoscaled materials with definite properties, and in looking for the mechanism of the so called "self-assembling" of boron- and carbon-based materials to propose, predict and create nanodevices towards manufacturing of useful solids [1].

Our first contribution in the field of nanostructured materials was novel structural formations of boron clusters proposed by Boustani for the first time. In 1994 he predicted the quasiplanarity for boron clusters [2] and in 1997 nanostructures in tubular forms [3, 4]. Further contributions followed in a series of theoretical and experimental studies exploring the evidence of the new formations. On one side, the quasiplanarity was confirmed by A. Ricca et al. [5], F. L. Gu et al. [6], J. E. Fowler et al. [7], P. L. Cao et al. [8], A. A. Shvartsburg et al. [9] and J. Aihara [10], theoretically, and by D. E. Bergeron et al. [11] and H. J. Zhai et al. [12] experimentally. The first application of the quasiplanarity was carried out as B12 cluster embedded in graphitic fragments by N. H. March et al. [13].

One the other side, the nanostructures were issued similarly. Theoretically, they were confirmed by Lipscomb et al. [14], experimentally, by D. Ciuparu et al. [15] in form of boron single-wall nanotubes, by L. M. Cao et al. [16] C. J. Otten et al. [17], S. Iijima et al. [18], J. Z. Wu et al. [19]

and X. M. Meng et al. [20], in form of nanowires, by Z.Wang et al. [21] in form of nanobelts and by T. T. Xu et al. [22] in form of nanoribbons. All these groups succeeded to synthesize crystalline as well as amorphous boron nanostructures. In the current paper we determined the total energy of B_{96} species at the B3LYP version of the density functional theory and the band structure in form of density of states. The stability of the observed α-boron, and of proposed boron nanotubes with different diameters are calculated and compared. These boron nanotubes are generated from the topological structures [3] and with the help of the "Aufbau Principle" proposed for boron clusters [23].

2. Computational Methods

The theoretical basis for the current work are the standard ab initio approaches for solving the many-electron problems in atoms, clusters, and solids, the Hartree-Fock (HF) self-consistent-field (SCF) and the density functional theory (DFT) [24]. These important concepts are the kernels of a variety of program packages that we use for our simulations, depending on the size of the system to be examined. For small to large sized clusters (up to 100 atoms), we use quantum chemical methods like multi-configurational HF as well as different kinds of DFT methods, ranging from the local spin-polarized DFT-approaches (LSD) to the non-local (computationally more demanding) spin-polarized DFT methods (NSD). Due to the fact that the size of the investigated systems is relatively large, it was advisable to use the standard minimal STO3G basis set and to consider symmetry constraints in form of point group symmetry, in order to simplify the Hamiltonian through the direct product of the irreducible representations. Also due to the large number of basis functions (five per atom) we did not consider structural optimisations. The first step of calculations was carried out at the restricted HF level using the STO3G basis set. Regarding the large number of the valence electrons (480 electrons) within the investigated system, we were not able to determine the electron correlation contribution at the HF level of theory, which only treats the exchange energy. Therefore, keeping the HF-SCF electron density matrix as starting density, we applied the DFT considering the nonlocal corrections to exchange and correlation B3LYP, given by Becke and Lee-Yang and Parr [25], respectively, using GAMESS-UK version 6.3 including the DFT [26].

In order to calculate the band structure and the density of states (DOS) of periodic unit cells of a-rhombohedral boron (Fig. 1a) and of boron nanotubes (Fig. 3a), we applied the VASP package [27], an ab initio density functional code, using plane-waves basis sets and ultrasoft pseudopotentials. The electron-electron interaction was treated within the local density approximation (LDA) with the Ceperley-Alder exchange-correlation functional [28]. The kinetic-energy cutoff used for the plane-wave expansion of

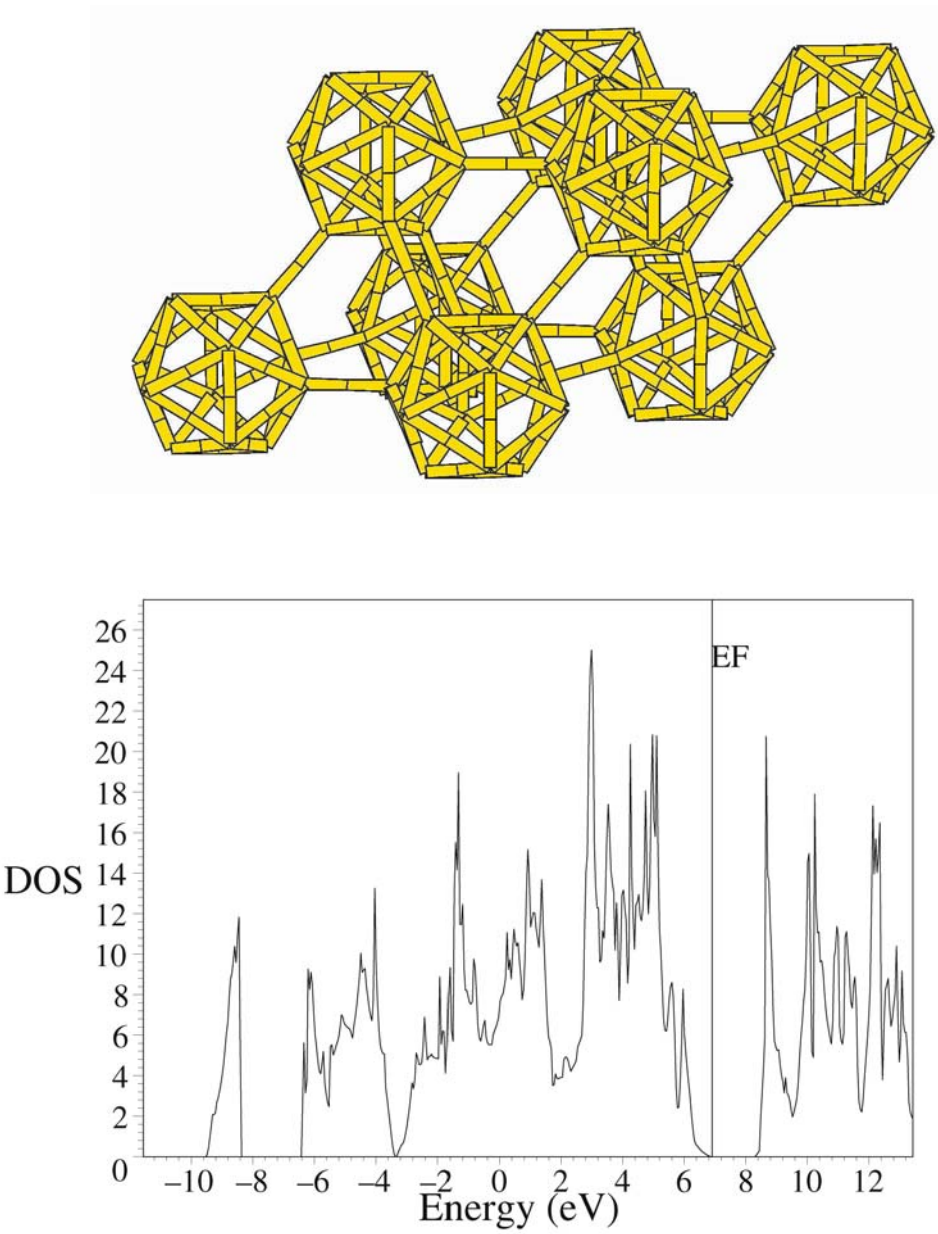

Figure 1. The a-rhombohedral unit cell of boron crystal (Fig. 1a) and the corresponding density of states DOS (Fig. 1b).

electronic wave functions was 321.4 eV for boron. The Brilloun zone was sampled on grids of (6x6x6) k points in the case of α-boron, and (5x5x5) k points in the case of boron nanotubes [29].

3. Results, Discussion and Conclusions

The investigated systems are the rhombohedral unit cell of α-boron crystals and boron nanotubes with different diameters. The α-boron B_{96} (Fig. 1a) is composed of eight connected icosahedra, centered at each vertex of the rhombohedral unit cell, representing crystalline boron, as a real system well known in nature. These almost compact and regular icosahedra form a network characterized by three-center and multi-center bonds. The unit cell of the α-boron has a space group R3m, a cell constant of 5.057 Angstrom a characteristic angle of 58.23 degrees, and a related dihedral angle of 52.93 degrees. As can be seen in (Fig. 1a) each icosahedron is bonded to six neighbouring icosahedra by direct B-B bonds along the threefold axis, and each of those almost perfectly coincides with an edge of the rhombohedral cell running through fivefold axes of the icosahedra. The average bond length lies between 1.67 and 2.10 . The DOS, given in (Fig. 1b), shows a band gap at the Fermi level of 1.57 eV.

Generally, nanotubes can be labelled by two indices (n,m), which indicate the way in which the graphene sheet is rolled onto a cylinder. The pair of integers (n,m) defines the Bravais lattice vectors, which determined the tube diameter. The combination (n,n) and (n,0) are for so called armchair and zig zag nanotubes, respectively. We generated (n,n) armchair nanotubes for n=24, 16, 12 and 8. These finite nanotubes are consisting of two 48-, three 32-, four 24-, and six 16-rings, respectively, as shown in (Fig. 2a to 2d). The corresponding diameters are 2.352, 1.557, 1.321 and 0.822 nanometers, respectively. The average bond length lies between 1.65 and 1.95 . They are characterized by three-center and multi-center bonds.

We would like to remind that all tubular structures are composed of 96 boron atoms, the same number of atoms in the elemental α-boron unit cell of boron crystals. The purpose is simply having clusters of the same size, in order to be energetically comparable. On one hand, α-boron is a real component existing in nature, and on the other hand, single-wall nanotubes so far have been predicted and also synthesized [15]. In this case we calculated the total B3LYP energies and determined the structure stability as follows: $E_b = (nE_1 - E_n) / n = E_1 - E_n / n$, where E_b is the binding energy per atom, E_1 the atomic energy, E_n the cluster energy, and n the cluster size. In our case, the cluster size n is 96. Beside the energy of the atomic boron, all obtained B3LYP energies and the corresponding binding energy per atom for each cluster are given in Table 1.

As can be seen in Table 1, the energy difference ΔE of all nanotubes relative to α-boron lies between 2 and 31 eV. By examining the B3LYP

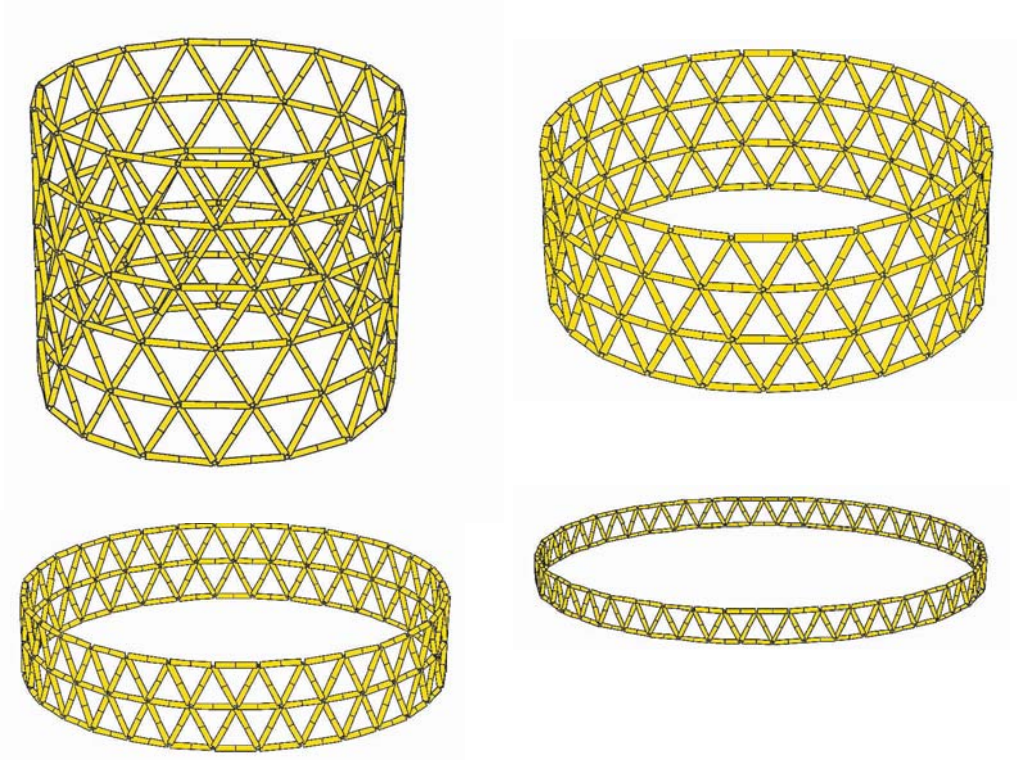

Figure 2. From the left: B_{96} cluster segments in form of two 48-rings (Fig. 2a), three 32-rings (Fig. 2b), four 24-rings (Fig. 2c) and six 16-rings (Fig. 2d) with the structures of (24, 24), (16,16), (12,12) and (8,8) armchair nanotubes, respectively.

Table 1

Specie	Cluster	Structure	B3LYP (a.u.)	E_b^1 (eV)	ΔE^2 (eV)
Crystal	α-boron	(5.057, 58.23, 52.94)[3]	-2353.45932	6.36	-0.0
Nanotubes	2x48-rings	$(2.352)^4$	-2354.59537	6.68	-30.9
	3x36-rings	$(1.636)^4$	-2354.25568	6.58	-21.7
	4x24-rings	$(1.321)^4$	-2353.96920	6.50	-13.9
	6x16-rings	$(0.822)^4$	-2353.53538	6.38	-2.1
B-Atom A(2P)			-24.28154		

1) Binding energy per atom.

2) The energy difference to the reference energy of α-boron.

3) The lattice distance (Å), rhombohedral (α) and dihedral (β) angles (grad) of α-boron unit cell.

4) The corresponding diameter (nanometer).

energies of boron nanotubes, it is easy to find out that the total energies are decreasing by increasing the diameter of the boron rings, and that the stability increases with increasing the diameters. The high stability of boron nanotubes can mainly be explained by the large number of directed sp2-hybridized s-bonds within the bent surfaces of the tubes, and by p-orbitals covering the inner and outer faces of the tubes, stabilizing the system even more.

Therefore, one can summarize two important statements from Table 1. The first one says that the stability of boron nanotubes is similar or higher than the stability of the real α-boron crystals. This statement confirms the same sequence of stability determined at the HF-SCF level of theory [30]. This phenomenon can only be explained by additional theoretical and experimental investigations. The second statement says that the larger the diameters the higher the stability. Finally, one of the most important properties is the electron density of states DOS of boron nanotubes. Figure 3b shows the DOS of (18,18) armchair, illustrated as puckered boron 36-ring. The DOS of (18,18) armchair dramatically changes in comparison to the DOS of α-boron, already shown in Fig. 1b. Boron nanotubes show a strongly conducting character, opposite to the semiconducting α-boron crystals.

One can conclude, that the predicted boron nanstructures were confirmed experimentally, namely in form of a single-wall [15], nanowires [16], nanobelts, [21], and nanoribbons [22]. However, much work remains to be done in the field of the boron nanotube chemistry and its possible potential applications as a hydrogen storage, electro-optics, semiconductors, supercoductivity and nanotechnology. The determination of the vibrational frequencies of boron nanotubes is of great interest for the infrared and raman spectroscopy. Finally, and according to our calculations the predicted boron nanotubes seem to be more stable than the real α-boron crystal. Nevertheless, further theoretical contributions are desirable for more insight into this phenomenon.

Acknowledgements

I. B. acknowledges the support of the German Research Foundation (DFG) and Fonds der Chemischen Industrie. I. B. and J. A. A. acknowledge the hospitality and support of the Donostia International Physics Center.

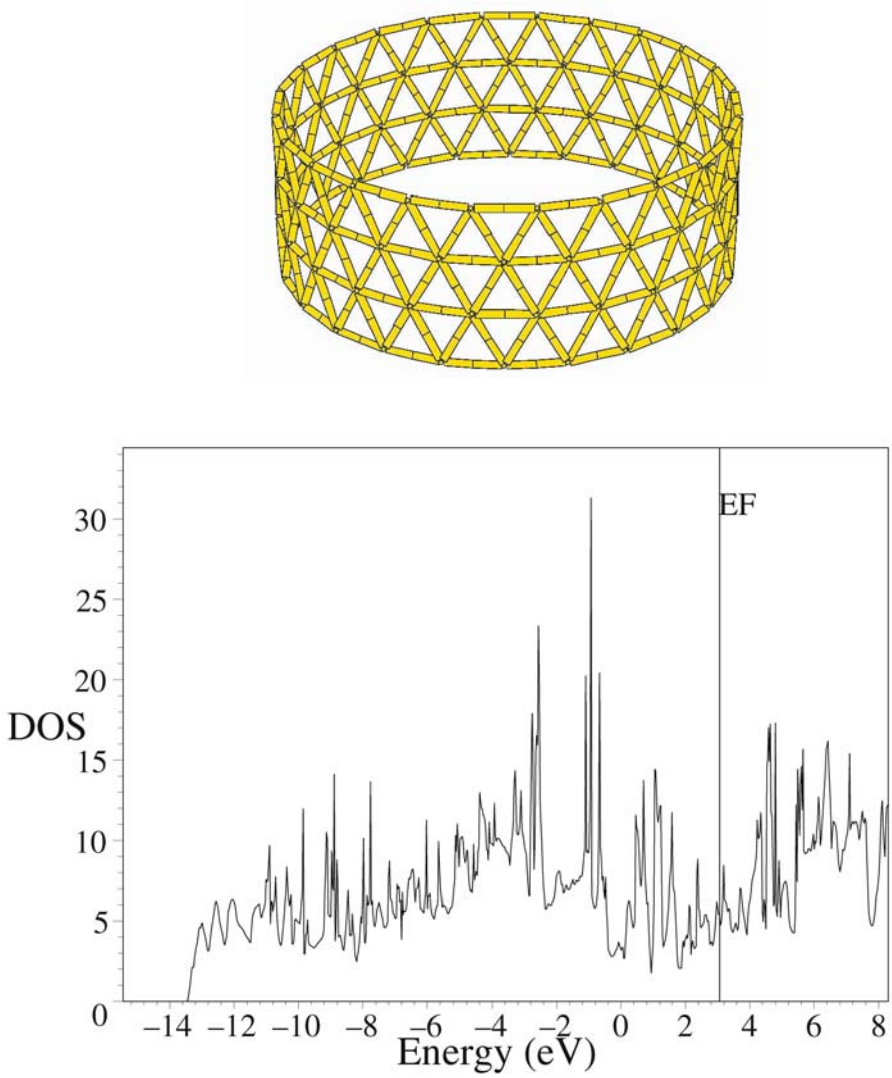

Figure 3. A Top view of puckered 36-ring (Fig. 3a) of (18,18) armchair with the corresponding density of states (Fig. 3b).

References

1. K. E. Drexler, in Nanosystems; Molecular Machinery, Manufacturing, and Computation, Wiley- Interscience publication, New York (1992).
2. I. Boustani, Int. J. Quantum Chem., 52, 1081 (1994).
3. I. Boustani, and A. Quandt, Europhys. Lett., 39, 527 (1997).
4. I. Boustani, A. Quandt, E. Hernandez, and A. Rubio, J. Chem. Phys. 110, 3176 (1999).
5. A. Ricca, and C. W. Bauschlicher, Chem. Phys. 208, 233 (1996).
6. F. L. Gu, X. Yang, A. C. Tang, H. Jiao, and P. V. R. Schleyer, J. Compt. Chem. 19, 203 (1998).
7. J. E. Fowler, and M. J. Ugalde, J. Phys. Chem. A 104, 397 (2000).
8. P. L. Cao, W. Zhao, B. X. Li, B. Song, and X. Y. Zhou, J. Phys.: Condens. Matter 13, 5065 (2001).
9. A. A. Shvartsburg, S. V. Mashkevich, and K. W. M. Siu, J. Phys. Chem. A 104, 9448 (2000).
10. J. Aihara, J. Phys. Chem. A 105, 5486 (2001).
11. D. E. Bergeron, and A. W. Castleman, Jr., Int. J. Spectrometry 230, 71 (2003).
12. H. J. Zhai, B. Kiran, J. Li, and L. S. Wang, Nature Materials Vol. 2, 12, 827 (2003).
13. A. Peeters, C. V. Van Alsenoy, N. H. March, D. J. Klein, and V. E. Van Doren, J. Phys. Chem. B 105, 10546 (2001)
14. A. Gindulyte, W. Lipscomb, and L. Massa Inorg. Chem. 37, 6544 (1998).
15. D. Ciuparu, R. F. Klie, Y. Zhu, and Lisa Pfefferle, J. Phys. Chem. B 108, 3967 (2004)
16. L. Cao, Z. Zhang, L. Sun, C. Gao, M. He, Y. Wang, Y. Li, X. Zhang, G. Li, J. Zhang, and W. Wang, Adv. Mater., 13, 1701 (2001).
17. C. J. Otten, O. R. Lourie, M. F. Yu, J. M. Cowley, M. J. Dyer, R. S. Ruoff, and W. E. Buhro, J. Am. Chem. Soc., 124, 4564 (2001).
18. Y. Zhang, H. Ago, M. Yumura, T. Komatsu, K. Uchida, and S. Iijima, Chem. Commun., 23, 2806 (2002).
19. J. Z. Wu, S. H. Yun, A. Dibos, D.-K. Kim, and M. Tidrow, Microelectronics Journal 34, 463 (2003).
20. X. M. Meng, J. Q. Hu, Y. Jiang, C. S. Lee, and S. T. Lee, Chem. Phys. Lett. 370, 825 (2003).
21. Z. Wang, Y. Shimizu, T. Sasaki, K. Kawaguchi, K. Kimura, and N. Koshizaki, Chem. Phys. Lett. 368, 663 (2003).
22. T. T. Xu, J.-G. Zheng, N. Wu, A. W. Nicholls, J. R. Roth, D. A. Dikin, and R. S. Ruoff, Nano Lett. 2004, submitted.
23. I. Boustani, Phys. Rev. B 55, 16426 (1997).
24. P. Hohenberg and W. Kohn, Phys. Rev. B 136, 864 (1964); W. Kohn and L. J. Sham, Phys. Rev. A 140, 1133 (1965).
25. A. D. Becke, Phys. Rev. A 38, 3098 (1988); C. Lee, W. Yang, and R. G. Parr, Phys. Rev. B 37, 785 (1988)
26. M.F. Guest, J.H. van Lenthe, J. Kendrick, and P. Sherwood, with contributions from R.D. Amos, R.J. Buenker, H. van Dam, M. Dupuis, N.C. Handy, I.H. Hillier, P.J. Knowles, V. Bonacic-Koutecky, W. von Niessen, R.J. Harrison, A.P. Rendell, V.R. Saunders, K. Schöffel, A.J. Stone and D. Tozer. (http://www.cse.clrc.ac.uk/qcg/gamess-uk/).
27. G. Kresse, and J. Furthmller, Comput. Mater. Sci. 6, 15 (1996); Phys. Rev. B 54, 11169 (1996).
28. D. M. Ceperley, and B. J. Alder, Phys. Rev. Lett. 45, 1196 (1980).
29. A. Quandt, A. Y. Liu, and I. Boustani, Phys. Rev. B 64, 125422 (2001).
30. I. Boustani, A. Quandt, and A. Rubio, J. Solid State Chem., 154, 269 (2000).

STOCHASTIC OPTIMIZATION METHODS FOR PROTEIN FOLDING

ALEXANDER SCHUG, THOMAS HERGES, ABHINAV VERMA AND WOLFGANG WENZEL

Forschungszentrum Karlsruhe , Institut für Nanotechnologie, P.O. Box 3640, 76021 Karlsruhe, Germany wenzel@int.fzk.de

Summary. We recently developed an all-atom free energy force field (PFF01) for protein structure prediction with stochastic optimization methods. We demonstrated that PFF01 correctly predicts the native conformation of several proteins as the global optimum of the free energy surface. Here we review recent folding studies, which permitted the reproducible all-atom folding of the 20 amino-acid trp-cage protein, the 40-amino acid three-helix HIV accessory protein and the sixty amino acid bacterial ribosomal protein L20 with a variety of stochastic optimization methods. These results demonstrate that all-atom protein folding can be achieved with present day computational resources for proteins of moderate size.

1 Introduction

Ab-initio protein tertiary structure prediction (PSP) and the elucidation of the mechanism of the folding process are among the most important outstanding problems of biophysical chemistry [1, 2]. The many complementary proposals for PSP span a wide range of representations of the protein conformation, ranging from coarse grained models to atomic resolution. The choice of representation often correlates with the methodology employed in structure prediction, ranging from empirical potentials for coarse grained models [3, 4] to complex atom-based potentials that directly approximate the physical interactions in the system. The latter offer insights into the mechanism of protein structure formation and promise better transferability, but their use incurs large computational costs that has confined all-atom protein structure prediction to all but the smallest peptides [5, 6].

It has been one of the central paradigms of protein folding that proteins in their native conformation are in thermodynamic equilibrium with their environment [7]. Exploiting this characteristic the structure of the protein can be predicted by locating the global minimum of its free energy surface without recourse to the folding dynamics, a process which is potentially much more efficient than the direct simulation of the folding process. PSP based on

J.-P. Julien et al. (eds.),
Recent Advances in the Theory of Chemical and Physical Systems, 557–572.

global optimization of the free energy may offer a viable alternative approach, provided that suitable parameterization of the free energy of the protein in its environment exists and that global optimum of this free energy surface can be found with sufficient accuracy [8].

2 Force field

We have recently demonstrated a feasible strategy for all-atom protein structure prediction [9, 10, 11] in a minimal thermodynamic approach. We developed an all-atom free-energy force field for proteins (PFF01), which is primarily based on physical interactions with important empirical, though sequence independent, corrections [11]. We already demonstrated the reproducible and predictive folding of four proteins, the 20 amino acid trp-cage protein (1L2Y) [9, 12], the structurally conserved headpiece of the 40 amino acid HIV accessory protein (1F4I) [10, 13] and the sixty amino acid bacterial ribosomal protein L20 [14]. In addition we showed that PFF01 stabilizes the native conformations of other proteins, e.g. the 52 amino-acid protein A [5, 15], and the engrailed homeodomain (1ENH) from *Drosophilia melangaster* [16].

We have recently developed an all-atom (with the exception of apolar CH_n groups) free-energy protein force field (PFF01) that models the low-energy conformations of proteins with minimal computational demand [17, 10, 11]. In the folding process at physiological conditions the degrees of freedom of a peptide are confined to rotations about single bonds. The force field is parameterized with the following non-bonded interactions:

$$V(\{\boldsymbol{r}_i\}) = \sum_{ij} V_{ij} \left[\left(\frac{R_{ij}}{r_{ij}} \right)^{12} - \left(\frac{2R_{ij}}{r_{ij}} \right)^{6} \right] + \sum_{ij} \frac{q_i q_j}{\epsilon_{g(i)g(j)} r_{ij}} + \sum_i \sigma_i A_i + \sum_{\text{hbonds}} V_{hb}. \tag{1}$$

Here r_{ij} denotes the distance between atoms i and j and g(i) the type of the amino acid i. The Lennard-Jones parameters (V_{ij}, R_{ij} for potential depths and equilibrium distance) depend on the type of the atom pair and were adjusted to satisfy constraints derived from as a set of 138 proteins of the PDB database [18, 17, 19]. The non-trivial electrostatic interactions in proteins are represented via group-specific dielectric constants ($\epsilon_{g(i),g(j)}$ depending on the amino-acid to which atom i belongs). The partial charges q_i and the dielectric constants were derived in a potential-of-mean-force approach [20]. Interactions with the solvent were first fit in a minimal solvent accessible surface model [21] parameterized by free energies per unit area σ_i to reproduce the enthalpies of solvation of the Gly-X-Gly family of peptides [22]. A_i corresponds to the area of atom i that is in contact with a ficticious solvent. Hydrogen bonds are described via dipole-dipole interactions included in the electrostatic terms

and an additional short range term for backbone-backbone hydrogen bonding (CO to NH) which depends on the OH distance, the angle between N,H and O along the bond and the angle between the CO and NH axis [11].

3 Optimization Methods

The low-energy free energy landscape of proteins is extremely rugged due to the comparatively close packing of the atoms in the native structure. Suitable optimization methods must therefore be able speed the simulation by avoiding high energy transition states, adapt large scale move or accept unphysical intermediates. Here we report on four different optimization methods, the stochastic tunneling method [23], the basin hopping technique [24, 25], the parallel tempering method [26, 27] and a recently employed evolutionary technique. The stochastic tunneling method and the basin hopping approach are an inherently sequential algorithms, which evolve a single configuration according to a given stochastic process. In contrast, parallel tempering and evolutionary techniques are inherently parallel optimization strategies that are well suited to presently available multiprocessor architectures with low bandwidth connections. Since all-atom protein structure prediction remains a computationally challenging problem it is important to search for suitable optimization methods that are capable to exploit such architectures, i.e. a high degree of parallelism with very little and optimally asynchronous communication is desirable.

3.1 Stochastic Tunneling Method

The stochastic tunneling technique (STUN) [23] was proposed as a generic global optimization method for complex rugged potential energy surfaces (PES). For a number of problems, including the prediction of receptor-ligand complexes for drug development [28, 29], this technique proved superior to competing stochastic optimization methods. The idea behind the method is to flatten the potential energy surface in all regions that lie significantly above the best estimate for the minimal energy (E_0). In STUN the dynamical process explores not the original, but a transformed PES,

$$E_{STUN} = \ln\left(x + \sqrt{x^2 + 1}\right) \tag{2}$$

which dynamically adapts and simplifies during the simulation. Here $x = \gamma(E - E_0)$, where E is the energy, E_0 the best energy found so far. The problem-dependent transformation parameter [23] γ controls the steepness of the transformation (we used $\gamma = 0.5(\text{kcal/mol})^{-1}$). The transformation in equation (2) ameliorates the difficulties associated with the original transformation [23], because $E_{STUN} \propto \ln(E/kT)$ continues to grow slowly for large energies. The ficticious temperature of STUN must be dynamically adjusted in

order to accelerate convergence. STUN works best if its dynamical process alternates between low-temperature "local-search" and high-temperature "tunneling" phases. At at finite temperature the dynamics of the system then becomes diffusive at energies $E \gg E_0$ independent of the relative energy differences of the high-energy conformations involved. On the untransformed PES, STUN thus permits the simulation to "tunnel" through energy barriers of arbitrary height.

3.2 Parallel Tempering

The parallel (or simulated) tempering technique [26, 27] was introduced to overcome difficulties in the evaluation of thermodynamic observables for models with very rugged potential energy surfaces and applied previously in several protein folding studies [30, 31, 32]. Low-temperature simulations on rugged potential energy surfaces are trapped for long times in similar metastable conformations because the energy barriers to structurally potentially competing different conformations are very high. The idea of PT is to perform several concurrent simulations of different replicas of the same system at different temperatures and to exchange replicas (or temperatures) between the simulations i and j with probability:

$$p = min(1, \exp\left(-(\beta_j - \beta_i)(E_i - E_j)\right)), \tag{3}$$

where $\beta_i = 1/k_B T_i$ and E_i are the inverse temperatures and energies of the conformations respectively. The temperature scale for the highest and lowest temperatures is determined by the requirement to efficiently explore the conformational space and to accurately resolve local minima, respectively. For proteins the temperatures must thus fall in a bracket between approximately 2-600 K. As described elsewhere [12] we have used an *adaptive temperature control* for the simulations: Starting with an initial, ordered set of geometrically distributed temperatures we monitored the exchange rate between adjacent temperatures. If the exchange rate between temperature i and i+1 was below 0.5%, then all temperatures above t_i were lowered by 10% of $t_{i+1} - t_i$. If the exchange rate was above 2%, then all temperatures above t_i were increased by the same difference.

To further improve the computational efficiency of PT we also use a *replication step*, in which the best conformation replaces the conformation at the highest temperature every 250,000 simulation steps. This mechanism results in a rapid, large scale exploration of the folding funnel around the best conformation found near the presently best conformation. The parallel tempering method was implemented in our program using the MPI communication library, which is available on most present-day parallel computational architectures with distributed memory. Since the communication effort is low (only the temperatures and energies need to be exchanged) and communication occurs only every few thousand steps, when replica exchange is attempted, this implementation scales very well with the number of processors.

3.3 Basin Hopping Method

An alternate approach to effectively eliminate high energy transition states of the PES is used in the basin hopping technique [24] (BHT), also known as Monte-Carlo with minimization. This method simplifies the original potential energy surface by replacing the energy of each conformation with the energy of a nearby local minimum. This replacement eliminates high energy barriers in the stochastic search that are responsible for the freezing problem in simulated annealing. In many cases the additional minimization effort to find an associated local minimum is more than compensated by the increase of efficiency of the stochastic search on the simplified potential energy surface.

For the protein simulations we replace a single minimization step with a simulated annealing run [33]. Within each SA simulation, new configurations are accepted according to the Metropolis criterion. The temperature is decreased geometrically from its starting to the final value, which must be chosen to be small compared to typical energy differences between competing metastable conformations, to ensure convergence to a local minimum (typically 2-5 K). Depending on the choice of the starting temperature, the SA search can deviate more or less significantly from its starting conformation. The individual relaxation step is thus parameterized completely by the starting (T_S), the a final temperature and the number of steps. We investigate various choices for the numerical parameters of the method, but have always used a geometric cooling schedule.

At the end of one annealing step the new conformation was accepted if its energy difference to the current configuration was no higher than a given threshold energy ε_T, an approach recently proven optimal for certain optimization problems [34]. Throughout this study we use a threshold acceptance criterion of 1 kcal/mol.

3.4 Evolutionary Strategies

While basin hopping and STUN are essentially sequential algorithms, PT provides some degree of inherent parallelism, which suits present day distributed architectures. In order to use even larger numbers of processors, we implemented an evolutionary strategy, in which the computational work is performed by many of independent client-computers that request tasks from a master-computer. The master maintains a list of open tasks comprising the active conformations of the population. Each client performs an increasingly extensive energy minimization on the conformation it is given. When the client returns a new conformation after completing its task, it may replace an existing conformation following a scheme that balances the diversity of the population and the continued energetic improvement of its members. Specifically the client performs either a Monte-Carlo (MC) or a simulated annealing (SA) [33] simulation of specified length on the conformation. Conformations are drawn randomly from the active population. When the client returns a

Figure 1. Overlay of the native(red) and folded (blue) structures of trp-cage protein [35], the HIV accessory protein [13] and the bacterial ribosomal protein L20 [14].

new conformation after completing its task, the result is stored. Additionally the new conformation replaces the energetically worst conformation in the active population, provided its energy is lower than the highest energy of the population and that it differs by at least 3Å backbone root mean square deviation (RMSB) from all members of the active population. If new conformation has an RMSB of less than 3Å to some conformation of the population, it replaces this conformation if its lower in energy.

This approach builds on the strength of the basin hopping technique, which is used for the individual step. Since stochastic optimization methods never locate the global optimum with certainty, several independent simulations must be undertaken to obtain a relative degree of confidence in the convergence of the methods. In the evolutionary approach the progress a single simulation has made towards the optimum is exploited, because the resulting conformation will become a member of the active population. As such it may replace less optimized conformations and speed the convergence of the overall population in comparison to a population of uncorrelated replicas.

4 Results

4.1 The trp-cage protein

Using the PFF01 force field we simulated 20 independent replicas of the 20 amino acid trp-cage protein [36, 6] (pdb code 1L2Y) with a modified versions of the stochastic tunneling method [23, 9]. Six of 25 simulations reached an energy within 1 kcal/mol of the best energy, all of which correctly predicted the native experimental structure of the protein(see Fig 1 (left)). We find a strong correlation between energy and RMSD deviation to the native structure for all simulations. The conformation with the lowest energy had a backbone root mean square deviation of 2.83 Å.

We also folded this protein with the parallel tempering method [12]. We found that the standard approach, which preserves the thermodynamic equilibrium of the simulated populations, did not reach very low energies even for

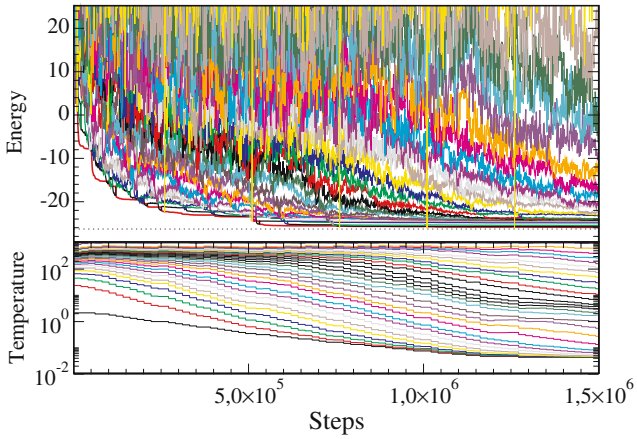

Figure 2. Energies (upper panel) and temperatures (lower panel) of the 30 replica modified parallel tempering simulation of the trp-cage protein reported in the text. The dotted line in the upper panel corresponds to the estimate of the global optimum of the free energy (obtained independently). The lower panel demonstrates a rapid equilibration of the temperatures during the simulation. The upper panel demonstrates the convergence of the energy and the rapid exchange of information between the different replicas as discussed in the text.

the low-temperature replicas. We believe that the reason for this convergence failure was the insufficient exchange probability between replicas at different temperatures. We therefore introduced the adaptive temperature control described in the methods section. Figure (2) shows the energies and corresponding temperatures for a simulation using thirty replicas. The temperature adjustment scheme results in a temperature distribution that permits frequent exchange of replicas and significantly speeds convergence. The best final structure associated with the lowest temperature in the simulation with 30 replicas had a RMSB deviation of 2.01 Å. We found convergence of the method using eight to thirty replicas. However, a minimal number of at least eight replicas appears to be required to fold the protein, for lower replica numbers it appears that even the adaptive temperature scheme fails to generate rapid replica exchange while spanning both high and low temperatures required for the speedy exploration of the free energy surface and the refinement of local minima respectively.

Finally we have folded the trp-cage protein with the basin hopping technique. In comparison with the stochastic tunneling method we noted that care must be taken with the parameterization of the basin hopping technique. First of all, very high starting temperatures above 600 K are required to permit a sufficient exploration of the free energy surface. This was also observed in the parallel tempering simulations (see Figure (2) bottom panel). As in PT, the lowest temperature had to be chosen in the range of 2-6 K to ensure

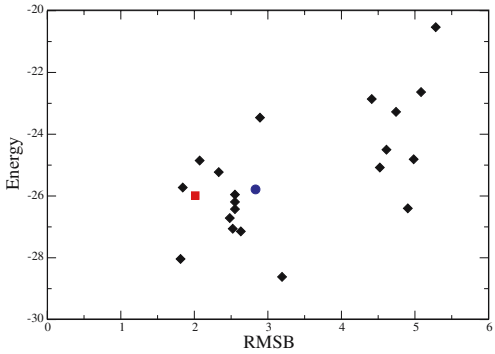

Figure 3. Energy vs. RMSB plot for the final energies of the twenty basin hopping simulations described in the text (diamonds). For comparison we also indicate the best energy result for the STUN method (circle) and for the thirty processor PT simulation (square).

that local minima are resolved well. In the stochastic tunneling method, the nonlinear transformation of the energy permits large scale relaxations through thermodynamically forbidden regions, in basin hopping this effect can only be achieved by raising the temperature to unphysical values. We cannot rule out the possibility that basin hopping simulations with low starting temperatures would converge eventually, however, it appears that such an approach would not be computationally competitive. Furthermore, we noted that the convergence of the basin hopping method is improved dramatically when the length of the relaxation run is moderately increased with the number of the basin hopping cycle. When we compared simulations comprised of basin hopping steps of constant length to simulations where the length increased with the square root of the cycle number, we found much lower energies for the latter after investing the same total number of function evaluations in each run.

Using the basin hopping method with a starting temperature of $T_s = 800K$ and a final temperature of $T_f = 3K$ the lowest six of 20 simulations converged to the native structure. A total of 12 of these simulations approached the native conformation as its estimate of the optimum. The energies and RMSB deviations of all simulations are shown in Figure (3). The plot indicates the existence of a set of structures with 2-3 Å RMSB deviation, which may correspond to the folding funnel, and a competing metastable conformation with about 5 Å RMSB. While all methods correctly identify the folding funnel, the basin hopping approach results in the lowest energies. Note that the second best simulation has an RMSB of only 1.8Å to the native conformation and loses in energy with less the 0.5 kcal/mol.

Name	RMSB	Energy	Secondary Structure Content
N	0.00		ccHHHHHHHHHclclbHHHHHHHHHHclcccHHHHHHHHHc
D01	2.34	-119.54	cHHHHHHHHHHHlclbcHHHHHHHHHHHHbHHHHHHHHHHc
D02	2.41	-117.52	cHHHHHHHHHHHlclbHHHHHHHHHHHHHbHHHHHHHHHHc
D03	2.76	-116.25	cHHHHHHHHHHHlclbHHHHHHHHHHHHHbHHHHHHHHHHc
D04	2.40	-115.85	cHHHHHHHHHHHlbbHHHHHHHHHHHHHbHHHHHHHHHHc
D05	2.43	-114.67	cHHHHHHHHHHHlclbHHHHHHHHHHcbHHHHHHHHHHc
D06	6.48	-114.06	cHHHHHHHHHHcccbHHHHHHHHHHHHbHHHHHHHHHHc
D07	2.57	-113.65	cHHHHHHHHHHHlbbcHHHHHHHHHHHHbHHHHHHHHHHc
D08	4.61	-107.72	cHHHHHHHHcclccHHHHHHHHHHHHlclHHHHHHHHc
D09	4.14	-106.29	cHHHHHHHHHHcbcbHHHHHHHHbblcHHHHHHHHHHc
D10	5.92	-103.88	cHHHHHHHHHHlcHHHHHHHHbcbcclbHHHHHHHHHc

Table 1. Energies (in kcal/mol) of the 10 lowest energy decoys obtained in the basin hopping simulations of the HIV accessory protein. The table shows the backbone RMS deviation to the NMR structure and secondary structure content. The first row designates the secondary structure content of the NMR structure.

4.2 The HIV accessory protein

Encouraged by this result, we applied a the modified basin hopping or Monte-Carlo with minimization (MCM) strategy [8, 25] to fold the structurally conserved 40-amino acid headpiece of the HIV accessory protein [10]. We performed twenty independent simulations and found the lowest five to converge to the native structure (see tbldecoyhiv) [14]. The first non-native decoy appears in position six, with an energy deviation of 5 kcal/mol and a significant RMSB deviation. The table demonstrates that all low-energy structures have essentially the same secondary structure, i.e. position and length of the helices are always correctly predicted, even if the protein did not fold correctly.

The good agreement between the folded and the experimental structure is also evident from Figure (1)(center), which shows the secondary structure alignment of the native and the folded conformations. The good physical alignment of the helices illustrates the importance of hydrophobic contacts to correctly fold this protein. An independent measure to assess the quality of these contacts is to compare the C_β-C_β distances (which correspond to the NOE constraints of the NMR experiments that determine tertiary structure) in the folded structure to those of the native structure. We found that 66 % (80 %) of the C_β-C_β distance distances agree to within one (1.5) standard deviations of the experimental resolution.

We also performed a simulation of the HIV accessory protein using the adapted parallel tempering method [13]. We used 20 processors of an INTEL XEON PC cluster and ran the simulation for a total of 30×10^6 energy evaluations for each configuration, which corresponds to approximately 500 CPU hours on an 2.4 GHz INTEL XEON processor. All simulations were started

with random conformations at high temperatures to allow for rapid, unbiased relaxation of the structures and the temperature distribution. The final conformation with the lowest energy/temperature had converged to within 1.23 / 2.46 Å backbone root mean square (RMSB) deviation to the best known decoy / NMR structure of the HIV accessory protein. The overlay of the experimental and the converged structure (see Figure (1)) demonstrates the good agreement between the conformations, the difference in NOE constraints demonstrates that not only short range, but also long range distances are correctly predicted. Considering the ensemble of final conformations, we find many structures closely resembling the native conformation. The RMSB deviations of the next four lowest conformations (all within 1.5 kcal/mol of the minimal energy of XXX) have RMSB deviations of 3.14/2.23/3.78/3.00 Å respectively to the native decoy.

4.3 The bacterial ribosomal protein L20

In the course of the simulations on the HIV accessory protein we explored methods to share information between the independent basin hopping simulations in order to improve the overall convergence. For the 60 amino acid bacterial ribosomal protein L20 (pdb-code 1GYZ) we thus experimented with the evolutionary technique described in the methods section. Starting from a seed population of random structures we performed the folding simulation in three phases: (1) generation of starting structures of the population, (2) evolutionary improvement of the population and (3) refinement of the best resulting structures to ensure convergence.

In phase (1) we performed high-temperature (500K) Monte Carlo simulations of 50,000 steps each. In these runs we reduced the strength of the solvent interactions (V_S) by 20% to facilitate the rapid formation of secondary structure. It has been argued that hydrophobic collapse competes with secondary structure formation in protein folding. In the collapsed conformational ensemble large scale conformational changes, such as those required for secondary structure formation, occur only rarely. The goal of this simulation phase was the generation of a wide variety of competitive starting conformations for further refinement.

At the end of this simulation we had gathered in excess of 17000 distinct decoys that were ranked according to their total energy as well as according to the individual energy terms of the force field (V_S,V_{LJ},V_{HB},$V_C(sidechain)$ and $V_C(backbone)$). For each criterion we selected the best 50 conformations and eliminated duplicates to arrive at a population of 266 starting structures for the phase (2) of the procedure. This population was relaxed in 14000 SA simulations as described in the methods section. At the end of this step we selected the 50 conformations best in total energy for further refinement. In phase (3) we performed 5500 SA simulations on this subpopulation. The length of the individual relaxation simulations was gradually increased from 10^5 steps per simulation to 2.3×10^6.

Name	Energy	RMSB	3-state secondary structure
1GYZ		0.01	ccHHHHHHHcccccccHHHHHHHHHHcccccccccHHHHHcHHHHHHHHHHHHHcccc
D01	-167.87	4.64	cHHHHHHHHHHHcccHHHHHHHHHHHcccccccccHHHHHcHHHHHHHHHHHHHHHcc
D02	-166.15	8.25	ccHHHHHHHHHHHcccHHHHHHHHHHHcccccccccHHHHHcHHHHHHHHHHHHHHHcc
D03	-165.91	4.41	cHHHHHHHHHHHcccHHHHHHHHHHHcccccccccccHHHcHHHHHHHHHHHHHHHcc
D04	-164.11	5.54	ccHHHHHHHHHHHcccHHHHHHHHHHHcccccccccHHHHHcHHHHHHHHHHHHHHHcc
D05	-163.99	3.79	cHHHHHHHHHHHcccHHHHHHHHHHHcccccccccHHHHHcHHHHHHHHHHHHHHHcc
D06	-163.93	4.04	cHHHHHHHHHHHcccHHHHHHHHHHHcccccccccccccccHHHHHHHHHHHHHHHcc
D07	-163.45	8.52	ccccHHHHHHHHHcccHHHHHHHHHHHcccccccccHHHHHcHHHHHHHHHHHHHHHcc
D08	-163.20	4.37	cHHHHHHHHHHHcccHHHHHHHHHHHcccccccccHHHHHcHHHHHHHHHHHHHHHcc
D09	-162.67	5.55	cHHHHHHHHHHHcccHHHHHHHHHHHcccccccccHHHHccHHHHHHHHHHHHHHHcc
D10	-162.52	3.78	cHHHHHHHHHHHcccHHHHHHHHHHHcccccccccccccccHHHHHHHHHHHHHHHccc

Table 2. Energies (in kcal/mol) of the 10 lowest energy decoys of the final population with backbone RMS deviation to the NMR structure and secondary structure content. The first row designates the secondary structure content of the NMR structure.. The letters H and c indicate amino acids in Helix and coil structure respectively. Green letters indicate correct, red incorrect secondary structure.

The energies and structural details of the best ten resulting conformations are summarized in Table (2). Again the best conformation had approached the native conformation to about 4.6 Å RMSB deviation. In total six of the lowest ten conformations approach the native structure, while four others misfolded. Note that the selection criterion for the active population (see methods section) precludes the occurrence of the same configuration to within 3 Å RMSB, this dominance of near native conformations of the total ensemble is particularly encouraging.

In order to quantify the overall improvement of native content during the simulation, we defined the native content of the simulated ensemble as a weighted average of the deviations of the population and the native conformation: For a population of size N we add 100(N-R+1)/N for each near-native decoy (RMSB less than 4Å) ranked at position R by energy to the total native score of this population. A score of 100 thus corresponds to a native decoy placed at the top position, while a near native decoy at the very bottom contributes just unity. Non-native conformations contribute nothing. Using this measure the final population contains in excess of 20% of near native conformations, its native score exceeds 800, increasing sixty-fold during the simulation phases (2) and (3).

5 Conclusion

Since the native structure dominates the low-energy conformations arising in all of these simulation, our results demonstrate the feasibility of all-atom

protein tertiary structure prediction for three different proteins ranging from 20-60 amino acids in length with a variety of different optimization methods. The free energy approach thus emerges as viable trade-off between predictivity and computational feasibility. While sacrificing the folding dynamics, a reliable prediction of its terminus, the native conformation — which is central to most biological questions — can be achieved.

The computational advantage of the optimization approach stems from the possibility to visit unphysical intermediate conformations with high energy during the search. This goal is realized with different mechanism in all of the employed stochastic optimization methods. In the stochastic tunneling method the nonlinear transformation of the PES permits the dynamical process to traverse arbitrarily high energy barriers at low temperatures, in basin hopping and parallel tempering, simulation phases at very high temperatures accomplish the same objective.

Our results indicate that the simple basin hopping method is very efficient in the determination of the global optimum of the free energy surface of realistic all-atom protein models. It is encouraging that the same structure was also found for the trp-cage protein using the parallel tempering and the stochastic tunneling method and also for the HIV accessory protein using the parallel tempering method. This finding indicates that the result of the folding approach is not an artefact of the optimization strategy. In direct comparison, however, we find that the basin hopping technique gave the lowest energies. Since it is virtually parameter free and very simple to implement it emerges as a natural work-horse for our approach.

Its one important disadvantage is the fact that different basin hopping simulations are completely independent of one another. Because the underlying optimization problem in all-atom protein folding is very difficult and the free energy surface is very rugged, several simulations must be undertaken to obtain a relative degree of confidence in the convergence of the approach. From this perspective it is desirable to design an optimization method in which different members of the simulated population can learn from one another. In the evolutionary approach we have explored here is one particularly simple scheme to ensure that the total computational effort is concentrated on the best conformations that arise at intermediate stages of the simulations. So far it lead to the folding of the largest protein at all-atom resolution, but much work remains to be done to optimize this approach.

6 Discussion

This review indicates that all-atom protein structure prediction with stochastic optimization methods becomes feasible with present-day computational resources. The fact that three proteins were reproducibly folded with different optimization methods to near-native conformation increases the confidence in the parameterization of our all-atom protein force field PFF01. The

presently available evidence indicates that the comparatively straightforward basin hopping routine is a good work horse to evolve individual conformations. The resolution of several independent basin hopping simulations may be enhanced by the use of evolutionary algorithms such as the one used for the bacterial ribosomal protein L20 . We note that the master-client model for this strategy is asynchronous and can be implemented outside the simulation program using the standard TCP/IP, FTP or HTTP protocols. Using generic libraries, such as MPI, it can also be easily implemented on MPP architectures. Since the amount of information that needs to be exchanged is very small, while the effort in a single basin hopping cycle is substantial, there is virtually no loss in an asynchronous parallel implementation. This makes the evolutionary approach investigated here suitable for present day GRID architectures. While the present results demonstrate proof of principle, much work, remains to be done to arrive at an optimal strategy.

Protein structure prediction with stochastic optimization methods requires two separate key ingredients: an accurate force field and efficient optimization techniques. One cannot overemphasize the importance of the interplay of optimization methods and force field validation. Rational force field development mandates the ability to generate decoys that fully explore competing low-energy conformations to the native state. The success of different optimization strategies depends strongly on the structure of the potential energy surface. As a result the development of efficient optimization techniques for all-atom protein structure prediction depends on the availability of a force field that stabilizes native conformations of proteins with appreciable hydrophobic cores. For helical proteins the bottleneck in *ab-initio* all-atom structure prediction now lies in the development of optimization strategies that significantly increase the system size and increase the reliability of the predictions. Based on the results reviewed here it is sensible investigate improvements of the evolutionary techniques based on the basin hopping method for this purpose.

The application of this methodology to a wide range of proteins will generate large decoy sets of metastable conformations that compete with the native structure of the protein. These decoy sets may in turn be used to improve the parameterization of the force field. By its very nature, the approximation of the free energy of the system mandates the use of implicit solvent models. This implies that interactions with the solvent and intramolecular electrostatic interactions must be parameterized in accurate, yet efficient effective models. Since both effects are highly nontrivial, the free-energy approach can only approximate, but not duplicate the results of all-atom explicit water simulations. The present evidence indicates that the native conformation is reproduced to 3-4 Å resolution with PFF01, but the results of the free energy approach could be refined in all-atom simulations that start from a set of low-energy decoys.

Acknowledgements

We thank the Fond der Chemischen Industrie, the BMBF, the Deutsche Forschungsgemeinschaft (grants WE 1863/10-2,WE 1863/14-1) and the Kurt Eberhard Bode Stiftung for financial support. Part of the simulations were performed at the KIST teraflop cluster.

References

1. D. Baker and A. Sali. Protein structure prediction and structural genomics. *Science*, 294:93–96, 2001.
2. J. Schonbrunn, W. J. Wedemeyer, and D. Baker. Protein structure prediction in 2002. *Curr. Op. Struc. Biol.*, 12:348–352, 2002.
3. N. Go and H. A. Scheraga. On the use of classical statistical mechanics in the treatment of polymer chain conformation. *Macromolecules*, 9:535–542, 1976.
4. P. Ulrich, W. Scott, W. F. van Gunsteren, and A. E. Torda. Protein structure prediction force fields: Paramterization with quasi newtonian dynamics. *Proteins, SF&G*, 27:367–384, 1997.
5. C. D. Snow, H. Nguyen, V. S. Pande, and M. Gruebele. Absolute comparison of simulated and experimental protein folding dynamics. *Nature*, 420:102–106, 2002.
6. C. Simmerling, B. Strockbine, and A. Roitberg. All-atom strucutre prediction and folding simulations of a stable protein. *J. Am. Chem. Soc.*, 124:11258–11259, 2002.
7. C. B. Anfinsen. Principles that govern the folding of protein chains. *Science*, 181:223–230, 1973.
8. Z. Li and H. A. Scheraga. Monte carlo minimization approach to the multiple minima problem in protein folding. *Proc. Nat. Acad. Sci. U.S.A.*, 84:6611–6615, 1987.
9. A. Schug, T. Herges, and W. Wenzel. Reproducible protein folding with the stochastisc tunneling method. *Phys. Rev. Letters*, 91:158102, 2003.
10. T. Herges and W. Wenzel. Reproducible in-silico folding of a three-helix protein in a transferable all-atom force field. Physical Review Letters (in press), http://www.arXiv.org: physics/0310146, 2004.
11. T. Herges and W. Wenzel. An All-Atom Force Field for Tertiary Structure Prediction of Helical Proteins. *Biophys. J.*, 87(5):3100–3109, 2004.
12. A. Schug, T. Herges, and W. Wenzel. All-atom folding of the trp-cage protein in an all-atom force field. *Europhyics Lett.*, 67:307–313, 2004.
13. A. Schug, T. Herges, and W. Wenzel. All-atom folding of the three-helix hiv accessory protein with an adaptive parallel tempering method. *Proteins* (in press), 2004.
14. A. Schug, T. Herges, and W. Wenzel. Reproducible folding of a four helix protein in an all-atom force field. J. Am. Chem. Soc. (in press), 2004.
15. H. Gouda, H. Torigoe, A. Saito, M. Sato, Y. Arata, and I. Shimanda. Three-dimensional solution structure of the b domain of staphylococcal protein a: comparisons of the solution and crystal structures. *Biochemistry*, 40:9665–9672, 1992.

16. U. Mayor, N. R. Guydosh, C. M. Johnson, J. G. Grossmann, S. Sato, G. S. Jas, S. M. V. Freund, D. O. V. Alonso, V. Daggett, and A. R. Fersht. The complete folding pathway of a protein from nanoseconds to micorseconds. *Nature*, 421:863–867, 2003.
17. T. Herges, H. Merlitz, and W. Wenzel. Stochastic optimisation methods for biomolecular structure prediction. *J. Ass. Lab. Autom.*, 7:98–104, 2002.
18. R. Abagyan and M. Totrov. Biased probability monte carlo conformation searches and electrostatic calculations for peptides and proteins. *J. Molec. Biol.*, 235:983–1002, 1994.
19. T. Herges, A. Schug, B. Burghardt, and W. Wenzel. Exploration of the free energy surface of a three helix peptide with stochastic optimization methods. *Intl. J. Quant. Chem.*, 99:854–893, 2004.
20. F. Avbelj and J. Moult. Role of electrostatic screening in determining protein main chain conformational preferences. *Biochemistry*, 34:755–764, 1995.
21. D. Eisenberg and A. D. McLachlan. Solvation energy in protein folding and binding. *Nature*, 319:199–203, 1986.
22. K. A. Sharp, A. Nicholls, R. Friedman, and B. Honig. Extracting hydrophobic free energies from experimental data:relationship to protein folding and theoretical models. *Biochemistry*, 30:9686–9697, 1991.
23. W. Wenzel and K. Hamacher. Stochastic tunneling approach for global optimization of complex potential energy landscapes. *Phys. Rev. Lett.*, 82:3003, 1999.
24. A. Nayeem, J. Vila, and H. A. Scheraga. A comparative study of the simulated-annealing and monte carlo-with-minimization approaches to the minimum-energy structures of polypeptides: [met]-enkephalin. *J. Comp. Chem.*, 12(5):594–605, 1991.
25. J. P. K. Doye and D. Wales. On potential energy surfaces and relaxation to the global minimum. *J. Chem. Phys.*, 105:8428, 1996.
26. G. J. Geyer. *Stat. Sci.*, 7:437, 1992.
27. K. Hukushima and K. Nemoto. Exchange monte carlo method and application to spin glass simulations. *Journal of the Physical Society of Japan*, 65:1604–1608, 1996.
28. H. Merlitz and W. Wenzel. Comparison of stochastic optimization methods forreceptor-ligand docking. *Chem. Phys. Lett.*, 362:271, 2002.
29. H. Merlitz, B. Burghardt, and W. Wenzel. Application of the stochastic tunneling method to high throughput screening. *Chem. Phys. Lett.*, 370:68, 2003.
30. U. H. E. Hansmann and Y. Okamoto. Numerical comparison of three recently proposed algorithms in the protein folding problem. *J. Comput. Chem*, 18:920, 1997.
31. U. H. E. Hansmann. *Eur. Phys. J. B*, 12:607, 1999.
32. C. Y. Lin, C. K. Hu, and U. H. Hansmann. Parallel tempering simulations of hp-36. *Proteins*, 53:436–445, 2003.
33. S. Kirkpatrick, C. D. Gelatt, and M. P. Vecchi. Optimization by simulated annealing. *Science*, 220:671–680, 1983.
34. J. Schneider, I. Morgenstern, and J. M. Singer. Bouncing towards the optimum: Improving the results of monte carlo optimisation algorithms. *Phys. Rev. E*, 58:5085–5095, 1998.
35. A. Schug, A. Verma, T. Herges, and W. Wenzel. Comparison of stochastic optimization methods for all-atom folding of the trp-cage protein. submitted to *Proteins,* 2005.

36. J. W. Neidigh, R. M. Fesinmeyer, and N. H. Anderson. Designing a 20-residue protein. *Nature Struct. Biol.*, 9:425–430, 2002.

INDEX

Progress in Theoretical Chemistry and Physics

1. S. Durand-Vidal, J.-P. Simonin and P. Turq: *Electrolytes at Interfaces.* 2000 ISBN 0-7923-5922-4
2. A. Hernandez-Laguna, J. Maruani, R. McWeeny and S. Wilson (eds.): *Quantum Systems in Chemistry and Physics.* Volume 1: Basic Problems and Model Systems, Granada, Spain, 1997. 2000 ISBN 0-7923-5969-0; Set 0-7923-5971-2
3. A. Hernandez-Laguna, J. Maruani, R. McWeeny and S. Wilson (eds.): *Quantum Systems in Chemistry and Physics.* Volume 2: Advanced Problems and Complex Systems, Granada, Spain, 1998. 2000 ISBN 0-7923-5970-4; Set 0-7923-5971-2
4. J.S. Avery: *Hyperspherical Harmonics and Generalized Sturmians.* 1999 ISBN 0-7923-6087-7
5. S.D. Schwartz (ed.): *Theoretical Methods in Condensed Phase Chemistry.* 2000 ISBN 0-7923-6687-5
6. J. Maruani, C. Minot, R. McWeeny, Y.G. Smeyers and S. Wilson (eds.): *New Trends in Quantum Systems in Chemistry and Physics.* Volume 1: Basic Problems and Model Systems. 2001 ISBN 0-7923-6708-1; Set: 0-7923-6710-3
7. J. Maruani, C. Minot, R. McWeeny, Y.G. Smeyers and S. Wilson (eds.): *New Trends in Quantum Systems in Chemistry and Physics.* Volume 2: Advanced Problems and Complex Systems. 2001 ISBN 0-7923-6709-X; Set: 0-7923-6710-3
8. M.A. Chaer Nascimento: *Theoretical Aspects of Heterogeneous Catalysis*. 2001 ISBN 1-4020-0127-4
9. W. Schweizer: *Numerical Quantum Dynamics*. 2001 ISBN 1-4020-0215-7
10. A. Lund and M. Shiotani (eds.): *EPR of Free Radicals in Solids*. Trends in Methods and Applications. 2003 ISBN 1-4020-1249-7
11. U. Kaldor and S. Wilson (eds.): *Theoretical Chemistry and Physics of Heavy and Superheavy Elements*. 2003 ISBN 1-4020-1371-X
12. J. Maruani, R. Lefebvre and E. Brändas (eds.): *Advanced Topics in Theoretical Chemical Physics*. 2003 ISBN 1-4020-1564-X
13. J. Rychlewski (ed.): *Explicitly Correlated Wave Functions in Chemistry and Physics*. Theory and Applications. 2003 ISBN 1-4020-1674-3
14. N.I. Gidopoulos and S. Wilson (eds.): *The Fundamentals of Electron Density, Density Matrix and Density Functional Theory in Atoms, Molecules and the Solid State*. 2003 ISBN 1-4020-1793-6
15. J.-P. Julien, J. Maruani, D. Mayou, S. Wilson and G. Delgado-Barrio (eds.) *Recent Advances in the Theory of Chemical and Physical Systems*. 2006 ISBN 1-4020-4527-1